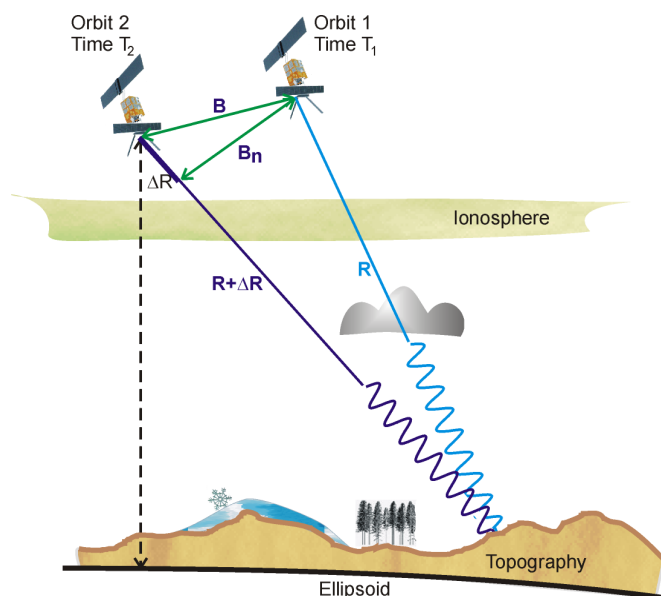


# THE USE OF SYNTHETIC APERTURE RADAR (SAR) INTERFEROMETRY TO RETRIEVE BIO- AND GEO-PHYSICAL VARIABLES

## FINAL REPORT

EUROPEAN SPACE AGENCY STUDY CONTRACT REPORT  
UNDER ESA CONTRACT No 16366/02/NL/MM



### PREPARED BY

Thomas NAGLER and Helmut ROTT

ENVEO (Prime Contractor), Exlgasse 39, A-6020 Innsbruck, AUSTRIA  
<http://www.enveo.at>

Ramon HANSSEN and Dmitri MOISSEEV

Delft University of Technology, Department of Geodesy, Delft, THE NETHERLANDS

Nico ADAM, Michael EINEDER and Bert KAMPES

Remote Sensing Technology Institute, German Aerospace Center, Wessling, GERMANY

Irena HAJNSEK and Konstantinos P. PAPATHANASSIOU

Microwaves and Radar Institute, German Aerospace Center, Wessling, GERMANY

Shane R. CLOUDE

AEL-Consultants, Cuper Fife, Scotland, UNITED KINGDOM

DATE: 20 February 2004



*The work described in this report was done under ESA contract. Responsibility for the contents resides in the author or organisation that prepared it.*





<b>ESA STUDY CONTRACT REPORT</b>			
ESA CONTRACT NO: 16366/02/NL/MM	SUBJECT: The Use of Synthetic Aperture Radar (SAR) Interferometry to Retrieve Bio- and Geo-Physical Variables		CONTRACTOR: ENVEO
ESA CR ( )No:	STAR CODE:	No OF VOLUMES: 1 THIS IS VOLUME NO: 1	CONTRACTOR'S REF: Final Report
<p>The report contains the detailed description of the work carried out in the study, aimed at identifying and developing new possibilities for retrieving bio- and geo-physical variables for land applications from interferometric SAR (InSAR) data. Based on literature review and theory various variables were identified as candidates for new InSAR algorithms for atmosphere, snow &amp; ice, and vegetation. The following parameters were selected for retrieval development: (i) atmospheric water vapour, (ii) snow water equivalent (SWE, the mass of snow on ground), and (iii) forest height. For each of these parameters theoretical modelling of radar wave propagation was carried out, test data sets were analysed and recommendations for further work and algorithm implementation were elaborated.</p> <p>PART A reports on theoretical work and data analysis for retrieving physical properties of the atmosphere, in particular columnar water vapour content. Emphasis is given on methods for resolving the acquisition ambiguity (isolating the atmospheric phase term for single dates) and for coherence optimisation. Test cases, based on ERS SAR, are presented for retrieving and interpreting the atmospheric phase signal in different climate zones. In PART B theory and test cases for SWE retrieval from repeat pass SAR data are presented, the effects of snow cover changes on coherence are analysed, and test cases for SWE retrievals are shown for ERS SAR data and for L-band airborne E-SAR data, suggesting clear preference for L-band as data source. PART C reports on theoretical modelling as basis for interpretation of polarimetric SAR signals of forests, a method to retrieve forest height from dual-polarized interferometric data (Light-Pol InSAR) is presented, examples for forest height estimation from single-pass L-band airborne SAR in dual-pol and quad-pol configuration are shown for various test sites, and possibilities and limitations of various polarisations and radar frequencies are discussed. PART D provides information on InSAR data processing issues in support of SWE and water vapour retrievals, with emphasis on man made targets.</p>			
The work described in this report was done under ESA Contract. Responsibility for the contents resides in the author or organisation that prepared it.			
AUTHORS: Thomas Nagler, Helmut Rott (ENVEO, Innsbruck, AT), Ramon Hanssen, Dmitri Moiseev (DEOS, Delft, NL), Irena Hajnsek, Konstantinos P. Papathanassiou (HR-DLR, Wessling, D), Shane R. Cloude (AELc, Scotland, UK), Nico Adam, Michael Eineder, Bert Kampes (IMF-DLR, Wessling)			
ESA STUDY MANAGER: N. Flourey (TOS-EEP)		ESA BUDGET HEADING: 060 - GSP	

*Amendment Record:*

15 December 2003	First Draft Version
20 February 2004	Final Version

---

## TABLE OF CONTENTS

### STUDY OVERVIEW

PART A - InSAR retrieval of atmospheric parameters

PART B - InSAR retrieval of snow and ice parameters

PART C - InSAR retrieval of vegetation parameters

PART D - Literature Review on InSAR methods for manmade targets

*This page is intentionally left blank.*

## STUDY OVERVIEW

The objective of the study for estimating bio- and geophysical parameters from SAR interferometry was to define new possibilities for retrieving bio- and geo-physical variables for land applications from interferometric SAR data and to develop and test prototype retrieval algorithms for these variables. The development of retrieval algorithms and application tests was carried out for geophysical variables of the following components of the global environmental system

- atmosphere
- snow and ice
- vegetation

Additionally the state of the art of InSAR methods for man-made targets was reviewed.

The report is organized in four parts (A to D), dedicated to InSAR retrievals of atmospheric parameters (*Part A*), of snow and ice parameters (*Part B*), vegetation / bare soil parameters (*Part C*) and review on InSAR retrievals from made targets (*Part D*). In the following sections an overview of the performed work is given and conclusions are drawn.

### InSAR retrieval of atmospheric parameters

In Part A of this study we focused on the estimation of atmospheric parameters. Atmospheric signal has been observed frequently in SAR interferograms, but is usually treated as a source of noise. However, it was recognized that of the many interferograms acquired during the ERS and Envisat missions, most of them do not have significant deformation, while topography is relatively well-known, making the atmospheric signal one of the most abundant data sources in the archives. The parameters of interest are all derived from their contributions to the refractive index, which is ionospheric electron density, pressure, temperature, relative water vapour pressure, and liquid water (clouds and precipitation). It was recognized that ionospheric electron density and pressure are long wavelength signals (relative to a 100x100 km interferogram) and that they may result in trends in the interferograms that cannot be distinguished from orbit errors. Therefore, by eliminating trends, the influence of these parameters is eliminated as well, for C-band radar. Of the remaining parameters, water vapour is clearly the most dominant and the most interesting parameter for estimation due to its significance for pin-point weather forecasting and global climate change, while the influence of temperature and liquid water needs to be estimated as well. Nevertheless, in terms of parameter estimation the most important intermediate parameter is the estimation of the atmospheric phase screen per acquisition, and not per interferogram. We developed different retrieval

algorithms to resolve this acquisition ambiguity and showed that the estimation of derived parameters such as water vapour is relatively straightforward.

The retrieval algorithms are based on time series processing of interferograms. Two main ideas are worked out in detail, the single-master stack and the cascade. The single-master stack has the most optimal APS ambiguity resolution properties, but is only very limitedly applicable due to the conditions on long-time coherence over large areas and baseline dispersion. A special case of the single-master stack is the permanent scatterer processing, which relaxes the conditions for spatially contiguous coherence preservation and baseline dispersion. Atmospheric contributions are estimated, but it was shown that the point noise on the PS observations significantly disturbs the APS estimation, to the effect that quantitative interpretation is not possible anymore. In fact, the prior information (on spatial smoothness) used to derive the part of the residual signal related to atmosphere via kriging algorithms is steering the solution. Therefore, the derived signal is forced considerably by those assumptions, making atmospheric phase screen estimation from a PS analysis rather unreliable. The second approach, cascade processing, is worked out in three alternative algorithms. The results of the single-master APS estimation are satisfying and interpretable, although the rank-deficiency in the problem causes 'leaking' of atmospheric signal between the estimations. Nevertheless, it is possible to estimate the APS and derive vertically integrated water vapour content from the delay signal.

For future applications of the technique, significant improvements can be expected using satellite observations in the L-band range, with a higher repeat-interval. In this context, mission proposals such as TerraSAR-L, currently under investigation, are supported.

## **InSAR retrieval of snow and ice parameters**

The state of the art of methods and applications of InSAR for snow and ice applications are briefly reviewed in Part B. This includes mapping and monitoring topography and motion of glaciers and ice sheets. Apart from these classical InSAR applications, three snow and ice variables, diagenetic snow / ice facies (related to penetration depth of radar waves), wet snow extent, and snow mass are identified for possible development of InSAR retrieval techniques. The status of knowledge on InSAR signals and possible methods for deriving these variables are discussed and the relevant factors for selecting a variable for algorithm development are identified. Assigning priority to need and innovation the snow water equivalent (the mass of snow on ground) was identified as the parameter with priority for algorithm development.

In chapter B.3 the theoretical basis for the development of a retrieval algorithm for mapping the snow water equivalent of dry snow is elaborated. The interaction of radar waves with snow covered terrain is modelled for various snow conditions and radar frequencies, in order to quantify the main factors for backscattering in dependence of target properties and to carry out a sensitivity study. The target coherence is studied for various snow properties. A model was developed to investigate decorrelation phenomena due to snow fall including surface, volume, and temporal decorrelation.

The physical basis and a concept for the SWE retrieval procedure is described and the magnitude of the main errors, including orbit accuracy, atmospheric variation, phase noise, and topographic phase removal, is estimated. For large areas the orbit inaccuracy is the main error source, while typical variations of the winter atmosphere are of little relevance for SWE retrieval. A prototype of the SWE retrieval algorithm using InSAR data is presented and the processing steps are described.

Test cases using different types of SAR data were analysed; ERS-1 SAR data of Phase-D with 3 day repeat cycle of an mountainous area in Eastern Austria, ERS 1/2 SAR Tandem data of high alpine areas to investigate the influence of wind drift on coherence and SWE retrieval, and a data set of 3 airborne E-SAR L-band fully polarimetric images. The InSAR based SWE maps are compared and locally validated using records of precipitation, snow height and air temperature from meteorological and climate stations, but the validation is limited because ground based information is available only on a very sparse grid. The airborne ESAR data at L-Band indicate good capability for retrieval of snow induced phase shifts and estimation of SWE. To fully assess and validate the capability of InSAR for SWE retrieval, the spatial sampling of standard snow measurements is too low. Dedicated experiments are still needed for accurate assessment of the applicability and accuracy of this method.

From the analysis of the test cases and modelling results the following conclusion can be drawn:

- The interferometric phase shift of repeat pass SAR data provides a physically based measure for mapping the spatial distribution of SWE.
- Temporal decorrelation due to differential phase delays at sub-pixel scale during snow fall and wind drift is the main limiting factor. In case of substantial snow fall, at C-Band coherence is often lost over large areas and little information can be retrieved, even over time spans of one or a few days only (ERS SAR Tandem data, ERS-1 Phase D 3-days repeat cycle). L-band is less sensitive to temporal decorrelation, but a large scale verification over rugged terrain is still missing.
- L-band is preferable for interferometric SWE retrievals because of better coherence and larger measurement range ( $2\pi$  ambiguity) than shorter wavelengths.
- Dedicated experiments with co-located spatially detailed field measurements are needed to further assess the capability of L-Band interferometry for SWE retrieval in mountainous terrain, because the standard snow measurement network is not sufficient for validation.

## **InSAR retrieval of vegetation parameters**

The estimation of forest height from fully polarimetric single baseline interferometric data (Pol-InSAR) is one of the big challenges in quantitative parameter estimation from SAR data (Part C). However, technical and/or mission operation constraints may favour a dual-polarimetric sensor design/operation instead of a fully-polarimetric one. Responding to this, the question about the applicability of a dual-polarimetric

interferometric acquisition mode (Lite-PolInSAR) for the estimation forest height is faced in the frame of this study.

In order to define the relevant framework, first a review of the development and current status of Pol-InSAR techniques, the inversion approaches, as well as their performance and validity/robustness has been performed. In agreement with ESA forest height has been selected as the parameter of interest and the appropriate test sites have been introduced. A validated - in terms of Pol-InSAR measurements- direct EM model for forest vegetation has been introduced and used first to validate the conventional two-layer (a random volume over a ground - RVoG) inversion model. Further, the direct model has been deployed to evaluate the behaviour of realistic forest conditions and - in combination with the inversion model - to analyse the obtained inversion performance.

Based on the previous steps, an inversion scheme for a Lite-PolInSAR observation scenario (i.e. dual-pol single-pass single-baseline) has been developed and its performance has been first analysed and validated against simulated data obtained from the direct model. Different polarisation pairs have been compared in order to conclude about the optimum dual-pol configuration. Finally, the Lite-PolInSAR inversion has been applied on experimental data (SIR-C / Kudara, Russia / C- and L-band and E-SAR / Fichtelgebirge, Germany / L-band) and the obtained results have been compared to the results and the inversion robustness obtained from the inversion of full Pol-InSAR data and against ground measurements.

The main conclusions that can be drawn are:

- The inversion of forest height from dual-polarimetric single-baseline InSAR data is in principle possible and has been demonstrated for different acquisition realisations.
- The RVoG model is - at least for the investigated forest scenarios - a sufficiently good approximation for forest scattering inversion at L-band (and C-band) in the sense that it allows a sensible estimation of forest height.

Orientation effects within the volume may lead - especially in a Lite-Pol inversion scenario to an underestimation of forest height. Comparing now the Lite-PolInSAR inversion performance to Quad-PolInSAR performance, the following points can be stated:

- Lite-PolInSAR leads - in general - to a larger estimated forest height estimation;
- The robustness lacks - at least in the presence of topographic variation.

However, the limitations arising from temporal decorrelation effects are significantly more severe than the ones arising from a Dual-Pol operation.



---

## **Literature review on InSAR methods for manmade targets**

In Part D InSAR methods and parameter retrieval techniques in respect to man-made objects, which are found mainly in urban areas, are discussed. An overview on the Permanent Scatterer Technique is presented, including the derivation of linear and non-linear motion estimation and the estimation of atmospheric phase screen. Physical parameters and products, which can be derived with this technique, and their use for various applications are reviewed.

*This page is intentionally left blank.*

# **PART A**

## **INSAR RETRIEVAL OF ATMOSPHERIC VARIABLES**

**Ramon HANSSEN and Dmitri MOISSEEV**

Department of Earth Observation and Space Systems, Faculty of Aerospace  
Engineering, Delft University of Technology  
Delft, THE NETHERLANDS

with contributions from

**Steven BUSINGER<sup>2</sup>, Freek van LEIJEN<sup>1</sup>,  
Joaquin Munoz SABETER<sup>1</sup>, and Falk AMELUNG<sup>3</sup>**

<sup>1</sup> Department of Earth Observation and Space Systems, Faculty of Aerospace  
Engineering, Delft University of Technology  
Delft, THE NETHERLANDS

<sup>2</sup> University of Hawaii, Department of Meteorology  
Hawaii, USA

<sup>3</sup> University of Miami, Marine Geology and Geophysics/RSMAS  
Florida, USA

*This page is intentionally left blank.*

## Table of Contents

<b>A.1</b>	<b>LITERATURE REVIEW .....</b>	<b>A-1</b>
A.1.1	History.....	A-1
A.1.2	Atmospheric structure and physics .....	A-2
A.1.3	Driving mechanisms .....	A-3
A.1.3.1	Decomposition of the refractivity .....	A-4
A.1.3.2	Isolating the wet delay .....	A-6
A.1.3.3	Contribution of temperature and water vapour pressure to wet delay . .....	A-7
A.1.3.4	Influence of droplets .....	A-10
A.1.3.5	Ionospheric influence .....	A-11
A.1.3.6	Turbulent mixing .....	A-12
A.1.3.7	Vertical stratification .....	A-15
A.1.4	Reported results .....	A-16
A.1.4.1	Identification .....	A-16
A.1.4.2	Meteorological interpretation.....	A-16
A.1.4.3	Statistical analysis.....	A-17
A.1.4.4	Atmospheric Phase Screen retrieval .....	A-21
A.1.5	Feasibility and challenges .....	A-21
<b>A.2</b>	<b>IDENTIFICATION OF VARIABLES AND TECHNIQUES.....</b>	<b>A-23</b>
A.2.1	Introduction.....	A-23
A.2.2	Overview of atmospheric variables .....	A-23
A.2.2.1	Hydrostatic delay .....	A-24
A.2.2.2	Ionospheric gradients .....	A-24
A.2.2.3	Temperature and water vapour .....	A-24
A.2.2.4	Influence of hydrometeors .....	A-24
A.2.3	Retrieval Techniques .....	A-25
A.2.3.1	Atmospheric interferograms .....	A-26
A.2.3.2	Single master stack .....	A-27
A.2.3.3	Permanent scatterer stack.....	A-29
A.2.3.4	Cascade interferograms.....	A-29
A.2.4	Challenge .....	A-30
A.2.5	Case study planning .....	A-31

---

<b>A.3</b>	<b>ELECTROMAGNETIC INTERACTION MODELING.....</b>	<b>A-33</b>
A.3.1	Introduction.....	A-33
A.3.2	Forward model: the deterministic case .....	A-34
A.3.3	Precipitation: hydrometeor analysis.....	A-35
A.3.4	Forward model: the stochastic case .....	A-37
A.3.4.1	Absolute variability.....	A-39
A.3.4.2	Kolmogorov turbulence .....	A-40
A.3.4.3	Model investigation .....	A-45
A.3.5	Conclusions.....	A-47
<b>A.4</b>	<b>RETRIEVAL ALGORITHMS .....</b>	<b>A-49</b>
A.4.1	Introduction.....	A-49
A.4.2	Ambiguity resolution: permanent scatterer case.....	A-49
A.4.2.1	Data .....	A-49
A.4.2.2	PS processing to isolate atmosphere .....	A-50
A.4.2.3	Variogram estimation.....	A-51
A.4.2.4	Results.....	A-51
A.4.2.5	Discussion.....	A-51
A.4.2.6	Conclusions.....	A-54
A.4.3	Ambiguity resolution, single master .....	A-56
A.4.4	Ambiguity resolution, cascade.....	A-59
A.4.4.1	Test for the Las Vegas area.....	A-60
A.4.4.2	Conclusion .....	A-70
A.4.5	Meteorological interpretation.....	A-70
A.4.5.1	Vertical stratification .....	A-71
A.4.5.2	18 April 1996 .....	A-74
A.4.5.3	24 August 1993 .....	A-74
A.4.5.4	29 May 1998 .....	A-75
A.4.5.5	18 February 2000 .....	A-76
A.4.6	Liquid water effects .....	A-77
A.4.7	Synthesis .....	A-78
A.4.8	Conclusions and recommendations.....	A-78
<b>A.5</b>	<b>REFERENCES.....</b>	<b>A-82</b>
<b>A.6</b>	<b>ACKNOWLEDGEMENTS.....</b>	<b>A-88</b>

## A.1 LITERATURE REVIEW

### A.1.1 History

Imaging radar remote sensing is frequently promoted as an active, all-weather technique, in comparison to optical techniques which need solar illumination and cloud free conditions. At the advent of radar interferometry for topography or deformation mapping, this adagium was still frequently used, ignoring its general focus on intensity in stead of phase measurements. For phase measurements, atmospheric refractivity plays an important role in delaying the electromagnetic signals, resulting in a spatially varying phase shift, also referred to as an atmospheric phase screen. Thus, repeat-pass radar interferometry is not weather independent. Since the first repeat-pass interferometric results with SIR-B (Gabriel and Goldstein, 1988; Goldstein *et al.*, 1988) and Seasat (Li and Goldstein, 1987; Gabriel *et al.*, 1989; Li and Goldstein, 1990) first reports on atmospheric induced distortion in radar interferograms appeared in the mid-nineties (Goldstein, 1995; Massonnet and Feigl, 1995; Tarayre and Massonnet, 1996; Hanssen and Feijt, 1996; Zebker *et al.*, 1997). The approaches to deal with the distortion varied from:

- attempts to detect and identify the atmospheric anomalies, (on relatively flat terrain or by using pair-wise logic, e.g. Tarayre and Massonnet (1994); Massonnet and Feigl (1995); Tarayre and Massonnet (1996); Tarayre (1996); Zebker *et al.* (1997); Beauducel *et al.* (2000))
- evaluation of the degradation of DEM accuracy due to atmospheric errors, e.g. Dupont *et al.* (1997); Hanssen (1998); Hanssen and Feijt (1996); Mattar *et al.* (1999); Hanssen and Klees (1997, 1999)
- attempts to eliminate, reduce, or suppress the atmospheric noise (by stacking multi-interferograms, by trying to use additional meteorological or GPS measurements, or by interpolation over small areas of deformation (Delacourt *et al.*, 1998; Kenyi and Raggam, 1995; ISTAR, 1998; Ferretti *et al.*, 2001; Hanssen *et al.*, 1998; Hanssen, 1998; Beauducel *et al.*, 2000; Shimada *et al.*, 2001; Crosetto *et al.*, 2002; van der Hoeven *et al.*, 2002; Webley *et al.*, 2002; Refice *et al.*, 2002; Wadge *et al.*, 2002))
- attempts to describe the stochastic behaviour of the atmospheric signal (Goldstein, 1995; Williams *et al.*, 1998; Hanssen, 1998, 2001; Di-Bisceglie *et al.*, 2001)
- attempts to analyse it from a meteorological point of view (Hanssen *et al.*, 1999, 2000, 2001)

Nowadays, reasonable consensus has been reached on the idea that atmospheric signal in interferograms cannot be characterized as a single isolated anomaly. Power law behaviour recognized in interferograms shows that the atmosphere affects the total interferogram, with increasing magnitudes for increasing spatial intervals (Goldstein, 1995; Ferretti *et al.*, 1999a; Hanssen, 2001). Elimination of the atmospheric signal using additional meteorological instrumentation on an operational basis is nearly

impossible, due to the lack of spatial resolution or coverage, temporal coincidence, full vertical profile, and accuracy.

### **A.1.2 Atmospheric structure and physics**

The main atmospheric layers related to radio wave propagation are the ionosphere and the neutral atmosphere. The ionosphere is often treated as a spherical shell between 60 and 600 km height and can be characterized by the ability of external sources to "knockoff" electrons from atoms, hereby creating *free* electrons which are not bound to their remaining ions. These external sources are mainly the solar ultraviolet and Rontgen radiation and energetic electrons of solar and magnetospheric origin. The number of (free) electrons is represented by the *electron density*, in electrons per m<sup>3</sup>. Radio signals traversing through the ionosphere are dispersively delayed along their paths by interactions with the free electrons. A dispersive delay means that the signal delay is frequency dependent, which is the key for, e.g., GPS or radar altimetry (dual-frequency) to estimate the ionospheric (or plasma) delay. Until now, spaceborne SAR sensors have operated either using only one frequency, or were orbiting at space shuttle altitudes (225 km), which is just in or below the main variations in ionisation (Afraimovich *et al.*, 1992). The atmosphere below about eighty kilometres naturally divides into two layers, the troposphere and the middle atmosphere, where the latter consists of the stratosphere and the mesosphere (North-West Research Associates, 2000). The troposphere is destabilized by radiative heating and by vertical wind shear near the surface. While radiative heating leads to convection, the vertical wind shear leads to baroclinic instability that manifests itself in synoptic-scale storms and frontogenesis. Unlike the troposphere, the overlying middle atmosphere is relatively weather-free. More precisely, the meteorological phenomena of the middle atmosphere do not resemble anything commonly experienced in the troposphere. The stratosphere is surprisingly dry, so cloud formation is almost nonexistent apart from noctilucent and polar stratospheric clouds (North-West Research Associates, 2000). Therefore, signal delay in the neutral part of the atmosphere is mainly originating from the troposphere.

Mesoscale Shallow Convection represents a specific class of atmospheric systems that could benefit from interferometric radar observations. *Mesoscale* systems have horizontal length scales between ten and a few hundred km. *Shallow* systems occupy the lower 1 to 2 km. This layer is referred to as the *planetary boundary layer*; the lowest part of the atmosphere, where the earth's surface has a profound effect on the properties of the overlying air. In this framework, convection represents mass motions of air resulting in vertical transport and mixing of its properties, which is a principal means of transporting heat. Atkinson and Zhang (1996) state three reasons why MSC are important. First, the transport of moisture, heat, and momentum to the free atmosphere are crucial for general circulation. Second, the net radiation budget of the earth, important for understanding the earth's climate system, is significantly influenced by stratocumulus clouds. MSC is related to the occurrence and forming of such clouds. Finally, as long as the process of MSC is not fully understood, there is a gap in the understanding of the dynamics of the planetary boundary layer. Fine-scale, high accuracy atmospheric parameters obtained from SAR interferometry may contribute to and improved understanding of MSC.



The influence of the atmosphere on electromagnetic waves in the microwave band (1 GHz - 30 GHz) can manifest itself in two forms (Hall *et al.*, 1996), if we limit ourselves to Earth-space configurations. First, there are the clear air effects of atmospheric gases and their associated refractive index changes, like signal delay, ray bending, absorption, reflection, and tropospheric scattering. Secondly, there are the effects of liquid and solid particles (clouds, precipitation, aerosols), like attenuation, cross polarization, scattering, and signal delay. Here we will discuss how the delay effects affect the phase measurements in repeat-pass SAR interferometry.

### A.1.3 Driving mechanisms

After extracting the phase contribution of a reference body, e.g. the ellipsoid, the relation between the interferometric (wrapped) phase observation  $\varphi_k^w$  of pixel  $k$  and the corresponding unknown parameters for repeat pass radar interferometry can be stated as (Hanssen, 2001):

$$E\{\varphi_k^w\} = -\frac{4\pi}{\lambda} \frac{B_{\perp,k}}{R_k \sin \theta_k} H_k + \frac{4\pi}{\lambda} D_k + \frac{4\pi}{\lambda} S_k^{t1} + -\frac{4\pi}{\lambda} S_k^{t2} - 2\pi w_k \quad (\text{A.1.1})$$

where the unknown parameters are the topographic height  $H_k$  [m], the deformation vector in slant direction  $D_k$  [m], the slant-atmospheric delay during acquisition 1  $S_k^{t1}$ , the slant-atmospheric delay during acquisition 2  $S_k^{t2}$ , and the integer ambiguity number  $w_k \in \mathbb{Z}$ .  $B_{\perp,k}$  is the perpendicular baseline for pixel  $k$ ,  $\theta_k$  is its look-angle, and  $R_k$  is its range.

Assuming that

- topography  $H_k$  is known with sufficient accuracy and resolution, (depending on the baseline)
- there is negligible deformation  $D_k$ , and
- data coherence is sufficient to enable unambiguous solution of the integer ambiguities  $w_k$ , using spatial phase unwrapping,

radar interferometry can be applied to study vertically integrated atmospheric refractivity variations. The parameters  $S_k^{t1}$  and  $S_k^{t2}$  in Equ. (A.1.1) reflect every type of slant atmospheric phase delay or advancement with respect to the propagation velocity in vacuum  $c$  (Feynman *et al.*, 1963). This can be due to the velocity variations along the geometric path between antenna and scatterer or due to the induced bending of the ray path (Bean and Dutton, 1968). For every point in three dimensional space, and for every moment in time, the electromagnetic properties concerning radio wave propagation are governed by the dimensionless refractive index  $n(x,y,z,t)$  of the medium. The phase velocity is expressed by  $v = cn^{-1}$ .

Under normal atmospheric circumstances the refractive index varies only slightly from its value in a vacuum ( $n = 1$ ), and therefore often the scaled-up refractivity  $N$  is used, with  $N = (n - 1)10^6$ . The slant-atmospheric delay for resolution cell  $k$  at acquisition time  $t_i$  can be written as (Hanssen, 1998)

$$S_k^{t_i} = 10^{-6} \underbrace{\int_0^H \frac{N}{\cos \theta_{\text{inc}}} dh}_{S_{k,\text{velocity}}^{t_i}} + \underbrace{\left( \int_0^H \frac{N}{\cos \theta_{\text{inc}}(h)} dh - R_k \right)}_{S_{k,\text{bending}}^{t_i}} \quad \text{A.1.2}$$

where  $\theta_{\text{inc}}$  is the incidence angle or zenith angle,  $H$  is the height of the satellite above the position of the scatterer, and  $R_k$  is the true slant range. In this equation we have separated the influence of propagation velocity and the bending of the ray path. For the propagation velocity part, measured along the true slant path the incidence angle  $\theta_{\text{inc}}$  is a constant. For the bending part, the incidence angle  $\theta_{\text{inc}}(h)$  is a variable along the ray path. Bean and Dutton (1968) have shown that even for extreme refractivities, the ratio  $S_{k,\text{bending}}/S_k$  approaches zero for incidence angles less than  $87^\circ$ . Therefore, for all SAR data available today the slant atmospheric delay can be considered a function of propagation velocity variations only, which reduces Equ. (A.1.2) to

$$S_k^{t_i} = 10^{-6} \int_0^H \frac{N}{\cos \theta_{\text{inc}}} dh. \quad \text{(A.1.3)}$$

As a rule of thumb, we may use

$$S_k^{t_i} \text{ [in mm]} = \frac{N}{\cos \theta_{\text{inc}}} \text{ [per km]}, \quad \text{(A.1.4)}$$

which is an approximation for the one-way path delay in mm, per km of signal path. Although Equ. (A.1.3) combined with Equ. (A.1.1) describes the fundamental functional relation between the interferometric phase and the integrated refractivity, decomposition of  $N$  in a number of physical parameters can provide new insights in atmospheric behaviour. This is mainly due to the fine resolution of the data, the high delay accuracy, and the all-weather capabilities. Using only one interferogram, an ambiguity will be introduced by the coherent superposition of two atmospheric states ( $S_k^{t_1}$  and  $S_k^{t_2}$ ). This ambiguity restricts the quantitative interpretation of the atmospheric signal to situations where events are dominant during one of the two SAR acquisitions. Nevertheless, several studies (Hanssen and Feijt, 1996; Hanssen *et al.*, 1998; Hanssen, 1998; Hanssen and Weckwerth, 1999; Hanssen *et al.*, 1999, 2000; Hanssen, 2001; Hanssen *et al.*, 2001) demonstrate the feasibility of meteorological interpretation. To circumvent the ambiguity problem, future applications of the technique can use "cascaded interferograms," in which every SAR image appears in two interferograms, or single master stacks (Ferretti *et al.*, 2001) (Figure A.1).

### A.1.3.1 Decomposition of the refractivity

For common radar frequencies, the refractivity  $N$  can be written as (Smith and Weintraub, 1953; Kursinski, 1997):

$$N = \underbrace{k_1 \frac{P}{T}}_{N_{\text{hyd}}} + \underbrace{\left( k_2' \frac{e}{T} + k_3 \frac{e}{T^2} \right)}_{N_{\text{wet}}} - \underbrace{4.028 \times 10^7 \frac{n_e}{f^2}}_{N_{\text{iono}}} + \underbrace{1.45W}_{N_{\text{liq}}}, \quad \text{(A.1.5)}$$

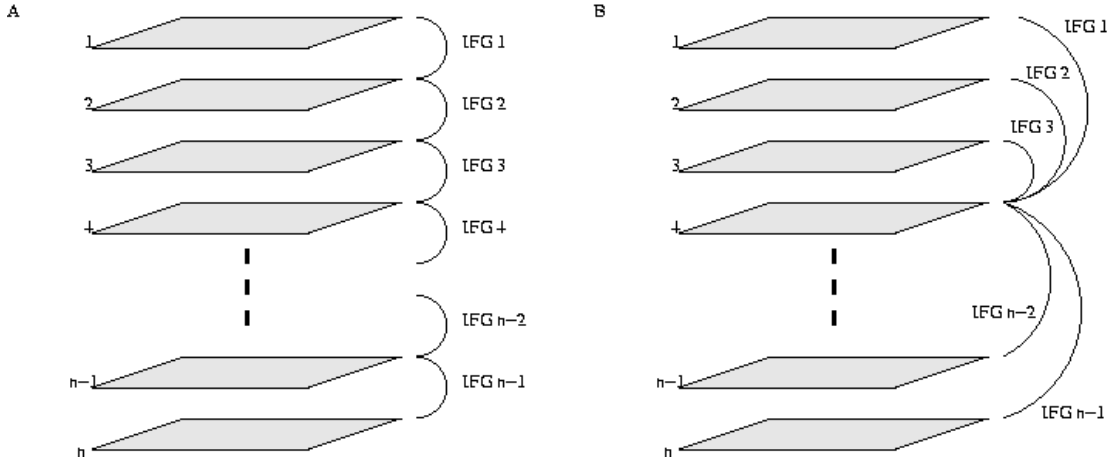


Figure A.1 A) *Cascaded* interferograms: every SAR image appears in two interferograms, except the first and last, and B) *single master stack*, where every interferogram refers to the same master image.

where  $P$  is the total atmospheric pressure in hPa,  $T$  is the atmospheric temperature in Kelvin,  $e$  is the partial pressure of water vapour in hPa,  $n_e$  is the electron number density per cubic meter,  $f$  is the radar frequency,  $W$  and is the liquid water content in g/m. The values  $k_1 = 77.6$ ,  $k_2 = 23.3$  and  $k_3 = 3.75 \times 10^5$  are taken from Smith and Weintraub (1953), but also results from Thayer (1974) are commonly used. The four refractivity terms are referred to as hydrostatic term, wet term, ionospheric term, and liquid term, respectively. Resch (1984) indicated that the first two parts are accurate to 0.5 percent. Using this representation of the refractivity we decompose Equ. (A.1.3) into

$$S_k^{t_i} = \frac{1}{10^6 \cos \theta_{\text{inc}}} \left\{ \int_0^H N_{\text{hyd}} dh + \int_0^H N_{\text{wet}} dh + \int_0^H N_{\text{iono}} dh + \int_0^H N_{\text{liq}} dh \right\}, \quad (\text{A.1.6})$$

where the four integrals are labelled the hydrostatic delay, the wet delay, the ionospheric delay, and the liquid delay, respectively.

As the total signal delay can be up to several meters<sup>1</sup> it is evident that the interferometric data--which were originally wrapped to half the radar wavelength interval (2.8 cm for ERS)--can never capture the full integrated values, unless some sort of independent absolute calibration is possible. As a result, we can regard every integral in Equ. (A.1.6) as the sum of two contributions. First, a fixed contribution (bias), which is constant for the whole scene. This value can be subtracted from the data. Second, a variable contribution dependent of the position in the image. In terms of the refractivity components, we can write

$$N(x, y, h) = \bar{N}(h_c) + \Delta N(x, y, h), \quad (\text{A.1.7})$$

where  $\bar{N}(h_c)$  is the mean refractivity for all values at height  $h_c$  within the interferogram area, see Figure A.2. The variable  $\Delta N(x, y, h)$ , with  $E\{\Delta N(x, y, h)\} = 0$ , is the lateral variation of the refractivity. Consequently, with  $S_k^{t_i} = \bar{S}^{t_i} + \Delta S_k^{t_i}$  we could write Equ. (A.1.6) as

$$\Delta S_k^{t_i} = \frac{1}{10^6 \cos \theta_{\text{inc}}} \left\{ \int_0^H \Delta N_{\text{hyd}} dh + \int_0^H \Delta N_{\text{wet}} dh + \int_0^H \Delta N_{\text{iono}} dh + \int_0^H \Delta N_{\text{liq}} dh \right\}. \quad (\text{A.1.8})$$

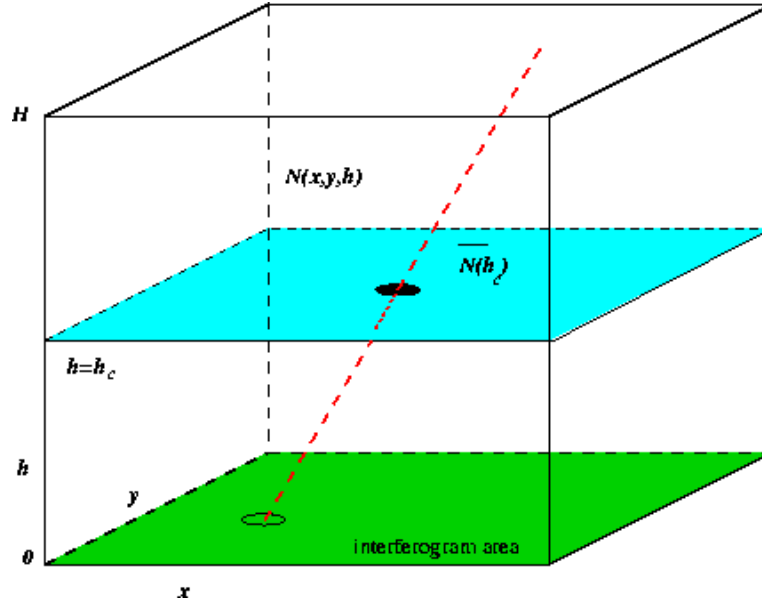


Figure A.2 The refractivity distribution  $N(x, y, h)$  in a 3D Cartesian space above the interferogram can be described by Equ. (A.1.7).

As a result of this (relative) representation, it is obvious that the influence of the four refractivity components depends on their lateral variability within the scene. Vertical variation of refractivity is of importance if (i) there is topography in the image and if (ii) the mean vertical refractivity profiles differ between the two acquisitions, see section A.3.7. In the next sections, we will try to isolate the separate terms of the delay.

### A.1.3.2 Isolating the wet delay

If we consider the contribution of the hydrostatic term in Equ. (A.1.5) on the zenith delay, we may write for point  $k$  at time  $t_i$ , using the ideal gas law  $P = \rho R_d T$ ,

$$S_k^{t_i} = \frac{1}{10^6 \cos \theta_{\text{inc}}} k_1 \int_k^a \frac{P}{T} dz = \frac{1}{10^6 \cos \theta_{\text{inc}}} k_1 R_d \int_k^a \rho(z) dz, \quad (\text{A.1.9})$$

where  $a$  is the antenna position. Since the measured total surface pressure can be written as

$$P_s = g_m \int_0^\infty \rho(z) dz, \quad (\text{A.1.10})$$

where  $g_m$  is the local gravity at the centre of the atmospheric column (Saastamoinen, 1972), which is approximated by

$$g_m = 9.784(1 - 0.0026 \cos 2\Phi - 0.00028z_0) \quad [\text{m/s}^2], \quad (\text{A.1.11})$$

dependent on the surface height  $z_0$  and latitude  $\Phi$ , the hydrostatic delay is obtained from a simple barometric measurement  $P_s$ :

$$S_{k,\text{hydrostatic}}^{\text{ti}} = k_1 \times 10^{-6} \frac{R_d}{g_m} P_s. \quad (\text{A.1.12})$$

Using these parameters and the surface pressure  $P_s$  measured with an accuracy of 0.4 hPa or better, this delay can be predicted with an accuracy of 1 mm or better (Bevis *et al.*, 1996). For the test sites used in Hanssen (2001),  $S_{k,\text{hydrostatic}}^{\text{ti}} = 2.275 \times 10^{-3} P_s$ , hence in the order of 2.3 m. For comparison, the wet delay is less than 0.3 m (Elgered, 1982).

Standard observations of surface pressure within a typical interferogram area of  $100 \times 100$  km show (i) minimal spatial variation, usually less than 1 hPa, and (ii) a smooth behaviour. This is due to the large scales of high and low pressure zones. Therefore, the hydrostatic delay observed in interferograms is smooth as well and manifests itself usually as a phase trend of maximally a few millimetres over the entire interferogram. Such phase trends are likely to occur due to orbit errors as well and are often corrected for using tie-points. As a result, the hydrostatic delay has a very limited influence on interferograms, and can be safely ignored for spatial scales of  $\sim 50$  km and smaller. If spatially distributed surface pressure measurements are available, these can be used to correct for the hydrostatic delay component.

The wet part of the delay or refractivity, parameterised by temperature  $T$  and the partial pressure of water vapor  $e$ , is much more spatially variable than the hydrostatic delay, while the variations have a considerable effect on the observed phase delay.

### A.1.3.3 Contribution of temperature and water vapour pressure to wet delay

The contribution of temperature and moisture (partial water vapour pressure) to the wet delay can be investigated by a sensitivity analysis. Within a range of  $-40^\circ\text{C}$  to  $40^\circ\text{C}$  for temperature and 0 hPa to 30 hPa for the partial pressure of water vapour, the partial derivatives of temperature and WV pressure to the wet refractivity can be computed:

$$\partial N_{\text{wet}} / \partial T = -\frac{k_2' e}{T^2} - \frac{2k_3 e}{T^3}, \quad (\text{A.1.13a})$$

$$\partial N_{\text{wet}} / \partial e = \frac{k_2'}{T} + \frac{k_3}{T^2}. \quad (\text{A.1.13b})$$

Note that a temperature increase yields a decrease in refractivity. Hence a localized area with a higher temperature will show up as a relative increase in propagation velocity, whereas a localized area with higher water vapour pressure will show up as a relative decrease in propagation velocity. Figure A.3 shows the ratio  $R = \frac{\partial N_{\text{wet}}}{\partial e} / \frac{\partial N_{\text{wet}}}{\partial T}$ . In

other words, we compare (i) the sensitivity of  $N_{\text{wet}}$  for a 1 hPa change in the partial pressure of water vapour  $e$  with (ii) the sensitivity of  $N_{\text{wet}}$  for a 1°C change in temperature  $T$ . If this ratio  $|R| > 1$  the refractivity is  $R$  times more sensitive for a 1 hPa change in  $e$  than for a 1°C change in  $T$ . On the horizontal axis, the partial pressure of water vapour is plotted, on the vertical axis the temperature. By combining a specific  $e$  and  $T$  value it is possible to evaluate the sensitivity ratio. Relative humidity isolines are superposed to show the likelihood of a specific  $e$ - $T$  combination. From Figure A.3, we may conclude that the sensitivity ratio  $R$  has a wide range of values. Although some very high ratio's are apparent for very dry air (less than 5 hPa water vapour pressure), we can safely state that  $4 < |R| < 20$ . The ratio is lowest for high temperatures combined with high partial water vapour pressures. These conditions are likely in hot and humid regions, especially near the earth's surface. For cloud development, reaching higher altitudes, temperatures drop with 6.5 K/km, which increases the ratio.

As a result, the *wet* part of the refractivity is in any scenario at least 4-20 times as sensitive to a 1 hPa change in the partial pressure of water vapour than to a 1°C change in temperature. Moisture variations of 1 g kg<sup>-1</sup> (1.2 hPa) are common even on a 1-km spatial scale (Weckwerth *et al.*, 1997). At 0°C, such a variation already produces 6 mm delay per vertical km.

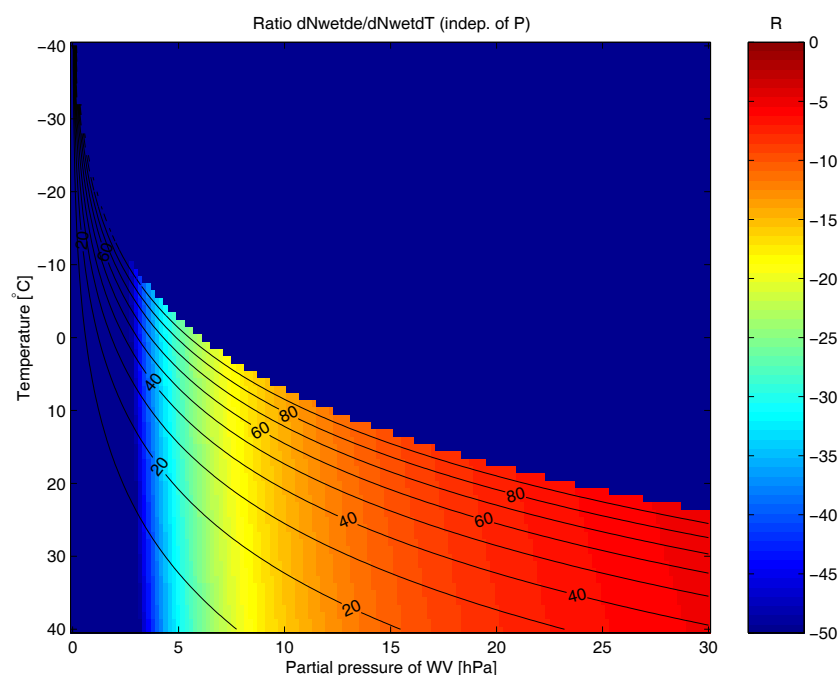


Figure A.3 Sensitivity ratio  $R = \frac{\partial N_{\text{wet}}}{\partial e} / \frac{\partial N_{\text{wet}}}{\partial T}$  of the wet part of the refractivity  $N_{\text{wet}}$ , dependent of the water vapour pressure  $e$  and of the temperature  $T$ . Relative humidity isolines are superposed.

A relationship which plays an important role in the definition of humidity is the *equation of state* for an ideal gas which has a meteorological form:

$$P_d = \rho_d R_d T, \quad (\text{A.1.14})$$

where  $R_d$  is the *specific gas constant*, which is  $287.053 \text{ J K}^{-1} \text{ kg}^{-1}$  for dry air,  $P_d$  is the pressure of the dry gas,  $\rho_d$  its density, and  $T$  the temperature in K. Equ. (A.1.14) is also known as the ideal gas law. It can be used to calculate *the partial water vapour pressure*  $e$  as a function of the *absolute humidity* or vapour density  $\rho_v$  and the absolute temperature  $T$ , since vapour behaves as an ideal gas in terrestrial conditions:

$$e = \rho_v R_v T, \quad (\text{A.1.15})$$

where  $R_v$  is the specific gas constant for water vapour, which is  $461 \text{ J K}^{-1} \text{ kg}^{-1}$ . The ratio of the gas constants  $R_d/R_v$  is therefore 0.622, often represented by  $\epsilon$ . The absolute humidity  $\rho_v$  is an objective measure for the amount of water vapour (in grams of equivalent liquid water) per cubic meter air. There is an upper limit for the amount of water vapour that a parcel of air can absorb. An additional input of water vapour would lead to condensation into clouds (ice crystals or water droplets), fog, dew, etc. This maximal value, the saturation point or dew point, is dependent of the temperature.

Table A.1

The relation between the air temperature and amount of liquid water a cubic meter air can absorb.

Air temperature [°C]	0	10	20	30
Absolute humidity [grams/m3]	4.8	9.4	17.3	30.4

Warm air can absorb more water vapour than cold air: it has a higher saturation point, cf. Table A.1. The saturation partial water vapour pressure  $e_s$  at temperature  $T$  is described by the *Clausius-Clapeyron* equation (Stull, 1995):

$$e_s = e_0 \exp\left(\frac{L}{R_v} \left(\frac{1}{T_0} - \frac{1}{T}\right)\right), \quad (\text{A.1.16})$$

where  $e_0 = 6.11 \text{ mbar}$ ,  $T_0 = 273 \text{ °K}$ , and  $L$  is the latent heat. Over a flat water surface,  $L = 2.5 \cdot 10^6 \text{ J kg}^{-1}$ , which is the latent heat of vaporization. In this case, cloud droplets are being formed. Over a flat ice surface,  $L = 2.83 \cdot 10^6 \text{ J kg}^{-1}$ , which is the latent heat of deposition, when ice crystals are being formed. For a temperature of  $20 \text{ °C}$ ,  $e_s = 23.7 \text{ mbar}$ , roughly 2.3 percent of the average total atmospheric pressure of  $1013 \text{ mbar}$ . Note that  $e_s$  does not depend on the pressure. The *relative humidity*  $RH$  is the ratio of the amount of water vapour in the air compared to the saturation amount of water vapour at that temperature:  $RH = (e/e_s) \cdot 100\%$ . For all practical purposes the relative humidity in water clouds is 100 percent. The partial pressure of water vapour can be computed from the relative humidity  $RH$  and the temperature  $T$ , using Equ. (A.1.16):

$$e = \frac{RH}{100} e_s(T). \quad (\text{A.1.17})$$

The humidity *mixing ratio*  $r$  is the ratio between the mass of water vapour and the mass

of dry air:

$$r = \frac{m_v}{m_d} = \frac{\epsilon \cdot e}{P_d}. \quad (\text{A.1.18})$$

The ratio between the mass of water vapour and the *total* pressure is called the *specific humidity*:

$$q = \frac{m_v}{m_d + m_v} = \frac{\epsilon \cdot e}{P_d + e}. \quad (\text{A.1.19})$$

As an example, for typical low tropospheric conditions,  $q = 10 \text{ g kg}^{-1}$ , and  $P_d + e = 1000 \text{ mbar}$ , so the partial pressure of water vapour  $e = 16 \text{ mbar}$ . The *precipitable water content* is the total amount of water vapour in a vertical column of the atmosphere, if it would all condense.

#### A.1.3.4 Influence of droplets

The phase shift of spaceborne C-band radar pulses caused by liquid water (droplets) can cause limited additional signal delay in the interferometric observations. The interaction of radar waves with droplets is a *forward scattering* problem: the wave induces a dipole moment in the droplet, which will act as a secondary wave front. After passing the droplet, the principal (undisturbed) wave front will interfere with the secondary wave front and hereby cause a phase shift.

Table A.2  
Liquid water content in clouds, after Hall *et al.* (1996) and Bean and Dutton (1968)

Type of cloud	Liquid water content [g/m <sup>3</sup> ]	Slant delay [mm/km]
Stratiform clouds	0.05-0.25	0.1-0.4
Small cumulus clouds	0.5	0.7
Cumulus congestus and cumulonimbus	0.5-2.0	0.7-3.1
Ice clouds	< 0.1	<0.1

Hall *et al.* (1996) have listed the liquid water content,  $W$ , of clouds, see Table A.2. The liquid water content is the particle number density times the volume per particle times the density of liquid water. Its maximum is usually found at  $\sim 2 \text{ km}$  above the cloud base, and can be related to the dielectric refractivity using the Clausius-Mossotti equation, (Solheim *et al.*, 1997):

$$N_{\text{cloud}} = \frac{3}{2} \frac{W}{\rho_w} \frac{\epsilon_0 - 1}{\epsilon_0 + 2}, \quad (\text{A.1.20})$$

where  $\epsilon_0$  is the permittivity of water and  $\rho_w$  is the density of liquid water. This relation is independent of the shape of the cloud droplet (Born and Wolf, 1980). Although the



permittivity of water is a weak function of temperature, it is possible to approximate Equ. (A.1.20) to within 1% by (Solheim *et al.*, 1997):

$$N_{\text{cloud}} = 1.45 W. \quad (\text{A.1.21})$$

Since the value of  $N_{\text{cloud}}$  reflects the difference with the vacuum refractive index, Equ (A.1.6) can be used to determine the additional delay  $S_{k,\text{cloud}}^{t_i}$  caused by the liquid water in clouds:

$$S_{k,\text{cloud}}^{t_i} \text{ [in mm]} = \frac{1.45}{\cos \theta_{\text{inc}}} W L, \quad (\text{A.1.22})$$

where  $L$  is the thickness of the cloud layer in km. Note that cloud-droplet refractivity is in fact *dispersive*. However, since the dispersive part of the refractivity is much smaller than the non-dispersive part it can be ignored for C-band frequencies. Table A.2 shows the zenith delay for four cloud groups. For repeat pass SAR interferometry, stratiform clouds and ice clouds do not cause large phase disturbances, due to their large horizontal extent and small additional delay. However, especially the cumulus type of clouds can result in a significant additional phase delay, as they have a relatively limited horizontal size combined with a large vertical height and liquid water content, see Figure A.4.

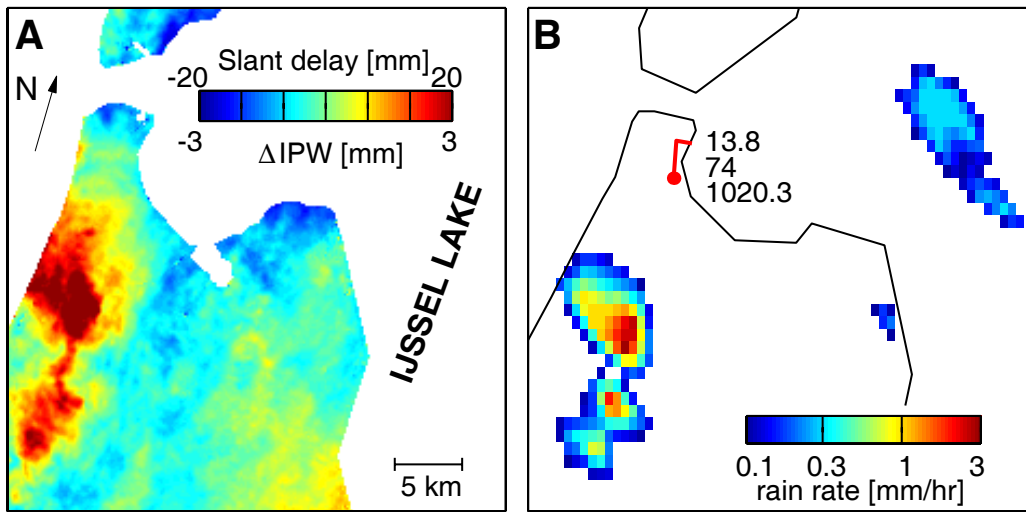


Figure A.4 Images of precipitation (Hanssen *et al.*, 1999). (A) The SAR interferogram (29 and 30 Aug 1995, 21:41 UTC) shows slant delay variation, mapped to zenith integrated precipitable water differences. The average of the undisturbed area is set to zero, yielding relative precipitable water estimates. (B) shows the weather radar rain rate (29 Aug 1995, 21:45 UTC). The surface wind velocity is 4.1 m/s, from 350 degrees, indicated by the wind barb. Temperature (°C), the percentage of relative humidity, and pressure (hPa) are plotted beside the station.

### A.1.3.5 Ionospheric influence

The ionospheric influence for C-band SAR follows from Equ. (A.1.5) and Equ. (A.1.6):

$$\begin{aligned}
S_{k,\text{iono}}^{t_i} &= \frac{1}{10^6 \cos \theta_{\text{inc}}} \int_0^H N_{\text{iono}} dh = -\frac{1}{10^6 \cos \theta_{\text{inc}}} \int_0^H 4.028 \times 10^7 \frac{n_e}{f^2} dh \\
&= -\frac{1}{10^6 \cos \theta_{\text{inc}}} \frac{K}{f^2} \text{TEC} \approx -1.54 \times 10^{-18} \text{TEC}.
\end{aligned}
\tag{A.1.23}$$

Taking the derivative of this function and using TEC-units (1 TECU =  $10^{16}$  electrons/m<sup>2</sup>), we obtain for C-band SAR

$$\partial S_{k,\text{iono}}^{t_i} / \partial \text{TECU} = -0.015. \tag{A.1.25}$$

In other words, for a repeat-pass interferometric cycle of 28 mm, a change in 1 TECU over the scene yields a phase ramp of approximately half a cycle. Of course, we have to take into account that an interferogram is the difference of two SAR acquisitions during different days, but at the same local time. The status of the ionosphere at both instances needs to be accounted for. Therefore, an identical TEC ramp in both images, e.g., due to the diurnal variation, will cancel in the interferogram.

Saito *et al.* (1998) used GEONET, the permanent GPS array of Japan with a mean distance between the receivers of 25 km, to map the two-dimensional TEC perturbations. TIDs, with a wavelength of 300-400 km, travelling with a speed of ~150 m/s, were observed. The amount of TEC variation was maximally 0.8 TECU. This would result in 1.2 cm phase variation in a C-band SAR interferogram. However, for these wavelengths and 100×100 km interferograms, such variations would result only in a slight curvature of the interferometric phase. Gray *et al.* (2000) observed ionospheric wave effects by examining the azimuth offset vectors during the coregistration of two SAR images over the Antarctic (81.3°S). This resulted in a wave-pattern with wavelengths of ~5 km which could be explained by a variation of 0.12 TECU (less than 2 mm zenith delay difference) during one of the SAR acquisitions. The variable electron content caused an erroneous Doppler frequency, resulting in an offset of the coverage of resolution elements in azimuth. In the interferometric phase these effects were not visible, likely due to their limited magnitude and the phase contribution of topography, deformation, and tropospheric signal. Therefore, Hanssen (2001) adapted the hypothesis that ionospheric effects may result in long wavelength gradients/curves over a single SAR image, but will not noticeably affect phase variations at scales less than, say, 50 km.

### A.1.3.6 Turbulent mixing

Three important observations characterize atmospheric signals in interferograms. First, the relative character of an interferogram does not enable absolute signal delay measurements. Hence, we can demean the interferogram, which implies that the expectation value of the atmospheric signal for an arbitrary pixel will be zero. As a consequence, there is no unique dependency on vertical variation in refractivity - different vertical refractivity distributions can result in the same total delay. Second, orbit errors can easily cause a nearly linear trend over the whole interferogram. Such trends are usually hard to distinguish from atmospheric signal delay trends, and are usually eliminated using some kind of residual flattening, for example using tie-points. This strategy is equivalent to a highpass filter for the atmospheric signal. Finally, we know that the amount of atmospheric signal within an interferogram is

highly variable in time: some interferograms seem to have no atmospheric influence at all, whereas others are contaminated significantly. This is also dependent on the climatological characteristics of the location. Nevertheless, for acquisition time intervals of 1 day or more the two states of the atmosphere appear to be practically uncorrelated.

Several studies have shown that the predominant part of the atmospheric signal in interferograms is caused by the water vapour distribution in the lower troposphere (Goldstein, 1995; Tarayre and Massonnet, 1996; Hanssen and Feijt, 1996; Tarayre, 1996; Zebker *et al.*, 1997; Hanssen, 1998; Hanssen *et al.*, 1999, 2001, 2000). This is a consequence of the fact that for microwave frequencies, the permanent molecular dipole moment of H<sub>2</sub>O dominates the variability of the refractive index. Moreover, the water vapour distribution can be considered to be an approximate passive "tracer" of the mechanical turbulence (Ishimaru, 1978). Therefore, the observed statistics of the atmospheric signal will be correlated with those of wind vortices, see, e.g., Hanssen *et al.* (2000).

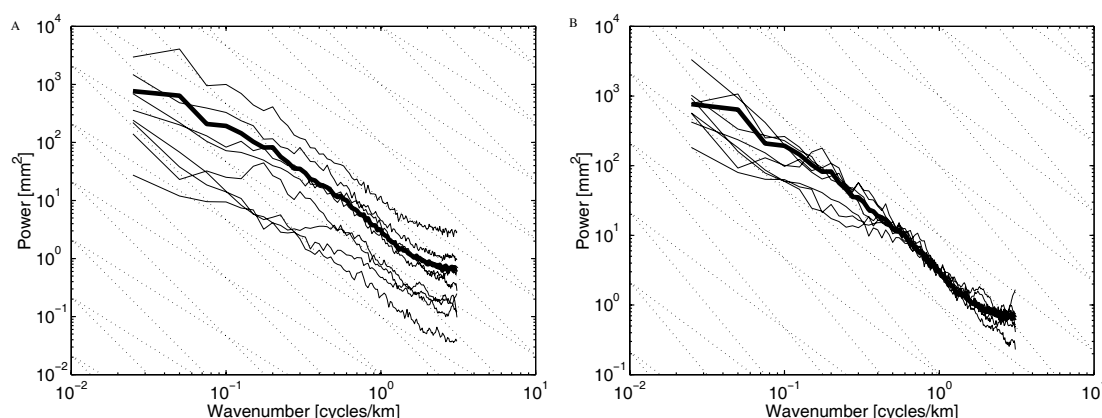


Figure A.5 The one-dimensional power spectra of eight atmospheric situations. (A) Absolute values. The diagonal lines indicate 5/3 and 8/3 power-law behaviour. The bold line is the average of all eight situations. (B) The same spectra multiplied with a factor to obtain the same power at 1 cycle/km.

Hanssen (2001) analysed 8 tandem interferograms with varying atmospheric signal, reaching from calm weather to strong storms. 50×50 km windows in the data are used to calculate a set of power spectra, written as

$$P_{\varphi}(f) = P_0(f/f_0)^{-\beta}, \quad (\text{A.1.26})$$

where  $f$  is some (spatial or temporal) frequency,  $P_0$  and  $f_0$  are normalizing constants, and  $-\beta$  is the *spectral index* (often  $1 < \beta < 3$ ). First the mean value of the window is subtracted, and both in azimuth and in range direction a linear trend is removed from the data. For these interferograms, the one-dimensional power spectra are shown in Figure A.5a, assuming isotropy. The diagonal lines in Figure A.5a indicate the slope

of  $-5/3$  and  $-8/3$  power-law functions. The data show that all atmospheric situations exhibit similar power-law behaviour, with slopes varying between  $-5/3$  and  $-8/3$  for the different scaling regimes. There is a range in the absolute power, indicated by the vertical position of the spectra in the graph, of almost two orders of magnitude, indicating more or less severe weather conditions. The bold line is the average of all eight situations. In Figure A.5b, all power spectra have been multiplied by a factor, yielding the averaged power for 1 cycle/km. Comparison of the shape of the power spectra shows that the data are not entirely scale-invariant, and three dominant regimes can be recognized, of which two are atmospheric while the third one probably reflects noise.

Regime I, with exponent  $\beta = 5/3$  and fractal dimension  $D_2 \approx 2.7$ , covers scales larger than the thickness of the turbulent layer. For these scales, between  $\sim 2$  km and the size of the interferogram ( $\sim 100$ - $200$  km), the approximation of two-dimensional turbulence can be applied. Over these scales the characteristics of the total atmospheric column dominate. For example, convective processes result in significant differences in the overall refractivity between updrafts (warm and moist) and downdrafts (cold and relatively dry). Although there is evidently atmospheric signal at scales larger than the interferogram size, we can safely ignore this since it is outside the measurement capabilities of the system. Stationarity of the physical process is always ensured due to the limitation of the earth's circumference, which enforces the flattening of the power spectrum for large scales. Based on VLBI observations it is proposed that the slope of the power spectrum is zero for scales larger than 3000 km (Treuhart and Lanyi, 1987).

Table.A.3

Three regimes of atmospheric delay as observed by radar interferometry  
\*, fractal dimension, †, Power-law exponent.

Regime	Scale (km)	$D_2^*$	$\beta^\dagger$
I	$> 2$	2.67 (16/6)	5/3
II	0.50-2.0	2.16 (13/6)	8/3
III	0.01-0.5	3.16 (19/6)	2/3

Regime II covers scales smaller than the thickness of the turbulent layer (the depth of the convective boundary layer, say 2 km), down to the resolution level. The integrated refractivity has a much smoother behaviour over these scales, indicated by the steeper power exponent  $\beta = 8/3$  and the lower fractal dimension  $D_2 \approx 2.2$ . The correspondence in the power slopes is clearly visible in Figure A.5b, where all curves overlap within this regime. The behaviour in this regime has been observed in several studies on SAR interferometry, see Goldstein (1995); Hanssen *et al.* (1998); Hanssen (1998); Ferretti *et al.* (1999a). Nevertheless, in contrast to some studies, the combination with regime I indicates that the signal cannot be considered scale-invariant for all spatial scales. In fact, assuming a  $-8/3$  power-law for scales larger than 5-10 km will increasingly underestimate the roughness and hence the variability of the atmospheric signal.

Table A.4

$P_0$ , rms, and main cloud type for eight interferograms (Cb, Cumulonimbus; Ci, Cirrus; St, Stratus; Sc, Stratocumulus; Cu, Cumulus. \* $P_0$  is the power initialization parameter at 1 cycle/km † The rms is computed over an area of  $\sim 50 \times 50$  km)

<i>Interferogram</i>	<i>A</i>	<i>B</i>	<i>C</i>	<i>D</i>	<i>E</i>	<i>F</i>	<i>G</i>	<i>H</i>
Code	Gd1	Gd2	Gd3	Gd4	Gd5	Gd6	Gd7	Gdex
Month/Year	7/95	8/95	12/95	3/96	4/96	5/96	8/96	2/96
$P_0^*$ (mm <sup>2</sup> )	11.2	4.7	0.6	0.5	0.8	2.5	4.7	0.3
rms† (mm)	15.2	6.7	7.1	2.7	6.2	8.0	8.0	8.5
Cloud	Cb	Ci	St/Sc	St/Sc	Ci	Cu	Cu	St

Regime III is unlikely to have an atmospheric origin, since there is no physical explanation for increased delay variation at such small scales. Instead, it is likely caused by high wavenumber noise in the data. This can be a result of decorrelation effects or, e.g., by interpolation errors when subtracting the reference DEM. In these examples, regime III noise starts to influence the data for wavelengths less than  $\sim 500$  m. Although the driving mechanisms differ from regime I and II, it can be advantageous to describe the statistical behaviour of regime III the same way, since the transitions between the regimes are gradual and the stochastic model can be constructed uniformly. The power exponent in regime III approaches  $\beta = 2/3$  and the lower fractal dimension  $D_2 \approx 3.2$  indicating the very rough behaviour at these scales.

Summarizing, the important observation from the power spectra is their similar shape, even though the atmospheric circumstances were extremely variable, ranging from calm, cold weather to severe storms with strong convection and humidity gradients. These weather situations covered two orders of magnitude in the power spectrum. Therefore, a reasonable approximation of the power spectra seems to be based on the three regimes, using only the  $P_0$  value (for 1 cycle/km wavenumbers) for initialisation, see Table.A.3. The  $P_0$ -values for the eight interferograms are listed in Table A.4.

#### A.1.3.7 Vertical stratification

Atmospheric stratification only considers variation of the refractivity along the vertical. Assuming an infinite number of thin atmospheric layers, each with constant refractivity, there will be no horizontal delay differences over flat terrain, even for different refractivity profiles during both SAR acquisitions. This is due to the fact that SAR interferograms are not sensitive to image-wide phase biases. However, for hilly or mountainous terrain a difference in the vertical refractivity profile during both acquisitions will affect the phase difference between two arbitrary resolution cells with different topographic height, and may cause an erroneous interpretation. This effect has been recognized during deformation studies of mount Etna by, e.g., Tarayre and Massonnet (1996); Massonnet and Feigl (1998); Delacourt *et al.* (1998); Ferretti *et al.* (1999a), and Beauducel *et al.* (2000).

Hanssen (2001) used 1460 radiosondes, acquired 4 times daily from 1 Jan. 1998 to 31 Dec. 1998, located in a moderate sea-climate at latitude  $52.10^\circ$  and longitude  $5.18^\circ$ , and analysed the statistics of the delay variation for every possible height interval.

This resulted in an empirical model for the standard deviation of the interferometric phase due to differential tropospheric stratification:

$$\sigma_{\varphi} = \frac{4\pi}{\lambda \cos \theta_{\text{inc}}} (33.7 + 0.08\Delta t) 10^{-3} \sin \frac{h\pi}{2h_s}, \quad 1 \leq \Delta t \leq 182, \quad 0 \leq h \leq h_s, \quad (\text{A.1.27})$$

where  $\Delta t$  is the time interval in days,  $h$  represents height in meters, and  $h_s = 5000$  m is a scale height. Above this height the variability of the refractivity is considered negligible. The estimated standard deviation has a precision better than 2-3 mm. For the accuracy of a height difference one can simply use

$$\sigma_{\varphi}(\Delta h) = \sigma_{\varphi}(h_2) - \sigma_{\varphi}(h_1). \quad (\text{A.1.28})$$

Assuming a Gaussian distribution, these results imply that approximately 33% of the interferometric combinations exhibit effects more severe than expressed in Equ. (A.1.27). For example, for a time interval of 175 days and a height interval of 2 km, 33% of the interferograms will have more than one phase cycle error due to vertical tropospheric stratification assuming ERS conditions. For a 100 m perpendicular baseline, this translates to a height error of 100 m or worse. For a 1-day interval and 2 km height interval it yields a height error of 76 m or worse.

The analysed dataset is restricted to one location on earth, which limits conclusions on global scales. However, since not the total refractivity but the variability of refractivity influences the signal in radar interferograms, it is expected that the results obtained here give a correct order of magnitude of the error.

Correction of the error due to vertical stratification is only possible using vertical profile measurements. Surface observations combined with a tropospheric model are in general unreliable, whereas integrated refractivity observations such as obtained using GPS are inadequate for correction.

## **A.1.4 Reported results**

### **A.1.4.1 Identification**

Identification of atmospheric signal in interferograms has been reported by many authors, e.g. Massonnet and Feigl (1995); Mattar *et al.* (1999); Rosen *et al.* (1996); Zebker *et al.* (1997); Tarayre-Oriot and Massonnet (1996); Tarayre and Massonnet (1994). Usually, this is a result of a priori knowledge of the topography or of the characteristics of the deformation signal. A general 'bumpy' phase behaviour is often attributed to atmospheric variability.

### **A.1.4.2 Meteorological interpretation**

Meteorological interpretation of the atmospheric signal is discussed by Hanssen (1998); Hanssen *et al.* (1999, 2000, 2001). Using additional meteorological observations (synoptic, weather radar, radiosondes, satellite imagery, and human

observation) it was possible to attribute specific phenomena in the differential interferograms to clouds, rain cells, laminar and turbulent flow, gravity waves, and fronts. The quantitative high accuracy delay observations could be attributed to mainly water vapour variability. For areas which contain both land and water areas, radar backscatter intensity over the water areas can be used to correlate wind observations with simultaneously observed water vapour distribution Hanssen *et al.* (2000).

#### A.1.4.3 Statistical analysis

Observations by Dupont *et al.* (1997) show phase variations with a low spatial frequency and an amplitude between 0.3 and 0.5 phase cycles in about 44 processed interferograms. In some interferograms, they observed localized phase variations with an amplitude of 1-3 phase cycles. Goldstein (1995) reports RMS phase variations of 0.1 phase cycles over the whole image, probably caused by turbulent mixing of water vapour and air, and maximum (peak-to-peak) variation of 1 phase cycle. Up to three phase cycles localized phase shift is observed by Tarayre and Massonnet (1996) corresponding with cumulus clouds, while Hanssen and Usai (1997) report wave effects with a wavelength of 1.5-2 km and an amplitude of 0.25 cycles, and localized phase shifts of up to 5 phase cycles. Zebker *et al.* (1997) analysed L-band and C-band data from SIR-C, and found RMS values between 0.04 and 0.16 phase cycles for L-band, which would convert to 0.17 and 0.68 phase cycles RMS for C-band.

Hanssen (1998) analysed 52 SAR images, corresponding with 26 analysed interferograms. The database of SAR images covers nearly every month of the year, see the histogram in Figure A.6a, except January. Therefore, all seasons have been sampled. Unfortunately, the limited duration of the ERS tandem mission does not permit a longer series of interferograms over one particular area. A consequence of the orbit configuration is that the diurnal cycle of the weather is only sampled at one nearly discrete time instant for every image. Therefore, the imaging times are always approximately 21:40 UTC for the *ascending* interferograms, and about 10:30 UTC for the *descending* interferograms. Variations between daytime and night time acquisitions could therefore not be studied.

A review of the observed *rms* phase values is shown in Table A.5. The *rms* values vary between 0.6 rad for interferogram gd4, and 3.6 rad for interferogram fa2. Note that the interpretation of the *rms* values is dependent on the area used for its calculation. For each of the 5 interferogram locations studied, the decorrelated areas (mainly water) varied in spatial coverage, and the combination of two interferograms in the *Flevoland ascending* series enabled a much larger surface for evaluation.

Figure A.6b shows the percentages of occurrence for the *rms* values, in eight categories. Root mean square values around 1.5 rad occur the most frequently in this series. Ordering the observed *rms* values based on the month of acquisition produces the histogram in Figure A.7. The months May and July have in this database phase variations with an *rms* which is double of the values observed in all other interferograms. Naturally, this is a consequence of only one or two interferograms, and it can therefore not be used for the derivation of general rules. However, it can be expected that 'summer'-thunderstorms, which occur often in this region, will produce strong phase artifacts in corresponding interferograms.

A classification of the observed effects can be based on the magnitude and the type and scale of the disturbance. Based on the *magnitude*, four classes are defined based on the observed rms values. The rms values are regarded to be representative for a Gaussian distribution, and can be used to find the 95% range of the distribution. The classes, labelled A, B, C, and D, are listed in Table A.6, together with the percentage of the analysed interferograms which fall in this range. Table A.5 indicates for each interferogram to what category it belongs.

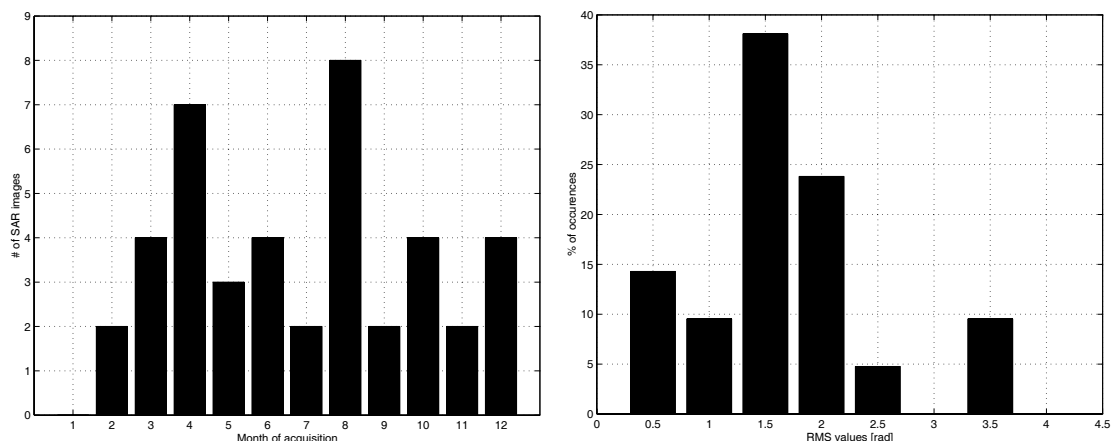


Figure A.6 A) Histogram showing the number of analysed SAR images, ordered by the month of acquisition. B) Histogram showing the *rms* values of the interferograms in the database and the frequencies of occurrence

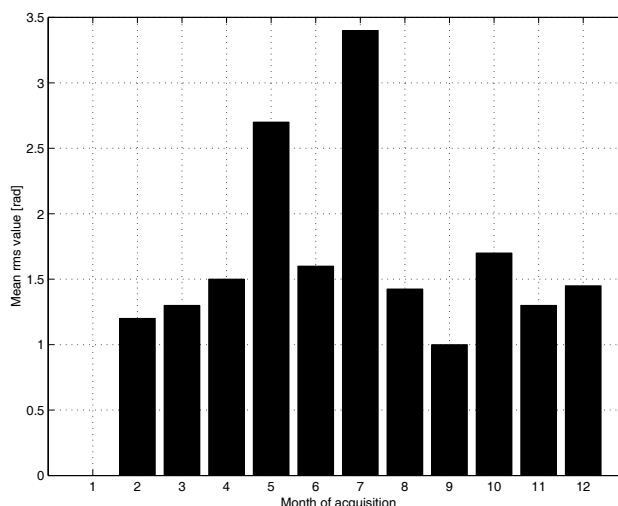


Figure A.7 Histogram showing the mean rms values, ordered by the month of acquisition



Table A.5

Statistics and observations in the interferograms. The rms values are listed, as well as the magnitude class, see Table A.6. Only cumulus or cumulonimbus clouds are indicated in the cloud category. Waves are observed mostly at small parts of the image. Striation indicates clear anisotropic behaviour of the observed patterns. Localized anomalies are defined as artefacts with a spatial extent of 20 km or less, and a phase disturbance of 2 rad or more. The keyword column describes special features of the interferogram.

<i>ID</i>	<i>rms (rad)</i>	<i>class</i>	<i>cloud</i>	<i>waves</i>	<i>striation</i>	<i>localized anomalies</i>	<i>keyword</i>
gd1	3.4	D	Cb		yes	yes	cells
gd2	1.5	B			yes	yes	pearls
gd3	1.6	C					dog ear
gd4	0.6	A		yes	yes		x-waves
gd5	1.4	B		yes	yes	yes	
gd6	1.8	C	Cu		yes	yes	cells
gd7	1.8	C	Cu		yes	yes	cells
gdex2	1.9	C		yes		yes	corner
cd1	1.0	B	Cb		yes	yes	cells
fd1	1.7	C	Cu		yes	yes	bean,cells
fd2	1.3	B	Cu	yes		yes	cells
fd3	1.3	B				yes	gradient
fd4	1.8	C	Cb			yes	cells
fd5	0.7	A				yes	
fd6	0.5	A		yes	yes		
fd7	1.7	B	Cu	yes	yes	yes	cells
fa1	2.0	C	Cu			yes	cells,intrusion
fa2	3.6	D	Cb			yes	sickle,line,cells
fa3	2.5	C		yes		yes	ramp
fa4	1.3	B				yes	intrusion
fa5	1.2	B		yes		yes	cells

Table A.6

Classification of the magnitude of atmospheric disturbance

Class	rms (rad)	95% range (rad)	Percentage
A	$< \pi/4$	$[0, \pi]$	14%
B	$[\pi/4, \pi/2]$	$[\pi, 2\pi]$	38%
C	$[\pi/2, \pi]$	$[2\pi, 4\pi]$	38%
D	$\pi <$	$[4\pi, \infty]$	10%

Based on the *type* of disturbance, *localized anomalies* are defined as those disturbances which occur on a spatial scale of less than 20 km, and have a magnitude of more than 2 radians. Within this definition, 17 of the 21 (combined) interferograms displayed this type of artefacts. These interferograms are listed in Table A.5. Furthermore, in the table it is shown if wave effects are observed. Waves have been observed perpendicular as well as parallel to the wind direction at some heights. These effects are mostly localized, and relatively small. Wave effects are observed in 8 of the 21 interferograms. Another effect is *striation*--where almost the whole interferogram is covered by a pattern with a clear orientation. Sometimes these effects could be defined as moisture transport in a more or less laminar flow. The possibility to find an orientation in the effects occurred in 10 of the 21 interferograms. Finally, one or two *keywords* have been chosen, which reflect the peculiarities of a specific interferogram. *Cells* occur most often, and indicate localized phase artefacts, which are quite discernible from the background. *Pearls* is a keyword for the 'string of pearls' effect, where a pattern is formed by many small circular anomalies, often aligned in a certain direction. The *dog ear* is specific for gd3, and shows a peculiar anomaly in the corner of the interferogram. The effect labelled *x-waves* shows wave-like effects in more than on direction. All other keywords refer to the shape of the observed anomalies.

An interesting relation is found by listing all the observations of cumulus or cumulonimbus clouds in Table A.5. It appears that in all cases in which these cloud types were observed, *cells* were observed in the interferogram. From this observation, it may be concluded that this type of cloud cover indicates strong local variations in relative humidity, which has a considerable influence on the SAR interferograms.

Atmospheric influences are observed in each of the 26 interferograms. The observed spatial scales reach from hundreds of meters to 100-200 km. For scales reaching the full image size it is difficult to discern them from errors in the satellite orbits. The magnitude of the effects is expressed in an rms value or in the extreme values observed in the interferogram. Observed rms values, obtained over a significant part of the image, reach from 0.5-3.6 radians. Assuming a Gaussian distribution, this implies that 95% of the observed phase values varies over a minimal range of 0.3 phase cycles up to a maximal range of 2.3 phase cycles. Extreme ranges of 4 phase cycles are found during thunderstorms at the two SAR acquisitions.

Observed atmospheric signatures are *isolated anomalies* with a spatial extent of 20 km or less, and a phase disturbance of 2 radians or more (in 18 of the 21 interferograms), *striation*, a pattern of linear features over a significant portion of the interferogram, (in 10 of the 21 interferograms), *wave effects*, identified as gravity waves or cloud/moisture streets with an amplitude mostly less than 1 phase cycle (in 8 of the 21 interferograms), *Frontal zones*, from smooth gradients to a very distinct 'wave crest' with a wavelength of just some 5 kilometres (in 5 of the 21 interferograms) and *overall atmospheric variation* which is observed in most of the interferograms. This is phase variation of a limited magnitude, and with varying wavelengths, perhaps best described as a 'bumpy' surface. This effect might be closely connected with turbulent behaviour of air and its constituents.

#### A.1.4.4 Atmospheric Phase Screen retrieval

Ferretti *et al.* (1996, 1998, 1999b, 1997, 2000, 2001); Refice *et al.* (2002) have shown that it is possible to retrieve the spatial atmospheric delay signal, referred to as the Atmospheric Phase Screen (APS) as a by-product of the permanent scatterers approach. In this approach a large set (more than, say, 30 images) is coregistered very accurately to a common master image. A priori known topography is subtracted from these data. By selecting single stable coherent points from the time series, often with characteristics similar to a corner-reflector, it is possible to estimate residual topography and linear deformation per interferogram with a submeter and millimetre accuracy, respectively. The residual signal after this estimation consists of atmospheric variability, non-linear motion and random noise. First, per point, a low frequency signal is estimated in time which is attributed to non-linear motion, since the atmospheric signal is assumed to be uncorrelated in time. Second, the residual (high-pass filtered) signal per interferogram is interpolated using a smoothing filter, ideally with characteristics similar to the expected atmospheric variability, but also a moving average window with a  $2 \times 2$  km window can be efficiently used. The interpolation result is assumed to be the interferogram APS, and the residues are considered to be point noise per pixel per interferogram.

By averaging all *interferogram* APS estimations an estimation of the *acquisition* APS of the master can be obtained. The accuracy of this estimation can be expressed by the structure function of the expected atmospheric signal variability per image divided by the number of images. This master APS is then subtracted from the interferogram APS estimations to obtain the *acquisition* APS of every slave image, with the same expected accuracy.

This methodology has been applied for sets of permanent scatterers in a number of test sites. Since most of the currently reported areas where rather small, on the order of  $10 \times 10$  km, a meteorological interpretation of the signal is very difficult. Small and mesoscale atmospheric structures such as cumulonimbus clouds and fronts can be easily detected in data which are at least  $50 \times 50$  km, since most of the additional meteorological sensors lack the resolution or the temporal coincidence.

#### A.1.5 Feasibility and challenges

Satellite radar interferometry can be applied to study vertically integrated atmospheric refractivity variations with a spatial resolution of 20 m and an accuracy of  $\sim 2$  mm, irrespective of cloud cover or solar illumination, over most land areas. Therefore, Interferometric Radar Meteorology (IRM) is a new technique for meteorological applications and atmospheric studies. The data are derived from the difference between the radar signal delay variations within the imaged area during two acquisitions with a temporal separation of one or more days. Hence, they reflect the **superposition** of the refractivity distribution during these two acquisitions. On short spatial scales integrated refractivity variations appear to be dominantly caused by spatial heterogeneities in the water vapour distribution, only slightly modulated by influences of liquid water and temperature. Hydrostatic delay gradients can be commonly ignored, as well as ionospheric influences for C-band radar.

The configuration of contemporary SAR satellites is currently far from optimal for operational meteorology. This is mainly due to the generally **infrequent repeat-**

**acquisition interval.** A related problem is the superposition of two atmospheric states: the **acquisition ambiguity**. It has been shown, however, that the interferometric combination of a series of SAR acquisitions can be used to identify the atmospheric influence per single acquisition (Ferretti *et al.*, 2000). Power consumption, high data rates, and significant signal processing effort form another challenge for **real-time operational applications**.

Nonetheless, IRM can be readily used for studying atmospheric dynamics such as mesoscale shallow convection (MSC), and provides unsurpassed insights, particularly in mapping the small-scale water vapour distribution. The main advantage of the technique is the combination of its imaging possibilities with quantitative delay estimates. ESA's tandem mission (August 1995-April 1996) acquired more than 110.000 tandem interferograms covering nearly the total global land surface (Duchossois *et al.*, 1996). Since surface deformation is practically excluded in these data, and topography can be considered known for many areas (especially after the data release from the SRTM mission, almost all of these interferograms can be used for atmospheric studies.

There are a number of limitations for the application of IRM. First, the technique is only applicable over land or ice areas. Second, whereas the time interval between the acquisitions should be as short as possible to reduce possible temporal decorrelation and optimise coherence, it has to be long enough to allow for the necessary atmospheric decorrelation. In other words, there needs to be some change in the atmospheric refractivity distribution. The latter condition can be somewhat relaxed if acquisitions are available very frequently. Third, topography needs to be known as a DEM with a vertical accuracy of ~10 m and a spatial resolution as fine as the SAR resolution. Using the results of the SRTM mission, this is currently feasible for latitudes between 58°S and 60°N. If the area is characterized by large elevation differences, atmospheric signal due to vertical stratification needs to be accounted for. Fourth, satellite orbits need to be of sufficient quality to remove residual phase gradients as good as possible, and to prevent DEM scaling errors. Very reliable orbit control allows for the retrieval of hydrostatic gradients. An ideal future system would benefit from a wide swath, e.g. by applying a ScanSAR mode, and could operate with a reduced spatial resolution. Such a system would have unique complementary characteristics with conventional meteorological techniques. Specific challenges are to improve the separation of temperature and water vapour pressure, the effect of droplets, and the effect of the ionosphere, to resolve the acquisition ambiguity, and to obtain more information of the three-dimensional distribution of refractivity.

## A.2 IDENTIFICATION OF VARIABLES AND TECHNIQUES

### A.2.1 Introduction

In the previous section it has been argued that Interferometric Radar Meteorology can be used to study vertically integrated atmospheric refractivity variations with a spatial resolution of 20 m and an accuracy of ~2 mm, irrespective of cloud cover or solar illumination. This potential enables new insights in atmospheric dynamics, such as mesoscale shallow convection and boundary layer structure.

In this section an overview is given of the possible atmospheric variables that influence interferometric phase observations, the potential for their estimation, their potential relevance, and possible retrieval techniques. It describes the scientific challenges and opportunities and suggests a number of case studies to demonstrate the proposed techniques.

### A.2.2 Overview of atmospheric variables

Variability in the atmospheric interferometric phase due to atmospheric delay,  $\delta_{ijt}^{IFG}$ , is due to the temporally and spatially heterogeneous distribution of refractivity, which can be written as a double-difference (in time and space) of the integrated refractivity

$$\delta_{ijt}^{IFG} = \frac{\partial}{\partial t} \frac{\partial}{\partial x} \int N(x, z, t) dz, \quad (\text{A.2.1})$$

where  $N$  is the refractivity as a function of altitude  $z$ , planar coordinates  $x$ , and time  $t$  (see also previous section). The spatial delay signal at time  $t_i$  is essentially a relative measurement with respect to an arbitrarily chosen reference point. There is a strong spatial correlation in  $\frac{\partial}{\partial x} \int N(x, z, t) dz$ . The differentiation with respect to time expresses the differencing of the two SAR acquisitions. For time intervals of  $\partial t > 1$  day (currently the shortest observed interval using the ERS-1/2 tandem mission) we assume no correlation between the signals. The refractivity can be decomposed into different constituents:

$$N([x, z, t]) = f(P[.], T[.], e[.], W[.], n_e[.]) + \varepsilon \quad (\text{A.2.2})$$

or in signal, trend, and noise components as

$$N([x, z, t]) = f(T[.], e[.]) + \underbrace{S(P[.])}_{\text{deterministic}} + \varepsilon(W[.], n_e[.]) \quad (\text{A.2.3})$$

These equations show that refractivity is decomposed of pressure,  $P$ , temperature,  $T$ , partial water vapour pressure,  $e$ , liquid water content,  $W$ , and ionospheric density,  $n_e$ . If these constituents would be independent, the integrated refractivity would be a sum of integrations over all constituents. Due to the correlation between the variables, this

is not possible. However, we can make a distinction between some of the parameters. A commonly used decomposition is in the hydrostatic (dry) delay and the *wet* delay.

#### **A.2.2.1 Hydrostatic delay**

By using readily available pressure measurements over the area of interest, we can estimate the contribution of the hydrostatic delay. It needs to be noted that the absolute hydrostatic delay is in the null space of the double difference observations, only lateral variability which is different in both images will be observed. Since pressure is a smoothly variable parameter which is well known from synoptic observations, it is of relatively poor importance to be estimated using interferometry. Therefore, in first instance it can be regarded deterministic and corrected for in the processing.

In the literature study (Chapter A.1) it was assumed that liquid water content (hydrometeors) composes a relatively small contribution to the delay variability. In the following we will analyse this in more detail, and, in chapter A.4 we will show case studies on the influence of liquid water on the total delay.

#### **A.2.2.2 Ionospheric gradients**

Ionospheric gradients are negligible for C-band radar except perhaps for polar areas. Reported influences have very long wavelengths and do not affect small scale variability in the delay (see Hanssen, 2001, pp.209-215, for a detailed discussion on ionospheric signal).

#### **A.2.2.3 Temperature and water vapour**

This leaves temperature and partial water vapour pressure as possible quantities of interest. Due to their correlation in the wet delay, their influence can only be jointly estimated. However, the signal delay is much more sensitive to water vapour variability than to temperature changes. See the literature review for a detailed discussion.

From a meteorological point of view, water vapour is the least understood parameter in atmospheric dynamics. Spatial resolutions are relatively poor (1 km and up) whereas radiometer measurements only observe the upper layers of the troposphere. Fine resolution observations obtained by InSAR, with high accuracies and of the entire atmospheric column are therefore valuable contributions to improved atmospheric understanding.

#### **A.2.2.4 Influence of hydrometeors**

The propagation delays induced by hydrometeors such as raindrops, snow, hail and cloud droplets have a small but detectable effect on the InSAR observations. It was shown that there is an increase in the zenith delay, as measured by SAR, associated with rain showers (Hanssen, 2001). Even though the most of the delay in this case is probably caused by the evaporation it is still important to estimate the contribution of the scattering on hydrometeors to the total signal delay.

Forward scattering from distributed hydrometeors causes a phase delay of a propagating wave. If weather radar data are available at the areas and times of the analysed SAR acquisitions, we will follow the following approach to quantify this effect.

In case of propagation through a medium filled with uniformly distributed scatterers, one can calculate the propagation phase as (Oguchi, 1983):

$$\varphi_{hv} = 10^{-3} 2 \frac{\pi}{k} \int \text{Re}(f_{h,v}(D)) N(D) dD \quad (\text{A.2.4})$$

where  $\varphi_{hv}$  is the propagation phase in  $\text{rad/km}$ ,  $k = \frac{2\pi}{\lambda}$ ,  $\lambda$  is the wavelength and  $N(D)$  is the number concentration per cubic meter and  $D$  is the equivolumic drop diameter.

The number concentration can be estimated from the rain measurements provided by weather radars. It is usually assumed to have an exponential form:

$$N(D) = N_0 e^{-\Lambda D} \quad (\text{A.2.5})$$

where  $N_0 = 8000 \text{ mm}^{-1} \text{ m}^{-3}$  where the slope  $\Lambda$  (Marshall and Palmer, 1948) is related to rainfall rate given in  $\text{mm h}^{-1}$  as:

$$\Lambda = \frac{4.1}{R^{0.21}} \quad (\text{A.2.6})$$

Finally we should calculate the scattering properties for different raindrop sizes and to determine the forward scattering amplitude  $f_{h,v}(D)$  in millimetres.

For this study we use weather radar measurements, see section A.4.6, to retrieve rain rates. By knowing the rain rates we can estimate the contribution of hydrometeors to the delay measurements. This can be used to calculate the error budget of our water vapour measurements as well as to reduce this effect on the measurements.

### A.2.3 Retrieval Techniques

Potential retrieval techniques for estimating atmospheric variables can be categorized in three categories:

- atmospheric interferograms,
- single master stacking, and
- cascaded interferograms.

For the second option, single master stacking there are two sub options: contiguous area interferometry and permanent scatterers interferometry. In this section, the basic ideas, limitations, and possibilities of each option is discussed.

### A.2.3.1 Atmospheric interferograms

The first option, atmospheric interferograms, refers to the conventional interferometry approach. A differential interferogram is created, where either an a priori DEM is subtracted or an interferometric DEM is calculated and subtracted in the three-pass mode. Under the assumption of zero deformation, this product will reflect double-difference atmospheric delay variability, which can be interpreted from a meteorological point of view. Using an a-priori DEM, its accuracy should be taken into account when assessing the quality of the atmospheric interferogram. Depending on the perpendicular baseline the influence of DEM errors can propagate into the interpretation accuracy. Using the three-pass method is not preferred, since it introduces a third and independent atmospheric signal that will be scaled (up or down) to match the height ambiguity of the atmospheric pair and hereby contaminate this atmospheric interferogram. If three-pass differential interferometry is the only means of extracting topography, the consequences should be well analysed.

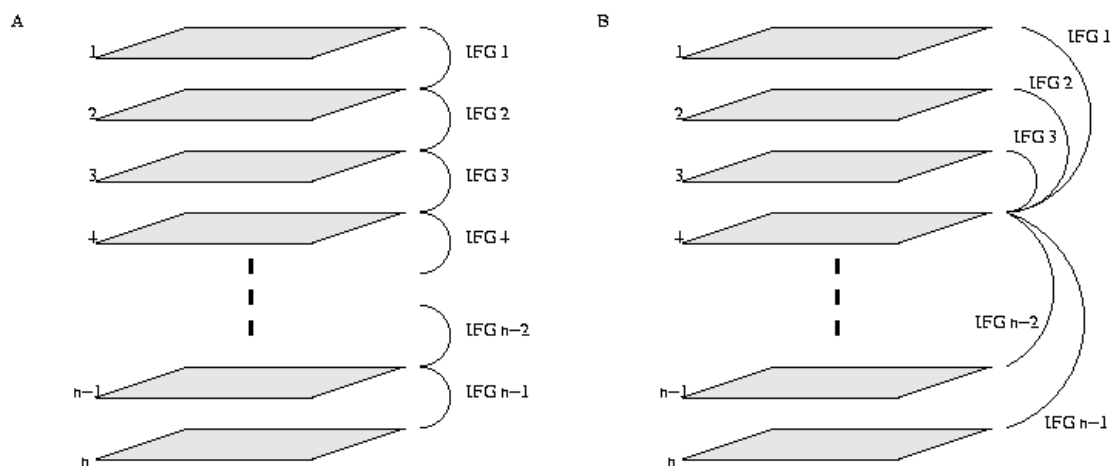


Figure A.8: A: cascaded interferograms. B: single master stack

The advantage of an atmospheric interferogram is that it can be composed of acquisitions with a short temporal baseline, and preferably a short perpendicular baseline. An ideal atmospheric interferogram would have zero-baseline and a temporal interval that is just enough to ensure complete decorrelation between the two atmospheric states, usually between 4 and 12 hours time difference. The interval for complete atmospheric decorrelation depends strongly on the meteorological conditions during the acquisitions, making general statements on the decorrelation time difficult.

Interpretation of atmospheric interferograms is easy when prominent atmospheric features, anomalies, are apparent in one of the two images. As long as the same type of anomaly is not present in both images (in this case the two would cancel each other in the interferogram), interpretation is possible, be it qualitatively.

The main limitation of atmospheric interferograms is its inherent ambiguity caused by the differencing of two acquisitions, referred to as the acquisition ambiguity. Although the sign of an anomaly, positive or negative, can often be used to attribute it



to one of the two images, using some a priori physical knowledge about the phenomenon, this is more difficult whenever the signal amplitude decreases or when strong anomalies are present during both image acquisitions. This is currently the most stringent limitation of differential atmospheric interferograms.

The second and third category of retrieval techniques are both based on the use of several acquisitions of a certain scene to suppress the effect of the acquisition ambiguity. Their difference lies in the method to do this.

### A.2.3.2 Single master stack

The single master stack approach computes interferometric differences of all acquisitions with one single ‘master’ image. For  $N+1$  SAR acquisitions (0 to  $N$ ), this results in  $N$  interferograms ( $I_1$  to  $I_N$ ) which are correlated since they all contain the same atmosphere of the master image. If  $t_1$  represents the atmospheric component of the phase value of a pixel in the master image, and  $S_1$  is the atmospheric signal for that pixel, we obtain

$$\begin{bmatrix} t_0 - t_1 \\ t_0 - t_2 \\ \vdots \\ t_0 - t_N \end{bmatrix} = \begin{bmatrix} I_1 \\ I_2 \\ \vdots \\ I_N \end{bmatrix} = \begin{bmatrix} S_0 - S_1 \\ S_0 - S_2 \\ \vdots \\ S_0 - S_N \end{bmatrix} \quad (\text{A.2.7})$$

Note that  $t_1$  does not necessarily to be the first image in time. Selection criteria for choosing  $t_1$  are based on its position in the baseline plot, preferably centered both in terms of perpendicular and temporal baselines, to ensure minimal decorrelation. Depending on the situation other considerations, such as Doppler centroid and stability and precise orbit availability might be important.

In matrix notation this is

$$\begin{bmatrix} I_1 \\ I_2 \\ \vdots \\ I_N \end{bmatrix} = \begin{bmatrix} 1 & -1 & & \\ & 1 & \ddots & \\ & & \ddots & \\ 1 & & & -1 \end{bmatrix} \begin{bmatrix} S_0 \\ S_1 \\ \vdots \\ S_N \end{bmatrix} \quad (\text{A.2.8})$$

where we assume in first instance that

$$E\left\{ \begin{bmatrix} S_0 \\ S_1 \\ \vdots \\ S_N \end{bmatrix} \right\} = \begin{bmatrix} 0 \\ 0 \\ \vdots \\ 0 \end{bmatrix}, \text{ and } D\left\{ \begin{bmatrix} S_0 \\ S_1 \\ \vdots \\ S_N \end{bmatrix} \right\} = \sigma^2 \begin{bmatrix} 1 & 0 & \dots & 0 \\ 0 & 1 & \ddots & \vdots \\ \vdots & \ddots & \ddots & 0 \\ 0 & \dots & 0 & 1 \end{bmatrix}. \quad (\text{A.2.9})$$

In other words, the relative atmospheric delay with respect to a reference pixel can be positive or negative, with expectation 0, while its dispersion is uncorrelated and equal for every acquisition.

As a result, the expectation value and dispersion of the interferograms is

$$E\left\{\begin{bmatrix} I_1 \\ \vdots \\ I_N \end{bmatrix}\right\} = \begin{bmatrix} 0 \\ \vdots \\ 0 \end{bmatrix}, \text{ and } D\left\{\begin{bmatrix} I_1 \\ \vdots \\ I_N \end{bmatrix}\right\} = \sigma^2 \begin{bmatrix} 2 & 1 & \cdots & 1 \\ 1 & 2 & & 1 \\ \vdots & & \ddots & \vdots \\ 1 & 1 & \cdots & 2 \end{bmatrix}. \quad (\text{A.2.10})$$

There is a strong correlation between the interferograms due to the common master image.

The obtained stack of interferograms is aligned to the master image and can be summed to

$$\begin{aligned} A &= \frac{1}{N} \sum_{i=1}^N I_i = \frac{1}{N} \begin{bmatrix} 1 & \cdots & 1 \end{bmatrix} \begin{bmatrix} I_1 \\ \vdots \\ I_N \end{bmatrix} \\ &= \frac{1}{N} \begin{bmatrix} 1 & \cdots & 1 \end{bmatrix} \begin{bmatrix} 1 & -1 & & \\ & 1 & & \ddots \\ \vdots & & \ddots & \\ 1 & & & -1 \end{bmatrix} \begin{bmatrix} S_0 \\ S_1 \\ \vdots \\ S_N \end{bmatrix} \\ &= S_0 + \frac{1}{N} \begin{bmatrix} -1 & \cdots & -1 \end{bmatrix} \begin{bmatrix} S_1 \\ \vdots \\ S_N \end{bmatrix} \\ &= S_0 + e \end{aligned} \quad (\text{A.2.11})$$

where we assume that the sum of all slave atmospheres (with expectation value 0) can be regarded as noise  $e$  with  $E\{e\}=0$ . Therefore, the summed stack will represent the atmosphere during the master acquisition only, and the best unbiased estimate will be

$$E\{A\} = S_0, \text{ and } \hat{S}_0 = A \quad (\text{A.2.12})$$

with variance

$$D\{\hat{S}_0\} = \sigma_{\hat{S}_0}^2 = \frac{\sigma^2}{N}. \quad (\text{A.2.13})$$

After this estimation, the atmospheric signals of the slave acquisitions can be estimated from

$$\hat{S}_i = \hat{S}_0 - I_i. \quad (\text{A.2.14})$$

Since the atmospheric variance  $\sigma^2$  is an absolute point measure, a more meaningful measure is the variance as a function of distance,  $\sigma^2(\rho)$ . Hanssen (2001) reports

$$\begin{aligned} 1 < \sigma_{I_i}(10km) < 18mm, \\ 1 < \sigma_{S_i}(10km) < 12mm, \end{aligned} \tag{A.2.15}$$

Thus, by averaging over  $N=16$  images, we expect to estimate  $\hat{S}_0$  with a standard deviation of  $0.25 < \sigma_{S_i}(10km) < 4mm$ .

The limitations of this approach are related to the coherence over the long time intervals and the necessity of many, say, more than 20 images to obtain a reasonable estimate in the averaging procedure. Furthermore, to avoid geometric (baseline) decorrelation, only a subset of the available acquisitions can be used. Topography and possible deformation signals have to be assumed known.

### A.2.3.3 Permanent scatterer stack

The limitation of the spatially contiguous coherent areas can be circumvented using the permanent scatterers approach (Ferretti *et al.*, 1999, 2000, 2001), (Hanssen and Ferretti, 2002a, 2002b). In this approach, physical scatterers are identified that have systematic phase behaviour in time. Under the assumption of uncorrelated atmospheres in time, residual elevation (topography) of the scatterers as well as systematic deformation behaviour may be estimated, leaving the atmospheric contribution as residuals on the measured signal. Again, sufficient acquisitions need to be available ( $>30$ ), although the limitations in the admissible baseline lengths is not present anymore, due to the point scattering characteristics of the permanent scatterers. Spatial interpolation of the residual signal per interferogram results in an atmospheric signal estimation, also referred to as an atmospheric phase screen. Averaging the stack results in the master atmospheric signal as described above.

Advantages of the PS method for atmospheric signal retrieval are the relaxed conditions regarding temporal and spatial decorrelation, which make the technique feasible for a whole new set of geographic areas, previously regarded unsuitable for repeat-pass interferometry. Disadvantages include the number of images necessary for the first order retrieval, considerable processing times, the spatial interpolation of the atmospheric signal (although this might not be necessary while searching for atmosphere instead of deformation). In general, over urban areas the PS density is usually sufficiently high ( $>25$  points/km<sup>2</sup>, or 1 point per 200x200 m block) to capture the atmospheric variability. A denser network does not add significantly new signal to the atmospheric phase screen (due to its power law behaviour the energy is decreasing fast over short distances), although it can improve the reliability of the estimation.

### A.2.3.4 Cascade interferograms

The third retrieval algorithm is referred to as cascade interferograms. Its use is based on the observations that (i) short time interval interferograms usually have high coherence, (ii) some interferograms show a relatively minimal amount of atmospheric phase variation (due to temperature conditions: cold air can hold less water vapour, or

more stable atmospheric conditions), (iii) if the atmospheric signal in one interferogram is known or minimal, the atmospheres in all linear combinations with images from this interferogram can be estimated uniquely. Therefore, the challenge is to find an interferogram with minimal atmospheric distortion and consecutively estimate all atmospheres in the cascade from this set.

The model for cascade interferogram atmospheric estimation is defined as

$$\begin{bmatrix} I_1 \\ I_2 \\ \vdots \\ I_N \end{bmatrix} = \begin{bmatrix} 1 & -1 & & \\ & 1 & -1 & \\ & & \ddots & \ddots \\ & & & 1 & -1 \end{bmatrix} \begin{bmatrix} S_0 \\ S_1 \\ \vdots \\ S_N \end{bmatrix} \quad (\text{A.2.16})$$

Suppose that the first interferogram exhibits minimal atmospheric distortion, that is,

$$I_1 = S_0 - S_1 \approx 0 \quad (\text{A.2.17})$$

We can write

$$\begin{bmatrix} 1 & 1 & & \\ 1 & 1 & 1 & \\ \vdots & & \ddots & \ddots \\ 1 & 1 & \cdots & 1 & 1 \end{bmatrix} \begin{bmatrix} I_1 \\ I_2 \\ \vdots \\ I_N \end{bmatrix} = \begin{bmatrix} \hat{S}_2 \\ \hat{S}_3 \\ \vdots \\ \hat{S}_N \end{bmatrix}. \quad (\text{A.2.18})$$

This can be used to obtain estimates for the atmospheric signal per acquisition. Note that it is not necessarily the first interferogram that needs to be the reference.

It is obvious that this approach is more opportunistic than the more rigorous single master approach. Nevertheless, it has the advantage that (i) the interferograms are generally more coherent due to the smallest time intervals, therefore, provide higher accuracy atmospheric parameters, (ii) that less image acquisitions may be needed to obtain an estimation, and (iii) that sub-pixel registration of the interferograms is not necessary. For both the single master and the cascaded interferogram approaches a reference atmosphere needs to be estimated only once; all future acquisitions can be estimated from this reference. Figure A.9 shows a simulation of the cascade interferogram estimation, using 9 SAR images.

#### A.2.4 Challenge

The main challenge of atmospheric parameter retrieval is to resolve the acquisition ambiguity. This step is inevitable to allow for unambiguous interpretation of atmospheric phenomena and to interest meteorologists and atmospheric scientists in the radar interferometric data. Further separation of the atmospheric constituents is currently not of prime interest, since the interpretation of the data as *wet delay* estimates with high resolution and accuracy provides sufficient new opportunities for improved insight in atmospheric dynamics. Moreover, to anticipate on possible future inclusion of radar delay data in atmospheric models does not require a separation of

constituents. In this case relative integrated refractivity field variations can be used to constraint the models.

### A.2.5 Case study planning

In the following chapters the processing and interpretation chain will be fine-tuned, and the procedure will be tested on a few test sites with different characteristics.

Processing concerns computing the differential unwrapped interferograms, using a DEM to subtract topographic signal if necessary. After single-master, PS, and cascade interferogram products are computed, the products will be analysed by subtracting a first order pressure gradient field, especially for topography. Then, the data will be further analysed using surface synoptic data, NOAA and Meteosat satellite data (VIS,WV,IR), and if available weather radar and radiosonde data. For the European sites, these data are obtained from BADC, ECMWF, or KNMI. For the US data, additional data are provided from NCAR, and NOAA, via the University of Hawaii.

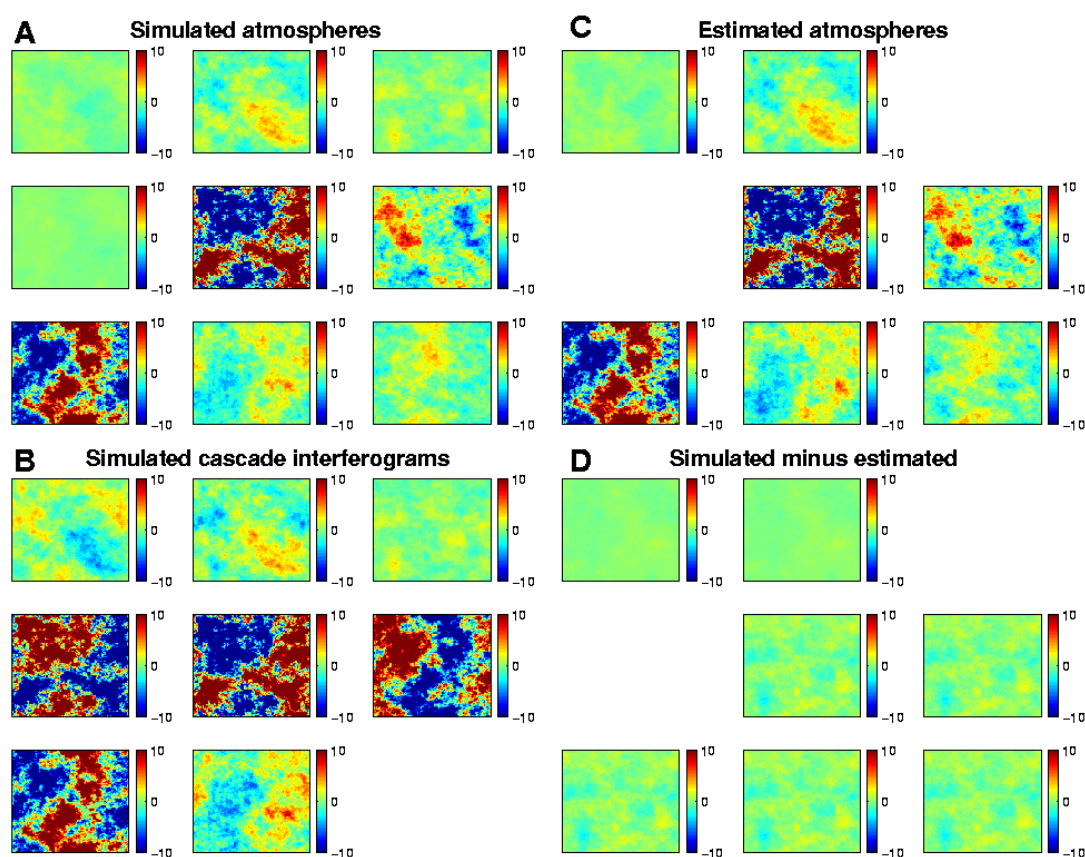


Figure A.9: Simulation of cascade interferograms approach. A: 9 simulated atmospheric signals in SAR images, simulated using power law regimes. Intensity of the atmospheric signals is randomly estimated from a Chi-squared distribution. B: 8 cascade interferograms derived from differencing the 9 SAR images. C: estimated atmospheric phase screen for every SAR acquisition time, except the ones corresponding to the interferogram with minimal phase variance. Compare C with A. D: Difference between simulated and estimated.

The PS method will be performed on the city of Berlin, where more than 60 datasets are available. Atmospheric phase screens will be computed using different *Kriging* procedures.

The contiguous stacking and cascaded interferograms will be performed on an area around Las Vegas, Nevada, using ERS acquisitions and over the big island of Hawaii, using Radarsat acquisitions. For the Las Vegas site the expected coherence is high, as observed in earlier studies. A sufficient amount of data is available but a definite selection is still to be made. The Hawaii site is characterized by high correlation (almost no vegetation on the higher parts of the volcano) and a large number of ancillary meteorological data available. 48 Radarsat acquisitions with various look angles are available, between September 2000 and June 2003.

## A.3 ELECTROMAGNETIC INTERACTION MODELING

### A.3.1 Introduction

In the previous part of this study, during which atmospheric variables and techniques of interest were identified, it has been shown that the lead variable of interest for this study is the integrated refractivity per acquisition. Even though the refractivity can be decomposed into water vapour, temperature, pressure, electron density, and hydrometeors, it is the inherent acquisition ambiguity (the superposition of two atmospheric states per interferogram) that limits the interpretation of the data.

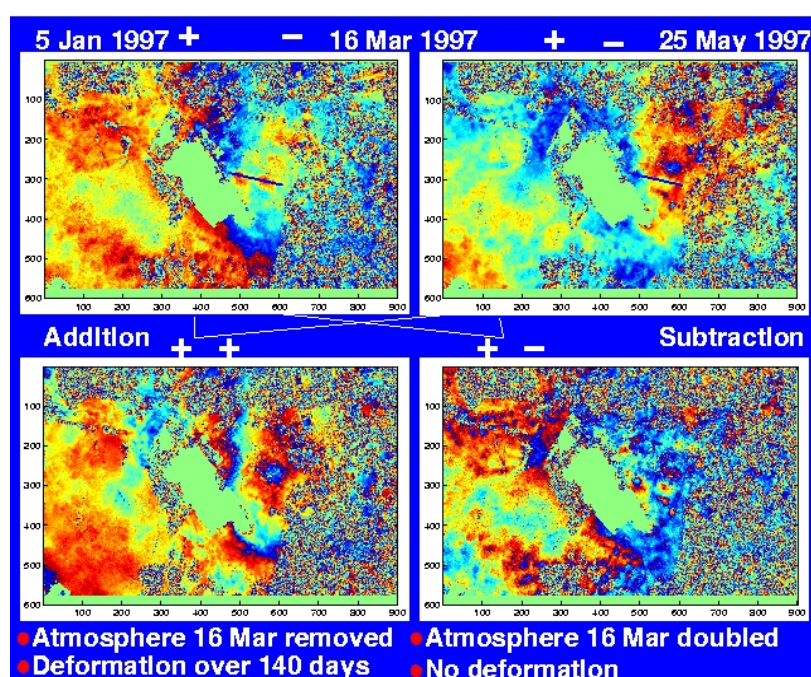


Figure A.10 Example of the acquisition ambiguity. By adding and subtracting two interferograms with a common image the atmosphere of that acquisition is either removed or doubled.

An example demonstrating the influence of the acquisition ambiguity is given in Figure A.10. Three SAR acquisitions have been used to create two interferograms, shown as the upper two images. In the first interferogram (*January-March*), the March acquisition is subtracted from the January acquisition. In the second interferogram (*March-May*), the March acquisition has a positive sign, since the May acquisition is subtracted from the March acquisition. As a result, in the summation of the two interferograms the March acquisition cancels, since  $(January - March) + (March - May)$  is equal to  $(January - May)$ . Hence, in that product, the lower left figure, the atmosphere of the March image is removed. Since there was surface deformation during these images, the surface deformation over the Jan-May period is visible. The subtraction of the two interferograms, in the lower right yields  $(January - March) - (March - May)$  which is equal to  $(Jan - 2 \times March + May)$ . As a result, all three

atmospheric states are visible in this combination, but the March acquisition is amplified by a factor of two, making it more prominently visible. Nevertheless, with three acquisitions and two interferograms it is still not possible to isolate the atmospheric phase screen belonging to one single acquisition uniquely.

In this report we focus on the electromagnetic interaction models for the atmospheric propagation. A forward model is presented indicating how, based on a spatial distribution of atmospheric parameters, the delay signal or atmospheric phase screen can be derived. This is presented both in a deterministic as well as a stochastic way, simulating a random turbulent atmosphere and its effect on the interferogram. Furthermore, we present further forward modelling studies on the propagation effects due to hydrometeors.

### A.3.2 Forward model: the deterministic case

Atmospheric signal in the radar interferograms manifests itself as a double-difference of slant-integrated refractivity: spatial variability within a radar scene is differenced between two acquisitions. This implies that the total delay signal, regarded as a mean value and variability around that mean, cannot be measured.

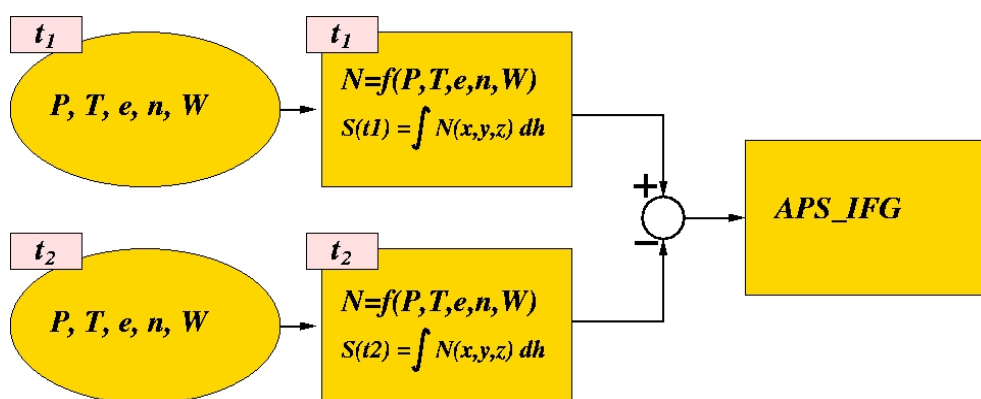


Figure A.11: Forward model for determining the interferometric atmospheric phase screen (APS\_IFG) from the atmospheric parameters.

The forward model can be sketched as in Figure A.11, cf. also section A.3 of WP21. In this scheme it is shown how the atmospheric parameters

- Pressure  $P$  [hPa],
- Temperature  $T$  [K],
- Relative water vapour pressure  $e$  [hPa],
- Electron density  $n$  [electron number/m<sup>3</sup>], and
- Liquid water  $W$  [g/m<sup>3</sup>] (and/or rain rate)

which are all a function of their three dimensional position  $(x, y, z)$  and time  $t$ , are combined to form the refractivity  $N(x, y, z, t)$ , via



$$N(x, y, z, t) = k_1 \frac{P}{T} + \left( k_2' \frac{e}{T} + k_3 \frac{e}{T^2} \right) - 4.028 \times 10^7 \frac{n_e}{f^2} + 1.45W \quad (\text{A.3.1})$$

where  $k_1 = 77.6$ ,  $k_2' = 23.3$ , and  $k_3 = 3.75 \times 10^5$  (Smith and Weintraub, 1953, Thayer, 1974).

If the refractivity field  $N(x, y, z, t = t_1)$  is known at the time of the first radar acquisition, we can calculate the delay per pixel by

$$S_k^{t_1} = 10^{-6} \int_0^\infty \frac{N(x, y, z, t_1)}{\cos \theta_{inc}} dh \quad (\text{A.3.2})$$

where  $\theta_{inc}$  is the incidence angle. Finally by subtracting these delay fields of the first and the second acquisition, we obtain the observed atmospheric phase screen of the interferogram, assuming that topographic, orbital, and deformation fringes have been accounted for:

$$APS_{IFG} = S_k^{t_1} - S_k^{t_2} \quad (\text{A.3.3})$$

Even though this forward model is rather exact, it is obvious that it relies on the condition that the five main contributions,  $P, T, e, n, W$  are known at every location and time. Even though most parameters are quite correlated in space and time, one should think of a minimum block size of, say, 50x50x50 m and a temporal resolution of, say, 30-60 minutes to obtain reasonable estimates of integrated refractivity per radar acquisition. This will never be possible using the currently available meteorological observation techniques and numerical models. For example a high resolution numerical weather prediction model uses block sizes of about 20 km horizontally.

Recognizing that application of the forward model sketched above to real-life situations is currently not possible in a deterministic setting, the question is whether it is possible to devise a forward model in a stochastic sense.

### A.3.3 Precipitation: hydrometeor analysis

The influence of liquid water (droplets and hydrometeors/precipitation) on the refractivity can be modelled as

$$N_{liq} = 10^{-3} \frac{2\pi}{k^2} \int_0^8 \text{Re}(f(D)N(D))dD \quad (\text{A.3.4})$$

where  $k$  is the wavenumber ( $k = 2\pi / \lambda$ , where  $\lambda$  is the 5.6 cm wavelength),  $f(D)$  is the forward scattering amplitude in millimetres,  $N(D)$  is the drop size density [ $\text{mm}^{-1}\text{m}^{-3}$ ], and  $D$  is the equivolumetric drop diameter in millimetres. Equivolumetric implies that we consider the diameter of a sphere with the same volume as the oblate spheroidal droplet. Note that we need the total distribution of both drop size and forward scattering amplitude.

The forward scattering amplitude is given as a function of the equivolumetric droplet diameter  $D$ , given for a horizontally polarized incidence angle by (Van de Hulst, 1959):

$$\begin{aligned}
 f(D) &= \frac{k^2}{24} D^3 (\varepsilon - 1) \chi \\
 \chi &= \frac{1}{1 + \lambda(e - 1)} \\
 \lambda &= \frac{1 - \lambda_3}{2} \\
 \lambda_3 &= \frac{1 + f^2}{f^2} \left(1 - \frac{1}{f} \tan^{-1} f\right) \\
 f &= e^{-2} - 1 \\
 e &= \begin{cases} 1.03 - 0.062D & 1 \leq D \leq 8 \\ 1 & 0 < D < 1 \end{cases}
 \end{aligned} \tag{A.3.5}$$

Thus, in the equation we integrate over all equivolumetric drop diameters  $D$  between 0 and 8 mm. In the definition of the forward scattering amplitude we used the conventional approach of modelling all raindrops that are larger than 1 mm as oblate spheroids. The value  $e$  is the ratio between the horizontal and the vertical axis of the spheroid, which is related to the equivolumetric drop size  $D$  (Pruppacher and Beard, 1970). The relative permittivity of water is denoted by  $\varepsilon$ , which is a complex value.

The drop size density  $N(D)$  can be written as a function of the equivolumetric drop diameter and the rain rate:

$$N(D) = N_0 \exp(-4.1R^{-0.21}D) \quad \text{for } 0 < D < 8 \tag{A.3.6}$$

where we denote the rain rate by  $R$ , given in mm/hr, and  $N_0 = 8000 \text{ mm}^{-1} \text{ m}^{-3}$ . Thus, the entire distribution of the drop size is assumed to have an exponential form (Marshall and Palmer, 1948). Note that we assume that the rain rate remains unchanged in the entire vertical column below the melting layer.

Using these equations we can calculate the refractivity due to liquid water as a function of the rain rate  $R$  only. The equivolumetric rain drop diameter  $D$  is usually truncated in the integration at 8 mm, since particles with a larger diameter are unstable.

In Figure A.12 the result of these calculations is given. It can be seen that for high rain intensities the path delay can be as high as several centimetres.

In the case that there is no precipitation, hence no hydrometeors, there is still liquid water in the clouds. In this case, we approximate the liquid water induced refractivity as (Hanssen, 2001)

$$N_{cloud} = 1.45W$$

where  $W$  is the liquid water content given in  $\text{g/m}^3$ .

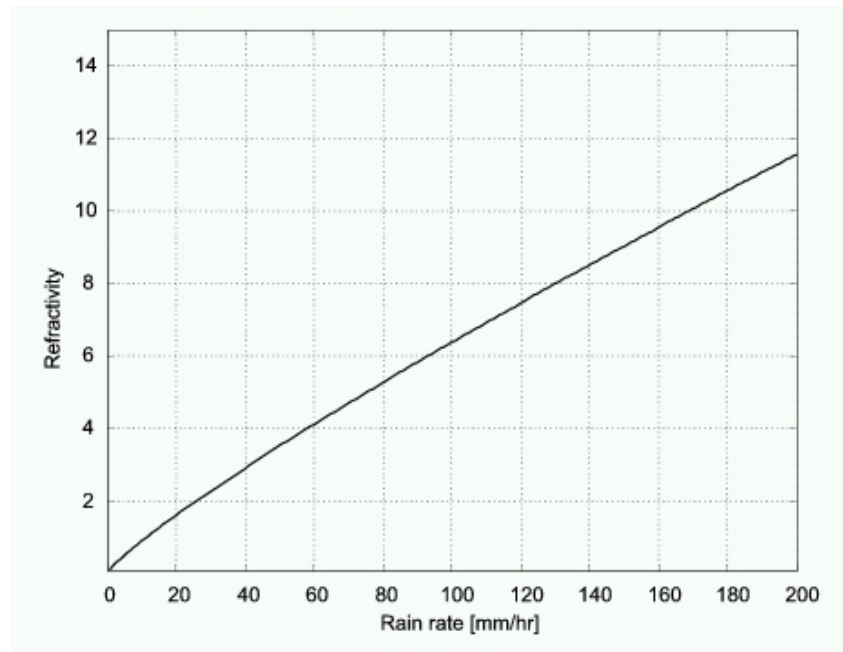


Figure A.12 Path delay as a function of the rain rate. This calculations are done for HH polarization of the transmit and receive antenna.

#### A.3.4 Forward model: the stochastic case

Previous studies have shown that atmospheric signal exhibits a scaling behaviour; the energy contained at specific spatial scales is exponentially related to the energy at different scales:

$$P_a(f) = P_0 \left( \frac{f}{f_0} \right)^{-\beta} \quad (\text{A.3.7})$$

or linearly in log-log:

$$\ln P_a(f) = -\beta \ln f + (\ln P_0 + \beta \ln f_0) \quad (\text{A.3.8})$$

where  $f$  is the spatial wavenumber,  $P_0$  and  $f_0$  are normalizing constants, and  $-\beta$  is the spectral index. Alternatively, this relation can be expressed by the structure function, covariance function, or 2D fractal dimension. All three expressions are valid within a limited range of scales due to physical restrictions.

Based on atmosphere-only, 1-day interval interferograms over relatively flat areas, it has been shown that atmospheric signal exhibits a scaling behaviour in two distinct regimes (Hanssen, 2001). For spatial scales less than the effective turbulent tropospheric thickness, say 2-5 km, the spectral index is close to -8/3, whereas for larger scales up to the interferogram sizes the spectral index decays to -5/3 and smaller. In fact, due to the removal of nearly linear trends induced by orbit errors the spectral index flattens over long distances. Thus, we have

$$P_a(f) = \begin{cases} P_0 \left( \frac{f}{f_0} \right)^{-\frac{8}{3}} & \text{for } 0 \leq \frac{f_0}{f} < 2 \text{ km} \\ P_0 \left( \frac{f_0}{2} \right) \left( \frac{f}{f_0} \right)^{-\frac{5}{3}} & \text{for } 2 \leq \frac{f_0}{f} < 50 \text{ km} \end{cases} \quad (\text{A.3.9})$$

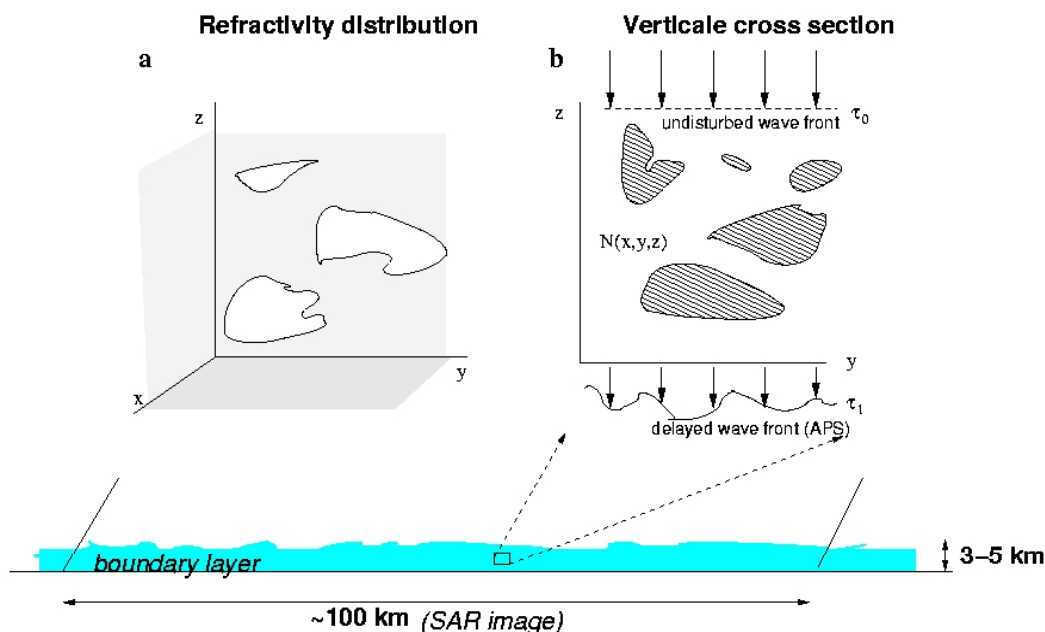


Figure A.13 The boundary layer is effectively a 2D medium. 3D characteristics are only expected for spatial scales less than 3-5 km, depending on the height of the boundary layer.

These observations correspond with Kolmogorov turbulence theory, which expects a spectral index of  $-5/3$  moving in any direction in a three-dimensional turbulent volume (Kolmogorov, 1941, Tatarski, 1961). Vertical integration of refractivity results in an atmospheric phase screen with a spectral index of  $-8/3$ . Here it is assumed that the horizontal spatial scales are less than the finite physical height of the turbulent medium, which relates to a 3D volume. Moving to larger scales, the medium becomes relatively more and more flat, effectively a thin, nearly 2D slice (Figure A.13). For these scales the roughness increases, resulting in the  $-5/3$  regime. For larger distances, further flattening of the spectra is expected.

Figure A.5, p. 13, illustrates the hypothesis of a scaling behaviour over two regimes. Independent atmospheric interferograms over an area in the Netherlands were used to obtain these observations. The flattening of the spectra at high wavenumbers is due to noise in the observations. The vertical position of these spectra is indicative for the amount of energy during that specific interferogram which is directly related to the instability of the boundary layer. It is important to note that the energy in the atmospheric signal varies over more than one order of magnitude. As a result, the

lowest spectrum in Figure A.5 corresponds with a nearly flat atmospheric phase screen.

Based on these observations we attempt to create a random filter that produces an atmospheric phase screen with a similar stochastic behaviour as the real-life situations, that is, with the  $-5/3$  and  $-8/3$  power law characteristics. Before continuing this discussion we will first look at the absolute energy to expect in the power spectra.

#### A.3.4.1 Absolute variability

The (relative) scaling behaviour of atmospheric signal as a function of distance is an elegant way for modelling or simulating an atmospheric phase screen for a radar acquisition. Nevertheless, the absolute amount of variability, expressed by the  $P_0$  coefficient, is necessary to obtain realistic values. For a specific location, it is important to know the likelihood of a specific value of the  $P_0$  coefficient. Since this is not readily available for these high spatial resolutions and accuracy, we used Zenith Total Delay variability derived from permanent GPS receivers of 138 EUREF stations over the year 2002, see Figure A.5. Hourly ZTD values were recorded with a mean standard deviation of 3.3 mm (Soehne and Weber, 2003).

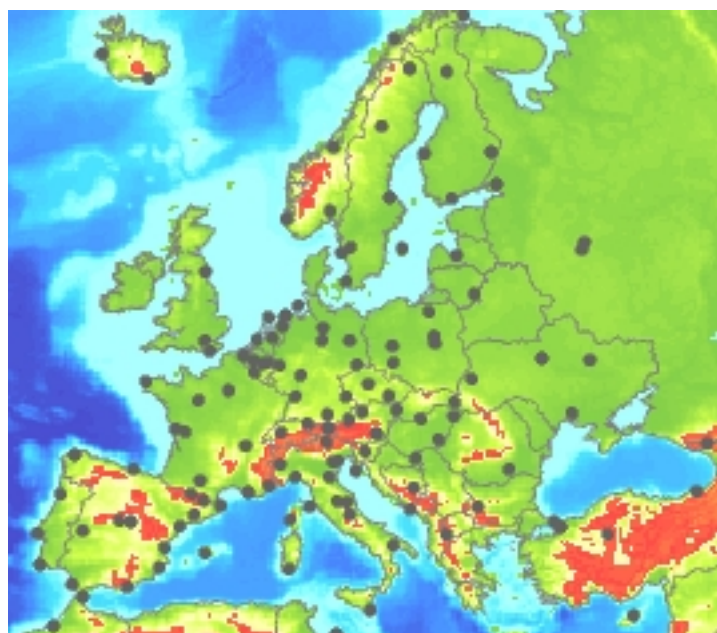


Figure A.14 The 138 permanent GPS stations of the EUREF network.

We assume that a specific weather situation can be expressed by analysing the variability of ZTD per day, using 24 measurements. This yields over 365 days of variances, which are related to instable, convective weather with much water vapour (high variances) or stable weather situations without much refractivity changes. Expressing these variances in a histogram gives an indication for the likelihood of a particular weather situation, parameterised by the delay variability. It is evident that the amount of variability during a full day is larger than during only a few hours, comparable with a spatial snapshot in an interferogram. Moreover, the GPS

observations do not reflect the small changes within the hourly sampling and use zenith averaging using satellites distributed over a wide part of the sky. Nevertheless, we assume that the obtained variances are a scaled version of the variability within a shorter time frame and over smaller spatial scales. The scale factor is not known. Under this assumption, the abundance of data in the EUREF network allows for deriving the necessary statistics.

Figure A.15 shows the histograms of the daily ZTD variability. For 114 stations with over 300 days of hourly observations, the histograms are shown in grey values. The average histogram is indicated by the bold black line. A best-fit  $\chi^2$  distribution is found for 2 degrees of freedom and a non-centrality parameter of 10, and indicated by the dashed line. The maximum likelihood value for daily ZTD variability is to be a standard deviation of 8 mm. Assuming that the distributions reflect the likelihood of a specific weather situation (in terms of electromagnetic wave propagation), it is interesting to observe that most stations show the same type of behaviour. A standard deviation of 3-4 cm or more has only a small likelihood, whereas most of the variability seems to be in the range 2 mm to 2 cm.

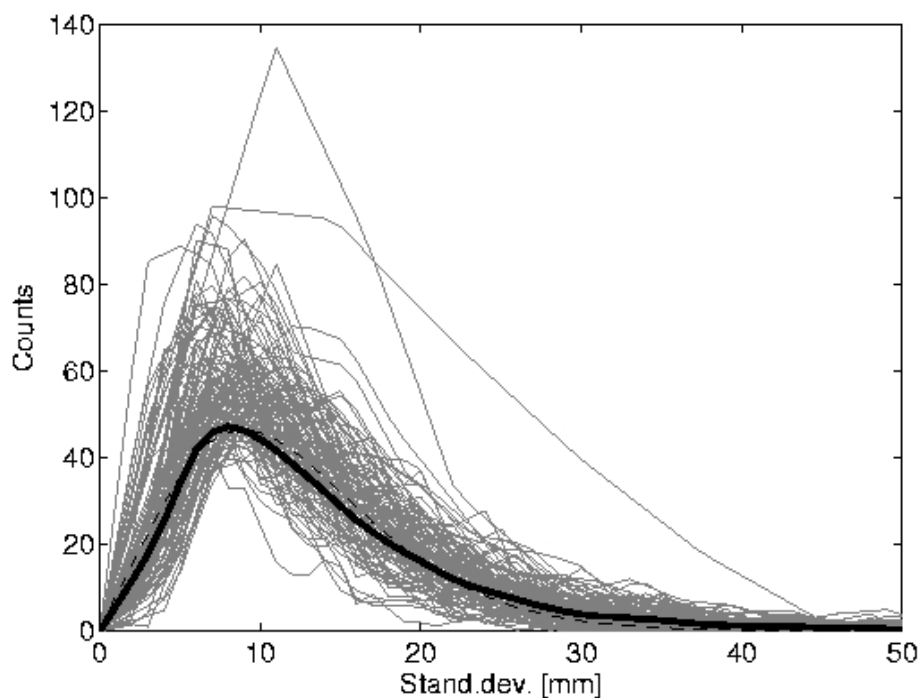


Figure A.15 Histograms of daily atmospheric delay variability (standard deviation) for 114 EUREF stations. The bold black line is the average distribution, and the dashed line shows a best-fit distribution.

#### A.3.4.2 Kolmogorov turbulence

To obtain a random simulator for an atmospheric refractivity distribution fulfilling the Kolmogorov turbulence characteristics (the two scaling regimes discussed in the previous chapter), the main considerations are that the simulation should be as close

as possible to reality and that the simulation should be initialised by easily obtainable meteorological observations.

This model consists of two steps. At the first step we estimate a boundary layer depth for both SAR acquisition days. Since the boundary layer is a layer where most atmospheric variability occurs, its depth should determine the scale change of the power law behaviour of the atmospheric signal. It is generally assumed that this transition occurs around 2 km. However, using radiosonde data we should be able to retrieve a more accurate estimate of this characteristic scale.

Often the boundary layer top is determined as the height where the first temperature inversion is observed. Therefore, by studying temperature height profiles we can estimate the boundary layer depth. In some cases, however, the temperature inversion is not well defined. Therefore, it is important also to study behaviour of dew point temperature, relative humidity and of virtual potential temperature.

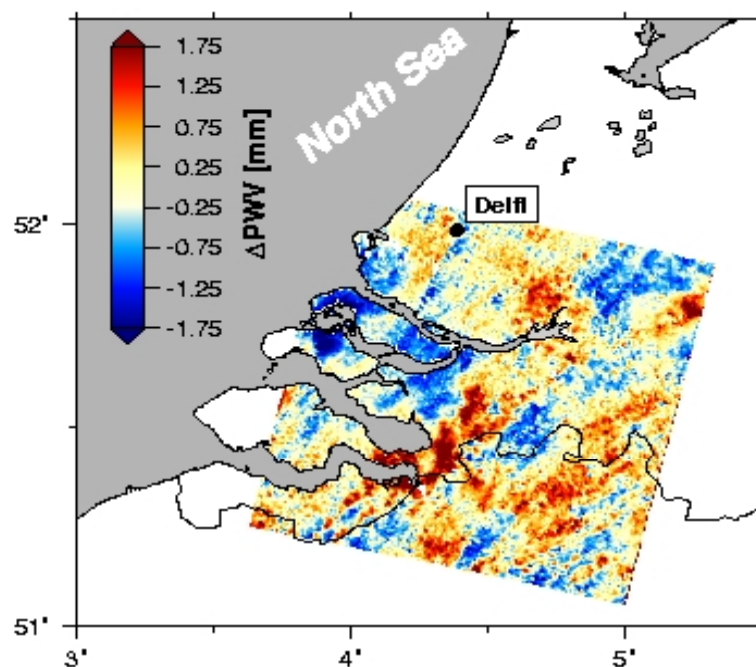


Figure A.16 Atmosphere -only interferogram over the south-west of the Netherlands

The virtual potential temperature is the temperature that dry air should have to have the same density as the moist air at the same pressure. We would expect that at the top of a boundary layer there is an increase in air temperature, decrease in dew temperature, abrupt decrease in relative humidity and increase in virtual potential temperature. In Figure A.17 the radiosonde measurements of virtual potential temperature  $q$ , temperature and Dew point, water vapour mixing ratio and relative humidity are shown. The expected behaviour of the observables is clearly seen on this figure. An automatic procedure for determining the boundary layer depth using all these parameters is used.

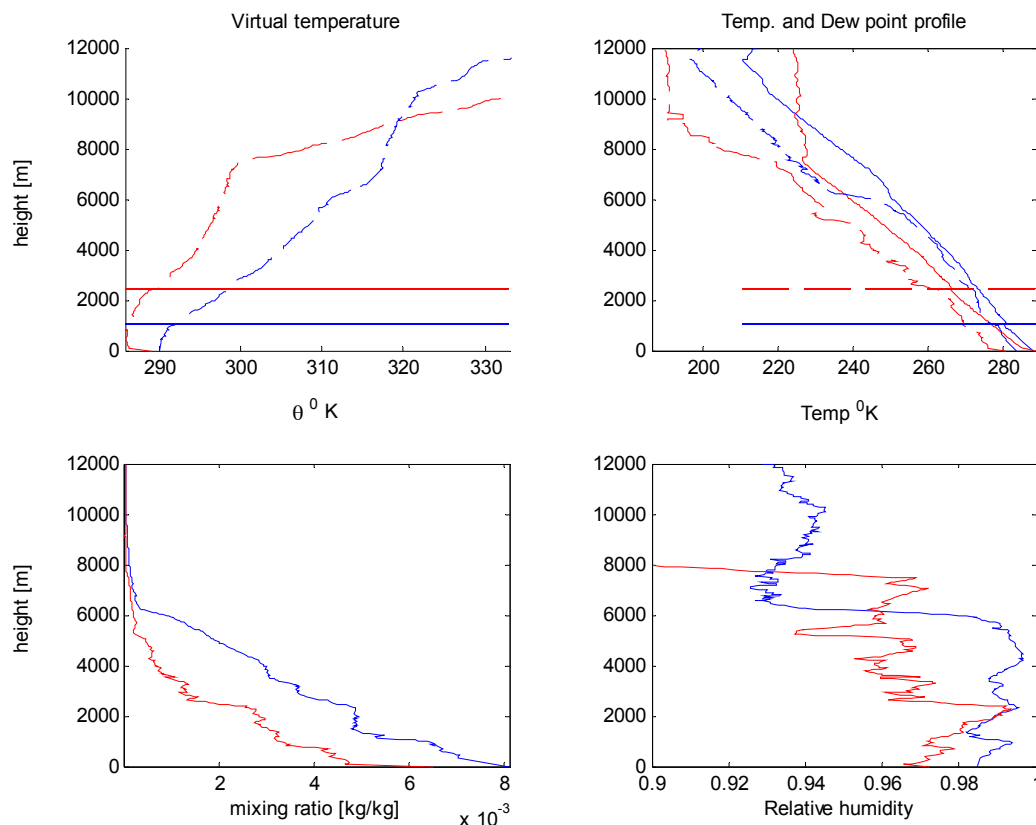


Figure A.17 Radiosonde measurements on 23 and 24 of April 2003 taken at 12.00 UTC. This picture shows virtual potential temperature  $q$ , temperature and Dew point, water vapour mixing ratio and relative humidity. From these observations the boundary layer depth was estimated for both days. It was found that it is equal to 1.062 km and 2.4345 km for the first and second day respectively.

To investigate relation between the mean boundary layer depth that as calculated as an average of boundary layer depths obtained from radiosonde measurements during the two days and the scale break observed on interferograms, we have studied 14 interferograms taken during the ERS1, 2 tandem mission in 1995 –1996. Figure A.18 shows the result of this study. It can be seen that there is a correlation between the boundary layer depth calculated from radiosonde observations and the InSAR scale break. The, sometimes, large variability in the estimate of the boundary layer depth is caused by larger differences in the meteorological conditions during the two observation days. The procedure of determining the scale break from the InSAR measurements is illustrated in the Figure A.19. From this figure we can see that the exact accuracy of the InSAR scale break is rather difficult to determine, but we expect that it is better than 1 km. It should also be noted that InSAR and radiosonde observations have 1.30 hour difference in time.



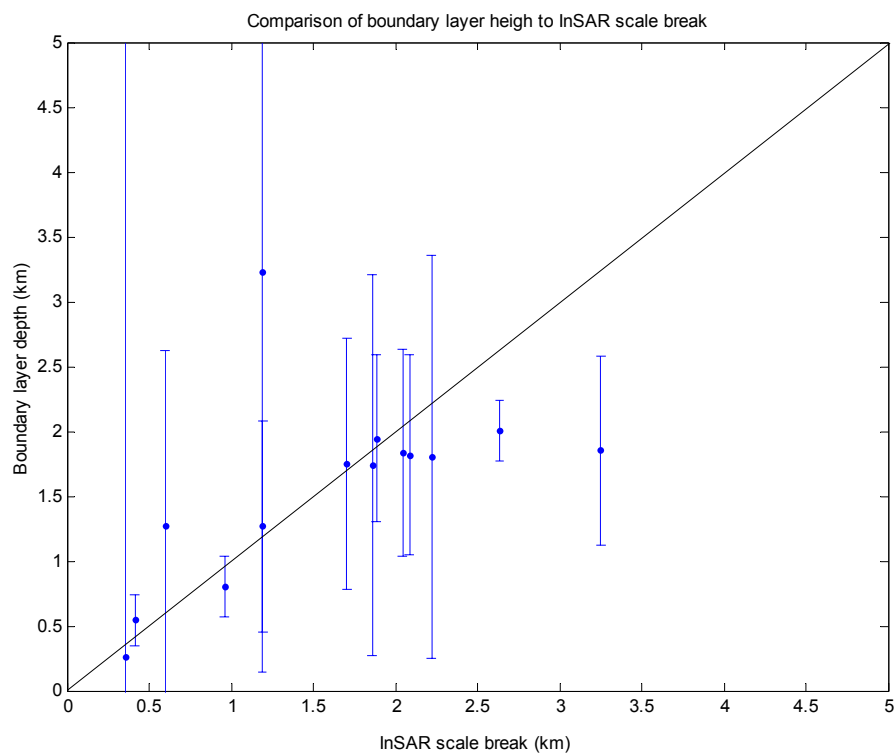


Figure A.18 Scale break as observed by InSAR versus mean depth of the boundary layer as measured by radiosondes during the two days. Error bars show variation of the boundary layer depth between two observation days.

Table A.7  
Observed mean values and *rms* of the  $\beta$  for different regimes

	> 2 km	0.6-2 km	< 0.6 km
MEAN	-1.29 (-1.66)	-2.81 (-2.66)	-0.91
RMS	0.54	0.96	1.18

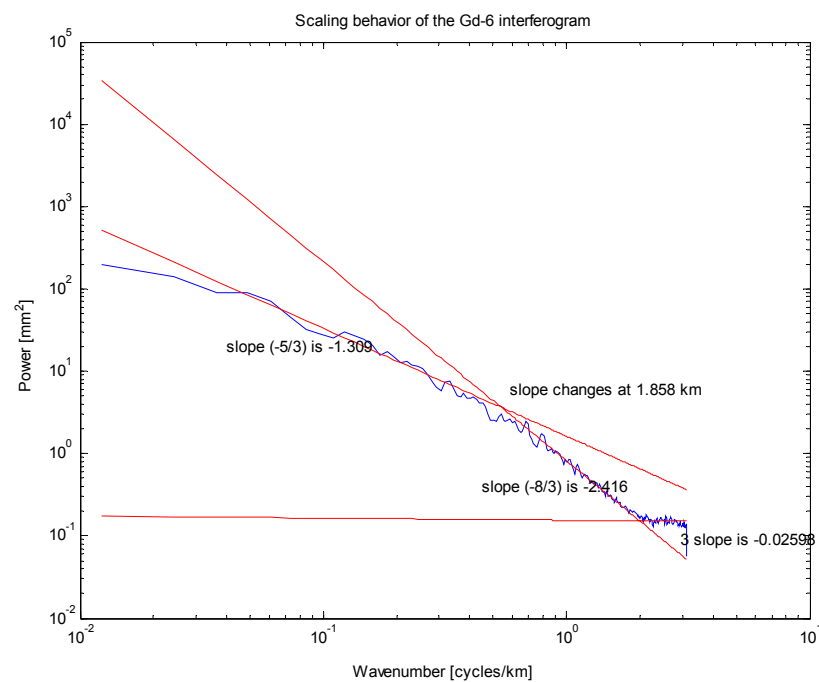


Figure A.19: An example of the scaling behaviour analysis. Three regions are identified and the exponents of the power behaviour are calculated. The flattening of the slope at the higher frequencies is probably caused by noise.

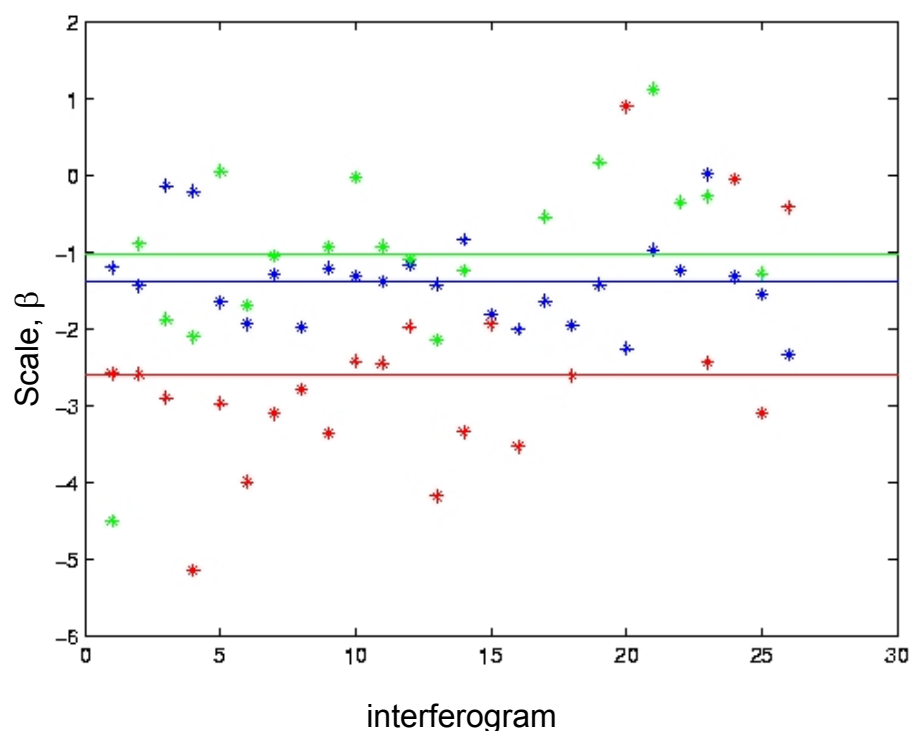


Figure A.20: Observed scales for different regimes and for all interferograms. Red stars correspond to the scales 2 km and 0.5 km. Blue stars correspond to the scales larger than 2 km and green stars to the scales smaller than 0.5 km.

The other step of our investigation was to study the exponents of the scaling behaviour of atmospheric signal in interferograms. For this purpose we have sought different  $\beta$  and  $P_0$ , such that we obtain a best power law fit to the data for the scales smaller than 0.5 km, larger than 0.5 km but smaller than 2 km and larger than 2 km. It is expected that due to finite boundary layer depth there will be two regimes in the scaling behaviour of the atmospheric water vapour, as was discussed in A.3.

In Figure A.19 an example of such analysis is shown. Also from this analysis we obtain the scale break. In the Table A.7 and on the Figure A.20 the overview of all observed  $\beta$  for different regimes are shown. It should be noted that the observed power laws are somewhat different from the theory prediction, denoted in parenthesis in the Table A.7, but there is a rather larger variance in  $\beta$  estimates. It is interesting to see that the mean value of  $\beta$ , for the scales larger than 2 km, obtained from our analysis is rather different from the expected value of  $-5/3$ . This can possibly have several causes. Errors in satellites orbits would cause tilts in the retrieved atmospheric phase screen (Hanssen, 2001), therefore adding a long wavelength disturbances to an atmospheric phase screen. Another phenomenon that can introduce a bias to our estimate of the scaling behaviour would be formation of clouds and cloud streets. It was shown (Feijt and Jonker, 2000) that the observed scaling behaviour of liquid water content can be sufficiently different from the behaviour predicted by the Kolmogorov theory and that this difference can be attributed to the life time of a cloud. Since both liquid particles and water vapour are tracers of the turbulence any over mechanism affecting their concentration would affect the observed scaling behaviour. Therefore as in work of Feijt and Jonker (2000) we can expect differences between observed and expected values of  $\beta$  and that differences can be explained by presence of clouds during satellite acquisitions.

Another interesting result of our analysis that is shown in Table A.7 is the presence of the third scaling regime. This regime manifests itself at the scales smaller than 0.6 km and is associated with the flattening of the observed power spectra. Also in this case there are several possible explanations. One of the possible reasons could be the effect of low resolution that would cause aliasing of higher frequencies into the lower frequencies in the power spectrum. To test this theory a signal with  $-5/3$  scaling behaviour was generated for the wavelength range of 50 to  $10^{-3}$  km. This signal was then sampled with a frequency of  $1/0.16$  km. This simulation was carried out to model multi looked InSAR observations with an effective resolution of 160 m. The result of this simulation was that the sampling has hardly any effect on the observed power spectra and cannot explain flattening of the spectra. Another possible explanation would be reduction of the coherence and therefore introduction of the noise to measurement. Also we should not exclude possible effects of atmosphere at these small wavelengths. Those effects could be formation of clouds and evaporation and condensation of water vapour. However, to our knowledge there is no literature that predicts such behaviour of water vapour. Therefore, we consider that this flattening is most probable caused by the noise.

#### **A.3.4.3 Model investigation**

In this section we want to simulate the observed scaling behaviour of atmospheric phase screen. Our goal is to verify whether using Kolmogorov theory and knowledge

of atmospheric boundary layer depth one can predict scaling break and observe two scaling regimes that are often observe.

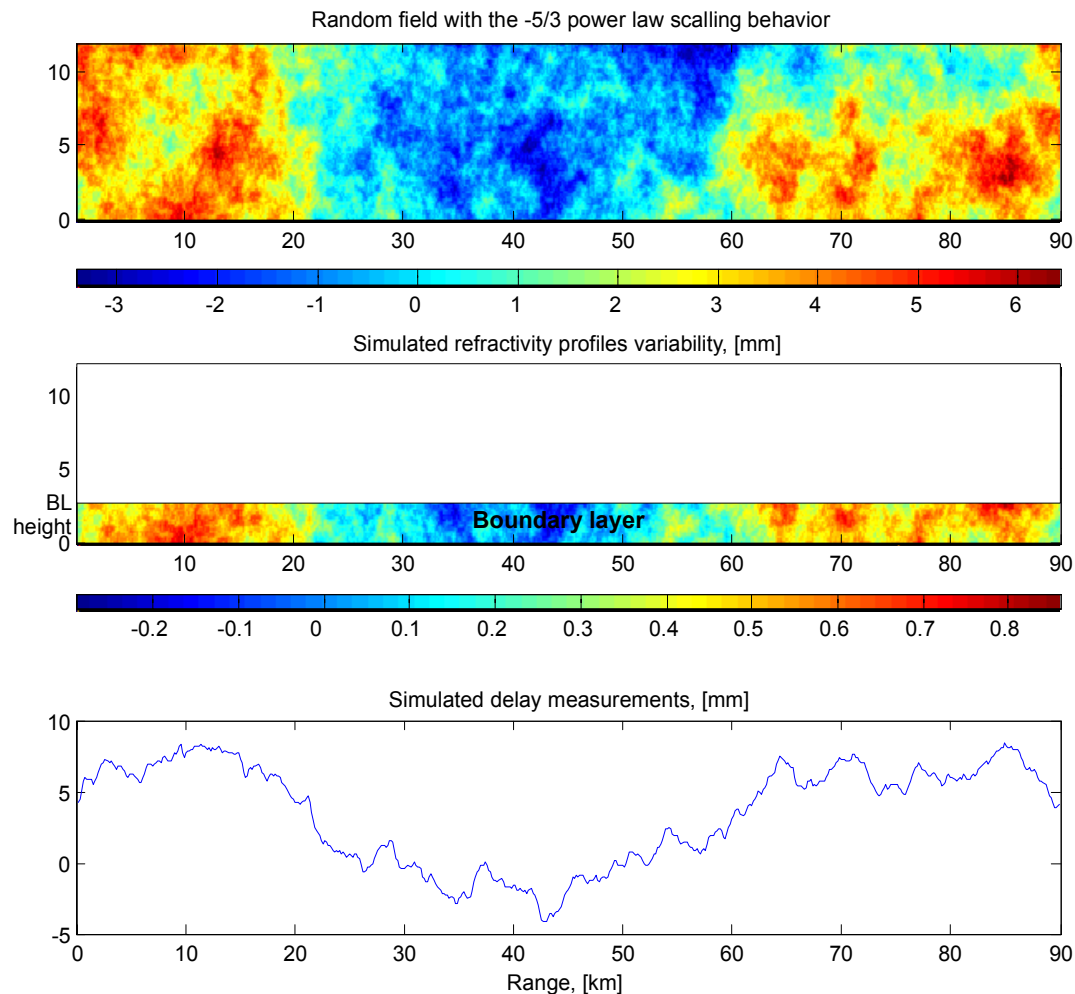


Figure A.21 Three steps of the model. At the first step a fractal simulator is used to generate a 2D signal with  $\beta = -1.3$ . At the second step the finite depth of the boundary layer is taken into account, the signal is truncated to allow atmospheric fluctuations only in the boundary layer. At this stage BL depths measured by radiosondes are used. And at the final stage height integration is performed and signal is weighted to have the same *rms* as the interferogram.

The basis of the model is formed by a fractal simulation of a signal showing a  $-5/3$  power law behaviour. For this study we have used the observed mean  $\beta = -1.3$  instead of  $-5/3$ . The choice for using this value of  $\beta$  was predetermined by the fact that clouds have a non negligible effect on scaling behaviour of the atmospheric phase screen and this effect should be taken into account. We have also limited ourselves to simulating refractivity in a vertical plane, but extension to a 3D volume is straightforward. The dimensions of the vertical plane are 90 km horizontal and 12 km vertical, see Figure A.21. Since we know that the refractivity distribution is most variable in the lower part of this region, the *boundary layer*, we have truncated the signal at the height of the boundary layer. The boundary layer height is determined from radiosonde measurements. This can be easily obtained by applying a vertical step function to the

signal. The signal that would be observed in an interferogram (combining two of these simulations) is shown in the lower subplot of Figure A.21. Using the periodogram method we have obtained the spectrum of the modelled signal as shown in Figure A.22. For this figure the modelled signal was multi-looked to obtain the same spatial behaviour as the interferogram.

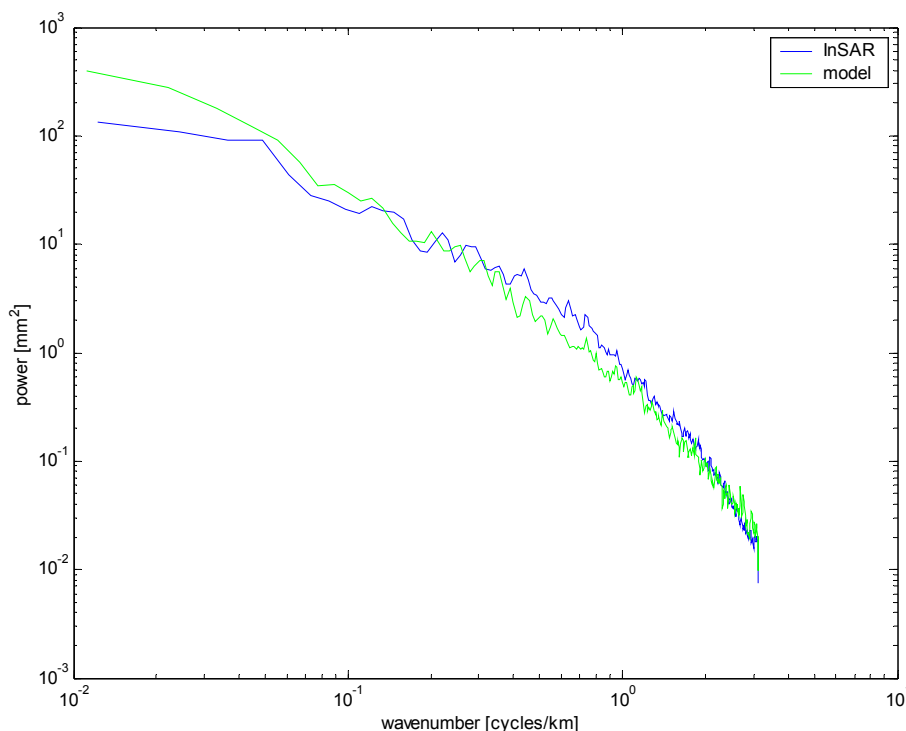


Figure A.22 Comparison between the simulation of a turbulent troposphere and the InSAR measurement. A  $-5/3$  signal is created using a fractal generator and restricted to the boundary layer only. Furthermore, the vertical integration yields the atmospheric phase screen shown in the Figure A.21. It should be noted that also effect of multi-looked is taken into account, which yields a further decrease in power for scales smaller than 0.5 km.

### A.3.5 Conclusions

In this section we discussed the forward models regarding the electromagnetic interaction of the radar waves with the atmosphere. We showed that forward modelling can be interpreted in two ways: deterministic modelling and stochastic modelling. In the former case, fine 3D resolution knowledge of the main atmospheric parameters influencing the refractivity is needed. Although this is the proper model for calculating the observed atmospheric phase screen in an interferogram, it is not very practical, since the information on the refractivity is hardly ever available. In the forward modelling we also showed how a component of the refractivity is due to hydrometeors. This component can be conveniently derived from rain rate values. Stochastic modelling concerns the simulation of a random refractivity distribution, showing the same stochastic behaviour as observed on earth. Initialisation of the

model is proposed by readily available radiosonde data, which can be used to determine the boundary layer depth. From the validation it appears that a forward stochastic model gives a good approximation of the real observed interferometric data.

## A.4 RETRIEVAL ALGORITHMS

### A.4.1 Introduction

In this chapter we present the prototype retrieval algorithms for resolving the acquisition ambiguity in Interferometric Radar Meteorology to estimate the atmospheric parameters water vapour and liquid water. These algorithms have been applied to the test sites Las Vegas, Berlin, Hawaii, and Flevoland. The Las Vegas site was used for the ambiguity resolution evaluation, the Berlin site for the permanent scatterer single-master stack approach, and the Flevoland site for some of the hydrometeor studies.

In sections A.4.2-A.4.4, retrieval techniques for resolving the acquisition ambiguity are described for permanent scatterers, single-master stacks and cascade stacks. The theory is further developed here and test results of the cascade interferograms approach for the Las Vegas area are shown. Section A.4.6 is a discussion on the influence of liquid water on the total observed delay. The chapter finishes with conclusions and recommendations in section A.4.8.

### A.4.2 Ambiguity resolution: permanent scatterer case

In the permanent scatterers InSAR analysis, the atmospheric contributions are estimated together with the deformation and topographic signal. Separation between the contributions is based on

- the assumption that atmosphere is not correlated over time spans of more than 1 day,
- the fact that spatial smoothness of the atmospheric delay signal can be characterized by a power-law (often a spatial low-pass filter),
- the fact that only topography is baseline-dependent, and
- the fact that deformation signal is usually correlated in time.

As a result, it is possible to investigate the derived atmospheric phase screen. Validation of this signal is very difficult though, mainly due to the lack of reference observations with sufficient spatial and temporal resolution, observing highly accurate vertically integrated refractivity. Therefore, we try to determine whether the stochastic behaviour of the retrieved APS corresponds with the behaviour as expected from theory. Such a confirmation (or refutation) could serve as a more objective (but secondary) indication of the reliability of the APS estimate.

#### A.4.2.1 Data

A stack of 70 ERS-1/2 acquisitions over the area of Berlin is analysed in this study. The total span of the perpendicular baseline is 2100 m. The time interval covered 8.5 years, from May 1992 to November 2000.

#### A.4.2.2 PS processing to isolate atmosphere

The aim of the permanent scatterer processing is to find sparsely distributed points with limited temporal decorrelation, and to estimate DEM error and linear deformation at these points using a time series approach (Kampes and Adam, 2003).

First the selection of a master has been performed from the stack of the images. The criterion is to choose the master as the image whose mean coherence is optimal as master of the stack of images. The magnitudes of all SLC images are calibrated for processor gain factors, range spreading loss and antenna pattern. Once the master is selected 7 interferograms of the stack were discarded as they presented a Doppler centroid frequency too large compared with the selected master.

The amplitude time series is used to select a large number of points that are most likely to possess a coherent phase in time. These points are expected to have large amplitudes and small amplitude dispersions. Nearly 100.000 points were selected. The phase of the selected points is first used to correct for global phase trends over the interferograms caused by orbit errors. The corrected data are then analysed with the PS network approach.

The model of observation equations relates a random vector  $y$  of phase observations with a vector  $x$  of unknown parameters, according to:

$$E\{y\} = Ax; D\{y\} = Q_y, \quad (\text{A.4.1})$$

where the matrix  $Q_y$  is the variance-covariance matrix (Teunissen, 2000). The dominant parameters affecting the interferometric phase are the topographic height, the deformation in slant direction, the slant-atmospheric delay during the first acquisition, the slant-atmospheric delay during the second acquisition, and an integer ambiguity number. Fortunately these components have different spectral properties which make it in principle possible to separate them. The topography is a linear function of the perpendicular baseline, and the velocity can be assumed to be a linear function of temporal baseline. Orbit errors are linear functions of the range and azimuth coordinates. The atmospheric phase is spatially correlated, but uncorrelated in time.

Noise is considered high frequency in all domains. The first goal is to obtain the unwrapped 'atmosphere plus noise' matrix by stepwise removing the other phase components, and then to remove the noise by spatial filtering with an averaging kernel.

The phase difference of nearby points is used to compute the DEM error differences and the linear velocity differences between points. A least squares adjustment and hypothesis testing step is then performed to obtain reliable estimates for the DEM error and linear velocity at these points, with respect to an arbitrary reference point. The phase is corrected for the estimated DEM errors and linear deformation, yielding the residual phase of atmosphere plus noise. Finally this phase has been unwrapped on a sparse grid.



### A.4.2.3 Variogram estimation

When a matrix containing atmospheric signal plus noise is isolated, the atmospheric phase can be analysed using its power spectrum, the covariance function or the structure function (variogram). Since the PS technique does not provide a regular grid of points available, a power spectrum can not be conveniently calculated through the 1-D FFTs. No restrictions regarding the preliminary estimation of the mean or stationarity are necessary to use the structure function. It can be applied to a network of sparsely distributed point as in our case, yielding a quantitative expression for the variance of the difference in atmospheric delay between two points separated by a distance  $\rho$ . Moreover it is also useful for the quality description.

The variogram of the stack of interferograms has been calculated using a subset of all Permanent Scatterers. (The initial number  $N$  of almost 100.000 permanent scatterers available requires a large number of computations due to the large number of possible combinations among permanent scatterers. Hence, a pre-processing step for data reduction is necessary. We select a reduced but statistically representative subset of points, randomly selected from all PS, based on their mean. The histogram of the atmospheric phase per interferogram shows in all the cases approximately a Gaussian distribution. We look for convergence between the mean of the total and the subset of permanent scatterers. At the moment when the mean of a subset of number of PSs is equal to that of the total, the process is ended. Following this procedure it was found that the convergence to the mean of all data was quite fast and with a number of 3000 randomly selected PS's the computing time decreases considerably. Moreover, there are still enough points to obtain smooth variograms.

### A.4.2.4 Results

The mean atmospheric residual phase has been subtracted for every interferogram. Figure A.23 shows an example of an atmospheric phase screen over the test area Berlin, Germany. Note, that a smoothing procedure has been applied to obtain this estimated. From the original data (unsmoothed) the variogram of every acquisition has been computed. Figure A.24 shows the superposed variograms for the 62 acquisitions.

All the variograms show the same structure but the standard deviation of the difference in the atmospheric delay ranges from 2 to 11 mm. The Kolmogorov power law slopes are shown as dotted lines.

### A.4.2.5 Discussion

The most important observation from the variograms in Figure A.24 is that they do not obey the expected Kolmogorov scaling behaviour, as expected for atmospheric signal. In order to interpret these results, a simulation in a controlled environment was performed. A 2D fractal signal was created with a variogram slope of  $2/3$  (fractal dimension  $8/3$ ). This is performed for three different power levels, indicated by the three rows in Figure A.25. The corresponding variograms are shown beside these plots, calculated from the PS positions in Berlin. The slope of the variograms represents the scaling behaviour correctly, and the vertical position of the variogram is an indication for the power of the variability.

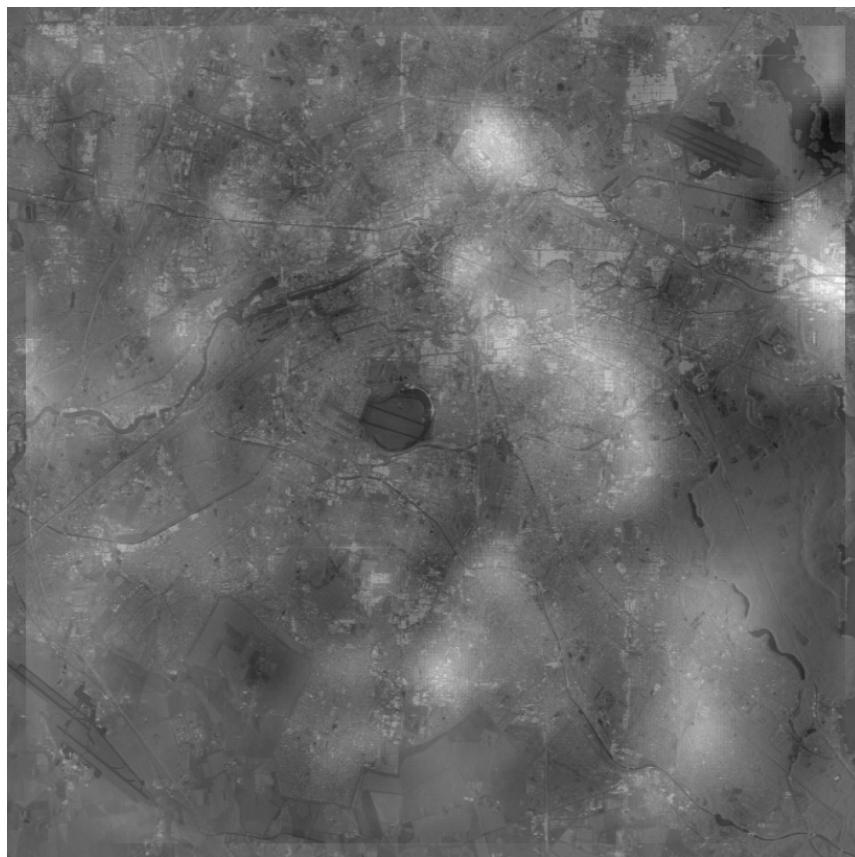


Figure A.23 Example of an atmospheric phase screen estimate over Berlin

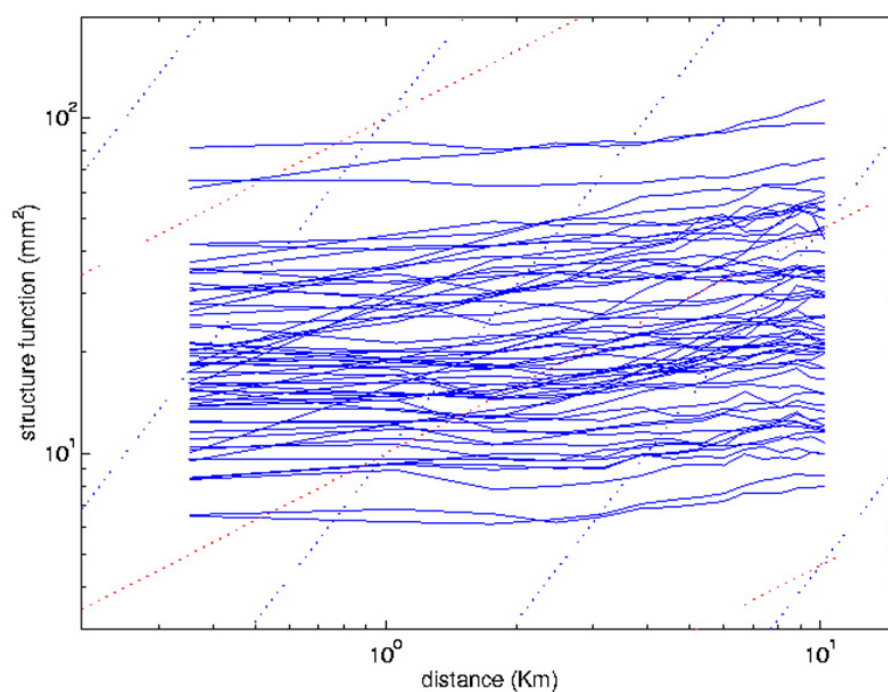


Figure A.24 Variograms of the presumed atmospheric phase screen in the stack of images.

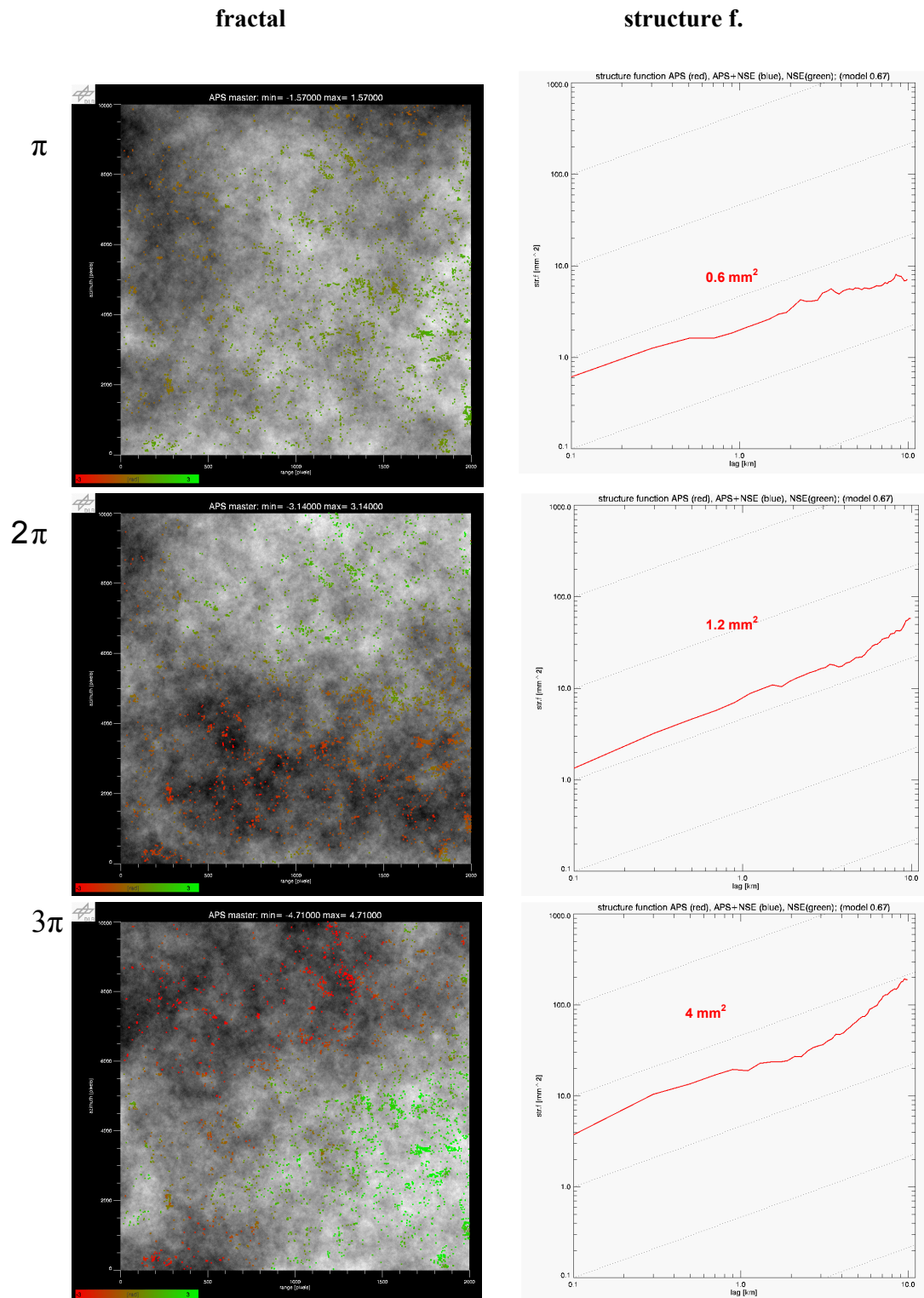


Figure A.25 Simulated atmospheric phase screens with a variogram slope of  $2/3$ . Three power levels ( $[-\pi/2, +\pi/2]$ ,  $[-\pi, +\pi]$ ,  $[-3\pi/2, +3\pi/2]$ ) were tested, and the variograms estimated from the locations of the PS over Berlin were calculated, similar as in Figure A.24. The variograms show the expected scaling behaviour, where the vertical position corresponds with the power of the variability.

From this simulation, we conclude that our algorithms are correct. A possible explanation of the anomalous behaviour of the variograms in Figure A.24 is that the PS observations still have a considerable amount of noise. For this reason, white noise (uncorrelated point noise) has been simulated and added to the simulated APS. Table A.8 lists the amount of simulations performed.

Table A.8

Simulation overview. The amount of simulations for atmospheric signal power plus additional uncorrelated noise with different standard deviations is listed

<i>Power\ noise (<math>\sigma</math>)</i>	<i>0</i>	<i>30</i>	<i>40</i>	<i>50</i>
0.5 cycle	10 sim	3 sim	3 sim	3 sim
1 cycle	10 sim	10 sim	10 sim	10 sim
1.5 cycle	10 sim	3 sim	3 sim	3 sim

Figure A.26 shows the effect of phase noise on the APS signal. Red lines indicate the simulated atmospheric phase screen, for three power levels, indicated by the three columns. Green lines show different point noise levels, for three noise levels (30, 40, and 50 degrees standard deviation, values which are considered to be realistic), indicated by the three rows. Blue lines show the ‘observed’ variograms. It is obvious that the observed functions cannot be interpreted in terms of their scaling behaviour anymore. In fact, the noise level ‘flattens’ the variograms, and only if either the noise level is very low, or the APS power very high, the slopes of the variograms may be interpretable.

#### A.4.2.6 Conclusions

The permanent scatterer technique is convenient for obtaining coherent interferometric phase information over a wide range of spatial and temporal baselines. The identification of reliable reflections within such an interferogram time series is instrumental in this approach. Residual signal, obtained after a first-order estimation of deformation and topographic signal, is likely to be largely due to the influence of the atmosphere. In literature, this signal is often referred to as the atmospheric phase screen. Practical experiments on the residual signal over a permanent scatterer analysis over Berlin shows that random phase noise is an important contribution to the error budget, which masks the true APS. Therefore, in practice it is very difficult to assess the quality of the estimated APS.

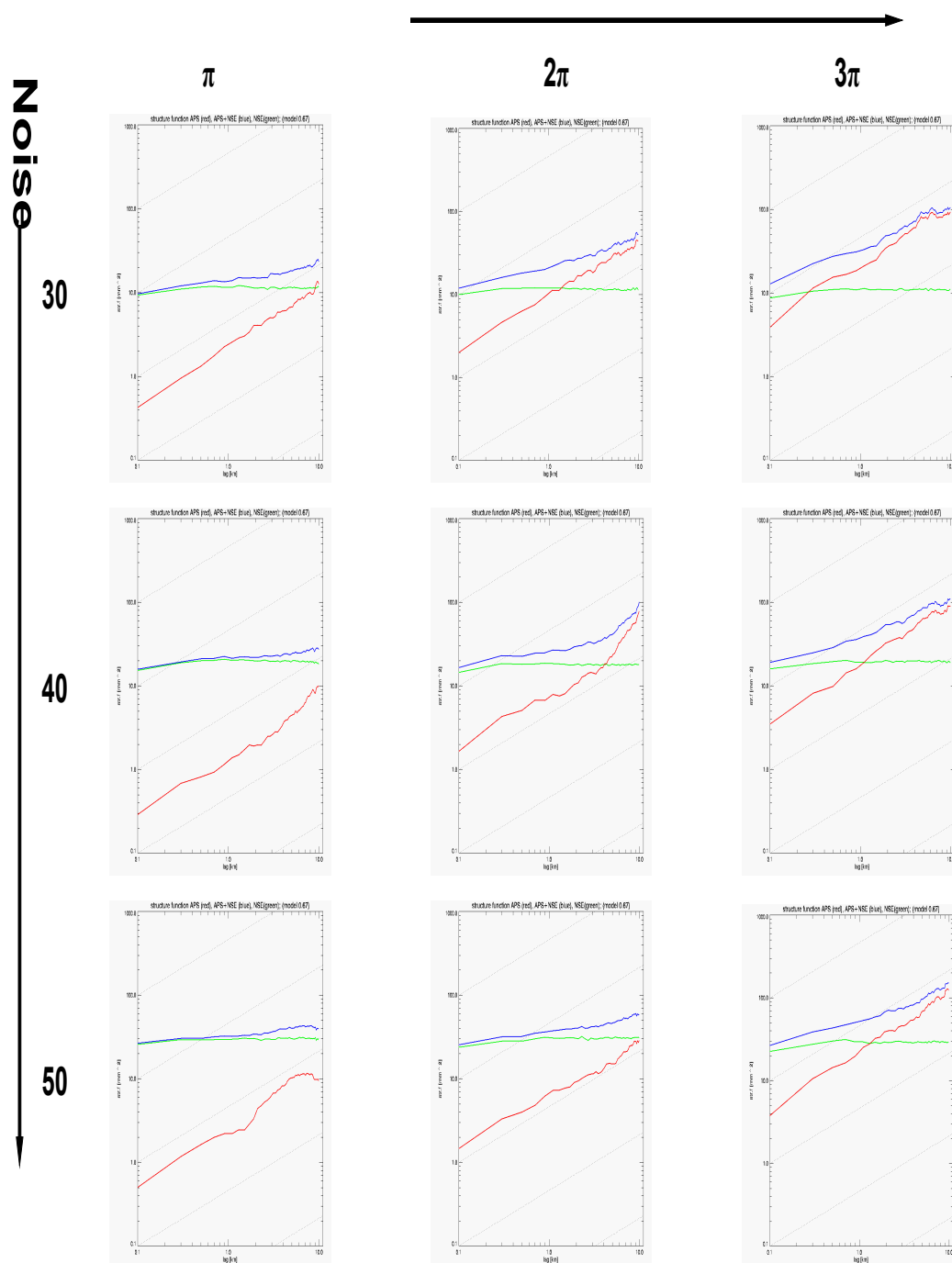


Figure A.26 Simulations showing the effect of uncorrelated (point) noise superposed on the atmospheric signal. Red lines indicate the simulated atmospheric phase screen, for three power levels, indicated by the three columns. Green lines show different point noise levels, for three noise levels (30, 40, and 50 degrees standard deviation), indicated by the three rows. Blue lines show the 'observed' variograms. It is obvious that the observed functions cannot be interpreted in terms of their scaling behaviour anymore.

**A.4.3 Ambiguity resolution, single master**

For  $N+1$  SAR acquisitions  $S_i$  the single master stack, with master  $S_0$ , is obtained for each pixel from

$$\begin{bmatrix} I_1 \\ I_2 \\ \vdots \\ I_N \end{bmatrix} = \begin{bmatrix} 1 & -1 & & \\ & 1 & \ddots & \\ & \vdots & \ddots & \\ & & & -1 \end{bmatrix} \begin{bmatrix} S_0 \\ S_1 \\ \vdots \\ S_N \end{bmatrix} \quad (\text{A.4.2})$$

Recall that the first and second order moments for  $S_i$  read

$$E\left\{ \begin{bmatrix} S_0 \\ S_1 \\ \vdots \\ S_N \end{bmatrix} \right\} = \begin{bmatrix} 0 \\ 0 \\ \vdots \\ 0 \end{bmatrix}, \text{ and } D\left\{ \begin{bmatrix} S_0 \\ S_1 \\ \vdots \\ S_N \end{bmatrix} \right\} = \sigma^2 \begin{bmatrix} 1 & 0 & \cdots & 0 \\ 0 & 1 & \ddots & \vdots \\ \vdots & \ddots & \ddots & 0 \\ 0 & \cdots & 0 & 1 \end{bmatrix}. \quad (\text{A.4.3})$$

As a result, the expectation value and dispersion of the interferograms is

$$E\left\{ \begin{bmatrix} I_1 \\ \vdots \\ I_N \end{bmatrix} \right\} = \begin{bmatrix} 0 \\ \vdots \\ 0 \end{bmatrix}, \text{ and } D\left\{ \begin{bmatrix} I_1 \\ \vdots \\ I_N \end{bmatrix} \right\} = \sigma^2 \begin{bmatrix} 2 & 1 & \cdots & 1 \\ 1 & 2 & & 1 \\ \vdots & & \ddots & \vdots \\ 1 & 1 & \cdots & 2 \end{bmatrix}. \quad (\text{A.4.4})$$

The system described can also be approached as a Gauss-Markoff model for the inverse problem of retrieving the atmospheric phase screens per acquisition. Obviously, the system contains a rank deficiency of 1. Hence, there is no unique solution. Two strategies to determine an optimal solution based on a specific criterion are proposed.

**Strategy 1**

The first strategy was described before and is based on the (possibly weighted) average of all interferograms, resulting in

$$\begin{aligned}
A &= \frac{1}{N} \sum_{i=1}^N I_i = \frac{1}{N} [1 \quad \dots \quad 1] \begin{bmatrix} I_1 \\ \vdots \\ I_N \end{bmatrix} \\
&= \frac{1}{N} [1 \quad \dots \quad 1] \begin{bmatrix} 1 & -1 & & & \\ 1 & & \ddots & & \\ \vdots & & & \ddots & \\ 1 & & & & -1 \end{bmatrix} \begin{bmatrix} S_0 \\ S_1 \\ \vdots \\ S_N \end{bmatrix} \\
&= S_0 + \frac{1}{N} [-1 \quad \dots \quad -1] \begin{bmatrix} S_1 \\ \vdots \\ S_N \end{bmatrix} \\
&= S_0 + e
\end{aligned} \tag{A.4.5}$$

where we assume that the sum of all slave atmospheres (with expectation value 0) can be regarded as noise  $e$  with  $E\{e\}=0$ . Therefore, the summed stack will represent the atmosphere during the master acquisition only, and the best unbiased estimate will be

$$E\{A\} = S_0, \text{ and } \hat{S}_0 = A \tag{A.4.6}$$

with variance

$$D\{\hat{S}_0\} = \sigma_{\hat{S}_0}^2 = \frac{\sigma^2}{N}. \tag{A.4.7}$$

To improve the estimate, a weighted averaging could be applied, for instance based on the atmospheric variance per interferogram, which can easily be derived from the data.

After this estimation, the atmospheric signals of the slave acquisitions can be estimated from

$$\hat{S}_i = \hat{S}_0 - I_i \tag{A.4.8}$$

## **Strategy 2**

A second strategy to determine a unique solution for the rank deficient problem is based on the well known Singular Value Decomposition (SVD), which uses a pseudo-inverse to estimate a minimal norm solution. The problem can be formulated as

$$\begin{bmatrix} A^T A & G \\ G^T & 0 \end{bmatrix} \begin{bmatrix} S \\ 0 \end{bmatrix} = \begin{bmatrix} A^T I \\ g \end{bmatrix} \tag{A.4.9}$$

where  $A$  is the normal matrix of system Equ (A.4.2),  $S$  are the unknown atmospheric phase screens per acquisition,  $I$  are the interferograms and  $G$  and  $g$  formulate a constraint. In this case,  $G$  is a vector of ones and  $g$  is zero. The first matrix on the left



hand site is now invertible, enabling the determination of the minimum norm solution of  $S$ .

It can be shown that the estimates for the atmospheric phase screens read

$$\begin{aligned}\hat{S}_i &= S_i - \frac{1}{N+1} \sum_0^N S_i \\ &= S_i + e\end{aligned}\tag{A.4.10}$$

with variance

$$D\{\hat{S}_i\} = \frac{\sigma^2}{N+1}\tag{A.4.11}$$

Hence, theoretically the SVD-method should give a slightly more accurate estimate of the atmospheric phase screens per acquisition.

Unfortunately, the practical application of single-master stacks is very cumbersome, since (i) coherence should be maintained over very long times to get a set large enough for reliable inversion (ii) baselines of this single master stack should be well within the critical baseline limit, (iii) no deformation should be present in the data. We tested the algorithms on a Radarsat data set with images from the big island of Hawaii, but deformation signals were too prominent for unambiguous estimation, see Figure A.27. The deformation of Mauna Loa can be identified since it is a similar feature over the volcano at many instances. Therefore, single master stacking is an option only feasible for, e.g., long-time coherent data as retrieved with an L-band system.

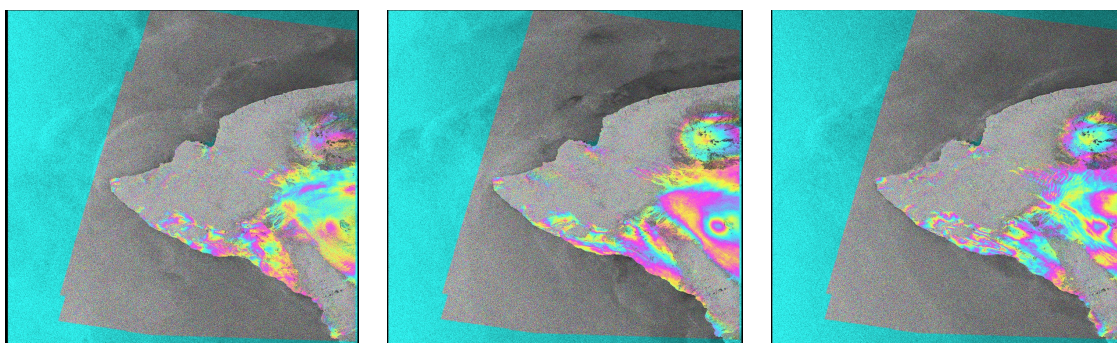


Figure A.27 Radarsat descending swath 2 over the west coast of Hawaii. The interferograms cover 2001-10-15/2002-08-23, 2001-10-15/2002-06-12, and 2001-10-15/2002-10-10, respectively (single master). The images show a combined deformation and atmosphere signal. Especially along the southern coast phase variations, probably due to water vapour in the master image, are visible. The last interferogram shows wave effects over the Mauna Kea western slopes.



#### A.4.4 Ambiguity resolution, cascade

Whereas the single-master approach estimates the master APS using a rigorous (weighted) averaging, experience shows that in a time series of radar interferograms there are always interferograms which show a negligible APS variability. Usually these situations occur during cold and stable weather situation, where the water vapour content is low. The idea behind the cascaded stack is to use this information.

The cascade stack is obtained from

$$\begin{bmatrix} I_1 \\ I_2 \\ \vdots \\ I_N \end{bmatrix} = \begin{bmatrix} 1 & -1 & & \\ & 1 & -1 & \\ & & \ddots & \ddots \\ & & & 1 & -1 \end{bmatrix} \begin{bmatrix} S_0 \\ S_1 \\ \vdots \\ S_N \end{bmatrix}. \quad (\text{A.4.12})$$

Again, this system can be regarded as a Gauss-Markoff model, with a rank deficiency of one. This rank deficiency can be circumvented by inserting a pseudo-observable  $S_k^*$  in the system. After inversion of the normal matrix, this leads to the solvable system

$$\begin{bmatrix} \hat{S}_0 \\ \hat{S}_{k-1} \\ \hat{S}_k \\ \hat{S}_{k+1} \\ \hat{S}_N \end{bmatrix} = \begin{bmatrix} 1 & \cdots & 1 & 1 & & \\ & \ddots & 1 & 1 & & \\ & & 1 & 1 & & \\ & & & 1 & & \\ & & & 1 & -1 & \\ & & & 1 & -1 & \ddots \\ & & & 1 & -1 & \cdots & -1 \end{bmatrix} \begin{bmatrix} I_1 \\ \vdots \\ I_{k-1} \\ S_k^* \\ I_k \\ \vdots \\ I_N \end{bmatrix}. \quad (\text{A.4.13})$$

Choosing  $S_k^* = 0$  and recalling that  $I_i = S_i - S_{i+1}$ , the estimates read

$$\hat{S}_i = S_i - S_k. \quad (\text{A.4.14})$$

Hence, all estimates are biased with a value equal to the atmospheric signal of the reference APS  $S_k$ . Obviously, this bias will be smallest by selecting the APS with minimal phase variance, which can be determined by comparing the phase variances of the (neighbouring) interferograms. This minimal variance can also be used for the construction of the vc-matrix of the estimated APS's, hence

$$D\{\hat{S}_i\} = \sigma_{I_k}^2. \quad (\text{A.4.15})$$

Recalling the averaging approach for the single-master stack, a *second strategy* to estimate the APS per acquisition can be deducted. Averaging of the estimated APS's  $\hat{S}_i$  obtained above (omitting  $\hat{S}_k$ ) leads to

$$\frac{1}{N} \sum_0^{N \setminus k} \hat{S}_i = \frac{1}{N} \sum_0^{N \setminus k} S_i - S_k. \quad (\text{A.4.16})$$

Because the expectation value of the first part of the right hand site is zero, this average is an estimate for the reference APS. Inserting this estimate as a new pseudo-observable in the functional model, this leads to the new estimates

$$\hat{S}_i = S_i - \frac{1}{N} \sum_0^{N \setminus k} S_i. \quad (\text{A.4.17})$$

Hence, the bias is now equal to the average of the APS's, omitting the reference APS. Therefore, the bias is smallest if the APS with largest phase variance is selected as reference. The precision of the estimates is

$$D\{\hat{S}_i\} = \frac{\sigma^2}{N+1}. \quad (\text{A.4.18})$$

Obviously, a weighted averaging could be performed as well. Moreover, only a subset of the estimated APS's can be used for the averaging, for instance based on the variance of the interferograms involved. However, it is difficult to give general recommendations in this perspective, because they are largely dependant on the data set used.

Finally, a *third strategy* to estimate the APS's is the application of Singular Value Decomposition. The procedure and the quality description are the same as was described in section A.4.3 for the single master case.

The cascade approach described here has the advantage over the single-master stack that the error can be 'chosen' opportunistically, since the error budget is fully determined by the interferogram with minimal phase variation. In contrast, single master stacking, especially in its unweighted form, minimizes the variance of the master atmospheric phase screen by averaging. This implies that (i) sufficient acquisitions need to be available, and (ii) the presence of a coincidental 'perfect' interferogram is not used. It needs to be noted that by weighting the single-master stack, comparable results can be obtained, although the possible decrease in coherence due to longer baselines can degrade the results.

#### **A.4.4.1 Test for the Las Vegas area**

The cascade approach is applied to a test set of the Las Vegas area. Figure A.28 shows the cascade, consisting of 33 interferograms. The cascade is shaped by a travelling salesman algorithm, (simulated annealing) conditioned by the trade-off between minimal effective baseline and temporal baseline length. Because large parts of the Las Vegas area are bare grounds, long term coherence was assumed. Hence, a short effective baseline was preferred to obtain optimal coherence.

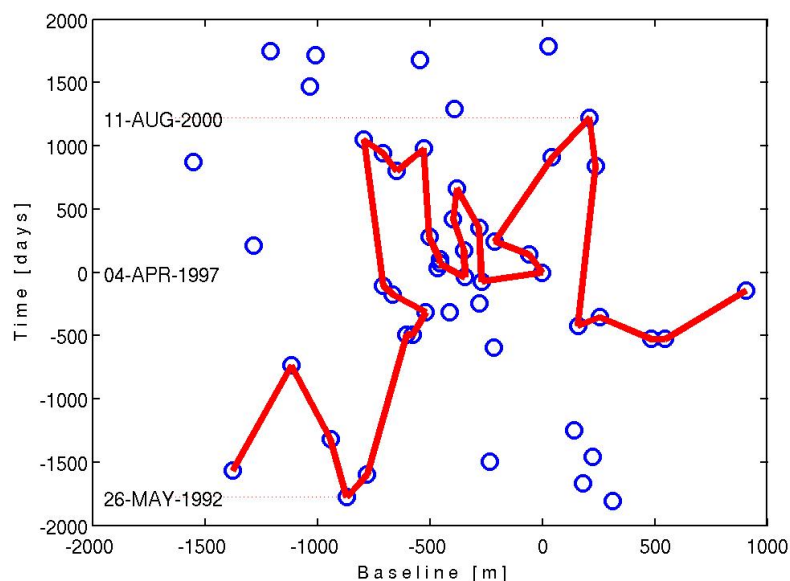


Figure A.28 Baseline plot of a cascade, consisting of 33 interferograms of the Las Vegas area.

The interferograms are processed by the genesis software (Eineder and Adam, 1997), using precise orbits and unwrapped by SNAPHU (Chen and Zebker, 2000). A SRTM-based reference DEM has been subtracted to remove the topographic signal. The phase in radians has been converted to zenith delay in mm. In order to reduce the computational load, the interferograms have been multilooked afterwards by a factor of 10 in range and a factor of 50 in azimuth, resulting in a pixel resolution of approximately 200 m.

Although long term coherence was assumed, some areas show low coherence, mainly caused by vegetation, combined with possible snow cover. This regional loss of coherence results in substantial phase unwrapping errors. Because these areas would affect the estimated APS's drastically, they are masked (see for instance Figure A.30). Moreover, remaining orbital trends in the interferograms can largely be reduced by subtraction of a linear plane. Neglecting the phase unwrapping errors would affect the estimated planes, hereby inducing another bias in the final estimates.

Depending on the processing, to cascade the interferograms two additional features have to be considered. First, the interferograms need to have the correct master-slave configuration according to the cascade order. Hence, a multiplication with factor -1 can be necessary. Second, apart from the obvious coregistration of the master and slave images for interferogram generation, the separate interferograms need to be coregistered as well. In many software-packages this will not be a standard procedure and therefore, as in our case, has to be done independently. Coregistration based on cross-correlation of the interferograms did not give satisfying results and because the amplitude images were not available, the coregistration is finally obtained by using the geographical coordinates of the corners of the interferograms. To verify the

procedure, the sum of interferograms in a circular cascade (see Figure A.29), which theoretically should result in a zero-plane, has been calculated. Figure A.30 shows the result.

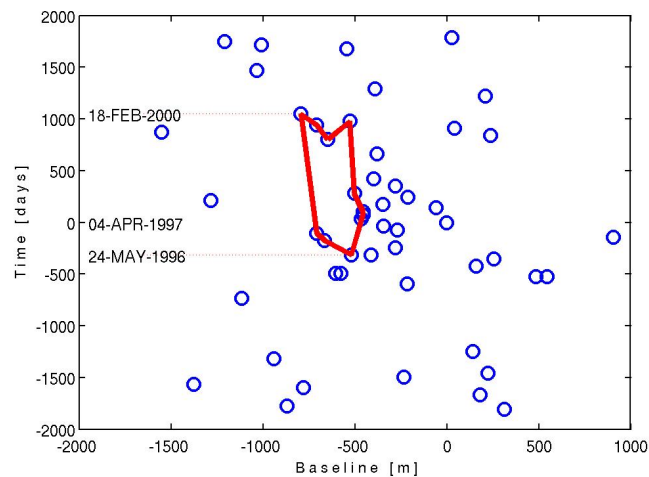


Figure A.29 Baseline plot of a circular cascade.

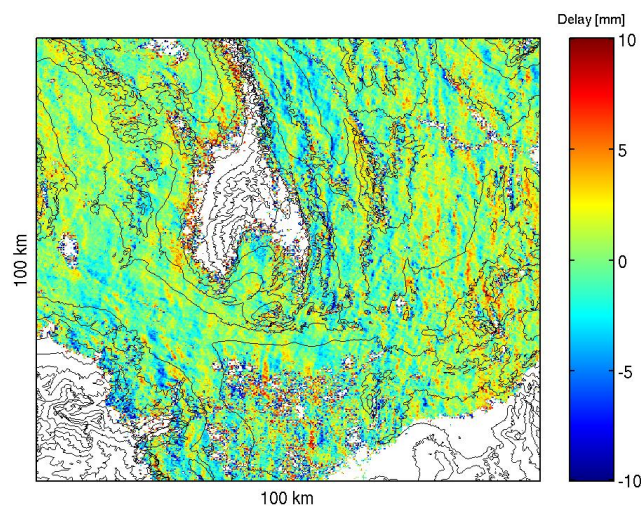


Figure A.30 Sum of interferograms in the circular cascade. Theoretically, the sum should be zero, however, co-registration and phase unwrapping errors induce a closure error.

Although the mean of the residual signal is approximately zero, still rather large fluctuations are visible (RMS = 3.79 mm). Based on the pattern, residual co-registration errors are assumed to be the major contributors. Furthermore, local phase unwrapping errors are visible, mainly on the border of the mask and in the urban area of Las Vegas in the middle/bottom of the image. Reference DEM errors are theoretically impossible, because the sum of the effective baselines is obviously zero, which results in cancellation of these errors.



The next pages show the cascaded interferograms and the results of the ambiguity retrieval. The first column shows the interferograms, starting at the right hand side of the cascade (Figure A.28). The second column contains the retrieved APS's by the first strategy described, using the APS with minimal variance as reference.

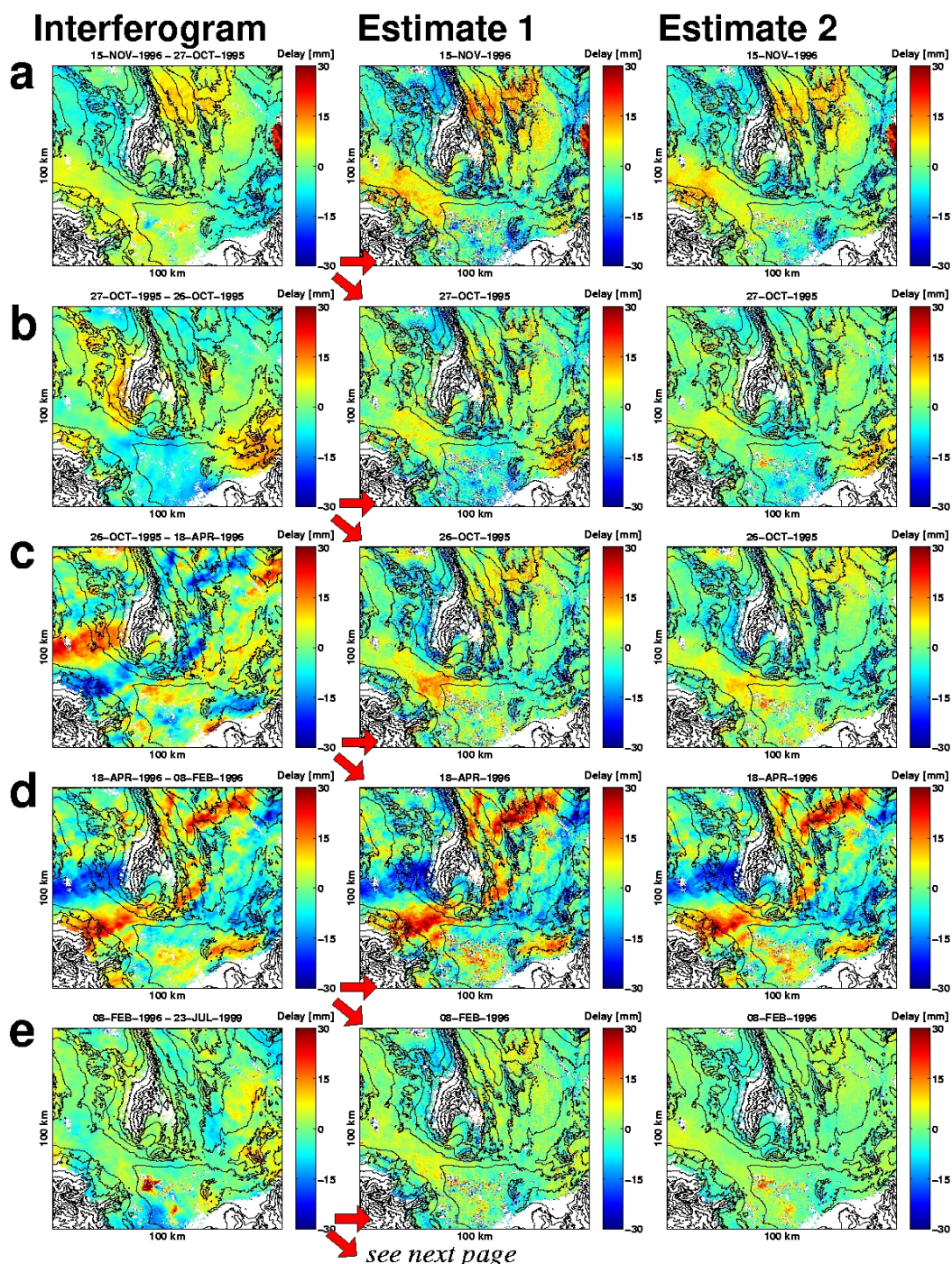


Figure A.31 Row A-E show the interferogram (first column), the APS estimate by the minimal variance method (second column) and the APS estimate by the averaging method (third column) for APS 1-5.



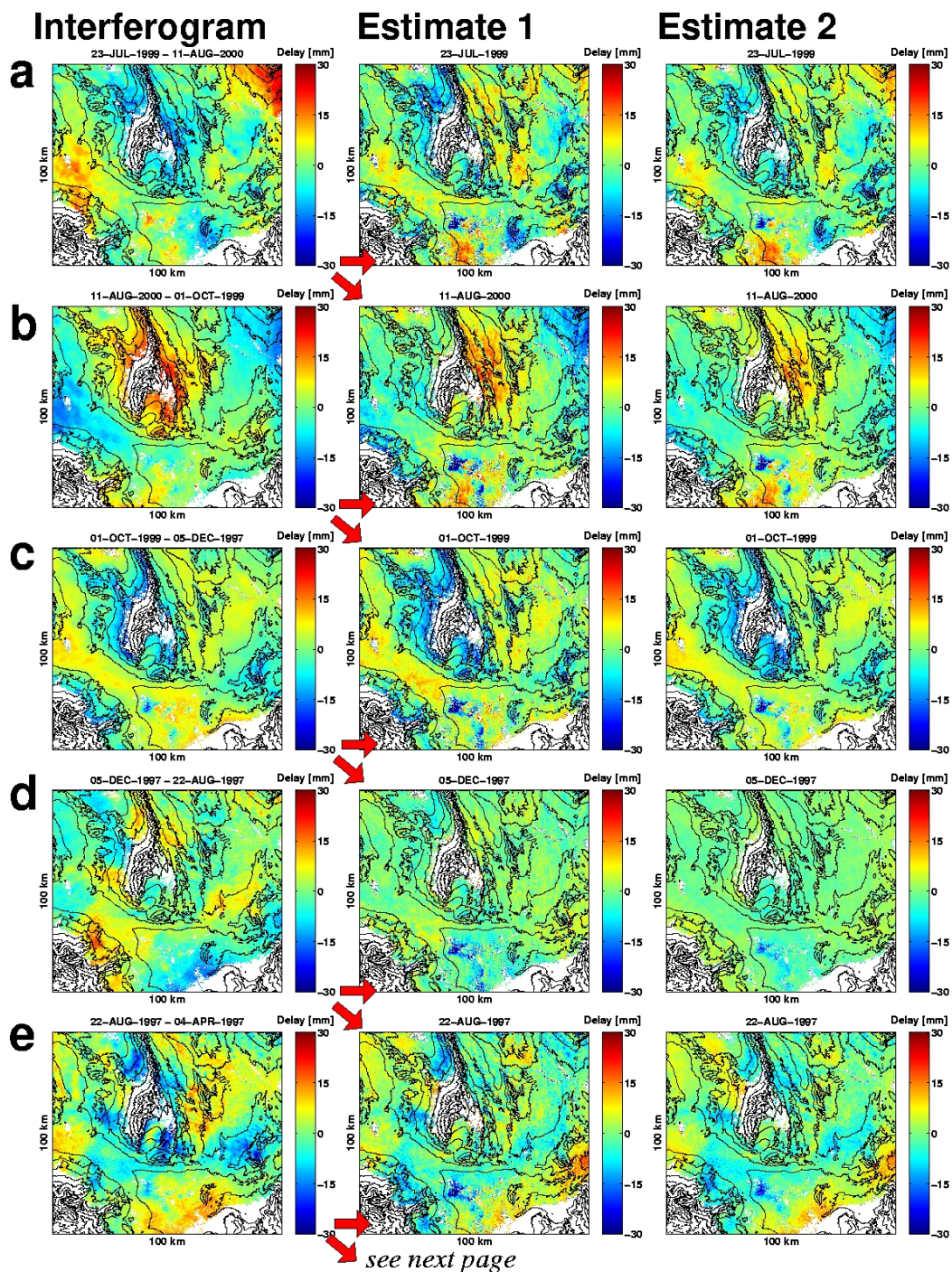


Figure A.32 Row A-E show the interferogram (first column), the APS estimate by the minimal variance method (second column) and the APS estimate by the averaging method (third column) for APS 6-10.

Consequence of this method is that the APS of the reference is put to zero, which can be seen in Figure A.36D. This APS was selected because the variance was assumed to be minimal, based on the variances of the interferograms involved (see Figure A.36C and D). The third column shows the estimates obtained by the averaging method. The SRTM-based DEM is used to generate contour lines, which serve as orientation. The



plots of the Singular Value Decomposition results are not shown, because they show large resemblance with those of the average method. This is discussed in more detail in a later stage.

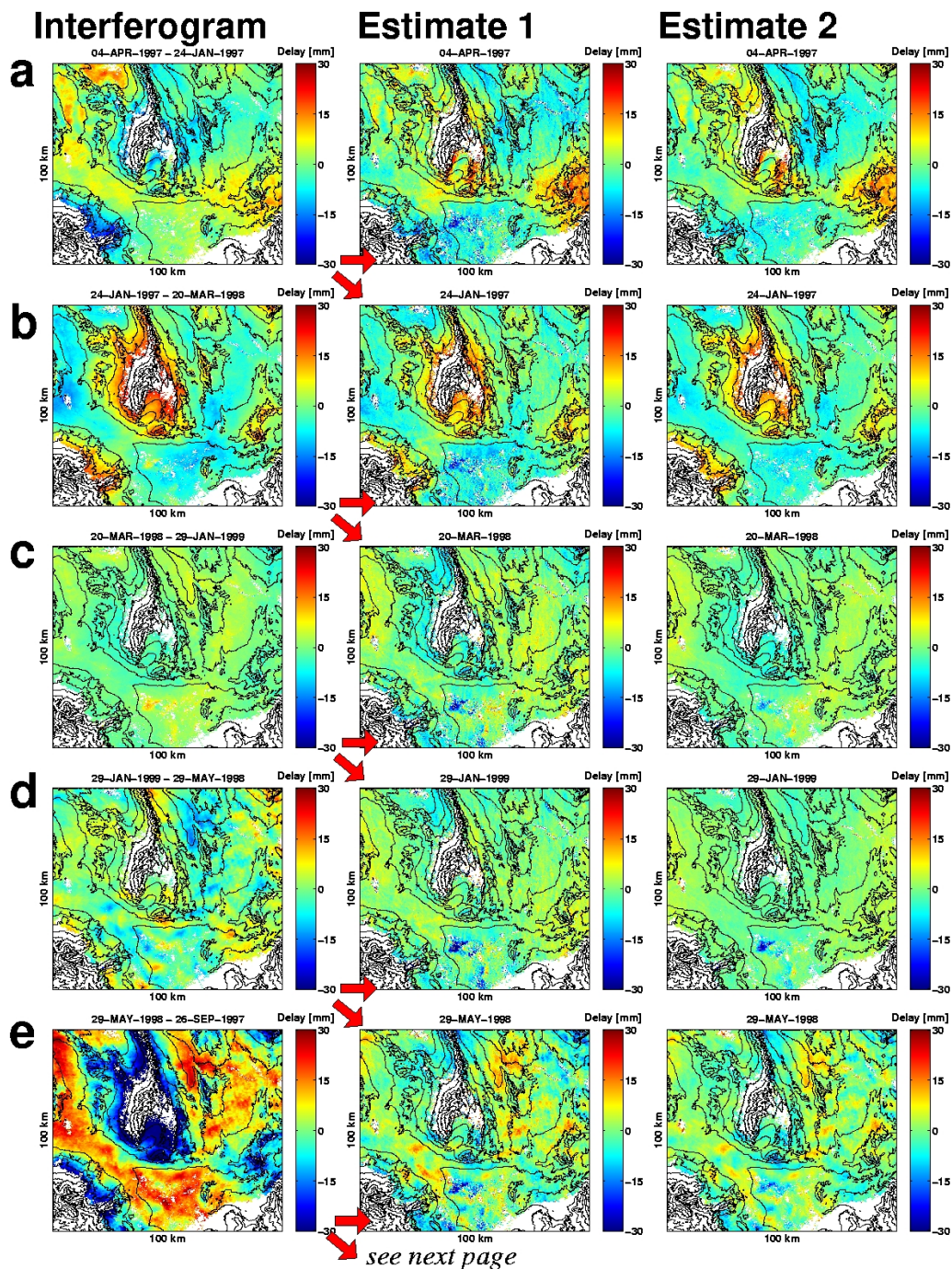


Figure A.33 Row A-E show the interferogram (first column), the APS estimate by the minimal variance method (second column) and the APS estimate by the averaging method (third column) for APS 11-15.



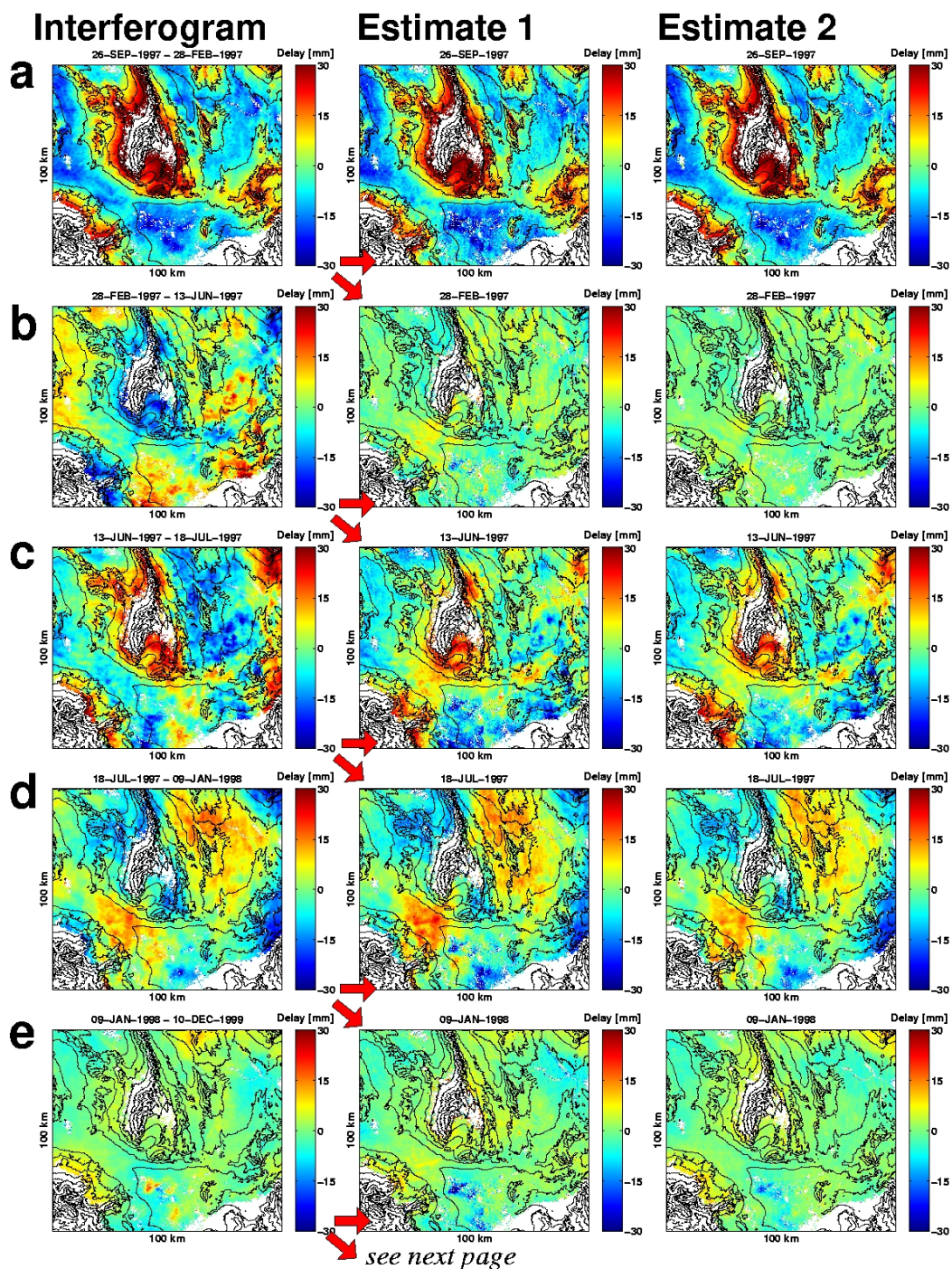


Figure A.34 Row A-E show the interferogram (first column), the APS estimate by the minimal variance method (second column) and the APS estimate by the averaging method (third column) for APS 16-20.



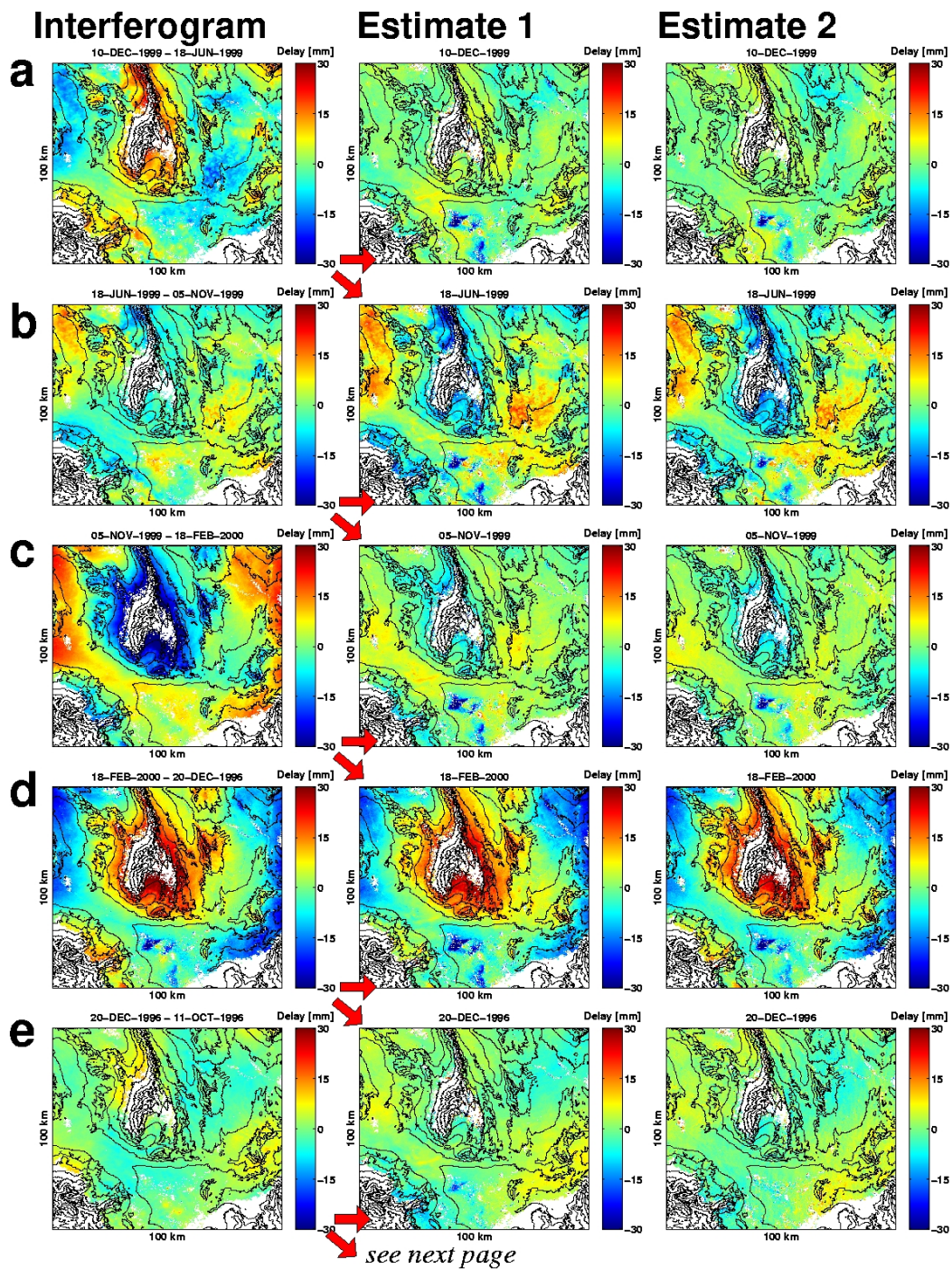
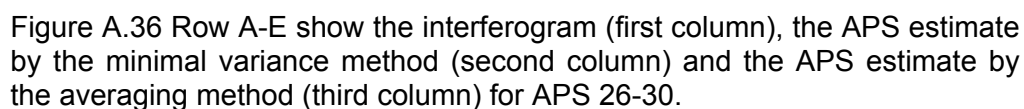


Figure A.35 Row A-E show the interferogram (first column), the APS estimate by the minimal variance method (second column) and the APS estimate by the averaging method (third column) for APS 21-25.







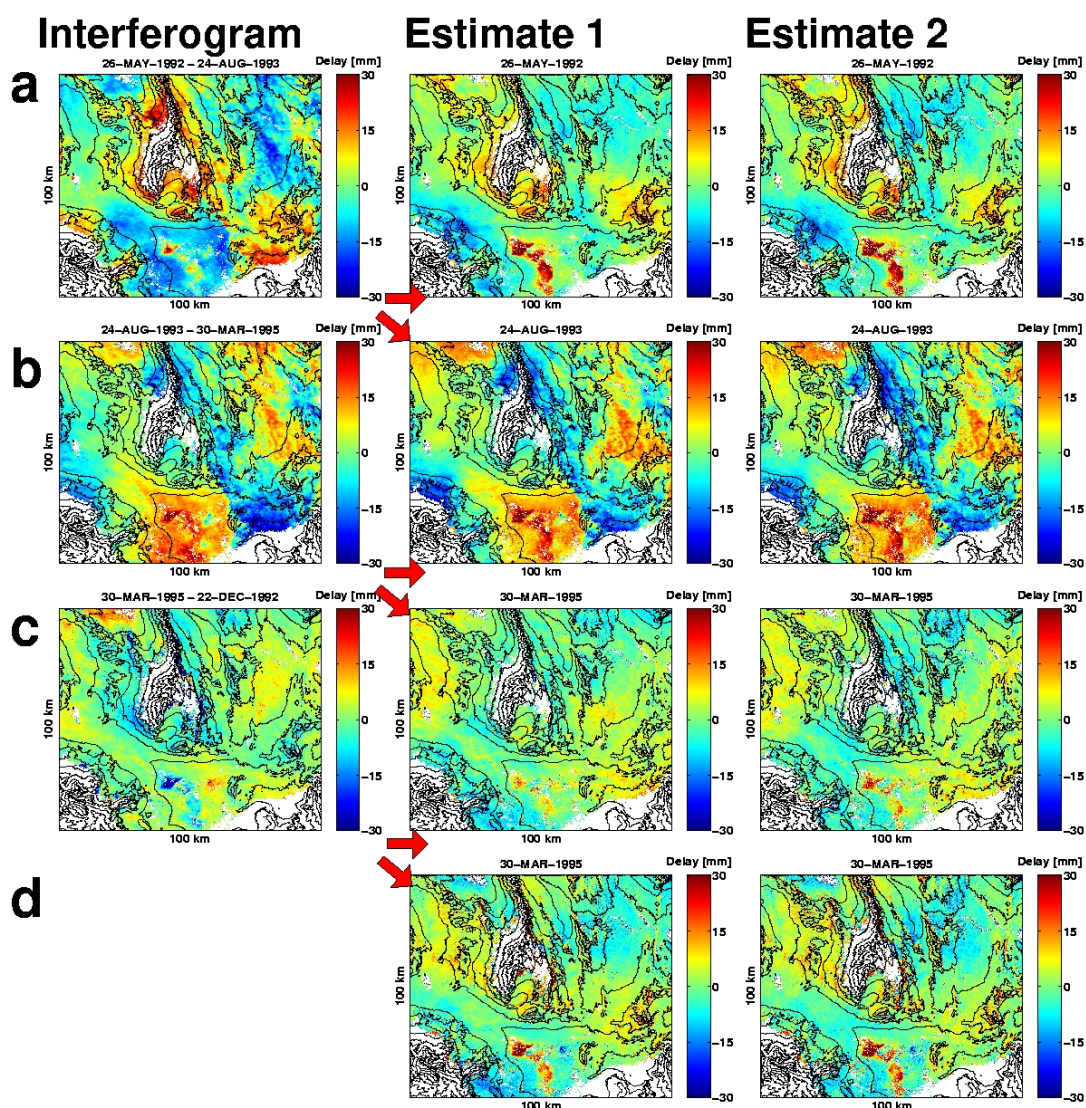


Figure A.37 Row A-E show the interferogram (first column), the APS estimate by the minimal variance method (second column) and the APS estimate by the averaging method (third column) for APS 31-34 (interferograms 31-33).

Generally, the results obtained by the various methods show large resemblance. The estimates by the averaging method (and SVD method) are somewhat smoother and show less noise (see for instance Figure A.31E). However, more test cases and comparisons with other atmospheric monitoring techniques are needed to draw conclusions in this perspective.

A number of APS estimates show a strong signal in the middle-bottom part of the image, see for instance Figure A.36E and Figure A.37A. This feature appears to be due to subsidence in urban Las Vegas. Dependent on the temporal baseline configuration, this feature is to some amount visual in practically all estimates. Estimation of a deformation model would enable the removal of the subsidence signal, giving rise to an estimate of the atmospheric signal above these areas.

Figure A.38 shows the difference between the estimated APS's by the SVD and the averaging method (which is equal for all estimates). The standard deviation reads 0.40 mm. The structure of the difference shows high correlation with the topography, suggesting an influence of the reference DEM. Further research has to clarify whether this assumption is correct.

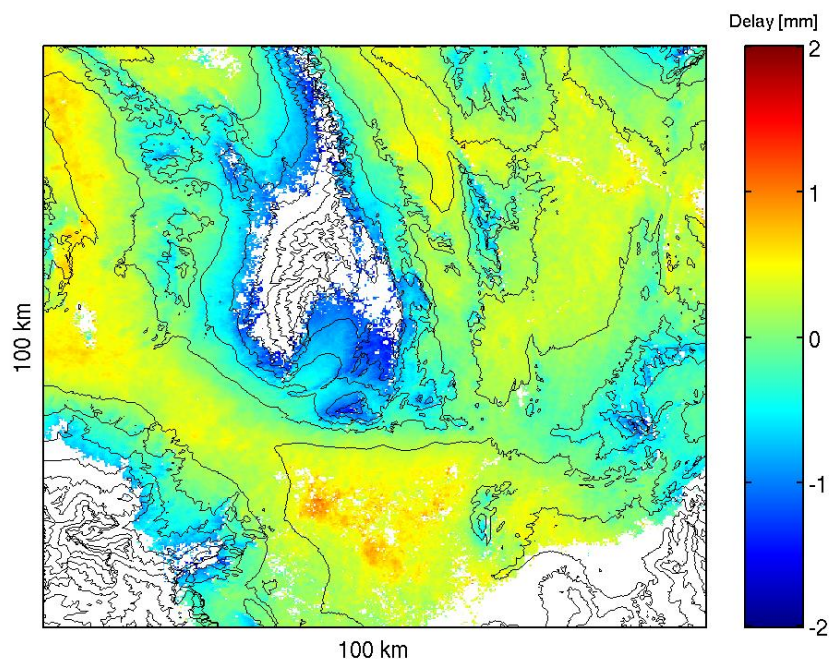


Figure A.38 Difference between the estimated APS's by the SVD and the averaging method.

#### A.4.4.2 Conclusion

The potential of the technique to retrieve the atmospheric phase screen (APS) per acquisition is shown and the resulting images give a unique tool to study atmospheric phenomenon. The three methods generate similar results, although the averaging and SVD method appear to reduce the noise. In the following, we will discuss a couple of single-acquisition APS estimates retrieved from the cascade stack.

#### A.4.5 Meteorological interpretation

Las Vegas, Nevada, is located in the south-western USA, east of the Sierra Nevada Mountains in California. Due to the Sierra Nevada, the entire state of Nevada lies in the rain-shadow desert and receives very little rainfall. The climate is usually extremely hot and dry. Las Vegas is located in a broad flat basin surrounded by barren mountains, oriented northwest-southeast, see Figure A.39, at an altitude of about 700m above sea level. The Spring Mountains, to the west, have average heights of 2000 m but peaks of 3 and 4 km. The Sheep Range to the north of Las Vegas is



clearly visible in all interferograms, and has a maximum height of 3.3 km at Hayford Peak. To the south, Mc Collough Range varies between 1 and 2.3 km, and to the east the terrain slopes down to Lake Mead and the Colorado River basin. Farther east the high mesa country of Arizona appears. Due to this complex topography, local atmospheric circulation is quite complex.

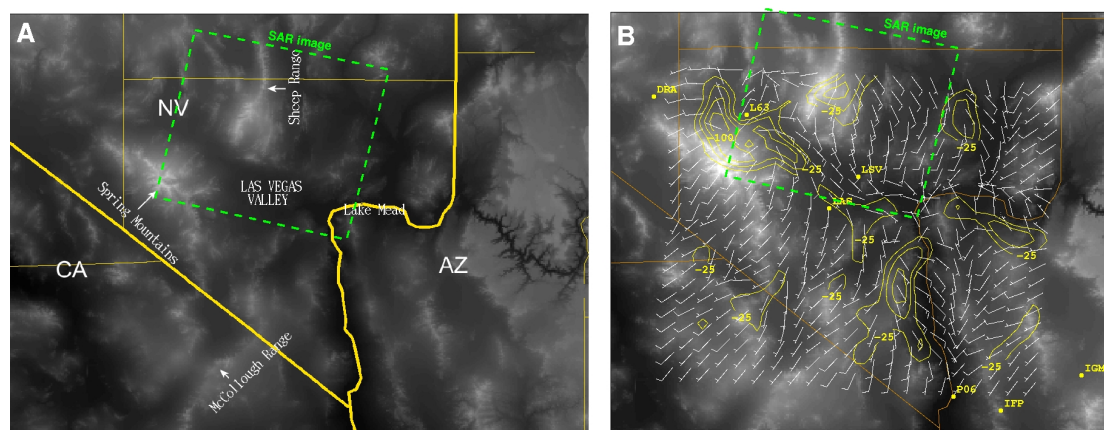


Figure A.39 (A) Topographic situation of the Las Vegas basin and the SAR image (B) Typical flow pattern associated with the Las Vegas Convergence Zone (LVCZ). Yellow isolines indicate moisture distribution.

Resulting mesoscale circulations depend on the nature and strength of the flow, the atmospheric stability, and diurnal solar forcing, which can induce a mountain-valley circulation. An arc-shaped convergence zone has been repeatedly observed to form in the low-level wind field, in the Las Vegas valley particularly under conditions of light, moderately unstable southwest flow (e.g., Runk 1996). Convergence lines also occur in the wakes of the Spring Mountains and the Sheep Range under stronger westerly flows are common (e.g., Mass 1981).

Meteorological interpretation for some selected datasets is presented here. We report on the effects of vertical stratification and select a few special cases.

#### A.4.5.1 Vertical stratification

A number of interferograms visualized in Figure A.31-Figure A.37 show a delay strongly correlated with topography. This phenomenon is assumed to be due to the vertical stratification effect described in section A.1.3.7. Vertical stratification occurs when the refractivity profiles of the atmosphere during the two acquisitions are not parallel. To verify the assumption of vertical stratification in the data, all interferograms are simulated based on radiosonde data. The radiosonde profiles were obtained at station Mercury, 100 km North-West of Las Vegas, just outside the interferogram. Measurements are available only at 6 hours before and 6 hours after the SAR acquisitions.

The refractivity profiles can be derived from the radiosonde data using the model (Equ. A.1.5)

$$N = \underbrace{k_1 \frac{P}{T}}_{N_{\text{hyd}}} + \underbrace{\left( k_2' \frac{e}{T} + k_3 \frac{e}{T^2} \right)}_{N_{\text{wet}}} - \underbrace{4.028 \times 10^7 \frac{n_e}{f^2}}_{N_{\text{iono}}} + \underbrace{1.45W}_{N_{\text{liq}}}, \quad (\text{A.4.19})$$

where the ionospheric and liquid water effects are omitted. The ionosphere does not add to the vertical stratification effect, because the ionosphere is situated at altitude higher than global topography-- only the refractivity below the highest ground point adds to the stratification. The liquid water content is unknown and its effect on stratification is neglected here. Using the temperature, relative humidity and pressure data from the radiosonde, in combination with the  $k$ -coefficients derived by Bevis *et al.* (1996), Equ. (A.1.16) and (A.1.17) can be used to obtain the necessary quantities to derive the refractivity profiles.

After differencing of the profiles, the stratification effect can be simulated by adapting the largest height as a reference. The resulting simulation and the original interferogram are shown for a case with and without stratification in Figure A.40. The differenced refractivity profiles used are shown in Figure A.41. The radiosonde launches of 6 hours before the SAR acquisitions are used. Missing data are due to the fact that the location of the radiosonde station is above the lowest points of the area, which causes the constant values over the lowest areas.

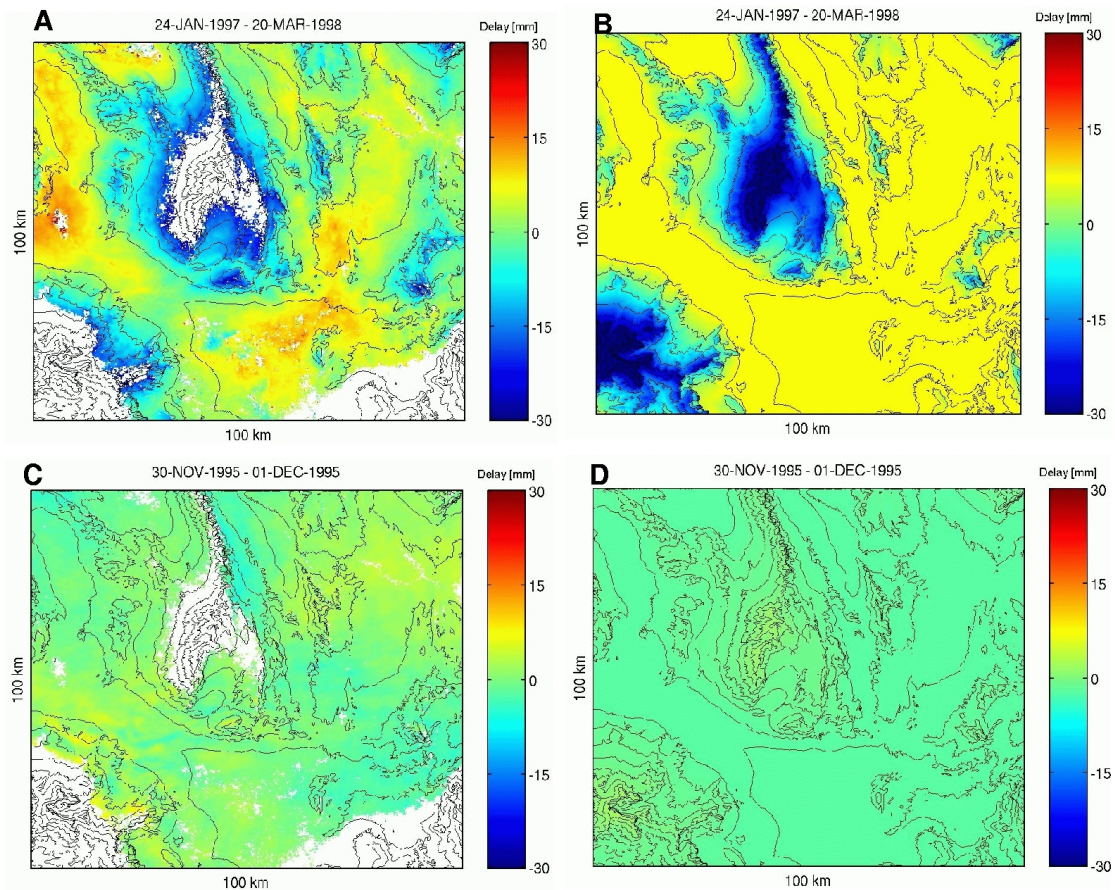


Figure A.40 Vertical stratification. (A) and (C) represent situations with and without a difference in vertical refractivity stratification, respectively. (B) and (D) reflect the expected signal based on the radiosonde vertical refractivity profiles.

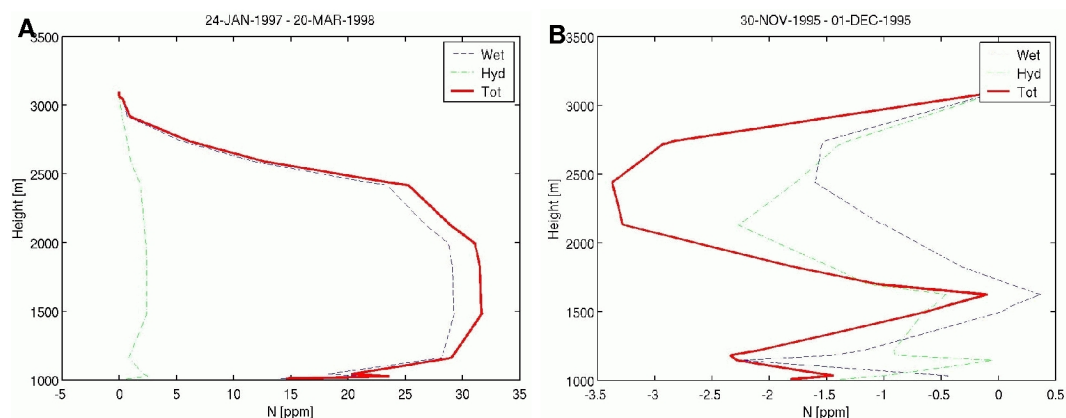


Figure A.41 Differential radiosonde profile (difference of two days) decomposed in the hydrostatic part, the wet part, and the total refractivity. (A) corresponds with Figure A.40A and (B) with Figure A.40B. It is clear to see that the differential profile (B) is one order of magnitude less than that of (A).

The correspondence between the original and simulated interferogram is shown in Figure A.42 by a cross section. The results using the sonde 6 hours before as well as 6 hours after the acquisition are given. The bottom plot shows the heights. It can be observed that there is a large resemblance between the original and simulated delay. A delay of 4 cm is visible in the top plot. Note that this effect would largely affect deformation measurements if not accounted for.

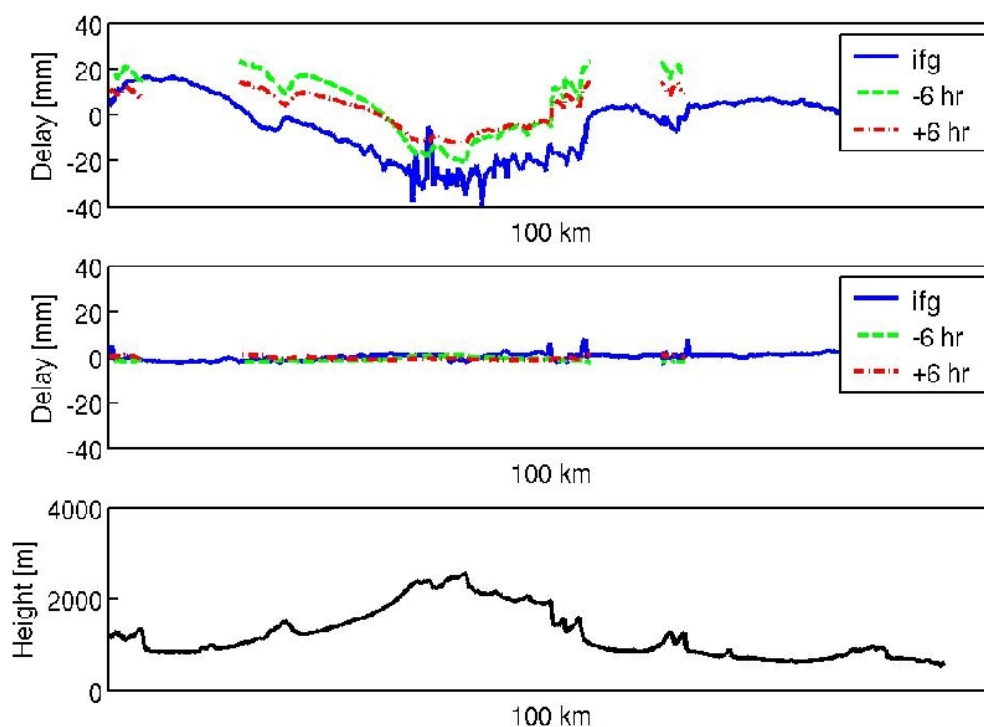


Figure A.42. Cross sections of the real and simulated interferograms. The upper graph shows the values for the first realization, the middle corresponds with the second one, and the lower is the corresponding topography.



**A.4.5.2 18 April 1996**

Meteorology in the Las Vegas basin is very complicated, due to the influence of all mountain ranges surrounding it. Figure A.43 shows a situation on 18 April 1996.

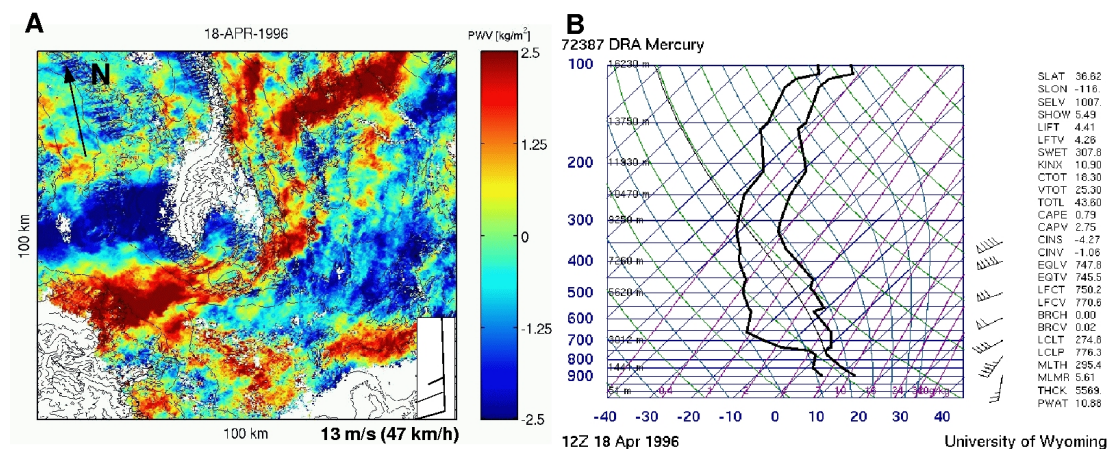


Figure A.43 The estimated water vapour distribution of 18 April 1996. (A) The cascade-derived estimate converted to relative PWV or IWV in kg/m<sup>2</sup>. The wind barb derived from the radiosonde profile is shown in the lower left (25 knots, or 13 m/s). (B) shows the radiosonde curves for temperature and dewpoint temperature.

A weak cold front passed over the region from the west the previous night. The Mercury sounding shows moisture neutral stability and ample moisture in the post-frontal westerly flow. The SAR shows bands of elevated PW in the wakes of both the Spring Mountains and the Sheep Range. The presence of convergence in the wake of mountains also occurs in Washington State where the phenomenon has been well documented (e.g., Mass 1981 and others see below)

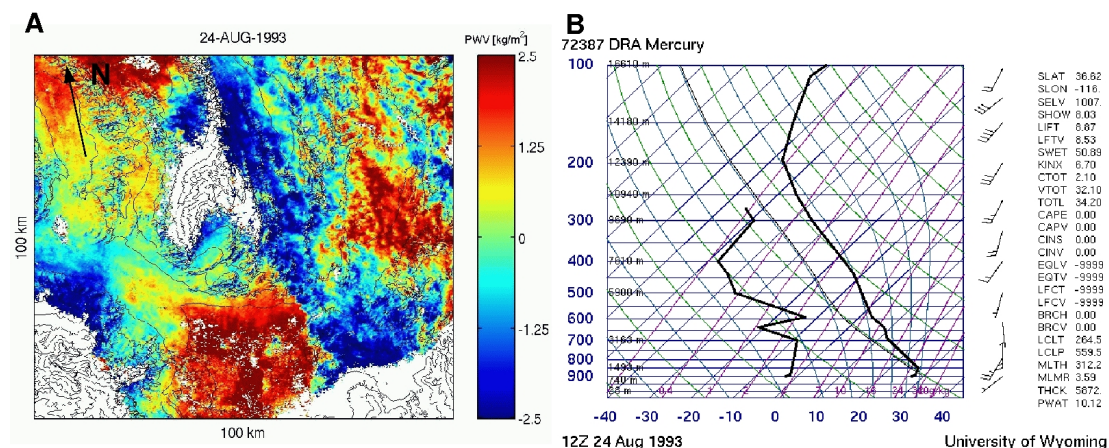
**A.4.5.3 24 August 1993**

Figure A.44 PWV distribution at 24 August 1993 and corresponding sounding from station Mercury.



Satellite imagery are consistent with the sounding data from Mercury, which indicate dry conditions in the troposphere and light southwest winds aloft. Variation in the PWV in the SAR image (with exception of the land subsidence limited to the centre of Las Vegas), therefore, must be interpreted as indicative of dry convective circulations that are influenced by terrain. Southwest winds are associated with the formation of the Las Vegas Convergence Zone (LVCZ). The pattern seen here is consistent with the formation stage of the LVCZ with the strongest rising motions along the south side of Las Vegas and a convergence line extending between the Spring Mountains and the Sheep Range. The implication here is that the SAR PWV analysis is able to identify convergence and vertical motion patterns in the absence of visible clouds. By extension, the SAR method could be applied to investigate the early stages in the formation of dry-line convection over the Great Plains, where severe thunderstorms are the frequent product.

#### **A.4.5.4 29 May 1998**

In this case satellite imagery, see Figure A.45, shows a weak front stalling near the southern boarder of Nevada. The sounding shows a moist-adiabatic lapse rate in the troposphere up to ~300 mb. Although there is some moisture in the profile, relatively large dewpoint depressions do not allow for instability. In this case variations seen in the SAR PWV image likely reflect mountain induced gravity waves.

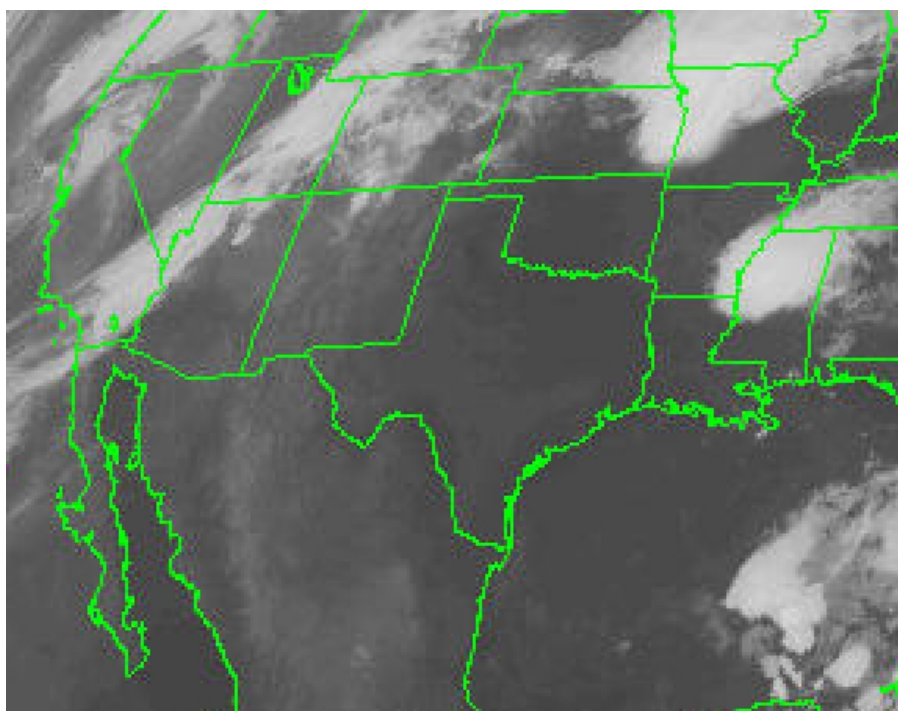


Figure A.45 GOES 9 Infrared channel at 29 May 1998, 12:15 UTC, showing the weak front near the southern boarder of Nevada.

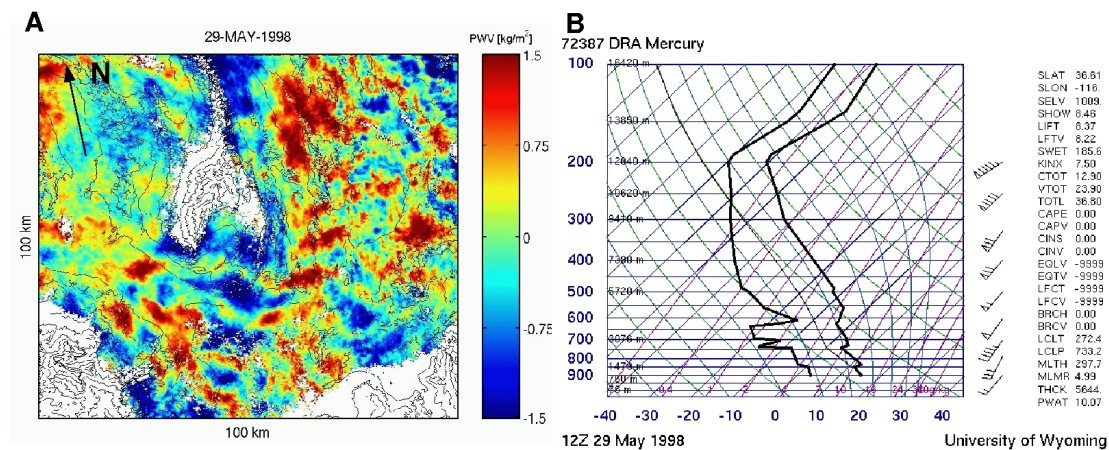


Figure A.46 Estimated water vapour field for 29 May 1998 (A) and the corresponding sounding (B).

#### A.4.5.5 18 February 2000

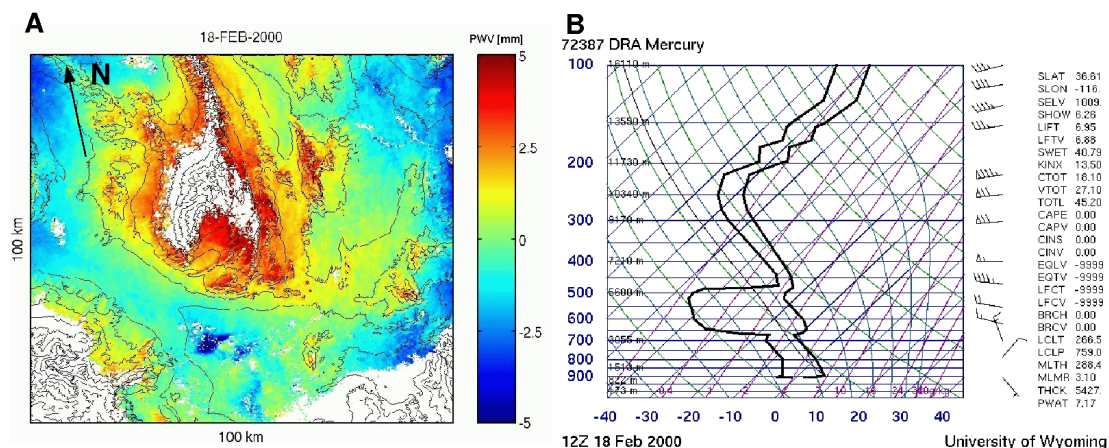


Figure A.47 PWV estimate for 18 February 2000 and corresponding sounding in Mercury.

In this case the southern Nevada is under the influence of a moderately strong westerly current (see water vapour imagery, Figure A.48, and sounding data) with baroclinic disturbances passing through. The sounding shows moist neutral conditions with moisture extending throughout the troposphere. At the time of the SAR image southern Nevada was just between two frontal systems, with lingering clouds and moisture anchored over the two mountain ranges in the image causing a difference in refractivity profiles (vertical stratification, see section A.4.5.1).

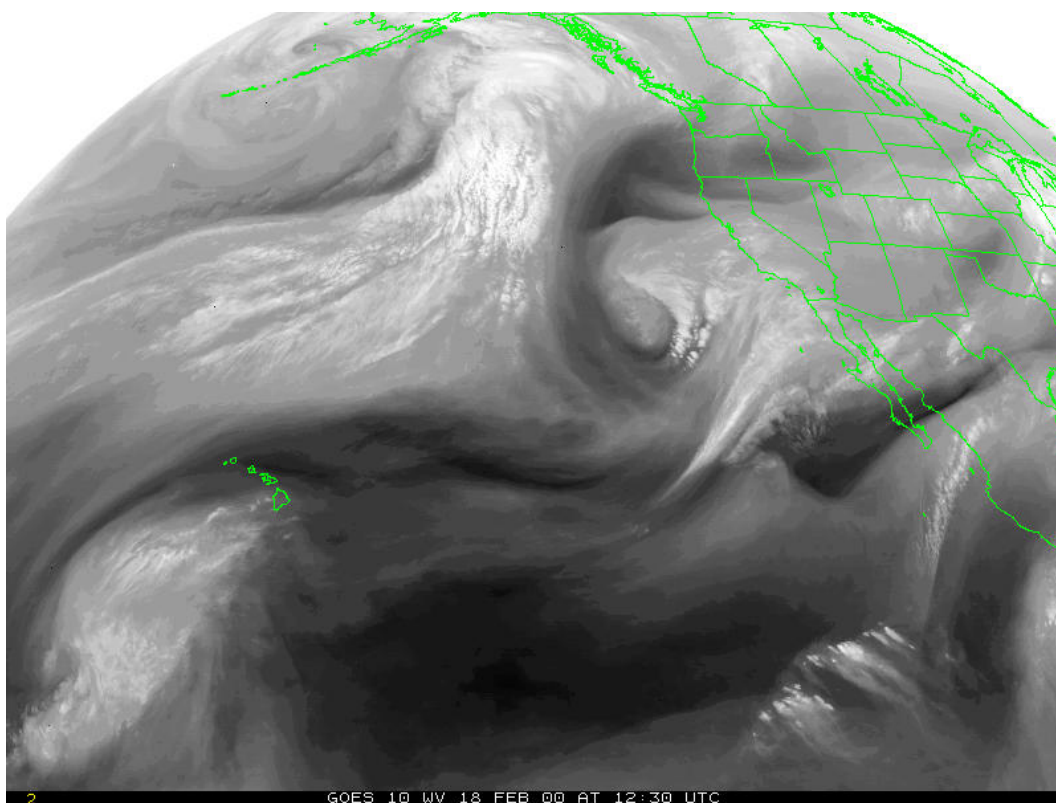


Figure A.48 Water vapour channel of GOES 10, 18 February 2000, 12:30 UTC

#### **A.4.6 Liquid water effects**

For this study we have used two interferograms. Both interferograms were acquired over Flevoland in the Netherlands. This area in the Netherlands is known for its extremely flat landscape. Since both interferograms were acquired with only one day difference in the satellites overpasses, no earth surface deformations are expected. The first interferogram was acquired on October 3 and 4, 1995 at 21.41 UTC. SAR frame numbers are 1053 and 1035, for ERS-1 orbit 22061 and ERS-2 orbit 2388, see Figure A.49. The perpendicular baseline is 393 m. This interferogram is a composition of two neighbouring scenes. The second interferogram was acquired at August 29 and 30, 1995, at 21.41 UTC. SAR frame number 1035, for ERS-1 orbit 21560 and ERS-2 orbit 1887. The perpendicular baseline is 80 m. The interferogram is shown in Figure A.50.

For these interferograms a phase unwrapping is performed using the minimal cost flow algorithm (Costantini, 1997). After the unwrapping the reference digital elevation model (DEM) was used to remove the topography. Furthermore, the spatial resolution was reduced to 160 x 160 m to reduce the speckle.

To eliminate the hydrostatic component of the troposphere the Saastamoinen model is used (Saastamoinen, 1972). This model determines hydrostatic delay estimates with an accuracy of 1 mm or better (Bevis *et al*, 1996). Moreover, the mean delay value calculated over the complete interferogram was calculated and subtracted for each interferogram. This processing step allows reducing an effect of ionosphere on the delay measurements, since an ionospheric delay has only long wavelength variability.

Therefore, the remaining delay signal after all the processing steps is expected to be only due to the propagation through the moist air and scattering on hydrometeors.

Weather radar data are obtained from the combination of two weather radars located in Schiphol and De Bilt, the Netherlands. These two radars are operating in C-band. Measurements from these two radars are combined into the reflectivity mosaic that covers completely the Netherlands. This mosaic is available every 15 min. From the observed reflectivity the rain rate is calculated using a standard Z-R relation

$$Z=200 R^{1.6} \quad (\text{A.4.20})$$

It should be noted that this relationship accuracy can be a factor 3 too large or too small, which causes one of the main uncertainties in the phase delay calculations.

#### **A.4.7 Synthesis**

In Figure A.49 and Figure A.50 comparisons between weather radar and InSAR measurements are shown. It can be seen that in all the cases the propagation delays caused by raindrops are much smaller than the observed delay. To estimate the signal delays due to the rain, we used Equ. (A.3.4) – (A.3.6) to calculate the path delay per vertical km. From radiosonde data we then obtain the height of the zero isotherm which was used to estimate the total path through the rain.

It should be noted that these calculations do not include estimations of the delay due to the melting layer of precipitations and due to the precipitating cloud above the melting layer. However, we expect that contribution of the melting layer is rather limited since it occupies the limited height range (usually in the order of few hundred meters). The precipitating cloud on the other hand can have a rather large height range, but due to the fact that the relative permittivity of ice is much smaller than the one of water the contribution of the precipitating cloud to the signal delay would be negligible.

Neither changes in pressure nor changes in temperature can explain the enhanced slant delay in the rain area. Therefore, the most probable explanation would be an increase in the water vapour concentration due to partial evaporation of the raindrops.

Based on these two examples we can argue that precipitation does cause an enhanced signal delay, less than 3% of the total observed slant delay. Therefore, the dominant contribution to the strong increase in delay over the areas of precipitation is an increase in water vapour concentration due to partial evaporation of raindrops.

#### **A.4.8 Conclusions and recommendations**

In this chapter on retrieval algorithms we have concentrated on the question how to resolve the acquisition ambiguity in the radar interferograms. In terms of atmospheric parameters it is relatively straightforward how to compute integrated water vapour content from the delay signal, assuming some knowledge on the pressure distribution and the temperature over the area of interest. The influence of liquid water was discussed and estimated to be less than 3% of the total observed delay.



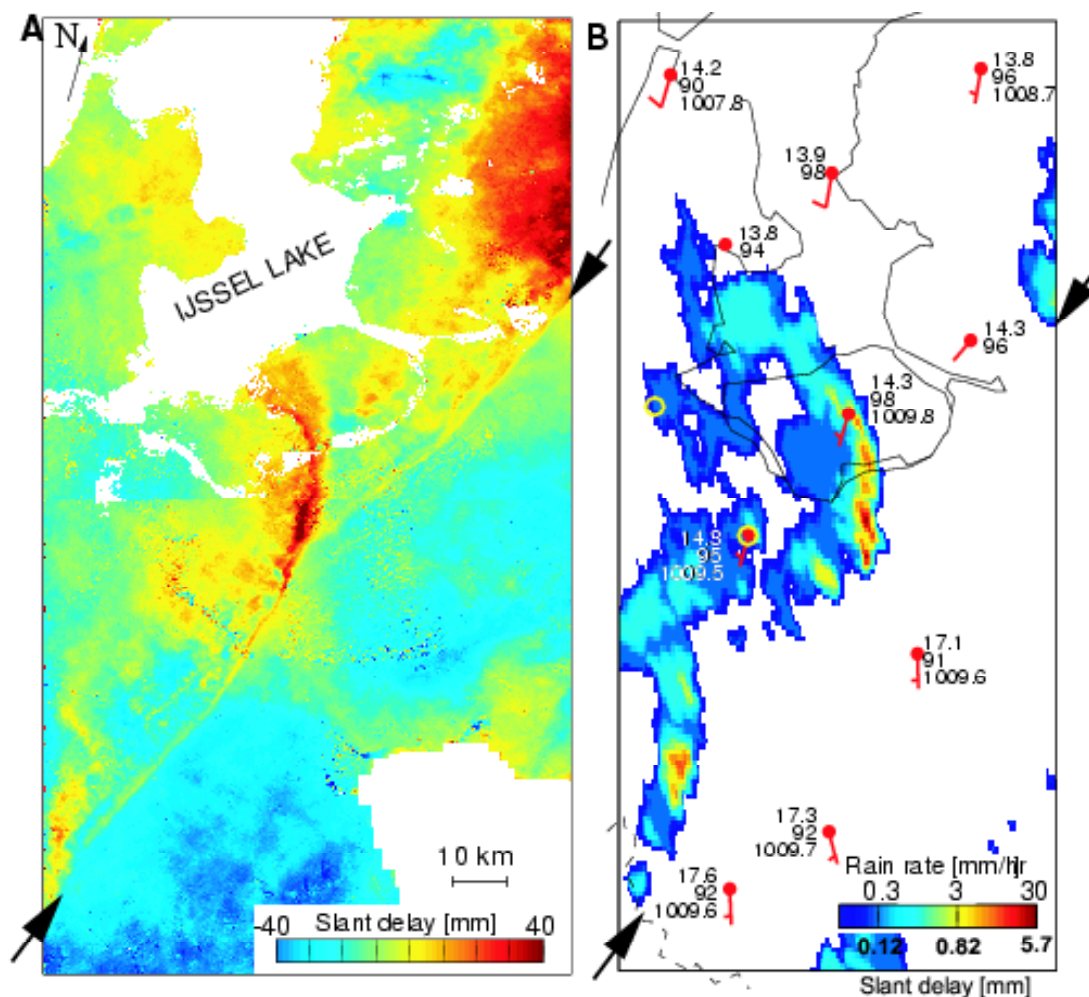


Figure A.49 The cold front observation (adapted from Hanssen *et al* 1999) (A) SAR interferogram of 3 and 4 October 1995, 21.41 UTC .The boundary of the cold front is clearly visible. (B) Weather radar image from 4 October 1995, 21.45 UTC. It can be seen that areas of large slant delay correspond to the areas of high rain intensity. In (B) the rain rate is used to calculate the slant delay due to droplets [mm]. It can be observed that propagation delay through rain is less than 3% of the total slant delay shown in (A).

Regarding the acquisition ambiguity resolution, it can be concluded that it is possible to obtain a reasonable estimate of the (precipitable) water vapour distribution per SAR acquisition using the single-master and the cascade approach. However, since the cascade approach can be tuned to use an optimal combination of baselines (temporal and perpendicular), this approach is probably the most promising for many areas of interest. Meteorological interpretation is possible and leads to new insights in mesoscale weather phenomena. In particular, the fine spatial resolution and the high accuracy is unprecedented.

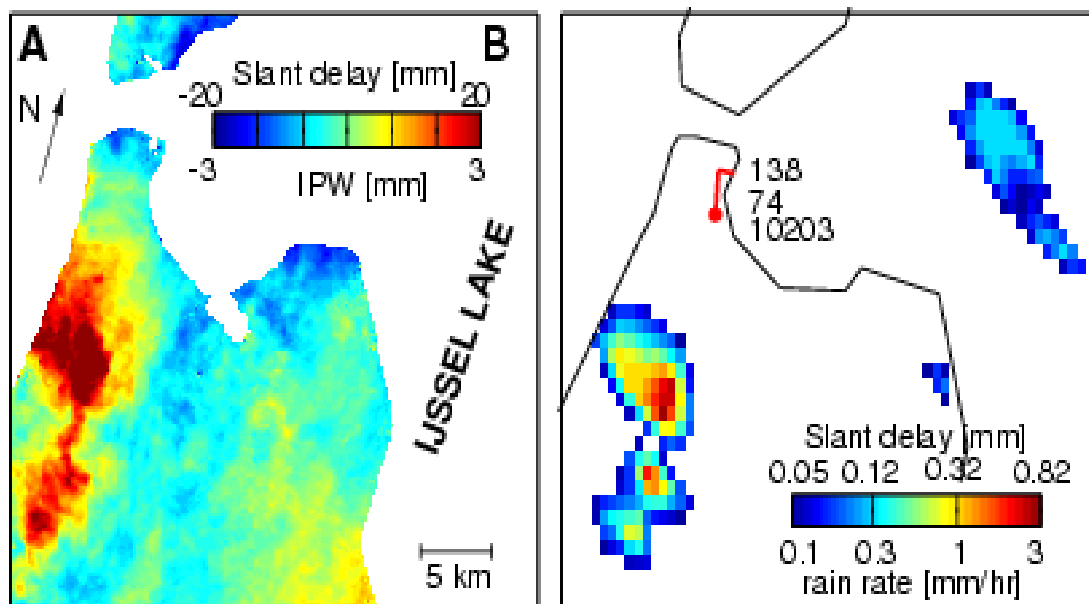


Figure A.50 Precipitation measurements. (A) SAR interferogram acquired on 29 and 30 August 1995. (B) Weather radar measurements taken on 29 August 1995. In this figure both rain rate and slant delay are depicted. The slant delay caused by propagation through the precipitation media is about 3% of the total observed delay.

The most important limitation to the reliability of the estimated APS per acquisition is the inherent rank defect in the system of equations. Nevertheless, when a large number (tens) of interferograms are available it is possible to perform a reliable adjustment (the single-master stack and the cascade approach) which give estimates of the APS per acquisition. Quantitative validation of the results is difficult due to the lack of supporting meteorological data with similar resolutions and accuracies and acquired at the same time as the radar data.

The importance of coherent and contiguous 2D phase information is underlined in the discussion on the estimation of APS from a permanent scatterer analysis. Noise on the data is the most important limitation here. Although it is possible to estimate a smooth signal using kriging algorithms, this is essentially a filtering step, in which the filter determines the amount of similarity between the experimental results and theory. Objective validation is difficult in these cases.

Based on the results from this study, it can be concluded that the use of Interferometric Radar Meteorology reached a higher level due to the resolution of the acquisition ambiguity, making it easier for meteorologists to interpret and use the SAR data for their analyses. In particular, the fact that all radar acquisitions can be analysed for their atmospheric signal makes both the archived and future data of SAR satellites extremely valuable. Nevertheless, it is necessary to convince the meteorological community from the benefits and potential of the technique, and to stimulate atmospheric studies in this field. Therefore, it is recommended to perform a full-scale and in-depth meteorological analysis of, say, 20 areas of interest in different climatological settings using the cascade technique. For example, using the severe

weather databanks it would be valuable to search for specific atmospheric circumstances where fine-resolution, high-accuracy data are usually lacking. Producing such a large set of examples is expected to be the best way to foster research in InSAR techniques for atmospheric science.

Further recommendations can be made to the development of L-band sensors, which combine less sensitivity to temporal decorrelation with a relaxed constraint on the maximum baseline length. This would lead to a larger percentage of meteorologically interpretable data. The combination of such an L-band sensor with ScanSAR<sup>1</sup> technology and a high orbital repeat frequency would lead to an optimal coverage of the world and wider, hence better interpretable, swaths. The slight reduction in spatial resolution is acceptable for such configurations.

---

<sup>1</sup> Note that burst synchronization would be essential for interferometric ScanSAR applications.

## A.5 REFERENCES

- Afraimovich, E. L., A. I. Terekhov, M. Y. Udodov, and S. V. Fridman (1992). Refraction distortions of transionospheric radio signals caused by changes in a regular ionosphere and by travelling ionospheric disturbances. *Journal of Atmospheric and Terrestrial Physics* 54(7/8), 1013-1020.
- Atkinson, B. W. and J. W. Zhang (1996, November). Mesoscale shallow convection in the atmosphere. *Reviews of Geophysics* 34(4), 403-431. Bean, B. R. and E. J. Dutton (1968). *Radio Meteorology*. New York: Dover.
- Beauducel, F., P. Briole, and J.-L. Froger (2000, July). Volcano wide fringes in ERS synthetic aperture radar interferograms of Etna. *Journal of Geophysical Research* 105(B7), 16391-16402.
- Bevis, M., S. Chiswell, S. Businger, T. A. Herring, and Y. Bock (1996). Estimating wet delays using numerical weather analysis and predictions. *Radio Science* 31(3), 477-487.
- Born, M. and E. Wolf (1980). *Electromagnetic Theory of Propagation Interference and Diffraction of Light*. New York: Pergamon Press.
- Chen, C.W. and H.A. Zebker (2000). Network approaches to two-dimensional phase unwrapping: intractability and two new algorithms. *Journal of the Optical Society of America A*, 17(3), 401-414.
- Chien, F.-C., and C. F. Mass, 1997: Interaction of a warm-season frontal system with the coastal mountains of the western United States. Part II: Evolution of a Puget Sound Convergence Zone. *Mon. Wea. Rev.*, **125**, 1730-1752.
- Costantini, M. 1998. A Novel Phase Unwrapping Method Based on Network Programming. *IEEE Trans. Geosci. Remote Sens.*, vol. 36, No 3, pp. 813-821.
- Crosetto, M., C. C. Tscherning, B. Crippa, and M. Castillo (2002). Subsidence monitoring using SAR interferometry: Reduction of the atmospheric effects using stochastic filtering. *Geophysical Research Letters* 29(9), 26-29.
- Delacourt, C., P. Briole, and J. Achache (1998, August). Tropospheric corrections of SAR interferograms with strong topography. application to Etna. *Geophysical Research Letters* 25(15), 2849-2852.
- Di-Bisceglie, M., A. Fusco, C. Galdi, and E. Sansosti (2001). Stochastic modelling of atmospheric effects in sar differential interferometry. In *International Geoscience and Remote Sensing Symposium*, Sydney, Australia, 9-13 July 2001, pp. cdrom, 3 pages.
- Duchossois, G., G. Kohlhammer, and P. Martin (1996, June). Completion of the ERS Tandem mission. *Earth Observation Quarterly* 55.
- Dupont, S., P. Nonin, L. Renouard, G. Pichon, and F. Bignone (1997). Atmospheric artifacts in ERS DTM. ISTAR's experience over multiple sites and large areas. In *Third ERS Symposium--Space at the Service of our Environment*, Florence, Italy, 17-21 March 1997.



- Eineder, M., and N. Adam (1997), A flexible system for the generation of Interferometric SAR products, *International Geoscience and Remote Sensing Symposium*, Singapore, 3-8 August 1997.
- Elgered, G. (1982). Tropospheric wet path-delay measurements. *IEEE Transactions on Antennas and Propagation* AP-30, 502-505.
- Feijt, A. and H. Jonker 2000. Comparison of scaling parameters from spatial and temporal distributions of cloud properties. *Journal of Geophysical Research*. 105 (D23): pp. 29089-29097
- Ferber, G. K., and C. F. Mass, 1990: Surface pressure perturbations produced by an isolated mesoscale topographic barrier. Part II: Influence on regional circulations. *Mon. Wea. Rev.*, **118**, 2597-2606.
- Ferretti, A., A. Monti-Guarnieri, C. Prati, and F. Rocca (1996). Multi baseline interferometric techniques and applications. In *'FRINGE 96' workshop on ERS SAR Interferometry*, Zurich, Switzerland, 30 Sep-2 October 1996.
- Ferretti, A., A. Monti-Guarnieri, C. Prati, and F. Rocca (1998). Multi-image DEM reconstruction. In *International Geoscience and Remote Sensing Symposium*, Seattle, Washington, USA, 6-10 July 1998, pp. 1367-1369.
- Ferretti, A., C. Prati, and F. Rocca (1999a, March). Multibaseline InSAR DEM reconstruction: The wavelet approach. *IEEE Transactions on Geoscience and Remote Sensing* 37(2), 705-715.
- Ferretti, A., C. Prati, and F. Rocca (1999b). Permanent scatterers in SAR interferometry. In *International Geoscience and Remote Sensing Symposium*, Hamburg, Germany, 28 June-2 July 1999, pp. 1-3.
- Ferretti, A., C. Prati, and F. Rocca (2000, September). Nonlinear subsidence rate estimation using permanent scatterers in differential SAR interferometry. *IEEE Transactions on Geoscience and Remote Sensing* 38(5), 2202-2212.
- Ferretti, A., C. Prati, and F. Rocca (2001, January). Permanent scatterers in SAR interferometry. *IEEE Transactions on Geoscience and Remote Sensing* 39(1), 8-20.
- Ferretti, A., C. Prati, F. Rocca, and A. Monti Guarnieri (1997). Multibaseline SAR interferometry for automatic DEM reconstruction. In *Third ERS Symposium--Space at the Service of our Environment*, Florence, Italy, 17-21 March 1997, ESA SP-414, pp. 1809-1820.
- Feynman, R. P., R. B. Leighton, and M. Sands (1963). *The Feynman Lectures on Physics: Commemorative Issue*, Volume 1. Reading, Massachusetts: AddisonWesley company, Inc.
- Gabriel, A. K. and R. M. Goldstein (1988). Crossed orbit interferometry: theory and experimental results from SIR-B. *Int.J. Remote Sensing* 9(5), 857-872.
- Gabriel, A. K., R. M. Goldstein, and H. A. Zebker (1989, July-10). Mapping small elevation changes over large areas: differential radar interferometry. *Journal of Geophysical Research* 94(B7), 9183-9191.
- Goldstein, R. (1995, September). Atmospheric limitations to repeat-track radar interferometry. *Geophysical Research Letters* 22(18), 2517-2520.

- Goldstein, R. M., H. A. Zebker, and C. L. Werner (1988, July). Satellite radar interferometry: Two-dimensional phase unwrapping. *Radio Science* 23(4), 713-720.
- Gray, A. L., K. E. Mattar, and G. Sofko (2000, May). Influence of ionospheric electron density fluctuations on satellite radar interferometry. *Geophysical Research Letters* 27(10), 1451-1454.
- Hall, M. P. M., L. W. Barclay, and M. T. Hewitt (Eds.) (1996). *Propagation of Radiowaves*. London: The Institution of Electrical Engineers.
- Hanssen R. and A. Ferretti. 2002a. Deformation monitoring by satellite radar interferometry: Design parameters and environmental factors affecting feasibility. *GIM International*, 16(9):52-57, September 2002.
- Hanssen R.F and A. Ferretti, 2002b, Parameter estimation in PS-InSAR deformation studies using integer least-squares techniques. *EOS Trans. AGU*, Fall Meet. Suppl., Abstract G62A-06, 83(47):F37, 2002.
- Hanssen, R. (1998). *Atmospheric heterogeneities in ERS tandem SAR interferometry*. Delft, the Netherlands: Delft University Press.
- Hanssen, R. and A. Feijt (1996). A first quantitative evaluation of atmospheric effects on SAR interferometry. In '*FRINGE 96*' workshop on ERS SAR Interferometry, Zurich, " Switzerland, 30 Sep-2 October 1996, pp. 277-282. ESA SP-406.
- Hanssen, R. and R. Klees (1997, November-18). Land subsidence monitoring with SAR interferometry: Assessment of the atmospheric errors. *EOS Transactions*, AGU 78(46), F144.
- Hanssen, R. and R. Klees (1999). An empirical model for the assessment of DEM accuracy degradation due to vertical atmospheric stratification. In *Second International Workshop on ERS SAR Interferometry*, '*FRINGE99*', Liege, Belgium, 10-12 ' Nov 1999, pp. 1-5. ESA.
- Hanssen, R. and S. Usai (1997). Interferometric phase analysis for monitoring slow deformation processes. In *Third ERS Symposium--Space at the Service of our Environment*, Florence, Italy, 17-21 March 1997, ESA SP-414, pp. 487-491.
- Hanssen, R. F. (2001). *Radar Interferometry: Data Interpretation and Error Analysis*. Dordrecht: Kluwer Academic Publishers.
- Hanssen, R. F. and T. M. Weckwerth (1999). Evaluation of spatial moisture distribution during CLARA 96 using spaceborne radar interferometry. In *Remote Sensing of cloud parameters: retrieval and validation*. 21-22 Oct 1999, Delft, The Netherlands, pp. 15-20.
- Hanssen, R. F., A. J. Feijt, and R. Klees (2001, May). Comparison of precipitable water vapour observations by spaceborne radar interferometry and Meteosat 6.7-m radiometry. *Journal of Atmospheric and Oceanic Technology* 18(5), 756-764.
- Hanssen, R. F., T. M. Weckwerth, H. A. Zebker, and R. Klees (1999, February-26). High-resolution water vapour mapping from interferometric radar measurements. *Science* 283, 1295-1297.

- Hanssen, R., B. Vermeersen, R. Scharroo, B. Kampes, S. Usai, R. Gens, and R. Klees (2000, February). Deformatiepatroon van de aardbeving van 17 augustus 1999 in Turkije gemeten met satelliet radar interferometrie. *Remote Sensing Nieuwsbrief* 90, 42-44.
- Hanssen, R., H. Zebker, R. Klees, and S. Barlag (1998). On the use of meteorological observations in SAR interferometry. In *International Geoscience and Remote Sensing Symposium*, Seattle, Washington, USA, 6-10 July 1998, pp. 1644-1646.
- Hanssen, R., I. Weinreich, S. Lehner, and A. Stoffelen (2000, June-15). Tropospheric wind and humidity derived from spaceborne radar intensity and phase observations. *Geophysical Research Letters* 27(12), 1699-1702.
- Ishimaru, A. (1978). Wave Propagation and Scattering in Random Media, Volume 2. New York: Academic Press. ISTAR (1998). Data quality analysis in support of the ERS tandem mission exploitation. *Technical Report ESRIN Contract No.12241/97/I-HGE*, ISTAR, Valbonne.
- Kenyi, L. W. and H. Raggam (1995, December). Feasibility of atmospheric effects in interferometric data and its interpretation. *Final presentation for ESA-ESTEC*, Noordwijk.
- Kursinski, E. R. (1997). *The GPS radio occultation concept: theoretical performance and initial results*. Ph. D. thesis, California Institute of Technology.
- Li, F. and R. Goldstein (1987). Studies of multi-baseline spaceborne interferometric synthetic aperture radar. In *International Geoscience and Remote Sensing Symposium*, Ann Arbor, 18-21 May 1987, pp. 1545-1550.
- Li, F. K. and R. M. Goldstein (1990, January). Studies of multibaseline spaceborne interferometric synthetic aperture radars. *IEEE Transactions on Geoscience and Remote Sensing* 28(1), 88-97.
- Marshall, J. and W. Palmer. 1948. The distribution of raindrops with size. *J. Meteorol.*, 5, 165-166, 1948.
- Mass, C. F., and D. P. Dempsey, 1985: A topographically forced convergence line in the lee of the Olympic Mountains. *Mon. Wea. Rev.*, **113**, 659-663.
- Mass, C., 1980: The Puget Sound Convergence Zone. *Weatherwise*, **33**, 272-274.
- Mass, C., 1981: Topographically forced convergence in Western Washington state. *Mon. Wea. Rev.*, **109**, 1335-1347.
- Massonnet, D. and K. L. Feigl (1995). Discrimination of geophysical phenomena in satellite radar interferograms. *Geophysical Research Letters* 22(12), 1537-1540.
- Massonnet, D. and K. L. Feigl (1998, November). Radar interferometry and its application to changes in the earth's surface. *Reviews of Geophysics* 36(4), 441-500.
- Mattar, K. E., A. L. Gray, D. Geudtner, and P. W. Vachon (1999, March). Interferometry for DEM and terrain displacement: Effects of inhomogeneous propagation. *Canadian Journal of Remote Sensing* 25(1), 60-69.
- NorthWest Research Associates, I. (2000). Atmospheric sciences. (Accessed 15 Jun, 2000) <http://www.nwra.com/>.

- Oguchi, T. 1983. Electromagnetic wave propagation and scattering in rain and other hydrometeors, *Proc. IEEE*, 71, 1029-1077.
- Pruppacher, H., and K. Beard. 1970. A wind tunnel investigation of the internal circulation and shape of water drops falling at terminal velocity in air. *Q. J. R. Meteorol. Soc.*, vol 96, pp. 247-256.
- Refice, A., F. Bovenga, S. Stramaglia, and D. Conte (2002). Use of scaling information for stochastic atmospheric absolute phase screen retrieval. In *International Geoscience and Remote Sensing Symposium*, Toronto, Canada, 24-28 June 2002.
- Resch, G. M. (1984). Water vapour radiometry in geodetic applications. In F. K. Brunner (Ed.). *Geodetic refraction*, pp. 53-84. Berlin: Springer-Verlag.
- Rosen, P. A., S. Hensley, H. A. Zebker, F. H. Webb, and E. J. Fielding (1996, October). Surface deformation and coherence measurements of Kilauea volcano, Hawaii, from SIR-C radar interferometry. *Journal of Geophysical Research* 101(E10), 23109- 23125.
- Runk, K.J., 1996: The Las Vegas convergence zone: Its development, structure and implications for forecasting. *NWS Western Region Tech. Attach.* 96-18, 21p.
- Saastamoinen, J. (1972). Introduction to practical computation of astronomical refraction. *Bulletin Geodesique* 106, 383-397.
- Saito, A., S. Fukao, and S. Miyazaki (1998, August). High resolution mapping of TEC perturbations with the GSI GPS network over Japan. *Geophysical Research Letters* 25(16), 3079-3082.
- Shimada, M., M. Minamisawa, and O. Isoguchi (2001). Correction of atmospheric excess path delay appeared in repeat-pass SAR interferometry using objective analysis data. In *International Geoscience and Remote Sensing Symposium*, Sydney, Australia, 9-13 July 2001, pp. cdrom, 3 pages.
- Smith, Jr., E. K. and S. Weintraub (1953, August). The constants in the equation for atmospheric refractive index at radio frequencies. *Proc. I.R.E.* 41, 1035- 1037.
- Solheim, F. S., J. Vivekanandan, R. H. Ware, and C. Rocken (1999). Propagation delays induced in GPS signals by dry air, water vapour, hydrometeors and other particulates. draft for *J. of Geoph. Res.* **104**, 9663-9670.
- Stull, R. B. (1995). *Meteorology Today For Scientists and Engineers*. St. Paul, Minneapolis: West Publishing.
- Tarayre, H. (1996). *Extraction de Modeles Numeriques de Terrain par Interferometrie Radar Satellitaire: Algorithmie et Artefacts Atmospheriques*. Ph. D. thesis, Institut National Polytechnique de Toulouse, Toulouse.
- Tarayre, H. and D. Massonnet (1994). Effects of refractive atmosphere on interferometric processing. In *International Geoscience and Remote Sensing Symposium*, Pasadena, CA, USA, 8-12 August 1994, pp. 717-719.
- Tarayre, H. and D. Massonnet (1996, May). Atmospheric propagation heterogeneities revealed by ERS-1 interferometry. *Geophysical Research Letters* 23(9), 989-992.

- Tarayre-Oriot, H. and D. Massonnet (1996). Atmospheric artifacts on interferograms. In '*FRINGE 96' workshop on ERS SAR Interferometry*, Zurich, Switzerland, 30 Sep-2 " October 1996, pp. 125-128.
- Thayer, G. D. (1974). An improved equation for the radio refractive index of air. *Radio Science* 9, 803-807.
- Treuhaft, R. N. and G. E. Lanyi (1987, March). The effect of the dynamic wet troposphere on radio interferometric measurements. *Radio Science* 22(2), 251-265.
- Van de Hulst, H.C. 1957. *Light Scattering by Small Particles*. New York, John Wiley, 1957.
- Van der Hoeven, A., R. F. Hanssen, and B. Ambrosius (2002). Tropospheric delay estimation and analysis using GPS and SAR interferometry. *Physics and Chemistry of the Earth* 27, 385-390.
- Wadge, G., P. W. Webley, I. N. James, R. Bingley, A. Dodson, S. Waugh, T. Veneboer, G. Puglisi, M. Mattia, D. Baker, S. C. Edwards, S. J. Edwards, and P. J. Clarke (2002, October). Atmospheric models, GPS and InSAR measurements of the tropospheric water vapour field over mount Etna. *Geophysical Research Letters* 29(19), 11/1-4.
- Webley, P. W., R. M. Bingley, A. H. Dodson, G. Wadge, S. J. Waugh, and I. N. James (2002). Atmospheric water vapour correction to INSAR surface motion measurements on mountains: results from a dense GPS network on Mount Etna. *Physics and Chemistry of the Earth, Parts A/B/C* 29(4-5), 363-370.
- Weckwerth, T. M., J. W. Wilson, R. M. Wakimoto, and N. A. Crook (1997, April). Horizontal convective rolls: Determining the environmental conditions supporting their existence and characteristics. *Monthly Weather Review* 125(4), 505-526.
- Whitney, W. M., R. L. Doherty, and B. R. Colman, 1993: A method for predicting the Puget Sound Convergence Zone and its associated weather. *Wea. Forecasting*, **8**, 214-222.
- Williams, S., Y. Bock, and P. Fang (1998). Integrated satellite interferometry: Tropospheric noise, GPS estimates and implications for interferometric synthetic aperture radar products. *Journal of Geophysical Research* 103(B11), 27,051-27,067.
- Zebker, H. A., P. A. Rosen, and S. Hensley (1997, April). Atmospheric effects in interferometric synthetic aperture radar surface deformation and topographic maps. *Journal of Geophysical Research* 102(B4), 7547-7563.

## **A.6 ACKNOWLEDGEMENTS**

The authors would like to express their special appreciation to Nico Adam, Michael Eineder, and Bert Kampes (DLR/Remote Sensing Technology Institute) for their collaboration in the data processing and constructive discussions. Falk Amelung is gratefully acknowledged for his help with the Radarsat data of Hawaii. Joaquin Munoz Sabater assisted in the analysis of the permanent scatterer APS estimation. Finally, we would like to thank Thomas Nagler and Helmut Rott for their organization, patience, and careful compilation of the final report, and Nicolas Floury for his critical and constructive comments.

## **PART B**

# **INSAR RETRIEVAL OF SNOW AND ICE PARAMETERS**

**Thomas NAGLER and Helmut ROTT**

ENVEO  
Innsbruck AUSTRIA

with contributions from

**Dana FLORICIOIU**

*This page is intentionally left blank.*



## Table of Contents

<b>B.1</b>	<b>LITERATURE REVIEW.....</b>	<b>B-1</b>
B.1.1	Introduction.....	B-1
B.1.2	Radar wave propagation in snow and ice .....	B-1
B.1.3	InSAR application for ice motion and topography .....	B-5
B.1.4	InSAR retrievals of snow and ice properties .....	B-7
B.1.4.1	Coherence of snow and ice .....	B-7
B.1.4.2	Possibilities for InSAR retrievals of snow and ice variables.....	B-9
B.1.4.2.1	Penetration depth / diagenetic snow and ice facies.....	B-9
B.1.4.2.2	Snow areal extent.....	B-10
B.1.4.2.3	Snow water equivalent (SWE).....	B-10
B.1.5	Summary and conclusions .....	B-12
<b>B.2</b>	<b>IDENTIFICATION OF VARIABLES AND TECHNIQUES .....</b>	<b>B-13</b>
B.2.1	Introduction.....	B-13
B.2.2	Diagenetic glacier facies .....	B-13
B.2.3	Snow extent.....	B-17
B.2.4	Snow water equivalent.....	B-20
B.2.5	Assessment and ranking.....	B-23
<b>B.3</b>	<b>ELECTROMAGNETIC INTERACTION MODELLING FOR SNOW COVERED TERRAIN</b>	<b>B-25</b>
B.3.1	Introduction.....	B-25
B.3.2	Radar backscatter modelling of snow covered terrain.....	B-25
B.3.3	Spatial and temporal decorrelation .....	B-32
B.3.3.1	Estimation of effects of $\gamma_{\text{surface}}$ and $\gamma_{\text{volume}}$ for snow covered ground.....	B-32
B.3.3.2	Estimation of effects of $\gamma_{\text{temporal}}$ related to snowfall .....	B-34
B.3.4	SWE retrieval based on interferometric phase shift .....	B-37
B.3.4.1	Error estimate for SWE due to phase noise .....	B-38
B.3.4.2	Error estimate for <i>SWE</i> due to the topographic phase .....	B-39
B.3.4.3	Error estimate of <i>SWE</i> due to orbit uncertainties.....	B-40
B.3.4.4	Effect of variations of atmospheric conditions .....	B-41
B.3.5	Summary and conclusions .....	B-43

---

<b>B.4</b>	<b>RETRIEVAL ALGORITHM AND TEST CASES .....</b>	<b>B-45</b>
B.4.1	Retrieval Algorithm .....	B-45
B.4.2	Test cases and data set .....	B-47
B.4.2.1	Analysis of ERS SAR 3-days repeat pass images .....	B-48
B.4.2.1.1	Test area A: Sonnseite .....	B-53
B.4.2.1.2	Test area B: Totes Gebirge .....	B-57
B.4.2.1.3	Test area C: Mur valley - Zeltweg .....	B-60
B.4.2.2	Analysis of ERS SAR Tandem data of a high alpine area.....	B-62
B.4.2.3	Airborne E-SAR L-band data of Test area Oberpfaffenhofen (InSAR processing by R. Scheiber, DLR-HF).....	B-63
B.4.3	Conclusions from test cases .....	B-68
<b>B.5</b>	<b>CONCLUSIONS AND OUTLOOK FOR SWE RETRIEVAL BY INSAR .....</b>	<b>B-69</b>
<b>B.6</b>	<b>REFERENCES .....</b>	<b>B-71</b>

## B.1 LITERATURE REVIEW

### B.1.1 Introduction

The literature regarding methods and applications of SAR interferometry over snow and ice is reviewed, with focus on papers that are of particular interest for development of new interferometric retrieval algorithms. The main application of InSAR over snow and ice has been mapping of surface topography and ice motion. Some hundred papers on these topics have been published. As this is a well established application, only some key papers are cited in this review (section B.1.3). Only few papers on retrievals of other physical properties of snow and ice have been published in the open literature. These are reviewed in section B.1.4. Because electromagnetic wave propagation in snow and ice is of relevance for the further work in this study, several key papers on this topic are reviewed in section B.1.2.

### B.1.2 Radar wave propagation in snow and ice

For the interpretation of interferometric signatures of snow and ice and for the development of InSAR retrieval techniques it is essential to know about the dominating interaction mechanisms of radar waves with these targets. In this section the main factors of relevance for backscattering from snow and ice in the L- to X-band range and key papers on related experimental and theoretical work are briefly summarized.

Snow is a mixture of air, ice crystals, and, if melting, liquid water. The percentages and distribution of these components in the snow volume may vary significantly, depending on the metamorphic state of the snow pack (Colbeck, 1982). In glacier ice air bubbles occupy only few per cent by volume (Paterson, 1994). In ice at melting point a water film forms at the grain boundaries. On glacier ice surfaces often tiny water-filled depression (cryoconite holes) develop due to selective melting. Sea ice is a mixture of ice, air bubbles and brine and may show highly diversified morphology depending on ice type, history of ice formation, and environmental conditions (Arcone *et al.*, 1986; Winebrenner *et al.*, 1992). Below we focus on the main microwave propagation and scattering characteristics of seasonal snow, glacier ice and polar firn.

The propagation of electromagnetic waves in snow is governed by the complex permittivity which is strongly dependent on liquid water content. In the 1 MHz to 10 GHz range the real part of the permittivity of pure ice is independent of frequency:  $\epsilon'_i = 3.185$  ( $T \cong -4^\circ\text{C}$ ), and the permittivity of dry snow,  $\epsilon'_s$ , depends on the density  $\rho_s$  (Mätzler, 1987). For  $\rho_s < 0.45 \text{ g cm}^{-3}$  the following polynomial fit matches very well the experimental data (Mätzler, 1996):

$$\epsilon'_s = 1 + 1.5995\rho_s + 1.861\rho_s^3 \quad (\text{dry snow}) \quad (\text{B.1.1})$$

The real part of the permittivity shows a very weak dependence on temperature as long as there is no liquid water in ice or snow (Mätzler, 1998). The imaginary part of

the permittivity of pure ice,  $\varepsilon''_i$ , and snow,  $\varepsilon''_s$ , varies with frequency and temperature. At  $T = 250\text{ K}$  the minimum of  $\varepsilon''_i \cong 10^{-4}$  is found near 1 GHz (Mätzler, 1998). Equ. (B1.2), developed by Hufford (1991) describes  $\varepsilon''_i$  in dependence on frequency,  $f$ :

$$\varepsilon''_i = \frac{\alpha}{f} + \beta f \quad (\text{B.1.2})$$

The parameters  $\alpha$  and  $\beta$  depend on temperature (Mätzler, 1996). As an example, the values for  $T = 260\text{ K}$  are:  $\alpha = 2.0 \cdot 10^{-4}$ ,  $\beta = 6.96 \cdot 10^{-5}$ . The imaginary part of the permittivity of dry snow can be calculated from the permittivity  $\varepsilon''_i$  by:

$$\varepsilon''_s = (0.48\rho_s + 0.52\rho_s^2) \varepsilon''_i \quad (\text{dry snow}) \quad (\text{B.1.3})$$

Neglecting attenuation due to scattering in the snow volume, in case of  $\varepsilon'' \ll \varepsilon'$  the penetration depth in dry snow can be estimated according to:

$$d_p = \frac{\lambda_0 \sqrt{\varepsilon'}}{2\pi \varepsilon''} \quad (\text{B.1.4})$$

This represents an upper limit of penetration. At C - band, for example,  $d_p = 90\text{ m}$  is derived with this equation for  $\rho_s = 0.5\text{ g cm}^{-3}$  and  $T = 260\text{ K}$ . Because the dielectric loss factor is so small, scattering in snow and ice plays even a role at frequencies which are comparatively large relative to the size of the scattering particles, as for example C-band. Experimental data measured at natural snow and cold polar firm (Figure B.1.1) show that the penetration is smaller than the numbers derived by Equ. (B.1.4), but the equation provides the right order of magnitude.

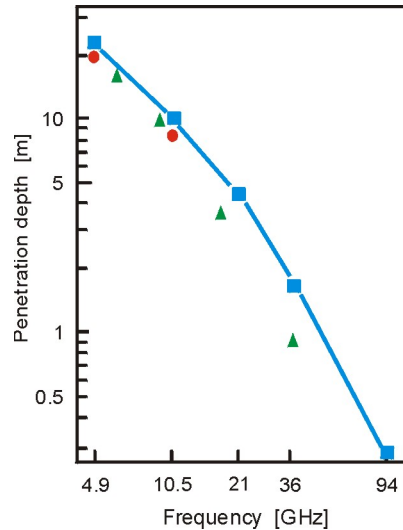


Figure B.1.1: Microwave penetration depth: ■ dry snow from measurements of alpine snowpack (Mätzler, 1987), ● field measurements of dry Antarctic firm (Rott *et al.*, 1993), ▲ inversion of SMMR data, Antarctic Plateau (Rott, 1989).

The measurements show penetration depths for dry Alpine and Antarctic snow of about 20 m at 5 GHz and about 10 m at 10 GHz. This has strong impact for the analysis and interpretation of InSAR data of dry snow and firn, as the scattering phase centre can be several meters below the snow surface. The effect of grain size on the penetration depth becomes obvious towards higher frequencies in Figure B.1.1, where  $d_p$  of Antarctic firn is somewhat smaller than of more fine-grained Alpine winter snow.

The penetration depth decreases strongly if snow contains liquid water. Using the equations for calculating the complex permittivity of wet snow of Mätzler (1987), Figure B.1.2 shows  $d_p$  in dependence of liquid water content,  $V_w$ , calculated according to Equ. (B.1.4). It is obvious that at X- and C-band the volume scattering contribution of snow during the melting period, with typical values for  $V_w$  of a few per cent by volume, is very small. At L-band the volume contribution is relevant, because  $d_p$  is of the order of 0.5 m to 1 m.

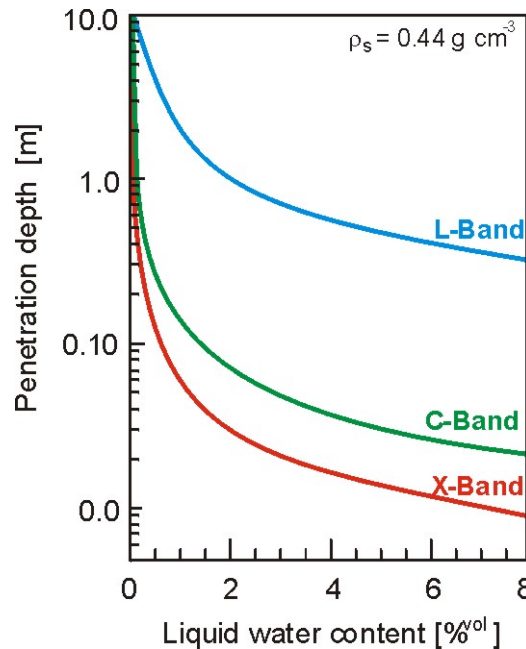


Figure B.1.2: Penetration depth,  $d_p$ , in wet snow as function of liquid water content,  $V_w$  (% by volume) at 1.24, 5.3 and 9.6 GHz.

The dielectric properties and penetration depth provide an important basis for estimating the layers which contribute to the radar signal of snow packs. Based on a first order radiative transfer model, the components contributing to backscattering from ground covered by a single snow layer can be written in terms of backscattering coefficient (Shi and Dozier, 2000b):

$$\sigma_{pp}^t = \sigma_{pp}^a + \sigma_{pp}^v + \sigma_{pp}^{gv} + T^2 \exp\left[-2\kappa_e d_s / \cos\theta_i\right] \sigma_{pp}^g \quad (\text{B.1.5})$$

where superscript  $t$ ,  $a$ ,  $v$ ,  $gv$ , and  $g$  refer to total backscattering, backscattering from the air-snow interface, direct volume contribution from the snow-pack, ground-

volume interaction and backscattering from the snow-ground interface, respectively.  $T$  is the power transmissivity for a plane boundary at the air-snow interface,  $\kappa_e$  the volume extinction coefficient and  $d_s$  the snow depth. The direct volume backscattering contribution from the snow pack is

$$\sigma_{pp}^v(\theta_i) = T^2(\theta_i) \left\{ \frac{3}{4} \omega \cos \theta_r \left[ 1 - \exp \left( \frac{-2\kappa_e d_s}{\cos \theta_r} \right) \right] \right\} \quad (\text{B.1.6})$$

where  $\omega$  is the volume scattering albedo. For most snow and ground surfaces the Integral Equation Model (IEM) is well suitable to estimate scattering at L- and C-band frequencies (Fung, 1994). Because snow is an aggregate of densely packed small particles forming an inhomogeneous medium, the standard radiative transfer approach with the phase function based on far field interaction does not accurately describe the volume scattering behaviour, though even this simple approach is suitable to obtain a first estimate. The **Dense Medium Radiative Transfer theory** (DMRT) takes into account the correlation between scatterers, where the wave interactions between different particles are weighted by the pair distribution function of particle positions (Wen *et al.*, 1990). This results in different expressions for the extinction coefficient and albedo compared to the classical radiative transfer equation (Fung and Chen, 1989). A DMRT solution, which takes into account size distributions of scatterers, has been applied to account for a sensitivity study on backscattering from snow in the 5 to 17 GHz range (West *et al.*, 1993). The results show that the size distribution is particularly important in the low frequency limit when scattering is strongly dependent on particle size.

In spite of the advancements of DMRT, forward modelling of backscatter from the natural snowpack is still not fully satisfactory, in particular if the calculations are done over a range of frequencies or in polarimetric mode (Floricioiu and Rott, 2001; Floricioiu, 1997). The main problem are the insufficient capabilities of present scattering models to accurately account for the structural and stratigraphic properties of natural snow. Layering related to different snowfall events and metamorphic states (Alley, 1988), grain clustering and sintering result in highly complex structures of snowpacks (Colbeck, 1997) which are difficult to measure and to take into account in scatter models.

Measurements at thin sections have been carried out to quantify the **textural properties** of polar firn for remote sensing applications by means of stereological measures (Alley, 1987). Mätzler (1997) and Wiesmann *et al.*, (1998) obtained statistical information about snow structure from digitised snow sections and used this information for microwave emission modelling. Zurk *et al.* (1997) used 2-D stereological data from snow samples to derive 3-D pair distribution functions for scattering calculations with the DMRT, resulting in a successful attempt to utilize measured quantitative data on snow texture for forward modelling. Field measurements show strong impact on layering for C- and X-band scattering and emission of polar firn (Rott *et al.*, 1993). Models accounting for layering have been developed and applied for microwave emission (West *et al.*, 1996), but such models are not yet available for radar scattering.

### B.1.3 InSAR application for ice motion and topography

SAR interferometry is widely used for surveying and monitoring mountain glaciers, high latitude glaciers, ice caps, and the large ice sheets of Antarctica and Greenland. It has become an important tool for studies of ice dynamics and ice/climate interactions. Many papers on this application of InSAR can be found in the *Journal of Glaciology*, in the special issue on Remote Sensing in Glaciology of *Annals of Glaciology* (Winther and Solberg, Eds., 2002), the Proceedings of the FRINGE Workshops (ESA, 1997; ESA, 2000a), the Proceedings of the ERS-Envisat Symposium (ESA, 2000b), and in the Proceedings of several other symposia, including the IGARSS conferences of the last several years. A summary of InSAR applications for glaciology is included in the overview paper by Rosen *et al.*, (2000). Because the application InSAR of InSAR for topography and motion of glaciers and ice sheets is well established, only some key papers are briefly discussed below and open issues are addressed.

The interferometric phase in repeat pass mode from a moving glacier for a pixel  $\mathbf{x}$  (position vector defined by azimuth and slant range coordinates) is made up by the following components:

$$\phi(\mathbf{x}) = \phi_{dis}(\mathbf{x}) + \phi_s(\mathbf{x}) + \phi_t(\mathbf{x}) + \phi_a(\mathbf{x}) + \phi_o(\mathbf{x}) \quad (\text{B.1.7})$$

where  $\phi_s$  and  $\phi_t$  are the geometric phase contributions due to across track position and topographic elevation, which depend on the baseline.  $\phi_a$  is the atmospheric phase contribution due to different propagation conditions in the two SAR images.  $\phi_o$  is a phase contribution due to changes of the scattering object. The **motion-related phase**,  $\phi_{dis} = 4\pi\Delta R_0/\lambda$ , is caused by displacement of the target in the direction of line-of-sight (**LOS**) of the satellite during the time interval between the two satellite data acquisitions.

Considering Equ. (B.1.7), it is obvious that certain assumptions are needed to retrieve topography and motion. More or less all of the InSAR retrievals carried out over ice sheets and glaciers assume that the **atmospheric phase contribution**,  $\phi_a$ , is negligible. The reason is that usually not sufficient InSAR pairs are available to account for the atmosphere. Because the atmospheric water vapour content in glacier regions is comparatively low, in particular in winter, this assumption probably does not cause any significant error in most cases, but under certain conditions may be disturbing. Also  $\phi_o$  is assumed to be zero, which is reasonable as shifts of the target phase would usually cause decorrelation.

After subtracting the flat earth phase contribution,  $\phi_s$ , using precise baseline data, the motion-related and topographic phase have to be separated. If no external digital elevation data (DEM) are available, the differential technique has to be applied, using at least two interferograms (Joughin *et al.*, 1996). Under the assumption that  $\phi_a$  and the ice velocity is the same in both interferograms [ $\phi_{dis}(1) = \phi_{dis}(2)$ ] a double-difference interferogram is formed:

$$\phi_1 - \phi_2 \approx \frac{-4\pi}{\lambda} \frac{(B_{n,1} - B_{n,2})}{\sin \theta_l R_0} \quad (\text{B.1.8})$$



where  $B_n$  is the perpendicular baseline,  $\theta_l$  is the radar look angle, and  $R_0$  the slant range. The topography, calculated with double-difference interferograms, is then rescaled to one of the interferograms and subtracted to obtain the motion-only interferogram.

A limiting factor for this method is the **condition of steady state velocity** for the two interferograms. Many glaciers reveal seasonal cycles of ice velocity related to water pressure (Paterson, 1994). In addition, surging glaciers exhibit large temporal variations of ice velocity (Björnsson *et al.*, in press; Kamb, 1987). Other factors causing large temporal changes of ice velocity are variations of geothermal heat flow and subglacial volcanic activity (Björnsson, 2002). In these cases it is necessary to use synthetic interferograms calculated from external DEMs to subtract the topographic phase (Björnsson *et al.*, 2001, Björnsson, 2002; Gudmundsson *et al.*, 2002). A problem is that accurate and current DEMs are often not available.

For most ice dynamic studies and for ice flow modelling the three-dimensional velocity vector is needed:

$$\mathbf{v} = v_x \hat{\mathbf{x}} + v_y \hat{\mathbf{y}} + v_z \hat{\mathbf{z}} = \mathbf{v}_h + v_z \hat{\mathbf{z}} \quad (\text{B.1.9})$$

where  $\mathbf{v}_h$  is the horizontal velocity vector. A widely used approach for estimating the three components of  $\mathbf{v}$  from the LOS velocity is the **surface parallel flow assumption**:

$$v_z = v_x \frac{\partial S(x, y)}{\partial x} + v_y \frac{\partial S(x, y)}{\partial y} = [\nabla_{xy} S(x, y)]^T \mathbf{v}_h \quad (\text{B.1.10})$$

where  $S$  is the surface height. In principle the velocity vector can be derived with this assumption for interferograms from a single look direction, but only if the flow direction differs sufficiently from the along-track direction (Nagler *et al.*, 2002). Therefore interferograms from both the ascending and descending passes are used to retrieve the 3-D velocity (Joughin *et al.*, 1998; Mohr *et al.*, 1998). If only an interferogram from a single look direction is available, an option to retrieve the velocity vector is the mapping of flowlines from optical and/or SAR images in combination with an external DEM, as applied with SIR-C interferometric data of Patagonian glaciers and verified with field data (Rott *et al.*, 1998).

The assumption that ice flows in direction of maximum surface slope is only reasonable if the surface flow is uniform over an area extending over at least 10 ice thicknesses, the *shallow ice assumption* (Paterson, 1994). Even for a steady-state glacier this assumption is not fully valid, because in the accumulation areas a negative vertical velocity component exists (downwards), and in the ablation area an upward component (Reeh *et al.*, 1999). For non steady-state glaciers the assumption of surface parallel flow can result in large errors also for the horizontal motion vector (Mohr *et al.*, 2003). A possibility for accurately deriving the field of the **3-D surface velocity** vector is the combination of InSAR analysis from ascending and descending orbits with airborne ice thickness maps, using the principle of mass conservation (Reeh *et al.*, 2003).

An important question for accurate retrieval of **surface topography of glaciers** and ice sheets is the penetration of the radar signal. Usually the InSAR analysis is carried

out at dry snow conditions because in case of melting the signal decorrelates rapidly. For dry snow and firn the penetration is substantial (Figure B.1.1), and the interferometrically derived surface topography may differ significantly from the true snow or ice surface. Rignot *et al.* (2001) compared airborne InSAR topography with laser altimetry data of Greenland and Alaska. On cold polar firn at Greenland summit the InSAR phase centre on the average was 9 m below the surface at C-band, and 14 m at L-band. Over glacier ice the difference was in general smaller, with the exception of cold marginal ice in northeast Greenland where they report on penetration up to 120 m at L-band. Comparison between laser altimetry and airborne C-band EMISAR interferometry showed a bias of 10 m at the high elevation zone of Geikie ice cap in East Greenland (Forsberg *et al.*, 2000).

### **B.1.4 InSAR retrievals of snow and ice properties**

Apart from the *classical* InSAR applications, namely topography and motion, interferometric coherence or phase shifts should also be able to provide information on certain physical properties of snow and ice.

Complementary to SAR amplitude images, InSAR data have been used for characterisation of *sea ice* type and for mapping ice movements. A case study, carried out in the Baltic with 3-day ERS-1 repeat pass SAR data indicated that both phase and coherence provide useful data for sea-ice dynamics and classification (Dammert *et al.*, 1997; 1998), but no retrieval algorithm has been developed. In a case study it was shown that ERS-1 coherence data from 3-day repeat pass are useful for monitoring changes of *river ice* (Li *et al.*, 1997).

For *perennial snow and ice and the seasonal snow cover* previous work suggests possibilities for retrieving the following variables:

1. Penetration depth (related to snow and ice diagenetic facies)
2. Snow extent
3. Snow mass (Snow Water Equivalent, SWE)

#### **B.1.4.1 Coherence of snow and ice**

A very important topic for InSAR applications of snow and ice is the question of temporal decorrelation. Because of rapid decorrelation, most of the work on glacier motion and topography is based on one-day repeat pass data (ERS tandem), followed by 3-day repeat pass data of the ERS ice phase. Only over the cold polar ice, such as interior of Antarctica, where ice motion is slow and accumulation is very small, coherence may be preserved over periods of several weeks, as demonstrated for ice motion analysis with 24-day cycle (Radarsat) and 35-day cycle (ERS) repeat pass data (Kwok *et al.*, 2000).

**The main factors for temporal decorrelation of snow and ice are:**

- Surface melt
- Snowfall
- Snow drift (wind erosion and deposition)
- Volume wavenumber shift (volume decorrelation in dry, transparent firn; dependent on baseline)

- Surface rotation and deformation at pixel and sub-pixel scale (e.g. in shear zones)
- Thermal noise (relevant for snow types with low  $\sigma^\circ$  or on backslopes)

At C-band **surface melt** of snow and ice often results in complete decorrelation even within one day (Rott and Siegel, 1997; Strozzi *et al.*, 1999). Because of the somewhat higher penetration in snow and ice also in melting conditions (Figure B.1.2), L-band coherence over one day may be sufficient for interferograms generation (Rott *et al.*, 1998).

**Snow redistribution** by wind (snow drift) and snowfall in the time interval between the image acquisitions also often cause complete decorrelation, as shown with ERS SAR tandem data of Alpine test sites (Rott and Siegel, 1997) and three-day repeat pass data of Alaska (Li and Sturm, 2003). Also Askne *et al.* (1997) found wind redistribution of snow an important factor for decorrelation of snow covered fields at time scales of several days.

**Volume decorrelation:** The interferometric coherence depends on the degree of spectral correlation between the radar measurements carried out under slightly different incidence angles,  $\theta$  and  $\theta + \Delta\theta$ . This results in a spectral wavenumber shift in not only at a surface (often called *baseline decorrelation*), but also in the vertical direction (Gatelli *et al.*, 1994). The wavenumbers in ground range,  $k_y$ , and in elevation,  $k_z$ , are:

$$|k_y| = \frac{2\omega}{c} \sin \theta ; \quad |k_z| = \frac{2\omega}{c} \cos \theta \quad (\text{B.1.11})$$

where  $\omega = 2\pi f$  is the radar frequency. The vertical components of the wavenumbers in the two SAR images of an interferogram are slightly shifted:  $k_z$  and  $\Delta k_z$ . Assuming that the volume contribution is a linear superposition of the signal of individual scatterers, the wavenumber shift is (Gatelli *et al.*, 1994):

$$\Delta k_z \cong \frac{-2\Delta\omega}{c \cos \theta} = \frac{-2\omega\Delta\theta}{c \sin \theta} \quad (\text{B.1.12})$$

The spectral correlation function for the signal from a box of vertical dimension  $\Delta z$  is:

$$\frac{\sin(\Delta k_z \Delta z / 2)}{\Delta k_z \Delta z / 2} \quad (\text{B.1.13})$$

Volume decorrelation plays a role if

$$|\Delta z| \geq \left| \frac{\lambda H \tan \theta}{2B_n} \right| \quad (\text{B.1.14})$$

where  $H$  is the satellite altitude and  $B_n$  is the normal baseline. As an example, for ERS with  $B_n = 250 \text{ m}$  complete decorrelation is expected for  $|\Delta z| \geq 38 \text{ m}$ . This shows clearly that volume decorrelation can be very relevant for dry polar firn and dry snow on firn areas of glaciers, but not for the seasonal snow cover.

**Surface rotation** of a target in respect to the radar look direction, as for example observed in shear zones along glacier margins or at boundaries of ice streams, is another geometrical factor causing decorrelation (Zebker and Villasenor, 1992). Complete decorrelation results for C-band (ERS) after a rotation of  $0.7^\circ$ . In zones of strong shear, as found close to fronts of calving glaciers, another factor for decorrelation can be deformation at sub-pixel scale.

#### B.1.4.2 Possibilities for InSAR retrievals of snow and ice variables

##### B.1.4.2.1 Penetration depth / diagenetic snow and ice facies.

Maps of penetration depth,  $d_p$ , of the radar signal in snow and ice is on one hand of interest for correcting interferometrically retrieved topography (section B.1.3), on the other hand  $d_p$  is also related to the diagenetic glacier facies, which is an important parameter for studies of ice dynamics and ice/climate interactions. Based on ERS interferograms over time intervals of 3 to 18 days, Rott and Siegel (1997) derived the degree of coherence,  $\gamma$ , for various types of polar snow and ice in Dronning Maud Land, Antarctica. Figure B.1.3 shows a clear dependence of  $\gamma$  on the normal baseline  $B_n$  for a site the Amundsen ice plateau with dry polar firn. Some of the data are slightly effected by temporal decorrelation. The relation between  $\gamma$  and  $B_n$  shows considerable variability in this region, depending on the metamorphic state and texture of the snow volume.

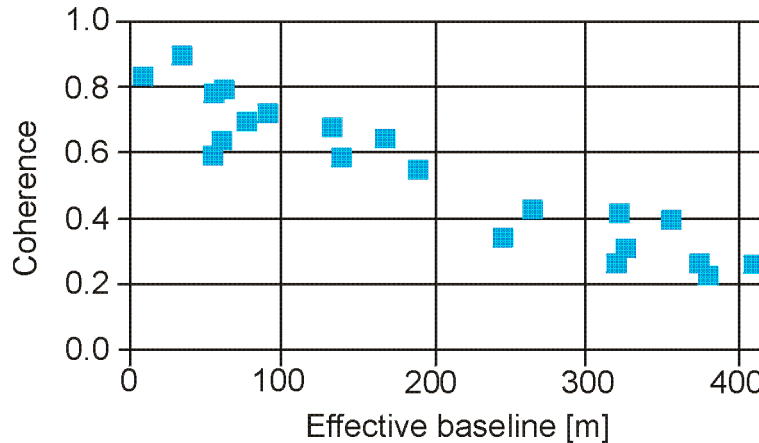


Figure B.1.3: Degree of coherence for dry polar firn in Dronning Maud Land, Antarctica, derived from ERS SAR data, in dependence of normal baseline (from Rott and Siegel, 1997).

Hoehn and Zebker (2000) developed a theoretical relation between the penetration depth of dry polar firn and coherence and applied this relation to calculate  $d_p$  over various test sites in Greenland, based on ERS InSAR data over 1 to 9 days time spans. Under the assumption that the volume consists of uniformly distributed and uncorrelated scattering centres and that  $\sigma^\circ$  varies only as function of depth  $z$ , they derived the following relation for the cross-correlation of the two SAR images:

$$\langle V_1 V_2^* \rangle = K \left( 1 - \frac{2R_r B_n}{\lambda R_0 \tan \theta} \right) \int \sigma^\circ(z) \exp \left[ -i \frac{4\pi}{\lambda \sin \theta_r} \sqrt{\varepsilon} z \delta \theta_r \right] dz \quad (\text{B.1.15})$$

where  $R_r$  is the slant range resolution in free space,  $\varepsilon$  is the permittivity, and  $\delta\theta_r$  is the difference of the refraction angle into the snow volume between the two SAR images. The spatial decorrelation consists of two components  $\gamma(\text{spatial}) = \gamma(\text{surface}) \cdot \gamma(\text{volume})$ . The decorrelation factor for the volume can be estimated by

$$\gamma_{vol} = \frac{1}{\sqrt{1 + \left( \frac{2\sqrt{\varepsilon} d_p B_n}{\lambda R_0 \tan \theta} \right)^2}} \quad (\text{B.1.16})$$

Hoen and Zebker (2000) found clear differences in the relation between  $\gamma(\text{volume})$  and  $B_n$  for different ice regions of Greenland. This study, as well as the investigations of Rott and Siegel (1997) suggest that InSAR coherence in combination with  $\sigma^\circ$  should provide a useful basis for retrieving diagenetic glacier facies. Detailed maps of penetration depth would also be of interest for support of Cryosat data analysis, because radar signal penetration plays an important role for radar altimetry retrievals.

#### **B.1.4.2.2 Snow areal extent**

The interferometric signal decorrelates rapidly over melting snow surfaces (Rott and Siegel, 1997). This offers in principle the possibility to map melting snow areas (Li *et al.*, 2001; Strozzi *et al.*, 1999). An automated algorithm for wet snow mapping has been developed by Nagler (1996), (Nagler and Rott, 2000), based on change detection of multitemporal SAR images. Because of the increase of  $\sigma^\circ$  of wet snow towards low incidence angles (Mätzler, 1987; Rott, 1997), classification using backscattering ratios is problematic at incidence angles below about 20°.

An **advantage of coherence as classifier for wet snow** is the fact that it shows little dependence on the incidence angle, which is of particular interest for applications in mountain areas.

A **disadvantage** is the need for short time spans because the classification is based on a coherence threshold. The SAR signals of wet snow decorrelate rapidly, but also other targets, such as forests, show rapid decorrelation (Askne *et al.*, 1997). For this reason repeat pass data of few-day time spans (preferably one day) would be needed for wet snow classification by means of coherence.

The possibility for classification of **dry snow** areas by means of coherence is still an open question. The coherence of Alpine areas covered with dry snow is very high in winter over one-day time intervals, as long as snow is dry and neither snowfall nor wind drift occur. Within 35 day repeat intervals the signal decorrelates usually completely over Alpine snow-covered areas also in case of dry snow.

So far only feasibility studies have been carried out for snow mapping by means of coherence, but no reports or articles have been published on development of an operational retrieval algorithm.

#### **B.1.4.2.3 Snow water equivalent (SWE)**

The mass of snow on the ground, the snow water equivalent (SWE), is a very important variable for determining the runoff from snow covered basins and for

climate research. SWE is defined as the product of snow density and depth, and represents the amount of water potentially available for runoff. Because SWE is very variable due to topographic effects affecting deposition during snow fall and redistribution by wind, estimation of SWE for an area is subject to large errors if extrapolated from *in situ* point measurements. Several attempts have been made to derive SWE from EO data in the microwave domain (active and passive), because microwaves provide the required penetration into the snowpack. Field experiments indicate that the relationship between backscattering coefficients and SWE is quite complex, since the backscattering from a dry snow cover depends not only on SWE but also on other properties of the snowpack.

An algorithm to estimate SWE from multifrequency polarimetric SAR data was developed by (Shi and Dozier, 2000a, 2000b). This algorithm seems to work under specific environmental conditions. It was developed and tested in the Californian Sierra Nevada using SIR-C data. We tested the algorithm with SIR-C data of the Alpine test site Ötztal, where it did not produce any reliable results. An other procedure to derive SWE from C-band SAR data was proposed by Bernier and Fortin (1998). They developed a model which links the scattering coefficient to the freezing depth of the underlying soil which is related to the snow depth. This algorithm also seems to require specific soil and snow conditions to be applicable. Theory and preliminary experimental data suggest Ku-band SAR as a suitable sensor for SWE mapping, which lead to the proposal of *SnowSat* for an Earth Explorer Mission (Rott *et al.*, 2003). Though this mission received excellent marks in the first round review, it was not selected for implementation in the final round. In summary, no widely applicable and robust algorithm for estimating SWE is yet available.

In principle the **phase shift in dry snow** offers the opportunity to map SWE by means of interferometric repeat pass SAR data (Gunteriusen *et al.*, 2001). For ground covered with dry winter snow the main scattering contribution at the L- to X-band range comes from the snow-ground interface. A uniform layer of snow with depth  $d_s$ , falling in the time interval between the acquisition of the two SAR images of an interferogram, causes the phase shift  $\Delta\phi_{SWE}$  given by

$$\Delta\phi_{SWE} = -\frac{4\pi}{\lambda_i} d_s \left( \cos\theta_i - \sqrt{\epsilon' - \sin^2\theta_i} \right) \quad (\text{B.1.17})$$

At  $\theta_i = 23^\circ$  a phase shift of one fringe is caused by a change  $\Delta SWE = 3.3 \text{ cm}$  at 5.3 GHz, which corresponds to  $d_s = 32.6 \text{ cm}$  for snow with density  $\rho_s = 0.1 \text{ gcm}^{-3}$  (typical for fresh snow) or  $d_s = 10.9 \text{ cm}$  with  $\rho_s = 0.3 \text{ gcm}^{-3}$  (average value for dry seasonal snow). At L - band the corresponding values for *SWE* and  $d_s$  are higher by a factor of about four.

Gunteriusen *et al.* (2001) show one example of a tandem interferogram from March 1997 for a test area in Norway where, after subtracting the topographic phase derived from an external DEM, they found a local phase shift which they attribute to the change of snow depth (Figure B.1.4). At that time the snow depth in this region was 1 to 4 m, the snow was dry, and only very little snowfall was observed at the nearest meteorological station, about 20 km away. The authors presume that the phase shift was caused by snow redistribution due to wind. According to our experience (Rott and Siegel, 1997) and the investigations of Li and Sturm (2003) in Alaska, wind

deposition or erosion causes significant decorrelation, because the snow layers built-up or deleted would usually not be uniform.

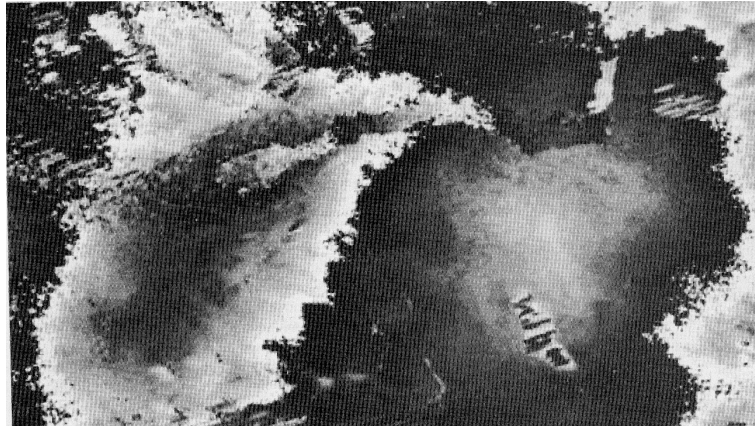


Figure B.1.4: Topographically corrected ERS tandem interferogram of 12/13 March 1997 from Heimedalen, Norway. Residual fringes are attributed to change of snow depth (from Guneriusen *et al.*, 2001).

Though theory confirms the possibility to estimate SWE, deposited in the time interval between two SAR image acquisitions, by means of phase shifts, clear experimental confirmation is still missing. The uniformity of the process of snow deposition at pixel scale, affecting coherence, plays probably a major role. In any case InSAR pairs with short time intervals (one to a few days) would be needed in case of C-band data. This can be relaxed with L-band.

Another possibility for mapping areal extent and depth of snow has been reported by Koskinen (2001). With C- and L-band airborne TOPSAR data they showed the possibility to estimate snow depth in case of melting snow by comparing the snow-covered DEM (with the signal coming from the snow-surface) with a snow-free DEM.

### **B.1.5 Summary and conclusions**

Theory and experimental investigations of radar propagation in snow and ice are reviewed. An overview of repeat pass InSAR methods and applications for mapping and monitoring topography and motion of glaciers and ice sheets is presented. Factors of relevance for coherence in snow and ice are discussed in detail.

The following snow and ice variables have been identified for which preliminary work suggest good possibilities for development of InSAR retrievals algorithms:

- Diagenetic glacier facies (related to SAR penetration depth)
- Snow extent (for wet snow)
- Snow mass (snow water equivalent, SWE)

The status of knowledge on InSAR signals and possible methods for deriving these variables are discussed, and needs and possibilities for further developments are briefly addressed.



## B.2 IDENTIFICATION OF VARIABLES AND TECHNIQUES

### B.2.1 Introduction

In the literature review (chapter B.1) the following variables of perennial snow and ice and the seasonal snow cover were identified as promising candidates for the development of new retrieval techniques based on radar interferometry:

1. Diagenetic glacier facies (related to SAR penetration depth)
2. Snow extent (if snow is wet)
3. Snow mass (snow water equivalent, SWE)

The physical background for retrieving these variables is reviewed in this chapter and the data sets available for development of retrieval algorithms in the project are specified.

### B.2.2 Diagenetic glacier facies

The diagenetic facies of a glacier or ice sheet refers to properties of the surface layer of snow and ice. The facies are related to the pattern of accumulation, ablation and snow metamorphosis and are basic information for studies of glacier mass balance and glacier/climate interactions (Paterson, 1994). The temporal evolution of these facies is, for example, a sensitive indicator of climate change.

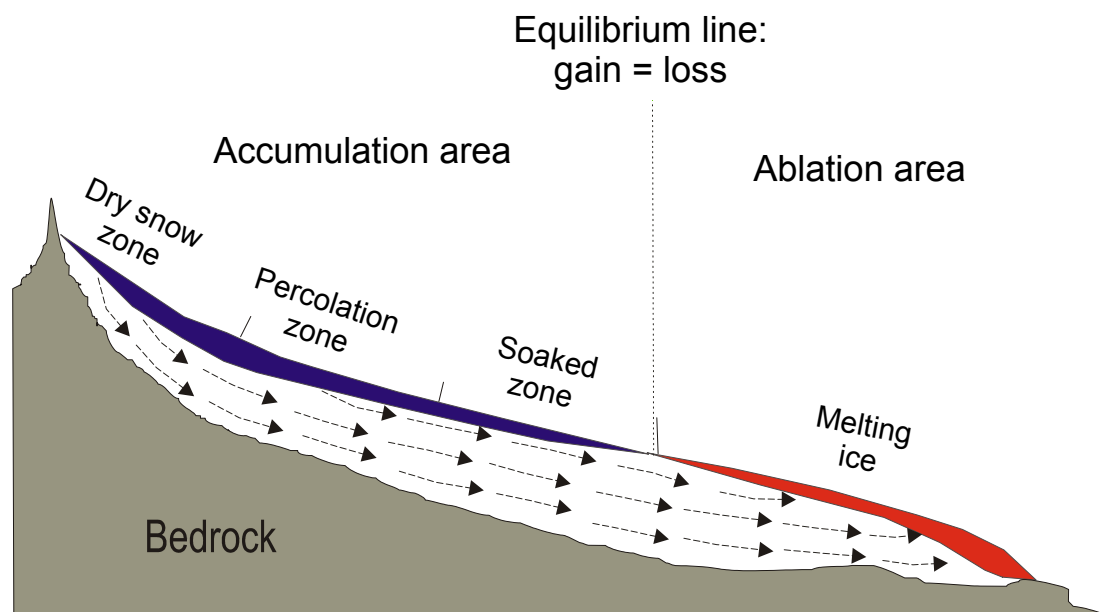


Figure B.2.1: Characteristic glacier zones (glacier facies).

The main glacier facies are the dry snow zone, percolation zone, soaked zone and ablation zone (Figure B.2.1), which can be further subdivided (Paterson, 1994). In the dry snow zone no melting occurs any time, so this zone is found only on ice sheets and upper zones of high latitude glaciers. In the percolation zone some surface melting occurs in summer, and the melt water penetrates a certain distance into the cold firn where it refreezes. In the wet snow zone, by the end of summer, all snow deposited during the last year is at melting point and melt water percolates to deeper layers which are also close to zero degree, though in some layers or at some locations temperatures below zero may persist. The ablation area, located below the equilibrium line, refers to the zone where the annual mass balance is negative.

Optical satellite imagery has been used for mapping glacier facies (Williams *et al.*, 1991), but this may lead to misclassifications, as optical data are only sensitive to surface properties of snow and ice. Because of the penetration capability SAR data are more suitable for analysis of glacier facies. Backscattering thresholds in single-term, or preferably multi-temporal, ERS SAR data (Nagler, 1996), Partington (1998) Ramage *et al.* (2000), and Radarsat data (Demuth and Pietroniro, 1999) were used for discriminating various glacier zones, but no objective methods is available for clearly relating the backscattering properties to physical properties of the glacier facies. Studies with multi-frequency polarimetric SAR suggest improvements for classification of snow and ice facies, but only limited data sets have been available so far (Floricioiu and Rott, 2001), (Rott and Davis, 1993), (Jezek *et al.*, 1993), (Foster *et al.*, 1996).

Penetration of radar waves in snow and ice is strongly dependent on the metamorphic properties of these targets and therefore also on the glacier facies. The penetration depth,  $d_p$ , would offer a quantitative measure for description of snow scattering and absorption properties (see chapter B.1) and should be a very useful classifier for mapping of glacier facies. Detailed maps of penetration depth would also be useful for correcting interferometric data of surface elevation of glaciers and ice sheets, because the scattering phase centre can be many meters below the surface. In addition, signal penetration plays an important role for radar altimetry retrievals.

In section B.1.4 the theoretical relation between the penetration depth of dry polar firn and coherence, developed by Hoen and Zebker (2000) was briefly described. In the following more details are presented. The viewing geometry, with interferometric acquisition from antennas  $A_1$  and  $A_2$ , is shown in Figure B.2.2(a). The spectral wavenumber shift due to volume scattering is illustrated in Figure B.2.2(b).

The spectral shift in direction  $z$  for two SAR signals, observed from the two angles  $\theta$  and  $(\theta+\Delta\theta)$ , is equivalent to (Gatelli *et al.*, 1994)

$$\Delta k_z \cong 2\omega\Delta\theta / c \sin \theta \quad (\text{B.2.1})$$

The coherence depends on the spectral correlation between the measurements in  $k_z$  and  $(k_z + \Delta k_z)$  which is related to the depth  $\Delta z$  of the volume contributing to the signal of a resolution element.

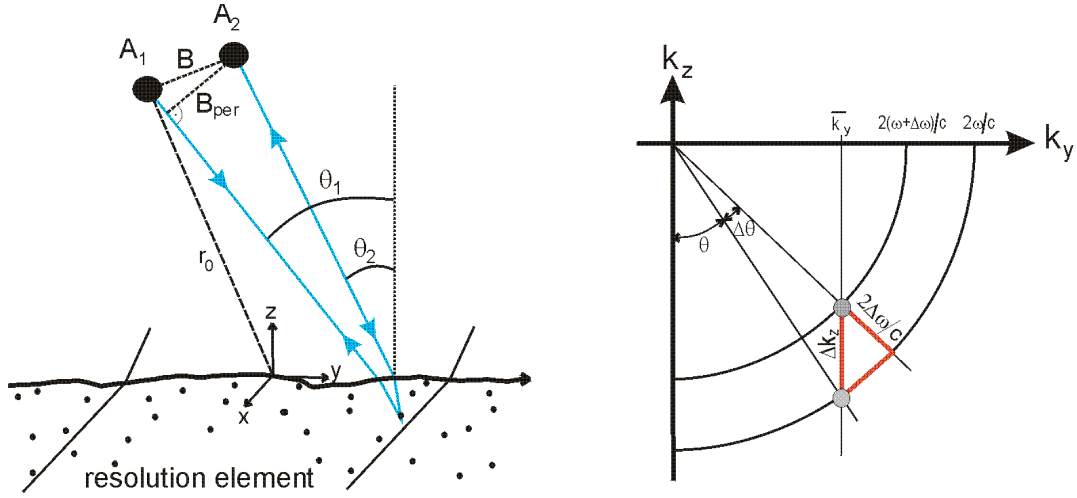


Figure B.2.2: (a) Interferometric viewing geometry for scattering from a snow volume (from Hoen and Zebker, 2000). (b) Wavenumber representation of the spectral shift (after Gatelli *et al.*, 1994).

The signals of a resolution element measured at the antennas A<sub>1</sub> and A<sub>2</sub> can be expressed by:

$$\begin{aligned} V_1 &= \iint f(y, z) \exp \left[ -i \frac{4\pi}{\lambda} (r_0 + y \sin \theta_1 - \sqrt{\epsilon} z \cos \theta_{r1}) \right] \cdot W_r(y, z) dy dz \\ V_2 &= \iint f(y, z) \exp \left[ -i \frac{4\pi}{\lambda} (r_0 + y \sin \theta_2 - \sqrt{\epsilon} z \cos \theta_{r2}) \right] \cdot W_r(y, z) dy dz \end{aligned} \quad (\text{B.2.2})$$

where  $f(y, z)$  is the complex backscatter function for each point in the volume,  $r_0$  is the range to the scattering centre,  $\epsilon$  is the permittivity of the medium, and  $\theta_r$  is the refraction angle.  $W_r(y, z)$  is the range-dependent system impulse response. The cross-correlation of the two signals is

$$V_1 V_2^* = \iiint f(y, z) f^*(y', z') e^{-i\beta(y, z)} \cdot W_r(y, z) W_r^*(y', z') dy dz dy' dz' \quad (\text{B.2.3})$$

where

$$\beta(y, z) = \frac{4\pi}{\lambda} \left[ y (\sin \theta_1 - \sin \theta_2) - \sqrt{\epsilon} z (\cos \theta_{r1} - \cos \theta_{r2}) \right]$$

Assuming that the volume consists of uniformly distributed and uncorrelated scattering centres, the backscatter function can be described by

$$\langle f(y, z) f^*(y', z') \rangle = \sigma^\circ(y, z) \delta(y - y', z - z') \quad (\text{B.2.4})$$

where  $\sigma^\circ$  is the normalized radar cross section of each point in the medium. In this case [with  $\theta = (\theta_1 + \theta_2)/2$ , etc.] the interferometric product is

$$\langle V_1 V_2^* \rangle = \iint \sigma^\circ(y, z) e^{-i\eta(y, z)} |W_r(y, z)|^2 dy dz$$

where

$$\eta(y, z) = \frac{4\pi}{\lambda} \left( y \cos \theta \delta\theta + \sqrt{\varepsilon} z \sin \theta_r \delta\theta_r \right) \quad (\text{B.2.5})$$

With an un-weighted radar transfer function the range-dependent system impulse response can be approximated by

$$W_r(y, z) = \text{sinc} \left( \frac{r}{R_r / \sqrt{\varepsilon}} \right) = \text{sinc} \left( \frac{y \sin \theta_r + z \cos \theta_r}{R_r / \sqrt{\varepsilon}} \right) \quad (\text{B.2.6})$$

where  $R_r$  is the slant range resolution in free space. Assuming that  $\sigma^\circ$  varies only as a function of depth [ $\sigma^\circ = \sigma^\circ(z)$ ], the interferometric signal is

$$\langle V_1 V_2^* \rangle = K \left( 1 - \frac{2R_r B_n}{\lambda r_0 \tan \theta} \right) \int \sigma^\circ(z) \exp \left[ -i \frac{4\pi}{\lambda \sin \theta_r} \sqrt{\varepsilon} z \delta\theta_r \right] dz \quad (\text{B.2.7})$$

where  $K$  is a system-dependent factor which cancels out for calculating the correlation coefficient (degree of coherence). This equation shows the two components of the spatial decorrelation:  $\gamma(\text{spatial}) = \gamma(\text{surface}) \cdot \gamma(\text{volume})$ . The term  $\gamma(\text{surface})$  is given in the first bracket, whereas  $\gamma(\text{volume})$  is represented by the integral. Evaluating the integral and normalizing results in

$$\gamma_{\text{volume}} = \frac{1}{\sqrt{1 + \left( \frac{2\pi \sqrt{\varepsilon} d_p B_n}{\lambda r_0 \tan \theta} \right)^2}} \quad (\text{B.2.8})$$

If the other factors of decorrelation are known, the penetration depth,  $d_p$ , can be derived by inverting this equation. Hoen and Zebker (2000) applied this relation to calculate  $d_p$  over four test sites in Greenland, based on ERS InSAR data over 1 to 9 days time spans, assuming a simple linear model for temporal decorrelation. Figure B.2.3 shows the plot of measured correlation from ERS SAR data versus  $B_n$  and the curves of the spatial correlation model calculated for several values of  $d_p$ . These data are for a test site in the central part of Greenland.

The analysis of Hoen and Zebker (2000) shows clear differences for  $\gamma(\text{volume})$  and the derived values of  $B_n$  for different ice regions of Greenland, suggesting the capability of this model for retrieving glacier facies.

The validity of the model is confirmed by the analysis of the coherence of ERS data in Dronning Maud Land, Antarctica, by Rott and Siegel (1997). A value of  $d_p = 20$  m is derived with the model for the coherence data of dry firn shown in Figure B.1.3. The field measurements, carried out in this area by Rott with a scatterometer/radiometer system, resulted in  $d_p = 21.7$  m at C-band (Rott *et al.*, 1993).

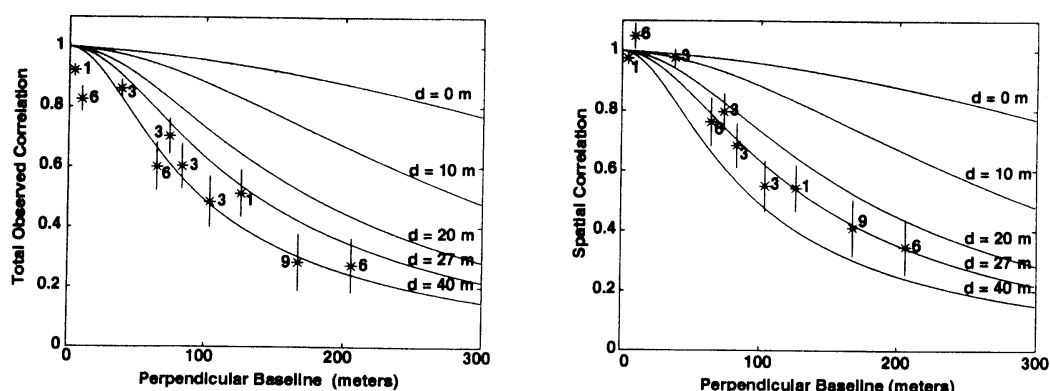


Figure B.2.3: Degree of coherence in dependence of perpendicular baseline from ERS data of a site in Central Greenland. The numbers refer to the time span in days. Right: with correction for temporal decorrelation. The curves were calculated with the spatial correlation model (from Hoen and Zebker, 2000).

These preliminary investigations suggest considerable potential of InSAR for retrieving penetration depth and glacier facies. In view of the theoretical work carried out so far, and the case studies, it should be possible to develop a robust retrieval algorithm. SAR data with short temporal baselines should be most suitable, because temporal decorrelation is the main disturbing factor for this application, which is based on spatial decorrelation. For this reason one day (tandem) and three-day (ice phase) ERS repeat pass data should be most useful.

### B.2.3 Snow extent

The areal extent of the snow cover is a basic variable for climate monitoring and for hydrology in mountain basins and high latitudes (Rott *et al.*, 2000). Because of the cloud penetration capability SAR is a very useful tool for snow mapping for these applications, requiring regular repeat observations. However, SAR so far has only been applied for mapping wet snow, because the signal of dry snow at C-band and L-band is very weak. An automated algorithm for wet snow mapping, based on change detection of multi-temporal SAR images, has been developed and applied with ERS SAR and Radarsat data by Nagler and Rott (2000).

The comparison of SAR snow maps with maps from optical imagery shows in general good agreement, with the exception of boundary zones of the snow cover and low SAR incidence angles. Figure B.2.4 shows the incidence angle dependence of the C-band backscattering cross section,  $\sigma^\circ$ , measured at a meadow at Leutasch (near Innsbruck) for snow-covered and snow-free conditions (Rott, 1997). The contrast of co-polarized  $\sigma^\circ$  of wet snow versus dry snow or snow-free surface is small at incidence angles  $\leq 20^\circ$ . This may result in misclassifications at foreslopes. Improvements in this respect can be expected by using a classifier, which is less dependent on the incidence angle, such as the interferometric correlation coefficient. But also the cross-polarized  $\sigma^\circ$  shows less variation with the incidence angle than the co-polarized signal (Figure B.2.4).

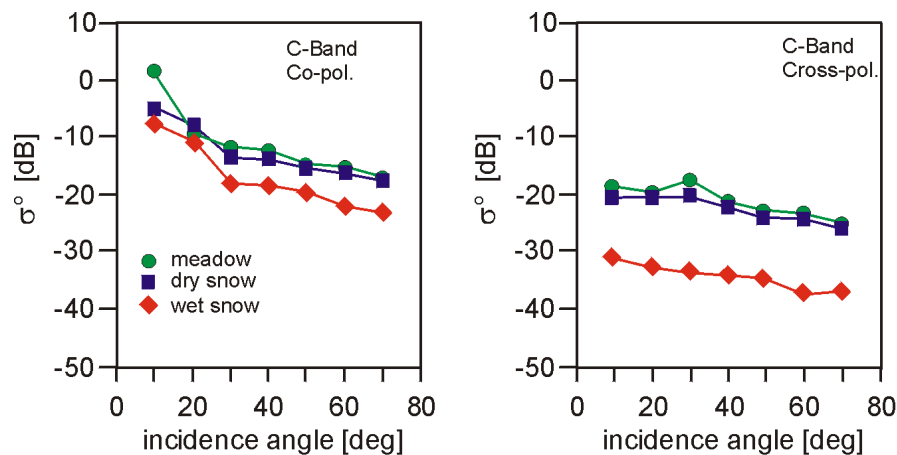


Figure B.2.4: Backscattering cross section,  $\sigma^\circ$ , at C-band co- and cross-polarization as function of the incidence angle,  $\theta$ , measured in Leutasch (Tyrol).

In connection with studies of glaciological InSAR applications it was observed that the interferometric signal of melting snow decorrelates rapidly, in case of typical spring or summer melt even within one day, as observed with ERS SAR one-day tandem data (Rott and Siegel, 1997). This offers in principle the possibility to map melting snow areas, using a threshold of the interferometric correlation coefficient,  $|\gamma|$ , as decision boundary. (Li *et al.*, 2001; Strozzi *et al.*, 1999).

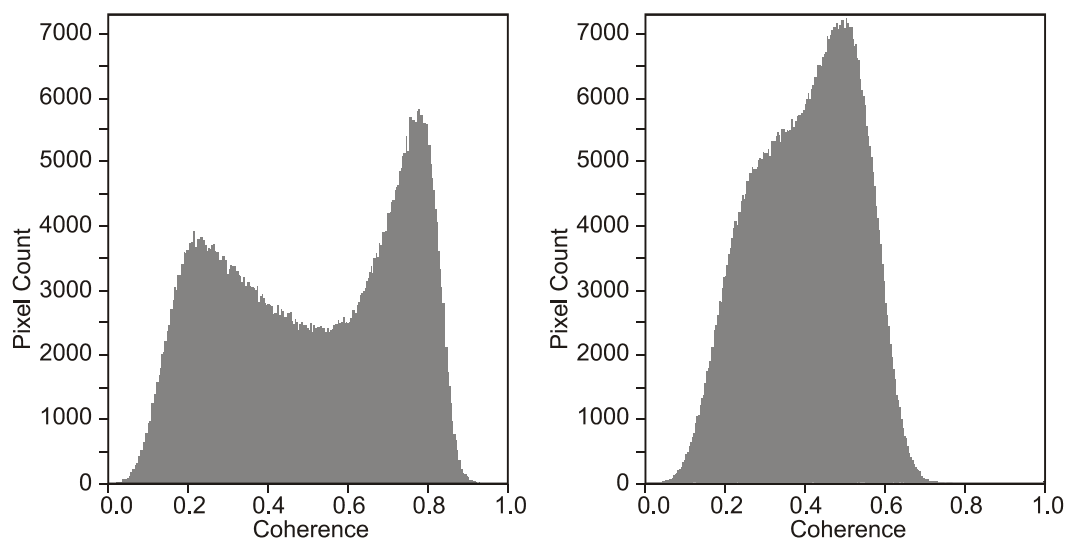


Figure B.2.5: Histogram of interferometric correlation coefficient,  $\gamma$ , for a high Alpine area in Ötztal Alps, Austria, from ERS tandem data of 23/24 Aug. 1995 (left) and 14/15 Feb. 1996 (right).

Figure B.2.5 shows a histogram of the degree of coherence of a high Alpine area in the Ötztal Alps in summer, with melting snow and ice surfaces, and in winter, when all surfaces were covered with dry winter snow. The secondary maximum at  $\gamma = 0.2$  in summer (23/24 August 1995) corresponds to snow and ice, that have melted

between the image acquisitions. In the example from winter (14/15 February 1996) this maximum does not exist, and the average  $\gamma$  is higher, though the highest coherence values of the summer interferograms are not reached. On both days in February weak snowfall was observed which reduced the coherence slightly throughout the image.

The example in Figure B.2.6 shows that the degree of coherence,  $\gamma$ , is a good classifier for melting snow and ice in high mountain areas above the timberline. A question for wider application is the discrimination against other targets. The signal of dense vegetation, in particular forests, decorrelates over short time spans (Wegmüller and Werner, 1997), so that  $\gamma$  would not be sufficient as single classifier.

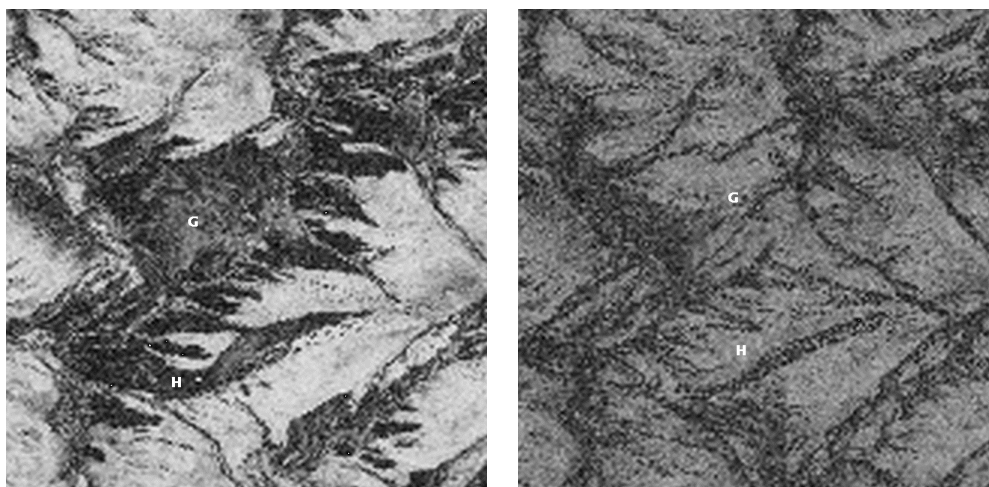


Figure B.2.6: Coherence image of a high Alpine area in the Ötztaler Alpen, Austria, with the glaciers Hintereisferner (H) and Gepatschferner (G). From ERS tandem data of 23/24 Aug. 1995 (left) and 14/15 Feb. 1996 (right).

In order to get an indication of effects of SAR frequency on coherence, we studied the interferometric correlation of various surface types in the region of Moreno Glacier, Patagonia, from one-day repeat pass data, acquired on 9/10 October 1994 by SIR-C / X-SAR (Figure B.2.7). At X-band and C-band melting snow and ice decorrelate almost completely, but the coherence of the dense beech forest is also very low. Only at L-band  $\gamma$  enables a clear separation of snow and ice from the other targets.

These examples suggest that coherence is of interest as classifier for melting snow and ice. The main points of consideration for developing a  $\gamma$ -based algorithm for snow mapping are:

- An advantage of coherence as classifier for wet snow is the reduced sensitivity to the incidence angle compared to  $\sigma^\circ$ .
- In order to avoid ambiguities with other targets, the combination of  $\gamma$  and  $\sigma^\circ$  is very promising.
- The need for short time spans limits the present database to one-day to three-day repeat pass data of ERS and SIR-C/X-SAR.
- The possibility for classification of dry snow areas by means of coherence should also be investigated.



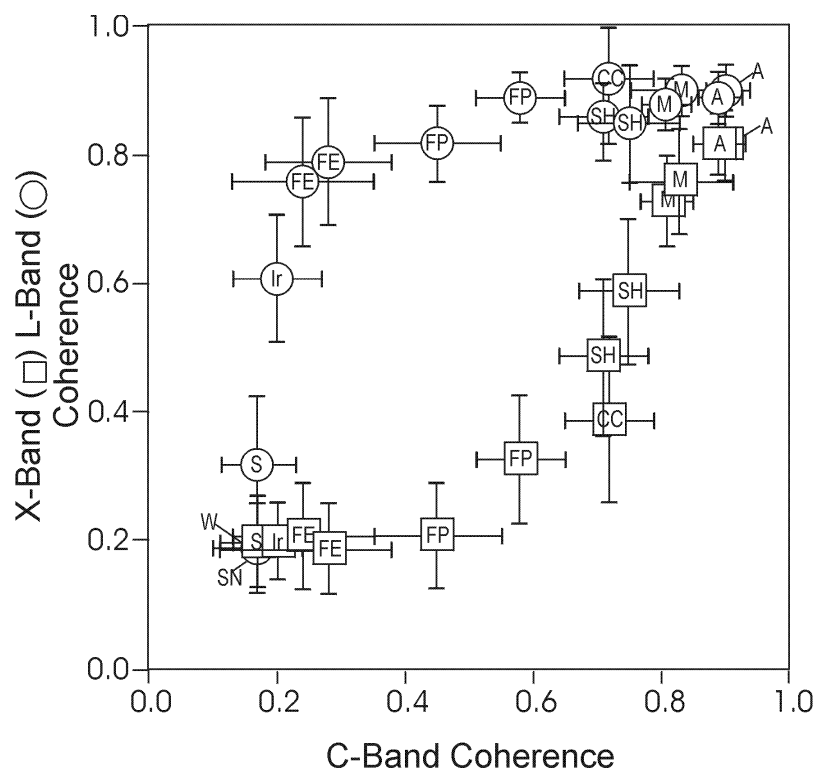


Figure B.2.7: Interferometric correlation coefficient,  $\gamma$ , at C-band versus X-band and L-band, from SIR-C/X-SAR data of 9/10 October 1994 in the region of Moreno Glacier, Patagonia. Surface types. S – melting snow, Ir – rough glacier ice, FE – evergreen beech forest, FP – Arctic beech, M – meadow, A – alluvium, SH – shrubs, W – water, CC – clear cut, SN – noise (radar shadow).

#### B.2.4 Snow water equivalent

The mass of snow on the ground, the snow water equivalent (SWE), is the most important hydrological variable for water resources management and flood prediction in high latitudes and in mountain basins where snow melt represents a substantial contribution to runoff (Bergström, 1995). In addition, SWE is a basic climate parameter, and also required for the initialisation and validation of land surface parameterisation in atmospheric circulation models. There is still a great deficit in the availability of spatially distributed SWE data, as made clear in the Third Assessment Report on Climate Change of IPCC (2001). Estimations of spatial SWE from meteorological data or point measurements of the snow pack results in large errors because of topographic effects during snowfall, snow redistribution by wind and selective melting processes (see e.g. Bales and Harrington, 1995; Essery and Yang, 2001; Slater *et al.*, 2001).

Because of the small spatial correlation length of SWE, remote sensing is considered as the only viable means to obtain spatially distributed information on this variable (Bales and Harrington, 1995). Considering the physical interaction mechanisms of radar waves with snow, SAR is the most promising sensor for SWE retrievals. However, in spite of some successful case studies on the use of SAR for mapping

SWE, no widely applicable and robust algorithm for estimating SWE is yet available as explained in chapter B1.

Whereas the previous work on SWE retrievals by SAR used single channel (Bernier and Fortin, 1998) or multi-channel, polarimetric backscattering coefficients (Shi and Dozier, 2000a; 2000b), a more robust approach was proposed by Guneriusson *et al.*, (2001) based on the phase shift in dry snow.

Assuming that the radar return from ground covered with a layer of dry winter snow results from the ground/snow interface, the phase difference  $\Delta\phi$  of a pixel between two repeat pass SAR images consists of the following contributions:

$$\Delta\phi = \Delta\phi_{flat} + \Delta\phi_{topo} + \Delta\phi_{dis} + \Delta\phi_{atm} + \Delta\phi_{snow} + \Delta\phi_{noise} \quad (B.2.9)$$

where  $\Delta\phi_{flat}$  and  $\Delta\phi_{topo}$  are the phase differences due to changes of the relative distance satellite-target for flat earth and for topography, respectively,  $\Delta\phi_{atm}$  is the phase difference due to changes in atmospheric propagation, and  $\Delta\phi_{noise}$  represents phase noise.  $\Delta\phi_{dis}$  represents the phase difference due to displacement of the target in line-of-sight of the radar beam (slant range).  $\Delta\phi_{snow}$  is the two-way propagation difference in the snow-pack relative to air.

In order to solve Equ. (B.2.9) in respect to the snow term, it is necessary to determine the other terms either by using information from external sources or by means of differential processing:

- $\Delta\phi_{flat}$  can be calculated accurately using precise ERS orbit data and/or a few ground control points across the scene.
- $\Delta\phi_{noise}$  is assumed to be a random component not introducing any bias. It can be reduced by low-pass filtering which is suitable for snow retrieval as the full SAR resolution would not be needed for SWE maps.
- $\Delta\phi_{dis} = 0$  can be assumed on non-glaciated areas, which means surface movement is negligible over the InSAR time span.
- $\Delta\phi_{atm} \approx 0$  is assumed as first approach, because in mountain areas in winter the one to three-day changes in atmospheric path length can be considered small compared to possible changes in snow pack path length. However, atmospheric effects and possible corrections were investigated in chapter B.3. It can be assumed that  $\Delta\phi_{atm}$  has a larger spatial correlation length than  $\Delta\phi_{snow}$ .
- $\Delta\phi_{topo}$ , the topographic phase needs to be derived from interferograms with  $\Delta\phi_{dis} = 0$ ,  $\Delta\phi_{snow} = 0$ ,  $\Delta\phi_{atm} = 0$  in the ideal case.  $\Delta\phi_{atm}$  may cause problems, but errors introduced by this factor can be reduced by using several interferograms and applying multi-baseline processing (Ferretti *et al.*, 1999). Another option is to use accurate digital elevation data from other sources, such as the SRTM mission.

After eliminating the other phase terms,  $\Delta\phi_{snow}$  can be interpreted in terms of *SWE* if the snow volume scattering effects can be neglected. The snow water equivalent, *SWE*, can be expressed either in terms of mass/area or water equivalent depth:

$$\begin{aligned} \text{SWE} &= \langle \rho_s \rangle d_s \quad [\text{kg m}^{-2}] \\ \text{SWE} &= [\langle \rho_s \rangle / \rho_w] d_s \quad [\text{m}] \end{aligned} \quad (\text{B.2.10})$$

where  $d_s$  is the snow depth,  $\rho_s$  and  $\rho_w$  are the density of snow and water, respectively;  $\langle \cdot \rangle$  denotes the mean value over the snow pack. In order to derive the phase shift due to accumulation of snow between two SAR images of an interferogram, the refraction into the snow pack needs to be taken into account (Figure B.2.8). The difference,  $\Delta R$ , of the geometric path in air versus the path with a snow layer present from the antenna to the same ground surface element is:  $\Delta R = \Delta R_s - (\Delta R_a + \Delta R_r)$ .

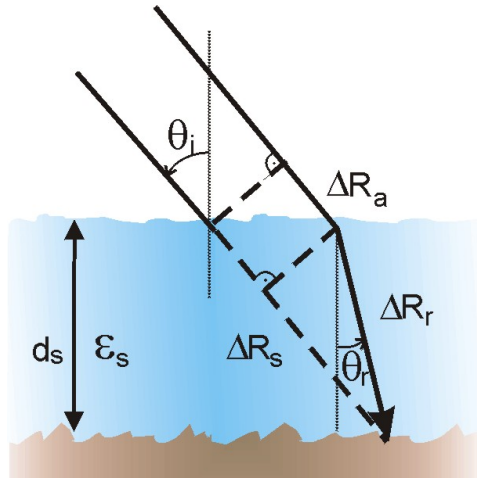


Figure B.2.8: Geometry of propagation path in snow.

A uniform layer of snow,  $d_s$ , falling in the time interval between the acquisition of the two SAR images of an interferogram, causes the following phase shift:

$$\Delta \phi_{\text{snow}} = -\frac{4\pi}{\lambda_i} d_s \left( \cos \theta_i - \sqrt{\epsilon' - \sin^2 \theta_i} \right) \quad (\text{B.2.11})$$

where  $\epsilon'$  is the real part of the permittivity of dry snow. For  $\rho_s \leq 450 \text{ kg m}^{-3}$  the following relation can be used to calculate  $\epsilon'$  from the snow density (Mätzler, 1996):

$$\epsilon'_{ds} = 1. + 1.60 \rho_s + 1.86 \rho_s^3 \quad (\text{B.2.12})$$

A linear approximation for Equ. (B.2.11) for  $\rho_s \leq 500 \text{ kg m}^{-3}$  can be used to estimate the sensitivity of the interferometric phase to  $\text{SWE}$ . For an incidence angle  $\theta_i = 23^\circ$  the phase shift due to a change of  $\text{SWE}$  is (Gunteriusen *et al.*, 2001):

$$\Delta \phi_{\text{snow}} = -\frac{4\pi}{\lambda_i} 0.87 \text{ SWE} \quad (\text{B.2.13})$$

This means that at the ERS wavelength one fringe is equivalent to 3.25 cm  $\text{SWE}$  or 32.5 cm of fresh dry snow with a typical density of  $100 \text{ kg m}^{-3}$ . For L-band ( $\lambda = 14$

cm,  $\theta_i = 23^\circ$ ) one fringe corresponds to an equivalent *SWE* of 14 cm. It is obvious that in case of major snowfall within the interferometric time span, the  $2\pi$  ambiguity may be a problem at C-band, but less at L-band.

The only example on phase shifts related to snow accumulation so far has been presented by Guneriussen *et al.* (2001) for a test site in Norway using ERS one-day repeat pass tandem data. However, this example is not fully conclusive, because of the lack of comparative data for validation, as discussed in section B.1.4.

There are several open questions that have to be studied for the development of a *SWE* retrieval algorithm based on ERS phase shifts:

- *The effect of snowfall on interferometric coherence.* Substantial inhomogeneity of snow deposition at sub-pixel scale very likely results in decorrelation. The feasibility and limits related to coherence need to be studied.
- *The required interferometric time span.* ERS SAR repeat pass data of the Alps in winter show in most cases complete decorrelation of snow covered areas for 5-week repeat-pass data. The coherence of one-day repeat pass data is in general very good, as long as the snow cover is dry. However, little has been known on effects of snowfall so far. Because the available tandem data of winter periods are quite limited, 3-day repeat pass data of the ERS ice phase are also very useful for studying these effects.
- *Effects of radar interaction with the snow cover.* The model above neglects the interaction of the radar waves with the snow volume. Though at C-band the losses in dry winter snow are quite small, it cannot be excluded that additional phase shifts are introduced by reflection at internal interfaces between layers of different density or by depth hoar layers with large grains.
- *Effects of land-cover type.* The algorithm requires a stable background signal of the ground below the snow pack. It should be investigated if different background targets have an effect on the *SWE* retrieval. The applicability for the main land cover types has to be studied.
- *Effects of radar frequency.* Theory suggests that the longer wavelengths (L-band) are more suitable for *SWE* retrieval by the proposed algorithm if only data of longer time spans are available, because of the reduced *SWE*-equivalent phase ambiguity and the better phase stability.

The proposed method for estimating *SWE* from interferometric phase shifts is only applicable for dry snow, because of the limited penetration and loss of coherence for melting snow. However, for many applications in snow hydrology (e.g. seasonal runoff forecasts) and climate monitoring this is not a severe constraint, because *SWE* close to the maximum accumulation, when the snow pack usually is still dry, is of main interest.

### **B.2.5 Assessment and ranking**

The main factors of relevance for prioritisation of the variables for algorithm development are summarized in Table B.2.1. There is significant interest for scientific and/or operational use for each of the three proposed variables, with the priority for spatially distributed data of *SWE*. This is particularly important for water

management, hydrological forecasting, flood risk management and climate research. Presently, there is no suitable method available for retrieving area-detailed SWE data, neither by means of remote sensing, nor by *in situ* measurements. For snow extent mapping alternate methods, using SAR and/or optical EO imagery, are in use. For mapping glacier facies a step forward can be expected by the proposed algorithm, because it would provide a better quantitative measure than existing EO-based algorithms.

Table B.2.1:  
Overview of relevant factors for selecting the variables for algorithm development.

	<b><i>Glacier Facies</i></b>	<b><i>Snow Extent</i></b>	<b><i>SWE</i></b>
<i>Operational need</i>	low	high	high
<i>Scientific need</i>	high	medium	high
<i>Alternate methods</i>	partial	yes	no
<i>SAR data for algorithm development</i>	good	good	good
<i>Data for validation</i>	suitable	good	Reasonable
<i>Development risk</i>	low	low	Medium
<i>Innovation</i>	medium	low-medium	High

Comprehensive SAR data sets for algorithm development are available in the ESA archives for all of the three proposed variables. Suitable SAR data sets and *in situ* data for validation have been available at ENVEO, and further C-Band data (in particular 3-day repeat pas ERS data) were ordered.

The feasibility for successful algorithm development is considered to be very high for glacier facies and snow extent, but the expected degree of innovation is medium to low. Regarding the algorithm development for SWE a certain risk of failure exists, mainly related to the question of temporal decorrelation in case of snowfall. On the other hand, the need for developing tools for spatially distributed SWE monitoring and the expected innovation are very high. Assigning priority to need and innovation, the following list of priority for algorithm development was proposed:

- (1) Snow water equivalent
- (2) Diagenetic glacier facies
- (3) Snow area extent

## B.3 ELECTROMAGNETIC INTERACTION MODELLING FOR SNOW COVERED TERRAIN

### B.3.1 Introduction

The water equivalent of the snow cover (*SWE*) was selected as variable for investigating an interferometric retrieval algorithm for snow and ice applications. In this chapter the theoretical basis for the development of a retrieval algorithm is elaborated. At first the interactions of radar waves with snow covered ground are modelled for various snow cover conditions and radar frequencies, in order to quantify the main factors for backscattering in dependence of target properties and to carry out a sensitivity study (section B.3.2). In section B.3.3 the target coherence is investigated in dependence of snow cover properties and SAR system parameters. Section B.3.4 deals with the physical basis of the retrieval algorithm. L- and C-band radar frequencies are considered, because at higher frequencies even modest amounts of snow accumulation would lead to decorrelation.

### B.3.2 Radar backscatter modelling of snow covered terrain

Backscattering from snow covered terrain is modelled with a one-layer model, where combined volume and surface scattering is calculated for a snow layer lying on a rough scattering surface (Figure B.3.1). The Integral Equation Model (IEM) is applied for surface scattering and the Rayleigh model for volume scattering. Snow is described as an inhomogeneous mixture of air, ice crystals, and (if wet) liquid water. The total backscattering coefficient at polarization *pp* (*hh* or *vv*),  $\sigma_{pp}^0$ , is calculated as the sum of backscattering at the air/snow interface,  $\sigma_{as}^0$ , backscattering in the snow volume with depth *d*,  $\sigma_{vol}^0$ , and the contribution from the snow/ground interface,  $\sigma_{sg}^0$ , which is attenuated due to propagation losses through the snow layer with the extinction coefficient,  $k_e$ , and due to transmission losses at the air/snow boundary, described by the power transmission coefficient,  $T_{as}$ :

$$\sigma_{pp}^0 = \sigma_{as}^0(\theta_i) + \sigma_{vol}^0 + \sigma_{sg}^0(\theta_t) \frac{\cos\theta_i}{\cos\theta_t} T_{as} T_{sa} \exp(-2k_e d / \cos\theta_t) \quad (\text{B.3.1})$$

Because dry snow is a low-loss medium at L- and C-band frequencies, the volume scattering contribution can be estimated with a first order model assuming independent Rayleigh scatterers:

$$\sigma_{vol}^0(pp) = \frac{1}{2} \omega_0 T_{as} T_{sa} \cos\theta_i [1 - \exp(-2\kappa_e d / \cos\theta_t)] P_{pp}(\cos\theta_t, -\cos\theta_t, \pi) \quad (\text{B.3.2})$$

where  $P_{pp}$  is the scattering phase function for polarization *pp*, and  $\omega_0$  is the single scattering albedo. We used the assumption of independent scatterers, because it provides the upper limit for the volume backscattering contribution of a snow layer. Scattering at the air/snow and snow/ground interfaces is calculated with the Integral Equation Model (IEM) of Fung (1994).

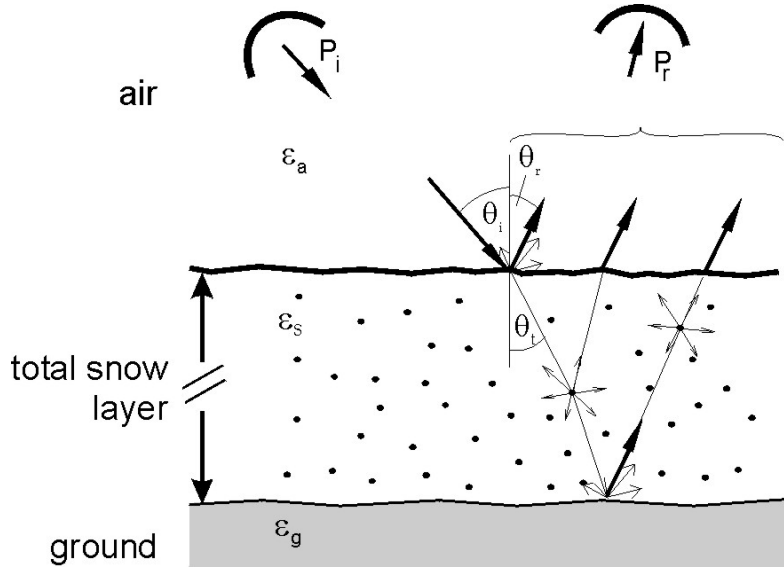


Figure B.3.1: Scattering processes of snow covered terrain with one homogeneous layer of snow.

The roughness of these surfaces is usually small to medium at L- and C-band ( $k\sigma_h < 1.5$ ), so that the co-polarized backscattering coefficients can be described by the following expression for single scattering from randomly rough surfaces:

$$\sigma_{pp}^0(surf) = \frac{k^2}{2} \exp\left(-2\sigma_h^2 k^2 \cos^2 \theta_i\right) \sum_{n=1}^{\infty} \sigma_h^{2n} \left| I_{pp}^n \right|^2 \frac{W^{(n)}(-2k \sin \theta_i, 0)}{n!} \quad (\text{B.3.3})$$

where

$$I_{pp}^n = (2k \cos \theta_i)^n f_{pp} \exp\left(-\sigma_h^2 k^2 \cos^2 \theta_i\right) + \frac{(k \cos \theta_i)^n \left[ F_{pp}(-k_S, 0) + F_{pp}(k_S, 0) \right]}{2} \quad (\text{B.3.4})$$

$W^{(n)}(-2k \sin \theta_i, 0)$  is the Fourier transform of the  $n^{\text{th}}$  power of the surface correlation function for  $k_s = k \sin \theta_i$ ; and  $f_{vv} = 2R_v / \cos \theta_i$ ,  $f_{hh} = 2R_h / \cos \theta_i$ , where  $R_p$  is the Fresnel reflection coefficient. The terms  $F_{pp}$ , depending on the reflection coefficient and incidence angle, are specified in Fung (1994).

We calculated the backscattering coefficients of ground covered with a layer of dry snow for a wide range of snow conditions, specified in Table B.3.1. The magnitudes of the variables are based on field observations during ERS SAR and SIR-C/X-SAR campaigns in the Tyrolean Alps. The snow permittivity was calculated with Equ. (B.2.12).

Figure B.3.2 to Figure B.3.5 show backscatter calculations for typical snow situations. In these examples volume scattering is calculated for grain radii of 0.3 mm, which is rather the upper limit for seasonal snow cover before extensive melt metamorphosis starts. Examples for the dry snow model calculations are shown for 3 m snow depth, which is a comparatively high value for seasonal snow cover (Figure B.3.2, Figure

B.3.3). In both cases (for rough and smooth soil surfaces) the backscatter signal is clearly dominated by the contribution of the snow/ground interface, at L-band as well as at C-band. This backscatter contribution is the basic background signal for *SWE* retrievals. The modification of this signal due to backscatter contributions of the snow volume or air/snow interface is negligible compared to the effects of differential phase shifts resulting from changes of propagation path length through the snow pack, as described in the next section.

Table B.3.1:  
Snow cover and soil variables used for backscatter calculations.

<b>Nr.</b>	<b>Variable</b>	<b>Case-I</b>	<b>Case II</b>
1	Snow surface roughness	4 mm	
2	Snow surface correlation length	110 mm	
3	Soil surface roughness	15 mm	10 mm
4	Soil surface correlation length	80 mm	134 mm
5	Soil permittivity, C-band	$\epsilon' = 17.0$ , $\epsilon'' = 3.2$	
6	Soil permittivity, L-band	$\epsilon' = 16.0$ , $\epsilon'' = 3.6$	
7	Snow depth	0.5 m	3.0 m
8	Snow density	300 kg m <sup>-3</sup>	
9	Snow particle radius	0.3 mm	1.0 mm
10	Snow permittivity, L-band	$V_w = 0\%$ , $\epsilon' = 1.53$ , $\epsilon'' = 0.0002$	$V_w = 0.5\%$ , $\epsilon' = 1.976$ , $\epsilon'' = 0.0144$
11	Snow permittivity, C-band	$V_w = 0\%$ , $\epsilon' = 1.53$ , $\epsilon'' = 0.0002$	$V_w = 0.5\%$ , $\epsilon' = 1.952$ , $\epsilon'' = 0.0479$

Snowmelt usually would result in comparatively rapid decorrelation, at least at C-band, as known from analysis of ERS SAR tandem data. At L-band this is not clearly known, because of the lack of interferometric data with various temporal baselines. For this reason we modelled the backscatter for a slightly wet snow pack of 0.5 m depth, assuming a liquid water content of 0.5 % by volume (Figure B.3.4, Figure B.3.5). For these conditions, the backscatter contribution of the ground surface at L-band is at least 10 dB higher than the contributions of the snow volume and the air/snow interface. This suggests that the L-band coherence might be preserved for slightly wet snow. Such conditions can be observed in the Alps in early spring, when the diurnal cycle of solar irradiation and refreezing causes moistening of the top snow layer whereas the main snow volume stays dry. At C-band total backscatter is reduced by at least 10 dB even for this slightly moist snow conditions, which confirms the findings of the SAR data analysis that such data are not useful for InSAR retrievals.



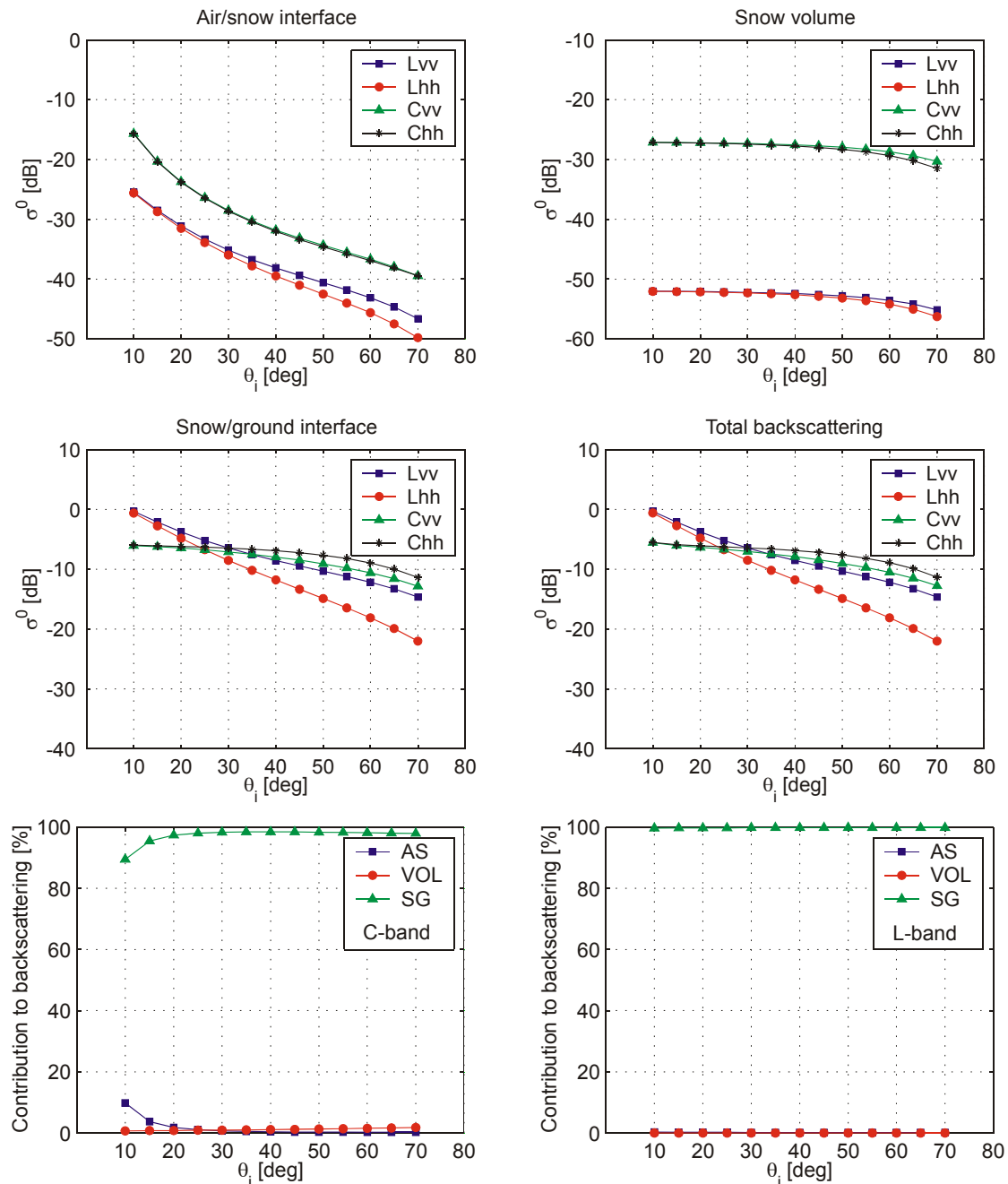


Figure B.3.2: L- and C-band co-polarized backscatter from snow covered ground (total and its three main components, in per cent of the total backscatter), for dry snow volume and rough soil surface. Selected parameters for model (referring to Table B.3.1): Soil roughness: Case I; snow depth: Case II; particle radius: Case I; snow wetness: Case I.

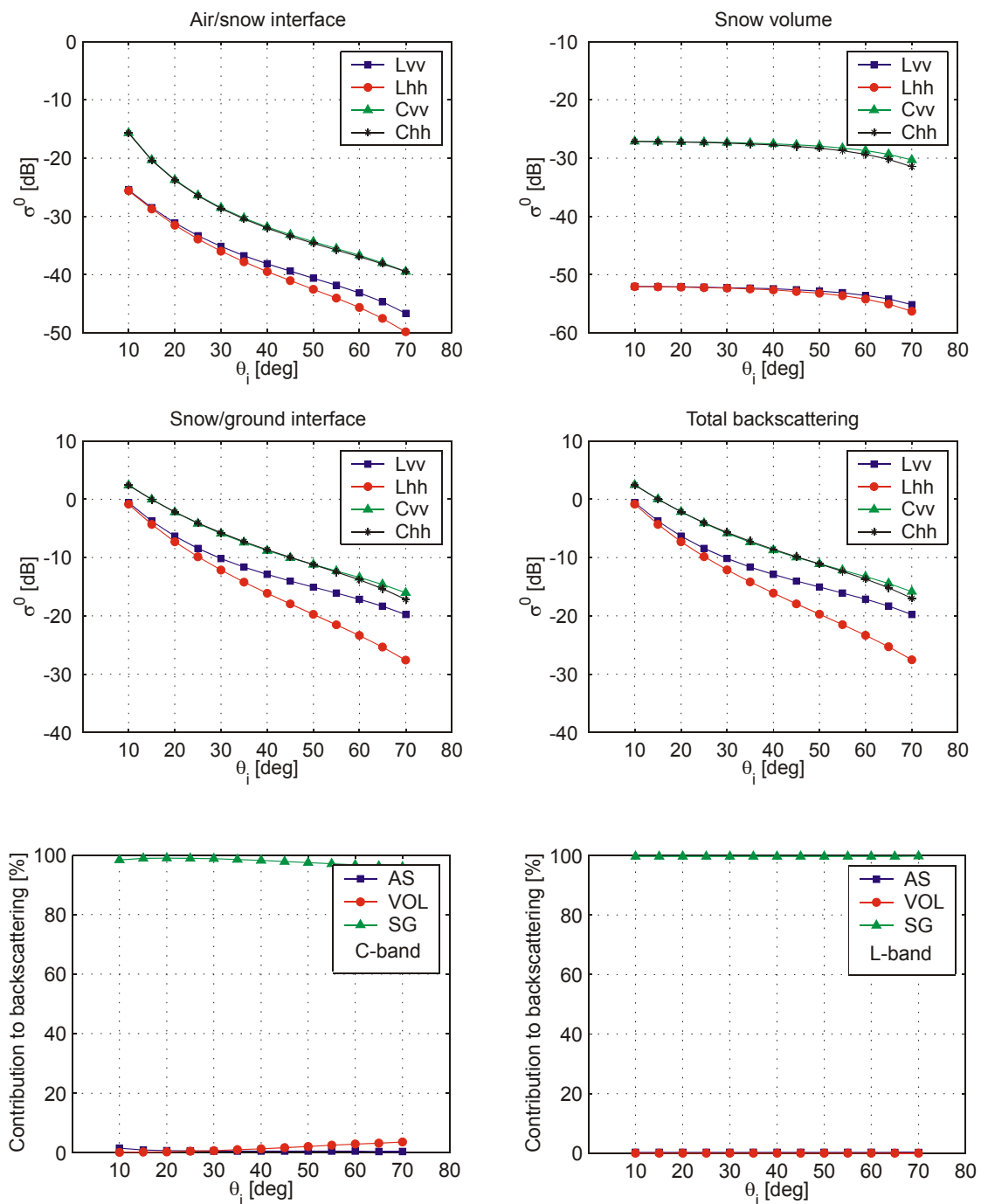


Figure B.3.3: As Figure B.3.2, but for dry snow volume and smooth soil surface. Selected parameters for model (referring to Table B.3.1): Soil roughness: Case II; snow depth: Case II; particle radius: Case I; snow wetness: Case I.

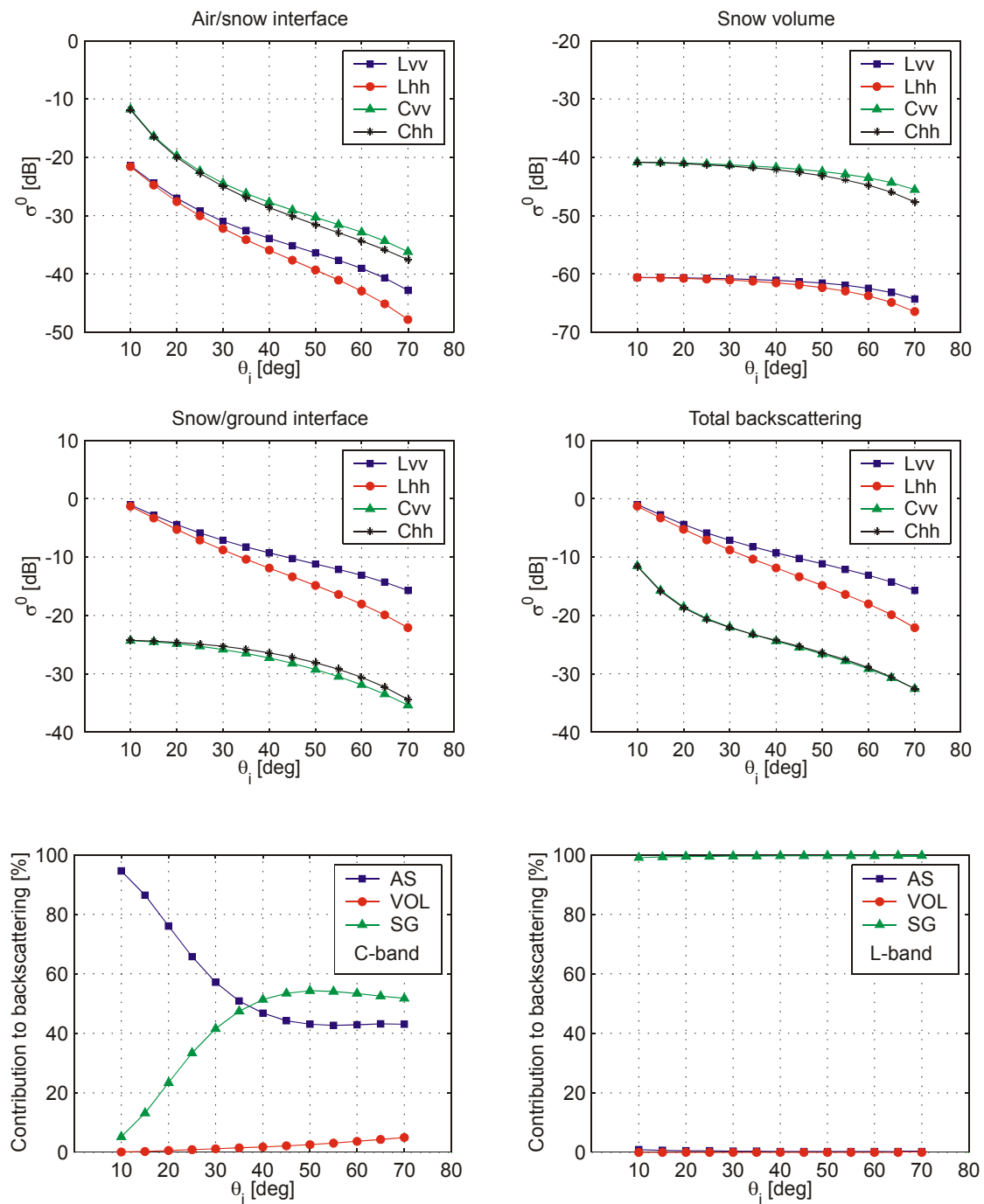


Figure B.3.4: As Figure B.3.2, but for slightly wet snow and rough soil. Selected parameters for model (referring to Table B.3.1): Soil roughness: Case I; snow depth: Case I; particle radius: Case I; snow wetness: Case II.

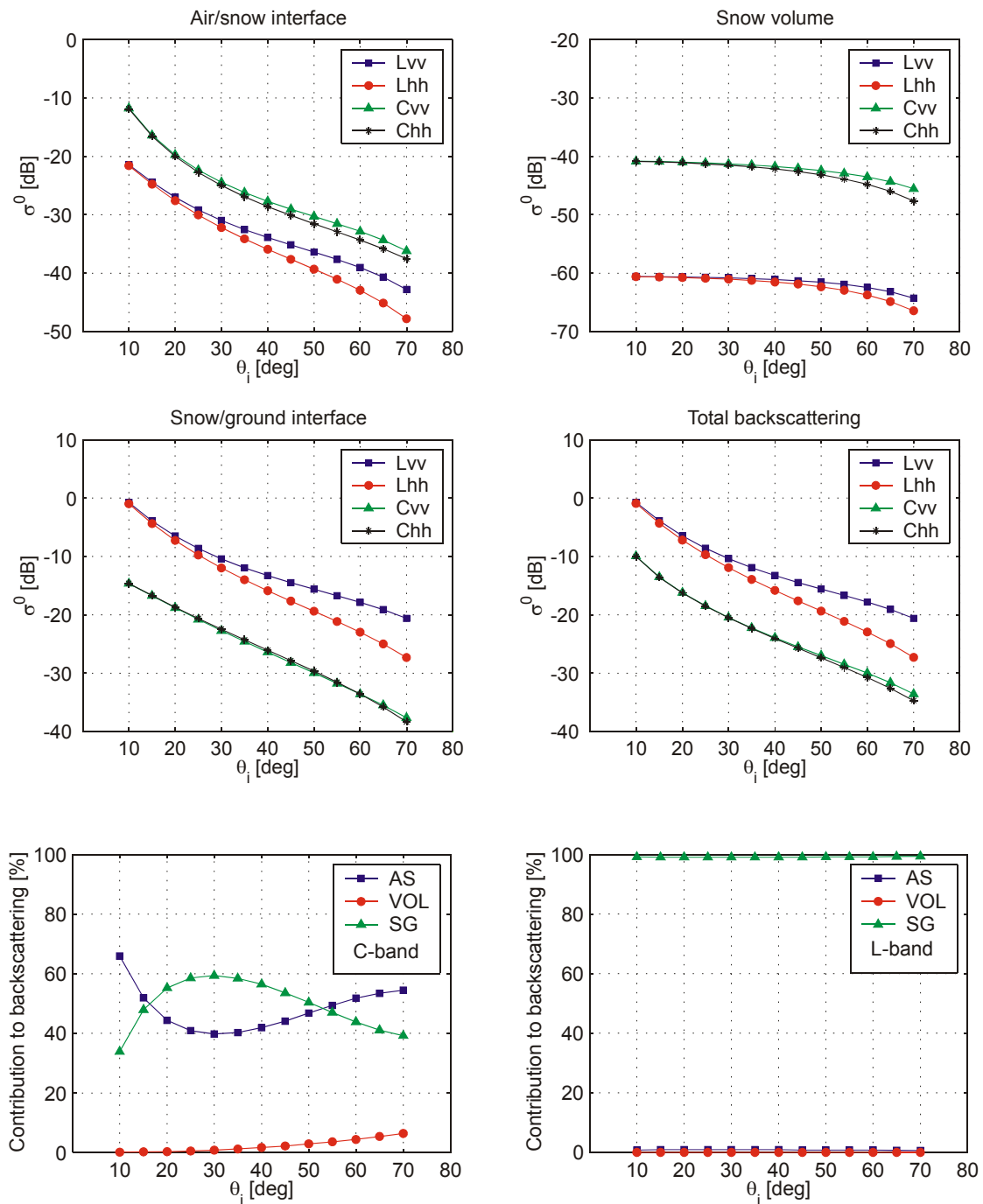


Figure B.3.5: As Figure B.3.2, but for slightly wet snow and smooth soil. Selected parameters for model (referring to Table B.3.1): Soil roughness: Case II; snow depth: Case I; particle radius: Case I; snow wetness: Case II.

### B.3.3 Spatial and temporal decorrelation

In order to estimate the coherence conditions for *SWE* retrievals we examine the main factors for decorrelation of repeat pass SAR data over snow covered terrain. The complex correlation coefficient of two SAR images is

$$\gamma = \frac{E\{V_1 V_2^*\}}{\sqrt{E\{|V_1|^2\} E\{|V_2|^2\}}} \quad (\text{B.3.5})$$

where  $E\{\cdot\}$  denotes the expected value. We consider the following main decorrelation phenomena:

$$\gamma_{\text{total}} = \gamma_{\text{thermal}} \cdot \gamma_{\text{surface}} \cdot \gamma_{\text{volume}} \cdot \gamma_{\text{temporal}} \quad (\text{B.3.6})$$

where

- $\gamma_{\text{thermal}}$  can be described by means of the signal-to-noise ratio (SNR). Assuming that the *SNR* is the same in both images, it can be written as 
$$|\gamma_{\text{thermal}}| = \frac{1}{1 + \text{SNR}^{-1}}$$
- $\gamma_{\text{surface}}$  describes the spatial baseline decorrelation for a radar echo from a distributed surface scatterer.
- $\gamma_{\text{volume}}$  describes the spatial baseline decorrelation due to spectral shift in a scattering volume.
- $\gamma_{\text{temporal}}$  is the temporal decorrelation caused by various changes of target backscattering properties (see sections B.2.2, B.2.3). Because the signal of melting snow decorrelates rapidly, and the radar beam does not penetrate sufficiently to enable *SWE* retrievals by the differential InSAR methods (at least at C-band), the analysis below focuses on temporal decorrelation due to snowfall under dry snow conditions.

#### B.3.3.1 Estimation of effects of $\gamma_{\text{surface}}$ and $\gamma_{\text{volume}}$ for snow covered ground

Because the propagation losses and signal contributions of dry snow are very small, the decorrelation at the snow/ground interface can be estimated without accounting for surface/volume interaction. In this case the only effect of the snow layer is the change of incidence angle at the ground surface due to refraction of the radar beam at the air/snow interface. The estimated spectral shift depends on the radar system transfer function. Assuming a surface scatterer with a high number of randomly distributed sub-scatterers in the resolution cell, the following expression is obtained for a *sinc*-system impulse response function, without spectral shift filtering (Bamler and Hartl, 1998):

$$|\gamma_{\text{surface}}| = 1 - \frac{2r_r B_n}{\lambda R_0 \tan \theta_i} \quad , \text{ for } B_n \leq B_{n,\text{crit}} \quad (\text{B.3.7})$$

The critical baseline,  $B_{n,crit}$ , is related to the slant range resolution,  $r_r$ , by

$$B_{n,crit} = \frac{\lambda R_0 \tan \theta_i}{2r_r} \quad (B.3.8)$$

where  $R_0$  is the slant range and  $\theta_i$  the local incidence angle at the illuminated slope.

For backscattering from a volume scattering medium, the wave number shifts in slant range (y) and in elevation (z) have to be considered. For a box with many small, randomly distributed, uncorrelated scatterers the spatial decorrelation results from spectral wave number shifts both in y and z direction:

$$\gamma_{\text{spatial}} = \gamma_{\text{surface}} \cdot \gamma_{\text{volume}} \quad (B.3.9)$$

The following expression for the z-component of the spatial decorrelation (the *volume* decorrelation) was derived by Hoen and Zebker (2000) for a snow layer with penetration depth  $d_p$  (see also Report WP20):

$$|\gamma_{\text{volume}}| = \frac{1}{\sqrt{1 + \left( \frac{2\sqrt{\epsilon} d_p B_n}{\lambda R_0 \tan \theta_i} \right)^2}} \quad (B.3.10)$$

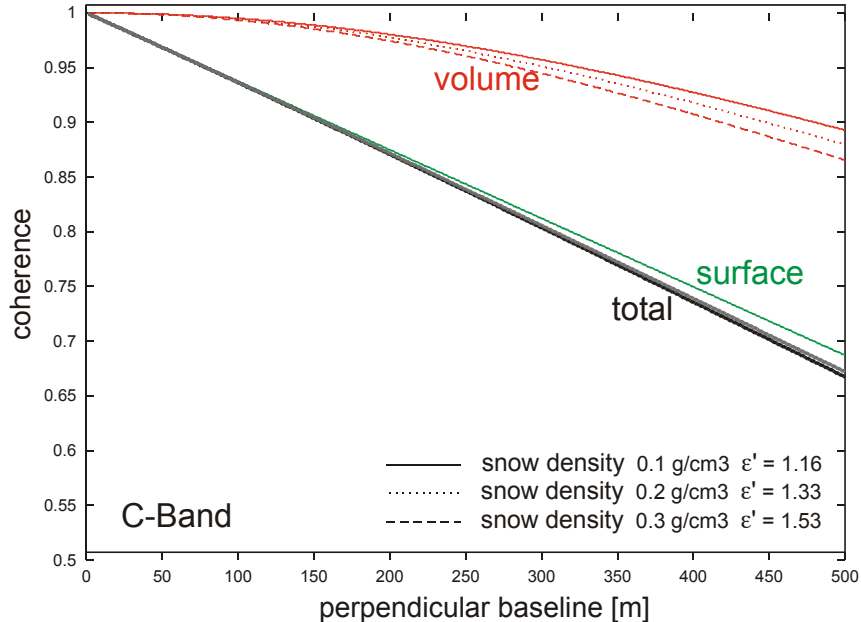


Figure B.3.6: Surface, volume and total spatial decorrelation estimates for different cases of dry snow, C - band, terrain angle  $-10^\circ$  (backslope), bandwidth 15.55 MHz, incidence angle (flat earth)  $23^\circ$ , snow depth 3 m.

This equation is valid for a semi-infinite layer of dry snow and ice, as found on glaciers and ice sheets. For this kind of medium the backscattering signal comes from the snow layer, except a very small contribution from the air/snow interface. For dry, fine-grained winter snow the signal contribution of the snow volume is very small (< 10 %), even if the snow depth reaches a depth of several metres in extreme cases. This means that the decorrelation originating from the scattering contribution of the snow pack can be neglected. More important is the spectral shift in y-direction for the signal contribution due to scattering at the snow/ground interface (Figure B.3.6 and Figure B.3.7).

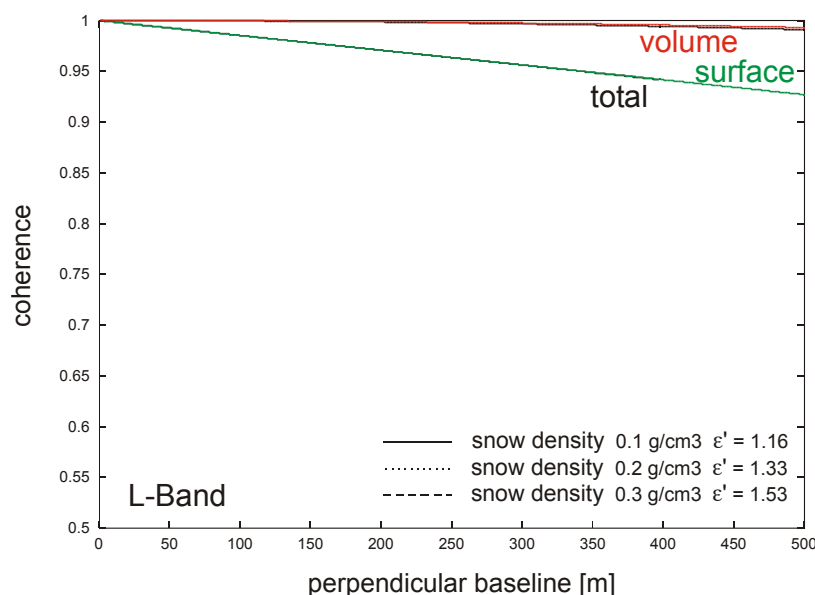


Figure B.3.7: As Figure B.3.6, but for L - band.

### B.3.3.2 Estimation of effects of $\gamma_{temporal}$ related to snowfall

The most disturbing effect for *SWE* retrievals by interferometry, however, is temporal decorrelation due to snowfall, snow drift or wind erosion. These effects cause phase shifts of the signal scattered back from the snow/air interface. These phase shifts vary within a surface resolution element, because the effects mentioned above modify the structure and roughness of a snow surface at sub-pixel scale.

Zebker and Villasenor (1992) derived an expression for temporal decorrelation due to change of the horizontal position  $\delta y$  and of vertical position  $\delta z$  of scattering elements in volume scattering media (e.g. wind induced motion in forests). Following this concept, we estimate the decorrelation for a snow layer deposited on a rough surface. In this case the change of phase delay in slant range  $\delta\phi_s$  has to be considered. Assuming that the phase delay is statistically unrelated to the position of a scattering element on a surface resolution cell, the cross-correlation of the two radar signals can be expressed by:

$$\langle V_1 V_2^* \rangle = \sigma^0 \int \exp[-i\delta\phi_s] p(\delta\phi_s) d(\delta\phi_s) \quad (B.3.10)$$

Because a uniform snow layer does not cause any decorrelation, only the differential phase delay due to non-uniform snow accumulation or erosion needs to be considered. The phase delay due to a change of snow depth  $\delta d_s$  (in direction of  $z$ ) (with constant snow density, as it is typical for fresh snow fall) depends on the radar wavelength and permittivity  $\varepsilon$  (Gunteriusen *et al.*, 2001):

$$\delta\phi_{SWE} = -\frac{4\pi}{\lambda_0} \delta d_s \left( \cos\theta_i - \sqrt{\varepsilon' - \sin^2\theta_i} \right) \quad (\text{B.3.11})$$

In Equ. (B.3.11) the permittivity is approximated by its real part,  $\varepsilon'$ , which is several orders above the imaginary part for dry snow at C- and L-Band (see Table B.3.1). Assuming that  $\delta d_s$  depends on the roughness of the snow surface,  $\delta\phi_{SWE}$  can be described by a Gaussian probability distribution for  $p(\delta\phi_s)$ . In this case, the temporal decorrelation is

$$|\gamma_{temporal}| = \exp \left[ -\frac{1}{2} \left( \frac{4\pi}{\lambda_0} \right)^2 \sigma_z^2 \left( \cos\theta_i - \sqrt{\varepsilon' - \sin^2\theta_i} \right)^2 \right] \quad (\text{B.3.12})$$

where  $\sigma_z$  is the standard deviation of the snow height, and  $\lambda_0$  is the vacuum wavelength. With this equation we calculate the upper limit of the temporal decorrelation in dependence of surface roughness. Two scales of snow surface roughness have to be considered:

1. The **smooth case**, which accounts for the small scale surface roughness. The reference value is the surface roughness of un-eroded snow, as measured with a laser profiler along a profile of 1.5 m length (Figure B.3.8). For this case a typical number for the standard deviation of surface roughness, as measured in the field, is  $\sigma_z \approx 5$  mm. This number can be assumed as initial value for an old snow cover before snowfall. After snow fall a perfectly flat surface is assumed. Such a situation might occur on horizontal surfaces, which are wind-sheltered, but would be rather the exception in mountain areas.
2. The more realistic **alpine case**, which has to be expected on sloping natural terrain, is characterized by surface roughness and undulations over a wide range of scales (Figure B.3.9). In addition, wind drift often plays an important role during snowfall. In this case the thickness of the deposited snow layer shows typical variations at the horizontal scale of metres and vertical scales of several centimetres; these dimensions are very relevant for C-band coherence at pixel scale. The high values of roughness at the meter scale are confirmed by Herzfeld (2002), who measured the roughness of snow surfaces in Colorado and glacier ice in Greenland over areas of  $100 \times 100 \text{ m}^2$ .

Figure B.3.10 shows the temporal decorrelation,  $|\gamma_{temporal}|$ , according to Equ. (B.3.12) at C- and L-band for three different snow densities in dependence of the surface roughness. At C-Band the coherence decreases rapidly with increasing standard deviation of the surface roughness; e.g. for  $\sigma_z = 50 \text{ mm}$  and snow density of  $0.2 \text{ g/cm}^3$ , which is characteristic for fresh winter snow, the resulting coherence is about 0.2 which means almost complete decorrelation. This effect would be even more



significant for snow with higher density, as in case of wind erosion. As shown in Figure B.3.10 coherence at L-band is much less sensitive to this effect.

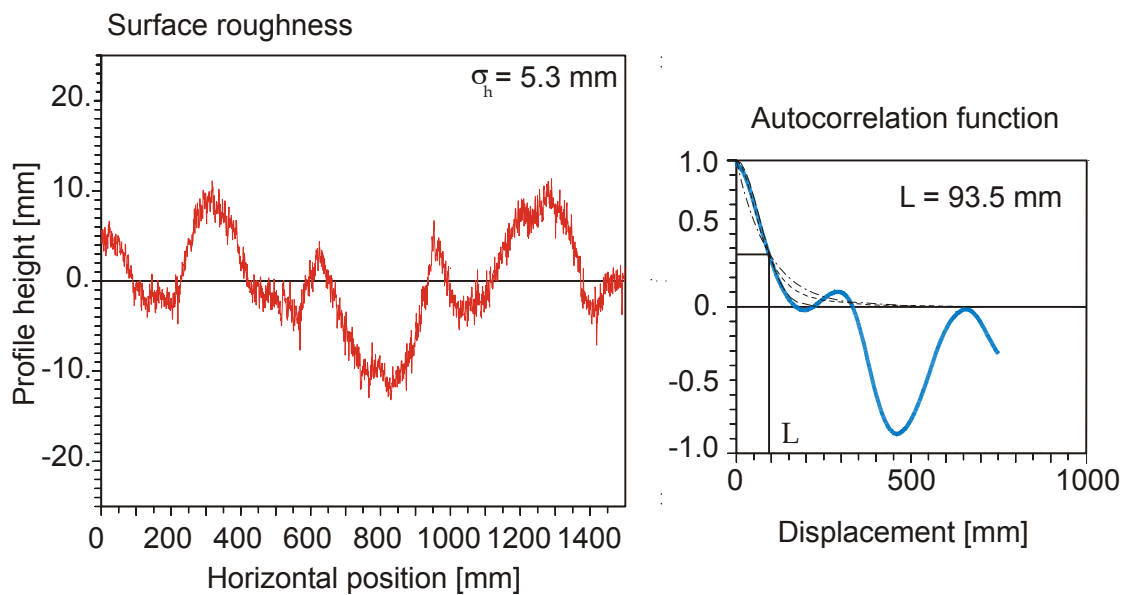


Figure B.3.8: Small scale surface roughness of snow measured with a laser profiler on the flat firn area of Hintereisferner Ötztal, on October 2, 1994.



Figure B.3.9: Winter snow pack after fresh snow fall, with surface roughness revealing undulations of various spatial scales (Alpbach, Tyrol).

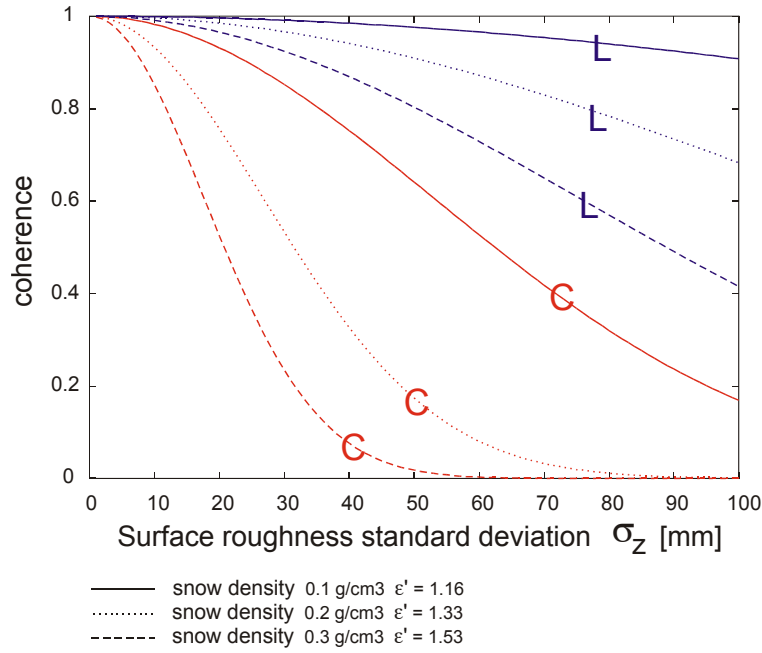


Figure B.3.10: Temporal decorrelation due to snowfall calculated for different snow densities according to Equ. (B.3.12).

#### B.3.4 SWE retrieval based on interferometric phase shift

In repeat pass SAR data the interferometric phase for a snow covered pixel with position vector  $\mathbf{x}$ , (defined by azimuth and slant range coordinates) is made up by the following components:

$$\Delta\phi(\mathbf{x}) = \Delta\phi_s(\mathbf{x}) + \Delta\phi_t(\mathbf{x}) + \Delta\phi_a(\mathbf{x}) + \Delta\phi_{SWE}(\mathbf{x}) + \Delta\phi_n(\mathbf{x}) \quad (\text{B.3.13})$$

where  $\Delta\phi_s$  and  $\Delta\phi_t$  are the geometric phase contributions due to slant range position and topographic elevation, which depend on the baseline,  $\Delta\phi_a$  is the phase contribution due to different atmospheric propagation conditions in the two SAR images,  $\Delta\phi_{SWE}$  is the phase shift due to snow accumulation or depletion, and  $\Delta\phi_n$  is phase noise.

In order to retrieve  $\Delta\phi_{SWE}$ , which is directly related to the change of SWE between the two image acquisitions, it is necessary to eliminate  $\Delta\phi_s$ ,  $\Delta\phi_t$ , and  $\Delta\phi_a$ .

According to Guneriusen *et al.* (2001) the phase change due to a change of SWE between the image acquisitions is given by

$$\Delta\phi_{SWE} = -2k \Delta d_s \left( \cos\theta_i - \sqrt{\epsilon' - \sin^2\theta_i} \right) \quad (\text{B.3.14})$$

with

$$\epsilon' = 1 + 1.6\rho + 1.8\rho^3 \quad (\text{B.3.15})$$

where  $\epsilon'$  is the real part of the permittivity of snow,  $\rho$  is the snow density, and  $\Delta d_s$  is the change of snow height between the two image acquisitions,  $k$  is the wave number.

Using a linear approximation for Equ. (B.3.15), valid for  $\rho < 0.45 \text{ g cm}^{-3}$ , the  $SWE$  can directly be related to the interferometric phase. For C-Band and  $\theta_i = 23^\circ$  the following relation is obtained

$$\Delta\phi_{SWE} = -\frac{4\pi}{\lambda} 0.87 SWE \quad (\text{B.3.16})$$

With these numbers one fringe corresponds at C-band to  $SWE = 3.2 \text{ cm}$  (at  $\theta_i = 23^\circ$ ) and at L-band to 16 cm. Figure B.3.11 shows  $\Delta\phi_{SWE}$  in dependence on  $SWE$  for three local incidence angles.

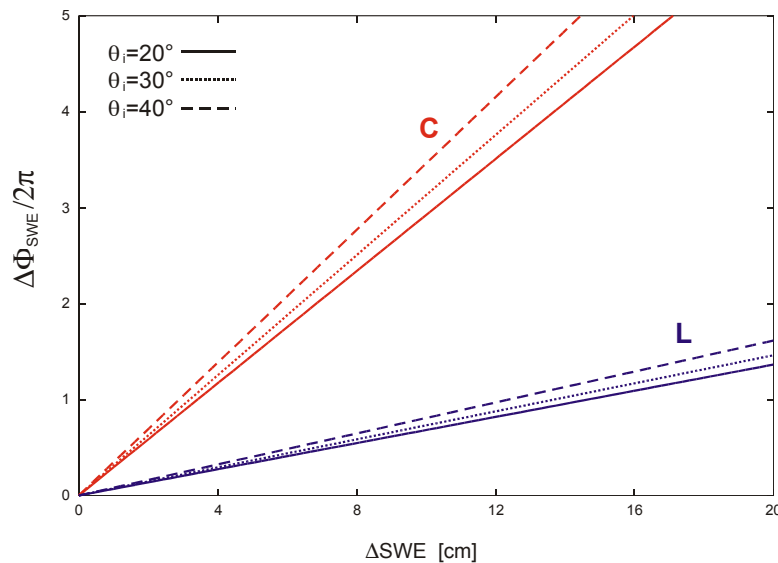


Figure B.3.11: Phase shifts in dependence of the change of snow water equivalent between two SAR images ( $SWE$ ) for different local incidence angles ( $\theta_i$ ) for C- and L-band.

#### B.3.4.1 Error estimate for $SWE$ due to phase noise

Table B.3.2 shows the sensitivity of  $SWE$  retrieval on phase noise for C-band and L-band. For ERS SAR with typical values of the signal to noise ratio of 10 to 20 dB the standard deviation of the phase ranges from about 40 to 15 degrees (Schwäbisch, 1995). In terms of  $SWE$  retrieval these values correspond to changes of  $SWE$  between 0.1 and 0.4 cm only, which would not be relevant for snow monitoring. At L-Band the phase noise introduces a somewhat higher variation in the  $SWE$  retrieval.

Table B.3.2:

Errors for  $SWE$  retrieval due to standard deviation of phase ( $\delta\phi$ ), incidence angle of  $23^\circ$ , at C-Band and L-Band.

	$\delta\phi = 10^\circ$	$\delta\phi = 25^\circ$	$\delta\phi = 40^\circ$	$\delta\phi = 55^\circ$
C-Band (5.6cm): $SWE$ [cm]	0.09	0.22	0.36	0.49
L-Band (24cm): $SWE$ [cm]	0.38	0.96	1.5	2.1

### B.3.4.2 Error estimate for *SWE* due to the topographic phase

To derive *SWE* from an interferogram, the topographic phase has to be subtracted. Typically, this can be done by differential processing, using at least one interferogram without *SWE* changes. If possible, several interferograms should be used for determining the topographic phase, to reduce effects of atmospheric phase variations and other phase noise. Another option would be to use an accurate digital elevation model for calculating the topographic phase, but standard digital elevation models are usually not accurate enough for this task.

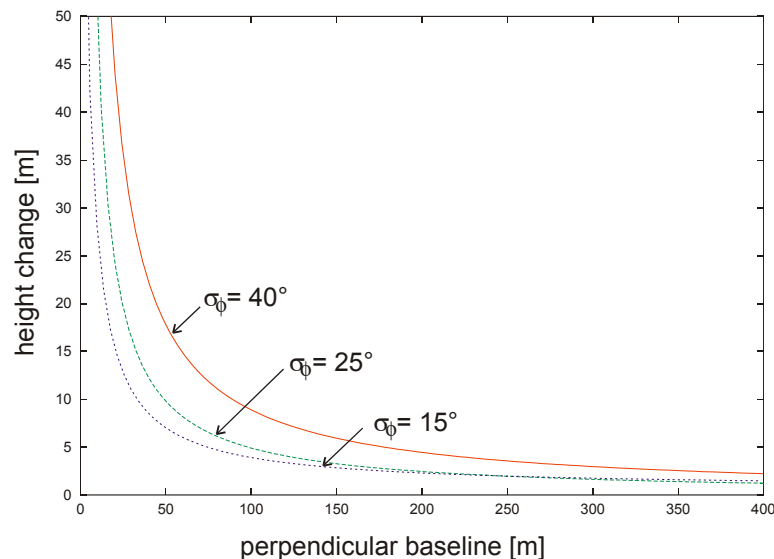


Figure B.3.12: Height error in dependence of the perpendicular baseline for various phase errors, C-band ( $\sigma_\phi$  ... standard deviation of phase, after Schwäbisch, 1995).

Differential processing requires rescaling of the baseline from the geometry of the topographic interferogram to the geometry of the *SWE*-image pair. The topographic phase is derived from image pairs acquired during snow free conditions or dry snow conditions without changes in the *SWE*. The sensitivity on height increases with increasing perpendicular baseline ( $B_{per}$ ). The estimation of the topographic phase is affected by phase noise resulting from temporal and geometric decorrelation. Figure B.3.12 shows the height error due to different standard deviations of the topographic phase. At small values of  $B_{per}$  the phase noise corresponds to large elevation changes; e.g. a phase standard deviation of  $40^\circ$  corresponds to a height error of 25 m and 5 m at  $B_{per} = 50$  m and 200 m, respectively. Therefore, phase noise is amplified or reduced due to the baseline rescaling up- or downwards, respectively. Because the rescaled topographic phase is subtracted from the *SWE*-interferogram, the effects of the uncertainty of the topographic phase depend on the relative baseline of the two differential interferograms. If appropriate SAR data are available, the  $B_{per}$  of the topographic image pair should clearly exceed the  $B_{per}$  of the *SWE*-image pair.

**B.3.4.3 Error estimate of *SWE* due to orbit uncertainties**

The impact of the accuracy of the orbit state vectors on the interferometric phase has been investigated by Reigber *et al.* (1996). It effects the estimation of the topographic phase and, consequently, the retrieval of *SWE*. The observed interferometric phase is given by

$$\phi = \frac{4\pi}{\lambda} (R_1 - R_2) = \frac{4\pi}{\lambda} \left( B_x \sqrt{1 - \frac{H^2}{R_1^2}} - B_y \frac{H}{R_1} \right) \quad (\text{B.3.17})$$

where  $H$  is the satellite height,  $R_1$  and  $R_2$  are the slant range distances of satellite position 1 and 2,  $B_x$  and  $B_y$  are the horizontal and vertical component of the baseline (see Hanssen, 2001, Figure 4.17 and Table 4.4, page 115). By differentiating with respect to  $B_x$ ,  $B_y$ , and  $H$  the sensitivity of the phase in respect to orbit errors is obtained:

$$\begin{aligned} \frac{\partial \phi}{\partial B_x} &= \frac{4\pi}{\lambda} \sqrt{1 - \frac{H^2}{R_1^2}} \\ \frac{\partial \phi}{\partial B_y} &= -\frac{4\pi}{\lambda} \frac{H}{R_1} \\ \frac{\partial \phi}{\partial H} &= -\frac{4\pi}{\lambda} \left( \frac{B_x H}{\sqrt{(1 - H^2 / R_1^2)} R_1^2} + \frac{B_y}{R_1} \right) \end{aligned} \quad (\text{B.3.18})$$

For *SWE* retrievals the effect of orbit inaccuracies have to be considered only for a limited area. Reigber *et al.* (1996) derived the impact of orbit uncertainties for test areas of local scale (5 km ground range extension) and regional scale (50 km ground range extension). The results are summarized in Table B.3.3. To assess the results they have to be related to phase noise due to temporal decorrelation, atmospheric perturbations, processing effects, changes in *SWE* etc. It should be noted that this phase noise acts mainly locally on the interferogram and not systematically on the image. According to Reigber *et al.* (1996) the *rms*-value of the phase noise (as derived from validation of radar topography maps, e.g. Schwäbisch, 1995) is on the order of 0.6 radian. Therefore, the impact of the orbit uncertainties is allowed to be on the order of 0.6 radian. The effect of orbits errors can be reduced by detrending the full phase image in azimuth and range using a linear polynomial model.

Table B.3.3 shows that orbit inaccuracies cause a tilt of the *SWE* in range, which becomes significant at regional scales if precise orbits are not available. The accuracies for different orbit types are summarized in Table B.3.4. For the estimation of *SWE* on single slopes (extending over a small range interval), and especially if precise orbits are used, the impact of orbit inaccuracies on *SWE* retrieval is negligible.

Table B.3.3

Systematic errors for surface height and *SWE* retrieval due to baseline errors of 0.05 m and 1 m, calculated for ERS SAR system parameters. The values are derived for areas with 5 km and 50 km ground range extension and for baselines of  $B_x = 50$  and 200 m, with ERS (Reigber *et al.*, 1996). The numbers show the maximum relative error calculated with  $d = d_{far\_range} - d_{near\_range}$ ;  $\phi$  ... interferometric phase,  $h$  ... elevation, *SWE* ... snow water equivalent

	$dB_x = 0.05\text{ m}$	$dB_y = 0.05\text{ m}$	$dB_x = 1.0\text{ m}$	$dB_y = 1.0\text{ m}$
$d\phi$ [5 km] [rad]	0.06	0.02	1.1	0.5
$d\phi$ [50 km] [rad]	0.5	0.2	10.2	4.6
Topographic Error $B_x = 50\text{m}$				
$dh$ (5 km) [m]	2	0.7	36	16.6
$dh$ (50 km) [m]	16	6.6	337.8	152.3
Topographic Error $B_x = 200\text{m}$				
$dh$ (5 km) [m]	0.5	0.2	9.1	4.1
$dh$ (50 km) [m]	4.1	1.7	84.4	38.1
Snow water equivalent Error				
$d(\text{SWE})$ (5 km) [cm]	-0.03	-0.01	-0.56	-0.26
$d(\text{SWE})$ (50 km) [cm]	-0.25	-0.10	-5.22	-2.36

Table B.3.4

Typical ERS orbit accuracies (after Closa, 1998)

Restituted orbits (produced by ESOC)	Along track accuracy 2 - 4 m Across track accuracy 1 - 2 m
Preliminary orbits (derived from fast delivery tracking data)	Radial accuracy 8 – 10 cm
Precise orbits - (produced by D-PAF)	Radial accuracy 8 – 10 cm
Delft Orbits	Radial accuracy 5 – 6 cm (only position)

#### B.3.4.4 Effect of variations of atmospheric conditions

The *SWE* estimation is affected by differences of atmospheric conditions (especially water vapour content) at the acquisition time of the images. In hilly and mountainous terrain the spatial scale of *SWE*-related phase differences should be typically much smaller than the scale of atmospheric phase variations, in particular if winter conditions are considered for the atmosphere. Nevertheless, it is not possible to

eliminate the atmospheric influence using only one image pair, as explained in Part A of this report and by Hanssen (2001). In order to estimate effects of variations in atmospheric conditions for *SWE* retrieval, we calculated phase shifts for a typical winter case in the Alps using radiosonde data.

Figure B.3.13 shows, as an example, the vertical temperature and humidity profiles from February, 9 and 12, 1996. For these dates ERS SAR images (Phase D, 3 days repeat cycle) are available. On February, 11, 1996 a frontal system passed the investigation area located in the Eastern Alps of Austria, causing snowfall and a change in the air mass. Figure B.3.14 shows the corresponding vertical profile of the scaled-up refraction index  $N$  (with  $N = (n-1) \times 10^6$ , where  $n$  is the refractivity) and the difference of  $N$  between both dates ( $\Delta N = N_{12Feb96} - N_{9Feb96}$ ).

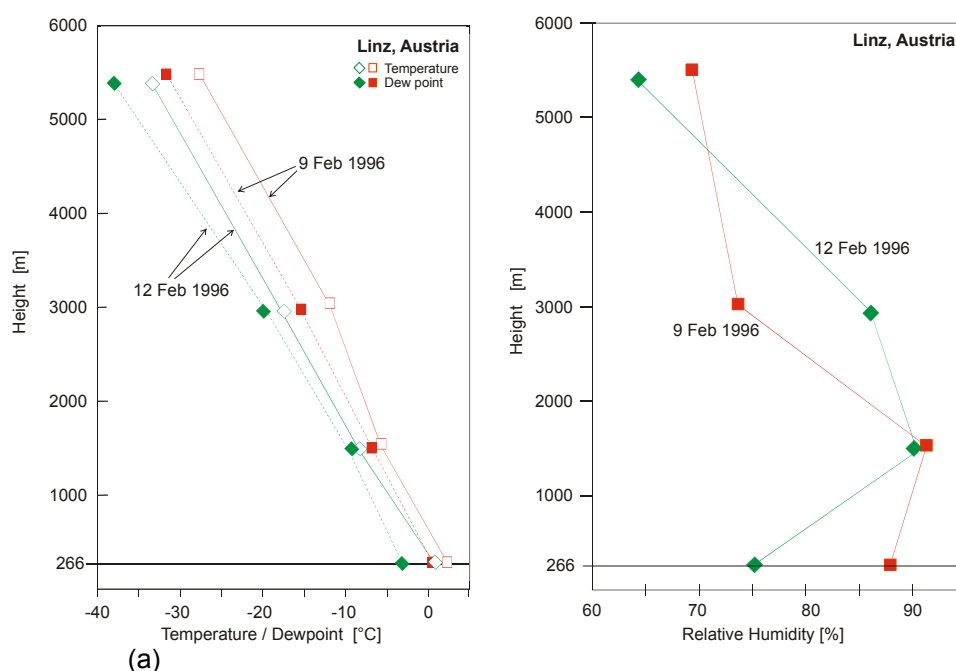


Figure B.3.13: Vertical profile of (a) air temperature and dew point, and (b) relative humidity, at synoptic station Linz, Austria (266 m).

To estimate the error due to atmospheric variations we calculate the phase shift for a slope extending from 1000 m to 2000 m in elevation. According to Figure B.3.14 the mean change for the 1 km thick layer would be  $\Delta N = -1$ . According to Hanssen (2001) the one-way path delay between the two acquisitions for typical ERS configuration and  $\Delta N = -1$  (incidence angle of  $23^\circ$ , C-band) is about -1 mm. This corresponds to a two-way phase delay of -13 degrees or -0.036 fringes. In terms of  $\Delta SWE$  this phase delay corresponds to a change of the snow water equivalent of 0.1 cm. Even a fivefold increase of the atmospheric effects, which should be the upper limit for winter conditions, would not introduce a significant bias in the *SWE* analysis, as variations of 0.5 cm *SWE* are of little relevance for an Alpine snowpack.



In the winter case with cold temperatures the atmospheric phase delay would cause only a negligible *SWE* bias over the slope. As shown by Hanssen (2001), other atmospheric conditions might introduce a significantly higher phase delays, but such conditions would lead to snowmelt which rules out the use of InSAR over snow covered areas because of decorrelation.

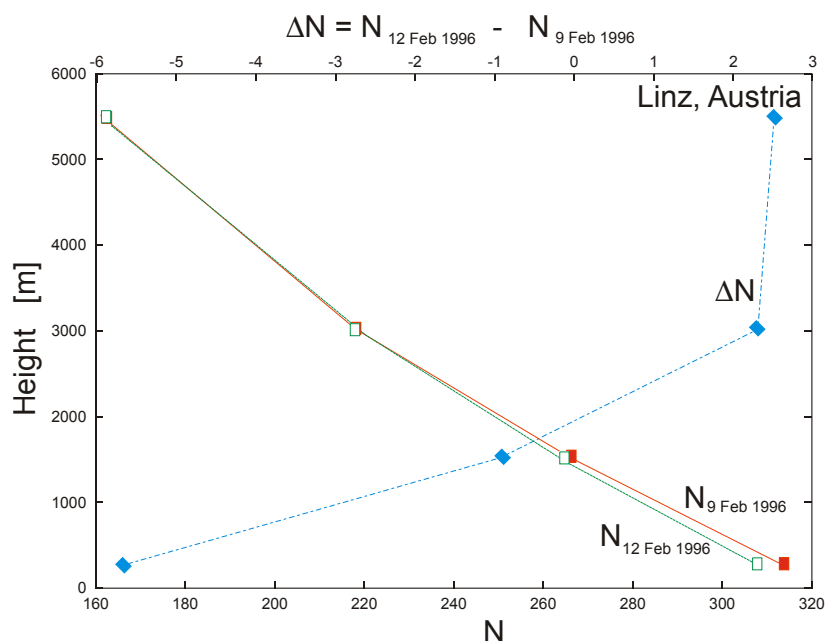


Figure B.3.14: Vertical profile of refraction index  $N$  and  $\Delta N$ , derived from radiosonde data of Linz for 9 and 12 February 1996.

### B.3.5 Summary and conclusions

The theoretical basis for the development of a retrieval algorithm to measure snow accumulation is elaborated, based on interferometric phase shifts due to temporal changes of snow water equivalent (SWE). A one layer model, which combines volume and rough surface scattering for a snow layer on rough ground, is applied to calculate the main backscatter contributions for L- and C-Band for various snow types (dry snow, slightly wet snow, different grain sizes, snow depth, surface roughness of the air-snow and snow-ground interface). As long as the snow is dry backscattering from the snow-ground interface dominates. At C-Band backscattering from the air-snow interface becomes more important already when the snow gets slightly wet, whereas at L-Band in this case the signal from the snow-ground interface still dominates if the snow pack is shallow.

In order to estimate the coherence conditions for *SWE* retrievals, the main factors for decorrelation (spatial and temporal) of snow covered terrain are examined for C- and L-band for different snow pack properties. To analyse the temporal decorrelation due to fresh snow fall in the time period between the SAR acquisitions, a simple model was developed, which accounts for the variation of dry snow accumulation within a SAR resolution element taking into account the roughness of natural terrain. It could be shown that at C-band coherence may decrease significantly or decorrelate in case of substantial snowfall if the snow surface and/or ground surface are rough at sub-



pixel scale, while at L-band the coherence is much better preserved. The physical basis for retrieving snow accumulation from phase differences is given, and the magnitude of the main error sources is calculated (phase noise, orbit inaccuracies, variations of atmospheric conditions). Table B.3.5 summarizes the effect of these error sources in terms of SWE retrieval for ERS system parameters. The impact of atmospheric variations is estimated using radiosonde data of a typical winter period. Because SWE retrievals require dry snow and consequently an atmosphere with low water vapour content, the disturbances due to changes of atmospheric propagation conditions are small.

Table B.3.5:

Summary on the order of errors of SWE retrieval for ERS SAR system parameters due to phase noise, orbit inaccuracies, and atmospheric variations (C-Band, incidence angle 23°). Details on each error source can be found in section B.3.4.1, B.3.4.3, 0.  $\delta\phi$  ... *standard deviation of phase*,  $dB_{x,y}$  ... *error of baseline in x- and y direction respectively*.

Error source	Phase Noise		Orbit inaccuracies		atmospheric phase shift	
Effect in SWE retrieval	local variation of retrieved SWE		systematic change of SWE in range direction (assumed: 5 km range extent)		SWE change with elevation (assumed: a slope with 1000 m elevation range)	
	$\delta\phi = 10^\circ$	$\delta\phi = 40^\circ$	$dB_{x,y} = 0.05 \text{ m}$	$dB_{x,y} = 1 \text{ m}$	typical case	extreme case
d(SWE) [cm]	0.09	0.36	0.03, 0.01	0.56, 0.26	~0.1	~0.5

The theoretical investigations suggest that C-band data should in principle be suitable for *SWE* retrievals, but L-Band should be better, mainly because of better preservation of coherence and larger measurement range for SWE within a  $2\pi$  phase cycle.

## B.4 RETRIEVAL ALGORITHM AND TEST CASES

### B.4.1 Retrieval Algorithm

Figure B.4.1 illustrates the basic idea of the SWE retrieval algorithm. It is based on the differential phase shift introduced by spatial differences in snow accumulation. This is analogous to motion mapping with differential InSAR. At least one reference point with zero or known SWE accumulation is necessary to determine the SWE accumulation in a region. The distribution of snow is highly variable in mountainous areas. On one hand snow height depends on the elevation, usually revealing an increase of precipitation with altitude. On the other hand snow on the ground may be redistributed due to wind, an effect which varies with the steepness and orientation of a slope and is governed by the dominating wind regime.

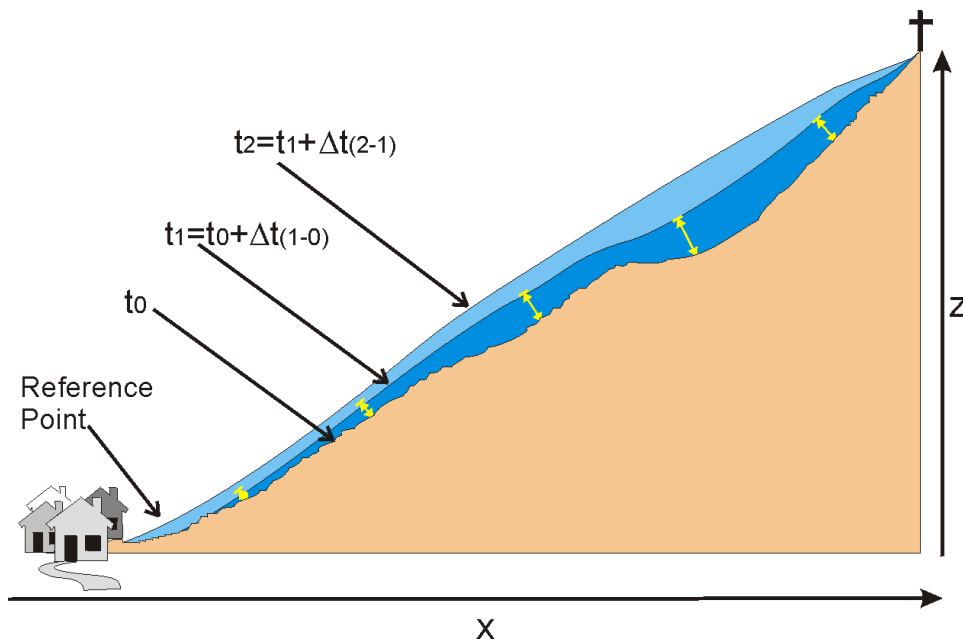


Figure B.4.1: Sketch of typical spatial distribution of snow in mountainous areas;  $x$  ... horizontal axis,  $z$  ... elevation,  $t_0, t_1$  and  $t_2$  correspond to dates with snow fall.

With the retrieval algorithm the SWE accumulated due to snowfall or wind drift within a time period  $(t_1 - t_2)$  is estimated using two SAR images, one image acquired at time  $t_1$ , before the snow fall, and the second image acquired at  $t_2$ , after the snow fall. According to Equ. (B.4.1) dry snow accumulated in the time interval will cause a phase shift  $\Delta\phi_{SWE}$ . Therefore, the  $\Delta\phi_{SWE}$  image reflects the spatial variations of the accumulated snow. To retrieve SWE maps at least one reference station with ground based measurements of snow accumulation (given as snow water equivalent) or a zero reference is required. Although in the Alps a dense network of meteorological stations and climate stations exists, most of the stations are located at low elevations near the valley floor. Only a few stations are located at higher elevations.

Figure B.4.2 summarizes the main processing steps and the data flow of the procedure for mapping changes of the SWE. As input for the procedure repeat pass SAR SLC images acquired before and after the snow fall are required. As first step interferometric processing is applied on the SAR image pair, including coregistration with sub-pixel accuracy to a common master scene, coherence estimation, calculation of the interferometric phase difference, filtering, and the removal of the flat earth phase contribution.

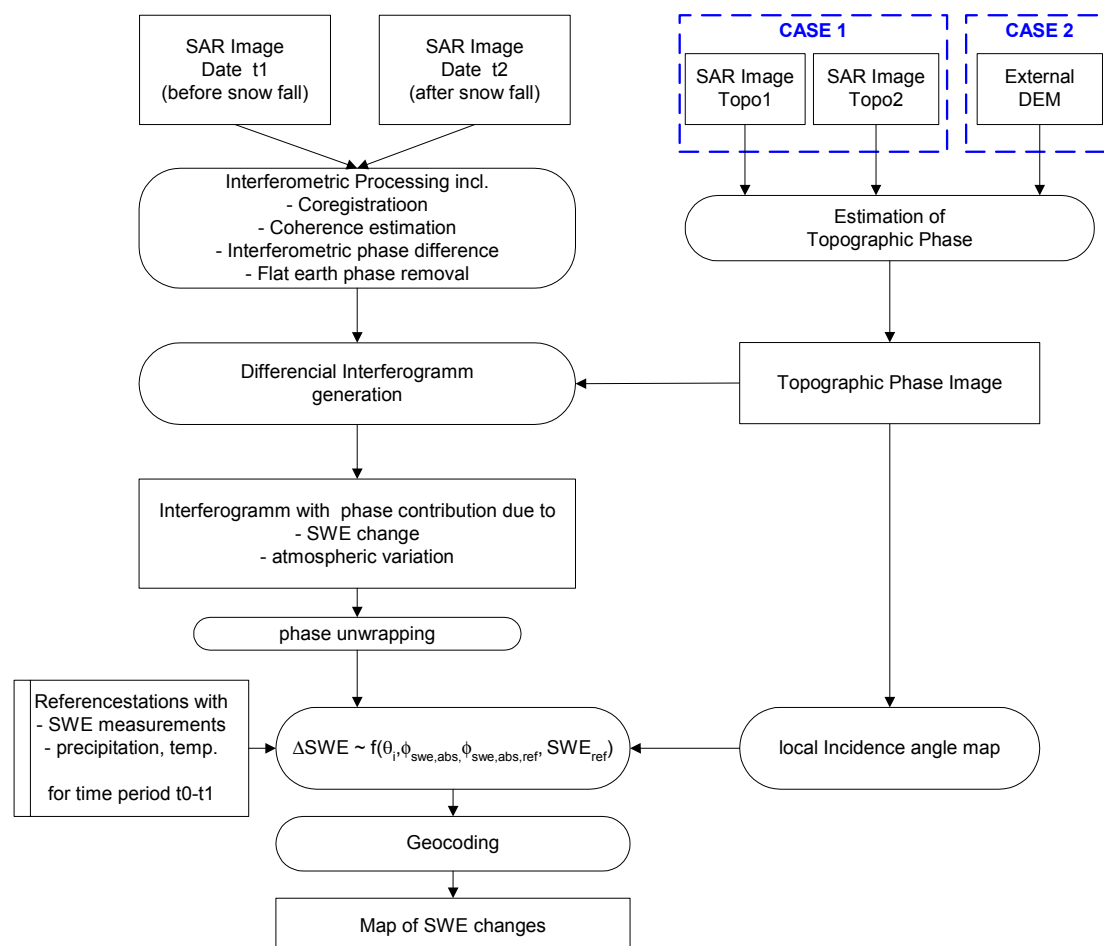


Figure B.4.2: Flowchart of main processing steps for mapping the snow water equivalent.

Then differential InSAR processing is carried out to remove the topographic phase contribution. Precise topographic phase removal is required because inaccuracies or errors (e.g. lost fringes) will directly affect the final map of SWE. The topographic phase can be estimated from repeat pass image pairs, which are not affected by snow fall. A multi-baseline approach, where several SAR image pairs with different perpendicular baselines are combined (Ferreti *et al.*, 1999) provides an accurate estimation of the topographic phase and has the further advantage that the influence of atmospheric variation for the topographic phase estimation is reduced. Optionally, the topographic phase can also be estimated from high precision digital elevation models and by calculating simulated topographic phase images.

After topographic phase removal the differential interferogram contains the phase contributions due to accumulated snow,  $\Delta\phi_{SWE}$ , and due to atmospheric variations,  $\Delta\phi_{atm}$ . In general,  $\Delta\phi_{atm}$ , varies from case to case and would require the knowledge of the vertical profile of water vapor and air temperature at the time of the image acquisitions to be separated. A good approximation are radiosonde measurements, which are carried out at selected meteorological stations on a daily basis (in general at 0h, 6 h, 12 h and/or 18 h UTC depending on the station). The influence of variation in the atmosphere on the SWE retrieval is discussed in detail in chapter B.3. For a slope of 1000 m elevation range the atmospheric variation under typical alpine winter conditions is on the order of 1 mm in terms of SWE, which is of little relevance for snow mapping in mountainous areas. Therefore the influence of atmospheric variation can be neglected in the retrieval algorithm.

After phase unwrapping  $\phi_{SWE,abs}$  (index *abs* for absolute phase) is transformed into *SWE* using the local incidence angle,  $\theta_i$ . The basic equations for SWE retrieval are

$$\begin{aligned}\phi_{SWE,abs} &= -2k \Delta d_s \left( \cos \theta_i - \sqrt{\varepsilon' - \sin^2 \theta_i} \right) \\ \varepsilon' &\approx 1 + 1.6\rho_s + 1.8\rho_s^3 \\ SWE &= \langle \rho_s \rangle d_s\end{aligned}\tag{B.4.1}$$

Applying a linear approximation for the snow density,  $\rho_s$ , which is quite accurate in the range of 0 – 0.5 g/cm<sup>3</sup>, *SWE* in dependence of the incidence angle is given by

$$SWE \approx \frac{\lambda}{4\pi} \frac{\cos(\theta_i)}{0.8} (\phi_{SWE,abs} - \phi_{SWE,abs.ref}) + SWE_{ref}\tag{B.4.2}$$

where  $\phi_{SWE,abs.ref}$  is the phase at the reference station and  $SWE_{ref}$  is the observed temporal change SWE at the reference station. Finally, the SWE image is transformed into a geographic map projection.

#### B.4.2 Test cases and data set

The procedure for mapping SWE described in the previous section was applied to various data sets:

- Data set 1: A series of ERS-1 repeat pass SAR images, acquired in Phase –D with 3 days repeat cycle, Eastern Austria.
- Data set 2: 4 ERS-1/2 SAR Tandem pairs of the Austrian Alps acquired in winter 1995 / 96, including the high alpine area Ötztal.
- Data set 3: Airborne E-SAR L-Band data of Oberpfaffenhofen (provided by DLR-HR).

Figure B.4.3 shows an overview on the location of the data sets, which are the basis for the investigations presented in the following sections.

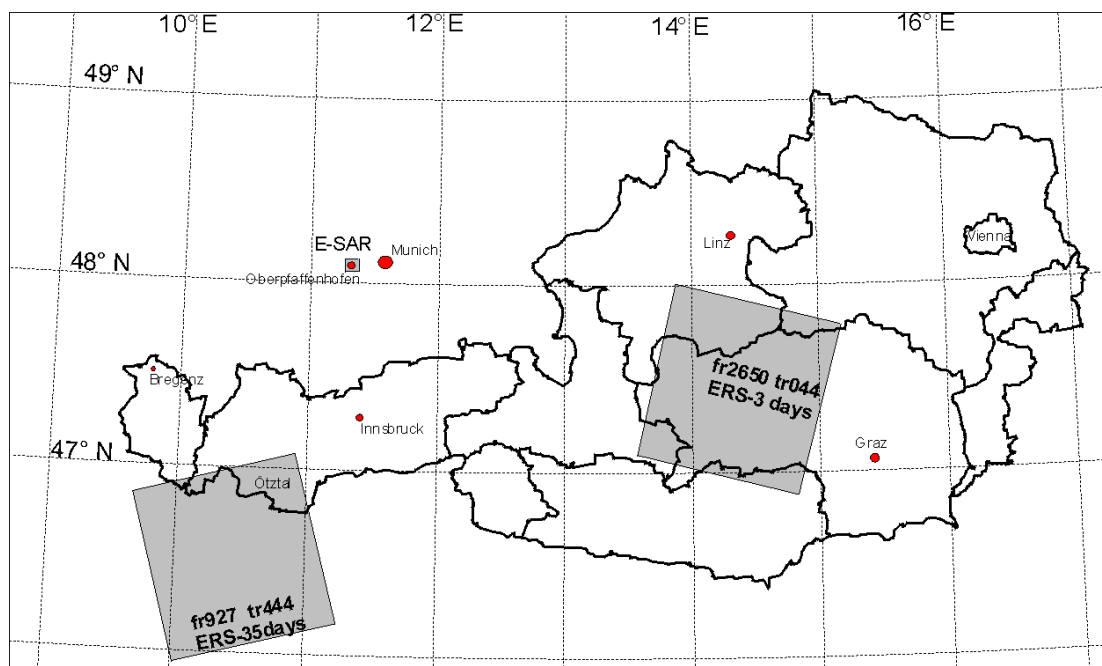


Figure B.4.3: Sketch map showing the location of data sets.

#### B.4.2.1 Analysis of ERS SAR 3-days repeat pass images

ERS SAR images of frame 2650, track 244 with a repeat cycle of 3 days, which were acquired during Phase D, are the basis for this analysis. The frame is located in Eastern Austria (Figure B.4.4), a mountainous regions with an elevation range between 400 m and 2700 m. The slopes are covered by forests and cultivated meadows up to about 2000 m elevation, above the tree line low alpine vegetation, bare soil and rocks are dominating.

About 50 meteorological stations, some of which equipped with automatic registration, provide hourly to daily measurements of meteorological parameters including air temperature, precipitation, total snow height and depth of fresh snow. Figure B.4.4 shows the location of the stations. Although the station network is well developed, most of them are located at lower elevations in the valleys, while only a few stations are situated at altitudes above 1500 m.

A time series of eight consecutive ERS SAR images acquired between 25 January 1994 and 18 February 2003 is used to investigate effects of fresh snow on coherence and to study capabilities for retrieving SWE by means of the interferometric phase. Figure B.4.5 shows the dates of ERS acquisitions used within this study together with meteorological records of temperature and snow height at the station Krippenstein (2005m). Based on the meteorological records two images pairs, which are affected by dry snow fall (25-31 January 1994, 9-12 February 1994) and two image pairs without or with negligible precipitation (3-6 February, 15-18 February) were selected. The images acquired in March 1994 were already available at DLR-IMF previous to the study, but because of warm temperatures and snowmelt they are not suitable for SWE retrieval. Table B.4.1 gives an overview of characteristics of these image pairs and summarizes qualitatively the occurrence of precipitation within the corresponding period.



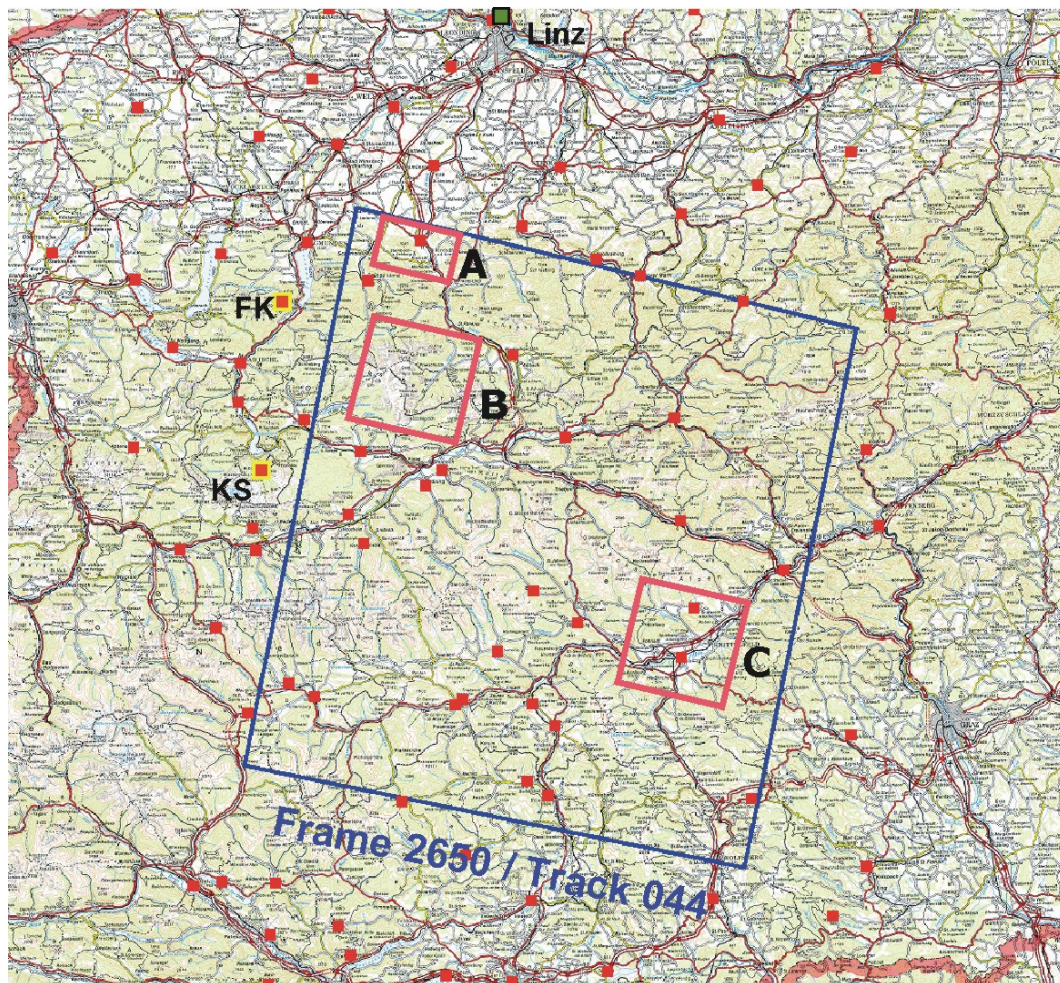


Figure B.4.4: Coverage of ERS SAR Phase D, frame 2650, track 044. Pink rectangles show the areas which were analysed in detail, (A) Sonnseite, (B) Totes Gebirge, (C) Zeltweg-Seckau. Red points correspond to the locations of meteorological and automatic climate stations. The radiosonde station Linz is shown as a green point. Mountain stations are Feuerkogel (FK), 1618m, and Krippenstein (KS), 2005 m.

Figure B.4.6 to Figure B.4.8 show interferograms of the full frame covering the periods with snow fall (25 – 31 January 1994, Figure B.4.6, 9-12 February 1994, Figure B.4.8) and without snow fall (3-6 February 1994, Figure B.4.7). In most areas with significant changes of the snow height the coherence is very low and no fringes are visible (Figure B.4.6, Figure B.4.8). In areas without or with little snow fall the coherence is sufficient for InSAR processing, as it is obvious in Figure B.4.7. In order to test the SWE retrieval algorithm three areas (A, B, and C) were selected for detailed analysis (Figure B.4.6).

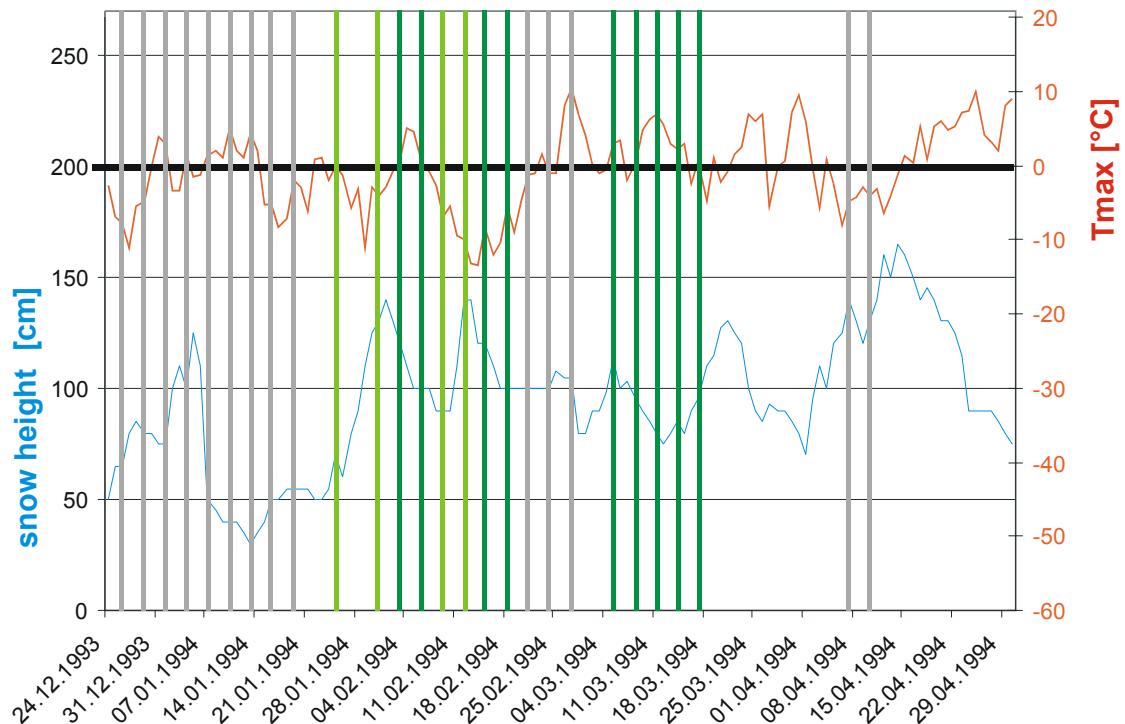


Figure B.4.5: Time series of snow height and daily maximum air temperature measured at the station Krippenstein (2005 m, see Figure B.4.4) from 24 December 1993 to 30 April 1994. Vertical bars indicate days with ERS SAR data acquisitions, available images are shown in green colour, grey bars indicate images not available at ENVEO.

Table B.4.1:

Perpendicular baseline and information on precipitation for interferometric pairs of repeat pass ERS scenes in the investigation period 25 January to 18 February 1994. ( $B_{\text{per}}$  ... perpendicular baseline).

<i>Date-1</i>	<i>Date-2</i>	<i>B<sub>per</sub></i>	<i>Period</i>	<i>Precipitation (qualitatively)</i>
25Jan94	31Jan94	42 m	6 days	snow fall / rain
31Jan94	3Feb94	-87 m	3 days	insignificant snowfall
3Feb94	6Feb94	-53 m	3 days	no precipitation
6Feb94	9Feb94	78 m	3 days	no precipitation
9Feb94	12Feb94	-122 m	3 days	snowfall
12Feb94	15Feb94	-57 m	3days	light snowfall
9Feb94	15Feb96	-179 m	6days	Snowfall
15Feb94	18Feb94	77 m	3days	no precipitation



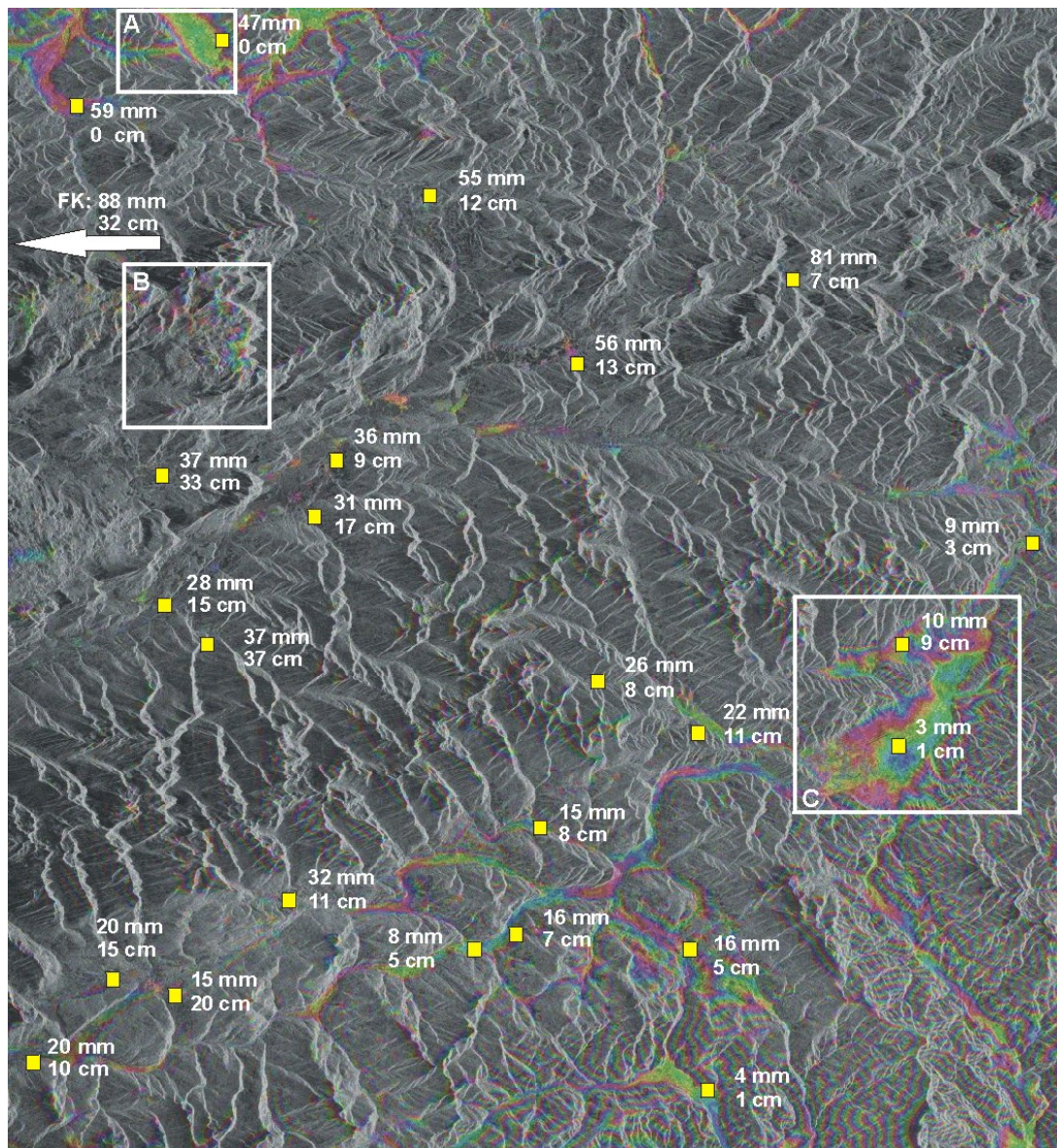
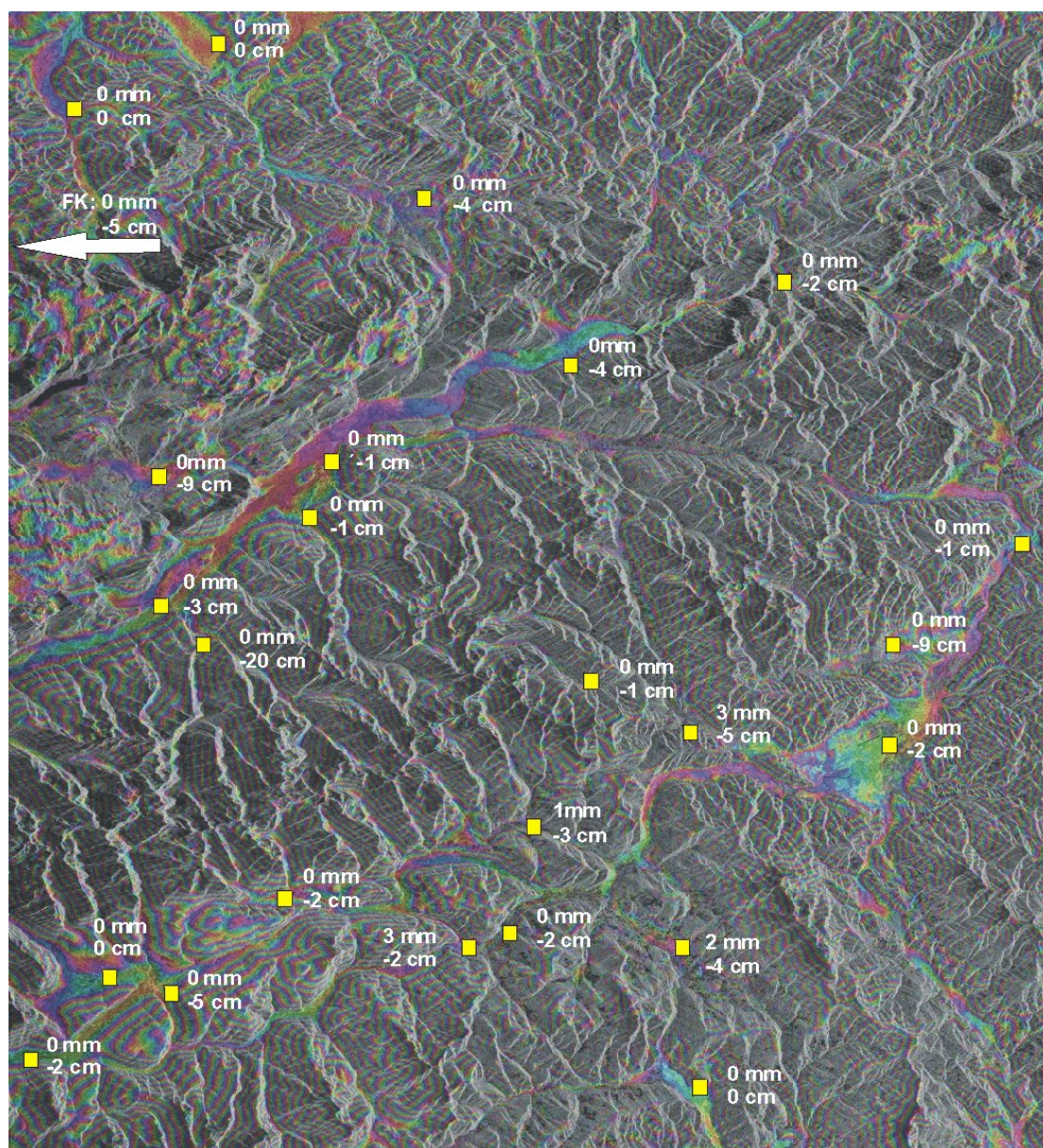


Figure B.4.6: Interferogram of 25 – 31 January 1994. Yellow squares represent meteorological stations. At each station two numbers are given, the upper number correspond to accumulated precipitation in mm and the lower number to the change of snow height in cm in the time period between image acquisitions. FK, station Feuerkogel (1618m, for location of this station see Figure B.4.4). A ... test area Sonnseite, B ... test area Totes Gebirge, C ... test area Zeltweg – Seckau.







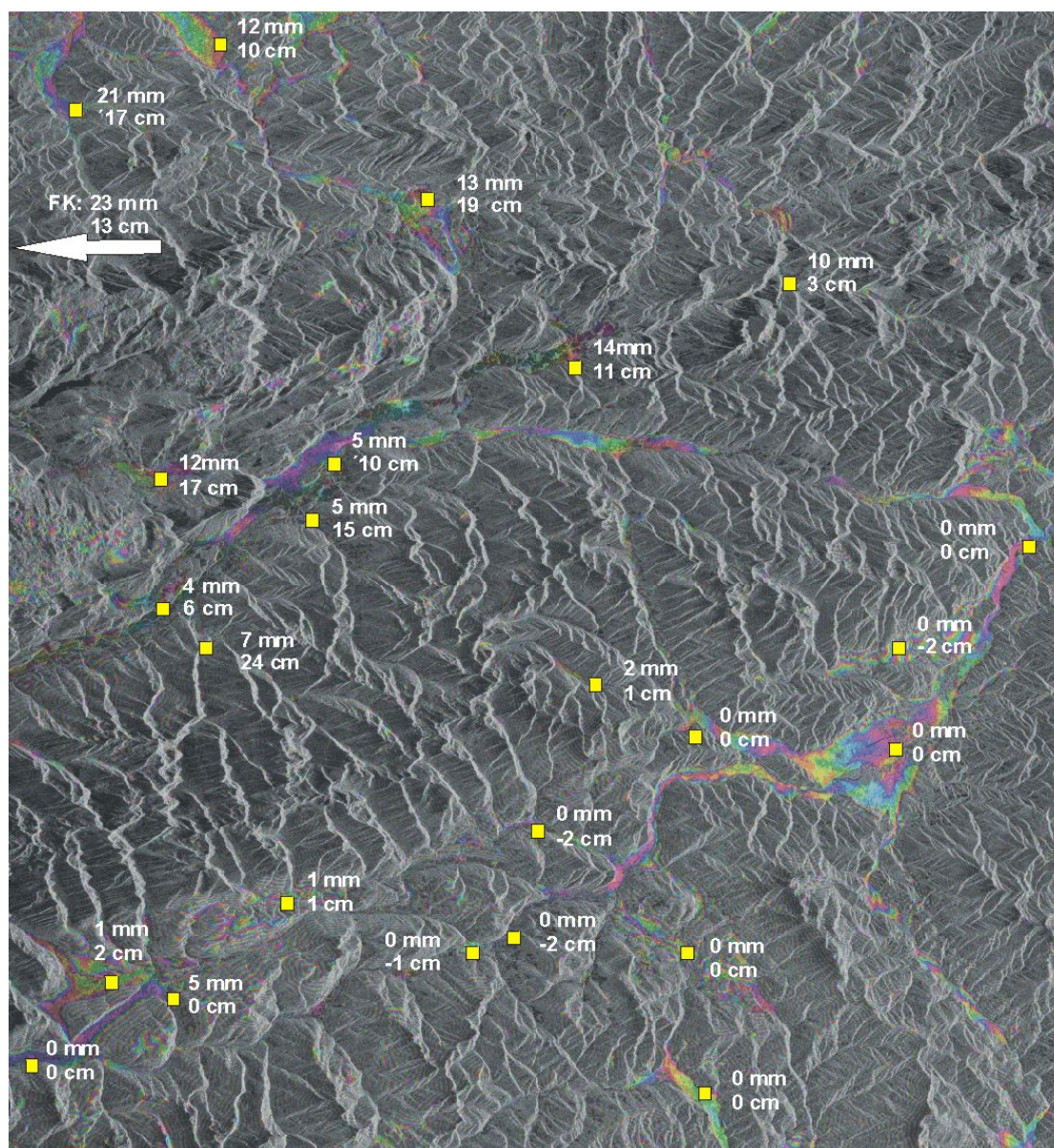


Figure B.4.8: As Figure B.4.6, but for 9-12 February 1994.

#### **B.4.2.1.1 Test area A: Sonnseite**

Figure B.4.9 (a) shows a map of the test area Sonnseite, which is a slope of about 350 m elevation difference ranging from 680 m to 913 m and Figure B.4.9 (b) a multitemporal amplitude image of the test area. To characterise the meteorological conditions within the investigation period two stations are available, the station Kirchdorf / Krems at 450 m elevation and, at high elevations, the station Feuerkogel, which is located about 16 km to the west-south-west of the test area at 1618 m elevation (Figure B.4.4).



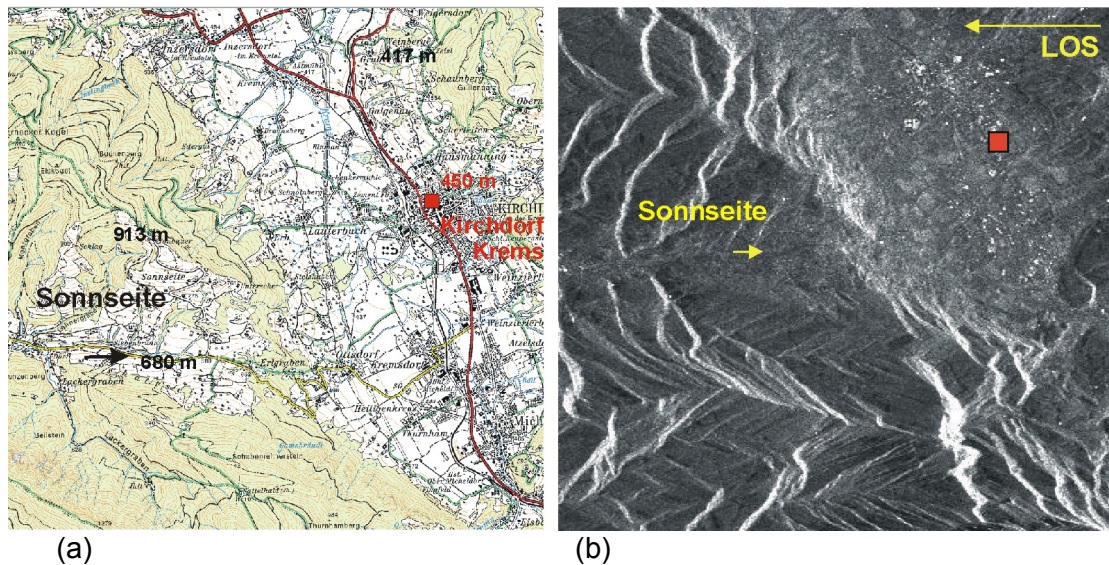


Figure B.4.9: (a) Topographic map of the test area Sonnseite, (b) multitemporal amplitude image in slant range projection, the red square shows the location of the meteorological station Kirchdorf – Krems (450 m elevation); the arrow the valley floor below the slope Sonnseite.

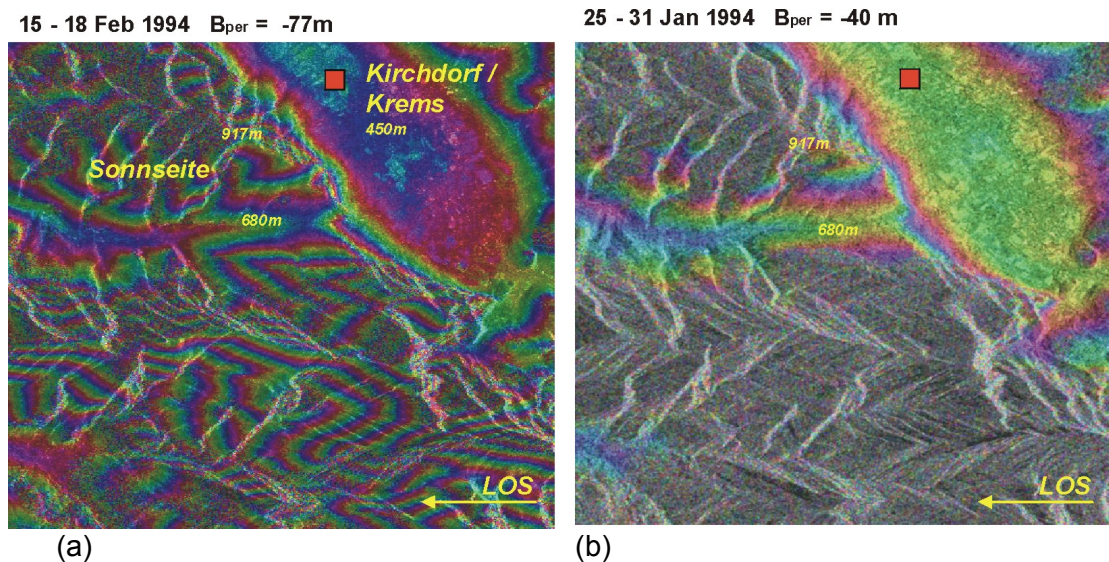


Figure B.4.10: Interferograms in slant range geometry of the test area Sonnseite. (a) 15 - 18 February 1994, without snow fall, (b) 25-31 January 1994, with snow fall.

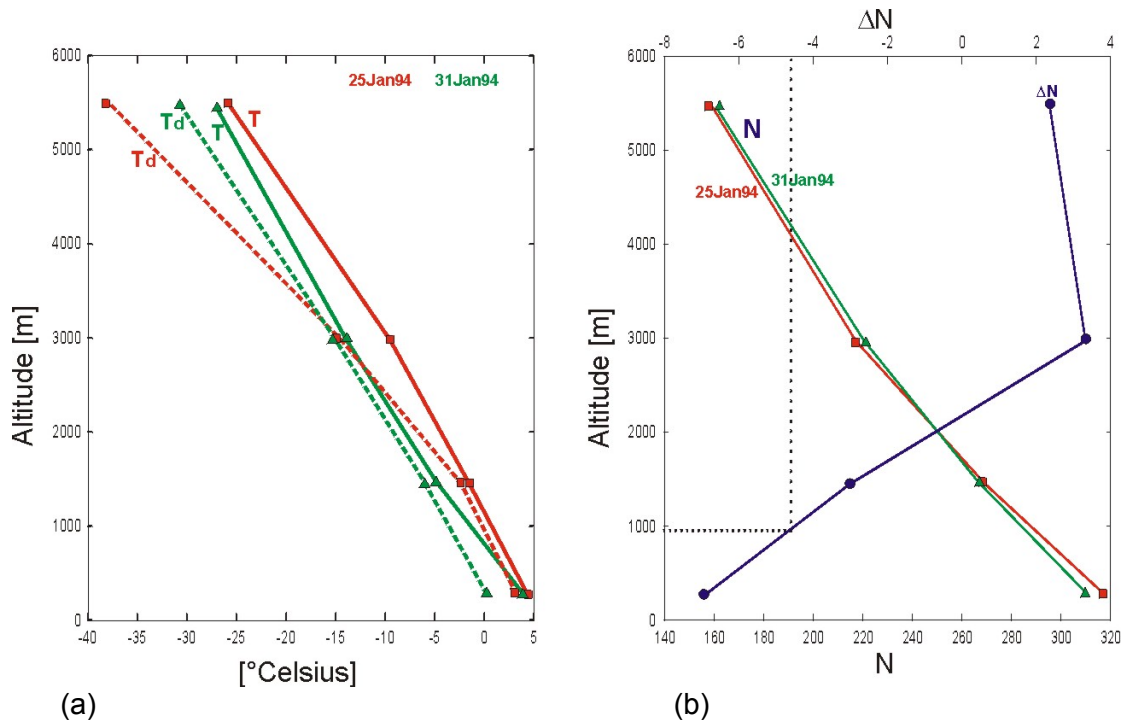


Figure B.4.11: (a) Radiosonde measurements of temperature (T) and dew point (Td) at station Linz, 25 and 31 January 1994, 6:00 UTC. (b) corresponding vertical profiles of refraction index N and the of  $\Delta N = (N_{31Jan1994} - N_{25Jan1994})$ .

The influence of atmospheric variations on the interferometric phase was estimated using the radiosonde measurements of the station Linz. Figure B.4.11 (a) shows the radiosonde measurements of the station Linz, at 6:00 UTC (about 4 h before the satellite overflight) indicating different atmospheric conditions during the image acquisitions. Along the Sonnseite slope with an elevation range of about 400 m (from about 600 m at bottom to about 1000 m at the top) the mean value of  $\Delta N$  is about  $-5$  (Figure B.4.11 b). This corresponds to  $\Delta\phi_{atm} = -0.47$  rad. The atmospheric influence on the 9-12 February image pair (see Figure B.3.13 and Figure B.3.14) shows a similar mean  $\Delta N$  of about  $-4$  for the elevation range 600m to 1000m. In each of the two cases the atmospheric influence is less than  $-0.27$  cm in terms of SWE (assuming  $23^\circ$  incidence angle), which is of little relevance for SWE retrieval.

The topographic phase was estimated using the image pair from 3-6 February 1994, where the coherence was good and which was not affected by snow fall. To check the quality of the topographic phase estimation, we formed the differential interferogram with the image pair from 15-18 February 1994, which was also not affected by snow fall. In the differential interferogram (Figure B.4.12) no significant phase trend is visible, which confirms the sufficient quality of the topographic phase estimation.



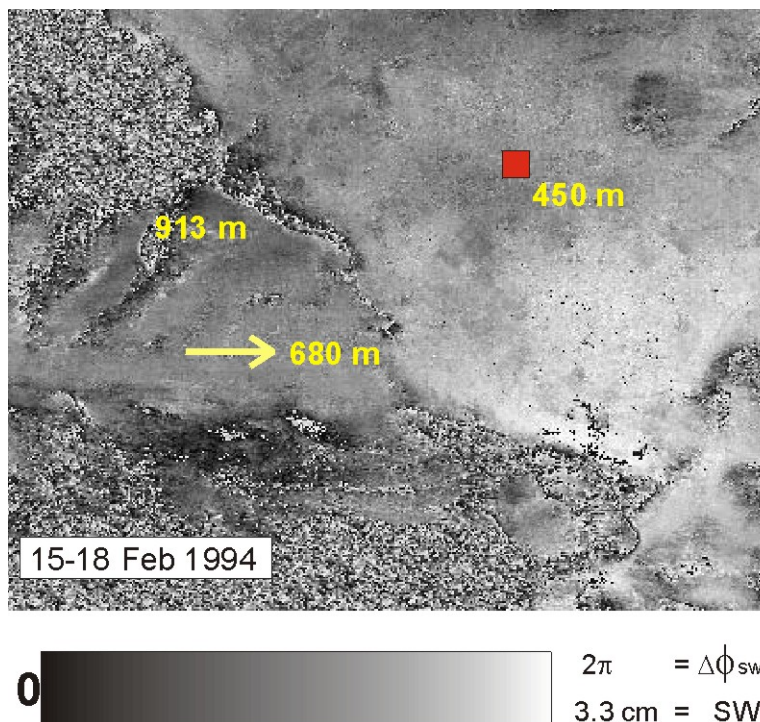


Figure B.4.12: Differential interferogram of 3-6 February and 15-18 February 1994. Both interferograms are not affected by snow fall.

Figure B.4.13a shows  $\phi_{swe}$  for the image pair 25-31 February 1994 after topographic phase removal. Within the time period 46.7 mm precipitation, predominately as rain, were measured at Kirchdorf / Krems at 450m, and no snow pack was formed. At high elevation the precipitation fell as snow, at Feuerkogel (1618m) 88.2 mm precipitation were measured and the snow depth increased from 60 cm to 92 cm. Therefore it can be concluded that in the upper part of the Sonnseite slope (elevations close to 1000 m) a snow pack was built up in this time period, but no observations are available at this site. According to Figure B.4.13a  $\phi_{swe}$  changed from  $-0.4$  rad to  $1.5$  rad from 680 m to 900 m elevation, which would correspond to a change of SWE of about 1 cm or an increase of the snow depth of 5 cm (assuming a density of  $0.2 \text{ g/cm}^3$ ) along the slope.

Figure B.4.13b shows  $\Delta\phi_{swe}$  of the image pair 9 – 12 February 1994. During this period 14 mm precipitation, mainly fallen as snow, were observed at Kirchdorf / Krems, where a snow pack of 10 cm was formed, while at Feuerkogel 23 mm precipitation and an increase of the snow height from 82 to 95 cm were measured. In the valley floor around Kirchdorf / Krems,  $\Delta\phi_{swe}$  shows small scale horizontal variations of up to 3 rad, which would corresponds to a variation of the fresh snow of 1.7 cm in terms of SWE (about 9 cm snow height assuming a density of  $0.2 \text{ g/cm}^3$ ). Due to missing *in-situ* snow measurements it cannot be verified that the observed phase variation is due to a change in SWE, and the small scale variation of  $\phi_{swe}$  may also be caused by other effects.

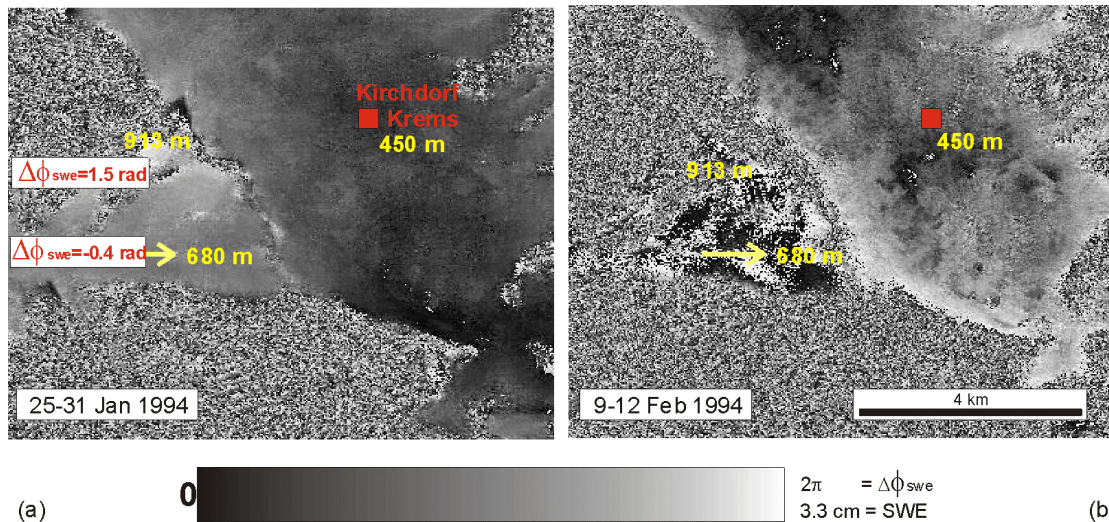


Figure B.4.13: Map of  $\phi_{SWE}$ , in slant range projection for the dates 25-31 January 1994 and 9-12 February 1994. The noise corresponds to areas of decorrelation (forested areas).

#### B.4.2.1.2 Test area B: Totes Gebirge

The test site Totes Gebirge covers an elevation range from about 700 m up to 2515 m at the peak Grosser Priel (Figure B.4.14). Above the forest line at about 2000m bare soils and rocks are the dominating surface classes.

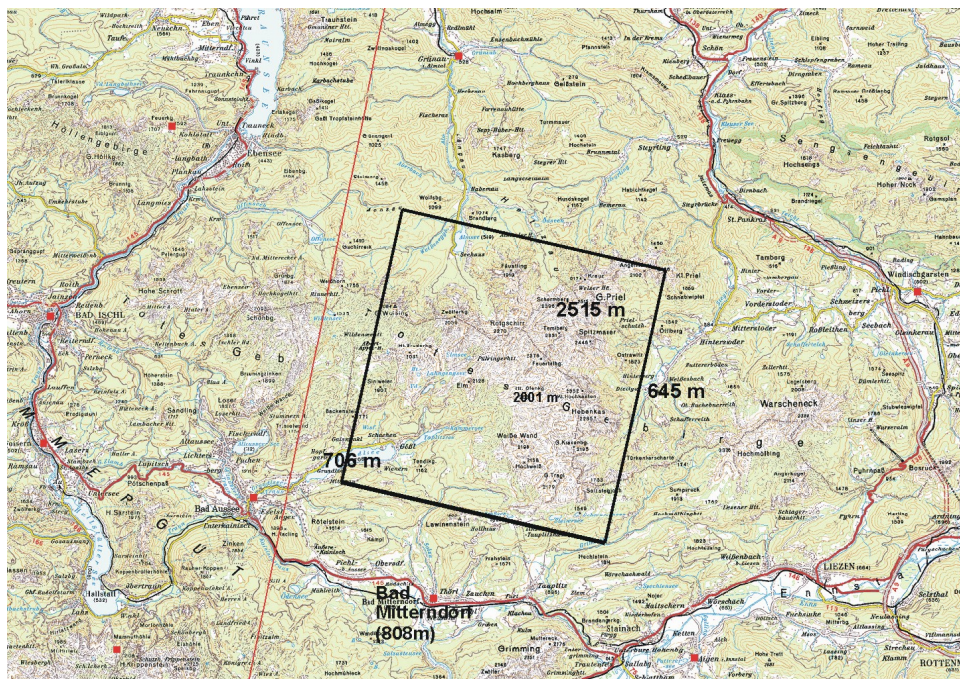


Figure B.4.14: Location of the test area Totes Gebirge. Red points indicate meteorological stations.



Several meteorological stations are located in the valleys close to the test area (red boxes in Figure B.4.14), but there are no observations available at the mountain plateau of the Totes Gebirge. As an example, Figure B.4.15 shows the records of precipitation, snow height and daily mean temperature record at Bad Mitterndorf, which is located at 808 m elevation in the south of the test area (Figure B.4.14). It should be noted that at higher elevations the increase of the snow pack was even higher; e.g. at Krippenstein (2005 m) the snow depth increased from 70 to 130 cm elevation in the period from 25 to 31 January (Figure B.4.4). This indicates a pronounced increase of precipitation with elevation. Based on the meteorological records four image pairs were selected to investigate the influence of snow fall on coherence:

- 25 - 31 January: 36.6 mm precipitation, 33 cm fresh snow at Mitterndorf
- 3 - 6 February: no snow fall or precipitation
- 9 - 12 February: 12.1 mm precipitation and 20 cm fresh snow were observed.
- 15-18 February: no snow fall or precipitation

Figure B.4.16 shows the coherence image of the test area for the selected image pairs. Image pairs not affected by precipitation (Figure B.4.16 b, d) show sufficient coherence, but if snow fall occurs the coherence is widely lost (Figure B.4.16 a, c). Figure B.4.17 shows as example two interferograms of the corresponding area. In the case of snow fall (Figure B.4.17 a) fringes could be detected only close to the mountain peaks, and the fringes a patchy structure, which does not allow unwrapping after applying the the topographic correction and does not enable the estimation of the SWE.

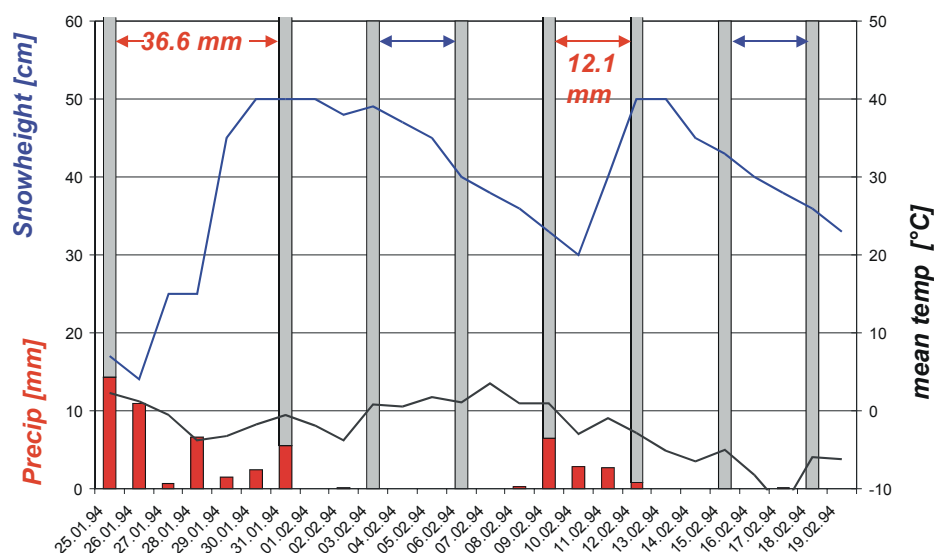


Figure B.4.15: Meteorological record of snow height, precipitation and daily mean temperature at station Bad Mitterndorf, 808m elevation. Grey bars indicate dates with ERS SAR image acquisitions.



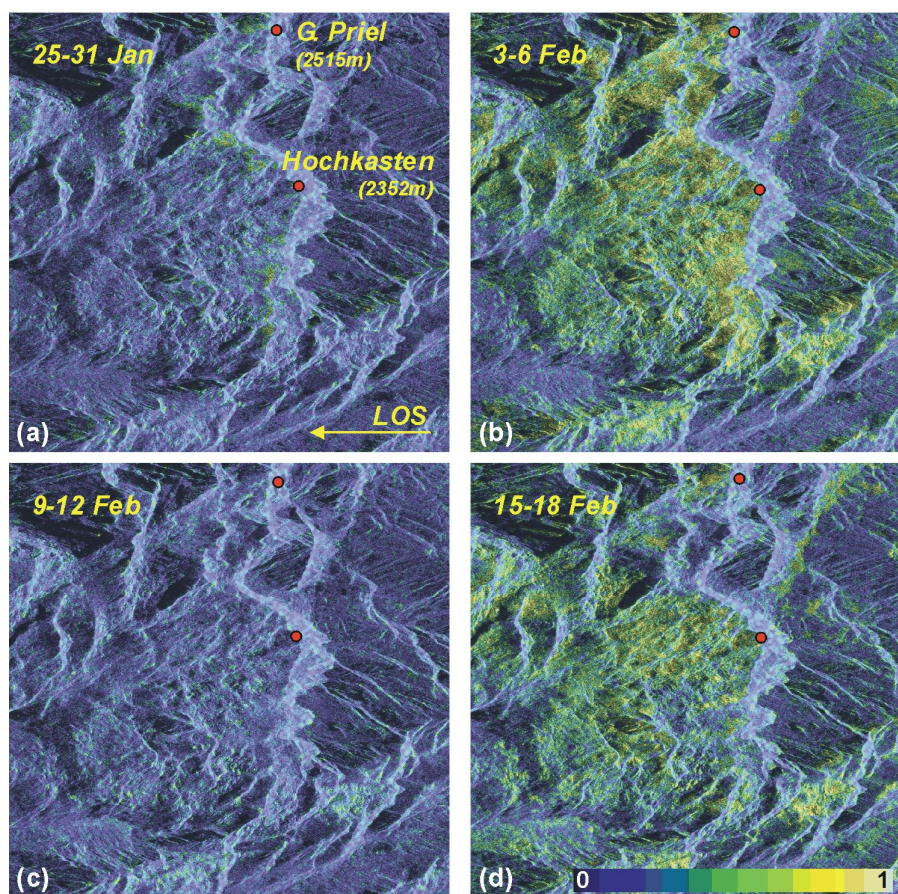
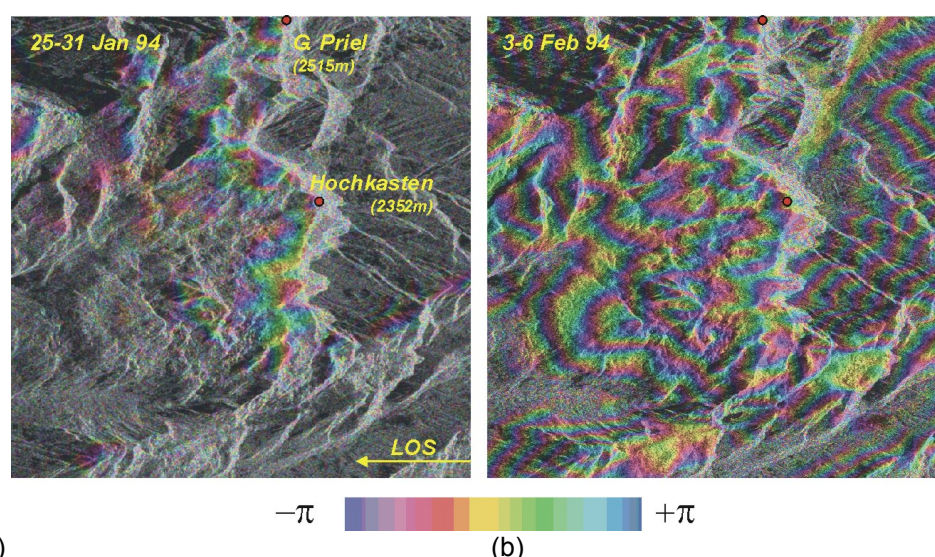


Figure B.4.16: Time series of coherence images in slant range geometry of the test area Totes Gebirge. (a) 25-31 January 1994 with snow fall; (b) 3-6 February 1994 without snow fall; (c) 9-12 February 1994 with snow fall; (d) 3-6 February 1994 without snow fall. (see also Figure B.4.15).



(a) (b)  
Figure B.4.17: Interferograms in slant range geometry for 2 time intervals, (a) 25-31 January 1994, with snow fall, (b) 3-6 February 1994, no precipitation observed.



**B.4.2.1.3 Test area C: Mur valley - Zeltweg**

The Mur valley at Zeltweg – Knittelfeld was selected as third test area within this frame. Figure B.4.18 shows a multitemporal amplitude image of this area. Precipitation and snow height measurements are available at Zeltweg (659 m) and Seckau (843 m). From 25 to 31 January 1994, 3 mm precipitation and 3 cm of new snow were recorded at Zeltweg, the snow depth increased only slightly from 11 cm on 25 January to 12 cm on 31 January. At Seckau, about 200 m above the Mur valley, 10 mm precipitation was recorded and the snow depth increased from 12 cm to 21 cm, at Oberzeiring 22 mm precipitation and an increase of the snow depth from 0 to 11 cm. The interferogram covering this period (Figure B.4.19b) shows sufficient coherence in the valley and lower parts of the slopes. For topographic phase removal the interferogram from the 15-18 February 1994 was used (Figure B.4.19a), which is not affected by snowfall and which shows good coherence for most areas. Based on the relation between  $\Delta\phi$  and  $SWE$ , a map of SWE accumulated in the period 25-31 January 1994 is calculated (Figure B.4.20). As reference point for the SWE map the precipitation value reported by the meteorological station Zeltweg was used. Within the urban area of Zeltweg SWE shows a value of about 0 mm (blue colour in Figure B.4.20). The green colour on the meadows and agricultural fields in the valley floor and near Seckau corresponds to SWE values of about 10 mm. Near the station Oberzeiring yellow to red colour tones corresponding up to about 20 mm SWE (or 10 cm snow depth assuming a snow density of  $0.2 \text{ g/cm}^3$ ) are shown. Though these values are plausible, they cannot be verified quantitatively, because of missing in-situ data at higher elevations.

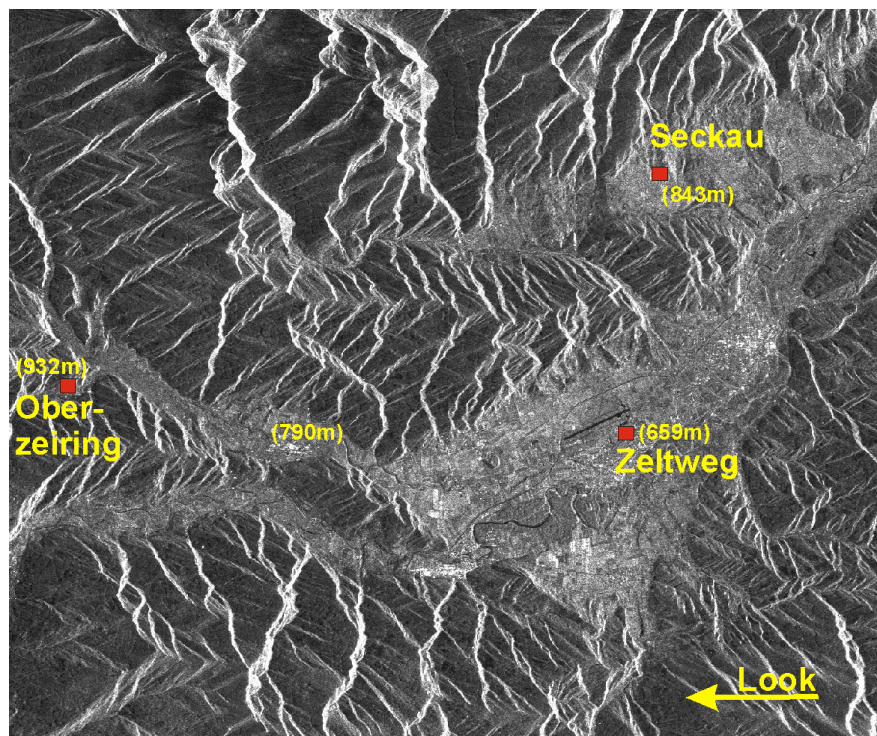


Figure B.4.18: Multitemporal amplitude image of the Mur-valley, red boxes show locations of the meteorological stations Zeltweg, Oberzeiring and Seckau.



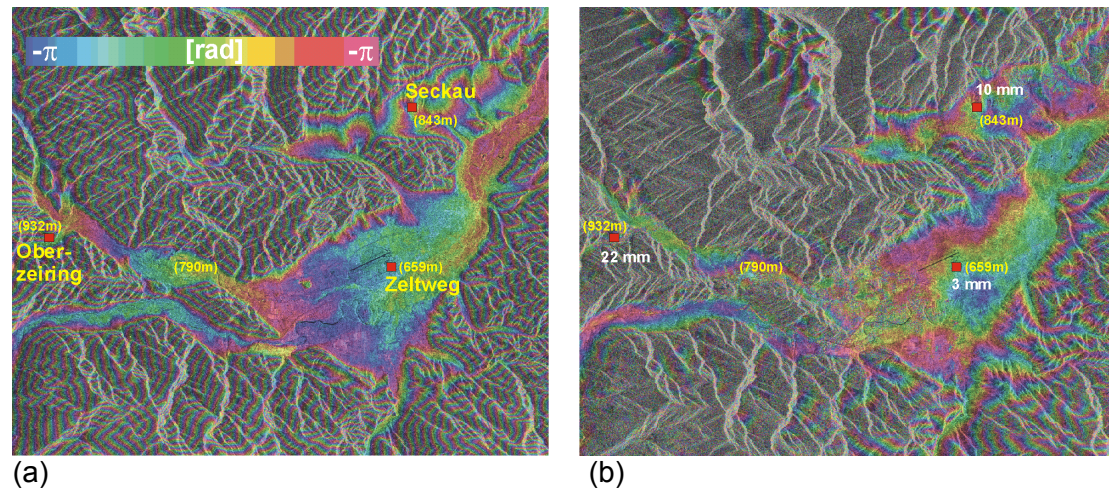


Figure B.4.19: Interferograms of the Mur-valley; (a) 15-18 February 1994, perpendicular baseline 77 m, no snow fall; (b) 25-31 January 1994, perpendicular baseline 42 m, white numbers give the accumulated precipitation at Zeltweg, Oberzeiring and Seckau.

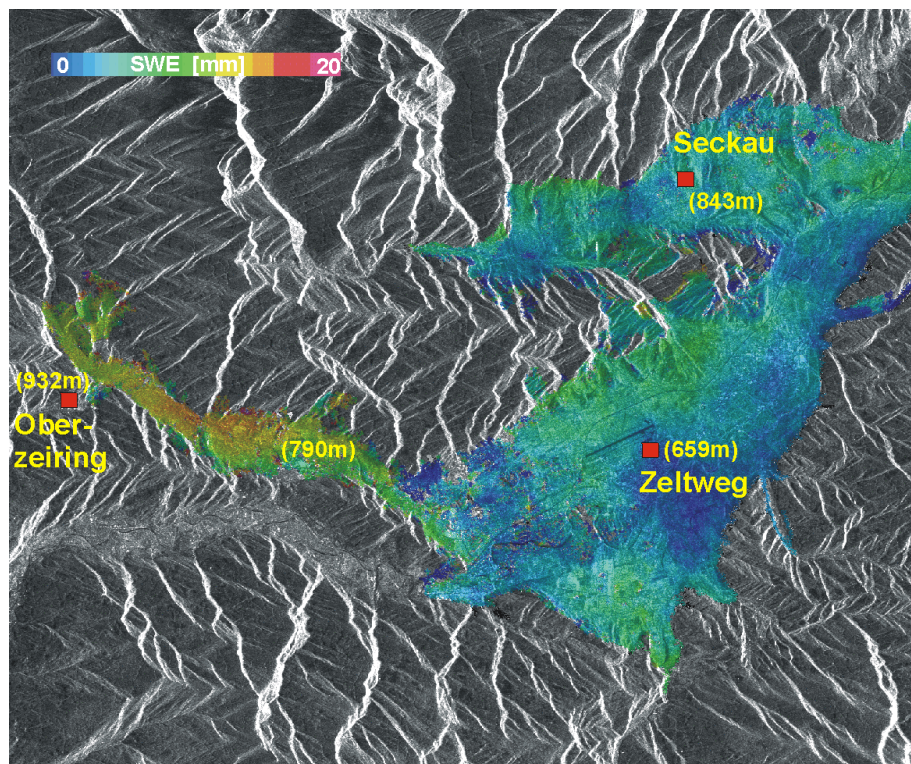


Figure B.4.20: Estimation of change of SWE from 25 to 31 January 1995, derived from Figure B.4.19b; as reference the station Zeltweg was used.



### B.4.2.2 Analysis of ERS SAR Tandem data of a high alpine area

A data set of 4 ERS SAR Tandem pairs (frame 927, track 444, ascending pass, acquisition time 21:27 UTC) covering the Ötztal, Austria, acquired during the winter season 1995 / 1996 is the basis for this analysis (Table B.4.2). It enables the investigation of the effect of snow drift on the coherence and the retrieval of SWE.

Figure B.4.21 shows four ERS SAR Tandem coherence images from December 1995 to March 1996 of the high alpine area in southern Ötztal, with the glacier plateau of Gepatschferner / Kesselwandferner. The image 14-15 February 1996 shows the best coherence over almost the whole area. The image pair 6-7 December 1995 shows poor coherence, which can be attributed to strong southerly winds (Föhn) according to the meteorological record of station Obergurgl (1938m). The wind increased during 6 December and caused snow drift and redistribution of snow. On large parts of the glacier plateau of Gepatschferner and the upper part of the Kesselwandferner no fringes can be produced (Figure B.4.22).

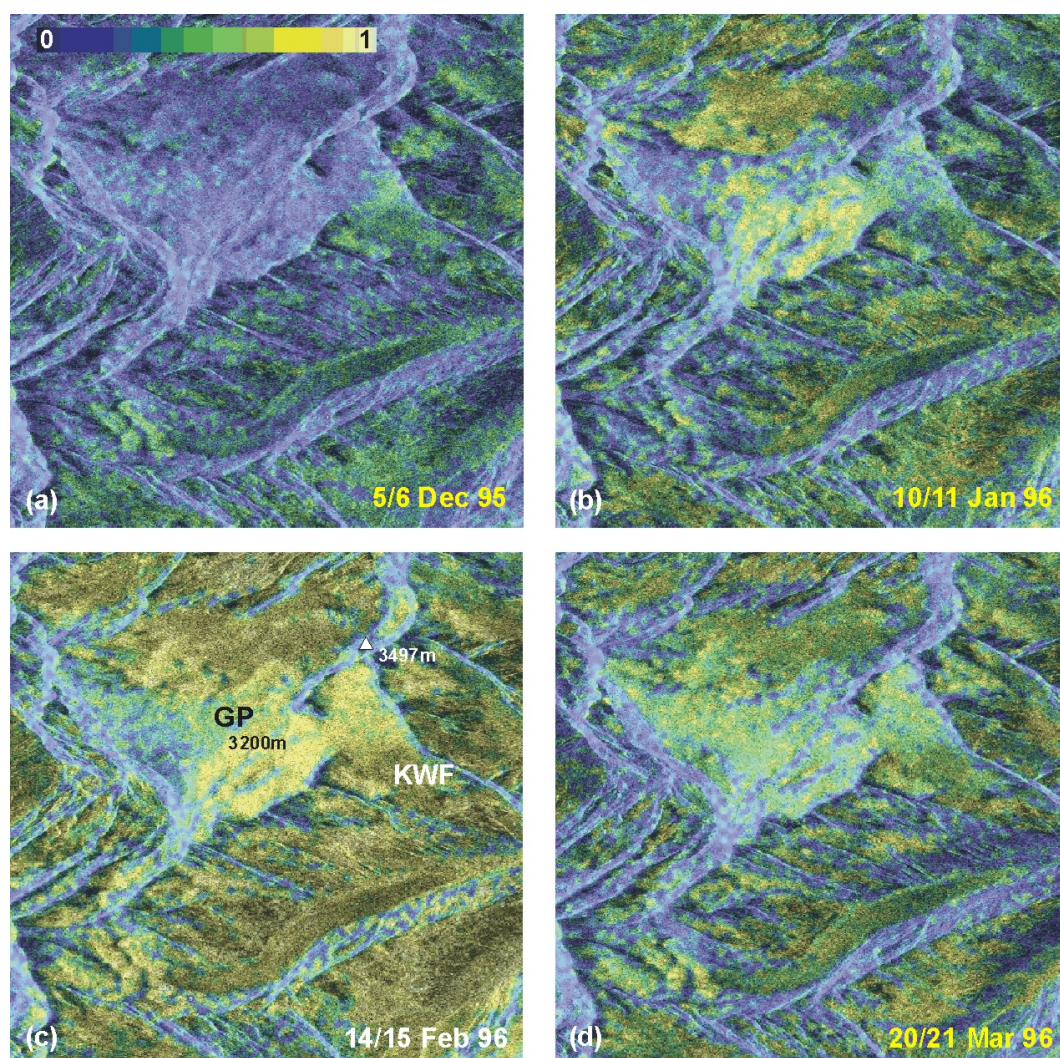


Figure B.4.21: Coherence images of ERS SAR Tandem data, frame 927, track 444. GP – Gepatschferner, KWF...Kesselwandferner.



Table B.4.2:  
List of ERS SAR Tandem data, frame 927, track 444, ascending pass.

<i>Acquisition Date</i>	<i>Perpendicular Baseline</i>
6 / 7 December 1995	210 m
10 / 11 January 1996	160 m
14 / 15 February 1996	135 m
20 / 21 March 1996	293 m

As test area for studying possible changes of SWE the upper part of the Kesselwandferner was selected, where the glacier is flat. For glaciated areas the ice motion has to be taken into account, but in the upper part of the glacier the motion (which is about 2 cm/day) is approximately along track and does not contribute to the interferometric phase. The differential analysis for the 5/6 December pair did not reveal any clear trend for differential phase change attributable to changes of SWE. This is not surprising, as redistribution of snow due to wind usually takes place at small spatial scale so that clear phase trends at larger scales (hundreds of metres to kilometres) are rather unlikely. In addition, the interferometric analysis was affected by the comparatively low coherence.

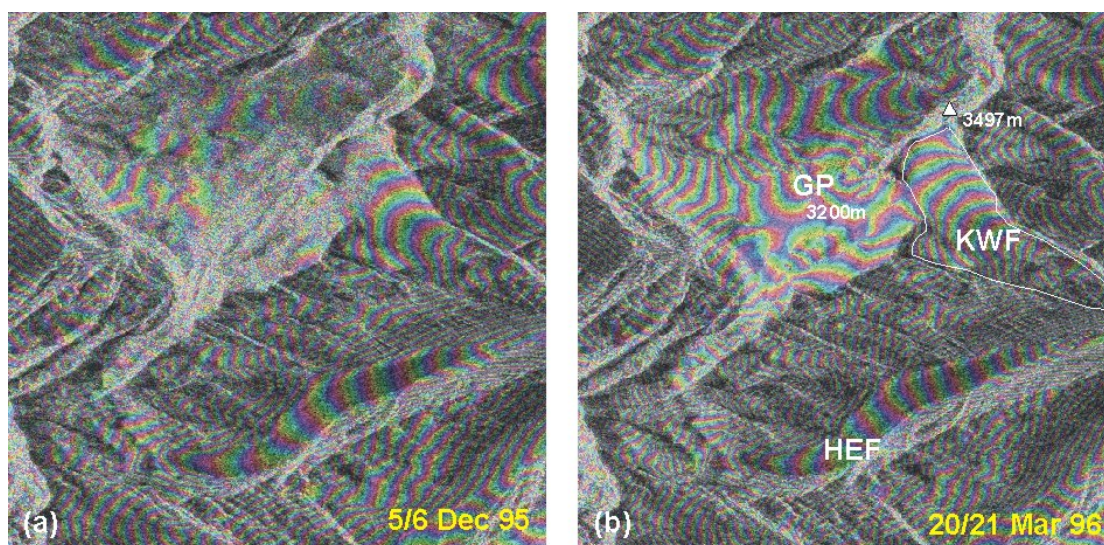


Figure B.4.22: Interferograms ERS SAR Tandem data (see Table B.4.2). The white polygon is the boundary of Kesselwandferner.

#### **B.4.2.3 Airborne E-SAR L-band data of Test area Oberpfaffenhofen (InSAR processing by R. Scheiber, DLR-HF)**

This investigation is based on a data set of repeat pass images of the airborne SAR system E-SAR of DLR operating at L-Band (1.3 GHz) in fully polarimetric mode which were acquired for vegetation studies. Table B.4.3 summarizes the parameters of the E-SAR system for this data set. The investigation area is the campus of DLR including the local airport (Figure B.4.23), where in two sub-areas 9 corner reflectors

are permanently mounted. The corner reflectors are used for E-SAR calibration flights and therefore the snow accumulated inside of the trihedral reflectors had been removed before the image acquisition. Two of the images were acquired within several minutes on 22 October 2002 when the site was snow free. The third data take was acquired on 20 February 2003, when the ground was fully covered by dry snow. The processing and interferometric product generation and corner reflector analysis was done by Rolf Scheiber and A. Misra (DLR-HF).

Table B.4.3:  
E-SAR system parameters used for image acquisitions at Oberpfaffenhofen  
on 22 October 2002, and 20 February 2003.

<i>Parameter</i>	<i>Value</i>
Frequency	L band ( 1.3GHz)
Wavelength	23.0544 cm
Pulse bandwidth	100 MHz
Chirp duration	5 $\mu$ sec
Sampling rate	100 MHz
PRF	400 Hz
Mode Of Operation	Repeat Pass
Velocity	96.0 m/s
Flight Altitude	3022.31 m
Polarization	Quad Pol (HH,VV,HV,VH)

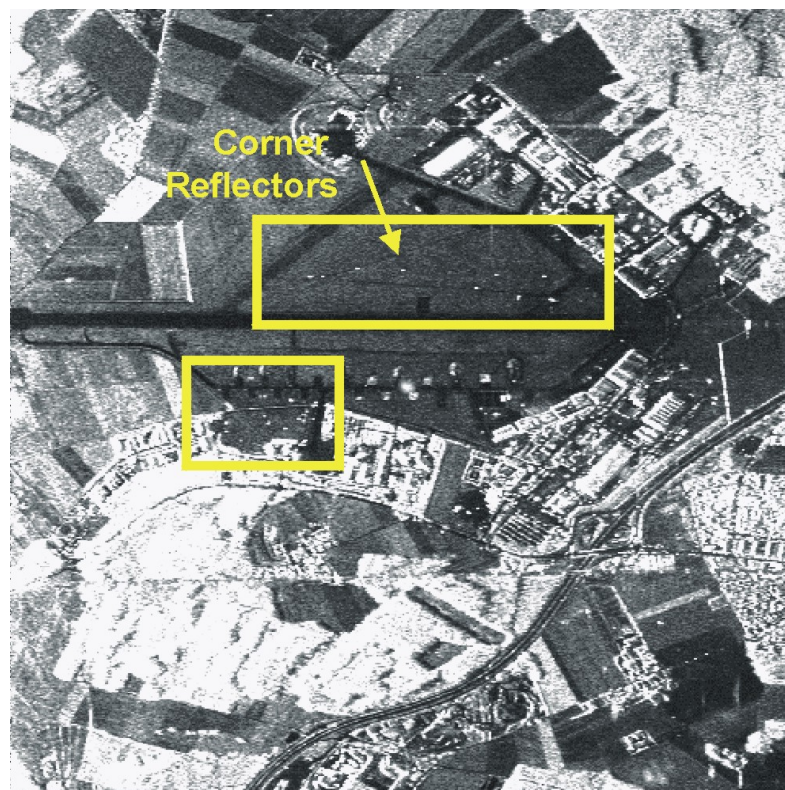


Figure B.4.23: Amplitude image of the test area Oberpfaffenhofen, yellow boxes indicate the areas with corner reflectors.



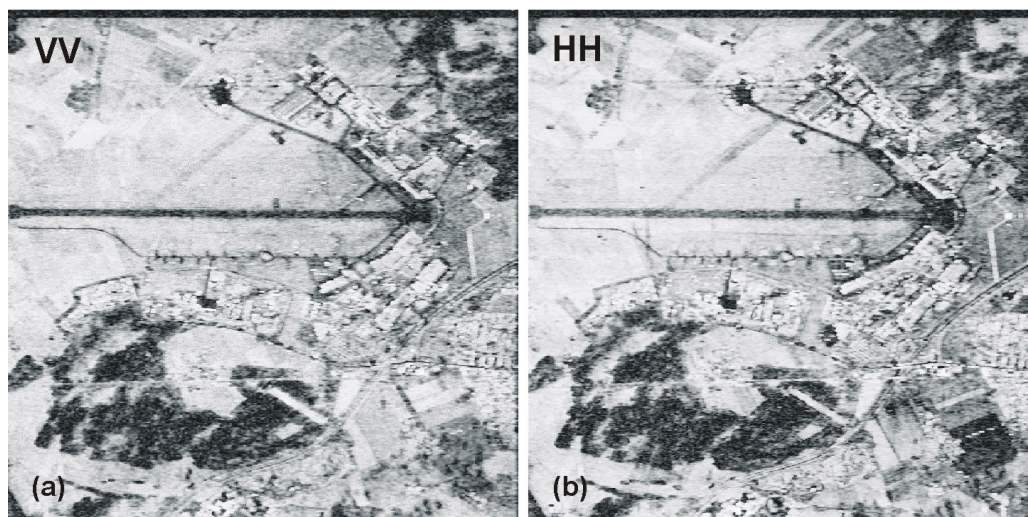


Figure B.4.24: Coherence images at (a) VV and (b) HH polarisation, of the image pair acquired on 22 October 2002 within half an hour time interval.

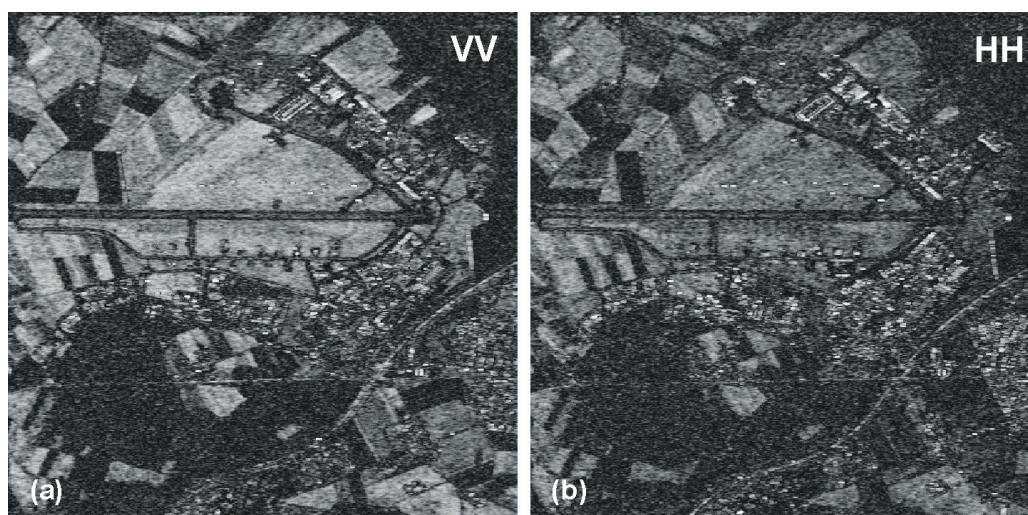


Figure B.4.25: Coherence images at (a) VV and (b) HH polarisation, of the repeat pass image pair acquired on 22 October 2002 and 20 February 2003.

Figure B.4.24 shows the coherence image at VV and HH polarisation of the image pair acquired on 22 October 2002. The data show high coherence at VV and HH polarisation, and the decorrelation is small except in forested areas.

The coherence images of the autumn/winter image pair from 22 October 2002 (snowfree) and 20 February 2003 (ground was covered by dry snow) are shown in Figure B.4.25. According to observations at adjacent meteorological stations the snow depth was between 10 to 20 cm in this region (Figure B.4.27). Compared to the on-day snow free interferogram (Figure B.4.24) the coherence is significantly lower at both polarisations. The decorrelation is probably mainly an effect of changes of the surface due to farming activities in autumn (agricultural fields), changes in the vegetation canopy, and changes of soil backscattering properties. The presence of the dry snow cover probably has only a small effect on coherence (section B.3.3).



Furthermore it should be noted that, as evident in Figure B.4.24 a and b, the correlation is slightly higher at VV than at HH polarisation.

To quantify the influence of the dry snow pack on the interferometric phase and estimate the snow water equivalent, the snow free corner reflectors were taken as stable reference points in respect to the surrounding areas. This enables the estimation of the influence of the snow pack on the phase as well as testing the SWE retrieval algorithm. Figure B.4.26 shows a detailed view of the area around the corner reflectors in the two interferograms. In the interferogram from 22 October 2002/20 February 2003, the snow free corner reflectors and roads show a consistent phase shift in respect to the surrounding snow covered meadows, while this interferometric phase shift is not visible in the interferogram of the image pair of 22/22 October 2002. Table B.4.4 lists the differential one way slant range distance for each of the corner reflectors, which is similar for HH and VV polarisation. The mean differential one way distance is 4.2 cm, which corresponds to an interferometric phase difference of  $\Delta\phi_{\text{SWE}} = -2.3$  rad. Using Equ. (B.4.1) and assuming a local incidence angle of 40 degrees it corresponds to a snow water equivalent of 4.3 cm, which corresponds to a snow height of 14 cm, 17cm and 21 cm for snow densities of 0.30, 0.25 and 0.20 g/cm<sup>3</sup>. As shown in Figure B.4.27 the InSAR based SWE agrees quite well with snow height measurements at neighbouring stations.

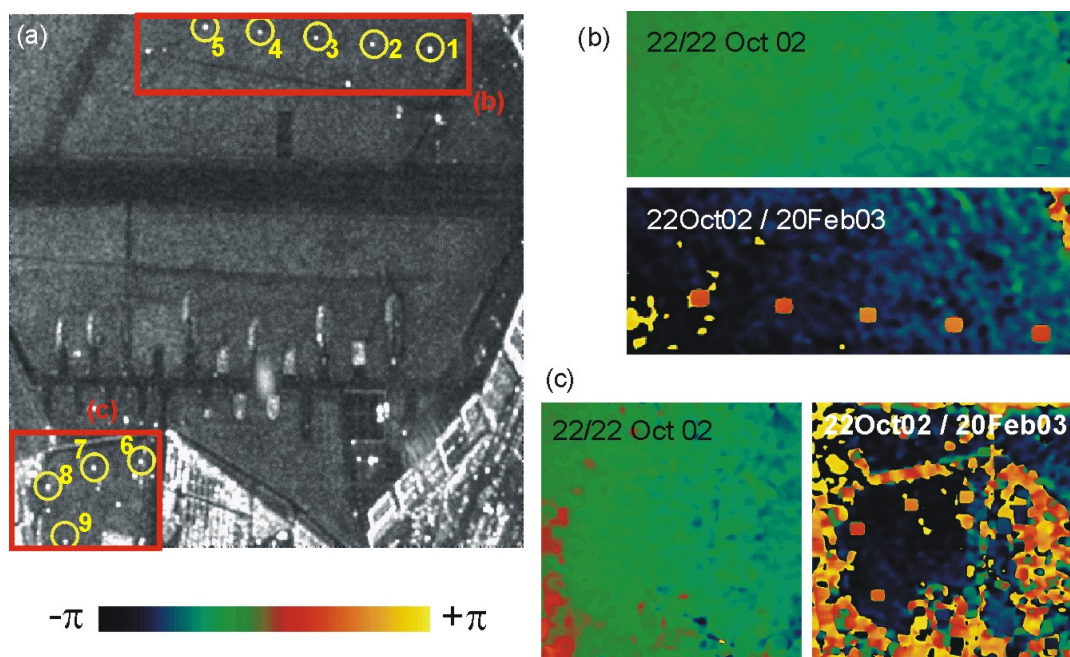


Figure B.4.26: (a) Amplitude image of the airport at Oberpfaffenhofen, yellow circles mark the corner reflectors. (b) and (c) Detailed view of the interferograms, VV Polarisation, of the image pair 22/22 October 2002 and 22 October 2002/20 February 2003. In the 22 October/ 20 February interferogram phase shifts are observed for the corner reflectors.

Table B.4.4:  
Summary of the differential one way slant range displacement between  
corner reflectors and meadows for the interferogram October 2002/ February  
2003, for VV and HH polarisation.

	<i>Differential displacement (VV Polarisation)</i>	<i>Differential displacement (HH Polarisation)</i>
CR-1	-0.05631 m	-0.05337m
CR-2	-0.03989 m	-0.04874 m
CR-3	-0.03976 m	-0.04661 m
CR-4	-0.04696 m	-0.04051 m
CR-5	-0.04357 m	-0.04348 m
CR-6	-0.03317m	-0.03202 m
CR-7	-0.03652m	-0.03618 m
CR-8	-0.04579 m	-0.04854 m
CR-9	-0.03641 m	-0.03480 m
<i>MEAN</i>	<i>-0.0426 m</i>	<i>-0.0420 m</i>
<i>Standard deviation</i>	<i>0.0072 m</i>	<i>0.0070 m</i>



Figure B.4.27: Sketch of locations of snow measurements on 20 February 2003. Numbers in green are ground observation, while the snow height retrieved from the corner reflector analysis of the E-SAR October 2003 / February 2003 image pair is shown in red. (assuming a snow density of  $0.25 \text{ g/cm}^3$ ).

### **B.4.3 Conclusions from test cases**

Based on an ERS 3-day repeat pass time series 3 test areas were analysed in detail. In the test area A (Sonnseite, section B.4.2.1.1) and C (Mur valley - Zeltweg, section B.4.2.1.3) the derived SWE map shows plausible values, but due to the relatively low density of the in-situ snow measurements compared to the spatial SWE variation they could not be verified quantitatively. In Test area C (Totes Gebirge, section B.4.2.1.3), a high mountain plateau with more snowfall than test area A and C, the influence of snow fall on the coherence is shown. In this case the signal decorrelated almost completely in periods with snow fall so that SWE retrieval was not possible. In the high Alpine test site Ötztal (section B.4.2.2) the coherence of ERS Tandem data was analysed to study effects of snow drift and wind erosion. Repeat pass airborne L-Band SAR data acquired by ESAR of DLR at the campus at Oberpfaffenhofen enabled the study of interferometric phase shifts in a snow pack. The coherence of a snow free and snow covered image acquired within 4 months was sufficient for interferometric analysis. This test case shows the high potential of the SWE retrieval by means of L-band InSAR.

From the analysis of the test cases the following conclusions are made:

- The differential interferometric phase shift of repeat pass SAR data provides a physically based measure for mapping the spatial distribution of SWE.
- The analysis of 3-day ERS repeat pass images with snowfall by means of InSAR processing in various Alpine test areas revealed patterns of differential phase shifts which agree with the trend of SWE accumulation inferred from a few field stations. Though the InSAR-retrieved SWE patterns are plausible, quantitative validation was not possible because the spatial density of the regular snow measurement network is not sufficient for verification, because the spatial variation of SWE and snow depths is very high.
- Temporal decorrelation due to differential phase delays at sub-pixels scale during snow fall and wind drift is the main limiting factor for InSAR processing of repeat pass images to retrieve the SWE. In case of substantial snow fall C-Band coherence is often very low and InSAR analysis is possible only over limited parts of the snowfall areas, even over time spans of one or a few days (ERS SAR Tandem data, ERS-1 Phase D 3-days repeat cycle). L-band is less sensitive to temporal decorrelation as suggested by theory and the analysis of the airborne data set, but a large scale analysis of L-band data is still missing.
- The atmospheric phase variation under winter conditions is typically of the order of a few mm (in terms of SWE) and can be neglected for snow hydrology applications.
- L-band is preferable for interferometric SWE retrievals because of better coherence and larger measurement range ( $2\pi$  ambiguity) than shorter wavelengths. This is particularly suitable for alpine snow packs with typical values of SWE of several hundreds millimetres.
- Dedicated experiments with detailed co-located field measurements of snow depth and SWE are needed to fully assess and verify the InSAR capability for SWE mapping.

## **B.5 CONCLUSIONS AND OUTLOOK FOR SWE RETRIEVAL BY INSAR**

The mass of snow on ground (the snow water equivalent, SWE) is a very important parameter for hydrology and water management of mountain areas and high latitude basins and for climate monitoring. Because of the high spatial variability of SWE, satellite-borne remote sensing seems to be the only viable means for SWE monitoring. However, the quest for sensors and methods to monitor SWE from space has only partly been successful up to now. Presently the only reasonable SWE product from satellites are SWE maps retrieved from microwave radiometric data, which due to the large footprints (typically several 100 km<sup>2</sup>) are not relevant for mountain areas and complex terrain. In addition, these products suffer from the sensitivity of high frequency microwave emission and scattering to snow grain size and snow pack morphology. The phase shift in snow at C-band or lower frequencies, studied in this project, offers a direct and elegant means to retrieve the SWE.

The analysis of ERS and airborne SAR data and theory confirm that the interferometric phase shift of repeat pass SAR data in a dry snow pack provides a physically based means for mapping the spatial distribution of SWE. For SWE retrieval the snow-induced phase shift has to be separated from the other phase terms, namely the topographic and atmospheric phase contributions. Model calculations show that under winter conditions the variations of the atmospheric phase delay play a small role for analysis of SWE at regional scale. The topographic phase can be determined from interferograms without snowfall. The main limitation for application of the method is caused by temporal decorrelation due to differential phase delays at sub-pixel scale induced by snow fall or wind re-distribution. In C-band SAR data these effects often cause complete decorrelation within time spans of a few days, sometimes even within one day. Therefore it is very unlikely that a SWE monitoring service can be based on C-band SAR interferometry because it lacks robustness.

Theory and the available airborne L-band repeat pass (October to February) interferograms confirm that L-band is much less affected by temporal decorrelation. In high Alpine areas typical SWE values in later winter are of the order of several hundred mm SWE, corresponding to snow-induced phase shifts of several fringes at L-band. Because of better coherence and larger measurement range, the investigations strongly suggest that L-band is preferable for interferometric SWE mapping compared to shorter wavelengths.

In order to fully assess the potential of L-band for SWE retrieval, it is recommended to carry out dedicated experiments with airborne and spaceborne SAR during which snow depth is measured at test fields in a narrow grid comparable to the pixel size of the sensor. The standard grid of snow stations in Austria, for example, has a density of about one station per 100 km<sup>2</sup> in area, which is unsuitable for validating the SWE algorithm. Although the available L-band airborne data suggest that VV polarization is preferable to HH because of better coherence, investigations with a larger data set are needed to clearly assess the impacts of polarization, incidence angle, chirp bandwidth and repeat pass interval for SWE retrieval.

In summary, L-band repeat pass SAR interferometry is a promising candidate for SWE mapping and monitoring, which could lead to a major break-through for snow hydrology, water management and cryospheric research.

## B.6 REFERENCES

- Alley R.B. 1987. Texture of polar firn for remote sensing. *Ann. Glaciol.* 9, 1-4.
- Alley R.B. 1988. Concerning the deposition and diagenesis of strata in polar firn. *J. Glaciol.* 34(118), 283-290.
- Arcone S.A., A.J. Gow and S. McGrew. 1986. Structure and dielectric properties at 4.8 and 9.5 GHz of saline ice. *J. Geophys. Res.* 91(C12), 14281-14303.
- Askne J., P. Dammert and G. Smith. 1997. Interferometric SAR observations of forested areas. Proc. 3<sup>rd</sup> ERS Symposium, Florence, Italy, 14-21 March 1997, *ESA SP-414, Vol.I*, 337-344.
- Bales R.C. and F. Harrington. 1995. Recent progress in snow hydrology. *Rev. Geophysics*, Supplement, July 1995, 1011-1020.
- Bamler R. and P. Hartl. 1998. Synthetic Aperture Radar Interferometry. *Inverse Problems*, vol.14, pp. R1-R54.
- Bergström, S. 1995. The HBV Model. In *Computer Models of Watershed Hydrology*, edited by V.P. Singh. (Highlands Ranch, Colorado: Water Resources Publications), 443-476.
- Bernier, M. and J.P. Fortin. 1998. The potential of time series of C-band SAR data to monitor dry and shallow snow cover. *IEEE Trans. Geosc. Rem. Sens.* 36 (1), 226 - 243.
- Björnsson, H. 2002. Subglacial lakes and jökulhlaups in Iceland. *Global and Planetary Change* 35, 255-271.
- Björnsson, H. F. Pálsson, and G. E. Flowers. In press. Surges of ice caps in Iceland. *Ann. Glaciol.* 36.
- Closa J. 1998. The influence of orbit precision in the quality of the ERS SAR interferometric data. *ES-TN-APP-APM-JC01*. <http://earth.esa.int>. 9 pp.
- Colbeck, S.C. 1982. An overview of seasonal snow metamorphism. *Rev. of Geophysics and Space Physics* 20, 63-79.
- Colbeck, S.C. 1997. A review of sintering of seasonal snow. *CRREL Report 97-10*. USACRREL, Hanover. N.H. 12 pp.
- Dammert P.B.G., M. Leppäranta and J. Askne. 1997. Sea ice displacement measured by ERS-1 SAR interferometry. Proc. 3<sup>rd</sup> ERS Symposium, Florence, Italy, 14-21 March 1997, *ESA SP-414, Vol.II*, 923-930.
- Dammert P.B.G., M. Leppäranta and J. Askne. 1998. SAR interferometry over Baltic sea ice. *Int. J. Rem. Sensing*, 19(16), 3019-3037.
- Demuth, M. and A. Pietroniro. 1999. Inferring glacier mass balance using Radarsat: results from Peyto Glacier, Canada, *Geografiska Annaler*, 81A, 521 - 540.
- ESA. 1997. ERS SAR Interferometry. Proc. Fringe 96 Workshop, 30 Sept.-2 Oct. 1996, Zürich, CH, Vol. I & II, *ESA SP-406*, 376 & 159 pp.



- ESA. 2000a. Proc. of Fringe'99, Liege, 11-12 November 1999. *ESA SP-478*. (CD)
- ESA. 2000b. Proc. of ERS-ENVISAT Symposium, Gothenburg, Sweden, 16-20 Oct 2000. *ESA SP-461*. (CD)
- Essery R. and Z-L Yang. 2001. An overview of models participating in the snow model intercomparison project (SNOWMIP). [www.cnrm.meteo.fr/snowmip-/model\\_review.htm](http://www.cnrm.meteo.fr/snowmip-/model_review.htm).
- Ferretti, A., C. Prati, and F. Rocca. 1999. Multibaseline InSAR DEM reconstruction: The wavelet approach. *IEEE Trans. Geosc. Rem. Sens.*, 37, 705-715.
- Floricioiu D.. 1997. *Polarimetric Signatures and Classification of Alpine Terrain by Means of SIR-C / X-SAR*. PhD Thesis, University of Innsbruck, Austria.
- Floricioiu, D. and H. Rott. 2001. Seasonal and short-term variability of multifrequency, polarimetric radar backscatter of alpine terrain from SIR-C/X-SAR and AIRSAR data. *IEEE Trans. Geosc. Rem. Sens.*, 39(12), 2634 –2648.
- Forsberg R., K. Keller, C.S. Nielsen, N. Gundestrup, C.C. Tscherning, S.N. Madsen and J. Dall. 2000. Elevation change measurements of the Greenland Ice Sheet. *Earth Planets Space* 52, 1049-1053.
- Foster, R. C., B. L. Isacks and S. B. Das. 1996. Shuttle imaging radar (SIR-C/X-SAR) reveals near-surface properties of the South Patagonian Icefield. *J. Geophysical Res.*, 101 (E10), 23169 - 23180.
- Fung, A. 1994. *Microwave Scattering and Emission Models and their Applications*. Artech House Inc.
- Fung, A. and M.F. Chen. 1989 Modelling of microwave emission and scattering from snow and soil. *Adv. Space Res.* 9 (1), 297-306.
- Gatelli F., A.M. Monti Guarnieri, F. Parizzi, P. Pasquali, C. Prati and F. Rocca. 1994. The wavenumber shift in SAR interferometry. *IEEE Trans. Geosc. Rem. Sens.* 32(4), 855-865.
- Gudmundsson, S., M. T. Gudmundsson, H. Björnsson, F. Sigmundsson, H. Rott and J. M. Carstensen. 2002. Three-dimensional glacier surface motion maps at the Gjálp eruption site, Iceland, inferred from combining InSAR and other ice displacement data. *Ann. Glaciology*, 34, 315-322.
- Guneriussen, T., K.A., Høgda, H. Johnson and I. Lauknes. 2001. InSAR for estimating changes in snow water equivalent of dry snow. *IEEE Trans. Geosc. Rem. Sens.* 39(10), 2101-2108.
- Hanssen R. 2001. *Radar Interferometry – Data Interpretation and Error Analysis*. Kluwer Acad. Pub. 308 pp.
- Herzfeld U.C., 2002: Vario functions of higher order – definition and application to characterization of snow surface roughness. *Computers and Geoscience*, 28, pp. 641-660.
- Hoën, E.W., and H.A. Zebker. 2000. Penetration depths inferred from interferometric volume decorrelation observed over the Greenland Ice Sheet. *IEEE Trans. Geosc. Remote Sensing*, 38(6), 2571-2583.

- Hufford, G. 1991. A model for the complex permittivity of ice at frequencies below 1 THz. *Int. J. Infrared and Millimeter Waves*, 12, 677-682.
- IPCC. 2001. Climate Change 2001: The Scientific Basis. Contribution of Working Group I to the Intergovernmental Panel on Climate Change (IPCC). J.T. Houghton *et al.*, Eds. Cambridge Univ. Press, 944 pp.
- Jezek, K. C., M. R. Drinkwater, J. P. Crawford, R. Bindenschadler and R. Kwok. 1993. Analysis of Synthetic Aperture Radar data collected over the southwestern Greenland ice sheet. *J. Glaciol.* 39 (131), 119 - 132.
- Joughin I., R. Kwok and M.A. Fahnestock. 1998. Interferometric estimation of three-dimensional ice-flow using ascending and descending passes. *IEEE Trans. Geosc. Remote Sensing*, 36 (1), 25-37.
- Joughin, I., D. Winebrenner, M. Fahnestock, R. Kwok and W. Krabill. 1996. Measurement of ice-sheet topography using satellite-radar interferometry. *J. Glaciol.*, 42 (140), 10-22.
- Kamb, B. 1987. Glacier surge mechanism based on a linked cavity configuration of the basal water conduit system. *J. Geoph. Res.* **92**, 9083-9100.
- Koskinen J.T. 2001. Snow monitoring using interferometric TOPSAR data. *Proc. IGARSS'01*, Sydney, AUS, 9-13 July 2001, IEEE, 2866-2868.
- Kwok R., M.J. Siegert and F.D. Carsey. 2000. Ice motion over Lake Vostok, Antarctica: constraints on inferences regarding the accreted ice. *J. Glaciol.*, 46(155), 689-694.
- Li, S., C. Benson, L. Shapiro and D. Kenneson. 1997. Aufeis in the Ivishak River, Alaska, mapped from satellite radar interferometry. *Rem. Sens. Env.* 60(2), 131-139.
- Li, Z., Gou H.D., Li X.W. and C.L. Wang. 2001. SAR interferometry coherence analysis for snow mapping. *Proc. IGARSS'01*, Sydney, AUS, 9-13 July 2001, IEEE, 2905-2907.
- Li, S. and M. Sturm. 2003. Patterns of wind-drifted snow on the Alaskan Arctic Slope detected with ERS-1 interferometric SAR. *J. Glaciol.*. Vol 48, No 163, 495-504.
- Mätzler, C. 1987. Applications of the interaction of microwaves with the natural snow cover, *Remote Sensing Review*, 2, 259-387.
- Mätzler, C. 1996. Microwave permittivity of dry snow. *IEEE Trans. Geosc. Remote Sensing*, 34(2), 573-581.
- Mätzler, C. 1997. Autocorrelation functions of granular media with free arrangement of spheres, spherical shells or ellipsoids. *J. Appl. Phys* 81(3), 1509-1517.
- Mätzler, C. 1998. Microwave properties of ice and snow. In: Schmitt, B., de Bergh, C., and Festou, M., Editors: Solar System Ices, Kluwer Academic Publ. Astrophysics and Space Science Library, Vol. 227. 832 pp.
- Mohr, J. J., N. Reeh and S.N. Madsen. 1998. Three-dimensional glacial flow and surface elevation measured with radar interferometry. *Nature*, 391, 273-276.

- Mohr J., N. Reeh and S.N. Madsen. 2003. Accuracy of three-dimensional glacier surface velocities derived from radar interferometry and ice-sounding radar measurements. *J. Glaciol.*, Vol 49, No 169, 210-222.
- Nagler T. and. H. Rott, 2000. Retrieval of Wet Snow by Means of Multitemporal SAR Data. *IEEE Trans. Geosci. Rem. Sens.*, Vol 38, No 2, March 2000, 754-765.
- Nagler T., C. Mayer, and H. Rott. 2002. Feasibility of DINSAR for mapping complex motion fields of Alpine ice and rock glaciers. *Proc. of 3rd Int. Symposium on Retrieval of Bio- and Geophysical Parameters from SAR Data for Land Applications, Sheffield, UK, 11-14 Sept. 2001. ESA SP-475*, 377-382.
- Nagler, T., 1996. *Methods and Analysis of Synthetic Aperture Radar Data from ERS-1 and X-SAR for Snow and Glacier Applications*. PhD Thesis, University of Innsbruck, Austria.
- Partington, K. C. 1998. Discrimination of glacier facies using multi-temporal SAR data. *J. Glaciol.*, 44 (146), 42 - 53.
- Paterson, W. S. B. 1994. *The Physics of Glaciers*. 3rd edition. Elsevier.
- Ramage, J. M., B. L. Isacks and M. M. Miller. 2000. -Radar glacier zones in southeast Alaska, USA: field and satellite observations. *J. Glaciol.*, 46 (152), 287-296.
- Reeh, N., S.N. Madsen and J.J. Mohr. 1999. Combining SAR interferometry and the equation of continuity to estimate the three-dimensional glacier surface-velocity vector. *J. Glaciol.*, 45, 533-538.
- Reeh N., J.J. Mohr, S.N. Madsen, H. Örter and N. Gundestrup. 2003. Three-dimensional surface velocities of the Storstrømmen glacier derived from radar interferometry and ice-sounding radar measurements. *J. Glaciol.*, 49, 201-209.
- Reigber C., Y. Xia, H. Kaufmann, F.H. Massmann, L. Timmen, J. Bodechtel, M. Frei. 1996. Impact of precise orbits on SAR interferometry. *Proc. FRINGE'96*. <http://www.geo.unizh.ch/rsl/fringe96/papers/reigber-et-al/>, 9 pp.
- Rignot E., K. Echelmeyer and W. Krabill. 2001. Penetration depth of interferometric synthetic-aperture radar signals in snow and ice. *Geoph. Res. Letters*, 28 (18), 3501-3504.
- Rosen, P. A., S. Hensley, I. R. Joughin, F. K. Li, S. N. Madsen, E. Rodriguez and R. M. Goldstein. 2000. Synthetic Aperture Radar Interferometry. *Proc. of the IEEE*, 88(3), 333-385.
- Rott H. 1989. Multispectral microwave signatures of the Antarctic ice sheet. In: *Microwave Radiometry and Remote Sensing Applications*, Ed. P. Pampaloni, VSP, Utrecht, NL: 89-101.
- Rott H. 1997. Capabilities of microwave sensors for monitoring areal extent and physical properties of the snowpack. In: *Land Surface Processes in Hydrology, NATO ASI Series I: Global Environmental Change Vol. 46*, Eds. S. Sooroshian, H.V. Gupta, J.C. Rodda. Springer Verlag Berlin, 135-167.
- Rott H. and R. Davis 1993. Multifrequency and polarimetric SAR observations on alpine glaciers. *Annals of Glaciology* 17, 98-104.

- Rott H., K. Sturm and H. Miller. 1993. Active and passive microwave signatures of Antarctic firn by means of field measurements and satellite data. *Annals of Glaciology* 17, 337-343.
- Rott, H., and A. Siegel. 1997. Glaciological Studies in the Alps and in Antarctica Using ERS Interferometric SAR. *ERS SAR Interferometry, Proc. ESA Fringe 96 Workshop, Zürich. Oct. 1996. ESA SP 406*, Vol. II, 149-159.
- Rott, H., M. Stuefer, A. Siegel, P. Skvarca and A. Eckstaller. 1998. Mass fluxes and dynamics of Moreno Glacier, Southern Patagonia Icefield. *Geoph. Res. Letters*, 25 (9), 1407-1410.
- Rott H., M. Baumgartner, R. Caves, G. Glendinning, B. Johansson, H. Kleindienst, T. Nagler, O. Pirker, S. Quegan, S. Voigt and G. Wright. 2000. HYDALP, Hydrology of Alpine and High Latitude Basins, Final Report Institut für Meteorologie und Geophysik, *Universität Innsbruck, Mitteilung Nr. 4 (2000)*, 201 pp.
- Schwäbisch M. 1995. *Die SAR Interferometrie zur Erzeugung digitaler Geländemodelle*. PhD Thesis, DLR. 124p.
- Shi, J. and J. Dozier. 2000a. Estimation of snow water equivalent using SIR-C/X-SAR, Part I: Inferring snow density and subsurface properties, *IEEE Trans. Geosc. Rem. Sens.*, 38 (6), 2465-2474.
- Shi J.C, and J. Dozier. 2000b. Estimation of snow water equivalent using SIR-C/X-SAR, Part II: Inferring snow depth and particle size. *IEEE Trans. Geosc. Remote Sensing*, 38(6), 2475-2488.
- Slater A.G. and 33 others. 2001. The representation of snow in land surface schemes: Results from PILPS 2(d). *J. of Hydrometeorology* 2, 7-25.
- Strozzi, T., U. Wegmüller and C. Mätzler. 1999. Mapping wet snow with SAR interferometry. *Int. J. Rem. Sensing*, 20(12), 2395-2403.
- Wegmüller U. and C. Werner. 1997. Retrieval of vegetation parameters with SAR interferometry. *IEEE Trans. Geosc. Remote Sensing*, 35(1), 18-24.
- Wen, B., L. Tsang, D. Winebrenner, and A. Ishimaru. 1990. Dense medium radiative transfer theory: Comparison with experiment and application to microwave remote sensing and polarimetry. *IEEE Trans. Geosc. Remote Sensing*, 28 (1), 46-59.
- West R., L. Tsang and D.P. Winebrenner. 1993. Dense Medium Radiative Transfer Theory for two scattering layers with a Rayleigh distribution of particle sizes. *IEEE Trans. Geosc. Remote Sensing*, 31 (2), 426-437.
- West R.D., D.P. Winebrenner, L. Tsang and H. Rott. 1996. Microwave emission from density-stratified Antarctic firn at 6 cm wavelength. *J. of Glaciology*, 42(140): 63-76.
- Wiesmann A., C. Mätzler and T. Weise. 1998. Radiometric and structural measurements of snow samples. *Radio Science* 33(2), 273-289.
- Williams R.S., D.K. Hall and C.S. Benson. 1991. Analysis of glacier facies using satellite techniques. *J. Glaciol.*, 37 (125), 120-128.

- 
- Winebrenner D.P. and 14 others. 1992. Microwave sea ice signature modelling. In: *Microwave Remote Sensing of Sea Ice. Geophys. Monograph 68, AGU*, 137-175.
- Winther J.-G. and R. Solberg. 2002. Chief Editors, Proc. of the Fourth Int. Symposium on Remote Sensing in Glaciology, College Park, MD, 3-8 June 2001. *Ann. Glaciology*, 34, 464 pp.
- Zebker H.A. and J. Villasenor. 1992. Decorrelation in interferometric radar echos. *IEEE Trans. Geosc. Remote Sensing*, 30(5), 950-959.
- Zurk L.M., L. Tsang, J-C- Shi and R.E. Davis. 1997. Electromagnetic scattering calculated from pair distribution functions retrieved from planar snow sections. *IEEE Trans. Geosc. Remote Sensing*, 35(6), 1419-1428.

## **PART C**

### **INSAR RETRIEVAL OF VEGETATION PARAMETERS**

**Konstantinos PAPATHANASSIOU and Irena HAJNSEK**

Microwaves and Radar Institute,  
German Aerospace Centre,  
Wessling, GERMANY

**Shane R. CLOUDE**

AEL-Consultants,  
Cuper, Scotland, UNITED KINGDOM



*This page is intentionally left blank.*

## Table of Contents

<b>C.1</b>	<b>LITERATURE REVIEW.....</b>	<b>C-1</b>
C.1.1	Introduction.....	C-1
C.1.2	Polarimetric SAR interferometry.....	C-4
C.1.3	Forest parameter estimation from Pol-InSAR data.....	C-6
C.1.3.1	Scattering and inversion models.....	C-6
C.1.3.2	Random volume over ground scattering model.....	C-7
C.1.3.3	RVoG model inversion.....	C-9
C.1.3.4	RVoG model validation.....	C-12
C.1.4	Surface parameter estimation from Pol-InSAR data.....	C-15
C.1.4.1	SAR polarimetry.....	C-15
C.1.4.2	Interferometric effects.....	C-16
C.1.5	Summary and conclusions.....	C-19
<b>C.2</b>	<b>IDENTIFICATION OF VARIABLES AND TECHNIQUES .....</b>	<b>C-21</b>
C.2.1	Physical vegetation and surface parameters.....	C-21
C.2.2	Selected data sets.....	C-22
C.2.2.1	Oberpfaffenhofen test site, Germany.....	C-22
C.2.2.2	Fichtelgebirge test site, Germany.....	C-23
C.2.2.3	Kudara test site, Russia.....	C-25
C.2.3	Tasks and methodology.....	C-25
<b>C.3</b>	<b>ELECTROMAGNETIC INTERACTION MODELLING .....</b>	<b>C-27</b>
C.3.1	Introduction.....	C-27
C.3.2	Coherent EM scattering model for InSAR studies.....	C-27
C.3.2.1	Direct-ground scattering.....	C-29
C.3.2.2	Volume scattering.....	C-29
C.3.2.3	Ground-volume and ground-volume-ground interactions.....	C-30
C.3.3	Pine forest InSAR scattering model.....	C-39
C.3.4	Layer coherence model for tree height estimation.....	C-46
C.3.5	Experimental validation.....	C-49

<b>C.4</b>	<b>RETRIEVAL ALGORITHMS FOR TREE HEIGHT AND TEST CASES.....</b>	<b>C-51</b>
C.4.1	Introduction.....	C-51
C.4.2	Tree height estimation algorithm using light polinsar modes.....	C-51
C.4.3	Scots pine forest simulations for L-band POLINSAR.....	C-53
C.4.4	Results of tree height algorithm assessment .....	C-55
C.4.4.1	Random canopy results .....	C-55
C.4.4.2	Scots pine forest results .....	C-59
C.4.4.3	Errors due to orientation effects in volume scattering .....	C-64
C.4.5	Experimental validation .....	C-66
C.4.6	Conclusions and recommendations.....	C-74
<b>C.5</b>	<b>REFERENCES .....</b>	<b>C-77</b>
<b>C.6</b>	<b>ACKNOWLEDGEMENTS.....</b>	<b>C-85</b>

## C.1 LITERATURE REVIEW

### C.1.1 Introduction

Synthetic Aperture Radar (SAR) Interferometry (InSAR) is today an established technique to measure terrain topography [1]. The estimation of the topographic height relies on parallax measurement using the phase difference between two SAR images of the same area acquired - at both ends of a spatial baseline - under slightly different look angles. However, the fact that the parallax is measured in terms of phase with an accuracy of fractions of the wavelength, makes SAR interferometry much more accurate than standard triangulation techniques.

Beside the generation of digital elevation models (DEM's) SAR interferometry plays also an important role in quantitative parameter estimation. The interferometric observables - i.e. the interferometric phase and coherence - are very sensitive to structural properties of the scatterers within a scene. This sensitivity arises mainly from two physical effects. The first one is the decorrelation of the individual speckle patterns due to the different projections of the scatterers height distribution into the two images, known as volume decorrelation. This leads to a degradation of the correlation between the two images and provides sensitivity to the vertical extension and EM density of the scatterer. The second one is the different interferometric behaviour of volume scatterers and structures with an isolated scattering centre. While the scattering contributions of volume scatterers - as they occur at different heights - appear as the coherent integration of their phasors over the volume height, the contributions from scatterers with an isolated scattering centre are added in phase. As a consequence, the interferometric observables are sensitive to the structural characteristics of scatterers. Furthermore, temporal and Signal-to-Noise (SNR) decorrelation effects depend additionally to the structural also on geometrical, and dielectric properties of the scatterers in a scene. Hence, with respect to the information content, interferometric observables are important for the investigation of natural volume (for example vegetation or media with low dielectric constant (ice or dry sand), surface and mixed (volume and surface) scatterers.

Based on the sensitivity of the interferometric observables to structural properties of vegetation, a variety of (Semi-) Empirical Models have been developed in order to establish relations between interferometric coherence values at a certain frequency and / or polarisation and vegetation height or forest biomass based on data regressions [14,15,16,17,22,23]. Further application of regression techniques to coherence for forestry can be found in [94,95], and agriculture applications [96]. Unfortunately, the interferometric observables are not directly (and/or unambiguously) related to individual scatterer parameters, so that a straightforward parameter inversion / regression is not possible [4]. Different scattering structures -e.g. different vegetation heights, densities, and or biomass levels - can lead to the same coherence values and become indistinguishable [4,36,37,40]. Furthermore, the semi-empirical nature, of these algorithms lack in generalisation and their application on different vegetation

conditions is not possible without comprehensive a priori information and / or restricting assumptions.

One key step for single channel systems was the extension of the interferometric observation space by temporal observation diversity by means of **multi-temporal** observations. The variation of the interferometric coherence and phase with temporal resolution, given by the repeat-pass time interval, enable to interpret and/or evaluate changing processes occurring on different time scales described by the amount of temporal decorrelation. Interferometric data collected continuously over a long time period have been successfully employed to determine the influence of perturbations of the propagation medium (atmospheric effects). They have been also used to interpret natural changing processes and relate them - mainly on an empirical basis - to different scattering processes for classification purposes [14,15,16,17,22,23] or to map seasonal variations in vegetation growth [94]. However, there are critical limitations on the effectiveness of multi-temporal interferometric data for quantitative parameter inversion. The interferometric coherence provides information about the amount of change, so that different natural processes may lead to the same amount of temporal decorrelation in the same time interval. Hence, generalised modelling or interpretation of temporal decorrelation without additional information about environmental conditions becomes very difficult.

Additionally, for volume scatterers temporal decorrelation is superimposed to volume decorrelation making - especially at higher frequencies as at X- or C-band - the discrimination of volume parameters and temporal effects ambiguous. Consequently, the advantage of more observables drops away as the number of unknown parameters necessary to describe temporal changes effects increases too.

Thus, a relation - in form of a scattering model or empirical correlation - linking the observables to the wanted parameters has to be established. In order to establish this relation for different coherent scattering problems, different approaches - model based and empirical - have been followed in the literature over the last years. Regarding a single baseline, single frequency and single polarisation interferometric acquisition, all approaches lead to unsatisfactorily inversion results. The problem lies in the complexity of the EM scattering process that requires even for simple scattering models more parameters to be described than the number of available interferometric observables. Empirical approaches suffer also under the limited number of available observables, which do not allow a complete interpretation of the interferometric information.

In order to extend the interferometric observation space, several multi-parameter interferometric approaches have been followed over the last few years:

**Multi-Baseline** approaches were the first ones addressed in the literature concerning model-based inversion of vegetation parameters from interferometric data [2,3,4,5,6]. Based on multi-baseline ERS-1/2 data the problem of vegetation height estimation from interferometric data was addressed for the first time [2,3]. Temporal decorrelation - affecting especially higher frequencies - was the main limitation of these approaches. Latter investigations based on dual-baseline interferometric data acquired (quasi-) simultaneously, where successful in

estimating parameters as tree height, canopy extinction, and underlying topography [4,5,6]. The availability of more baselines allows potentially the estimation of vertical vegetation structure profiles [7,8,9]. However, for the case of repeat pass implementations, temporal decorrelation effects limit the performance or even the applicability of these approaches.

**Multi-frequency** methods make use of the frequency dependent behaviour of the interferometric observables primarily caused by the frequency dependent penetration properties of EM waves. First approaches were based on the use of a high and a low frequency in order to estimate directly vegetation height in terms of the height difference between the two interferograms [10,11,12,13]. Experiments demonstrated that this approach leads to an underestimation of the vegetation height due to the fact that neither the higher frequency measures the top of the vegetation nor the vegetation layer is transparent at the lower frequency [13]. Model based inversion of dual- or multi-frequency InSAR data is also “problematic” due to the fact that several parameters of the scattering process dependent on the operation frequency, leading thus to under-determined inversion problems.

**Quad-Pol:** approaches: One alternative - and very promising - way to extend the interferometric observation space is the introduction of polarisation diversity. Scattering polarimetry is sensitive to the shape, orientation and dielectric properties of scatterers. This allows the identification and separation of scattering mechanisms of natural media employing differences in the polarisation signature for purposes of classification and parameter estimation [18,19]. Thus, the combination of the qualitative information provided from polarimetry and interferometry is very promising concerning the extraction of forest or other structure parameters, as it will be reported in the next section.

**SAR Tomography** has been demonstrated for the first time using L-band multi-baseline data of DLR’s E-SAR system [20,21]. This technique allows a real three-dimensional imaging of volume scatterers as is the case at lower frequencies for vegetation of forest scatterers. Thus, it makes possible apart from height and underlying topography estimation an unambiguous evaluation of vertical backscattering profiles. The main limitation of this technique - at least for conventional SAR sensor configurations - is the large number of acquisitions (more than five) required for its implementation.

With respect to application fields now, forest applications are the most developed - with respect to multi-parameter InSAR. Over the last years several groups have been working on the interpretation and inversion of multi-parameter InSAR data over forested terrain. Compared to forest, agricultural applications are in general underdeveloped and not clearly addressed, evaluated and/or validated. The existing work relies on the adoption of approaches developed for forest vegetation without accounting for the different structural characteristics of agricultural vegetation. The activities on these fields will be reviewed in the section 3. Regarding now non-vegetated scatterers, - first experimental results indicate that - multi-parameter InSAR data may have a challenging and interesting impact also in the classical - remote



sensing and EM - problem of surface parameter estimation. The actual status on this field will be reviewed in section 4.

### **C.1.2 Polarimetric SAR interferometry**

Polarimetric Synthetic Aperture Radar Interferometry (Pol-InSAR) is a recently developed and fast evolving radar remote sensing technique, based on the coherent combination of radar polarimetry and SAR interferometry. The main reason why the potential of combining polarimetry and SAR interferometry was not evaluated until the late nineties was mainly the lack of appropriate experimental data. On the one hand side, fully polarimetric airborne data are available to the scientific community since the early eighties while the SIR-C/X-SAR mission in 1994 offered the first fully polarimetric spaceborne data sets. On the other hand side, repeat-pass interferometric data are widely available since the launch of ERS-I in 1991. However, the first interferometric data takes acquired in a fully polarimetric mode were recorded on board of the space shuttle during the last three days of the second SIR-C/X-SAR mission in October 1994.

The combination of polarimetry and interferometry started to be studied in 1995 on the basis of the SIR-C/X-SAR data sets. The first scientific publication about polarimetric effects in SAR interferometry appeared in May 1996 where the polarisation dependent interferometric coherence behaviour was reported addressing the supposition that interferograms at different polarisations correspond to different scattering centres located at different heights [24].

Starting from these early observations, polarimetric interferometry evolved fast in the following two years (1996-1998). First, the theoretical framework of vector interferometry - necessary to account for a polarimetric observation vector - has been worked out [25,26,27,28,29]. The problem of the polarisation dependency of the interferometric coherence has been addressed and the analytical solution for optimum polarisations states that maximise the interferometric coherence has been derived and applied to experimental data [25,28,29]. This way, it was possible to form interferograms with a significant higher interferometric coherence than the ones obtained from conventional polarisations allowing an improving the accuracy of derived DEM's. This was a first important result showing the potential to increase the performance of conventional interferometry by using a fully polarimetric interferometric system configuration.

Furthermore, the coherence optimisation algorithm leads - apart from the optimum polarisation state - to other two optimised polarisation states, each one a optimum solution in different subspaces. Thus, the coherence optimisation algorithm has been alternatively interpreted as a coherent decomposition into three independent interferograms [25,26]. Each of these interferograms can be regarded to correspond to a different deterministic scattering process occurring at the same or at different height inside the resolution cell. Hence, it was possible to decompose the scattering process into three different scattering contributions and to estimate their height location in a relative as well as absolute sense. The phase difference between the optimum interferograms obtained by the application of the algorithm on the SIR-C data turned

out to be strongly correlated with the actual forest height [30]. This was a major result indicating the potential of the coherent combination of polarimetry and interferometry. Even if during the next years these results proved to be of limited validity, it was essential in enforcing the scientific work on polarimetric interferometry.

Motivated by these results different groups independently from each other applied the optimisation algorithm on laboratory and/or scatterometer data [31,32]. The optimum interferograms have been analysed with respect to DEM optimisation [32,34] as well as with respect to vegetation height extraction and validated against ground measurements [32,33]. The results were in accordance with the results obtained from the SIR-C data supporting the drawn conclusions. Moreover, a more empirical approach for estimating the optimum polarisation states based on the principle of coherence signature plots was addressed, leading to the same polarisation states as the analytical estimation approach [32].

An important step forward was done with the successfully implementation of repeat-pass interferometry - at longer wavelengths as at L- and P-band - by airborne SAR systems. This enabled the acquisition of fully polarimetric interferometric SAR data using a conventional polarimetric airborne SAR [35]. Polarimetric interferometric data acquired with a variety of spatial baselines over well known test sites become available and led to a break-through in understanding, development, and validation of the new technology.

The analysis of first multi-baseline L-band airborne polarimetric interferometric data permitted for the first time an interpretation of interferograms at different polarisations widely unaffected by temporal decorrelation [36,37,38,39,40]. The key observation was that (at longer baselines than the ones available by the SIR-C data) the optimum coherence values over vegetated and/or forested areas are not more equal to one and degrade with increasing interferometric baseline. This is an unambiguous indication for that even the optimum polarisation states are affected by volume decorrelation, a fact with important implications. Consequently, volume scattering is present in the whole polarimetric space so that there is no polarisation state without volume scattering contributions and hence no interferogram corresponding to the ground can be generated. Furthermore, at L-band vegetation scattering includes interactions with the vegetation layer as well as with the underlying ground. The analysis of the data indicated strongly that also ground scattering has to be assumed to be three-dimensional, i.e. to be present in all polarisation states [36,37,40].

Both observations make clear that in general it is not possible to separate entirely volume and surface scattering contributions of vegetation scattering in terms of optimum interferograms. Consequently, an unbiased estimation of vegetation height in terms of phase difference between the optimum interferograms is in general not possible, as it leads to an underestimated estimation.

Analogous experimental observations leading to the same results and conclusions have been reported by several independent groups. In [41,42,43,44] the analysis of airborne and space multi-baseline SAR data results on the same conclusions about the separability of ground and volume scattering contributions. In- and outdoor

scatterometer experiments in [45,46] over agricultural vegetation types (maize, rice and sorghum) led also to similar results regarding the underestimation of vegetation height extracted from phase differences between interferograms at different polarisations.

### **C.1.3 Forest parameter estimation from Pol-InSAR data**

#### **C.1.3.1 Scattering and inversion models**

The absence of any direct relation between physical forest parameters (e.g. forest height, density, etc.) and interferometric observables, necessitates the consideration of model based estimation approaches [47]. Model based parameter inversion may be regarded as a two-step procedure: In a first step, a (coherent) scattering model  $[M]$  that relates the scattering parameters to the interferometric observables has to be established:

$$\begin{bmatrix} \text{Interferometric} \\ \text{Observables} \end{bmatrix} = [M] \begin{bmatrix} \text{Scattering} \\ \text{Parameters} \end{bmatrix} \quad (\text{C.1.1})$$

Then, in a second step, the scattering parameters can be estimated from the interferometric observables from the inversion of the scattering model as

$$\begin{bmatrix} \text{Scattering} \\ \text{Parameters} \end{bmatrix} = [M]^{-1} \begin{bmatrix} \text{Interferometric} \\ \text{Observables} \end{bmatrix} \quad (\text{C.1.2})$$

The scattering model is essential for the accuracy of the estimated parameters. On the one hand the model must contain enough physical structure to interpret the radar observables, while on the other hand it must be simple in terms of parameters in order to be determinable with a limited number of observables [5, 47]. This trade off is mirrored in the two approaches, which have been followed in the literature: direct and statistical scattering models

- Direct models are based on a detailed description of the scatterer in terms of discrete particle or equivalent dielectric constant distributions and model the radar observables by solving the corresponding Maxwell equations. As a detailed description of the scatterer's structure can be incorporated in terms of particle size, shape and orientation, direct models they are characterised by precise structural vegetation description paying the price of a large number of over-parameterisation.
- Statistical models - as already indicated by their name - use macroscopic statistical and/or symmetry derived properties of the scatterer to state about its

scattering behaviour. They are not so detailed as direct models but have the advantage to be describable by a significant smaller number of parameters.

Direct models are in general too complex in terms of parameters and lead in general to underestimated inversion problems. They can be solved unambiguously only by introducing simplifying assumptions or a priori information and have therefore a constrained applicability. In [48,49] vegetation height was extracted by using a coherent scattering model based on the combination of a fractal-tree model [50] and a  $\Delta k$  interferometric simulator [51,52,53]. This was possible only by using a priori information about tree species (for performing the modelling) and a precise ground elevation model [45,48]. However, direct models can play an important role in concerning the understanding and parameterisation of scattering processes in forest environments and thus in the development of accurate simplified inversion models. For the quantitative parameter estimation from polarimetric interferometric SAR data, statistical models have been proved to be more suited leading to promising results and will be considered in the following.

### C.1.3.2 Random volume over ground scattering model

In the case of forest scattering at lower frequencies, a realistic scattering model has to consider both, the vegetation layer and ground interactions. A simple statistical model to describe such a scenario is the random volume over ground scattering model [7,36,37,40]. Accordingly, the vegetation is modelled as a single layer of thickness  $h_V$  containing a volume with randomly oriented particles and scattering amplitude per unit volume  $m_V$ . This random volume, as shown schematically in Figure C.1.1, is located over a ground scatterer positioned at  $z=z_0$  with scattering amplitude  $m_G$ . The ground is seen through the vegetation layer by an interferometric system operating at wavelength  $\lambda$  with physical baseline  $B$  under a mean incident angle  $\theta_0$ . In this case, the complex interferometric coherence  $\tilde{\gamma}$  after range spectral filtering, may be written as

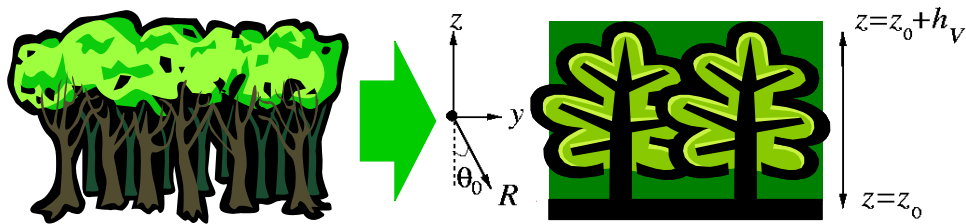


Figure C.1.1: Random Volume over Ground Scattering Model.

$$\tilde{\gamma}(\vec{w}) = \exp(i\phi_0) \frac{\tilde{\gamma}_V + m(\vec{w})}{1 + m(\vec{w})} \quad (\text{C.1.3})$$

$\tilde{\gamma}_V$  denotes the complex coherence for the volume alone, which depends on the extinction coefficient  $\sigma$  for the random volume, and its thickness  $h_V$  as

$$\tilde{\gamma}_V = \frac{I}{I_0} \quad \text{where} \quad \begin{aligned} I &= \int_0^{h_V} \exp(i\kappa_z z') \exp\left(\frac{2\sigma z'}{\cos\theta_0}\right) dz' \\ I_0 &= \int_0^{h_V} \exp\left(\frac{2\sigma z'}{\cos\theta_0}\right) dz' \end{aligned} \quad (\text{C.1.4})$$

$\phi_0$  is the phase related to the ground topography and  $m$  the effective ground-to-volume amplitude ratio accounting for the attenuation through the volume

$$m(\vec{w}) = \frac{m_G(\vec{w})}{m_V(\vec{w})I_0} \quad (\text{C.1.5})$$

The extinction coefficient corresponds to a mean extinction value for the vegetation layer, and is a function of the density of scatterers in the volume and their dielectric constant.  $\kappa_z$  is the effective vertical interferometric wavenumber after range spectral filtering, which depends on the imaging geometry and the radar wavelength

$$\kappa_z = \frac{\kappa\Delta\theta}{\sin(\theta_0)} \quad (\text{C.1.6})$$

$\Delta\theta$  is the incidence angle difference between the two interferometric images induced by the baseline. According to Equ. (C.1.3), the effective scattering centre is located above the ground at a height that depends on the ground-to-volume amplitude ratio  $m$  as well as the attenuation length of the vegetation layer.

Equ. (C.1.3) - (C.1.6) address the coherent random volume over a ground scattering problem as a four parameter problem regarding: 1) the volume thickness  $h_V$ , 2) the volume extinction coefficient  $\sigma$ , 3) the effective ground-to-volume amplitude ratio  $m$ , and, 4)  $\phi_0$  the phase related to the underlying topography.

This random volume over ground model has been used in several vegetation parameter inversion scenarios from multi-parameter InSAR data. In [2,3] it has been used in an early form for the estimation of forest height from single polarisation multi-baseline / temporal ERS (C-band) data and in [7] for the estimation of forest parameters and underlying topography from multi-baseline airborne (TOPSAR C-band) interferometric data. Finally, in [36,37,40,69] the random volume over ground model is used for the inversion of single-baseline fully-polarimetric InSAR data.

The only alternative scenario, apart from a random volume over a depolarising ground, which may interpret the experimental observations, is the presence of orientation effects in the volume (vegetation layer) [36,37]. The oriented volume problem has been considered in [54] and [55] where the analytical solution of the problem as well as experimental validation has been shown. However, as will be

discussed in the following, the evaluation of a large amount of experimental data has shown for forest vegetation at wavelengths up to L-band orientation effects - at least for forest vegetation - can be excluded.

In [57,58] an interesting alternative approach to analyse polarimetric interferometric data was addressed. Super-resolution techniques (ESPRIT Algorithm) have been used in order to estimate the number of inherent effective scattering centres in the data and their height difference. The application of the technique on the SIR-C data sets at L-band, indicated the existence of two dominant inherent scattering centres, corresponding to the ground and forest canopy. These results are in accordance and strengthen the random-volume-over-ground scattering model assumption.

### C.1.3.3 RVoG model inversion

It is designative that, even this simple two layer model leads to an underestimated inversion problem for a conventional single-channel single-baseline interferometric system. Consequently, in the absence of a priori information and/or simplifying assumptions, multi parameter interferometric configurations are needed for its inversion. The random volume over ground scattering model can be inverted by a single frequency, fully polarimetric, single baseline configuration or by a single frequency, single polarisation, multi-baseline configuration.

**Multi-baseline single frequency single polarisation interferometry:** By varying the baseline all four model parameters (Height, Extinction, Underlying Topography and Ground to Volume amplitude ratio) remain the same. The only parameter that changes is the effective vertical wavenumber ( $kz$ ). So, any additional baseline offers two more observables while at the same time do not introduce additional unknowns. Accordingly, the inversion of the RVoG scattering model can be (in principal) performed using only two baselines, in form of an non-linear optimisation problem with four unknowns and four observables [7]:

$$\begin{bmatrix} \text{Forest Height} \\ \text{Canopy Extinction} \\ \text{Underlying Topography} \\ \text{Ground / Volume scattering} \\ \text{amplitude} \end{bmatrix} = [M]^{-1} \begin{bmatrix} \text{Interferometric Phase and Coherence} \\ \text{from two (or more) Baselines} \end{bmatrix} \quad (\text{C.1.7})$$

The availability of more baselines allows potentially the estimation of vertical vegetation structure profiles [8,9]. However, in order to obtain two baselines a well-conditioned inversion problem, the two baselines have to be significantly different. The use of long baselines implies a loss in interferometric coherence due to volume decorrelation that can be compensated only at the expense of spatial resolution. Furthermore, the realisation of large baselines at airborne single-pass implementations - especially at lower frequencies (i.e., L- or P-band) - can be difficult and feasible only with high technological effort. The acquisition in repeat pass mode introduces temporal decorrelation effects that limit the performance or even the applicability of the approach.



**Single-baseline single frequency fully polarimetric interferometry** is the second way to invert the RVoG model. As the propagation through the volume is scalar, i.e. the extinction coefficient  $\sigma$  is independent of polarisation, the random volume contribution on the interferometric coherence  $\tilde{\gamma}_v$  is polarisation independent. Polarisation influences the interferometric coherence only through the variation of the ground/volume amplitude ratio  $m$ . Accordingly, any additional polarimetric channel operating in a single baseline interferometric mode increases the number of observables by two, but at the same time introduces one additional unknown parameter: the ground-to-volume amplitude ratio for the new polarisation [35,40]. Consequently, the inversion of the RVoG scattering scenario using a single baseline requires at least three independent polarisations, and therefore, fully polarimetric interferometric data [37,40].

$$\begin{bmatrix} \text{Forest Height} \\ \text{Canopy Extinction} \\ \text{Underlying Topography} \\ \text{Ground/Volume scattering} \\ \text{amplitude for each polarisation} \end{bmatrix} = [M]^{-1} \begin{bmatrix} \text{Interferometric Phase and Coherence} \\ \text{in three Polarisation} \end{bmatrix} \quad (\text{C.1.8})$$

In principal, the inversion problem as stated above can be solved by using any three orthogonal polarisation states. However, the performance of the non-linear inversion depends on the choice of the three selected polarisations. The key point for achieving high parameter estimation accuracy is a well-conditioned inversion problem. The analysis of the inversion performance has shown that polarisations characterised by a wide ground-to-volume amplitude ratio spectrum lead to best parameter estimation performances [40,65,66]. The polarisations obtained from the coherence optimisation algorithm are characterised by the widest possible ground-to-volume amplitude ratio spectrum and therefore, lead to the best conditioning of the inversion problem. Conventional polarisations, as for example the linear polarisations HH, HV, and VV, lead in general to a sub-optimum inversion performance.

A more severe problem arises from the fact that this six-dimensional optimisation problem has in general no unique solutions [40], and a regularisation is required in order to establish uniqueness [67,68,69]. One way to overcome this problem - without increasing the number of observables introducing a second baseline - is to force the smallest  $m = 0$  ( $m_1 > m_2 > m_3 = 0$ ) [69,70].

Regarding the forest height estimation, the effect of this assumption is not serious [70], as the errors introduced by the assumption are compared to the intrinsic uncertainties in the data. However, as mentioned above, there is no polarisation channel that can be considered to have a zero ground scattering component. Therefore, it is of importance to ensure minimisation of the ground to volume ratio employing the optimum polarisation channels as the cross-polarised channel does not necessarily minimise the ground component. However, the most elegant way to overcome this ambiguity problem, is by introducing a second baseline [9]. This allows an unambiguous and unrestricted estimation of all model parameters [9].

Up to now, the inversion performance of this technique has been validated for deciduous as well coniferous forest stands in different European test sites with flat and

mountainous terrain predominantly at L-band. In all cases the estimation accuracy of forest height lies on the order of 10% [37,40,61,72,73] indicating the stability and robustness of the approach. Recently, tree height inversion results obtained using the same approach at P-band over tropical forest have been reported in the literature [63].

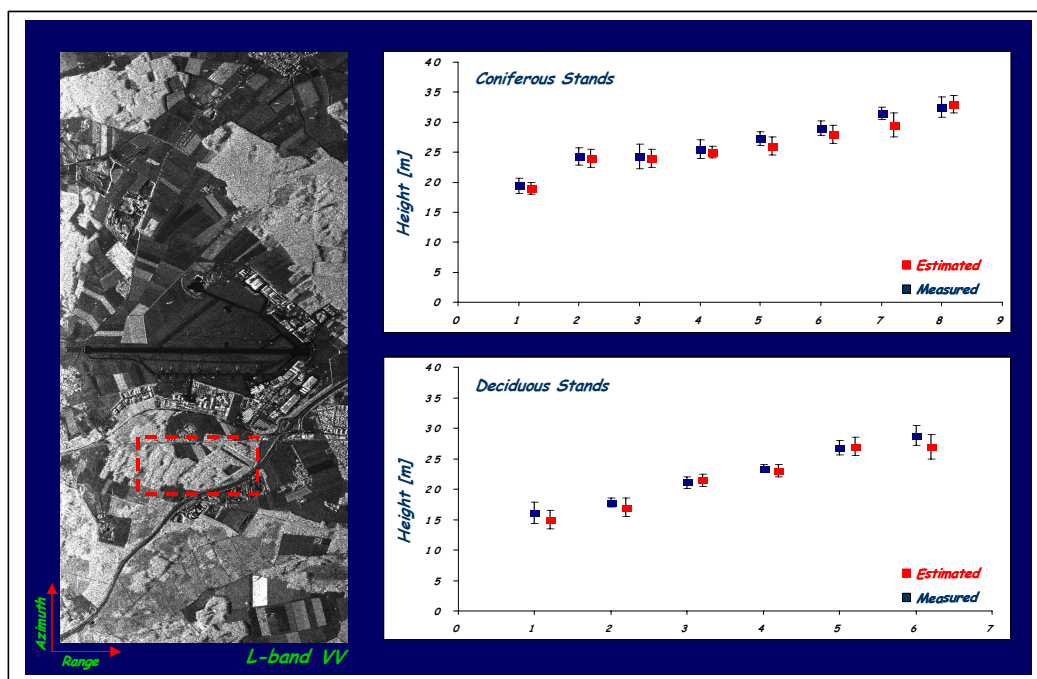


Figure C.1.2: Left: L-band SAR Image. Right: Forest Height: Estimated and measured.

Figure C.1.2 shows tree-heights (estimated and measured) obtained from the inversion of single-baseline single frequency fully polarimetric interferometric data from the Oberpfaffenhofen test site in Germany.

The performance of the inversion technique has been also tested using laboratory and ground-based scatterometer data in more controlled experimental environments. The obtained results are similar to the results reported to be obtained from SAR data. The estimation of vegetation height is good, while the estimated of the other parameters indicating the estimation ambiguity problem mentioned above [71]. While the inversion of forest height has been validated against accurate ground measurements, the other obtained parameters, i.e. forest extinction, underlying topography, and ground scattering amplitudes, have not been validated up to now mainly because of the lack of accurate ground measurements.

There are main advantages of the single-baseline fully polarimetric mode compared to the multi-baseline single polarisation approach. The first one is that additional to the volume parameters, the inversion of polarimetric interferometric data provides also estimates about the effective ground-to-volume amplitude ratio at the different polarisations. This information about the ground scattering under the vegetation layer

may open the way for the parameter estimation of vegetation covered terrain. The second one is that it requires only a single baseline. This can be essential regarding space-borne implementation scenarios.

However, the inversion of the random-volume-over-ground scattering model consumes five out six available observables. There is no - much - more remaining information that will allow the consideration of a more complicated vegetation structure. Therefore, extension of the scattering model requires either the use of a priori information or more observables, as for example by using one or more additional baselines.

### C.1.3.4 RVoG model validation

The significance of any scattering model depends on its ability to fit experimental observations. Therefore, it is essential for any model-based parameter estimation to ascertain about the validity of the underlying model. One of the big advantages of the RVoG model is that it is possible to prove its validity from single-baseline polarimetric interferometric data without the need of any other information. The key for this is hidden in the geometrical interpretation of the model.

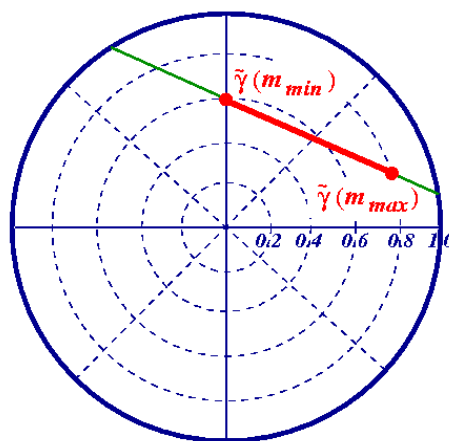


Figure C.1.3: Geometrical Interpretation of the RVoG Scattering Model

One key steps in understanding the role of polarisation in the RVoG scattering model is its geometrical interpretation. To obtain a geometrical interpretation of Equ. (C.1.3), it is important to recognise that the only parameter that varies with polarisation is the ground-to-volume amplitude ratio  $m$ . Thus Equ. (C.1.3) can be rewritten as

$$\tilde{\gamma}(\vec{w}) = \exp(i\phi_0) \left[ \tilde{\gamma}_v + \frac{m(\vec{w})}{1+m(\vec{w})} (1 - \tilde{\gamma}_v) \right] \quad (\text{C.1.9})$$

This is the equation of a straight line in the complex plane, generated by the real parameter  $m$ . The line is going through the constant point  $\exp(i\phi_0) \tilde{\gamma}_v$  with direction

$\exp(i\phi_0)(1 - \tilde{\gamma}_v)$ . Accordingly, the RVoG model predicts that the variation of the complex coherence as a function of polarisation is along a straight line inside the complex unit circle [59,60,40]. In other words, by changing the polarisation state of the two interferometric images forming the interferogram, the loci of the corresponding complex coherences lie on a line inside the complex unit circle. The movement along a direction on the line corresponds to a monotonic (increasing or decreasing) change in  $m$ .

Hence, a direct assessment of the validity of the RVoG model is possible by forming interferograms using different polarisations, plotting their complex coherences on the complex unitary circle and measuring their deviation from a straight line [60,74]. This can be performed by means of chi-square statistics. Using  $N$  different polarisations for forming an interferogram one obtain  $N$  complex coherence values  $\tilde{\gamma}_i$ . If the RVoG model is valid then the real and imaginary parts of  $\tilde{\gamma}_i$  have to satisfy

$$\text{Im}\{ \tilde{\gamma}(\bar{w}) \} = A \text{ Re}\{ \tilde{\gamma}(\bar{w}) \} + B \quad (\text{C.1.10})$$

To measure how well the data satisfy this condition accounting for the intrinsic variance of amplitude and phase of the estimated complex coherences when  $|\tilde{\gamma}_i| \leq 1$  a chi-square merit function can be used which in this case is

$$\chi^2(A, B) = \sum_{i=1}^N \frac{\text{Im}\{ \tilde{\gamma}(\bar{w}_i) \} - A \text{ Re}\{ \tilde{\gamma}(\bar{w}_i) \} - B}{\sigma_{\text{Imi}}^2 + A^2 \sigma_{\text{Rei}}^2} \quad (\text{C.1.11})$$

$\sigma_{\text{Rei}}^2$  and  $\sigma_{\text{Imi}}^2$  are the standard deviations of the Real and Imaginary part of  $\tilde{\gamma}_i$  respectively, and can be estimated directly from the data. Minimisation of Equ. (C.1.11) by setting the partial derivatives of  $\chi^2(A, B)$  with respect to  $A$  and  $B$  to be zero, allows a least-squares determination of  $A$  and  $B$ ,

$$\partial \chi^2 / \partial A = 0 \quad \text{and} \quad \partial \chi^2 / \partial B = 0 \quad (\text{C.1.12})$$

Note that while the condition - and thus the resulting equation - for the intersection point is linear, the condition for the slope is non-linear, due to the appearance of  $A$  in the denominator of Equ. (C.1.11). The agreement between the data and the model can be expressed by the “goodness” of the fit given by the probability  $Q$

$$Q = \Gamma\left(\frac{N-2}{2}, \frac{\chi^2}{2}\right) \quad \text{with} \quad 0 \leq Q \leq 1 \quad (\text{C.1.13})$$

where  $\Gamma(...)$  is the incomplete gamma function. Large  $Q$  values indicate a good agreement between data and model while low  $Q$  values make the application of the RVoG model questionable.

Using this simple but essential concept a variety of Pol-InSAR data sets acquired over different test sites - including the ecologically important temperate, boreal and tropical forests - by different sensors have been evaluated with respect to the validity of the RvoG model. Figure C.1.4 shows the  $Q$  maps obtained over the Kudara, Russia test site (SIR-C/L-band) as a representative site for boreal forest conditions.

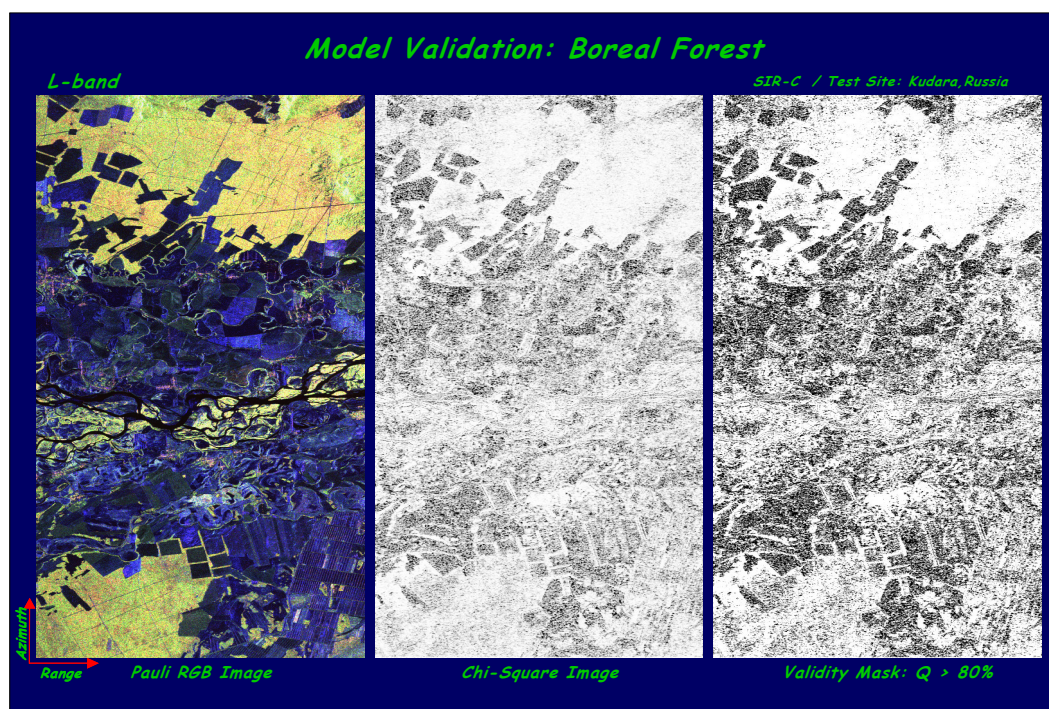


Figure C.1.4: Left: SAR Image, Middle  $Q$  Map, Right Mask for  $Q > 80\%$  for the Kudara Test Site.

The chi-square test can be seen as an indirect way of testing the assumption of the Random Volume (RV). In general, high  $Q$  values indicate a *good* line fit and verify thus the Random Volume (RV) assumption as orientation effects introduce deviations from the line. Regarding the inversion performance the “line test” do not provide evidence. This becomes clear by looking at the case where the line shrinks to a point. Assuming the baseline not to be zero, this means that all polarisations lead to interferograms with the same coherence values (less than one). This indicates the presence of a random volume (no orientation effects and no ground scattering). In this case the RV assumption is valid, but inversion is not possible due to the fact that all complex observables are the same.

The inversion performance depends mainly on the length of the visible line. Longer lines lead to more accurate parameter estimates than shorter lines (in general) [66].

However, the chi-square test fails (i.e. a high probability  $Q$  does not reflect validity of the RV assumption) in the case of very low coherences. In this case the variance of real and imaginary part of the complex coherences is so big that make *every fit a good fit*. This becomes clear by looking to the river at the middle of the Kudara test site on

Figure C.1.4. The river itself is totally decorrelated but appears with high  $Q$  values in the  $Q$ -map. Yet, both scenarios (i.e., equal coherences and very low coherences) can be recognised directly and can be accounted in the interpretation of the  $Q$  maps.

A final uncertainty in the interpretation of the chi-square test is the question about how strongly orientation effects bend the line. This is a function of baseline and for some baseline configurations uncertainties in the interpretation may be possible. However, a strong variation of  $Q$  with baseline is an indication for such cases. Nevertheless, the *line test* is a very valuable test as it allows data scrolling and conclusions about large image parts.

### **C.1.4 Surface parameter estimation from Pol-InSAR data**

The sensitivity of microwave scattering to the dielectric properties and the geometric structure of bare soil surfaces makes radar remote sensing a challenge for a wide range of environmental issues related to the condition of natural surfaces. Especially, the potential for retrieving soil moisture with a high spatial and/or temporal resolution represents a significant contribution to hydrological and meteorological modelling, as well as to economical optimisation of agricultural procedures.

Surfaces are characterised in terms of their material and geometrical properties. One of the main parameters describing the material properties of surfaces is the volumetric soil moisture content. The relation to the radar backscatter signal is given primarily by the dielectric constant. The geometric properties are described by the spatial roughness scales in both, horizontal and vertical directions, in terms of the surface RMS height  $s$  and the surface correlation length,  $l$  respectively. In the scattering problem both parameters are scaled by the actual wavelength in terms of  $ks$  and  $kl$  ( $k=2\pi/\lambda$ ) [75,76,77,78].

#### **C.1.4.1 SAR polarimetry**

The main problem for the quantitative estimation of soil moisture and/or surface roughness from SAR data lies in the separation of their individual effects on the (coherent) backscattered signal. Polarimetry plays an important role as it allows a direct or indirect separation of roughness and moisture induced effects. The scattering problem of electromagnetic waves from randomly rough surfaces has been an actual research topic over decades and is still not satisfactorily solved, as no exact closed-form solutions exist hitherto. However, for many practical applications, approximate solutions are sufficient [79,80,81]. As there is no linear relationship between the surface parameters and the backscattering signal scattering models or empirical relations have been developed for their estimation. In the field of radar remote sensing the most common approximation methods are based on the evaluation of backscattering amplitudes considering single or dual-channel SAR data. The choice of an appropriate scattering model is essential for the quantitative estimation of the surface parameters. On the one hand side, the model must contain enough physical background and on the other hand it should have a right balance between the amount of observables and the desired parameters. As the observed object (natural surfaces) is



complex a priori information and/or assumptions help to simplify the inversion problem [82,83,84]. Hence, in order to obtain an accurate soil moisture estimates, scattering models require information about the surface roughness or the roughness is considered as a disturbing effect and conditions are developed in order to minimise its influence.

However, an independent estimation of roughness conditions is not possible by using a single polarisation and single- frequency SAR data. By increasing the number of observables - using fully polarimetric data - the number of surface parameters and their estimation accuracy increases [85,86,87]. However, the main limitation of using polarimetric backscattering amplitude models is their insufficiency to predict / interpret secondary scattering and depolarisation effects, resulting in a biased surface parameter estimates.

A large class of natural surface scatterers, is characterised by secondary and multiple scattering effects. With increasing surface roughness, relative to the wavelength implied, the effect of multiple scattering becomes stronger, generating an adequate |HV| scattering component. Also the case of vegetation-covered surfaces can not be accounted with surface scattering models. Dihedral scattering due to small correlation lengths characterised by |HH| > |VV|, and/or diffuse scattering (|HV| contribution), affecting the backscattered signal. Both effects lead to a violation of the requirements, or to a biased estimation of the roughness and moisture parameters.

#### C.1.4.2 Interferometric effects

While the problem of soil-moisture / roughness estimation of bare surfaces has been extensively analysed in terms of conventional polarimetric SAR data, the information content of interferometric data regarding these parameters has not been illuminated sufficiently. In the following we review the different decorrelation contributions on the interferometric coherence with respect to the estimation of surface parameters.

The interferometric coherence (between two images S1 and S2 acquired from slightly different look angles) is given by

$$\gamma := \frac{|\langle S_1 S_2^* \rangle|}{\sqrt{\langle S_{11} S_{11}^* \rangle \langle S_{22} S_{22}^* \rangle}} \quad (\text{C.1.14})$$

For a single pass interferometric system (i.e. ignoring temporal decorrelation) two are the main decorrelation contributions [1]

$$\gamma = \gamma_{\text{Spatial}} \gamma_{\text{SNR}} \quad (\text{C.1.15})$$

$\gamma_{\text{Spatial}}$  expresses the decorrelation caused by the different projections of the scatterer reflectivity into the two SAR images due to their slightly different acquisition angles. Thus, it is a baseline dependent contribution which can be splitted into two individual contributions:

$$\gamma_{Spatial} = \gamma_{Range} \gamma_{Volume} \quad (C.1.16)$$

$\gamma_{Range}$  describes the decorrelation due to the different projections of the ground-range scattering reflectivity. On the other side,  $\gamma_{Volume}$  expresses the decorrelation caused by the different projections of the vertical distribution of the scattering reflectivity.  $\gamma_{Volume}$  is given by the Fourier transformation of the vertical distribution of the scatterer. Assuming a homogeneous scatterer distribution with an effective height of  $s_V$ ,  $\gamma_{Volume}$  becomes

$$\gamma_{Volume} \sim \frac{\sin(\kappa_z s_V)}{\kappa_z s_V} \quad (C.1.17)$$

where  $\kappa_z = (\kappa \Delta \theta) / \sin(\theta_0)$  is the vertical wavenumber,  $\Delta \theta$  baseline induced difference in the incidence angles and  $\theta_0$  the reference incidence angle.

$\gamma_{SNR}$  expresses the decorrelation caused by the uncorrelated additive noise contributions in the two interferometric images [88]

$$\gamma_{SNR} = \frac{1}{1 + (SNR)^{-1}} \quad (C.1.18)$$

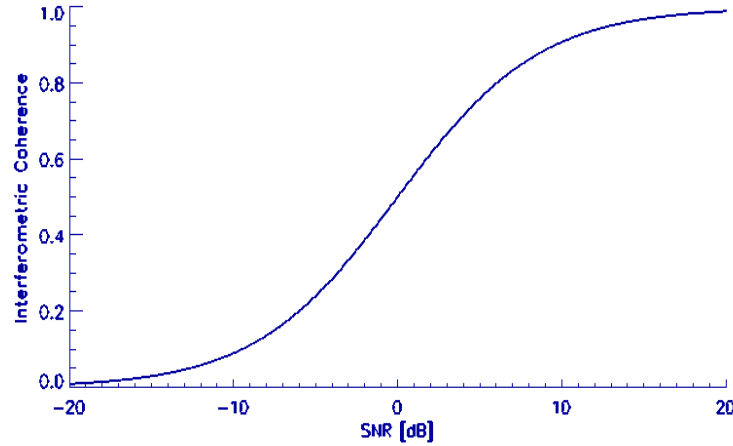


Figure C.1.5: SNR decorrelation as a function of the interferometric coherence.

It depends on the backscattering intensity of the scatterer and is independent of the interferometric baseline. Figure C.1.5  $\gamma_{SNR}$  is plotted against SNR. For  $SNR = 0$  [dB]  $\gamma_{SNR} = 0.5$ , for SNR values below -10 [dB]  $\gamma_{SNR}$  drops below 0.1 while for SNR values above 15 [dB]  $\gamma_{SNR} \sim 1$ .

Concerning now the information content of the individual coherence contributions with respect to geometrical and dielectric surface parameters the following conclusions can be stated:

- $\gamma_{Range}$  depends (in first order) on the correlation properties of the ground range reflectivity spectrum. The variation of the statistical parameters of the surface (i.e. roughness and correlation length) effects mainly the amplitude distribution of the ground range reflectivity spectrum but not its correlation properties. Thus, the amount of  $\gamma_{Range}$  does not provide directly information about the surface characteristics.
- $\gamma_{Volume}$  is sensitive to height variations in the order of tenths of  $2\pi/\kappa_z$ . After filtering the image spectra a total correlation for surface scatterer and changes depending only on the volume decorrelation can be observed. This observation was first addressed in [89] using multi-baseline interferometric ERS-1 SAR data to derive experimental results and has been confirmed using simulated multi-baseline interferometric SAR data. The approach has a high potential with respect to vegetation parameters estimation. Considering the estimation of surface parameters, the sensitivity to height variations of  $\gamma_{Volume}$  in relation to the height variation of natural surfaces which are characterised by a rms-height  $s$  being in the order of tenths of centimetres is very small. The vertical wavenumber has to be on the order of  $\sim 10$  to provide sensitivity of  $\gamma_{Volume}$  to  $s$ . Such  $\kappa_z$  values exceed the critical baseline for most realistic system configurations.
- $\gamma_{SNR}$  contains information of the surface characteristics, as the backscattered intensity depends on both, geometric and dielectric properties of the surface.

Recapitulating, the baseline dependent contributions of the interferometric coherence do not contain practical useful information about the underlying surface properties. After spectral filtering of both images to a common ground-range bandwidth  $\gamma_{Range} = 1$ , so that  $\gamma_{Spatial} = 1$ . Thus, the only remaining contribution sensitive to roughness and dielectric constant conditions of a surface scatterer is  $\gamma_{SNR}$ . Its information content, for a given system noise level, is in principal nothing more than the information about the backscattered intensity. Yet, the sensible difference between  $\gamma_{SNR}$  and intensity lies in the speckle: while conventional SAR images are affected by speckle, the two interferometric images - after spectral filtering - contain the same speckle contributions which cancel each other out by forming the interferogram.

A theoretical treatment of surface roughness effects in SAR interferometry, where surface roughness is addressed as a volume decorrelation source, is given in [90]. However, the required baselines configurations exceed by far the critical baseline of existing and planned conventional interferometric systems. A more realistic approach combining a coherent polarimetric scattering model to interpret the contributions roughness and moisture content of interferometric observables over rough surfaces at different polarisations has been addressed in [91,92,93].

The estimation of surface parameter from interferometric observables is still under investigations but the first observations indicating that the interferometric coherence could help to extend the validity range of conventional polarimetric models.

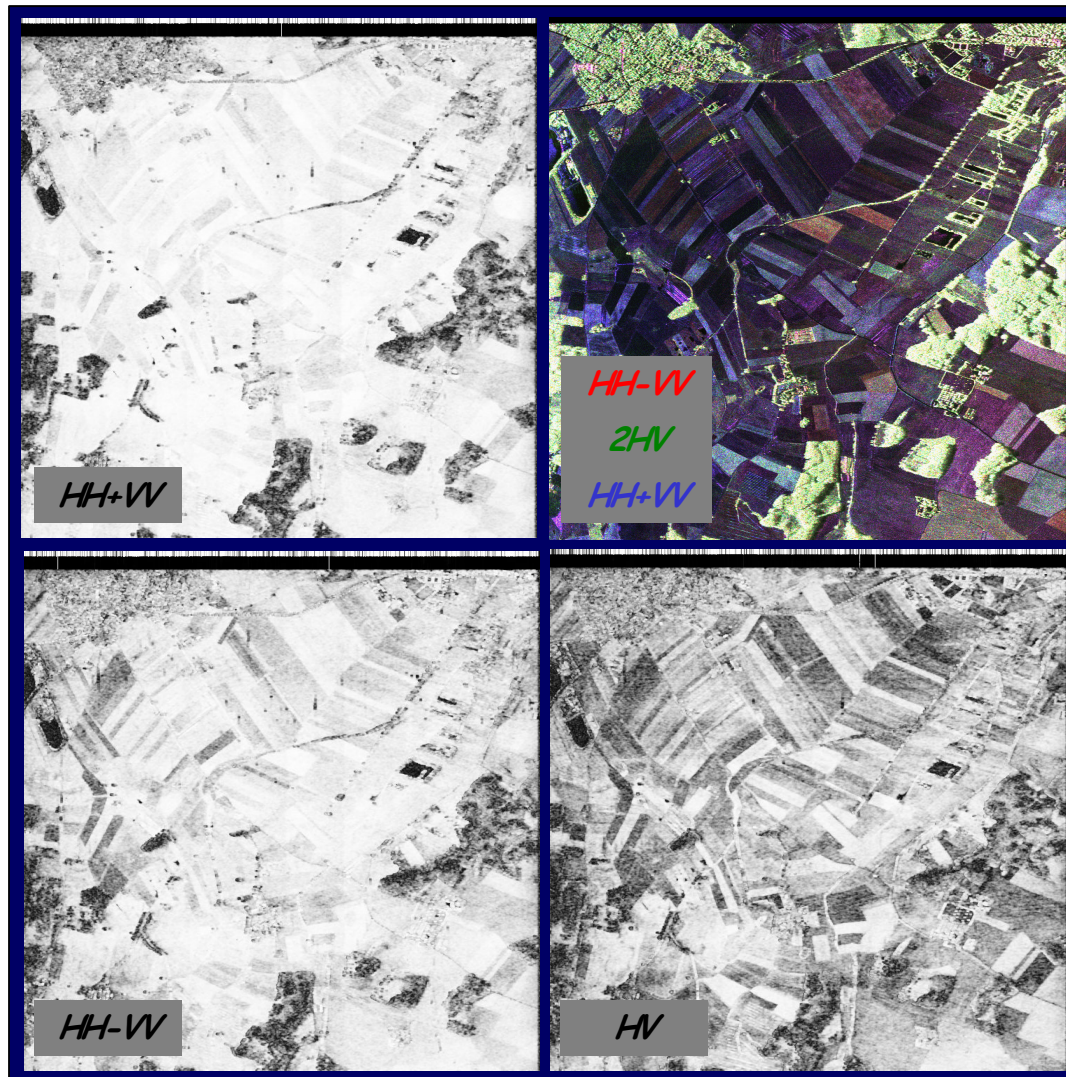


Figure C.1.6: Interferometric coherences at different polarisations over bare fields [91].

### C.1.5 Summary and conclusions

The literature review on quantitative vegetation and surface parameter estimation from multi-parameter InSAR data can be summarised in the following points:

- There is no direct relation between scattering parameters and interferometric observables (phase and coherence) at any frequency or polarisation. Hence, a direct estimation of bio-/geo-physical vegetation and/or soil parameters from interferometric data is in general not possible.
- Nevertheless, accurate forest parameter estimation has been demonstrated based on the inversion of scattering model that relate the scattering parameters to the interferometric observables.

- However, due to the complexity of the vegetation and surface scattering processes, the robust inversion of scattering models requires an extended observation vector in terms of multi-parameter InSAR observations.

Regarding the possible ways of extending the observation vector now

- Frequency diversity is not the optimal choice because several parameters of the scattering process are frequency dependent. Consequently, too many model parameters change with frequency leading (in general) to ill-conditioned inversion problems.
- Temporal diversity provides information about the dynamic behaviour of scatterers and allows qualitative conclusions as well as classification of scattering parameters. However, the presence of temporal decorrelation limit seriously the performance of model based quantitative parameter estimation.
- Baseline diversity is one promising ways to extend the observation vector. The change of baseline does not affect the main parameters of vegetation and surface scattering models and leads so to well conditioned inversion problems. The main constrain is - again - the effect of temporal decorrelation when the baselines are obtained in a repeat pass mode.
- Polarisation diversity is an alternative effective way to extend the observation space. The propagation through forest canopy layer(s) is - at least at C- and L-band – widely independent of polarisation so that the number of volume parameters in the inversion process does not increase by adding more polarimetric observations. Also here, the main constraint arises from temporal decorrelation effects. However, the fact that only a single baseline is required makes implementation scenarios more feasible.

Regarding the scattering models used for quantitative parameter estimation following points can be made:

- Statistical scattering models seem to be more promising than direct models. The main reason for this is that they are addressed in terms of a small number of parameters, and thus their inversion can be performed using realistic observation vectors. However, their correctness in terms of ability to fit the experimental data (and thus the underlying scattering process) has to be warranted.
- The most used statistical scattering model for vegetation scattering is the random-volume-over-ground scattering model. It fits sufficiently several experimental observations over different forested environments at C-, L-, and/or P-band and its inversion led to sensible estimation results.

## C.2 IDENTIFICATION OF VARIABLES AND TECHNIQUES

### C.2.1 *Physical vegetation and surface parameters*

Comparing vegetation (forest and agriculture) and surface (vegetated and bare) parameter estimation, the best understood and most developed and validated applications are the ones concerning forest parameters. Keeping in mind that the main objective of this study is to evaluate parameter estimation with reduced observation vectors we propose to focus on inversion scenarios for forest parameters. Regarding the forest parameters that can be potentially estimated from the inversion of multi-parameter interferometric data, following parameters are identified:

1. Tree/ forest height is one of the most important parameters in forestry along with dbh/ basal area<sup>1</sup> and tree species. Being a standard parameter in forest inventories, tree height is hard to be measured on the ground and typical estimation errors are given with 10%, yet increasing with forest height and density. All three parameters, height, dbh and tree species, are used to calculate the biomass of a tree, or the forest as the sum of all trees.

Inventory tables for managed (here: single species, single layer) temperate forests [94] suggest that by only using the parameter mean tree height, forest biomass can be estimated with an error of +/- 15% due site conditions and different forest management [95], or species [97].

Since table-conform forests refer to an ideal situation, it is necessary to test the height-biomass allometry with real forest inventories data. When assuming that no forest (especially not a natural one) is really mono-layered, it becomes clear that the mean tree height is not very representative. It will even differ when different inventory directives set different dbh limits, thereby including or excluding smaller trees. Probably, the most significant forest height unit for a number of applications is the upper canopy height, or in forestry terms h100, the height of the 100 highest trees (per hectare). Already in 1973, the FAO recommended the upper canopy height as a prime forest parameter in global ecosystem classification [96]. An h100-biomass allometry does not substantially differ from the table-derived mean height-biomass allometry since in mono-layered forests the difference between mean height and h100 does not exceed 2m. Tested for its suitability using real forest inventory from montane temperate spruce forests (managed), it could be shown, that h100 explains biomass with an  $r^2$  of 0.80, mainly affected by varying stand densities, and basal area with an  $r^2$  of 0.74, mainly affected by the species composition [98].

According to the results published in the literature, its estimation can be performed with an accuracy of about 10-20%. This, combined with the fact

---

<sup>1</sup> Dbh: diameter at breast height: 1.35m; basal area: cross-section of all trees at breast height: 1.35m



that forest height cannot be estimated - on a global scale - with comparable accuracy or spatial resolution by any other remote sensing technique make the verification of the extraction of vegetation height from polarimetric interferometric data a very important objective of this study.

2. Underlying topography is an important commercial parameter as it allows the correction of the vegetation bias always present in conventional interferometry. Stable underlying topography estimation from dual polarised interferometric data may be of particular interest with respect to ASAR / ENVISAT like configurations.
3. Forest biomass is essential for ecological modelling and forest inventory and is today the big unknown for global ecosystem change modelling. Its direct (regression based) estimation from SAR data has been subject of many studies and is restricted by relative low saturation levels that make a global biomass inventory by means of conventional SAR techniques very limited. On the contrary, allometric estimation of forest biomass from forest height is almost unsaturated and is a good candidate for a global above ground biomass inventory. Because of the actual scientific and political demand for accurate biomass estimation, the question of biomass estimation from polarimetric interferometric SAR data is proposed as one of the key objectives of this study.
4. Canopy extinction: The density of the vegetation cover affects the radar signature through extinction of the forward propagating wave. This extinction is related to structural attributes such as the leaf area index (LAI) of the canopy and canopy density.

**In accordance with ESA forest height has been selected as the parameter for further investigation in the frame of this study.** Its importance in ecological and commercial applications combined with the potential to be estimated from reduced observations vectors – as required by ESA's Statement of Work - have been the main reasons for this decision.

## **C.2.2 Selected data sets**

### **C.2.2.1 Oberpfaffenhofen test site, Germany**

The test site is a mixed forest/urban/agricultural region surrounding the DLR centre in Oberpfaffenhofen, near Munich in Germany. The forested area includes homogeneous beech and pine stands with different ages and heights as well as mixed forest stands. Figure C.2.1 shows the L-band SAR amplitude images at three different polarisations.

**SAR data:** For this test site, a large number of multi-baseline, multi-temporal, fully polarimetric interferometric data sets at L-band are available. The data are collected by DLR's E-SAR system continuously over the last years. Some of the available SAR data are summarised in Table C.2.1

Table C.2.1  
Available SAR data for the Oberpfaffenhofen test site.

<i>Frequency</i>	<i>Polarisation</i>	<i>Interferometry</i>	<i>Spatial Baselines</i>	<i>Temporal Baselines</i>
L-band	HH-HV-VH-VV	Repeat-Pass	5	10 min.
X-band	VV	Single-Pass	1	-



Figure C.2.1: HH, HV, and VV SAR amplitude images at L-band of the proposed Oberpfaffenhofen test site.

**Ground measurements:** The available ground measurements include forest height, canopy density, and species measured at a sufficient large number of sample points and geographically referenced information on topography. Optical and multi-spectral remote sensing data sets are also available.

### C.2.2.2 Fichtelgebirge test site, Germany

The Fichtelgebirge area, is a mountainous region with representative managed forests stands of varying structure and age for two dominant commercial forest species: European beech (*Fagus sylvatica* L.) and Norway spruce (*Picea abies* Karst. L.). The Fichtelgebirge area varies in topography, edaphic situation, and forest management practices from 650 m a.s.l. to 1054 m a.s.l.. The variability of its site climate, terrain, and soils in combination with two monospecific forest types with a resulting large gradient in tree age, stand height, stand density, and biomass (from 100 tons/ha up to 400 tons/ha) renders it as an excellent test site for this study.

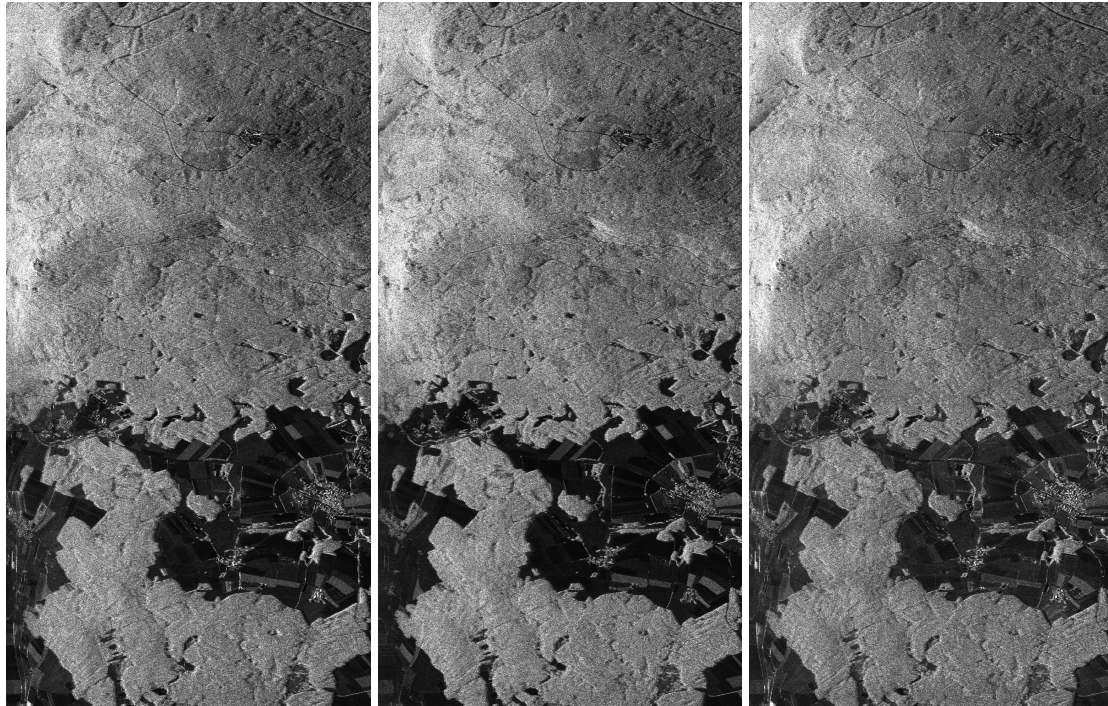


Figure C.2.2: HH, HV, VV amplitude images at L-band of the Fichtelgebirge test site.

**SAR data:** E-SAR Airborne repeat pass interferometric fully polarimetric data at L-band with multiple baselines acquired using different imaging geometries. X-band single pass interferometric data for topographic reference. Available SAR data are summarised in Table C.2.2.

Table C.2.2:  
Available SAR data for the Fichtelgebirge test site.

<i>Frequency</i>	<i>Polarisation</i>	<i>Interferometry</i>	<i>Spatial Baselines</i>	<i>Temporal Baselines</i>
L-band	HH-HV-VH-VV	Repeat-Pass	3	10 min.
X-band	VV	Single-Pass	1	-

**Ground measurements:** A extensive ground measurements data base from forest inventory (Forest Inventory 2002; DbH and height measurements of statistically sampled tree within 400m<sup>2</sup> circles, regular 4 ha grid) and measurements of biomass and forest structure (University of Bayreuth, Germany, and Max Plank Institute, Jena, Germany) is available for this study. The data sets include geographically referenced information on topography, geology, soils, tree species distribution, forest inventory biomass as well as several areas with very detailed plot measurements of site conditions, tree biometric and tree growth parameters.

### C.2.2.3 Kudara test site, Russia

The test site is a mixed agricultural-forested region without strong topographic variations crossed by the Selenga River. It is located over the SE Baikal Lake Selenga River delta region of Buriatia in East Siberia, Russia. Figure C.2.3 shows the L-band SAR amplitude images at three different polarisations.

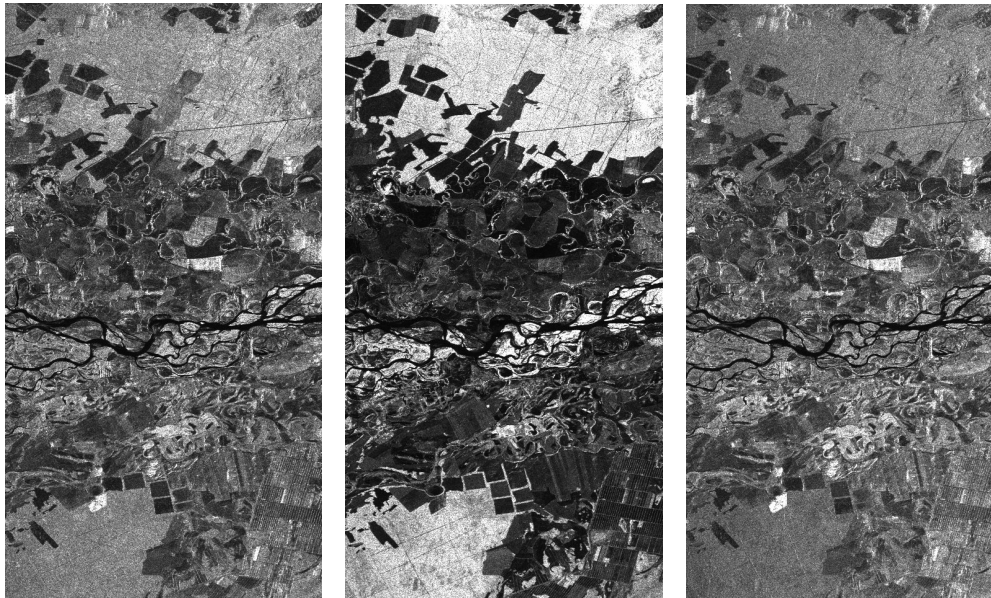


Figure C.2.3: HH, HV, and VV amplitude images at L-band of the Kudara test site.

**SAR data:** The site comprises three fully polarimetric repeat-pass interferometric data sets at C- and L-band acquired by the shuttle-borne SIR-C sensor in October 1994. The temporal baseline between the acquisitions is about 24 hours. The available SAR data are summarised in Table C.2.3.

Table C.2.3:  
Available SAR data for the Kudara test site.

<i>Frequency</i>	<i>Polarisation</i>	<i>Interferometry</i>	<i>Spatial Baselines</i>	<i>Temporal Baselines</i>
C-band	HH-HV-VH-VV	Repeat-Pass	2	24 hours
L-band	HH-HV-VH-VV	Repeat-Pass	2	24 hours

### C.2.3 Tasks and methodology

Based on the conclusions drawn out of the literature review, the list of proposed parameters and the selected test sites we propose the following tasks for this study:

**Task 1:** Evaluation of the forest height estimation accuracy using single baseline fully polarimetric InSAR data. This estimation accuracy will be the reference for the evaluation of the following tasks. For this task the following steps are proposed:

- Implementation of the inversion algorithm for the *Random-Volume-over-Ground scattering model* for a single baseline and application on the data.
- Validation of the obtained forest height estimates against the ground measurements

**Task 2:** Evaluation of the influence of a successive reduction (dual- and pseudo dual-pol.) or modification of the interferometric observation vector (multi-temporal dual-pol. instead of single-baseline quad-pol.) on the number of parameters that can be estimated and on their estimation accuracy. Emphasis will be given on scenarios providing a similar observation vector as provided by the ASAR configuration. The following steps are proposed for this task:

- Simulation of the inversion performance for the different inversion scenarios.
- Implementation of the most promising inversion scenarios and application on the experimental data.
- Validation of the obtained parameter estimates against the ground measurements.

**Task 3:** Evaluation of the impact of available a priori information (as for example the availability of an available DEM) on the different parameter inversion scenarios as well as the required accuracy for this a priori information. For this task the following steps are proposed:

- Simulation of the inversion performance for the different inversion scenarios.
- Implementation of the most promising inversion scenarios and application on the experimental data.

Validation of the obtained parameter estimates against the ground measurements.

## **C.3 ELECTROMAGNETIC INTERACTION MODELLING**

### ***C.3.1 Introduction***

In chapter C.2 tree height was selected as a promising key parameter for land surface InSAR retrieval. Therefore, this chapter is on the development and validation of direct EM scattering models to predict the complex coherence of forested terrain. Two approaches will be considered, the first based on a 3-D coherent EM model and the second on a simplified 2-layer representation of the coherence. The output of the rigorous EM model will be compared with the simplified version with a view to using the latter as the basis for height estimation via model inversion as part of chapter C.4.

### ***C.3.2 Coherent EM scattering model for InSAR studies***

To enable an assessment of coherence sensitivity to parameter variation, a full Maxwell equation based wave propagation and scattering model is used to generate test InSAR data. A capability to model forest scattering in detail has been developed at DSTO, Adelaide, Australia [108, 106]. The simulation employs a 3-D, voxel-based, vector wave propagation and scattering model, combined with detailed descriptions of tree architectures used to model the forest canopy [108, 106, 107, 103]. A more complete description of the simulation is available in [107]. In the following, some of the more salient features are described briefly.

The calculations incorporate techniques for the prediction of low frequency attenuation and scattering from forests, using enhanced wood and soil permittivity models. Rough ground effects are included in ground-target and ground-volume interactions. The forest SAR model has been validated at VHF against observation. Predictions at L-Band have been compared with SAR observations of other pine forests and the clutter and attenuation models yield values comparable with observation.

Importantly, the simulation software has been rigorously tested and validated against theoretical predictions at L-Band. Calculations for direct-ground, direct-volume, ground-volume and ground-volume-ground interactions have all been tested and shown to reproduce correct theoretical results.

The simulation is fully polarimetric, entirely coherent and deterministic, and is able to account for volume decorrelation effects in polarimetric radar interferometry. Penetration and scattering are calculated as functions of wavelength and polarisation and depend upon tree and canopy biophysical properties. Simulated SAR images are the coherent superposition of focused scattering events, each arising from a tiny element of the scene. For example, the scattering amplitude *in-situ* is estimated for each branch element as a function of platform position: the voxel method permits



modelling of the effects of canopy inhomogeneity on the local mean field. A mathematical model for the simulated coherent SAR image is

$$\underline{\underline{P}}(x_0, R_0) = \sum_j \underline{\underline{F}}_j \hat{Q}(x_0, R_0, \underline{s}_j) \quad (\text{C.3.1})$$

where

$\underline{\underline{P}}(x_0, R_0)$  is the polarimetric pixel value at cross range  $x_0$  and range  $R_0$   
 $\underline{\underline{F}}_j$  is the polarimetric scattering amplitude associated with the scene element, and  
 $\hat{Q}(x_0, R_0, \underline{s}_j)$  is the complex system point spread function depending upon the *effective scattering centre*  $\underline{s}_j$ .

Scattering amplitudes may be averaged both in azimuth and frequency. Each element has an *effective scattering centre*. For first order returns this is simply the centre of the element. For higher order returns, involving multiple reflections, the effective scattering centre is determined rapidly at run-time using knowledge of the scattering path and the antenna motion. The simulated SAR images are given in ground range and azimuth.

Direct-ground contributions are calculated from ground facet elements using a hybrid deterministic/stochastic approach. Ground facet RCS values depend on local incidence through a physical scattering model (the Bragg or small perturbation model), to which speckle is added. Direct-volume, ground-volume and ground-volume-ground interactions are calculated. All volume terms originate from the forest canopy. This is modelled as tree structures described as collections of dielectric, absorbing cylinders and pine needles. The (complex, phase containing) system point spread function is determined from SAR imaging geometry, bandwidth and processing options. The platform motion is ideal, and the platform is modelled as having a straight, uniform trajectory.

To test the model, the SAR simulator was first employed in a limited sense to simulate coherent backscatter from a random canopy above a flat ground. A point spread function matched to the airborne DLR E-SAR system was used with 0.69m azimuthal resolution and 1.38m ground range resolution. Simulations were carried out at L band (23cm wavelength) and at 45 degrees angle of incidence from 3km altitude with 10m and 20m horizontal baselines. The random canopy has a uniform density and height of 10m. Branch dimensions are Gaussian with mean length 1.5 m and standard deviation 0.2m. Branches have a uniformly random orientation distribution and constitute a mean volume fraction of 0.2%. This example provides a convenient check of the algorithm performance.

Before a sensitivity analysis of the coherent SAR simulator is shown a brief description of the various components of the simulator are provided.

### C.3.2.1 Direct-ground scattering

A digital terrain map (DTM) is interpolated and divided into triangular facets of sufficiently small size as to ensure fully developed speckle. A physical model is adopted for the ground RCS, which depends upon ground permittivity, in turn dependent upon soil moisture and frequency. For low frequency the small perturbation model (SPM) with Gaussian correlation has been deemed sufficient. The effective scattering centre is determined simply as the facet centre, and the centre of focus simply the projection of this point onto the SAR imaging plane, which may be done using near-field or far-field models. Local speckle statistics are assumed Gaussian and scattering amplitude values are drawn from distributions using the mean RCS for the facet as determined from local incidence. Speckle phase may be added to the ground return at this stage using a correlated speckle phase model. This model contains a speckle phase correlation distance which depends upon surface roughness, surface correlation length, wavelength and incidence angle. The correlated speckle phase model reduces to uncorrelated speckle phase for short wavelength and surface correlation length, as well as for large surface roughness.

The scattering amplitude is scaled by attenuation tensors determined from line-of-sight visibility through the canopy, and averaged over frequency and Doppler bandwidths. Thus, for the ground facet scattering amplitude it can be stated that:

$$\underline{\underline{F}}_{ground} = \langle \underline{\underline{\gamma}}_s \underline{\underline{S}}_{ground} \underline{\underline{\gamma}}_i \rangle \quad (C.3.2)$$

where the angular brackets denote the Doppler and frequency averaging,  $\underline{\underline{\gamma}}_s$  is the attenuation suffered over the return scattering path,  $\underline{\underline{\gamma}}_i$  the attenuation suffered over the incident path and  $\underline{\underline{S}}_{ground}$  is the unattenuated ground facet scattering amplitude.

The attenuation parameters depend upon the detail of canopy constitution and are calculated in the first order smoothing approximation based on knowledge of the scattering properties of the forest canopy, if present. Direct-ground returns may be shadowed by targets when these are included in the calculation.

### C.3.2.2 Volume scattering

The forest environment has been modelled using detailed tree architecture models for Scots Pine, provided by the University of Joensuu, Finland [107]. These take the form of collections of dielectric cylinders, with detailed information concerning sapwood and heartwood dimensions, and needle distributions. Moisture content plays a dominant role in determining attenuation by the canopy and this information is vital for correct estimation of effective canopy permittivity. The forest is described using a map of tree positions and heights, and these heights are used to extract from the tree architecture database the tree model whose dimensions most closely match the tree at the location. The trees are placed in position above the ground surface, described itself by the DTM.

Having arranged trees to form a forest canopy the calculation proceeds to take into account canopy inhomogeneity by subdividing the canopy volume into smaller sub-volumes termed “voxels”. Each voxel has dimensions commensurate with the SAR system resolution, and each contains many tree elements, which are subdivided on input to have dimensions well below the same resolution. Canopy effective permittivity is then mapped into voxels by examining voxel occupancy, and determining the contribution to mean permittivity from individual branch elements based upon knowledge of their dimensions, orientations and water contents. Note that target scattering attenuation is calculated in exactly this way, and that volume scattering events may be shadowed by targets in the same way as direct-ground scattering. To calculate direct forest clutter, each branch element is addressed in turn. The scattering centre is taken to be the centre of the branch element, and the scattering amplitude is calculated using the infinite cylinder approximation [102]. Contributions to the SAR image are averaged in Doppler and frequency as in the direct-target case so that we may (as before) write

$$\underline{F}_{\text{volume}} = \langle \underline{\gamma}_{\text{volume}} \underline{S}_{\text{volume}} \underline{\gamma}_{\text{volume}} \rangle \quad (\text{C.3.3})$$

Note that there is no calculation of multipath between tree elements since this has in theory already been taken into account in the mean-field model. This model employs the distorted Born approximation [109], which states that the local field at the scatterer is the same as the mean field at that location, which estimate incorporates multiple scattering.

Needle scattering is estimated in a statistical manner, by simulating short random walks using a physical scattering model for needles, and scaling these short walks depending upon the number of needles associated with each branch element. Calculation of direct tree scattering is purely deterministic, although the efficiency of the calculation could be improved by extending the statistical technique employed for needles to smaller branches in the upper canopy.

When determining the attenuation dyadics the voxels intersected by the line connecting the scattering tree element and the platform are determined. Passage of the wave through each voxel attenuates the wave by an amount that depends upon both the effective permittivity of the voxel, and the distance travelled through that voxel. The total attenuation is the cumulative effect of passage of the wave through all intersected voxels. Figure C.3.1 demonstrates the geometry of this voxel based approach. Voxel shading indicates the typical variation in mass density (and therefore attenuation) throughout the canopy determined from the voxel occupancies.

### C.3.2.3 Ground-volume and ground-volume-ground interactions

In general the ground has arbitrary roughness and many different scales of variation in height. The model calculations are limited to the case that the ground may be assumed locally flat (not curved), but roughened and tilted. Let the word “volume” in the following refer to any short element of the tree, be it in the trunk or stem, in the primary branches (those with origins in the stem), or in the secondary canopy.

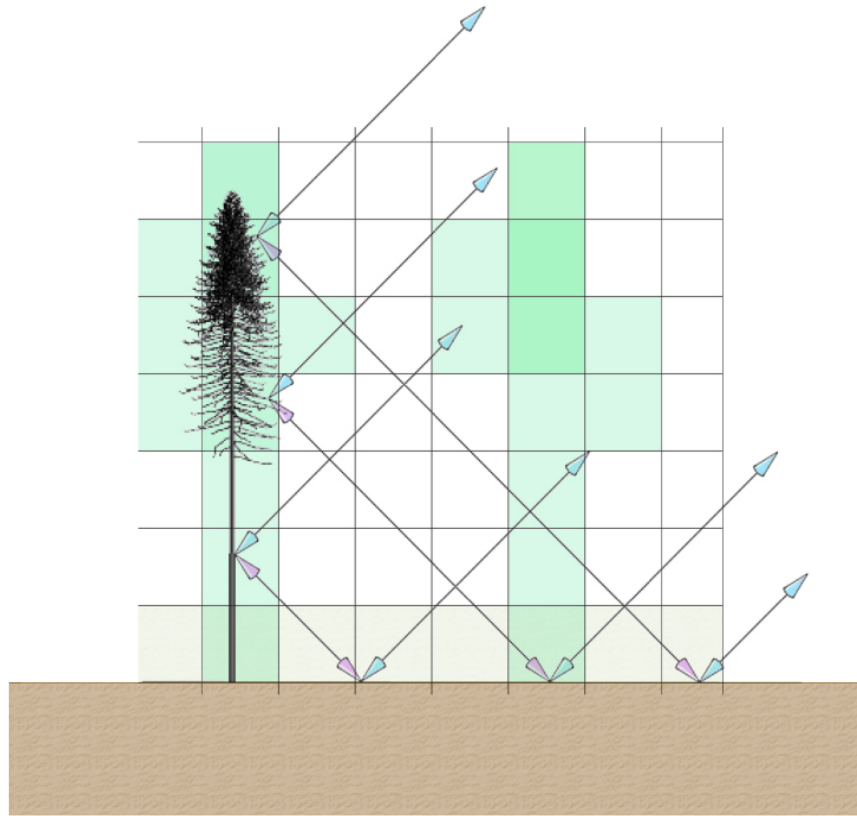


Figure C.3.1: Diagram indicating voxel subdivision of forest canopy (left) and a variety of scattering mechanisms incorporated into the calculations

Ground-volume interactions have effective scattering centres located as the projection of the volume centre in the locally flat, mean surface. The local, flat surface for each tree is determined by fitting to the digital elevation map in the vicinity of each tree (Figure C.3.2). Similarly, ground-volume-ground interactions have effective centres located at the reflection of the volume centre in the locally flat, mean surface. Scattering amplitudes for these interactions are calculated using the same infinite cylinder approximation, with ground reflection coefficients being calculated as follow. The ground acts as a primary reflecting surface in the multi-path chain. Ground and volume elements are distinguished only by their reflection properties. The ground is modelled as a rough dielectric surface, with Fresnel reflection coefficients scaled according to the surface roughness. Averaging of these interactions in Doppler and frequency is again possible if desired.

Ground-volume and ground-volume-ground contributions may thus be written in the forms

$$F_{\text{ground-volume}} = \langle \gamma_{\text{s}} S_{\text{ground-volume}} \gamma_{\text{r}} R_{\text{ground}} \gamma_{\text{i}} \rangle \quad (\text{C.3.4})$$

$$F_{\text{ground-volume-ground}} = \langle \gamma_{\text{s}} R_{\text{ground}} \gamma_{\text{r}}^- S_{\text{ground-volume-ground}} \gamma_{\text{r}}^+ R_{\text{ground}} \gamma_{\text{i}}^{(n)} \rangle$$

Predictions for forest clutter at L-band have been made for a forest stand with density similar to that at Tuusula [103]. No observational data has yet been made available for comparison, but typical predicted clutter levels at 45 degrees elevation of  $-4\text{dB}$  (HH)  $-11\text{dB}$  (HV) and  $-8\text{dB}$  (VV) are consistent with those reported in the open literature for similar forests.

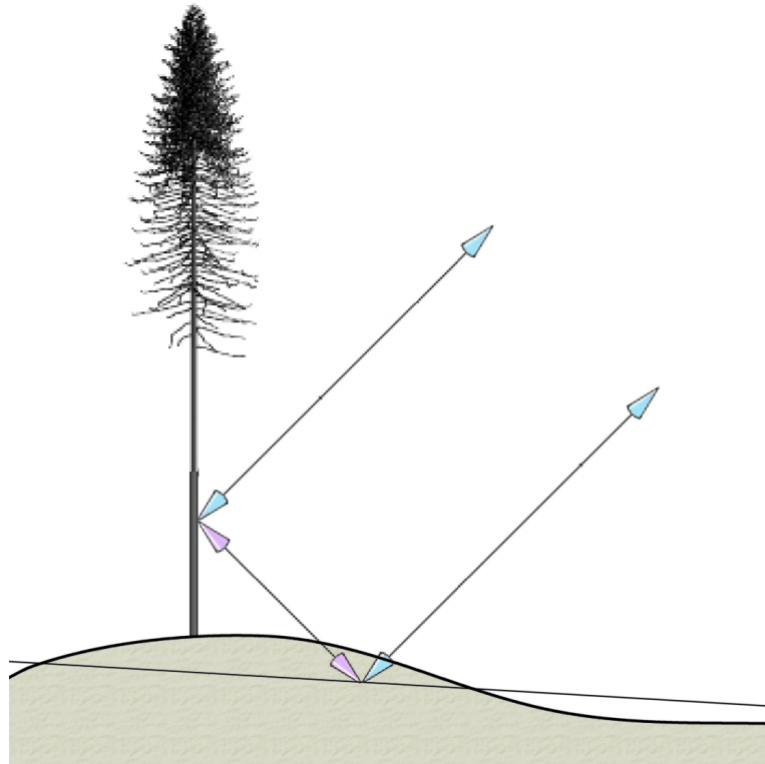


Figure C.3.2. Model for ground-volume interactions using a local mean slope.

Figure C.3.3 shows an interferogram of the test case for the 10m baseline ( $k_z = 0.12$ ). The canopy causes a loss of coherence, manifested as an increase in phase variance. Figure C.3.4 shows the corresponding phase for the 20m baseline with and without flat earth removal. From a qualitative viewpoint the phase variance has now increased, as expected due to the increased volume decorrelation with a longer baseline.

Figure C.3.5 confirms these observations by showing the histograms of the interferometric coherence for the three polarisation channels HH, HV and VV. In all cases the coherence was estimated using a window corresponding to an effective number of looks (ENL) of around 100.

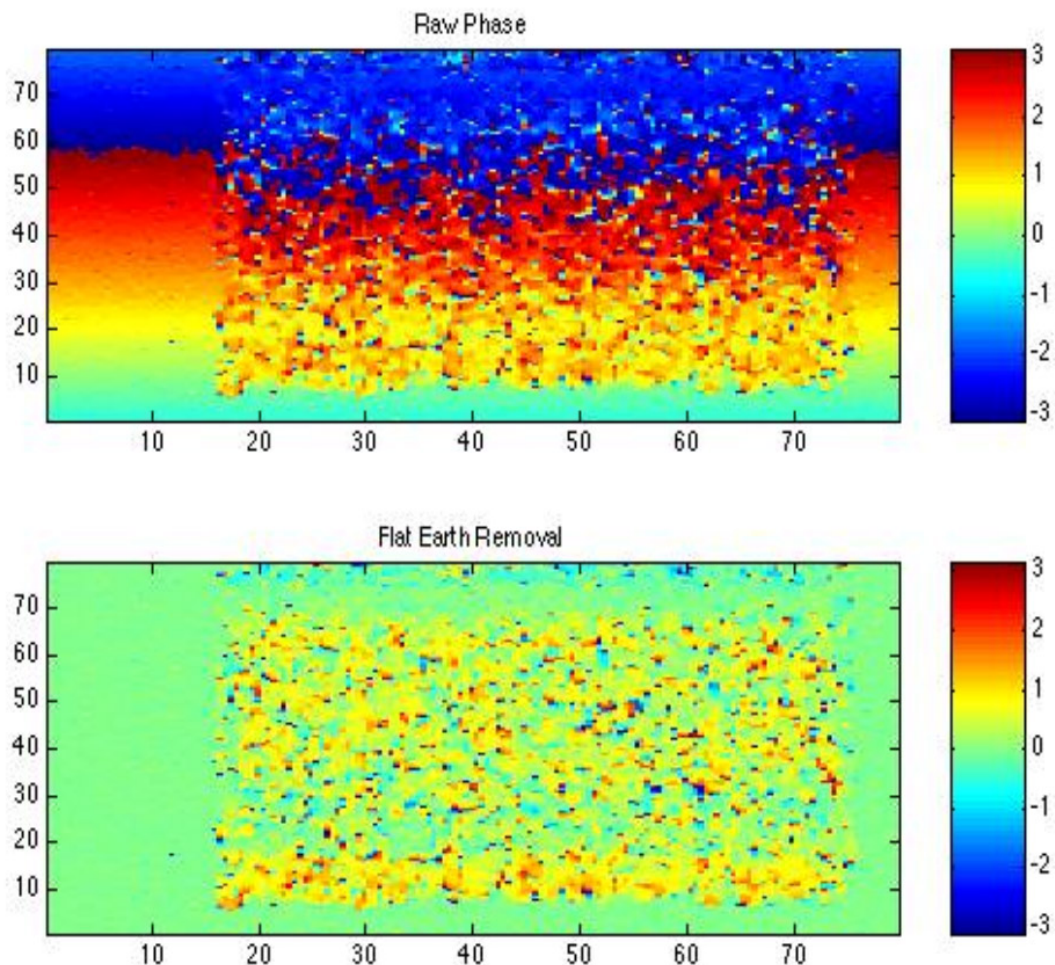


Figure C.3.3: Interferogram for 10m baseline and random canopy simulation (horizontal: azimuth (m); vertical: ground range (m))

In Figure C.3.5a the results are obtained from the 10 m baseline. It can be seen that the highest coherence is obtained for the cross-polarised or HV channel. The lowest is obtained for the HH with VV lying between the two. This rank ordering indicates that there are no strong differential propagation effects in the model. If for example the VV extinction was higher than the HH then one would expect VV to have the highest coherence and HV to lie between the two copolarised channels. The fact that this does not occur confirms that the canopy is being correctly modelled as a random volume. It will be shown later on that the change of coherence with polarisation is due to the presence of surface scattering components in the copolarised channels.

With the increase of baseline to 20 m (Figure C.3.5b) the coherences have decreased as expected. Again the rank ordering is preserved with HV having the highest coherence and HH the lowest. Again, the variation with polarisation is consistent with the effect of residual surface scattering on the observed InSAR coherence.



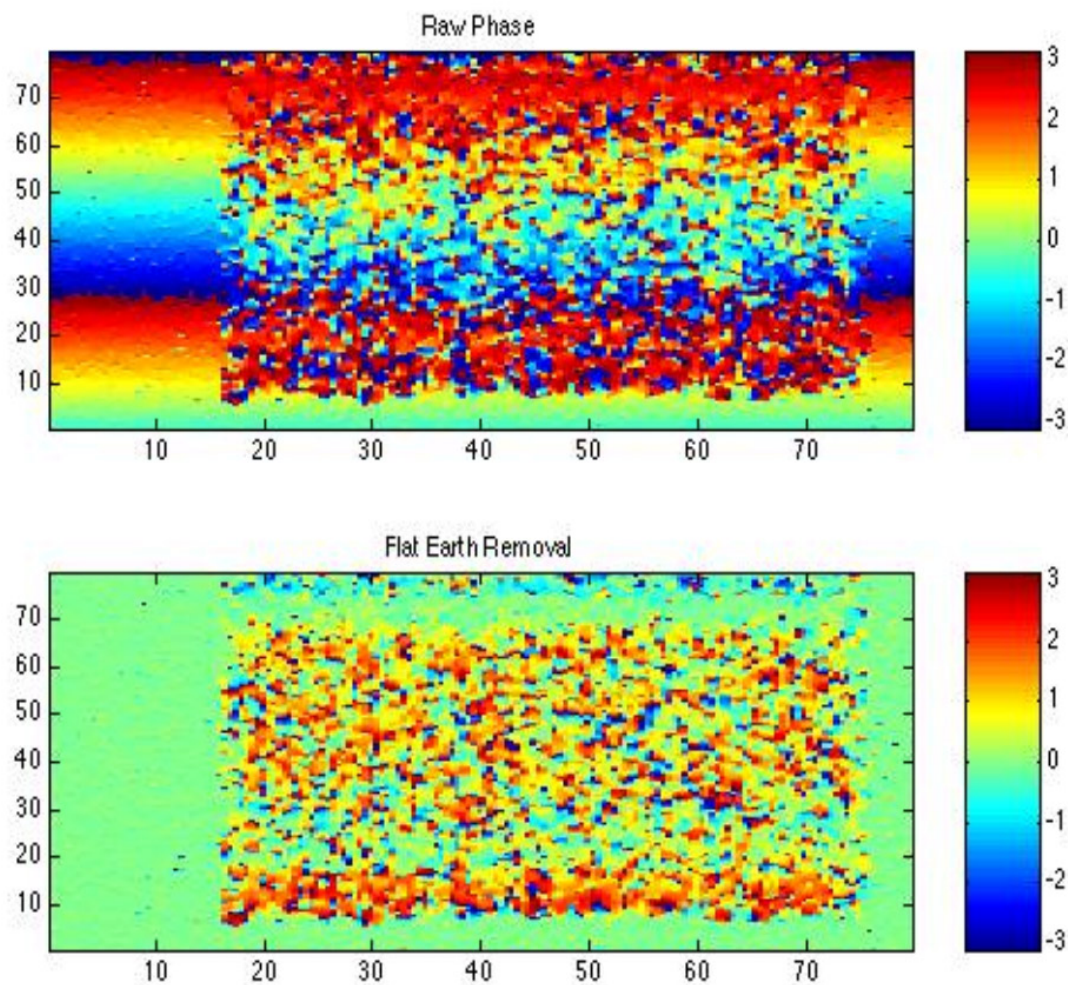


Figure C.3.4: Interferogram for 20m baseline and random canopy simulation

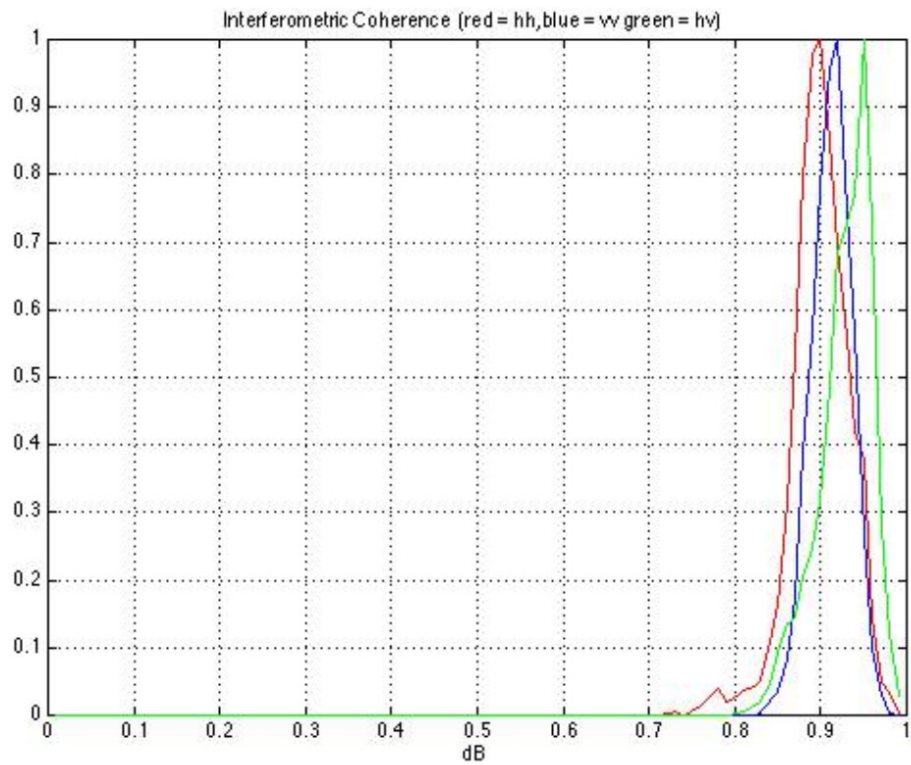
One advantage of using the modelling approach is that it becomes possible to separate the various contributions and to check on the level of volume and surface scattering. For example, in Figure C.3.6 and Figure C.3.7 only a polarimetric analysis of the direct volume scattering is performed. The corresponding entropy/alpha values are shown in Figure C.3.6 [99]. For a random canopy these should lie along the lower bounding curve, corresponding to azimuthal symmetry. It becomes clear that the points do show this symmetry as expected. Also, for a random canopy the RCS in the HH-VV channel should equal that in the HV+VH channel, and both should be smaller than that in HH+VV. Figure C.3.7 shows example histograms taken from the volume component of the simulation, again confirming this symmetry assumption.

These tests confirm that the volume component is random. The most important consequence of this for InSAR is that the extinction becomes independent of polarisation. This is confirmed in Figure C.3.8 where the histograms in HH and VV for the RCS of the surface components only are shown. The following can be noted: The distribution is bimodal, the upper maximum is due to pixels from nonvegetated surface scattering while the lower is from pixels beneath the canopy. The difference

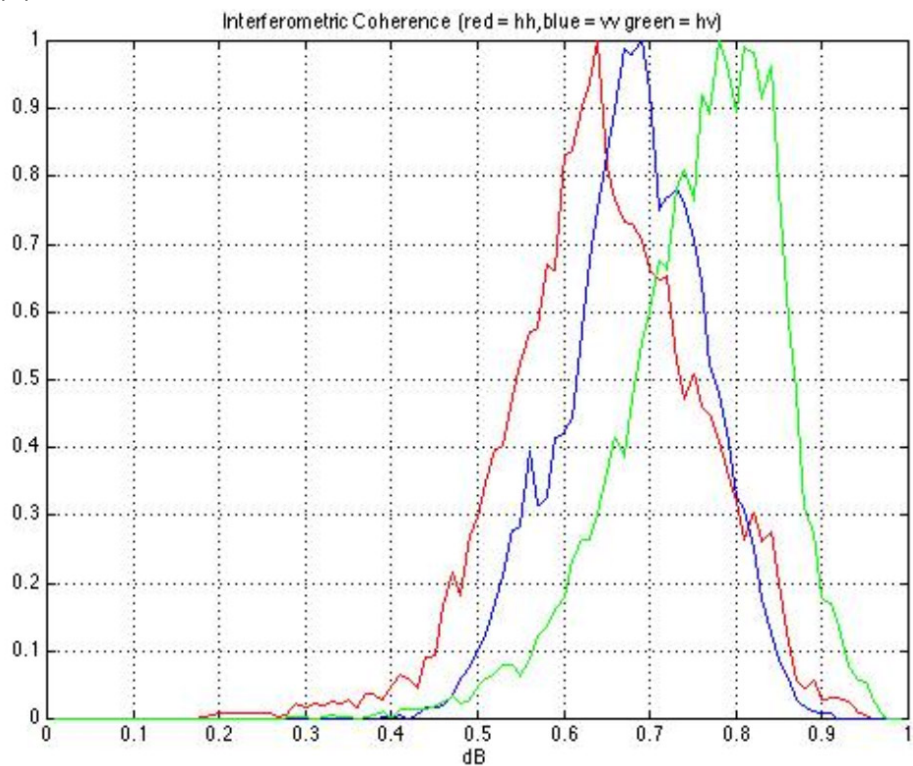
between peaks is a measure of the total 2-way extinction through the vegetation. This is around 10dB for Figure C.3.8. This corresponds to a 1-way extinction rate of 0.35 dB/m. The difference between peaks does not depend on polarisation confirming that the propagation component of the simulation does not introduce any numerical differential effects.

Finally, in Figure C.3.9 the ratio of surface scattering (including extinction) to volume scattering is formed to obtain directly  $\mu$ . Quantifying this ratio is central to the development of efficient inverse models for tree height [40, 100]. Note that the surface component also includes second order surface-volume and volume-surface interactions, as these have a phase centre on the surface and hence in interferometry appear like ground components. It is obvious that the HV channel has the smallest ratio as expected. However, it is not zero (and the direct surface scattering model used in the simulation is the first order Bragg model with zero cross-polarisation). This is explained by the presence of surface volume interactions giving an apparent HV component from the surface. Note that the mean value is still smaller than -10dB. The largest  $\mu$  values occur in the HH-VV channel. Here a combination of direct Bragg surface scattering plus a strong ground/volume dihedral return occurs. This pushes the mean ratio above 0dB. The HH+VV channel lies between these two extremes. It will be shown that these ratios are consistent with the coherence histograms shown in Figure C.3.5

Combining the observation of random volume scattering, scalar extinction properties and  $\mu$  values lying in the range +10 to -10dB it can be concluded that such a scenario is well suited to the application of tree height estimation studies. This is not surprising, as a very simple and homogeneous canopy model has been simulated. Of more interest is the results obtained for more realistic forest scattering models taking into account the structural properties of real trees with more natural gap and topography variations. The modelling of such a scenario will be considered in the following.



(a)



(b)

Figure C.3.5: Interferometric Coherence Histograms of canopy simulation for 3 polarisation channels (a) 10m baseline , (b) 20m lower.

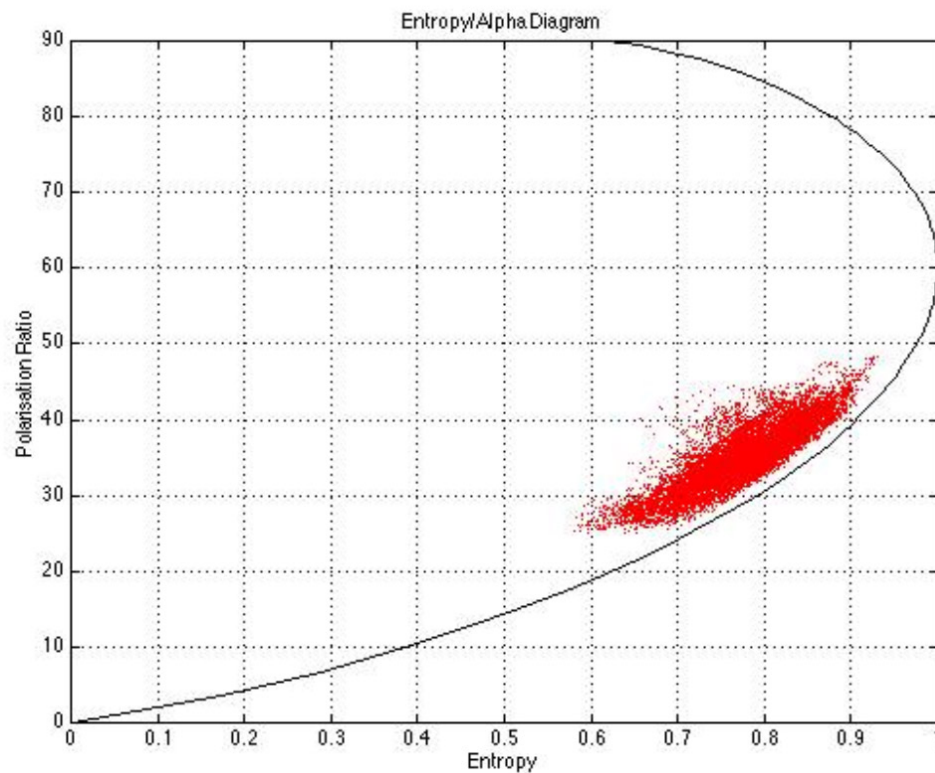


Figure C.3.6: Entropy/Alpha Diagram for Volume Scattering Components in random canopy simulation

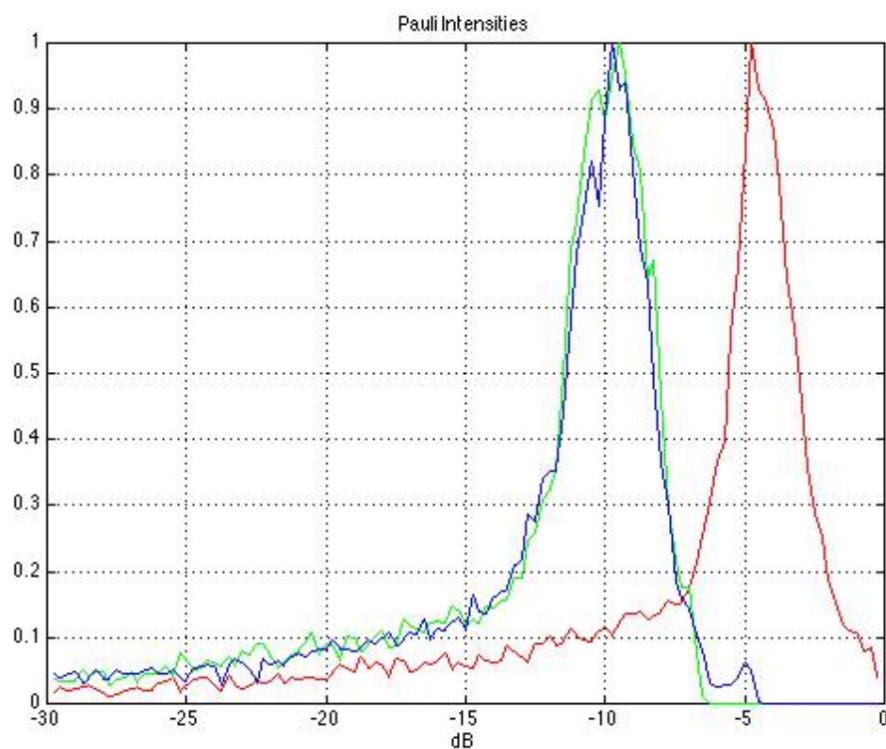


Figure C.3.7: Histograms of RCS in the Pauli Channel (red = HH+VV, green=HV, blue = HH-VV)



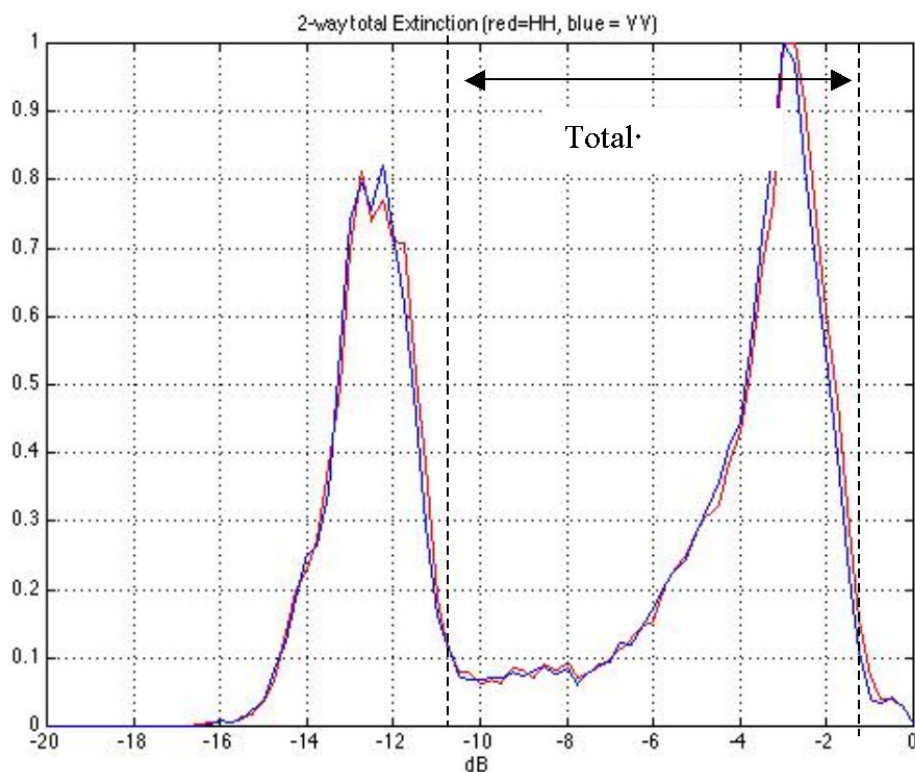


Figure C.3.8: Histograms of RCS of surface scattering for HH(red) and VV(blue) in random canopy simulation showing the effects of extinction by the canopy

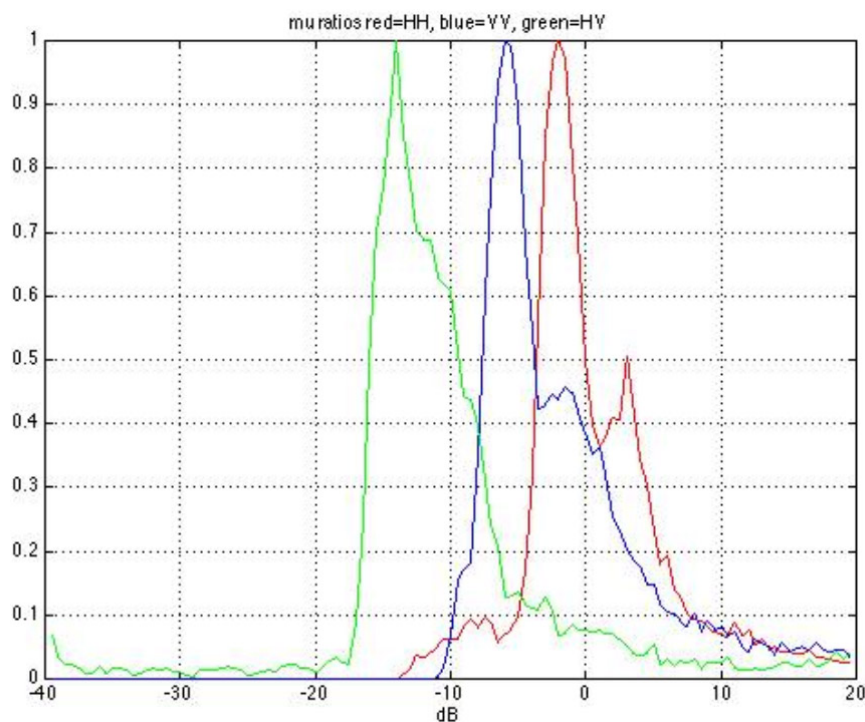


Figure C.3.9: Estimates of the ratio of surface-to-volume scattering in the three Pauli matrix channels (red = HH, blue=VV, green=HV)

### **C.3.3 Pine forest InSAR scattering model**

Having validated the basic components of the Pol-InSAR simulator, it was next applied to a more complicated but biologically accurate tree architectural model for Scots Pine. This model was provided by Prof. Seppo Kellomäki and Dr Veli-Pekka Ikonen of the Faculty of Forestry, University of Joensuu, Finland and further details of its structure and implementation in the SAR simulator can be found in [107, 103]. Figure C.3.10 shows an optical picture of the simulated forest and the DEM used for the forest floor. The SAR system parameters remain unchanged (L band E-SAR configuration and 45 degrees angle of incidence). The forest has a road through its middle and also gaps taken from *in-situ* measurements of tree positions. In this way the model better simulates the natural variability of a single species forest. Figure C.3.11 shows the tree height distribution with a mean around 18m. Baselines of 10 and 20m were again used in the Pol-InSAR simulation.

Figure C.3.12 shows simulated interferograms (with and without flat earth removal) for the two baselines. Again, the increase of phase variance with baseline due to the presence of the volume scatterers can be noted. Figure C.3.13 shows histograms of the interferometric coherence for different polarisations demonstrating the fact that the coherence decreases with baseline - as expected - and that the coherence is a function of polarisation. The rank order is the same as that seen for the random canopy, with HV having the highest coherence and HH the lowest. This again leads us to conclude that there are no dominant differential propagation effects, although the VV coherence is this time closer to HV and so some weak differential effects may be occurring.

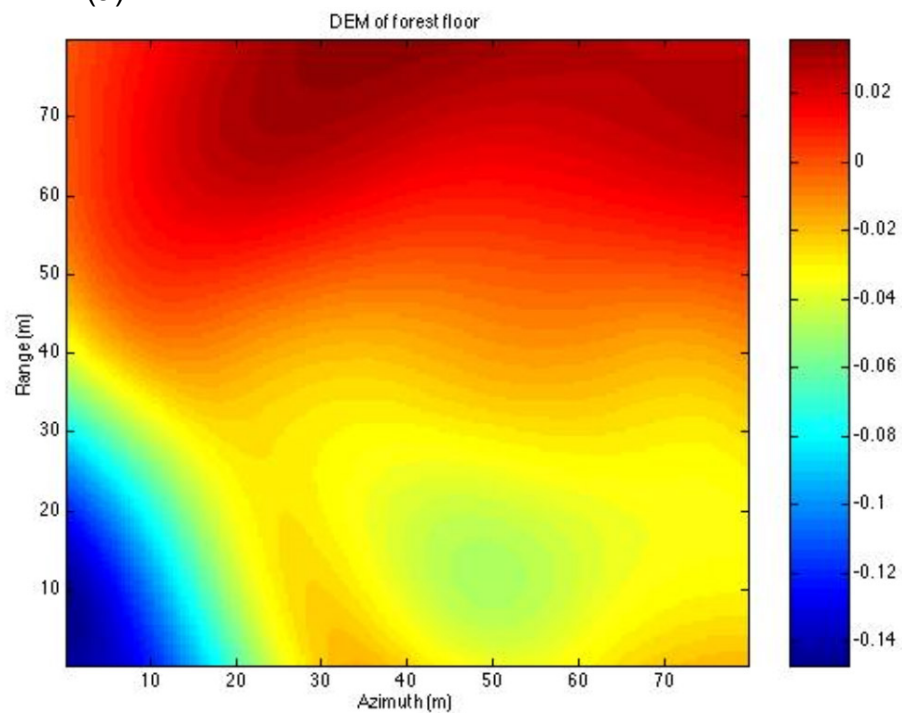
Figure C.3.14 and Figure C.3.15 show the entropy/alpha analysis [99] and Pauli scattering coefficients for the volume scattering components only. The  $H/\alpha$  values lie again close to the azimuthally symmetric curve but are slightly displaced from it compared to the random canopy results. This indicates some residual structure in the canopy returns. This structure is not however visible in the Pauli histograms of Figure C.3.15. These show equality of HH-VV and HV+VH as expected of a random canopy. Hence any residual orientation effects in the canopy are not visible in the intensity and only weakly visible in the polarimetry ( $H/\alpha$ ).

Turning to wave propagation effects through the canopy, Figure C.3.16 shows estimates of the two way total extinction in HH and VV. These were obtained by taking the ratio of surface scattering with and without the vegetation in place and show that the extinction here is a function of polarisation. There is now a much wider spread of extinction values but the mean extinction in VV is higher than that in HH. This qualitatively agrees with published data on L-band forest extinction which is estimated between 10 and 12 dB [101]. Hence while the scattering behaviour is close to that of a random volume, there are some predicted differential extinction effects which will influence the observed phase centre in InSAR applications. Note that most published forest height estimation techniques [40, 100] assume that the extinction is scalar and so such differential effects will be a potential source of error. While differential extinction effects in Pol-InSAR have been considered in the literature [54, 55] as yet there have been no published inversion algorithms taking these into account. In Section C.4 the magnitude of this error will be investigated in order to see if such effects will be significant in tree height estimation.





(a)



(b)

Figure C.3.10: Pine Forest Model used for InSAR simulations: (a) tree structure, (b) digital elevation model (DEM).

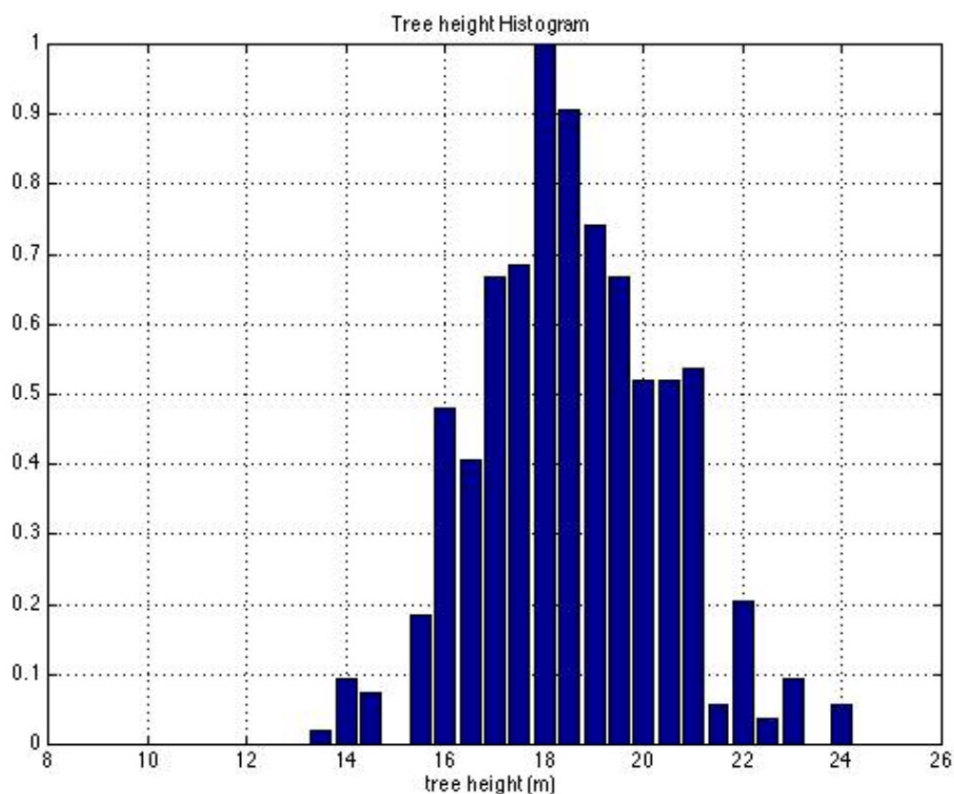


Figure C.3.11: Tree Height Distribution for Simulated Forest

Finally, in Figure C.3.17 the  $\mu$  ratios taken from the separated volume and surface+surface/volume components are shown. A much lower HV ratio than for the canopy simulations is obtained. This is due to the smaller amount of canopy vegetation giving rise to small ground/canopy interactions. This is good for tree height estimation as the inversion algorithm requires ground regularisation, which assumes that in at least one polarisation channel the ground scattering can be ignored (see [100]). Figure C.3.17 makes evident that this is a good approximation for HV.

The HH-VV channel has the highest  $\mu$  values, again due to ground/trunk interactions, but these are somewhat less than in the case for the random canopy.

Concluding, the InSAR coherence signatures of the pine forest simulations show general agreement with those expected from the random canopy analysis. However there are two important distinguishing features, namely the presence of differential extinction in the volume and also lower values of  $\mu$ , the ratio of surface-to-volume scattering.

In the following, the implications of these for tree height retrieval algorithms are investigated.

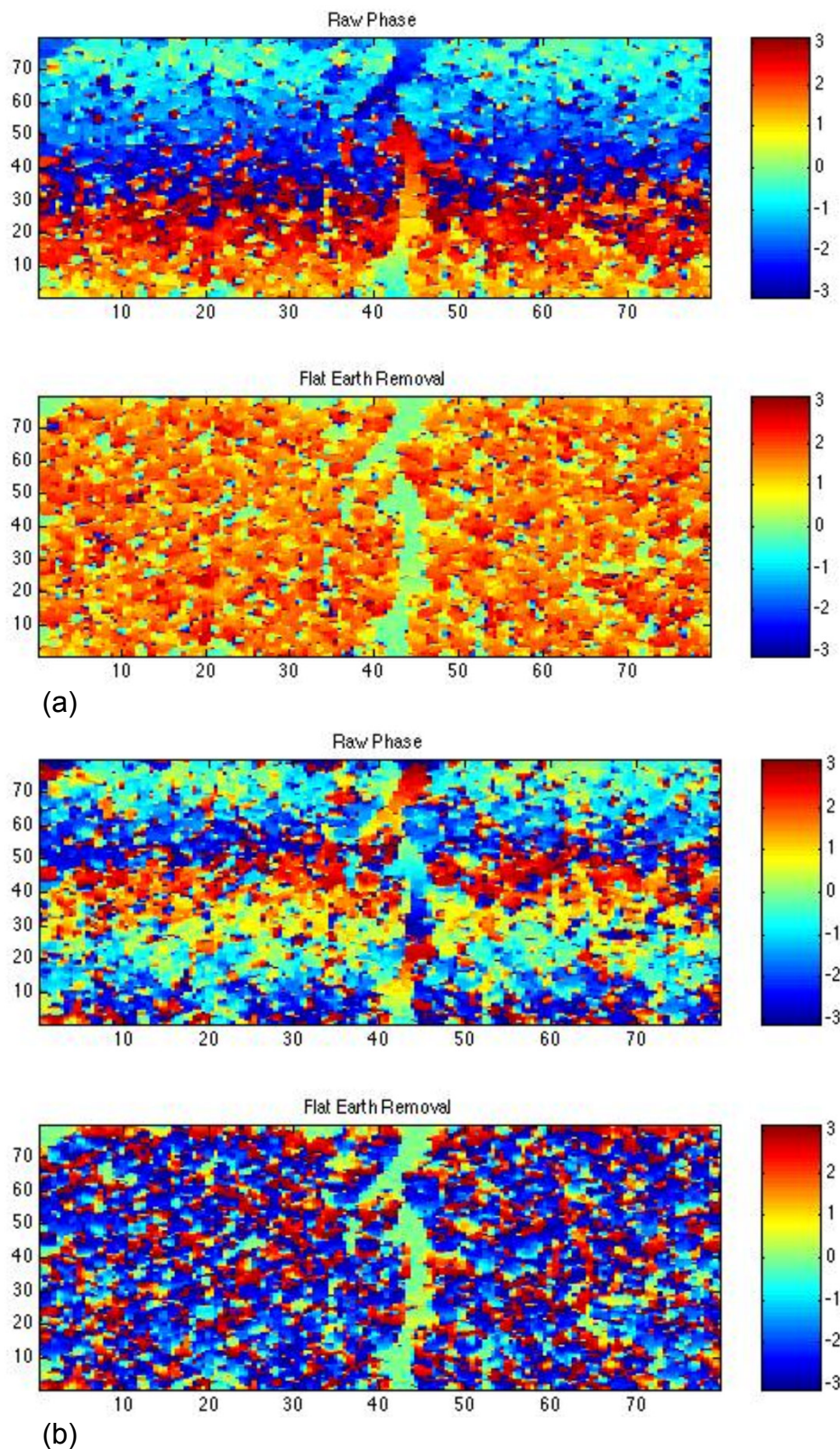
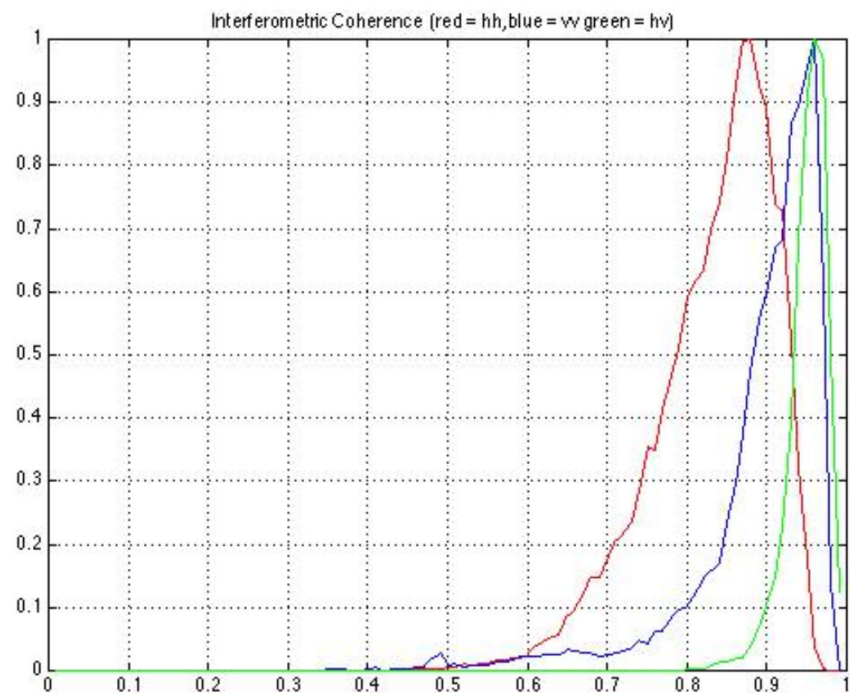
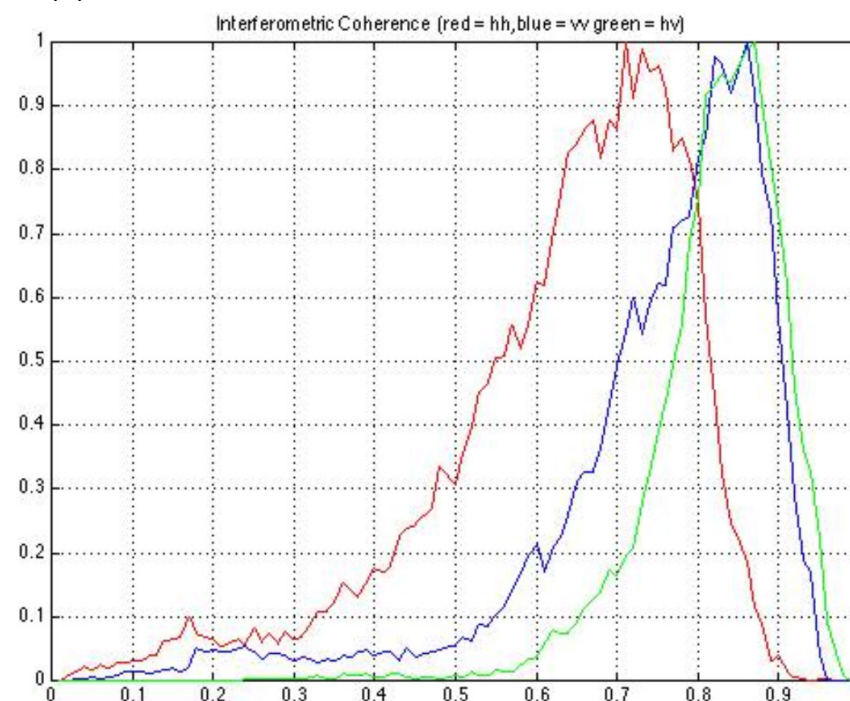


Figure C.3.12: Interferograms of Pine Forest Simulation: (a) 10m baseline, and (b) 20m baseline.





(a)



(b)

Figure C.3.13: Interferometric Coherence Histograms of forest simulation for 3 polarisation channels: (a) 10m baseline, and (b) 20m baseline.

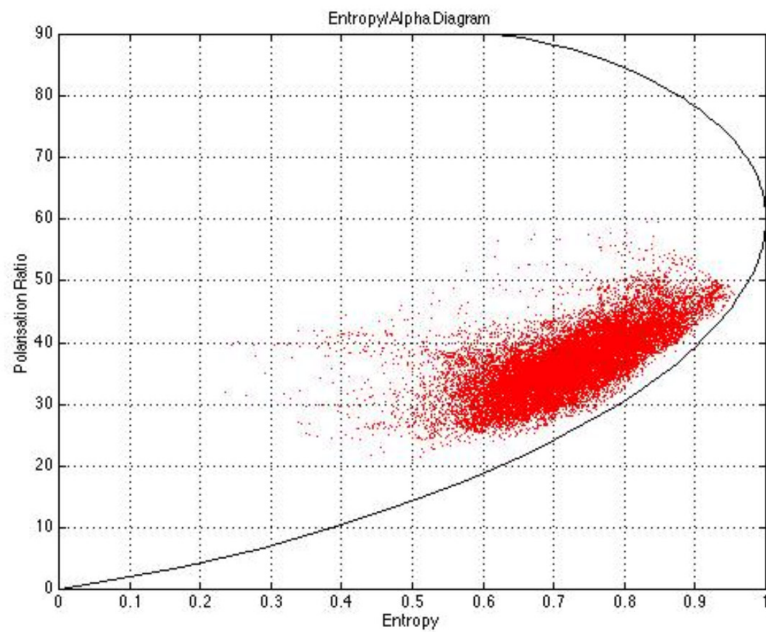


Figure C.3.14: Entropy/Alpha Diagram for Volume Scattering Components in forest simulation

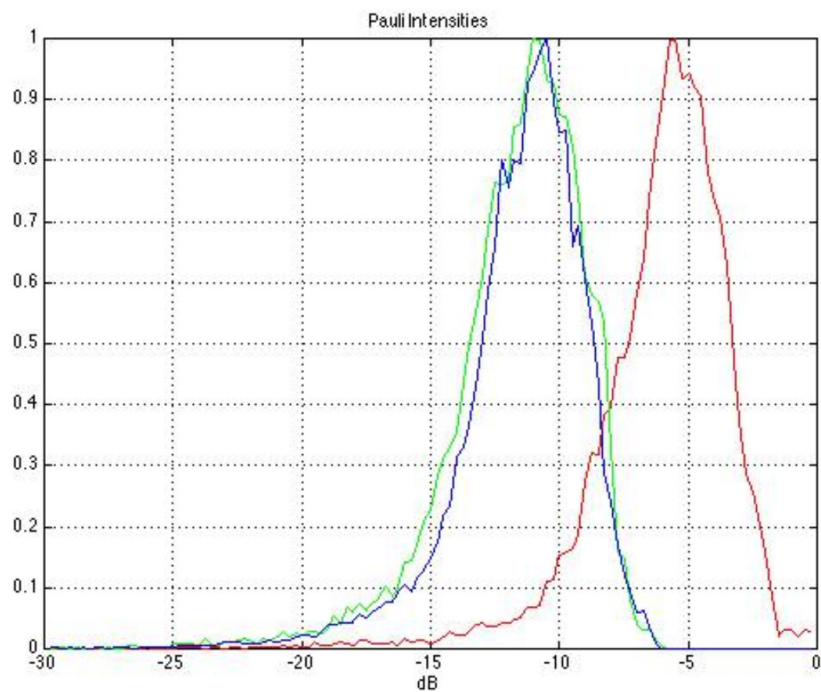


Figure C.3.15: Histograms of volume scattering in the Pauli Channels (red = HH+VV, green=HV, blue = HH-VV)

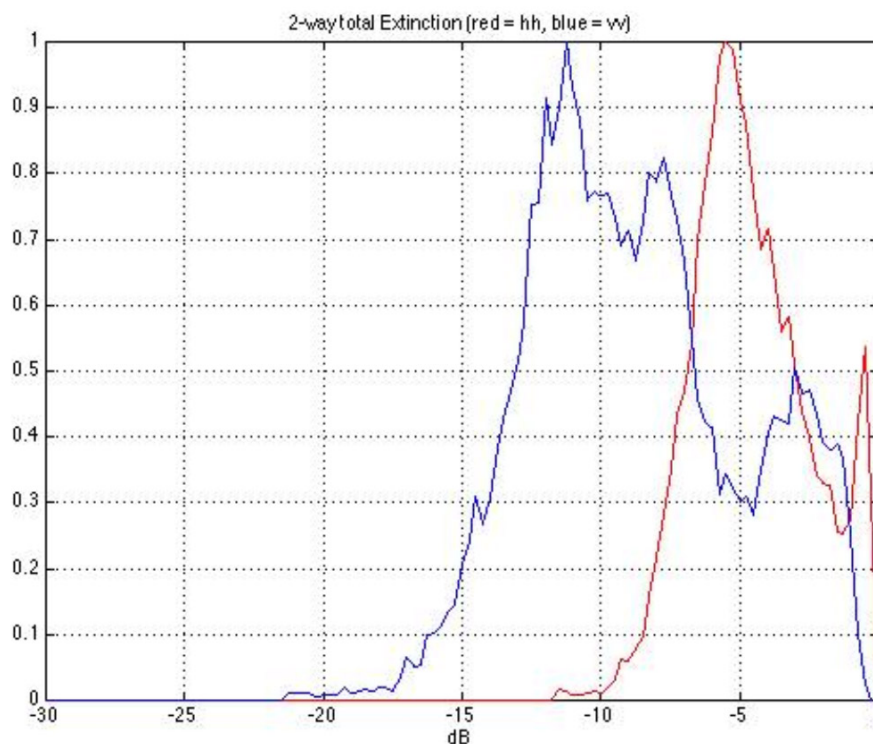


Figure C.3.16: Histograms of ratio of surface scattering with and without vegetation for HH(red) and VV(blue) forest simulation

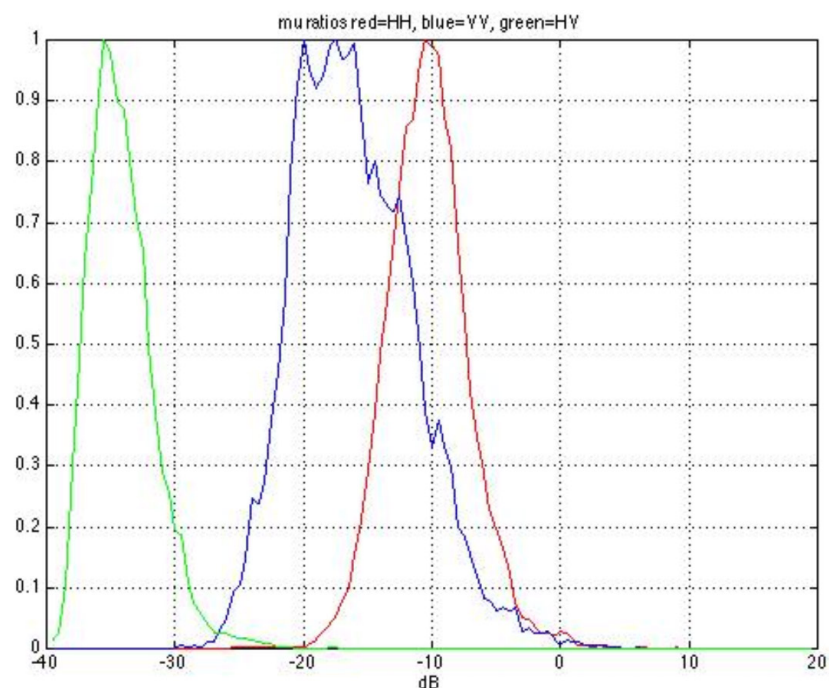


Figure C.3.17: Estimates of the ratio of surface-to-volume scattering in the three Pauli matrix channels (red = HH, blue=VV green=HV): forest simulation



### C.3.4 Layer coherence model for tree height estimation

In the previous section the coherence predictions of a direct EM scattering model for forested terrain have been analysed. However, this model is too complicated for inversion and simplified models, which are nonetheless capable of predicting the observed coherence variations from the full direct simulations have to be developed. Such a model has been developed based on a simplified 2-layer hypothesis [40, 100]. For vegetated land surfaces, the interferometric coherence at polarisation  $\underline{w}$  can be expressed in the form of straight line in the complex coherence plane as shown in Equ. (C.3.5).

$$\tilde{\gamma}(\underline{w}) = e^{i\phi} \left( \tilde{\gamma}_v - \frac{\mu(\underline{w})}{1 + \mu(\underline{w})} (1 - \tilde{\gamma}_v) \right) \quad (\text{C.3.5})$$

where  $\gamma_v$  is the volume coherence due to the presence of vegetation (and for random media is independent of polarisation) and  $\mu$  is the ratio of surface to volume scattering defined in Equ. (C.3.6).

$$\mu(\underline{w}) = \frac{2\sigma}{\cos\theta \left( e^{\frac{2\sigma h_v}{\cos\theta}} - 1 \right)} \frac{\underline{w}^{*T} T_g \underline{w}}{\underline{w}^{*T} T_v \underline{w}} \geq 0 \quad (\text{C.3.6})$$

This ratio is a function of the surface properties, vegetation height and extinction as well as the volume scattering coefficient. Importantly  $\mu$  is positive semi-definite. This observation can be used to estimate 3 parameters, ground topography, vegetation height and extinction by minimising the following function.

$$\min_{h_v, \sigma} L_1(\lambda) = \left\| \tilde{\gamma}_1 + \lambda \left( e^{i\phi_{1b}} - \tilde{\gamma}_1 \right) - e^{i\phi_{1a}} \frac{p}{p_1} \frac{e^{p_1 h_v} - 1}{e^{p h_v} - 1} \right\| \quad 0 \leq \lambda \leq 1 \quad (\text{C.3.7})$$

where  $\begin{cases} p = \frac{2\sigma}{\cos\theta} \\ p_1 = p + ik_{z1} \end{cases}$

where  $\gamma_1$  is the coherence with maximum vegetation bias in the radar data (typically the HV interferometric coherence channel) and  $\phi_{1a}$  and  $\phi_{1b}$  are the unit circle intercept points of the coherence line. These too require estimation from the radar data, usually by employing a least squares line fit to multiple coherence estimates made in different polarisation channels. The phase  $\phi_{1a}$  is the ground topography and hence if a DEM is available then this parameter may be estimated separately.  $K_{z1}$  is the vertical wave number of the interferometer, itself a function of the baseline, wavelength and sensor height. The angle  $\theta$  is the mean angle of incidence. Both  $\theta$  and  $k_{z1}$  can be estimated from the sensor geometry and used in Equ. (C.3.7) to estimate tree height.

Note that there are a family of height/extinction solutions to Equ. (C.3.7), depending on the value of  $\lambda$ . For single baseline sensors regularisation is required, usually by

ground regularisation which amounts to setting  $\lambda = 0$ . This corresponds to assuming that  $\gamma_1 = \gamma_v$ . A measure of the fit between data and model is then obtained as the coherence error residue (CER), defined as shown in Equ. (C.3.8)

$$CER = \left\| \tilde{\gamma}_v - \tilde{\gamma}_{vest} \right\| = \left\| \tilde{\gamma}_1 - \frac{2\sigma e^{i\phi_a}}{\cos\theta_o (e^{2\sigma h_v / \cos\theta_o} - 1)} \int_0^{h_v} e^{ik_z z'} e^{\frac{2\sigma z'}{\cos\theta_o}} dz' \right\| \quad (C.3.8)$$

Equ. (C.3.7) will be used as the basis for height inversion studies carried out in chapter C.4. Here, a validation of this simple 2-layer model versus the full wave propagation simulator will be addressed.

As input to the 2-layer model tree height, mean extinction and  $\mu$  values in each of the three polarisation channels are required. These can be obtained from the simulations in Section C.3.3. Table C.3.1 summarizes the input parameters to the model.

Table C.3.1:  
Model Parameters used for 2-layer simulations of coherence

	<i>Random Canopy</i>	<i>Forest</i>
$K_z$ (10m baseline)	0.13	0.26
$K_z$ (20m baseline)	0.13	0.26
AOI $\theta$	$\pi/4$	$\pi/4$
Extinction $\sigma$	0.35 dB/m (one way)	0.6 dB/m (one way)
Ratio $\mu_{HH}$	-3 dB	-10 dB
Ratio $\mu_{VV}$	-6 dB	-20 dB
Ratio $\mu_{HV}$	-13 dB	-35 dB

The values of Table C.3.1 were obtained from the full model analysis. The only major change is the extinction for the forest. It was found that a better model fit was obtained using a higher extinction than observed in the data. This is a well known problem with the single baseline method. It assumes a uniform layer of vegetation from ground to top of canopy. The trees in the simulation however have elevated canopies and so the phase centre is offset from the ground. This is compensated in the simple 2-layer model by an increase in the apparent extinction. As there is no interest here in extinction estimation this is not a serious error.

Table C.3.2 shows results for the predicted coherences in the three polarisations. On comparison with Figure C.3.5 and Figure C.3.13 a very good prediction is obtained, both of the absolute levels and of the rank positioning of coherence with polarisation.

Figure C.3.18 shows a graphical representation of these results; the complex coherence points for each of the three polarisations HH, VV and HV inside the unit circle and the line fit through the coherence points for both 10 and 20m baselines are

shown. Note that both lines cut the unit circle through the point (1,0) as expected for a ground phase of zero degrees as expected in this simulation.

Table C.3.2:  
Estimated Coherence Values using 2-layer model

2-Layer Coherence model	10m baseline random canopy	20m baseline random canopy	10m baseline forest	20m baseline forest
HH coherence	0.898	0.620	0.848	0.704
VV coherence	0.912	0.675	0.945	0.837
HV coherence	0.942	0.787	0.957	0.852

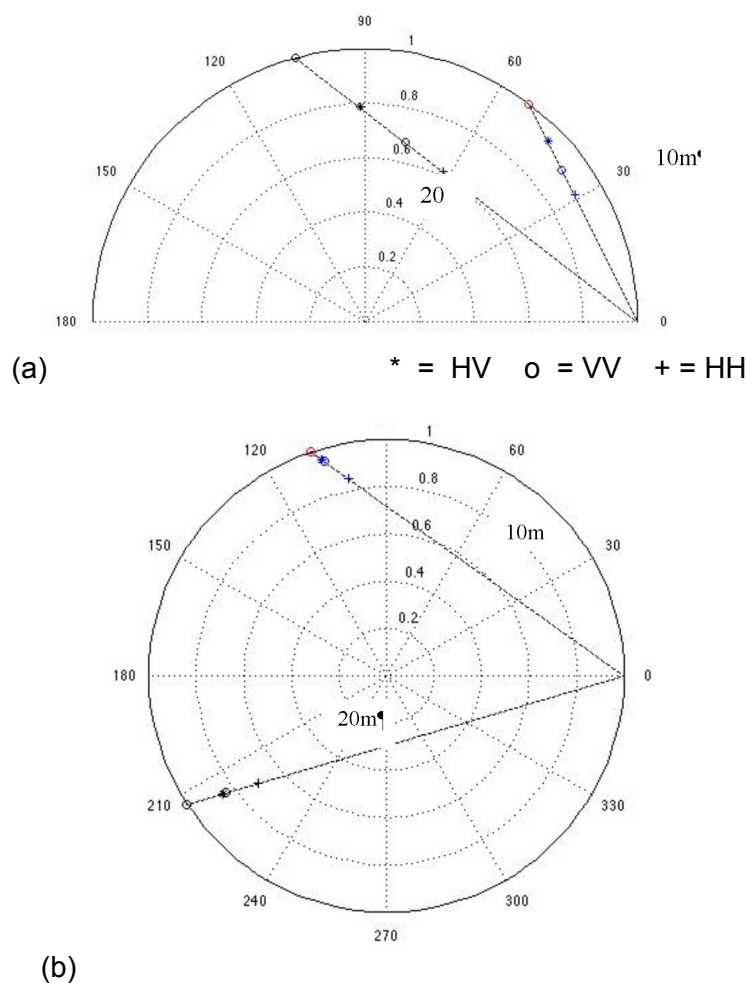


Figure C.3.18: Dual baseline predictions of complex coherence using simple two-layer model (a) random canopy, (b) and forest model.

Concluding, this simple model is capable of predicting the coherence structure, even for the full forest model. The only problem is the use of an artificially high extinction value due to the canopy structure in the forest. In the next work package the accuracy of height retrievals based on Equ. (C.3.7) will be further investigated.

### C.3.5 Experimental validation

Based on the geometrical interpretation of Equ. (C.3.5) the validity of the underlying model can be assessed by measuring how good the experimental data fit a straight line by means of chi-square statistics. The approach has been already addressed and discussed in chapter C.1. Using this simple but essential concept a variety of polarimetric interferometric data sets acquired over different test sites – by different sensors – were evaluated with respect to the validity of the RvoG model. Figure C.3.19 shows the Q probability map (where white indicates a high probability and a good agreement between data and model while black indicates a low probability and thus a strong deviation between data and model) obtained over the Fichtelgebirge/Germany test site (E-SAR/L-band) as a representative site of temperate CE forest. A very high agreement between model and data is obtained over the whole forested region – independent from topographic variations. In Figure C.3.20, the corresponding Q map for a boreal forest from the Kudara/Russia test site (SIR-C/L-band) indicates also the validity of the RvoG model. Finally, in Figure C.3.21 the Q map for a test site of tropical rain forest in Amazon/Brazil (AeroSensing/P-band).

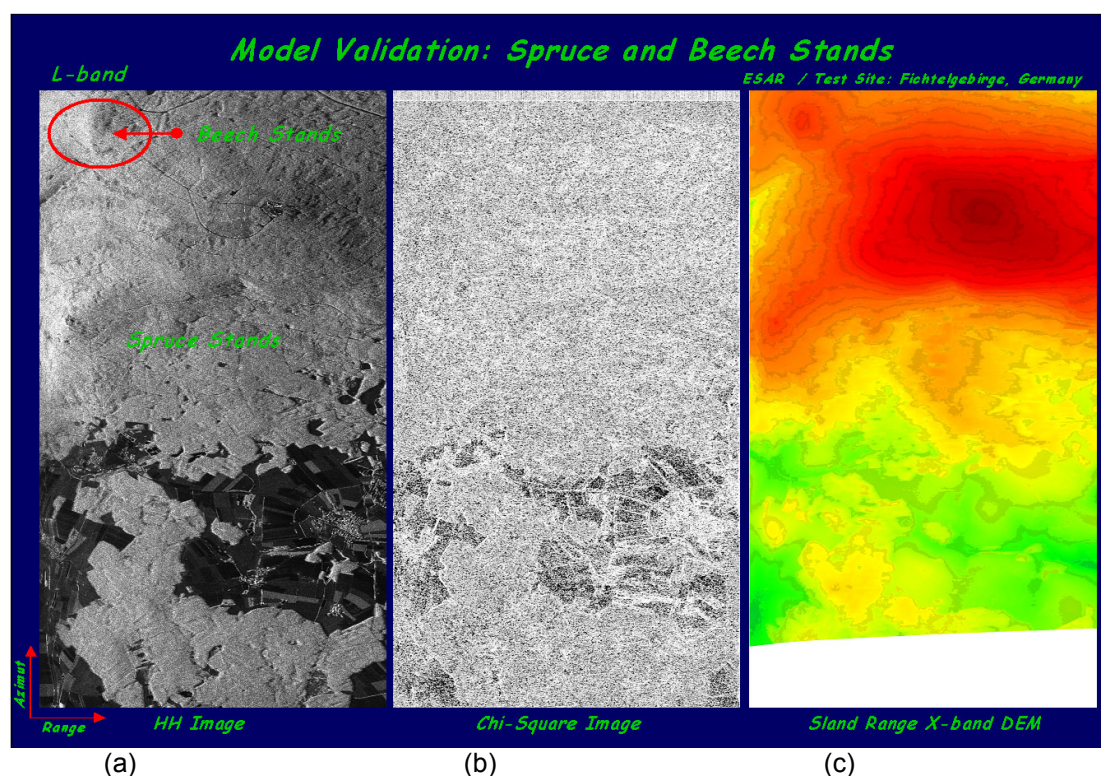


Figure C.3.19: (a) SAR Image, (b) Q Map (white Q=1, black Q=0), (c) DEM of the Fichtelgebirge Test Site.



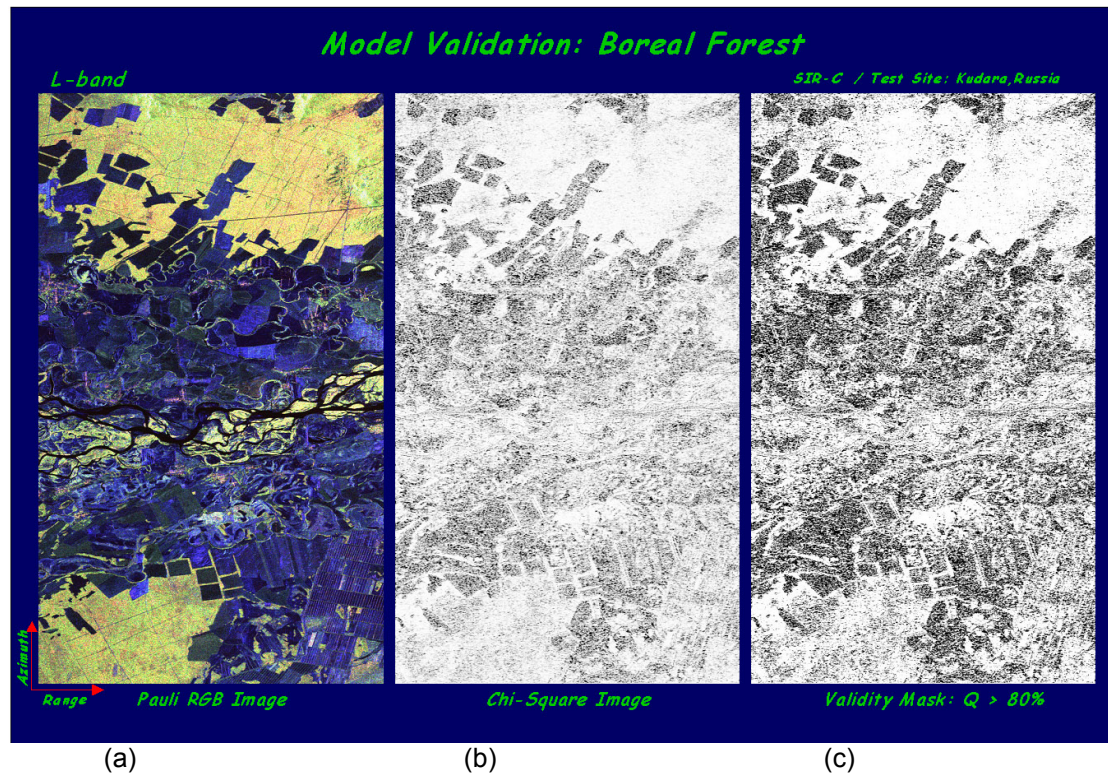


Figure C.3.20: (a) SAR Image, (b) Q Map, (c) Mask for  $Q > 80\%$  for the Kudara Test Site.

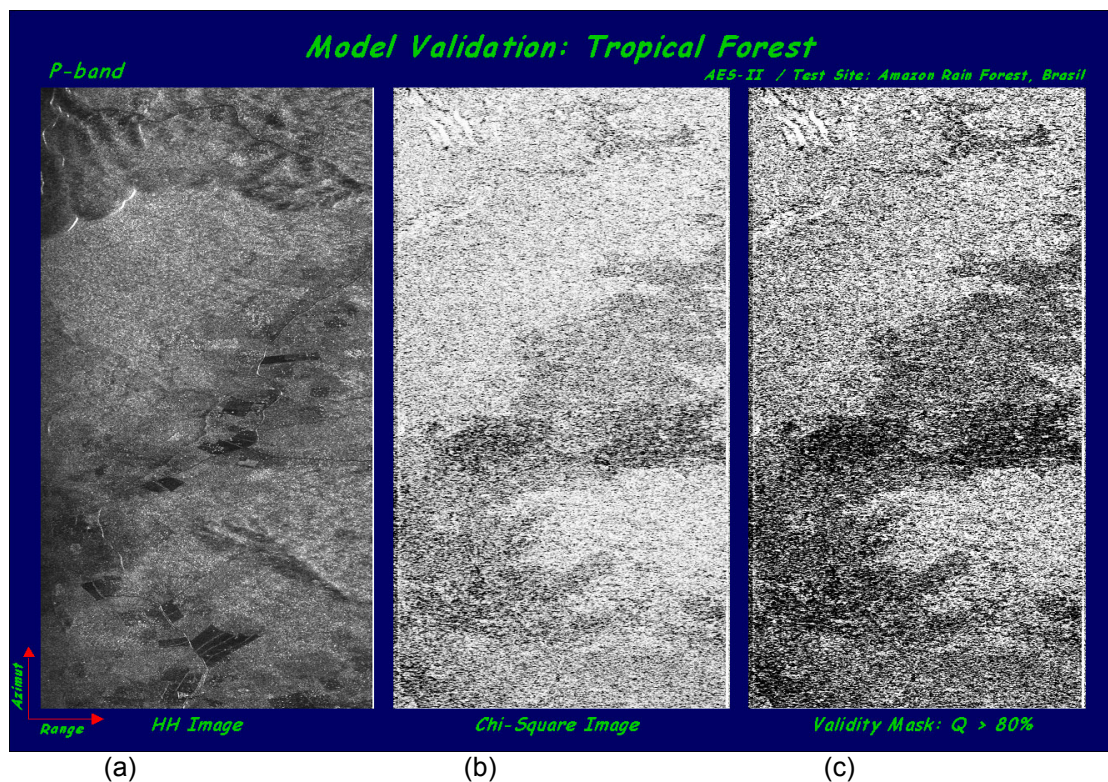


Figure C.3.21: (a) SAR Image, (b) Map, (c) Mask for  $Q > 80\%$  for the Amazon Test Site.

## C.4 RETRIEVAL ALGORITHMS FOR TREE HEIGHT AND TEST CASES

### C.4.1 Introduction

In the chapter C.2, tree height was selected as a key promising parameter for land surface InSAR retrieval. Subsequently, in chapter C.3, a direct EM scattering model has been validated to predict the complex coherence of forested terrain. We showed that a simplified 2-layer coherence model was able to predict the mean coherence structure of detailed Scots pine forest simulations employing a full vector wave propagation and scattering code. The main limitation of the simplified model was the need to make an assumption of isotropic wave propagation inside the volume. However, it was demonstrated in chapter C.3 that in the 3D tree simulations V polarisation had a higher extinction than H and hence this assumption is not strictly valid. Here we investigate the implications of such differential extinction on tree height retrieval.

We first develop a new algorithm for estimating tree height by inverting the 2-layer model. Previous versions of this model inversion have assumed access to full scattering matrix data [110]. However, there are several system advantages to be had by deploying sensors constrained to transmit only a single polarisation and receive dual orthogonal states. Important examples are V transmit and V/H receive (as in the ENVISAT ASAR), H transmit and V/H receive (as in the JAXA ALOS-PALSAR) and left or right circular transmit with left and right circular receive. In the near future data will be widely available for these limited or ‘light’ polarimetric modes. For this reason the development of tree height estimation algorithms employing these modes is of great topical importance. Here we compare different light polarisation modes and determine the best for L band forest applications.

### C.4.2 Tree height estimation algorithm using light polinsar modes

According to the 2-layer model, the observed complex coherence for forested terrain is a coherent mixture of volume and surface scattering [110] which can be written as a function of polarisation  $\underline{w}$  in the form shown in Equ. (C.4.1)

$$\tilde{\gamma}(\underline{w}) = e^{i\phi} \tilde{\gamma}_v + L(\underline{w})(e^{i\phi} - e^{i\phi} \tilde{\gamma}_v) \quad \tilde{\gamma}_v = \frac{p}{p_1} \frac{e^{p_1 h_v} - 1}{e^{p h_v} - 1} \quad \text{where} \quad \begin{cases} p = \frac{2\sigma}{\cos\theta} \\ p_1 = p + ik_z \end{cases} \quad (\text{C.4.1})$$

where  $h_v$  is the tree height,  $\sigma$  the mean extinction and  $k_z$  the vertical wavenumber of the interferometer. The real factor  $L$  is a function of the ground-to-volume scattering ratio and lies in the range  $0 \leq L \leq 1$ . The phase  $\phi$  is the true ground topographic phase. In lightpol modes, we have access to just 2 interferograms corresponding to vectors  $\underline{w}_1$  and  $\underline{w}_2$ . For uniqueness in the inversion we need to associate one of these with the



special case  $L = 0$  [110] i.e. to assume that in one of the observed channels the ground-to-volume scattering ratio is zero. Based on an understanding of scattering behaviour at L band this can be taken as the cross-polarised HV channel for linear lightpol modes and must be approximated by cross circular LR for circular modes. The 2-state form of the coherence equations is then shown in Equ. (C.4.2)

$$\begin{aligned}\tilde{\gamma}_1 &= e^{i\phi} \tilde{\gamma}_v \\ \tilde{\gamma}_2 &= e^{i\phi} \tilde{\gamma}_v + L(w)(e^{i\phi} - e^{i\phi} \tilde{\gamma}_v) = \tilde{\gamma}_1 + L(e^{i\phi} - \tilde{\gamma}_1) \\ \Rightarrow Le^{i\phi} &= \tilde{\gamma}_2 - \tilde{\gamma}_1(1-L) \\ \Rightarrow \phi &= \arg(\tilde{\gamma}_2 - \tilde{\gamma}_1(1-L))\end{aligned}\tag{C.4.2}$$

We see that to find the phase (and hence height) from measurements of  $\gamma_1$  and  $\gamma_2$  we first need to estimate  $L$ . This can be obtained from Equ. (C.4.2) as the solution of a quadratic equation as shown in

$$\begin{aligned}AL^2 + BL + C &= 0 \Rightarrow L = \frac{-B - \sqrt{B^2 - 4AC}}{2A} \\ A &= |\tilde{\gamma}_1|^2 - 1 \quad B = 2\text{Re}((\tilde{\gamma}_2 - \tilde{\gamma}_1)\tilde{\gamma}_1^*) \quad C = |\tilde{\gamma}_2 - \tilde{\gamma}_1|^2\end{aligned}\tag{C.4.3}$$

To ensure that  $L$  is always non-negative, the negative root must always be chosen. In this way we have a unique estimate of the ground phase with no need for the ambiguity resolution issues associated with fully polarimetric data [110].

In practice there may also be some a prior information about the underlying ground topography available to the user. This may take the form of an external digital terrain model (DTM) for example, from which the ground topography can be derived. In this case we can modify Equ. (C.4.2) for the phase estimate to accommodate such information so that we have in general

$$\hat{\phi} = K\phi_{DTM} + (1-K).\arg(\tilde{\gamma}_2 - \tilde{\gamma}_1(1-L)) \quad 0 \leq K \leq 1\tag{C.4.4}$$

where the factor  $K$  can be varied according to the accuracy and availability of the reference DTM. In this study we take extreme values to consider both cases of  $K = 0$  and  $K = 1$ . Future studies could address the development of more general statistical methods for selecting  $K$ .

Having determined the phase estimate from Equ. (C.4.3) and (C.4.4), we can then employ the observed coherence  $\gamma_1$  together with the model for volume decorrelation to obtain height and extinction estimates as a solution of the following least squares equation

$$\min_{h_v, \sigma} Q_1 = \left\| \tilde{\gamma}_1 - e^{i\hat{\phi}} \frac{p}{p_1} \frac{e^{p_1 h_v} - 1}{e^{p h_v} - 1} \right\| \quad \text{where} \quad \begin{cases} p = \frac{2\sigma}{\cos \theta} \\ p_1 = p + ik_z \end{cases}\tag{C.4.5}$$

The accuracy of these estimates depends on the phase centre separation of the two polarisations 1 and 2. State 1 is constrained by the requirement to have zero ground-to-volume scattering ratio in Equ. (C.4.5) and so it follows that state 2 should be chosen to have the *highest* possible ground to volume ratio so that its phase is well separated from 1. In the linear basis for example, state 1 can be selected as HV and, because of reciprocity, state 2 can therefore be HH or VV and still comply with a lightpol mode. However generally HH will have a higher effective ground-to volume scattering ratio than VV due to the stronger influence of surface-volume dihedral interactions. In the circular base, copolarised LL or RR can also be selected to maximise ground-volume interactions but then the cross polar channel LR must be taken as state 1 to comply with the lightpol mode requirements. Generally the cross circular will have a higher ground-to-surface ratio than the cross linear and so we can expect larger height errors in Equ. (C.4.5). However the accuracy of the inversion in 5 also depends on the accuracy of the ground phase estimate in 4 and so in practice the benefits of cross linear or circular are not so easy to establish in advance. To confirm these ideas and to establish whether linear or circular lightpol modes are better for forest height retrieval we turn to apply these algorithms to detailed 3-D coherent SAR simulations of forest scattering.

### **C.4.3 Scots pine forest simulations for L-band POLINSAR**

To provide a realistic test case for the investigation of tree height retrieval using light POLInSAR, we employ data from the DSTL coherent SAR simulator [107]. In addition to the test random canopy model described in chapter C.3, a stand of Scots Pine was simulated as shown in Figure C.4.1. Here we show a stand of dimensions 150m x 150m containing 1240 trees. On the left we show detail of one tree, illustrating the complexity of the 3-D structure model used for the SAR simulation. Shown in the lower part of Figure C.4.1 is a side view for a transect through the forest. Note the crown depth which is around 50% of the tree height.

A key advantage of using a simulation such as this is the control the user has over the input parameters. This makes it easy to assess the accuracy of any inversion scheme. For example, the tree height is known exactly and in this case is well approximated by a Gaussian with a mean around 18m with a standard deviation of 0.6m as shown in Figure C.4.2

The stand density selected is 0.055 stems/m<sup>2</sup> which corresponds to a moderate tree density. The forest stand model is then employed in a coherent L band SAR simulation with the following system parameters :

Frequency :	1.25 GHz	Vertical Baseline :	0 m
Sensor height :	3 km	Range resolution :	1.381065
Angle of Incidence :	45 degrees	Azimuth resolution :	0.690532
Horizontal baseline :	10 m		

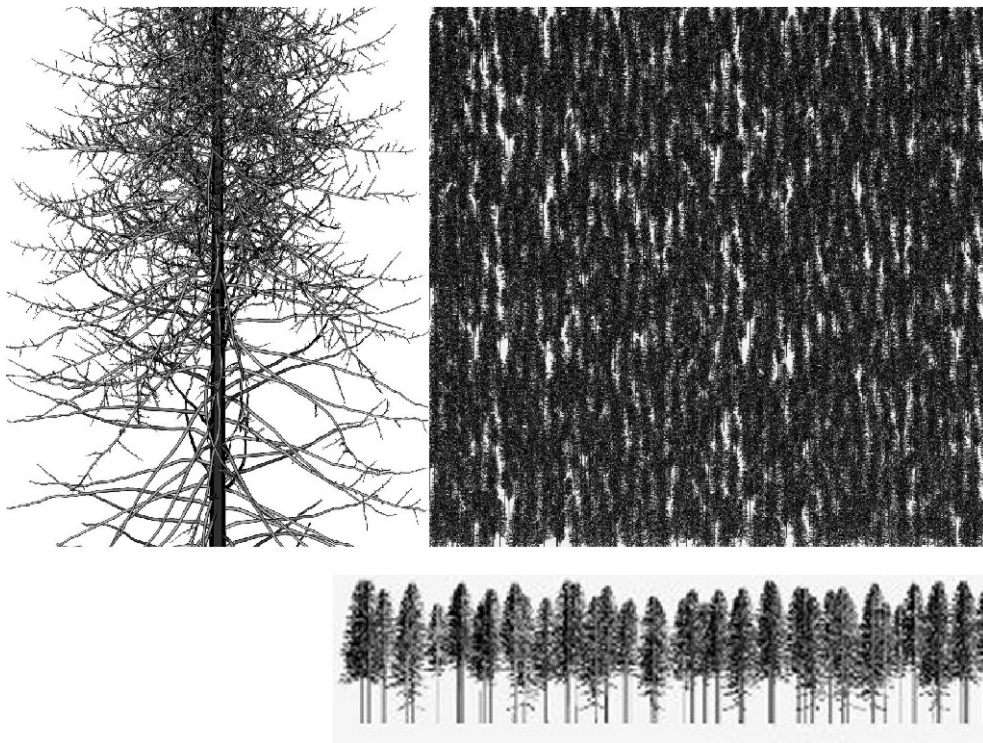


Figure C.4.1: Scots Pine Forest Stand used for POLInSAR simulation

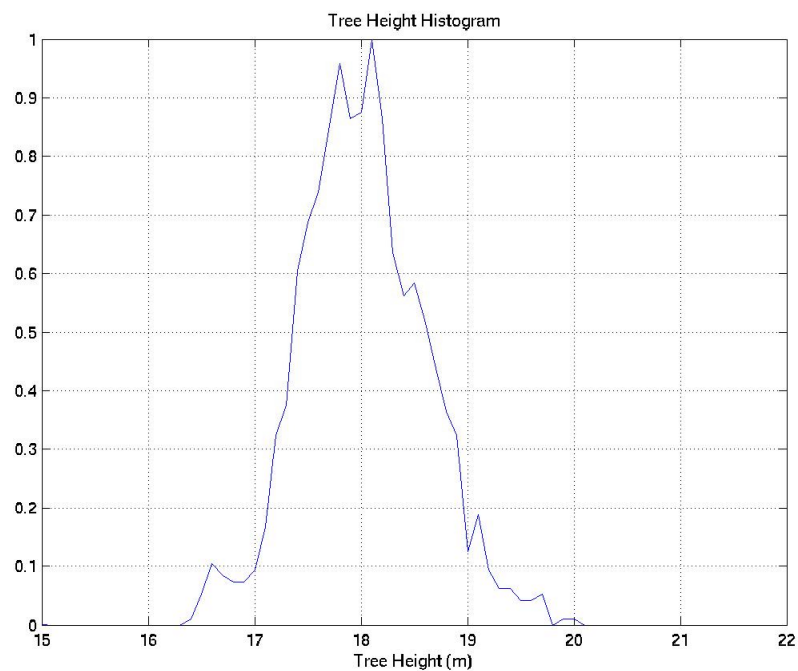


Figure C.4.2: Histogram of Tree heights used in forest stand simulation.

These system parameters closely match those of the DLR airborne E-SAR, which is the major experimental source of POLInSAR data. The parameters above lead to a vertical wavenumber  $k_z = 0.123$  or a  $\pi$  height of 25m. Hence we avoid phase ambiguities, even for the tallest trees in the scene. We now turn to consider the results of applying the light polinsar height retrieval algorithm to this data set.

#### **C.4.4 Results of tree height algorithm assessment**

In order to establish some performance bounds on light POLInSAR tree height retrieval, we apply the inversion algorithm of Equ. (C.4.3) – (C.4.5) to two simulated L-band data sets, a random canopy and Scots pine forest stand.

##### **C.4.4.1 Random canopy results**

We begin with an estimate of the ground phase i.e. with vegetation bias removal. In the simulations the flat earth removal can always be designed to ensure that the true ground phase is 0 degrees. With this in mind we start with application of the light polinsar algorithm to the random canopy data. In Figure C.4.3- Figure C.4.5 shows phase histograms for the canopy response. In black we show the cross-pol phase which clearly has a bias (and relatively high coherence). In red we show the phase estimate assuming  $K = 0$  in Equ. (C.4.4) and using HV together with HH (Figure C.4.3) and VV (Figure C.4.4) and then LR with LL (Figure C.4.5). In all cases we have used a high effective number of looks  $ENL = 1000$ .

In Figure C.4.3 we see that the mean ground phase for HH/HV is correctly predicted to be zero while the effective coherence is a little worse than the HV channel (which in this simulation corresponds to the optimum coherence). The VV/VH estimate in Figure C.4.4 is poorer, with a lower effective coherence and a residual bias to the phase. Finally in Figure C.4.5 the circular polarisation response shows good bias removal but has a lower coherence in the cross-polar reference channel. These results confirm the expectations of section C.4.2 that HH/VH is the best lightpol choice for ground topography estimation.

Figure C.4.6 shows sample phase images for the random canopy using the VH/HH mode. On the left is the single look HV phase, where the canopy is clearly seen as a vegetation bias. On the right we show the ground phase estimate based on multilook averaging and application of Equ. (C.4.4) (with  $K = 0$ ).

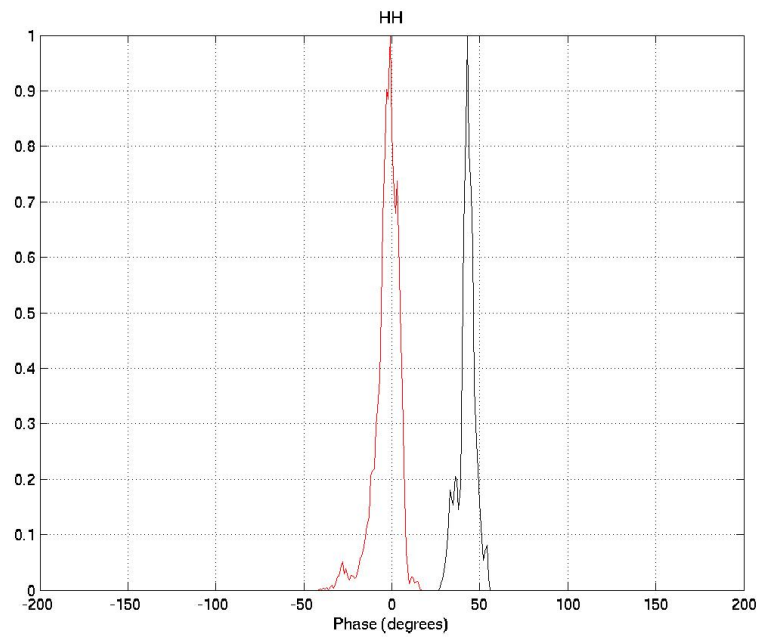


Figure C.4.3: Histogram of Ground Phase Estimate (in red) for light pol mode VH/HH for the random canopy simulations.

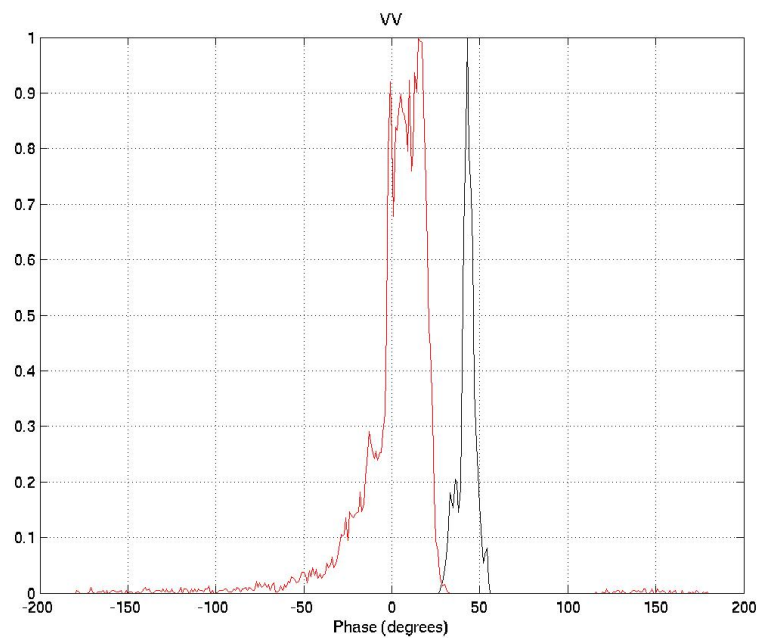


Figure C.4.4: Histogram of Ground Phase Estimate (in red) for light pol mode VH/VV for the random canopy simulations.

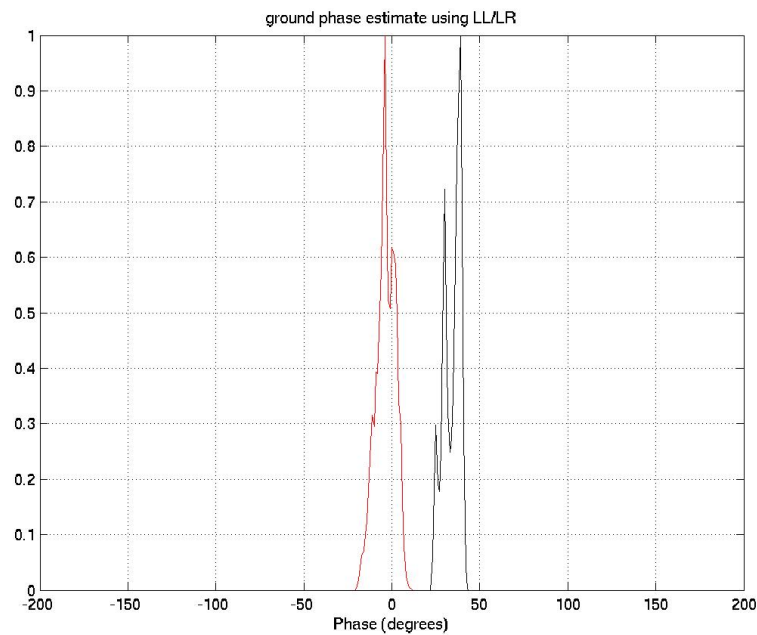


Figure C.4.5: Histogram of Ground Phase Estimate (in red) for light pol mode LL/LR for the random canopy simulations

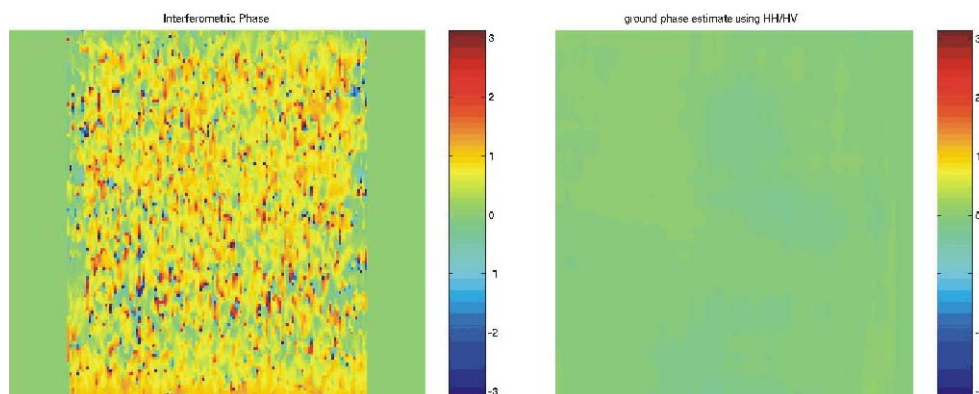


Figure C.4.6: Phase Images for Random Canopy (HV single look phase (left) and multi-look ground phase estimate (right))

To further demonstrate that this good ground estimate is due to the presence of ground-volume dihedral returns, we show in Figure C.4.7 the ground phase estimate for HH-VV/HV combination. Here we see very good bias removal with an effective coherence higher than HH in Figure C.4.3. This is due to the better phase centre separability of HV and HH-VV, with the latter having a phase centre closer to the ground. However to achieve the performance of Figure C.4.7 we require a fully polarimetric system, with switching on transmit and dual channel receive which is not consistent with the lightpol constraints. These results do however demonstrate that fully polarimetric systems will generally have superior accuracy to lightpol configurations.



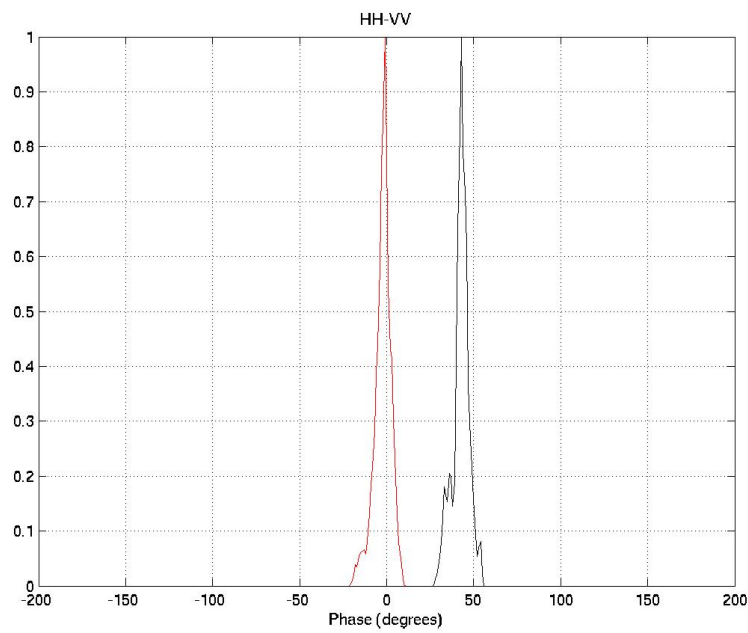


Figure C.4.7: Histogram of Ground Phase Estimate (in red) for HH-VV/HV for the random canopy simulations

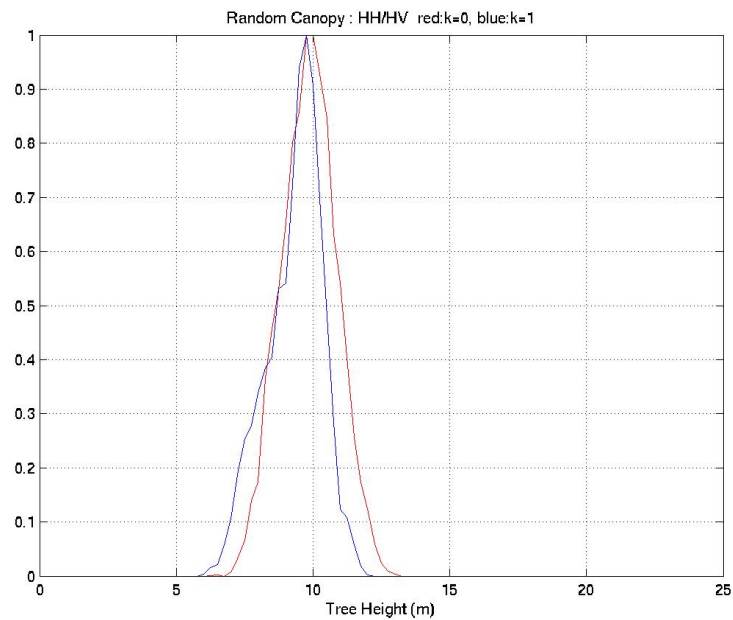


Figure C.4.8: Histograms of Height Estimates for random canopy simulations using HH/HV and K= 0 (red), K = 1 (blue).

If we now employ these phase estimates in Equ. (C.4.5), we can estimate the height of the canopy. The true height is uniform at 10m. From the above analysis we would expect the HH/VH combination to give the best lightpol accuracy. Figure C.4.8 shows histograms of the height estimates for the extreme cases of  $K = 0$  in red (no a prior DTM) and  $K = 1$  in blue (true DTM available) in this mode. We see that both estimates are good with an accuracy around 10%. These results are encouraging for the use of lightpol modes for tree height retrieval but are not typical of real forest environments, as the homogenous canopy is a poor model for true vertical structure. For this reason we now turn to consider application of the same algorithms to the Scots Pine forest simulations of Figure C.4.1.

#### C.4.4.2 Scots pine forest results

We begin again with estimation of the underlying ground phase from pairs of interferograms corresponding to various lightpol modes using Equ. (C.4.4) with  $K = 0$ . Figure C.4.9 - Figure C.4.12 show histograms of results obtained across the whole forest stand. We note the following features:

- The best ground estimate is again obtained for the fully polarimetric HH-VV and HV combination of Figure C.4.12, although there remains a bias of a few degrees and a lower effective coherence than observed for the random canopy results.
- The HH/HV combination shows only a 60% reduction in vegetation bias and again displays a lower coherence than the random canopy results.
- The VV/HV results show a vegetation bias that is actually increased by the processing rather than reduced. This we trace to differential extinction effects in the volume as we show in section 4.3
- The RR/RL results look similar to the HH/HV combination, although we note an increased bulge in the histogram for negative phase angles which will cause overestimation of height in the parameter retrieval stage.

To demonstrate the detailed differences between the linear HV/HH and circular LR/LL lightpol modes we show in Figure C.4.13 phase images of the forest stand. On the left we show the raw phase of the volume reference interferogram (HV or RL) and on the right the processed ground phase estimation. We can see positive and negative errors in the ground phase, with deeper negative errors for circular than for linear. These are the source of the bulge in the histogram of Figure C.4.11.

Again these errors can be traced to differential extinction effects in the volume, although we note that the performance of HH and LL is superior to the VV channel. This is due to the fact that the extinction in the forest is always higher for VV than it is for HH (see section C.4.4.3).

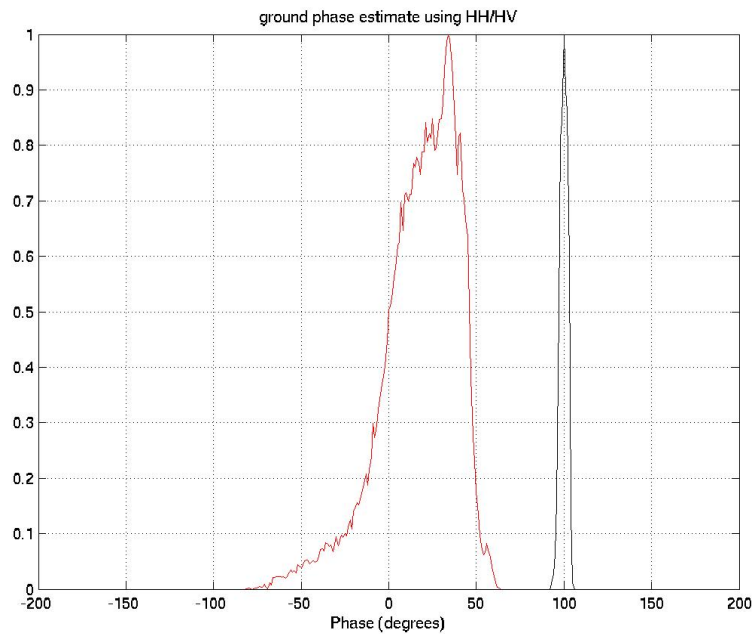


Figure C.4.9: Histogram of Ground Phase Estimate (in red) for light pol mode VH/HH for the Scots Pine forest simulations.

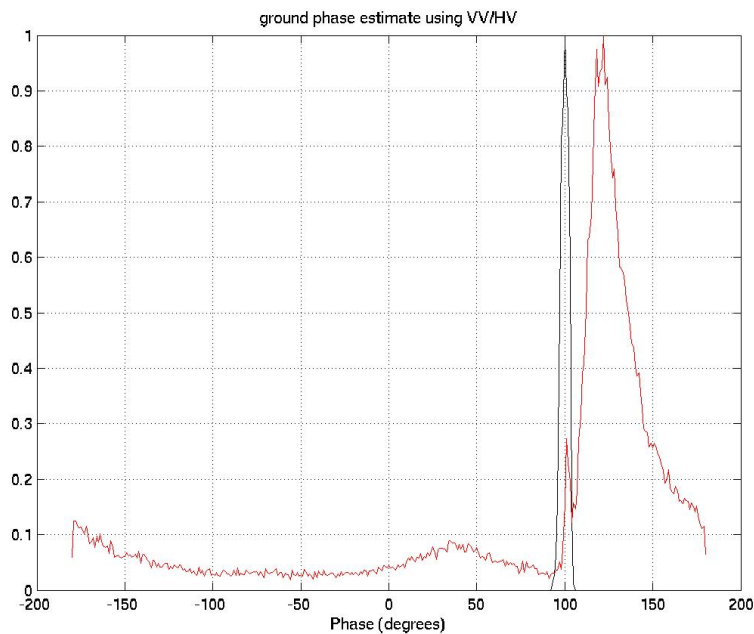


Figure C.4.10: Histogram of Ground Phase Estimate (in red) for light pol mode HV/VV for the Scots Pine forest simulations.

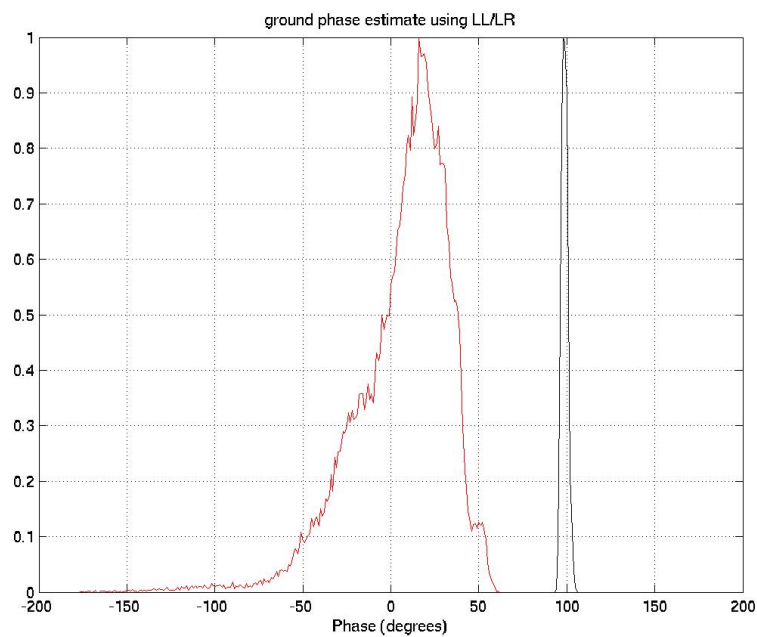


Figure C.4.11: Histogram of Ground Phase Estimate (in red) for light pol mode LR/LL for the Scots Pine forest simulations.

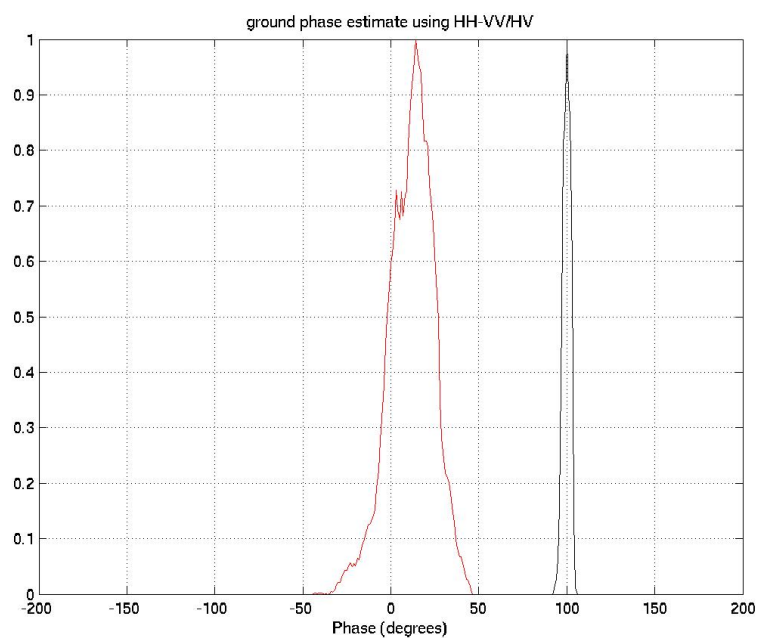


Figure C.4.12: Histogram of Ground Phase Estimate (in red) for light pol mode HH-VV/HV for the Scots Pine forest simulations.

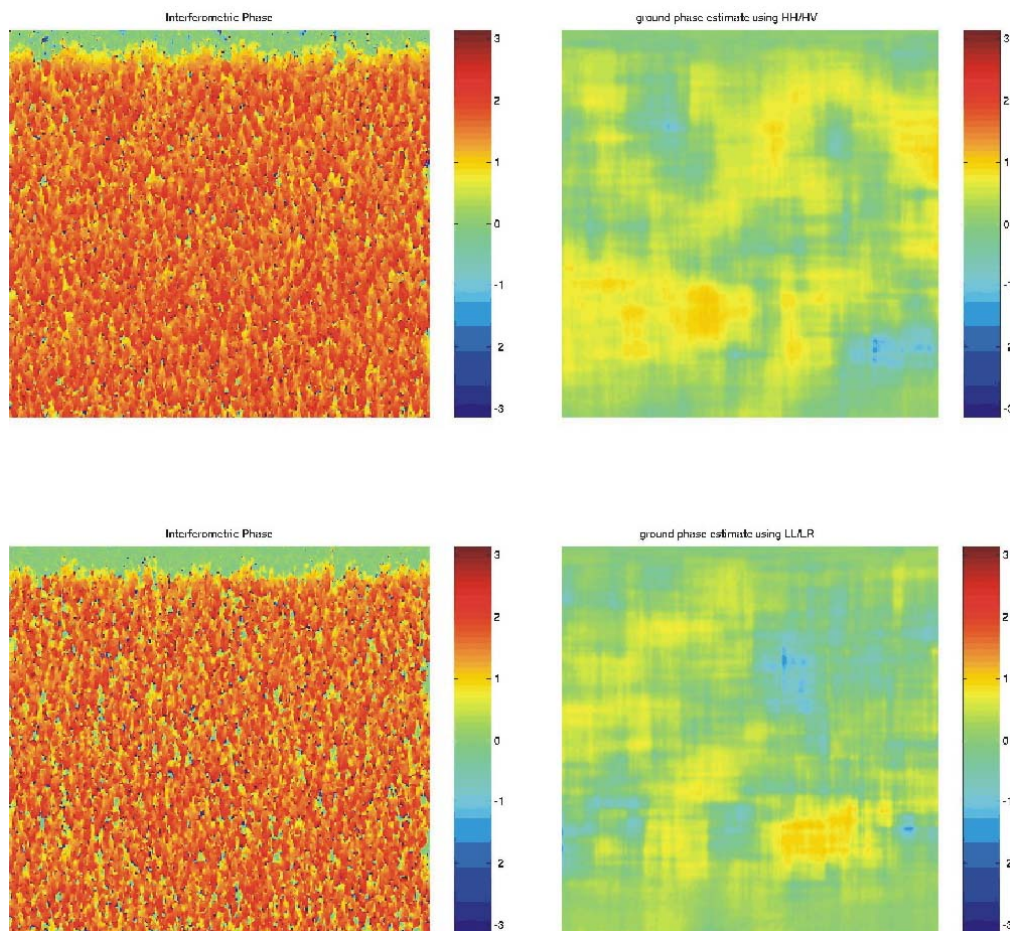


Figure C.4.13: Phase Images for Scots Pine Forest (VH/VV upper and LR/LL lower).

We now use these phase estimates in the height estimation routine (Equ. (C.4.5)). Figure C.4.14 and Figure C.4.15 show histograms of height estimates across the stand for the extreme cases of  $K = 0$  and  $K = 1$ . Figure C.4.14 shows the linear lightpol case. We see that the mean height is underestimated when we have no DTM and the width of the distribution is very wide with some trees appearing over 20m in height. This tendency to overestimate tree height is more pronounced in the circular lightpol case. Figure C.4.15 shows the corresponding histogram. Here we note a bulge at heights above 20m which corresponds to those pixels in Figure C.4.13 with the large negative phase estimate. In both Figure C.4.14 and Figure C.4.15 when  $K = 1$  we see good agreement between the estimate and true height distribution.

We conclude from this that the accuracy of tree height estimation depends critically on the accuracy of the topographic phase estimate. In cases where a DTM is available then the choice of Lite-pol mode is not critical. However when no DTM is available then the accuracy of the phase estimate depends on polarisation. From our initial analysis it seems that HH/HV is the best mode for L band Lite-pol estimation of tree height.

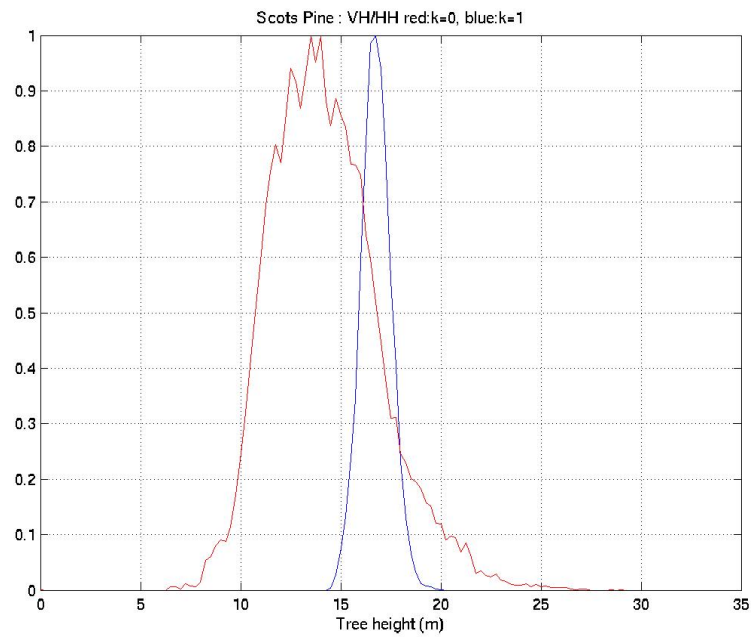


Figure C.4.14: Height Histograms for VH/HH Mode (K=0 red and K=1 blue).  
Note that the Quad-pol performance is also given by the blue histogram.

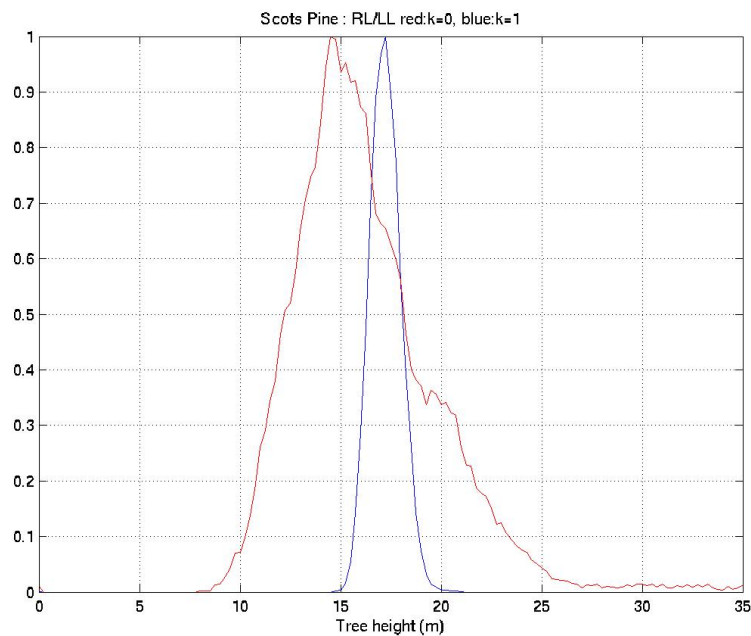


Figure C.4.15: Height Histograms for RL/LL Mode (K=0 red and K=1 blue).  
Note that the Quad-pol performance is also given by the blue histogram.



### C.4.4.3 Errors due to orientation effects in volume scattering

According to section C.4.2 we obtained poorer height estimates in lightpol modes for the pine forest than for the random canopy case. In this section we investigate further the source of these errors.

Figure C.4.10 shows that the poorest performance of all Lite-pol modes occurs when V polarisation is transmitted. In this case the ground phase is estimated as being higher in the canopy than the reference volume component HV. This can be explained by considering the effects of differential extinction on the coherence variation as we now demonstrate.

Figure C.4.16 shows the total 2-way extinction through the forest layer. These estimates were obtained directly from the SAR simulations by separating the ground component with and without the vegetation in place. Here we see a higher extinction in VV than in HH. Figure C.4.17 shows a histogram of the corresponding differential extinction, which we see has a mean around 8dB. In the random canopy case the extinction in HH and VV were found to be the same. Hence the differences seen in Figure C.4.16 are due to structural properties of the Scots Pine tree model used in the forest simulation and not to errors in the simulation procedure.

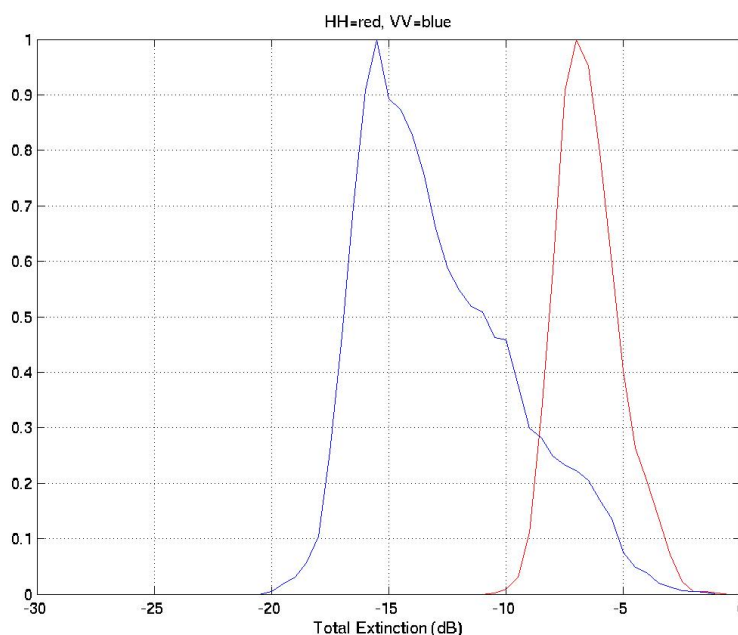


Figure C.4.16: Extinction Histograms for VV (blue) and HH(red)

In the modelling process itself, voxel occupancy is determined from size and orientation distributions taken from actual field measurements. However the voxel size must be determined by the user as a compromise between resolution and statistical sampling of these distributions. Hence it is unclear at this stage whether such large differential extinctions are physical or an artefact of the model quantisation. Comparison with the literature on extinction measurements in forests

shows that VV is generally higher than HH at L band but the magnitude of the difference is smaller than observed in these simulations. Further work is required to establish the fidelity of the differential extinction modelling capabilities of the simulator.

Nonetheless, if we accept the principle that at L band the VV extinction is always greater than or equal to HH then we can explain the observed results as follows. The volume coherence for a random medium (like the canopy simulations) has an invariant complex coherence with polarisation. This is shown schematically as overlapping points in the complex plane as shown in the top of Figure C.4.18. This is the case we assume for model inversion and hence leads to good results for the random canopy simulations. However if VV has a higher extinction than HH then the points will split as shown in the lower part of Figure C.4.18, with HV remaining unchanged but with VV moving to the left while HH moves to the right.

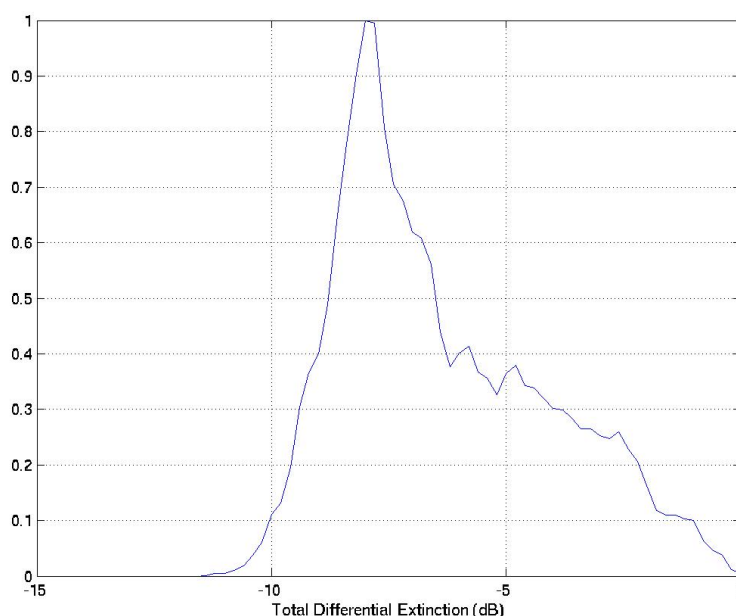


Figure C.4.17: Differential Extinction Histogram VV > HH.

The key observation is that the lower extinction (HH) will always move in the direction of the ground topography, as lower extinction implies a lower phase centre in the volume. On the contrary the highest extinction (VV) will move further away from the ground and have a higher phase centre in the canopy than the crosspolar channel. This is just the behaviour observed in Figure C.4.10. Further, although the HH coherence moves towards the ground phase it does not do so along the line joining the HV coherence to the ground phase unit circle point. Hence use of HH and HV as a Lite-pol pair will still lead to ground phase errors, as the line through these two will not generally intersect the unit circle at the correct place. Hence differential extinction can be used to explain the errors observed in Figure C.4.9 - Figure C.4.12.

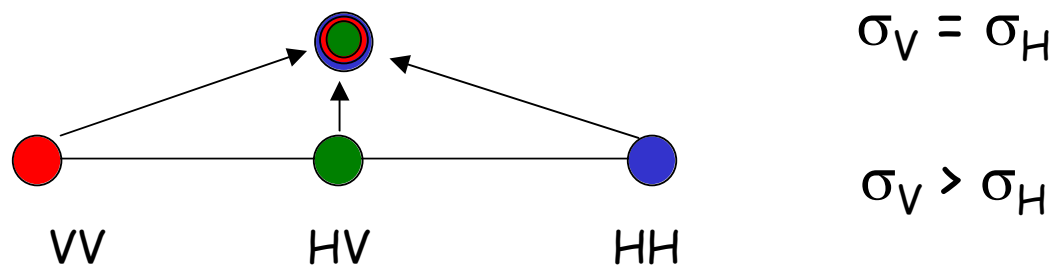


Figure C.4.18: The effect of differential extinction on volume coherence in the complex plane

To further assess whether the magnitude of these observed errors is due to statistical sampling or to real tree structure will require two further stages of investigation:

- To apply the algorithms to real SAR data collected over forest test sites. However such real data will have additional coherence errors due to temporal decorrelation, signal to noise ratio and mis-registration, which must be accounted for in any quantitative analysis.
- To investigate the effects of varying voxel size on extinction estimation in the SAR simulator.

The first of these can be explored within this project by using existing forest SAR data collected by the DLR E-SAR system while the second lies outside the scope of this project and remains for future study.

#### C.4.5 Experimental validation

In the following, the selected experimental data will be analysed in order to demonstrate the effects/potential of Lite-Pol InSAR Configurations. The first data set has been acquired during the second SIR-C/X-SAR space shuttle mission in 1996 over the Kudara test site located close to the lake Baikal / Russia. Fully polarimetric data at L- and C-band have been acquired in a repeat-pass interferometric mode with a temporal baseline of about 48 hours. Figure C.4.19 shows a RGB representation of the three Pauli basis polarisations (Red: HH-VV, Blue: HH+VV, Green: HV+VH). The forested areas are located on the bottom and on the top of each image and appear green at C-band (HV) while the red component at L-band indicates the presence of significant dihedral scattering component (HH-VV) - especially in the forested areas on the top of the image. In the middle, the Selegna river crosses the image surrounded by woodland and vegetated or bare agricultural fields.

According to the discussion in the previous sections, the use of Lite-Pol configuration(s) for forest height inversion has - under the assumption of the RVoG model - two potential limitations compared to Quad-Pol configurations. The first one arises from the contraction of the “visible part” of the straight line in the complex space - predicted by the RVoG model - in Lite-Pol acquisitions. This leads, in general,

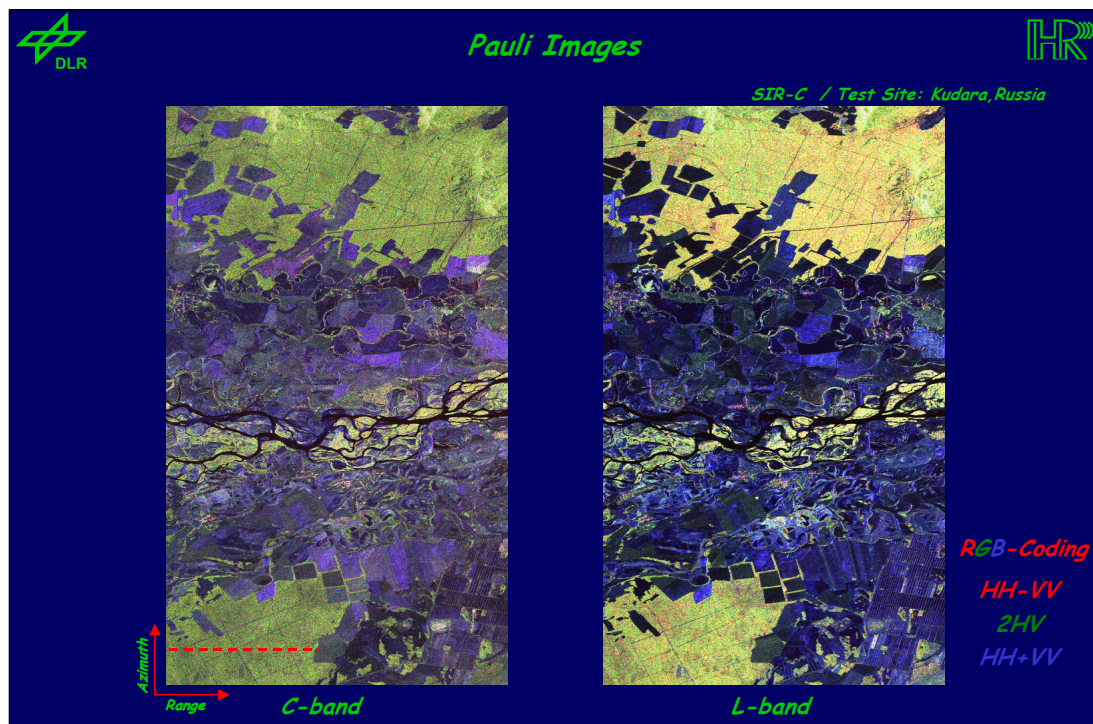


Figure C.4.19: Pauli Images of the Kudara test site: Left: C-band, Right: L-band.

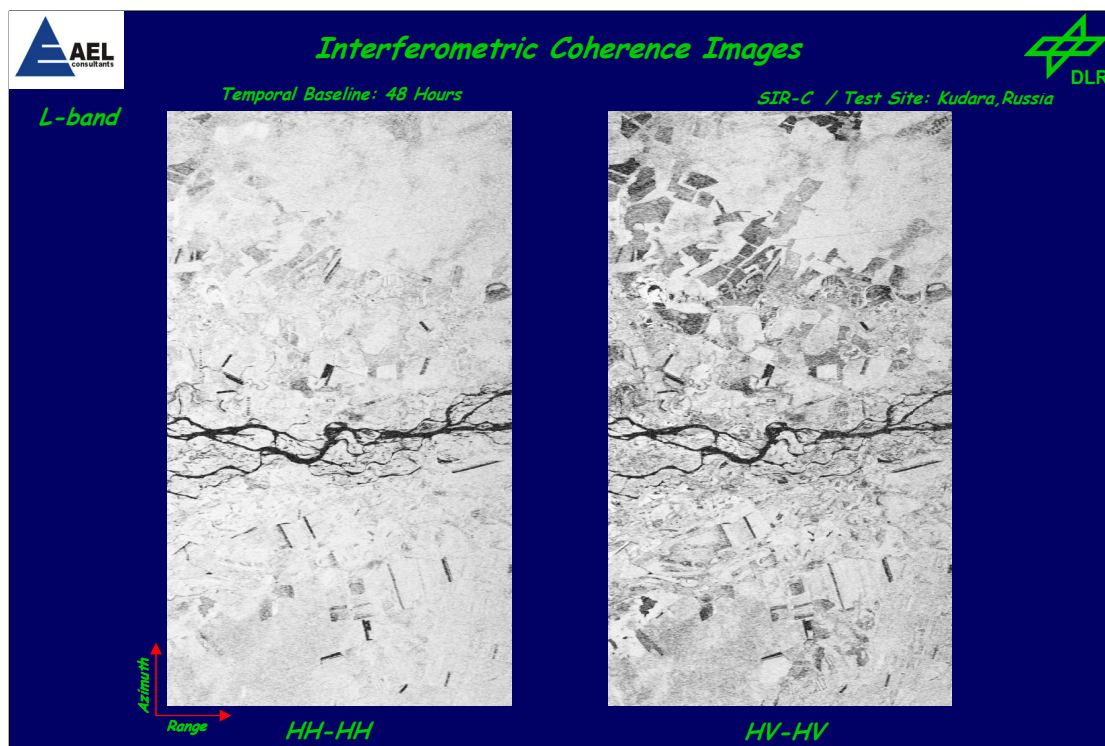


Figure C.4.20: Left: HH-HH, Right: HV-HV Coherence Maps (L-band).



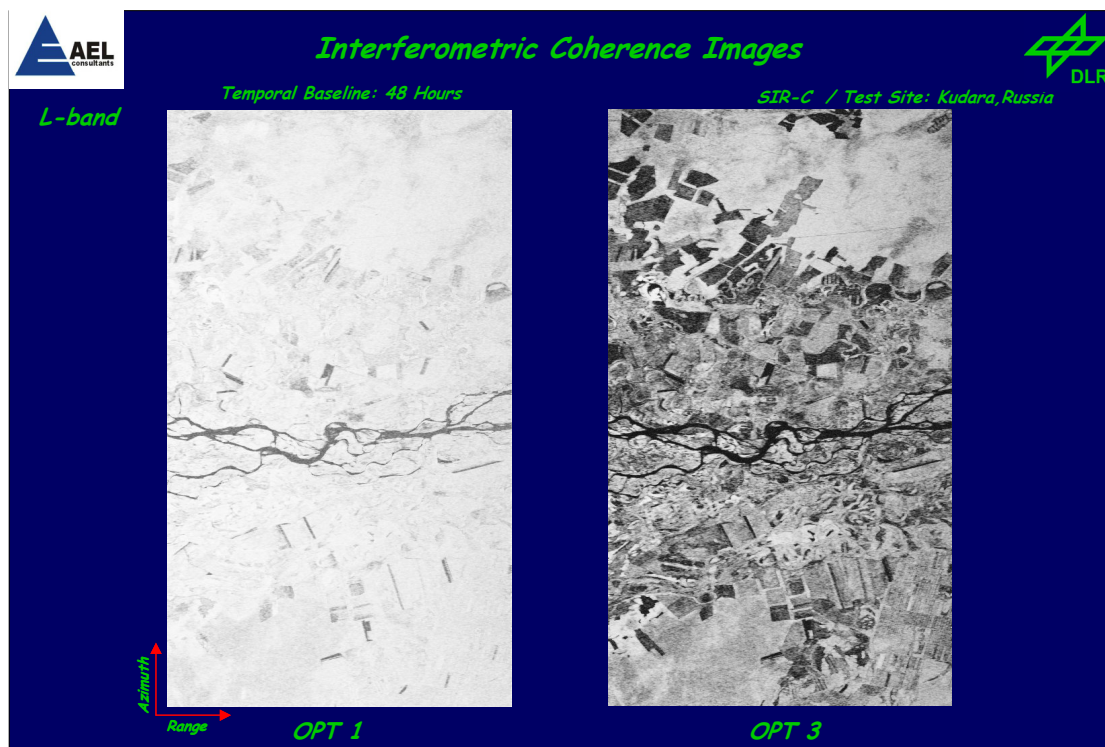


Figure C.4.21: Left: 1<sup>st</sup>, Right: 3<sup>rd</sup> optimum coherence map (L-band).

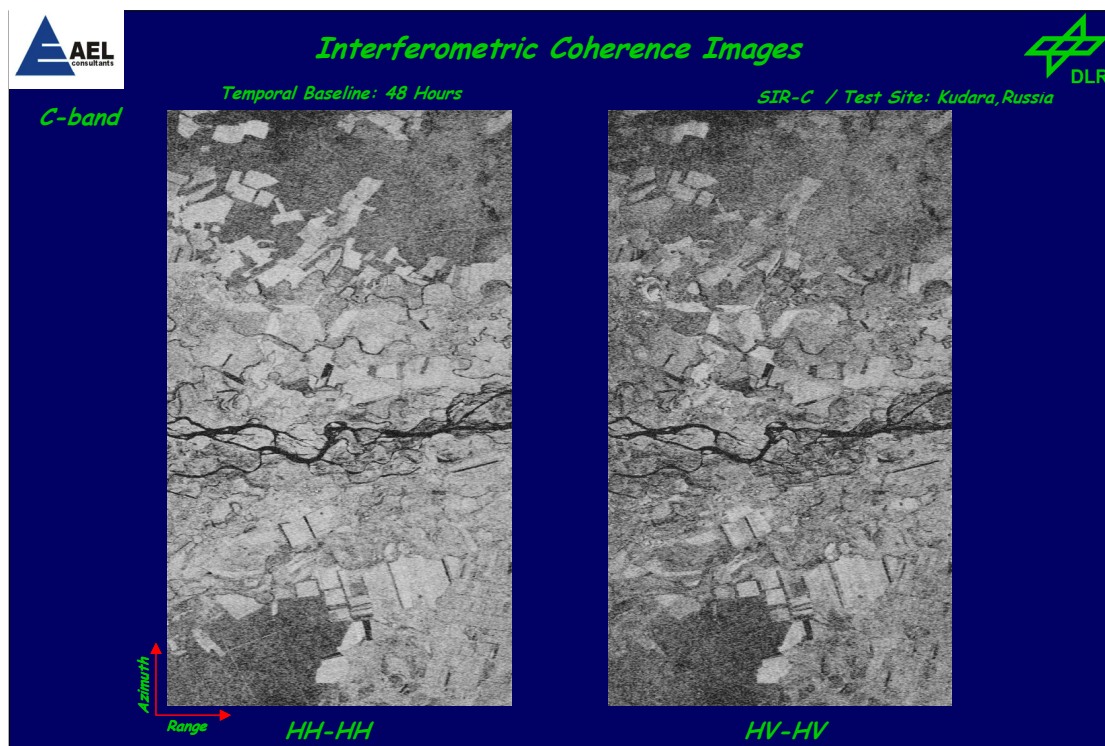


Figure C.4.22: Left: HH-HH, Right: HV-HV coherence map (C-band).

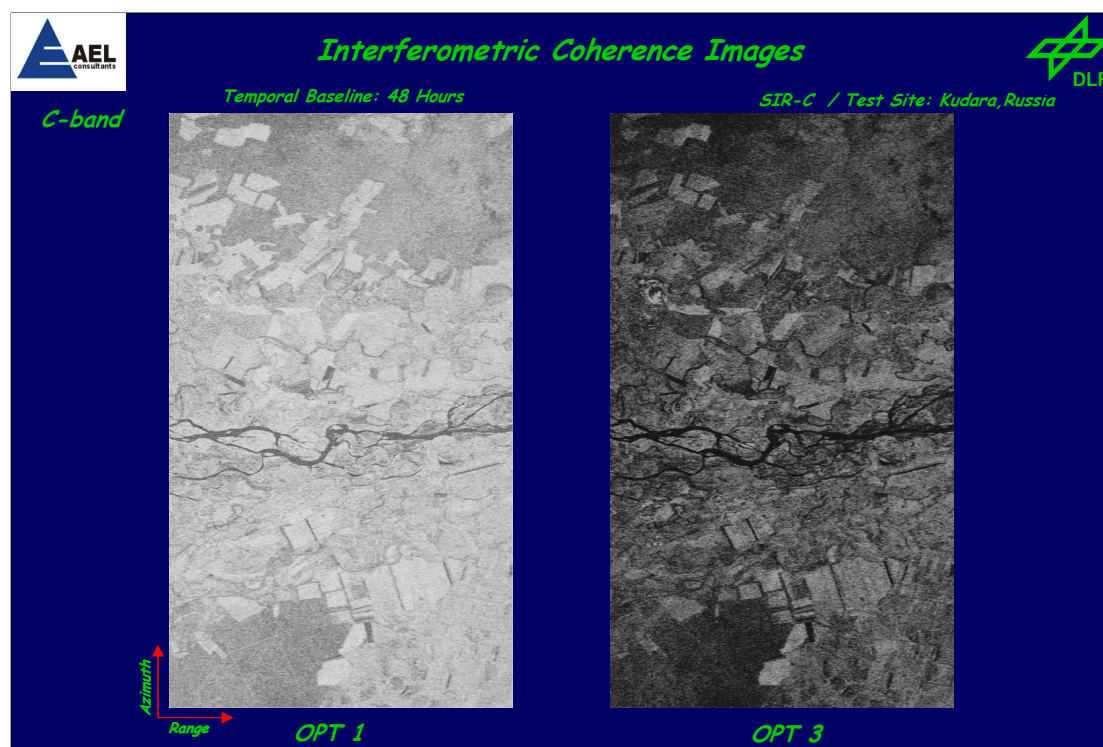


Figure C.4.23: Left: 1<sup>st</sup>, Right: 3<sup>rd</sup> Optimum Coherence Maps (C-band).

to a degraded Lite-Pol estimation performance compared to the inversion performance obtained from Quad-Pol acquisitions. To demonstrate this effect the interferometric coherence maps for the HH-HH and HV-HV interferograms obtained from a Lite-Pol acquisition are shown in Figure C.4.20 (L-band) and 22 (C-band) and compared to the coherence maps of the two extreme optimum polarisations (1<sup>st</sup> and 3<sup>rd</sup>) obtained from a Lite-Pol acquisition shown in Figure C.4.21 (L-band) and 23 (C-band).

It becomes clear that the contrast between the optimum coherences is significantly higher than the contrast between the HH-HH and HV-HV coherences over the whole extent of the forested areas at both frequencies. At C-band is the effect especially strong. Accounting the constant topographic conditions over the whole image, the difference in the contrast reflects - at first order - the difference in the length of the “visible part” of the RVoG model.

To demonstrate this in a direct way, the coherence signatures of two forest points within the scene are shown in Figure C.4.24 (L-band) and 25 (C-band). On the left hand side the loci of the 1<sup>st</sup> and 3<sup>rd</sup> optimum (complex) coherences are indicated by the two green points while on the right hand side the green points indicate loci of the HH-HH and HV-HV (complex) coherences. The effect of a smaller “visible line segment” becomes clear: The contraction of the visible line segment can vary from moderate (lower point) to dramatic (higher point). In the first case the inversion robustness is not very different between the Lite-Pol and Quad-Pol scenario, while in the second case inversion robustness degrades significant in the Lite-Pol scenario.



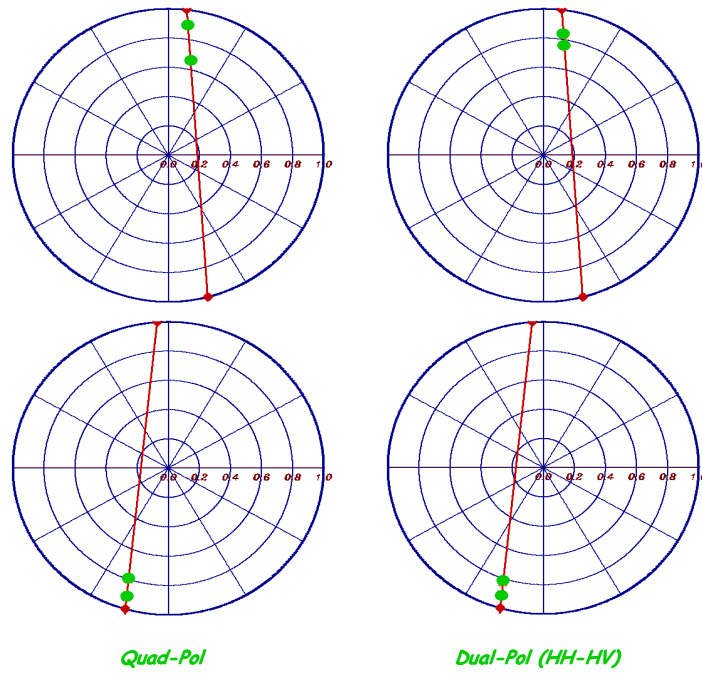


Figure C.4.24: Coherence Signatures: Left Quad, Right: Dual-Pol (L-band).

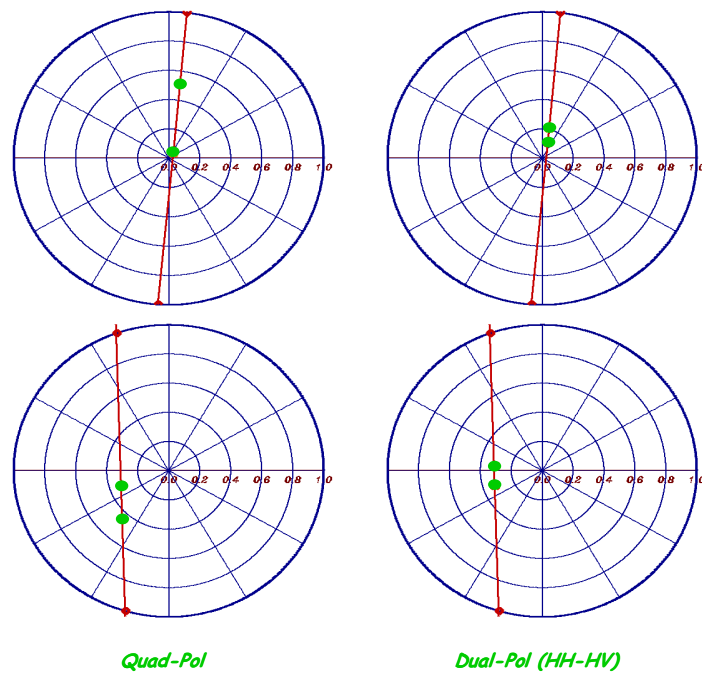


Figure C.4.25: Coherence Signatures: Left Quad, Right: Dual-Pol (L-band).

The second effect is a potential estimation bias introduced by the regularisation condition of no-ground scattering in one of the available polarisations, that is required for the unique inversion of forest height from a single baseline Pol-InSAR acquisition.

While for flat terrain conditions the assumption of no ground contribution in the HV channel may be adequate, in the presence of terrain topography a significant ground component could be introduced in the HV channel. While in the case of a Quad-Pol observation vector this effect can be compensated – by the coherence optimisation process- in the case of Lite-Pol the availability of just two channels does not allow any compensation. Consequently, the use of the HV channel for forest height inversion can lead - depending on the forest conditions - to a more or less significant height bias.

In Figure C.4.26 and Figure C.4.27, two forest height profiles obtained from the inversion of two Lite-Pol (top) and Quad-Pol (bottom) Pol-InSAR data range profiles at L-band are shown. The triangles indicate the estimated height values for every sample and the red line represent the mean height of whole estimates. It can be seen that in both cases the mean values obtained from the Lite-Pol data inversion and the ones obtained from the Quad-Pol data inversion are very close to each other, and no bias becomes visible – in accordance with what one will expect due to the flat terrain conditions. However, it also becomes clear that the height standard variation is higher for the Lite-Pol estimates than for the Quad-Pol estimated – mainly a consequence of the shorter “visible line parts”.

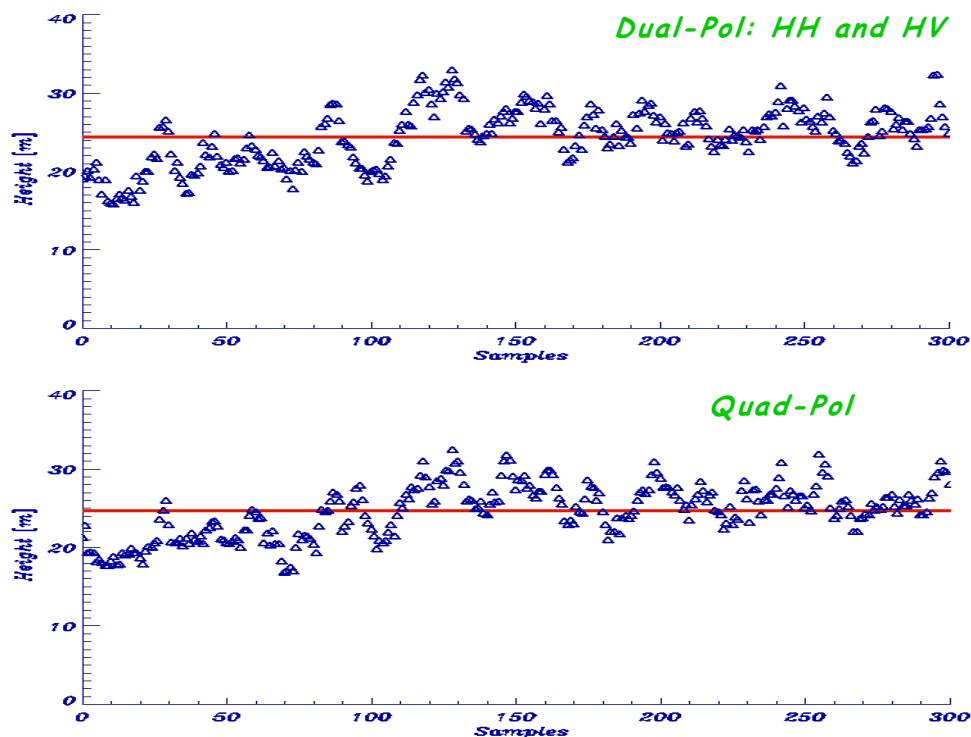


Figure C.4.26: Inverted height profiles. Top: Lite-Pol, Bottom: Quad-Pol.

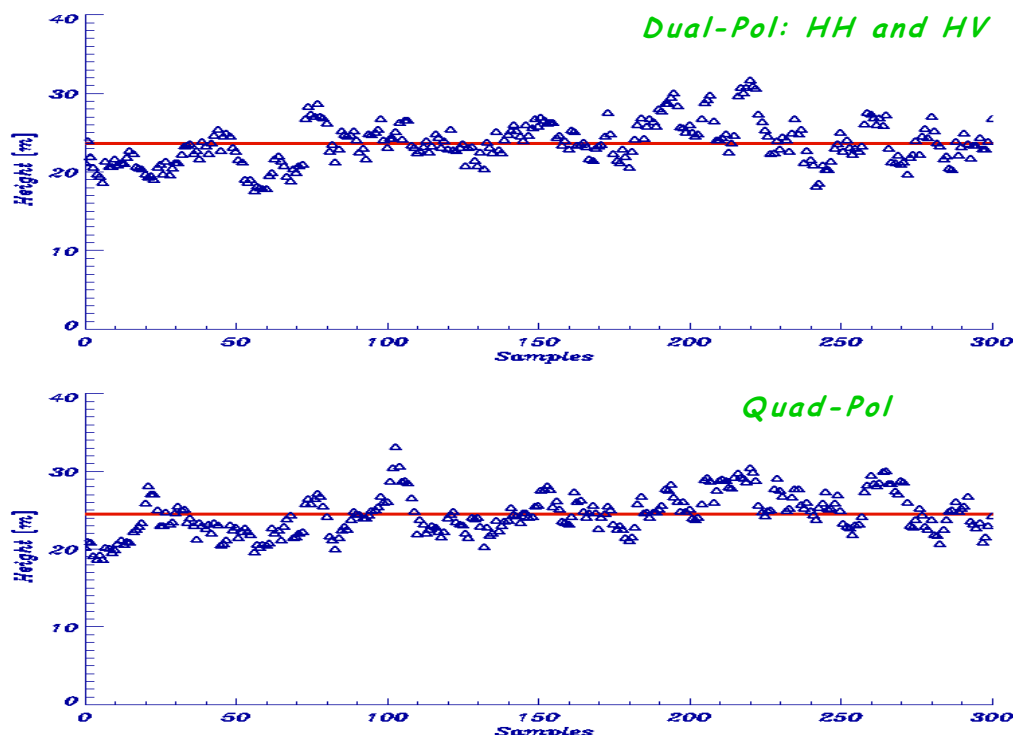


Figure C.4.27: Inverted height profiles. Top: Lite-Pol, Bottom: Quad-Pol.

Finally, in order to evaluate the effect of topography on the Lite-Pol InSAR forest height estimates, the Lite-Pol inversion approach is applied on the proposed test site of Fichtelgebirge / Germany, and the obtained results are compared to the results obtained from the inversion of full Quad-Pol InSAR data. As already stated in chapter C.3, the main test areas of the Fichtelgebirge site are located at the slopes of Schneeberg, that introduces an about 700m height variation over 1.5 kilometres and are dominated by Norway spruce (*Picea abies* about 95%).

Two test stands have been selected and are shown in Figure C.4.28. The histograms of the obtained inversion results are shown in Figure C.4.29 (Test Area 1) and 30 (Test Area 2). The blue histogram represents the results obtained from the inversion of the Quad-Pol data while the orange histograms correspond to the results obtained from the Lite-Pol approach (i.e. Dual-Pol, Channels: HH and HV). In both cases, the Lite-Pol results are characterised by a underestimation of the mean value and a higher variance compared to the Quad-Pol results that fit in these area the ground-measurements better than 10% [111]. For Test Area 1 (mean ground measured height about 18-19 meters) the Quad-Pol results are characterised by a mean value of about 18.8 meters and a variance of 4 meters while the Lite-Pol results have a mean value of about 16 meters and a variance of 6.5 meters. For Test Area 2 (mean ground measured value about 19-22 meters) the Quad-Pol results have a mean value of about 20.5 meters and a variance of 4 meters while the Lite-Pol results have a mean value of about 18.5 meters and a variance of 4.5 meters.

Also these results are in accordance with the physical interpretation performed in the previous sections: Lite-Pol configurations are still capable to provide sensitive forest

height estimates, however with a larger variance compared to the results obtained from Quad-Pol configurations. Quad-Pol configurations allow more robust inversion results primarily due to the higher ability to compensate terrain effects and the more accurate estimation of ground topography.

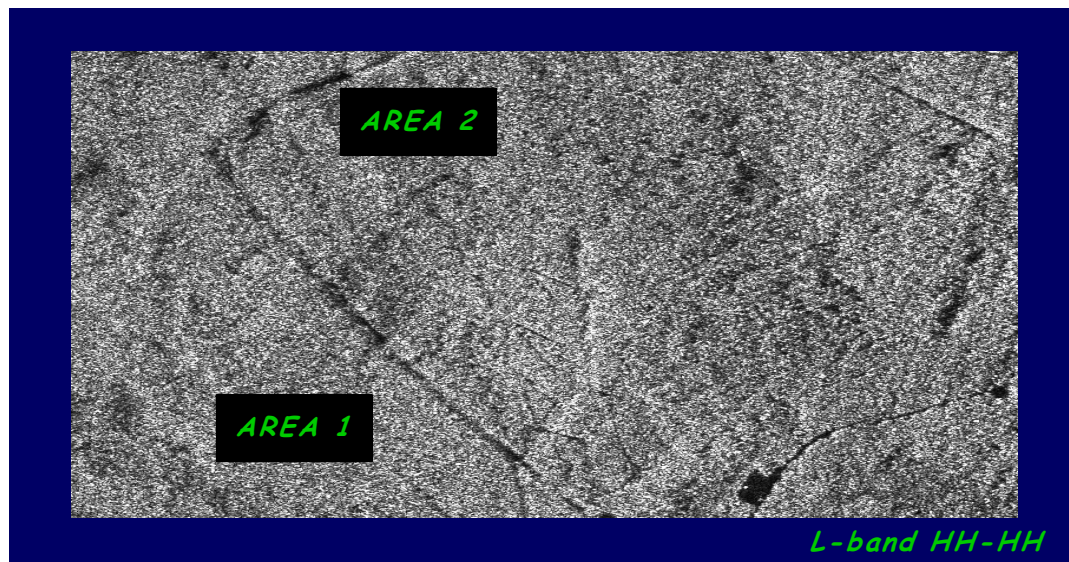


Figure C.4.28: Test Areas for the Fichtelgebirge test site.

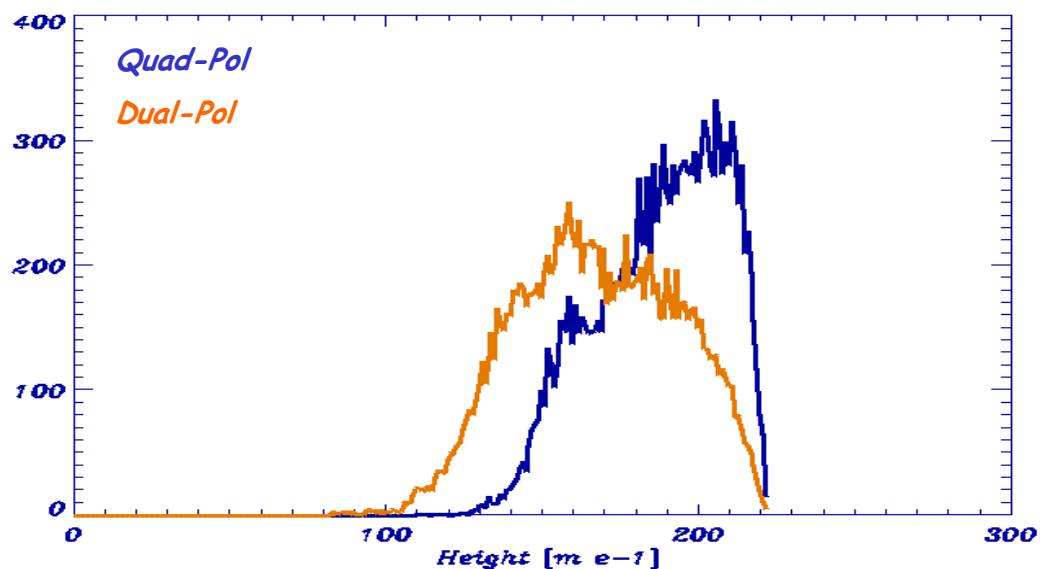


Figure C.4.29: Histograms of estimated forest height for Test Area 1.

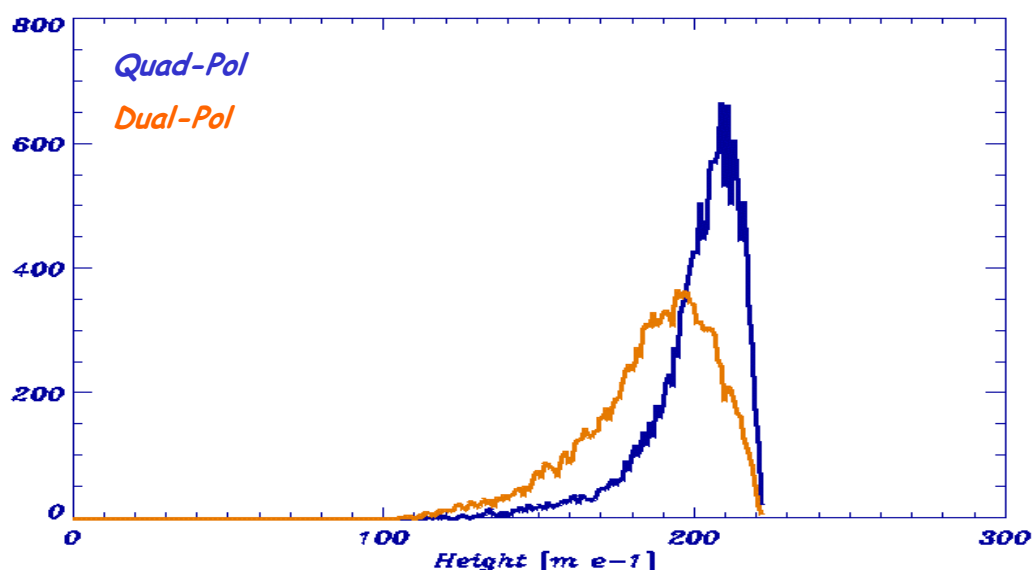


Figure C.4.30: Histograms of estimated forest height for Test Area 1.

#### C.4.6 Conclusions and recommendations

Concluding the work on forest height estimation, the following comments can be made:

Model-based estimation of forest height in terms of Light-pol (Dual-pol) InSAR is in principle possible. Indeed, in the frame of this study has been demonstrated that the Random-Volume-over-Ground (RVoG) scattering model can be used for the inversion of forest height from a dual-pol single baseline InSAR configuration based on a modified (with respect to the quad-pol scenario) inversion methodology. The height estimates – obtained from simulated as well as from experimental data sets – show an overall estimation accuracy of about 15-20% and are sensible enough to make an impact on forest applications. However, the estimation performance depends critically on a series of parameters.

The first key point towards accurate forest height estimation is the precise estimation (or knowledge) of the phase related to the underlying topography. In the Dual-pol InSAR case, model-based estimation of the underlying topography from the data is by far not so successful as in the Quad-pol InSAR case and becomes - with decreasing overall coherence values - less robust and less accurate. It follows that, external ground elevation models - when available – may increase significantly the estimation accuracy of forest height by providing accurate information about underlying topography and its variation. However, DEM's obtained from InSAR techniques are of limited suitability for providing the required underlying topography information. The inherent vegetation bias can reach up about 80% of the forest height - depending on the operation frequency and the forest structure - making the estimation of ground topography very inaccurate. The required accuracy of a true ground topography DEM,

as well as the quantification of the error introduced by a certain terrain variation have to be answered in future investigations.

A second aspect that influences directly the estimation performance of forest height is the presence of orientation effects within the forest canopy. Oriented canopy structure can lead to a polarisation dependent wave propagation through the vegetation volume and violates the assumptions of the RVoG model. The relevance of orientation effects depends strongly on the forest type/structure and the operation frequency. Regarding the influence of frequency, orientation effects are expected, in general, to be stronger at lower (e.g. P-band) than at higher frequencies (e.g. X-, or C-band). At L-band - an intermediate frequency band - the presence and intensity of orientation effects may vary from case to case depending on forest structure.

The Scots Pine forest stand simulation indicates the presence of significant orientation effects at L-band with differential extinctions on the order of 5-10 dB/m. However, the accuracy of those differential extinction estimates is questionable the modelling of vegetation extinction is in general affected by large error-bars. In contrary to these results, the analysis of several experimental Pol-InSAR data sets at L-band over temperate and boreal forest types (predominantly Pine, Spruce and/or Beach stands) do not indicate the presence of strong orientation effects – at least not as strong to effect the forest height estimation accuracy.

The lack of vegetation (forest and agriculture) extinction measurements and its variation with polarisation in the literature, for almost all key radar frequencies (X-, C-, and L-band) makes a critical evaluation of the obtained results very difficult. Thus, the organisation and support of experimental vegetation extinction/ attenuation measurement campaigns, especially with respect to future Pol-InSAR missions, is strongly recommended.

In addition, acquisition and evaluation - with respect to forest height estimation and quantification of the effect of differential extinction - of experimental Pol-InSAR data over forest types characterised by different structure than the ones reported in the literature is also suggested. This will allow a wider validation of the proposed methodology and of the underlying assumptions.

In the absence of a ground elevation model the accuracy of the underlying phase estimation – and consequently the accuracy of the forest height estimation - depends critical on the choice of the polarisation pair. The performed analysis indicated that HH-VV and HV is the pair that leads to the best estimation performance. Under the constraint of a single transmission channel, HH and HV appears to provide the best results having at the same time the highest robustness against orientation effects. Light-pol using circular polarisation LL and LR also provided satisfactory performance, at least in the simulated data sets used in this study. However, the fact that the circular performance is no better than the one obtained from the linear configuration combined with the fact that there are no plans for a near future makes the circular LL and LR pair to be of secondary importance.

Compared now to the Quad-pol InSAR case, the main impairment regarding forest height estimation introduced by a Light-pol InSAR configuration is in terms of



robustness and estimation accuracy. A Quad-pol InSAR configuration allows, as already mentioned above, a more accurate and/or robust estimation of the underlying topography phase as it allows to generate more statistical samples - in terms of linear combinations of the three independent polarisation states - required for a better estimation. In the Light-pol InSAR case, the availability of only two polarisations - that in both proposed configurations (HH and VH or LL and LR) do not correlate - affects the formation of appropriate linear combinations and limits thus the estimation accuracy/robustness.

In addition, a Quad-pol InSAR configuration permits a more accurate approximation of the assumption of no ground scattering in one polarisation that is required for the regularisation of the inversion problem, especially in the presence of terrain variation. The availability of Quad-pol data allows a better compensation of terrain induced ground scattering components, while in the Light-pol InSAR case the assumption of no ground scattering is always approximated by the Cross-pol channel. An external ground topography DEM becomes also on here of importance as it may permit the removal of the ground scattering components introduced by the terrain variation. The accuracy requirements are in this case not so strict as for the estimation of the phase related to the ground.

However, the main limitation for the application of the developed methodology is temporal decorrelation - inherent in all repeat-pass implementations of InSAR. Temporal decorrelation reduces the InSAR coherence and leads - if not accounted - to a sensitive overestimation of forest height. In its most general form, temporal decorrelation can affect directly the underlying RVoG inversion model making forest height estimation with a Light-Pol (or even Quad-Pol) InSAR configuration unreliable. However, the most common temporal decorrelation sources- as for example wind induced movement of the scatterers within the canopy layer - do not affect directly the underlying model, making forest height estimation a solvable but underdetermined problem at least for a for a single baseline Pol-InSAR acquisition. The most promising way to deal with this problem is by facing moderate decorrelation effects – guaranteed by very small temporal baselines – with an extended observation vector in terms of multiple interferometric observations at different baselines – a scenario that can be realised in the frame of a mission. In this way height retrieval with a reasonable error bar can be made possible (even for Light Pol systems). Promotion for the development of the related methodology and its validation is highly recommended as a possible break-through will allow a significant upgrade of near future spaceborne SAR mission applications.

## C.5 REFERENCES

1. Bamler, R., and P. Hartl. 1998. Synthetic Aperture Radar Interferometry. *Inverse Problems*, vol. 14, pp. R1-R54.
2. Hagberg, J.O., L.M. Ulander, and J. Askne. 1995. Repeat-Pass Interferometry over Forested Terrain. *IEEE Trans. Geosci. Rem. Sens.* Vol. 33, no. 2, pp. 331-340.
3. Askne, J., P.B. Dammert, L.M. Ulander, and G. Smith. 1997. C-Band Repeat-Pass Interferometric SAR Observations of the Forest. *IEEE Trans. Geosci. Rem. Sens.*, vol. 35, no. 1, pp. 25-35.
4. Treuhaft, R.N., M. Moghaddam, and B.J. Yoder. 1997. Forest Vertical Structure from Multibaseline Interferometric Radar for Studying Growth and Productivity. *Proc. IGARSS'97*, Singapore, 3-8 August 1997..
5. Treuhaft, R.N., S.N. Madsen, M. Moghaddam, and J.J. van Zyl. 1999. Vegetation Characteristics and Underlying Topography from Interferometric Data. *Radio Science*, vol. 31, pp. 1449-1495.
6. Treuhaft R.N., B.E. Law, and P.R. Siqueira. 1999. Estimating Forest Vertical Structure from Multialtitude, Fixed Baseline Radar Interferometric and Polarimetric Data, *Proc. IGARSS'99*, Hamburg, Germany, 28 June - 2 July 1999.
7. Treuhaft R.N., and P.R. Siqueira. 2000. The Vertical Structure of Vegetated Land Surfaces from Interferometric and Polarimetric Radar. *Radio Science*, vol. 35, no. 1, pp. 141-177.
8. Treuhaft, R.N., B.E. Law, G.P. Asner, and S. Hensley. 2000. Vegetation Profile Estimation from Multialtitude, Multifrequency, Radar Interferometric and Polarimetric Data. *Proc. IGARSS'00*, Honolulu Hawaii, 24-28 July 2000.
9. Cloude S R. 2002. Robust Parameter Estimation using dual baseline polarimetric SAR Interferometry. *Proc. IGARSS'02*, Toronto, Canada, Vol.2, pp 838-840, July.
10. Schwaebisch, M., C. Hofmann, J. Moreira, C. Wimmer and S. Oh. 1999. Operational Processing of Airborne P-band InSAR Data for Ground Topography Estimation. *Proc. IGARSS'99*, Hamburg, Germany, 28 June - 2 July.
11. Ulbricht, A. Reigber, R. Horn, A. Potsis, and A. Moreira. 2000. Multi-frequency SAR Interferometry: DEM Generation in L- and P-band and Vegetation Height Estimation in Combination with X-band. *Proc. 3rd European Conference on Synthetic Aperture Radar EUSAR 2000*, pp. 51-54, Munich, Germany, 23-25 May.
12. Hensley S, E Chapin, A Freedman, C Le, S Madsen, T Michel, E Rodriguez, P Siqueira, K Wheeler. 2001. First P-band Results Using the GeoSAR Mapping System. *Proc. IGARSS 2001*, Sydney, Australia, (CD-ROM), July 2001.
13. Mura, J C, L Bins, F Gama, C Freitas, J dos Santos, L V Dutra, 2001. Identification of Tropical Forest in the Brazilian Amazon Based on DEM differences between P and X band Interferometric Data. *Proc. IGARSS'01*, Sydney, Australia, (CD-ROM), July 2001

14. Wegmüller, U., and C.L. Werner, 1995. SAR Interferometric Signatures of Forest. *IEEE Trans. Geosci. Rem. Sens.*, vol. 33, no. 5, pp. 1153-1161, 1995.
15. Wegmüller, U., and C.L. Werner. 1997. Retrieval of Vegetation Parameters with SAR Interferometry. *IEEE Trans. Geosci. Rem. Sens.*, vol. 35, no. 1, pp. 18-24.
16. Papathanassiou, K.P., and M. Coltelli. 1996. Interpretation of Multifrequency Coherence Maps. *Proc. European Conference on Synthetic Aperture Radar, EUSAR'96*, pp. 225-230, Koenigswinter, Germany, 26-28 March.
17. Papathanassiou, K.P., A. Reigber, and M. Coltelli. 1996. On the Interferometric Coherence: A Multifrequency and Multitemporal Analysis. *Proc. FRINGE '96 Workshop*, ESA, Zurich, Switzerland, pp. 319-330, 20 Sept. -2 Oct. 1996.
18. Boerner, W.M., et al. 1998. *Polarimetry in Radar Remote Sensing: Basic and Applied Concepts. Chapter 5 in F.M. Henderson, and A.J. Lewis, (ed.) Principles and Applications of Imaging Radar.* vol. 2 of Manual of Remote Sensing, (ed. R.A. Reyerson), 3<sup>rd</sup> Edition, John Willey & Sons, New York, 1998.
19. Cloude, S.R., K.P. Papathanassiou, and E. Pottier. 2001. Radar Polarimetry and Polarimetric Interferometry. *IEICE Trans. Electronics*, vol. E84-C, no. 12, pp. 1814-1822, December.
20. Reigber A. and A. Moreira, 2000. First Demonstration of SAR Tomography Using Multibaseline L-band Data. *IEEE Trans. Geosci. Rem. Sens.*, vol. 38, no. 5, pp. 2142-2152, 2000.
21. Reigber A.. 2002. Airborne Polarimetric SAR Tomography. DLR report, ISRN DLR-FB-2002-02.
22. Wagner W. *et al.* 2000. The Use of Coherence Information from ERS Tandem Pairs for Determining Forest Stock Volume in SIBERIA. *Proc. IGARSS'00*, Honolulu Hawaii, 24-28 July.
23. W. Wagner et al. 2001. SAR Imaging for Boreal Ecology and Radar Interferometry Applications. *SIBERIA Project Final Report*, EC Environment and Climate Program, Theme 3, Area 3.3, June.
24. Papathanassiou, K.P., and J.R. Moreira. 1996. Interferometric Analysis of Multifrequency and Multipolarisation SAR Data. *Proc. IGARSS'96*, pp. 1227-1229, Lincoln, 27-31 May.
25. Cloude, S.R. and K.P. Papathanassiou. 1998. Polarimetric SAR Interferometry. *IEEE Trans. Geosci. Rem. Sens.*, vol. 36, no. 5, pp. 1551-1565, September.
26. Papathanassiou, K.P., and S.R. Cloude. 1997. Polarimetric Effects in Repeat-Path Interferometry. *Proc. IGARSS'97*, pp. 1926-1928, Singapore, 3-8 August.
27. Papathanassiou, K.P., and S.R. Cloude. 1998. Phase Decomposition in Polarimetric SAR Interferometry. *Proc. IGARSS'98*, pp. 2184-2186, Seattle, 3-8 August.
28. Cloude, S.R. and K.P. Papathanassiou. 1997. Polarimetric Optimisation in Radar Interferometry. *Electronics Letters*, vol. 33, no. 13, pp. 1176-1178, June.
29. Cloude, S.R., and K.P. Papathanassiou. 1997. Coherence Optimisation in Polarimetric SAR Interferometry. *Proc. IGARSS'97*, pp. 1932- -1934, Singapore, 3-8 August.

- 
30. Gabriel, J., C. Schmullius and K.P. Papathanassiou. 1999. Tree Height Estimation using Polarimetric SAR Interferometry. *Proc. IGARSS'99*, Hamburg, Germany, 28 June - 2 July.
  31. Lopez-Sanchez, J.M., L. Saques, J. Fortuny, X. Fabregas, A. Broquetas, A.J. Sieber and S.R. Cloude. 1999. Laboratory Experiments of Polarimetric Radar Interferometry: DEM Generation and Vegetation Height Estimation. *Proc. IGARSS'99*, Hamburg, Germany, 28 June - 2 July.
  32. Saques, L., J.M. Lopez-Sanchez, J. Fortuny, X. Fabregas, A. Broquetas, and A.J. Sieber. 2000. Indoor Experiments on Polarimetric SAR Interferometry. *IEEE Trans. Geosci. Rem. Sens.*, vol. 38, no. 2, pp.671-684.
  33. Saques, L., J.M. Lopez-Sanchez, X. Fabregas, A. Broquetas, J. Fortuny, and A.J. Sieber. 2000. Crop Height Retrieval by Polarimetric Radar Interferometry: Indoor and Outdoor Results with Ground Based Systems. *Proc. 3rd European Conference on Synthetic Aperture Radar EUSAR 2000*, pp. 787-790, Munich, Germany, 23-25 May.
  34. Nico, G., J.M. Lopez-Sanchez, J. Fortuny, D. Tarchi, D. Leva, and A.J. Sieber. 2000. Assessment of the Impact of the Polarimetric Coherence Optimisation on Phase Unwrapping. *Proc. 3<sup>rd</sup> European Conference on Synthetic Aperture Radar EUSAR 2000*, pp. 523-526, Munich, Germany, 23-25 May.
  35. Papathanassiou, K.P., A. Reigber, R. Scheiber, R. Horn, A. Moreira, and S.R. Cloude. 1998. Airborne Polarimetric SAR Interferometry. *Proc. IGARSS'98*, pp. 1901-1904, Seattle, 3-8 August.
  36. Papathanassiou, K.P., A. Reigber, and S.R. Cloude. 1999. Vegetation and Ground Parameter Estimation using Polarimetric Interferometry Part I: The Role of Polarisation. *Proc. CEOS SAR Workshop*, Toulouse, 26-29 October.
  37. Papathanassiou, K.P., A. Reigber, and S.R. Cloude. 1999. Vegetation and Ground Parameter Estimation using Polarimetric Interferometry Part II: Parameter Inversion and Optimal Polarisation. *Proc. CEOS SAR Workshop*, Toulouse, 26-29 October.
  38. Papathanassiou, K.P., S.R. Cloude, and A. Reigber. 2000. Single and Multibaseline Polarimetric SAR Interferometry over Forested Terrain. *Proc. 3rd European Conference on Synthetic Aperture Radar EUSAR 2000*, pp. 123-126, Munich, Germany, 23-25 May.
  39. Papathanassiou, K.P., S.R. Cloude, A. Reigber, and M-W. Boerner. 2000. Multi-baseline Polarimetric SAR Interferometry for Vegetation Parameters Extraction. *Proc. IGARSS'00*, pp. 2762-2764, Honolulu Hawaii, 24-28 July.
  40. Papathanassiou, K.P. and S.R. Cloude. 2001. Single baseline Polarimetric SAR Interferometry. *IEEE Trans. Geosci. Rem. Sens.*, vol, 39, no. 11, pp. 2352-2363, November.
  41. Stebler, O., P. Pasquali, D. Nuesch. 2000. Investigation of multi-baseline singular value estimation within POL-InSAR measurements. *Proc. European Conference on Synthetic Aperture Radar EUSAR 2000*, 23-25 May, Munich, Germany, pp. 257-260.

42. Stebler, O., P. Pasquali, R. Brodbeck, and D. Nüesch. 2000. Multibaseline Pol-InSAR for the Estimation of Scattering Processes and their Spatial Distribution Within Vegetation Layers. *Proc. IGARSS'00*, Honolulu Hawaii, 24-28 July.
43. Stebler, O., E. Meier, D. Nüesch. 2001. Multi-baseline airborne Pol-InSAR measurements for the analysis and inversion of scattering processes within vegetation media. *Proc. 3rd International Symposium on Retrieval of Bio- and Geophysical Parameters from SAR Data for Land Applications*, 11-14 September, Sheffield, UK.
44. Stebler, O., E. Meier, D. Nüesch. in press. Multi-baseline polarimetric SAR interferometry - first experimental spaceborne and airborne results. *ISPRS Journal of Photogrammetry and Remote Sensing (P&RS)*.
45. Saques, L., X. Fabregas, A. Broquetas. 2000. Extraction of Vegetation Structure and Surface Parameters using Polarimetric and Interferometric SAR Techniques. *Proc. IGARSS'00*, Honolulu Hawaii, 24-28 July.
46. Lopez-Sanchez, J.M., J. Fortuny, A.J. Sieber, L. Saques, M. Bara, X. Fabregas, A. Broquetas. 2000. Experimental Comparison of Different Scattering Mechanism Selections for Vegetation Height Retrieval by PolInSAR. *Proc. IGARSS'00*, Honolulu Hawaii, 24-28 July.
47. Reigber, K., K.P. Papathanassiou, S.R. Cloude, and A. Moreira. 2001. SAR Tomography and Interferometry for Remote Sensing of Forested Terrain. *Frequenz-Die Zeitschrift fuer Telecommunication*, vol. 55, pp. 119-122, April.
48. Kobayaschi, Y., K. Sarabandi, L. Pierce and G. Dobson. 2000. An Evaluation of the JPL TOPSAR for Extracting Tree Heights. *IEEE Trans. Geosci. Rem. Sens.*, vol. 38, no. 6, pp. 2446-2454, 2000.
49. Brown C.G. and K. Sarabandi. 2001. Model Based Estimation of Forest Canopy Parameters Using Polarimetric and Interferometric SAR. *Proc. IGARSS'01*, Sydney, Australia, 9-13 July.
50. Lyn, Y.C. and K. Sarabandi. 1999. Monte Carlo Coherent Scattering Model for Forest Canopies using Fractal Generated Trees. *IEEE Trans. Geosci. Rem. Sens.*, vol. 37, no. 1, pp.440-451.
51. Sarabandi, K., 1997.  $\Delta k$ -Radar Equivalent of Interferometric SARs: A Theoretical Study for Determination of Vegetation Height. *IEEE Trans. Geosci. Rem. Sens.*, vol. 35, pp.1267-1276.
52. Sarabandi, K. and Y.C. Lyn. 1997. Simulation of Interferometric SAR Response for Characterizing the Scattering Phase Centre Statistics of Forest Canopies. *IEEE Trans. Geosci. Rem. Sens.*, vol. 35, no. 1, pp.115-125.
53. Sarabandi, K., and A. Nashabibi. 1999. Analysis and Application of Backscattered Frequency Correlation Function. *IEEE Trans. Geosci. Rem. Sens.*, vol. 37, no. 4, pp.1895-1906.
54. Treuhaft, R., and S.R. Cloude. 1999. The Structure of Oriented Vegetation from Polarimetric Interferometry. *IEEE Trans. Geosci. Rem. Sens.*, vol. 37, no. 5, pp. 2620-2624, 1999.
55. Cloude, S.R., K.P. Papathanassiou, and M-W. Boerner. 2000. The Remote Sensing of Oriented Volume Scattering using Polarimetric Radar Interferometry.

- Proc. International Symposium on Antennas and Propagation ISAP'00*, Fukuoka, Japan, 22-25 August.
56. Reigber, K.P. Papathanassiou, S.R. Cloude and A. Moreira. 2000. SAR Tomography and Interferometry for the Remote Sensing of Forested Terrain. *Proc. 3rd European Conference on Synthetic Aperture Radar EUSAR 2000*, pp. 137-140, Munich, Germany, 23-25 May.
  57. Yamada H., Yamaguchi Y., Roiquez E., Kim Y., and W.M. Boerner. 2001. Polarimetric SAR Interferometry for Forest Canopy Analysis by using Super-Resolution Method. *Proc. IGARSS'01*, 9-13 July, Sydney, Australia, 2001.
  58. Yamada H. Submitted-2001. Polarimetric SAR Interferometry Based on the ESPRIT Algorithm. *Submitted to IEEE Trans. Geosci. Rem. Sens.*
  59. Cloude, S.R., K.P. Papathanassiou, and M-W. Boerner. 2000. A Fast Method for Vegetation Correction in Topographic Mapping using Polarimetric Radar Interferometry. *Proc. 3rd European Conference on Synthetic Aperture Radar EUSAR 2000*, pp. 261-264, Munich, Germany, 23-25 May 2000.
  60. Isola, M., and S.R. Cloude. 2001. Forest Height Mapping using Space-Borne Polarimetric SAR Interferometry. *Proc. IGARSS'01*, 9-13 July, Sydney, Australia.
  61. Cloude, S.R., K.P. Papathanassiou, I. Woodhouse, J. Hope, J.C. Suarez Minguez, P. Osborne, and G. Wright. 2001. The Glen-Affric Project: Forest Mapping using Polarimetric Radar Interferometry. *Proc. IGARSS'01*, 9-13 July, Sydney, Australia.
  62. Stebler, O., E. Meier, D. Nüesch. 2001. Multi-baseline airborne Pol-InSAR measurements for the estimation of scattering processes within vegetation media. *Proc. IGARSS'01*, 9-13 July, Sydney, Australia.
  63. Brandfass, M., C. Hofmann, J.C. Mura, J. Moreira, and K.P. Papathanassiou. 2001. Parameter estimation of Rain Forest Vegetation via Polarimetric Radar Interferometric Data. *Proc. SPIE 2001*, Toulouse, France, August 2001.
  64. Papathanassiou, K.P., T. Mette, R. Zimmermann and S.R. Cloude. 2001 - in print. Forest Biomass Estimation using Polarimetric SAR Interferometry. *Proc. ASAR'01* (in print), Montreal, Canada, 1-4 October 2001.
  65. Cloude, S.R., K.P. Papathanassiou, and A. Reigber. 2000. Polarimetric SAR Interferometry at P-Band for Vegetation Structure Extraction. *Proc. 3rd European Conference on Synthetic Aperture Radar EUSAR 2000*, pp. 249-252, Munich, Germany, 23-25 May.
  66. Cloude, S.R., K.P. Papathanassiou, A. Reigber, and M-W. Boerner. 2000. Multi-Frequency Polarimetric SAR Interferometry for Vegetation Structure Extraction. *Proc. IGARSS'00*, pp. 129-131, Honolulu Hawaii, 24-28 July.
  67. Brandfass, M., C. Hofmann, J.C. Mura, and K.P. Papathanassiou. 2001. Polarimetric SAR Interferometry as Applied to Fully Polarimetric Rain Forest Data. *Proc. IGARSS'01*, 9-13 July, Sydney, Australia.
  68. Tabb, M., and R. Carande. 2001. Robust Inversion of Vegetation Structure Parameters from Low Frequency Polarimetric Interferometric SAR. *Proc. IGARSS'01*, 9-13 July, Sydney, Australia.



- 
69. Cloude, S.R., and K.P. Papathanassiou. 2002. A 3-Stage Inversion Process for Polarimetric SAR Interferometry. *Proc. European Conference on Synthetic Aperture Radar, EUSAR'02*, pp. 279-282, Cologne, Germany, 4-6 June.
  70. Papathanassiou, K.P., I. Hajnsek, A. Moreira and S.R. Cloude. 2002. Forest Parameter Estimation using a Passive Polarimetric Micro-Satellite Concept. *Proc. European Conference on Synthetic Aperture Radar, EUSAR'02*, pp. 357-360, Cologne, Germany, 4-6 June.
  71. Ulbricht, X. Fabregas, L. Saques. 2001. Applying Polarimetric Interferometric Methods to Invert Vegetation Parameters from SAR Data. *Proc. IGARSS'01*, 9-13 July, Sydney, Australia.
  72. Papathanassiou, K.P., S.R. Cloude, and A. Reigber. 2000. Single and Multibaseline Polarimetric SAR Interferometry over Forested Terrain. *Proc. 3rd European Conference on Synthetic Aperture Radar EUSAR 2000*, pp. 123-126, Munich, Germany, 23-25 May.
  73. Papathanassiou, K.P., T. Mette, I. Hajnsek, G. Krieger and, A. Moreira. 2002. Passive Polarimetric Micro-Satellite Concept for Global Biomass Mapping', *Proc. PI-SAR Workshop (cd-rom)*, Tokyo, Japan, 29-30 August.
  74. Papathanassiou, K.P., I. Hajnsek, T. Mette, and S.R. Clouse. 2002. Model Based Forest Height Estimation for Forest Biomass Estimation. *Recent Advances in Remote Sensing Workshop (Proc. in print)*, Valencia, Spain, 16-20 September.
  75. Allmaras, R. R, Burwell, R.E & R.F. Holt. 1967. Plow-layer porosity surface roughness from tillage as affected by initial porosity and soil moisture at tillage time. *Soil Sci. Soc. Am. P.*, vol. 31, pp. 550-556.
  76. Dobson, M. C. Ulaby, F. T., Hallikainen, M. T. and EL-Rayes, M A. 1985. Microwave Dielectric Behaviour of Wet Soil - Part II: Empirical Models and Experimental Observations. *IEEE Trans. Geosci. Rem. Sens.*, vol. 23, no. 1, pp. 35 - 46, 1985.
  77. Beckmann, P. and Spizzichino A. 1963. *The scattering of electromagnetic waves from rough surfaces*. Pergamon Press, p. 503.
  78. Mattia, F. and Le Toan, T. 1999. Backscattering properties of multi scale rough surfaces. *J. Electromagn. Waves Applicat.*, vol. 13, pp. 491-526, 1999.
  79. Oh, Y., K. Sarabandi and F. T. Ulaby. 1992. An Empirical Model and an Inversion Technique for Radar Scattering from Bare Soil Surfaces. *IEEE Trans. Geosci. Rem. Sens.*, vol. 30, no. 2, pp.370 - 381.
  80. Dubois, P. C. and J. J. van Zyl. 1995. An Empirical Soil Moisture Estimation Algorithm Using Imaging Radar. *IEEE Trans. Geosci. Rem. Sens.* vol. 33, no.4, 1995, pp. 915 - 926.
  81. Borgeaud, M. and Noll, J., 1994. Analysis of Theoretical Surface Scattering Models for Polarimetric Microwave Remote Sensing of Bare Soils. *International Journal of Remote Sensing*. vol. 15, no. 14, pp. 2931-2942.
  82. Mattia, F., Le Toan, T., Souyris, J. C., De Carolis, G., Floury, N., Posa, F., Pasquariello, G..1997. The effect of Surface Roughness on Multi-Frequency Polarimetric SAR Data. *IEEE Trans. Geosci. Rem. Sens.*, vol. 35, no. 4, pp. 954-965.

- 
83. Zribi, M. V. Ciarelli, D. Vidal-Madjar. 1999. An Inversion Model of Soil Roughness Based on Two Radar Frequency Measurements. *Proc. IGARSS'99*, Hamburg 1999, vol. II, pp. 2528 - 2530.
  84. Davidson, M.W.J., T. Le Toan, F. Mattia, G. Satalino, T. Mannier, and M. Borgeaud. 2000. On the characterisation of agricultural soil roughness for radar remote sensing studies. *IEEE Trans. Geosci. Rem. Sens.*, vol. 38, no. 2, pp. 630-640.
  85. Hajnsek, I., K. P. Papathanassiou and S. R. Cloude. 2001. Additive Noise Filtering for Polarimetric Eigenvalue Processing. *Proc. IGARSS'01*, Sydney.
  86. Cloude, S. R., I. Hajnsek, and K. P. Papathanassiou. 1999. An Eigenvector Method for the Extraction of Surface Parameters in Polarimetric SAR. *Proc. CEOS SAR Workshop*, Toulouse 1999, ESA SP-450, pp. 693 - 698.
  87. Hajnsek, I. 2001. Inversion of Surface Parameters Using Polarimetric SAR. *DLR-Science Report*, vol. 30, ISSN 1434-8454, p. 224.
  88. Just, D. and R. Bamler. 1994. Phase Statistics of Interferograms with Applications to Synthetic Aperture Radar. *Applied Optics*, vol. 33, pp. 4361-4368.
  89. Gatelli, F., A. Monti Guarnieri, F. Parizzi, P. Pasquali, C. Prati, and F. Rocca. 2002. Airborne Polarimetric SAR Tomography, *DLR-Science Report*, vol. 02, ISSN 1434-8454, p. 154.
  90. Franceschetti, G. and Iodice, A. 1997. The effect of Surface scattering on IFSAR Baseline Decorrelation. *Journal of Electromagnetic Waves and Applications*, vol. 11, pp. 353-370.
  91. Hajnsek, I., K.P. Papathanassiou, A. Moreira and S.R. Cloude. 2002. The Potential of Surface Parameter Estimation from Interferometric SAR. *Proc. European Conference on Synthetic Aperture Radar, EUSAR'02*, pp. 275-278, Cologne, Germany, 4-6 June.
  92. Hajnsek, I., K.P. Papathanassiou, A. Moreira and S.R. Cloude. 2002. Surface Parameter Estimation using Interferometric and Polarimetric SAR. *Proc. IGARSS'02 (cd-rom)*, Toronto, Canada, 22-26 June.
  93. Cloude, S.R. and D. Corr. 2002. Surface Parameter Estimation using Interferometric and Polarimetric SAR. *Proc. IGARSS'02 (cd-rom)*, Toronto, Canada, 22-26 June.
  94. R. Schober. 1995. *Ertragstabellen wichtiger Baumarten*. J.D.Sauerlaender's Verlag, Frankfurt a. M., ISBN: 3793907309.
  95. Pretzsch H.. 2001. *Modellierung des Waldwachstums*. Ulmer (Eugen) Verlag, ISBN: 3800145553.
  96. T. Mette, K.P. Papathanassiou, I. Hajnsek, and R. Zimmermann. 2003. Above Ground Forest Biomass Estimation using Fully Polarimetric / Interferometric Radar Data. *Proc. POLinSAR Workshop on Applications of SAR Polarimetry and Polarimetric Interferometry* (<http://earth.esa.int/polinsar>), ESA-ESRIN - Frascati, Italy, 14-16 January.
  97. Mette, T., Hajnsek, I., Papathanassiou, K. 2003. *Height biomass allometry in temperate forests*. *Proc. IGARSS'02 (CD-ROM)*, Toronto, Canada, 21-25 July 2003.

- 
98. UNESCO. 1973. *International classification and mapping of vegetation*. Ecology and Conservation, 6, Paris.
  99. Cloude S.R., E. Pottier. 1999. An Entropy Based Classification Scheme for Land Applications of Polarimetric SAR". *IEEE Trans. Geosc. Remote Sensing*, Vol. 35, No. 1, pp 68-78.
  100. Cloude S.R. , K.P. Papathanassiou. 2003. A 3-Stage Inversion Process for Polarimetric SAR Interferometry. *IEE Proc. Radar, Sonar and Navigation*, Vol. 150, Issue 3, pp 125-134.
  101. Davis M. E. 1999. Technical Challenges in UWB Radar Development of Target Detection and Terrain Mapping. *Proc.1999 IEEE Radar Conference*.
  102. Karam, M. A. and A. K. Fung *et al.*, 1988. Electromagnetic Wave Scattering from some Vegetation Samples. *IEEE Trans. GRS*, Vol. 26, 6, p799.
  103. Kellomäki S., V.-P Ikonen, H. Peltola and T. Kolström. 1999. Modelling the Structural Growth of Scots Pine with Implications for Wood Quality. *Ecological Modelling*, 122, pp117-134.
  104. Kellomäki, S and Harri Strandman. 1995. A Model for the Structural Growth of Young Scots Pine Crowns based on Light Interception by Shoots, *Ecological Modelling* 80, 237-250.
  105. Kellomäki, S and Olavi Kurtio. 1991. A Model for the Structural Development of Scots Pine Crown based on Modular Growth. *Forest Ecology and Management*, 43 (1991) 103-123
  106. Williams M L. 2000. Simulating Low Frequency SAR Clutter from a Pine Forest. *Proc. 3<sup>rd</sup> European SAR Conference (EUSAR)*, 23-25 May, 2000, Munich, Germany, pp 149-152
  107. Williams M L., T Manninen, Seppo Kellomäki, Veli-Pekka Ikonen, Risto Sievänen, Mika Lehtonen, Eero Nikinmaa and Timo Vesala. 2003. Modeling the SAR Response of Pine Forest in Southern Finland. *Proc. IGARSS 03, Toulouse, France*. 1350-1352 pp.
  108. Williams M L..1999. Prediction and Observation of SAR Clutter from Vegetation Canopies. *Proc. IGARSS '99*, Hamburg, Germany, pp 1983-1985.
  109. Williams M. L., S. Quegan and D. Blacknell, 1997. Distribution of backscattered intensity in the distorted Born approximation: application to C-band SAR images of woodland, *Waves in Random Media*, 7, pp 643-660.
  110. Cloude S.R., K.P. Papathanassiou. 2003. A 3-Stage Inversion Process for Polarimetric SAR Interferometry. *IEE Proc., Radar, Sonar and Navigation*, June 2003.
  111. Papathanassiou K.P., I. Hajnsek, T. Mette, and A. Moreira.2003. Model Based Forest Parameter Estimation from Single Baseline Pol-in-SAR Data: the Fichtelgebirge Test Case. *Proc. POLinSAR WS on Applications of SAR Polarimetry and Polarimetric Interferometry* (<http://earth.esa.int/polinsar>), ESA-ESRIN Frascati, Italy, 14-16 January, 2003.

## **C.6 ACKNOWLEDGEMENTS**

The biologically accurate tree architectural models for Scots Pine used in this work were provided by Prof. Seppo Kellomäki and Dr Veli-Pekka Ikonen of the Faculty of Forestry, University of Joensuu, Finland. Dr. Mark Williams of DSTO, Australia, carried out the SAR simulations used in this study.

*This page is intentionally left blank.*

# **PART D**

## **Literature Review – Man-Made Objects**

**Nico ADAM, Michael EINEDER and Bert KAMPES**

Remote Sensing Technology Institute, German Aerospace Center,  
Wessling, GERMANY



*This page is intentionally left blank.*

## Table of Contents

<b>D.1</b>	<b>INTRODUCTION.....</b>	<b>D-1</b>
<b>D.2</b>	<b>STRUCTURE OF THE REVIEW .....</b>	<b>D-1</b>
<b>D.3</b>	<b>OVERVIEW OF PREVIOUS STUDIES.....</b>	<b>D-2</b>
<b>D.4</b>	<b>PROPERTIES OF MAN-MADE OBJECTS (PERMANENT SCATTERER) .....</b>	<b>D-3</b>
<b>D.5</b>	<b>PERMANENT SCATTERER ALGORITHM INVENTED BY POLIMI .....</b>	<b>D-5</b>
D.5.1	PS general problem formulation .....	D-6
D.5.2	PS base algorithm .....	D-7
D.5.3	PS Atmospheric Phase Screen (APS) estimation.....	D-8
D.5.4	PS linear phase residual (LPR) and non-linear motion estimation ....	D-9
<b>D.6</b>	<b>IMPROVEMENTS AND VARIANTS OF THE PS PROCESSING.....</b>	<b>D-10</b>
<b>D.7</b>	<b>APPLICATIONS BASED ON THE PS ALGORITHM .....</b>	<b>D-12</b>
<b>D.8</b>	<b>CONCLUSION .....</b>	<b>D-15</b>
<b>D.9</b>	<b>EXAMPLES .....</b>	<b>D-17</b>
<b>D.10</b>	<b>REFERENCES.....</b>	<b>D-20</b>

*This page is intentionally left blank.*

## D.1 INTRODUCTION

A comprehensive literature review has been carried out for the special SAR interferometry application of man-made objects. Existing bio- and geophysical retrieval algorithms and relevant techniques are reviewed. Their status and interferometric data base requirements are assessed. Special attention is paid to promising concepts which could be the basis for the development of new retrieval algorithms.

InSAR applications (DEMs, coherence analysis and surface motion) are restricted mainly by temporal and spectral data decorrelation. The temporal decorrelation results in a lack of interferograms composed of long-time separated acquisitions. Consequently, the temporal statistical properties of the observed variables (i.e. seasonal periodicities and temporal mean) can not be utilized. The restriction of the data analysis on man-made features on a sparse spatial grid requires completely new estimation methods. Man-made objects have the property to be long-term stable regarding scattering effects. Therefore, they allow long-time span and time series analysis. The use of local measurements on a pixel by pixel basis avoids the need for phase unwrapping which is the most difficult InSAR processing step. The interferometrically observed variables topography, atmospheric delay and surface motion can be separated from each other. This technique results in an improved accuracy measuring the different effects and offers the potential for new applications. Publications regarding this technique are compiled and analysed in this section. Emphasis is put on promising concepts which may lead to new interferometric products.

## D.2 STRUCTURE OF THE REVIEW

Previous studies about the retrieval of geo- and biophysical parameters are reviewed in section D.3. The relevance of the known applications for man-made features and urban areas is revised in the context of permanent scatterers. In section D.4, properties and resulting advantages of man-made objects in SAR interferometry (InSAR) are gathered.

Pioneering work was performed by scientists at the Politecnico di Milano (POLIMI). The retrieval algorithms invented by POLIMI are presented starting with the general formulation of the estimation problem. Afterwards, POLIMI's permanent scatterer base algorithm for linear motion is described. The extension of the estimation for the atmospheric phase screen (APS) follows. The non-linear motion estimation found by the POLIMI scientists is described in the next subsection.

Many scientists focus on the optimisation of particular processing steps of the permanent scatterer technique. Rarely, they have a dedicated application in mind but contribute to the better understanding and consequently to the operational use of the

new technique. Their work is presented in the section D.6. An alternative algorithm is described as well.

POLIMI's permanent scatterer algorithms form the basis for various geophysical applications, which are summarized in section D.7. Most applications for the monitoring of geophysical parameters are based on the measurement of the change of range distance, which e.g. can be considered as subsidence. Many scientists found relations between the observed subsidence and various geophysical effects. Finally the different geophysical parameters, applications and possible data products are summarized including some examples of DLRs software development in the framework of permanent scatterers.

### D.3 OVERVIEW OF PREVIOUS STUDIES

A special issue of the *IEEE Transactions on Geoscience and Remote Sensing* with research papers on “*Retrieval of Bio- and Geophysical Parameters from SAR Data for Land Applications*” (Vol. 35, No. 1, January 1997) was already published in 1997. The articles emphasize that retrieval algorithms for bio- and geophysical parameters are considered as well-established but have nevertheless not lost any of its importance. Although there used to be several interferometric applications e.g. Wegmüller and Werner (1995) and Askne *et al.* (1997) the permanent scatterer technique was not yet established. The techniques presented in the special issue covered the following topics:

- Vegetation and land cover
- Forestry
- Agriculture
- Soil Moisture/ Roughness
- Urban/ Geology

Unfortunately, they can neither directly be applied to man-made objects nor permanent scatterers. As the permanent scatterer technique is restricted to areas with stable scattering targets, which are predominantly found in urban areas, vegetation parameters and forestry applications are left out from the field of applications.

A very good insight into the importance of urban areas is provided by Henderson and Xia (1997). According to their view, urban areas

- occupy a relatively small portion of the Earth's surface
- represent one of the most complex, intricate and variable of all land covers
- over 70% of the world's population in developed countries live in urbanized areas
- the economic importance and land values of urban areas are among the highest of all land uses
- urban areas are the most rapidly expanding and changing elements of the landscape

- monitoring changes is considered to be important for the allocation and conservation of natural resources and planning.

They also list the following SAR applications in urban areas:

- settlement detection
- population estimation
- urban analysis, i.e. identification of man-made features (industrial sites, shopping centres, commercial areas) using multi-polarized imagery.

Another paper by Xia and Henderson (1997) reviews the understanding of the relationships between radar response patterns and the bio- and geophysical parameters in urban areas. It investigates the intensity and patterns of radar returns from urban features. The authors specify the following applications:

- dielectric properties of urban features (high absolute values for the complex dielectric constant for metallic features)
- surface roughness of urban features (rough surfaces produce returns of relatively strong intensity for a wide range of depression angles)
- landform characteristics
- type, amount and pattern of vegetation cover
- settlement history
- local climate and seasonal changes

Both authors have performed a very comprehensive literature review and present an extensive bibliography but no retrieval algorithms themselves. In spite of the importance of the mentioned applications this report is restricted to interferometric techniques utilizing man-made features as the permanent scatterer technique.

## **D.4 PROPERTIES OF MAN-MADE OBJECTS (PERMANENT SCATTERER)**

Interferometric observations are affected by phase noise and therefore are limited in their application. The following effects result in phase noise contributions:

- temporal changes of the scatterer
- different look angle
- volume scattering

Man-made features are scatterers with exceptionally advantageous properties in comparison to distributed scatterers or clutter. The restricting effects mentioned earlier have only little influence on the result.

Usai (1997) and Usai *et al.* (1999, 2000) studied the coherence for selected features in long time interferograms (time span 3 1/2 years). They observed in almost totally decorrelated interferograms that some features maintain high coherence even over a



time scale of years. They recognized that these stable scatterer properties apply mainly to man-made features (anthropogenic features). Therefore it was investigated whether this information can still be used to assess terrain deformations by means of the differential technique and to use it for long term monitoring. For this reason, the authors investigated the phase stability in time and the spatial homogeneity of the detected coherent scatterers. The experiments already consider the atmospheric influences on the interferometric measurement. Consequently, they performed a spatially relative phase estimation referring to one reference scatterer. Likewise the interferometric pairs are processed referring to one and the same master. They noted that weather, seasonality, satellite configuration under which the slave scenes have been acquired may affect the coherence more than the time interval between master and slave. Based on these observations, they predicted the extension of a range of new InSAR applications and proposed the monitoring of slow deformation processes like land subsidence and plate tectonics.

Ferretti *et al.* (2000a) did a more thorough investigation of the properties of permanent scatterers (PS). They estimated the permanent scatterer density as a function of phase noise (shown for several cities: Milan, Paris, Los Angeles). Consequently, their estimations can be tuned on the one hand regarding spatial resolution (permanent scatterer density) and on the other hand regarding accuracy (phase noise). For different applications individual demands are considered advantageous. The selection of scatterers which are used for the estimation is a key step in the processing chain. Two competing effects have to be balanced with each other. If the selection of the permanent scatterers is not severe enough the phase values are too noisy. An unreliable estimation is the consequence of this decision. If on the other hand only few permanent scatterers can be identified because of a very restrictive selection the spatial density will be too sparse. The POLIMI team found about  $100 PS/km^2$  in urban areas which can be identified and exploited for terrain deformation monitoring with a phase standard deviation less than 0.5 rad. This already shows the accuracy of the estimation of interferometric measurement contributions and reveals the high potential for geophysical applications.

Ferretti *et al.* (2001) presented a complete procedure for the identification of stable scatterers. In connection with this procedure they mentioned another very important property of these permanent scatterers. If the dimension of the permanent scatterer is smaller than a resolution cell, interferograms with baselines larger than the decorrelation baseline can be combined. Therefore, all available acquisitions of ERS can be exploited. Ferretti *et al.* (2001) presented an equation that provides the basis for the estimation of the phase stability  $\sigma_v$  out of the time series of the amplitude  $A$  for a single permanent scatterer.

$$\sigma_v \cong \frac{\sigma_A}{m_A} = D_A \quad (D.1)$$

This equation states that the amplitude dispersion index  $D_A$  is a good estimate for the phase dispersion  $\sigma_v$  and therefore for the phase stability. It is valid for high SNR values i.e.  $D_A < 0.3$ .  $\sigma_A$  is the temporal standard deviation and  $m_A$  is the temporal mean of the amplitude. This relation was found at POLIMI using numerical simulations and verified by comparison with their estimation results. This relation is

helpful on one hand for the identification of the PS and on the other for a preliminary guess of the obtainable estimation accuracy for a given stack of data.

## D.5 PERMANENT SCATTERER ALGORITHM INVENTED BY POLIMI

Ferretti *et al.* (1999a) presented the mathematical framework and examples for the Permanent Scatterer (PS) method. The published algorithm is the basis for all efficient permanent scatterer estimation procedures. The starting point is the interferometric observation equation for a single differential interferogram  $i$  which is part of the data stack generated from  $N + 1$  SLC scenes:

$$\phi_i = \frac{4 \cdot \pi}{\lambda} \cdot \Delta r_{Ti} + \Delta a_i + \Delta n_i + \varepsilon_{topo\_i} \quad (D.2)$$

with  $i = 1 \dots N$

$\lambda$  : is the radar wavelength

$\Delta r_{Ti}$  : is the target displacement in the LOS and is proportional to the targets displacement velocity  $v_r$

$\Delta a_i$  : is the atmospheric phase contribution

$\varepsilon_{topo\_i}$  : is the height error from the DEM compensation and is proportional to the perpendicular Baseline  $B_i$

$\Delta n_i$  : is the decorrelation noise

All  $N$  interferograms are processed relative to the same master scene. In order to eliminate atmospheric effects and baseline errors the low frequency components need to be removed from the single interferograms  $\phi_i$ . The estimation is performed pixel-by-pixel and a linear model for displacement is introduced. The authors introduced the following estimation equation:

$$\phi_i = C_{zi} \cdot \varepsilon_z + C_{vi} \cdot v_r \quad (D.3)$$

The factors are  $C_{vi} = \frac{4 \cdot \pi}{\lambda} \cdot T_i$  and  $C_{zi} \propto B_i$  ( $B_i$  is the perpendicular baseline). In this simple form, the presented algorithm can obtain two geophysical parameters: firstly, the linear displacement,  $v_r$ , and, secondly, an improved DEM utilizing  $\varepsilon_z$ . The POLIMI team compared the PS with a natural GPS network. Hence, many applications a GPS network can cope with are addressed. In their paper, they present slow terrain motion (<1 cm/ year) and a correction of the DEM at the PS locations.

### D.5.1 PS general problem formulation

In Ferretti *et al.* (2001) the estimation procedure is enhanced in order to separate and determine the DEM error  $\varepsilon_z$ , the atmospheric contributions  $\Delta a_i$  and the target motion  $v_r$ . For this reason, they can estimate with the presented algorithm the following geophysical parameters:

- millimetric terrain motion (detection and temporal evolution)
- sub-meter DEM accuracy
- atmospheric phase screen
- PS dimension i.e. the effective electromagnetic width of the PS.

The following general formulation of the problem and the estimation procedure originates from Ferretti *et al.* (2001). Note, that some variables are renamed in respect to the original publication in order to get a consistent naming within the document. Based on  $K+1$  ERS SAR images,  $K$  interferograms are formed with respect to the same master scene (index  $m$ ). The measured interferometric phase is given by:

$$\Phi = a^T + p_y \cdot y^T + p_x \cdot x^T + B \cdot h^T + T \cdot v^T + E \quad (D.4)$$

where

$H$ : number of PS

$a$ :  $K \times 1$  are constant phase values

$p_x$  and  $p_y$ : each is  $K \times 1$  and contains the slope values of the linear phase components along azimuth  $y$  and slant range  $x$  due to orbit and atmosphere ( $x$  and  $y$ : each is  $H \times 1$ )

$B$ :  $K \times 1$  contains the normal baseline values (for large areas baseline varies with location  $B$ :  $K \times H$ ) multiplied with  $\frac{4 \cdot \pi}{\lambda \cdot R \cdot \sin(\alpha)}$  (and corresponds now to the height to phase conversion)

$h$ :  $H \times 1$  contains the elevation of each PS

$T$ :  $K \times 1$  contains the time interval between the  $K$  slave images and the master multiplied with  $\frac{4 \cdot \pi}{\lambda}$  (and corresponds to a velocity to phase conversion)

$v$ :  $H \times 1$  contains the slant range (LOS) velocities of the PS's

$E$ :  $K \times H$  contains the residues (atmospheric effects different from linear components, phase noise due to temporal and baseline decorrelation, residual non-linear motion).

The above set of  $H \cdot K$  equations and  $3 \cdot K + 2 \cdot H$  unknown parameters ( $a$ ,  $p_x$ ,  $p_y$ ,  $h$ ,  $v$ ) is non-linear due to the wrapped phase values  $\Phi$ . The solution is obtained by an iterative algorithm.

**D.5.2 PS base algorithm**

The algorithm is described by Ferretti *et al.* (2001). The processing starts with the so called zero baseline steering. Utilizing a moderately accurate DEM (accuracy of 20 m is sufficient) the interferometric phase  $\Phi$  is corrected for the geometric DEM phase contribution. The obtained phase can then be considered observed from the same master orbit. Due to unavoidable orbit and DEM errors the compensation is not performed perfectly. The following observation equation results:

$$\Delta\Phi = a^T + p_y \cdot y^T + p_x \cdot x^T + B \cdot \Delta h^T + T \cdot v^T + E \quad (D.5)$$

where

$\Delta\Phi$  : is the differential phase

$p_x$  and  $p_y$  : residual linear (due to a small estimation area) components of orbit error and APS

$\Delta h$  : DEM error.

A system solution can be obtained if

- the space-time distribution of the acquisitions is uniform (as possible)
- the reference DEM is accurate ( $\pm 20m$ )
- the estimation area is small, i.e. APS and orbit error can be modelled by linear phase components
- the target motion is slow because of aliasing and can be approximated by a constant velocity.

The POLIMI team describes the retrieval algorithm for the parameters PS height error  $\Delta h$  and PS motion  $v$  as follows:

(D.6)

1. initialisation  
 $n = 0$  (iteration counter)  
 $\underline{\Delta\Phi}^{(0)} = \underline{\Delta\Phi} \quad \underline{\Delta h}^{(0)} = \underline{\delta h}^{(0)} = \underline{v}^{(0)} = \underline{\delta v}^{(0)} = \underline{0}$
2. repeat until convergence:
  - a) update vectors and iteration counter:  
 $n = n + 1$   
 $\underline{\Delta h}^{(n)} = \underline{\Delta h}^{(n-1)} + \underline{\delta h}^{(n-1)}$   
 $\underline{v}^{(n)} = \underline{v}^{(n-1)} + \underline{\delta v}^{(n-1)}$
  - b) test for end of iteration (finish if the following conditions are fulfilled)  
 $n > 1$  and  $\|\underline{\delta h}^{(n-1)}\|_{L_\infty} < T_h$  and  $\|\underline{\delta v}^{(n-1)}\|_{L_\infty} < T_v$  or  $n = N_{\max}$
  - c) compensate  $\underline{\Delta\Phi}$  for the phase caused by  $\underline{\Delta h}^{(n)}$  and  $\underline{v}^{(n)}$   
 $\underline{\Delta\Phi}^{(n)} = \underline{\Delta\Phi} - (B \cdot \underline{\Delta h}^{(n)} + T \cdot \underline{v}^{(n)})$

d) for each differential interferogram (each row  $k$ ) of  $\underline{\Delta\Phi}^{(n)}$  estimate

$a_k^{(n)}, p_{xk}^{(n)}, p_{yk}^{(n)}$  using a periodogram:

$$\{p_{xk}^{(n)}, p_{yk}^{(n)}\} = \arg \max \left\{ \left| \Gamma_k^{(n)}(p_{xk}, p_{yk}) \right| \right\}$$

$$a_k^{(n)} = \angle \Gamma_k^{(n)}$$

where:

$$\Gamma_k^{(n)} = \frac{1}{H} \sum_{i=1}^H e^{j \cdot \underline{\Delta\Phi}_{ki}^{(n)}} \cdot e^{-j(p_{xk} \cdot x_i + p_{yk} \cdot y_i)}$$

e) compensate the data for the estimated linear phase contributions:

$$\underline{\Delta\Phi}^{(n)} = \underline{\Delta\Phi}^{(n)} - \left( \underline{a}^{(n)} + \underline{p}_x^{(n)} \cdot \underline{X} + \underline{p}_y^{(n)} \cdot \underline{Y} \right)$$

f) for each PSC  $i$  estimate the residual velocity and DEM error

$\{\delta h_i^{(n)}, \delta v_i^{(n)}\}$  weighting each with the absolute value of  $\Gamma_k$

$$\{\delta h_i^{(n)}, \delta v_i^{(n)}\} = \arg \max \left\{ \left| \gamma_i^{(n)}(\delta h_i, \delta v_i) \right| \right\}$$

with

$$\gamma_i^{(n)} = \frac{1}{K} \sum_{k=1}^K \left| \Gamma_k^{(n)} \right| \cdot e^{j \cdot \underline{\Delta\Phi}_{ki}^{(n)}} \cdot e^{-j(B_k \cdot \delta h + T_k \cdot \delta v)}$$

### D.5.3 PS Atmospheric Phase Screen (APS) estimation

The result of the retrieval algorithm described before is the following:

- the DEM error:  $\underline{\Delta h}$ ,
- the LOS velocity:  $\underline{\Delta v}$ ,
- linear components of the APS:  $\underline{a}$ ,  $\underline{p}_x$ ,  $\underline{p}_y$ .

The residual phase  $\underline{E}$  corresponds to atmospheric effects  $\underline{E}_{atmo}$  and phase noise  $\underline{E}_{noise}$ :

$$\underline{E} = \underline{\Delta\Phi} - \left( \underline{a} + \underline{p}_x \cdot \underline{x} + \underline{p}_y \cdot \underline{y} + \underline{B} \cdot \underline{\Delta h} + \underline{T} \cdot \underline{v} \right) \quad (D.7)$$

$$\underline{E} = \underline{E}_{atmo} + \underline{E}_{noise} \quad (D.8)$$

Ferretti *et al.* (2001) showed the enhanced processing in order

1. to separate the noise and the atmospheric contribution from each other and
2. to separate the atmospheric contributions from the formed interferograms into the contributions of the single radar acquisitions.

ad 1) The strong correlation of atmosphere on short distances is utilized. By smoothing spatially the phase residues  $\underline{E}$ , the atmospheric effects  $\underline{E}_{atmo}$  and the noise are separated. The APS is sampled on a sparse irregular grid. Therefore an interpolation of the data is required. Ferretti *et al.* proposed the *Kriging* interpolation because it can perform the smoothing and the interpolation in one and the same processing step taking into account the power spectrum of  $\underline{E}_{atmo}$ .

ad 2) The atmospheric contribution in time is uncorrelated. Therefore the mean of the atmospheric components taken over all scenes corresponds to the master

$$APS_{master} = \frac{1}{K} \cdot \left\{ \underline{E}_{atmo} + \left( \underline{a} + \underline{p}_x \cdot \underline{x} + \underline{p}_y \cdot \underline{y} \right) \right\} \quad (D.9)$$

The APS relative to each single scene  $i$  is obtained by subtracting the  $APS_{master}$  from the corresponding atmospheric contribution

$$APS_i = E_{atmo_i} - APS_{master} \quad (D.10)$$

#### **D.5.4 PS linear phase residual (LPR) and non-linear motion estimation**

The POLIMI team further improved the estimation to be able to monitor non-linear displacement and to increase the estimation accuracy. Two advantages arise; firstly, the atmosphere, the noise and the non-linear motion can be separated from each other. And secondly, the displacement can be interpolated and predicted by a suitable model. Ferretti *et al.* (1999, 2000d) present the more general approach in detail. It is shortly summarized in this section.

The phase residual  $\underline{E}$  can contain a component of motion that does not match the linear motion model

$$\underline{E} = \underline{E}_{atmo} + \underline{E}_{noise} + \underline{E}_{nonlinear\_motion} \quad (D.11)$$

$\underline{E}$  is called the Linear Phase Screen (LPR) and is the superposition of the three effects atmosphere  $\underline{E}_{atmo}$ , noise  $\underline{E}_{noise}$  and non-linear motion  $\underline{E}_{nonlinear\_motion}$ . With a simple low-pass filtering for the separation of noise and APS the non-linear motion component is lost in the APS. A least mean square (LMS) estimation can separate the components  $\underline{E}_{atmo}$ ,  $\underline{E}_{noise}$  and  $\underline{E}_{nonlinear\_motion}$  from each other.  $\underline{E}_{atmo}$ ,  $\underline{E}_{noise}$  and  $\underline{E}_{nonlinear\_motion}$  are considered random variables und thus  $\underline{E}$  has a phase variance  $\sigma_w^2$  composed from the sum of the three.

$$\sigma_w^2 = \sigma_a^2 + \sigma_n^2 + \sigma_m^2 \quad (D.12)$$

The constant velocity model simplifies the mathematical framework. But the PS technique can cope with non-uniform target motion provided the following two conditions are satisfied:

- the PS density is high enough,
- the coherence is high enough (i.e.  $\sigma_w^2$  is low).

The data (composed of an uncorrupted signal and a disturbance) are optimally filtered in the time - space - domain. The uncorrupted signal is the non-linear motion. The atmosphere signal corresponds to the disturbance. To develop the optimal filter the subsidence mechanism is modelled with a diffusion process:

$$\frac{\partial^2 S}{\partial x^2} + \frac{\partial^2 S}{\partial y^2} = c \cdot \frac{\partial S}{\partial t} \quad (D.13)$$



The solution  $S(x,y,t)$  of the differential equation offers a model of the subsidence in space  $\{x,y\}$  and time  $t$ . The presented examples indicate the applicability of the above model for the subsidence mechanism. Consequently, the growing of a subsidence in space  $\{x,y\}$  can be interpolated and predicted. This sort of model can estimate the amount of the infilled or of the extracted volume  $V_0$ .

$$S(x,y,t) = \frac{c}{4 \cdot \pi \cdot t} \cdot V_0 e^{\frac{-c(x^2+y^2)}{4t}} \quad (D.14)$$

In the equation above,  $V_0$  is the amount of the infilled or of the extracted volume and  $c$  is the diffusion coefficient (the POLIMI team used  $c \approx 4 \cdot 10^{-4} \text{ m}^2 / \text{month}$ ). The displacement signal is described in the frequency – wavenumber - domain by

$$S(u,v,\omega) = \frac{V_0 \cdot c}{(u^2 + v^2)^2 + j \cdot \omega \cdot c} \quad (D.15)$$

The power spectrum of the signal is therefore

$$P_s = \sigma^2 \cdot \frac{c^2}{(u^2 + v^2)^4 + \omega^2 \cdot c^2} \quad (D.16)$$

The power spectrum  $P_A$  of the atmospheric disturbance depends only on the wavenumber  $k$  and the power  $Q_1$  and is described by the Kolmogorov law:

$$P_A = \frac{Q_1}{k^{8/3}} \quad (D.17)$$

The optimal filtered estimate  $\hat{S}$  of the subsidence is obtained from the measurements  $M$  by:

$$S = \frac{P_s}{P_s + P_A} \cdot M \quad (D.18)$$

Different geophysical effects require different models in order to describe and finally emulate their special space - time - behaviour. Each parameter in the model can be monitored by the procedure described above. The range of applications is therefore manifold and some examples will be presented in section D.7.

## D.6 IMPROVEMENTS AND VARIANTS OF THE PS PROCESSING

In contrast to the techniques described before, Fruneau *et al.* (1999) presented a much simpler algorithm in order to detect slow deformations in urban areas with standard atmospheric conditions. Only few scenes are required und their acquisitions span a time range of about three years only. It was recognized that the detection of very low subsidence rates over long time span in urban areas is not limited by the coherence loss on the required time scale of observations. Firstly, it was tried to compensate the

atmospheric effects. But the team reports that the correction of tropospheric effects utilizing standard weather information (temperature, pressure, relative humidity) does not perform as expected. For this reason, they suggest a simple solution to cope with the atmospheric influences: the addition of interferograms. Unfortunately there are no details about the selection of scenes regarding their baseline and temporal distance in order to form the interferograms and the final combination of the interferograms. The presented example shows clearly the dimension of the subsidence. Its temporal evolution is mentioned as another application.

Other scientists focus on the optimisation of particular processing steps of the permanent scatterer technique. Rarely, they have a dedicated application in mind but contribute to the better understanding and consequently to the operational use of the new technique. Colesanti *et al.* (2002a) merges independent data sets covering the same area. This sort of data stacks can be obtained by

- ascending and descending acquisitions and
- overlapping areas from adjacent tracks.

Several advantages result. Firstly, the increased number of data sets significantly increases the number of PS. It is reported that only 30% of PS are common in different interferometric stacks with the same pass direction. The other much larger part contributes to a more dense PS distribution. Secondly, the combination of different data sets enables the cross validation and a quality assessment. It is obvious that this is an essential point for an operational monitoring.

Furthermore, Colesanti *et al.* (2002b) suggest simple but effective models for the permanent scatterer processing in order to monitor non-linear motion. The application of the presented models requires a processing of the data as described in section D.5, i.e. the interferograms are compensated with regard to atmosphere before. The models help to discriminate deformation from residual topography and noise. Different geophysical effects are assigned to various models:

- Ground deformations caused by exploitation of ground water resources or withdrawal of oil or gas, mining activities, underground excavations are described by higher order polynomials.
- Seasonal effects e.g. periodically varying ground water level (dry summers and wet winters), reversible ground deformation (reversible compaction of the aquifer system) can be described by a linear displacement and a periodical contribution:

$$\Phi_{1,m,i} = \frac{4 \cdot \pi}{\lambda} \cdot v_{1,m} \cdot T_i + A_{i,m} \cdot \cos\left(\frac{2 \cdot \pi}{\tilde{T}} \cdot (T_i - T_{0,1,m})\right) \quad (D.19)$$

Assuming a one year periodicity  $\tilde{T}$ , the variables  $v$ ,  $A$  and  $T_0$  can be estimated. In (Colesanti *et al.*, 2002b) sample images for the spatial estimation of the amplitude  $A$  and the temporal offset  $T_0$  of periodical effects are shown. Consequently, various geophysical effects on ground can be spatially separated.

Another interesting problem is picked up by Refice *et al.* (2002a). The measured atmospheric phase screen is given on a sparse grid (at the PS locations) and needs to be transformed from a relative phase into an absolute phase. This processing step

requires firstly a phase unwrapping (PU) and secondly an interpolation. It is well known that the scaling information is an important tool for the description of natural processes. Therefore, the team investigates the use of scaling information in the process of PU on sparse data. Indeed, the power law behaviour of the data variogram is used as an a priori constraint for an optimisation procedure (simulated annealing). The presented algorithm was tested with simulated data.

As pointed out in section D.5, the PS technique is based on the iterative separation of the different contributions to the interferometric phase. Alternatively, Inglada and Adragna (2002) propose to apply the Independent Component Analysis (ICA) in order to decompose the ground subsidence and the APS. Their simulation indicates that the ICA based algorithm can separate non-linear displacements, e.g. seasonal effects and linear down - and uplift of subsidence areas and the APS.

## D.7 APPLICATIONS BASED ON THE PS ALGORITHM

The PS algorithm described in section D.5 forms the basis for various geophysical applications. In this section, the reported applications are summarized. Most applications for the monitoring of geophysical parameters are based on the measurement of the change of range distance which is usually considered as subsidence. Many scientists found relations between the observed subsidence and various geophysical effects.

Due to the advanced PS processing Ferretti *et al.* (2000c) can monitor linear and non-linear motion which includes in particular periodical subsidence and uplift. By applying time series analysis of the phase residues Ferretti *et al.* (2000b) can show examples of collapsing buildings. They are also able to show the dilation of a metallic building (e.g. La Cite des Sciences in Paris) caused by temperature variation. Based on this measurement

- the temperature can be measured if material is known or
- the material can be determined from its thermal dilation coefficient if the temperature is known.

Le Mouelic *et al.* (2002) measured a subsidence in Paris. They demonstrated that the uplift correlates to underground water level (elastic deformation of the ground, not simply compaction). Finally, they were able to monitor the amplitude and shape of the deformation.

Colesanti *et al.* (2000) use the PS technique to locate seismic faults (i.e. a fracture of rocky mass marked by the offset of one side with respect to the other) with high spatial resolution. They can monitor the evolution of the displacement in the LOS and utilize this information to classify the faults into Strike-Slip faults or into Dip-Slip faults. The displacement rate discontinuity across active faults can be determined by the PS technique. The measured LOS discontinuity varies between 0.5 and 2.5 mm/year and shows the outstanding accuracy and potential of the PS technique. Colesanti *et al.* (2000) plan to assess and understand the effects of slight seismic events utilizing the PS technique.

Dehls *et al.* (2002) applied the PS technique in barren rocky non-urban areas. The team states to monitor geophysical parameters on different scales:

- creep phenomena in blocky avalanche deposits (steep slopes are covered with blocky colluvium and large blocks of the slopes creep down due to gravity up to 5 mm/ year),
- subsidence by compaction of material (dam at a lake shows a compaction which rate is proportional to the thickness of the dam material about 4-5 mm/ year) and
- postglacial uplift (isostatic uplift in response to the melting of the last ice sheets approximately 9 mm/ year) but it is stated as “difficult to quantify yet”.

Additionally, Dehls *et al.* (2002) investigate the problem of snow cover, especially the snow coat of variable thickness on PS. It was observed, that as long as the snow cover is thin, the survival rate of natural PS is high. Finally, the problem was solved by the selection of suitable snow free scenes.

Using the PS technique, Mora *et al.* (2001) monitored subsidences causing problems in buildings. They compare the results obtained by D-InSAR and the PS technique and conclude that both measurements agree with the available GPS measurements.

Refice *et al.* (2002b) utilize the PS technique to monitor landslides. It is reported that the PS technique helps to overcome the difficulties which occur with this application:

- limited spatial extend of landslide areas,
- rainy weather conditions associated with movement events and
- decorrelation due to vegetation, strong topographic contributions.

Additionally, they present the temporal phase history for an industrial hangar. The temporal evolution of this PS follows clearly a sinusoid like oscillation with a periodicity of one year. The team assumes that the signal is caused by a thermal expansion and contraction of a metallic roof or by seasonal swelling of clayey soil under the construction's foundations.

A new geophysical application which is not based on the influence of the change of range distance is proposed by Ferretti *et al.* (2001). The PS dimension can be estimated and is to be interpreted as the *electromagnetic width* of the scatterers. Usually, point scatterers are assumed to be utilized with the PS technique. But these optimal point scatterers are not given in reality. The estimation of the mean effective electromagnetic width in range  $\Delta$  is derived by the POLIMI team as follows: The coherence  $\gamma$  depends on the effective baseline  $B_{eff}$  due to the spectral shift

$$\gamma = \left| \frac{\sin(k \cdot \Delta / 2)}{k \cdot \Delta / 2} \right| \quad (D.20)$$

with

$$k = \frac{4 \cdot \pi}{\lambda \cdot R \cdot \tan(\alpha)} \cdot B_{eff} \quad (D.21)$$

The electromagnetic width in range  $\Delta$  can be obtained by a parameter fit through the dispersion of the residual phase values (measured coherence  $\Gamma_k$  from section D.5.2) versus the effective baseline. Residual phase values means that the phase of each slave scene is corrected for terrain motion  $v$ , atmospheric effects APS, the orbit and height error (slave scene as seen from master orbit position)

$$\Gamma_k = \sum_{i=1}^H e^{j(\Phi - (APS + B \cdot \Delta h + T \cdot v))} \quad (D.22)$$

Various by-products result by the permanent scatterer technique processing each with its own applications. Man-made features simplify the co-registration of SLC scenes. Such co-registered stacks of scenes are on the one hand the data basis for the PS processing but on the other hand the stacks enable new applications and improved visualisations:

- super-resolution scenes: Prati and Rocca (1993) demonstrated the improvement of the slant range resolution utilizing the spectral shift by properly combining several scenes covering different parts of the reflectivity spectra.
- calibrated scenes for classifications: The temporal evaluation on radar data and especially the combination of data from different sensors e.g. ERS-1 and ERS-2 require the calibration of the scattered intensity. With the PS technique the calibration enables the comparability of the scattered intensity and finally the identification and selection of the PS. Laur *et al.* (2002) describe the calibration procedure for the sensors ERS-1 and ERS-2 and provide the required calibration parameters and its meaning. Bovenga *et al.* (2002) suggest a simplified calibration of such data stacks.
- calibrated temporal and spatial multi looked scenes: The multi image reflectivity map shows a significant speckle reduction but preserves the resolution of the image. The enhancement is expressed by the radiometric resolution (Bamler and Schättler, 1993). A straightforward processing consists of a simple incoherent summation of the available SAR scenes. Coltuc and Radescu (2002) show that this approach causes a non-uniform speckle reduction. At the same time, they present a procedure which results in a uniform speckle reduction. Therefore known algorithms developed to cope with speckle can be applied on this image.

In the framework of man-made features, super-resolution data and data with a high radiometric resolution obtained by temporal multi-looking can be utilized for instance in:

- road network extraction (Tupin *et al.*, 2002) and
- extraction of perennial structures (Datcu and Quartulli, 2002; Quartulli and Datcu, 2002a, 2002b)

## D.8 CONCLUSION

Until now the following interferometric applications are well established:

- DEMs,
- coherence,
- surface motion (e.g. glacier, landslides) and
- atmosphere.

The permanent scatterer technique invented by POLIMI enables the separation of the various interferometric contributions by utilizing man-made objects. Firstly, an exceptional accuracy results and secondly a range of new applications and data products are the consequence. The applications and the related data and by-products are listed in Table D.1.

The literature analysis shows that within only four years, the PS technique has evolved rapidly. For instance,

- the motion monitoring accuracy was improved from cm/ year to mm/ year
- the PS density was increased and
- the ability to track not only linear but also non-linear motion patterns was found.

Some restrictions in applications (e.g. tidal load) can result from the sun-synchronous orbit which means that the same area on ground is observed always at the same local time. Existing ERS data since 1991 enable a monitoring in the past even with high spatial resolution. Subsidence effects unknown so far can be detected, explained and their cause can be determined. The unique ERS data base gains an outstanding value from this application. Furthermore, the continuous monitoring of urban areas is guaranteed by the Envisat. The theoretical basis on the combination of the measurements of ERS and Envisat is explained by Gatelli *et al.* (1994) and Guaneri and Prati (2000).

Despite the enormous increase in accuracy only few groups in the world use the PS-technique because of the large data amounts necessary and the difficult processing. A new pre-processed PS-product might further stimulate applications and operational use. Therefore, the identification of permanent scatterer candidates (PSC) and the extraction of its interferometric data is an application itself and may result in a new interferometric basis data product. All reported applications are based on such a data set which currently can only be obtained with huge effort and costs as mentioned before. The data set should consist of:

- the complex values (composed of the calibrated intensity and the interferometric phase) for each PSC in the stack of scenes,
- the information about the acquisition time for each used scene,
- the information about observation geometry (baseline and look angle) for each PSC,
- the position of each PSC in slant range coordinates and
- a multi-image reflectivity map for the visualization.



Table D.1:  
Collection of physical parameters, applications and possible data products

physical parameter	application	data product
linear displacement	<ul style="list-style-type: none"> <li>- urban subsidence monitoring</li> <li>- landslides monitoring</li> <li>- mining monitoring</li> </ul>	<ul style="list-style-type: none"> <li>- subsidence map</li> <li>- time of collapse of single buildings</li> <li>- evolution of displacement over time (interpolation and prediction)</li> <li>- infilled or extracted volume</li> </ul>
nonlinear displacement	<ul style="list-style-type: none"> <li>- urban subsidence monitoring</li> <li>- volcano monitoring</li> <li>- earth quake warning</li> <li>- landslides monitoring</li> <li>- mining monitoring</li> <li>- temperature tracking</li> <li>- piezoelectric water level monitoring</li> </ul>	<ul style="list-style-type: none"> <li>- subsidence map</li> <li>- periodicity of effects (e.g. watering)</li> <li>- local temperature</li> <li>- material of single metallic buildings</li> <li>- evolution of displacement over time</li> <li>- time of building collapse</li> <li>- warning about building collapse</li> </ul>
DEM		- improved city DEM
APS		- (see section A)
temporal change		<ul style="list-style-type: none"> <li>- ensemble coherence (<math>\gamma_h</math>)</li> <li>- dispersion index <math>D_A</math></li> </ul>
phase stability and electromagnetic width of PS		<ul style="list-style-type: none"> <li>- phase dispersion (<math>\Gamma_k</math>)</li> <li>- electromagnetic width of PS (<math>\Delta</math>)</li> </ul>
calibrated intensity	<ul style="list-style-type: none"> <li>- road network extraction</li> <li>- perennial structures extraction</li> <li>- classification</li> </ul>	<ul style="list-style-type: none"> <li>- stack of calibrated intensities</li> <li>- multi-image <math>\sigma^0</math> map</li> </ul>
reflectivity	- road network extraction	- super resolution scene

The proposed data product reduces considerable the amount of data to deliver (some Mb instead of 40-80 SLC scenes). Due to the reduced costs and the simplified processing (co-registration of the scenes stack and its calibration is not needed any more), the number of users would increase and new applications will probably be found. Ferretti *et al.* (2001) present a complete procedure for the identification of PS. They show how to detect stable point scatterer candidates (PSC) without loss of resolution by utilizing a time analysis of the scenes' amplitude. The selection of the

PSC is based on the dispersion index  $D_A$ . It is described in section D.4. With the data set presented above the following geophysical parameter can be monitored:

1. millimetric terrain motion detection (linear, non-linear and periodical effects)
  - urban subsidence
  - seismic faults
  - sliding areas
  - volcanoes (lava compaction)
  - earthquake co-seismic dislocations and strain accumulation
  - piezoelectric water level (Fruneau *et al.*, 1999) and (Mouélic *et al.*, 2002)
  - thermal dilation of metal enabling the determination of material or of the temperature
2. sub meter DEM accuracy improvement
3. atmospheric phase screen monitoring: With repeat pass interferometry the radiation travel path can be affected differently by the atmosphere. The sources of the changes are differences in atmospheric humidity distribution and concentration, temperature and pressure between the two acquisitions (Ferretti *et al.*, 2000c). Further separation of the different effects can result from the combination of the data with the one obtained from other remote sensing sensors. Fruneau *et al.* (1999) mentions weather fronts and convective cells. This topic is described in detail in section A.
4. PS dimension, i.e. the electromagnetic width of the PS from the phase dispersion  $\Gamma_k$  of each interferometric scene
5. ensemble phase coherence for each PS:  $\gamma_h$

## D.9 EXAMPLES

This sections shows some examples of results in the framework of permanent scatterers using software developed at the Remote Sensing Technology Institute of DLR.

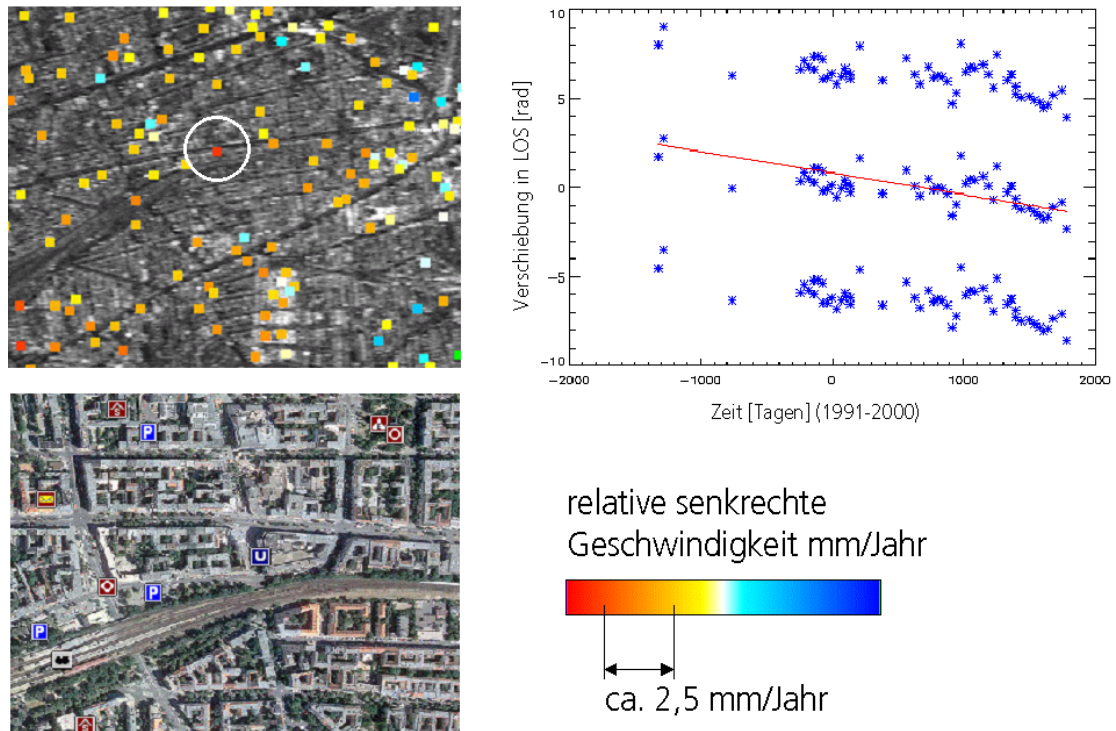


Figure D.1: Example of a relative linear velocity estimation, the subsidence corresponds to an underground station and amounts to about 2.5 mm/ year

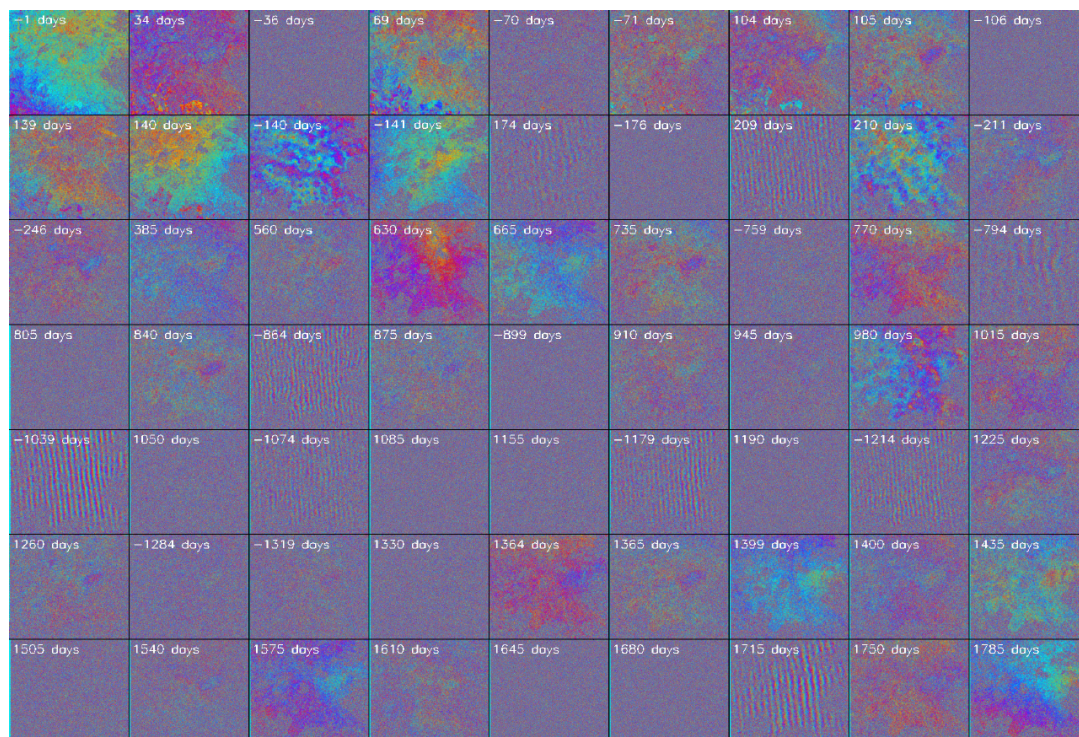


Figure D.2: Differential interferometric data stack of Berlin

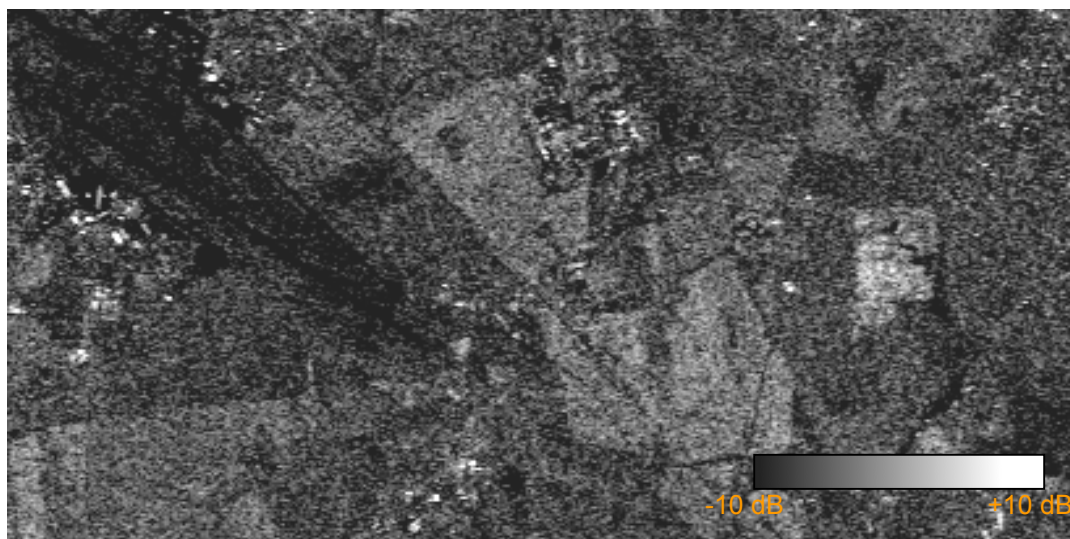


Figure D.3: Calibrated  $\sigma^0$  image with 5 geometric looks resulting in 20 x 20 m resolution on ground and a 2 dB radiometric resolution



Figure D.4: Calibrated  $\sigma^0$  image with 320 (theoretical) looks still with 20 x 20 m resolution on ground and up to 0.3 dB radiometric resolution



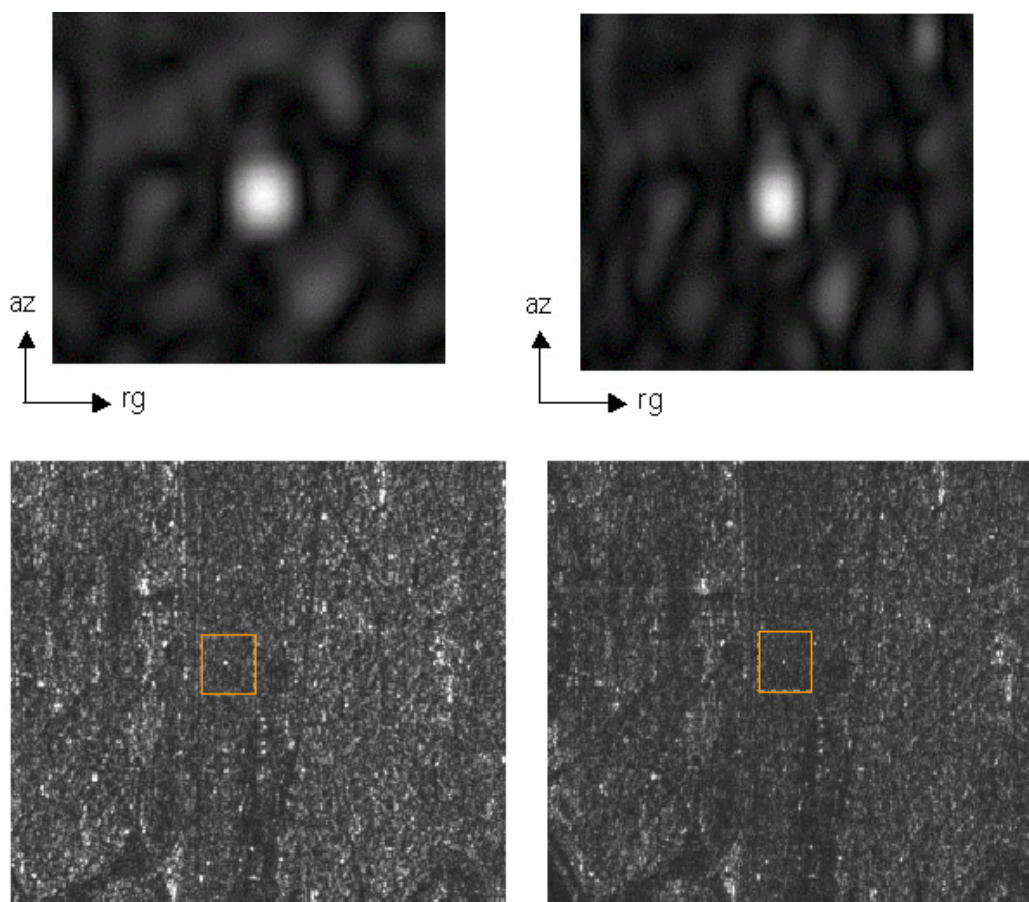


Figure D.5: Super resolution example, left column one look SLC image with a measured range 3dB width of 1.2 samples for this point target. But in the right column the range 3 dB width is improved to 0.88 samples

## D.10 REFERENCES

- Askne, J. I. H., P. B. G. Dammert, L. M. H. Ulander and G. Smith. 1997. C-Band Repeat-Pass Interferometric SAR Observations of Forest. *IEEE Trans. Geosc. Rem. Sens.*, Vol. 35, No. 1, 25-35.
- Bamler and Schättler. 1993. *SAR Data Acquisition and Image Formation*. SAR Geocoding: Data and Systems (Ed. G. Schreier), Wichmann, 1993, 81-82.
- Bickel D. L., W. H. Hensley and D. A. Yockey. 1997. The Effect of Scattering from Buildings on Interferometric SAR Measurements. *Proc. IGARSS 1997*, CDROM
- Bovenga F., A. Refice and R. Nutricato. 2002. Automated Calibration of Multi-temporal ERS SAR Data. *Proc. IGARSS 2002*, Toronto, Canada, 24-28 June 2002, CDROM.
- Colesanti C., A Ferretti, C Prati, and F Rocca. 2000. Monitoring Known Seismic Faults Using the Permanent Scatterers (PS) Technique. *Proc. IGARSS 2000*, Honolulu, Hawaii, 24-28 July 2000, CDROM.

- Colesanti C., A Ferretti, C Prati, and F Rocca. 2002a. Full Exploitation of the ERS Archive: Multi Data Set Permanent Scatterers Analysis. *Proc. IGARSS 2002*, Toronto, Canada, 24-28 June 2002, CDROM.
- Colesanti C., R. Locatelli and F. Novali. 2002b. Ground Deformation Monitoring Exploiting SAR Permanent Scatterers. *Proc. IGARSS 2002*, Canada, 24-28 June, Toronto, CDROM.
- Coltuc D., R. Radescu, 2002. On the Homomorphic Filtering by Channel's Summation. *Proc. of IGARSS 2002*, Toronto, Canada, 24-28 June 2002, CDROM.
- Datcu M. and M. Quartulli. 2002. Structural Modelling for Scene Understanding from Meter Resolution SAR – Part I – On the Quality of Model Based SAR Despeckling and Information Extraction. *Submitted IEEE Trans. Geosc. Rem. Sens.*
- Dehls J. F., M. Basilico and C. Colesanti. 2002. Ground Deformation Monitoring in the Ranafjord Area of Norway by Means of the Permanent Scatterer Technique. *Proc. IGARSS 2002*, Toronto, Canada, 24-28 June 2002, CDROM.
- Ferretti, A., C. Prati and F. Rocca. 1999a. Permanent Scatterers in SAR Interferometry. *Proc. IGARSS 1999*, Hamburg, Germany, 28 June-2 July 1999, 1528-1530.
- Ferretti, A.; C. Prati and F. Rocca. 1999b. Non-Uniform Motion Monitoring Using the Permanent Scatterers Technique. *Proc. FRINGE99*, Liège, Belgium, [http://earth.esa.int/pub/ESA\\_DOC/fringe1999](http://earth.esa.int/pub/ESA_DOC/fringe1999).
- Ferretti, A., C. Prati and F. Rocca. 2000a. Analysis of Permanent Scatterers in SAR Interferometry. *Proc. IGARSS 2000*, 24-28 July 2000, Honolulu, Hawaii, CDROM.
- Ferretti A., F. Ferrucci, C. Prati, F. Rocca, 2000b. SAR Analysis of Building Collapse by Means of the Permanent Scatterers Technique. *Proc. IGARSS 2000*, Honolulu, Hawaii, 24-28 July 2000, CDROM.
- Ferretti, A., C. Prati, and F. Rocca. 2000c. Measuring Subsidence with SAR Interferometry: Applications of the Permanent Scatterers Techniques. *Proc. Sixth International Symposium on Land Subsidence*, Vol. 2, Ravenna, 24-29 September 2000, 67-79.
- Ferretti, A., C. Prati, and F. Rocca. 2000d. Nonlinear Subsidence Rate Estimation Using Permanent Scatterers in Differential SAR Interferometry. *IEEE Trans. Geosc. Rem. Sens.*, Vol. 38, No. 5, September 2000, 2202-2212.
- Ferretti, A., C. Prati, and F. Rocca. 2001. Permanent Scatterers in SAR Interferometry. *IEEE Trans. Geosc. Rem. Sens.*, Vol. 39, No. 1, January 2001, 8-20.
- Fruneau B., J. P. Rudant, D. Obert and D. Raymond. 1999. Small Displacements Detected by SAR Interferometry on the City of Paris (France). *Proc. FRINGE99*, Liège, Belgium, 10-12 Nov 1999, [http://earth.esa.int/pub/ESA\\_DOC/fringe1999](http://earth.esa.int/pub/ESA_DOC/fringe1999)
- Gatelli, F., A. M. Guarnieri, F. Parizzi, P. Pasquali, C. Prati, and F. Rocca. 1994. The Wavenumber Shift in SAR Interferometry. *IEEE Trans. Geosc. Rem. Sens.*, Vol. 32, 855-865.



- Guarnieri A. M. and C. Prati. 2000. ERS-ENVISAT combination for interferometry and super-resolution. *Proc. ERS-Envisat symposium 2000*, 16-20 October, Gothenburg, Sweden.
- Hanssen R. F. 2001. *Radar interferometry: Data Interpretation and Error Analysis*. Kluwer Academic Press, Dordrecht, 308p.
- Henderson F. M. and Z. G. Xia. 1997. SAR Applications in Human Settlement Detection, Population Estimation and Urban Land Use Pattern Analysis: A Status Report. *IEEE Trans. Geosc. Rem. Sens.*, Vol. 35, No 1, 79-85.
- Inglada J. and F. Adragna, 2002. Blind Source Separation Applied to Multitemporal Series of Differential SAR Interferograms. *Proc. IGARSS 2002*, 24-28 June, Toronto, Canada, CDROM.
- Laur H., P. Bally, P. Meadows, J. Sanchez, B. Schättler, E. Lopinto and D. Esteban. 2002. Derivation of the Backscattering Coefficient  $\sigma^0$  in ERS SAR PRI Products. *Document No. ES-TN-RS-PM-HL09*, September 2002, <http://earth.esa.int/ESC2>
- Le Mouélic S., D. Raucoules, C. Carnec, C. King and F. Adragna. 2002. Ground Uplift in the City of Paris (France) Revealed by Satellite Radar Interferometry, *Proc. IGARSS 2002*, Canada, 24-28 June, Toronto, CDROM.
- Mora O., J. J. Mallorqui, J. Duro and A. Broquetas. 2001. Long-term Subsidence Monitoring of Urban Areas Using Differential Interferometric SAR Techniques. *Proc. IGARSS 2001*, 9-13 July, Sydney, Australia, CDROM.
- Nutricato R., F. Bovenga, and A. Refice. 2002. Optimum Interpolation and Resampling for PSC Identification. *Proc. IGARSS 2002*, Toronto, Canada, 24-28 June 2002, CDROM.
- Prati, C. and F. Rocca. 1993. Improving Slant-Range Resolution with Multiple SAR Surveys. *IEEE Transactions on Aerospace and Electronic Systems*, Volume: 29 Issue: 1, Jan. 1993, 135 –144.
- Quartulli M. and M. Datcu. 2002a. Information Fusion for Scene Understanding from Interferometric SAR Data in Urban Environments. *Submitted IEEE Trans. Geosc. Rem. Sens.*
- Quartulli M. and M. Datcu. 2002b. Structural Modelling for Scene Understanding from meter resolution SAR – Part II – Stochastic Geometric Modelling for Urban Scene Understanding from Single SAR intensity Images with Meter Resolution. *Submitted IEEE Trans. Geosc. Rem. Sens.*
- Refice A., F. Bovenga, S. Stramaglia and D. Conte. 2002a. Use of Scaling Information for Stochastic Atmospheric Absolute Phase Screen Retrieval. *Proc. IGARSS 2002*, Toronto, Canada, 24-28 June 2002, CDROM.
- Refice A., F. Bovenga, L. Guerriero and J. Wasowski. 2002b. DInSAR Applications to Landslide Studies. *Proc. IGARSS 2002*, Canada, 24-28 June, Toronto, CDROM.
- Tupin F., B. Houshmand and M. Datcu. 2002. Road Detection in Dense Urban Areas Using SAR Imaginary and the Usefulness of Multiple Views. *Accepted by IEEE Trans. Geosc. Rem. Sens.*

- 
- Usai, S. 1997. The Use of Man-made Features for Long Time Scale InSAR. *Proc. IGARSS 1997*, Singapore, 3-8 August 1997, 1542-1544.
- Usai S. and R. Klees. 1999. SAR Interferometry on Very Long Time Scale: A Study of the Interferometric Characteristics of Man-Made Features. *IEEE Trans. Geosc. Rem. Sens.*, Vol. 37, No. 4, 2118-2123.
- Usai S. and R. Klees. 2000. An Analysis of the Interferometric Characteristics of Anthropogenic Features. *IEEE Trans. Geosc. Rem. Sens.*, Vol. 38, No 3, 1491-1497.
- Wegmüller U. and C. L. Werner. 1995. SAR Interferometric Signatures of Forest. *IEEE Trans. Geosc. Rem. Sens.*, Vol. 33, No. 5, pp. 1153-1161.
- Xia Z. G. and F. M. Henderson. 1997. Understanding the Relationships between Radar Response Patterns and the Bio- and Geophysical Parameters of Urban Areas. *IEEE Trans. Geosc. Rem. Sens.*, Vol. 35, No 1, 93-101.







Innsbruck, AUSTRIA

Email: [office@enveo.at](mailto:office@enveo.at)

WWW: <http://www.enveo.at>